

DEVELOPMENT OF A STRUCTURAL DESIGN METHODOLOGY FOR
CEMENTITIOUS SPRAYED APPLIED PIPE LININGS IN GRAVITY
STORM WATER CONVEYANCE CONDUITS

By

AMIN DARABNOUSH TEHRANI



DISSERTATION

Submitted in Partial Fulfillment of the Requirements

for the Degree of

DOCTOR OF PHILOSOPHY

THE UNIVERSITY OF TEXAS AT ARLINGTON

Arlington, Texas

August 2020

Copyright © by Amin Darabnoush Tehrani 2020

All Rights Reserved



ACKNOWLEDGEMENTS

I would like to express my deep sense of gratitude to my supervising professor, Dr. Mohammad Najafi, for his continued support throughout my Doctoral studies. This achievement would not have been successfully completed without his valuable knowledge and advice.

I would like to thank my committee members, Dr. Chao, Dr. Kermanshachi and Dr. Rosenberger, for providing me with their valuable comments that helped to improve the quality of the presented research from various prospective.

This dissertation includes results of a pool-funded project through the National Cooperative Highway Research Program (NCHRP) and funded by seven departments of transportation (DOTs) of Ohio DOT (project leader), DelDOT, FDOT, MnDOT, NCDOT, NYSDOT and PennDOT. I would like to thank the Principal Investigator (PI) of this project, Dr. Najafi, the DOT representatives, specifically Mr. Jeffrey Syar, Mr. Brian Carmody, Ms. Sherry Little, Mr. Matthew S. Lauffer, Mr. Charles Smith, Mr. Paul Rowekamp, Mr. Carlton Spirio, Mr. Nicholas Dean, and Co-PI of this project, Dr. Xinbao Yu, for their technical and financial support.

In addition, I would like to thank, Standard Cement Materials Inc., Contech Engineering, Forterra Pipe and Precast, HVJ Associates, MTS Systems Corporation, and Micro-Measurement for providing us with various products and services that were most essential for these research project. Many thanks Mr. Mario Tamez, Dr. Firat Sever, Mr. Lynn Osborn, Mr. Chip Johnson, Mr. Mark Garrison, and Mr. Ed Kampbell.

I would like to give my warmest thanks to my friends; Dr. Zahra (Ellie) Kohankar Kouchesfehani, Mr. Farzam Yazdani, Dr. Amir Tabesh, Dr. Masoud Ghahremannejad, Dr. Arash Emami Saleh, Dr. Maziar Mahdavi, Dr. Himen Hojat Jalali, Dr. Armin Soltanzadi and Mr. Mark Hurley. Their motivation and heartwarming support are always appreciated.

Many thanks go to my colleagues at CUIRE, Samrat Raut, Hiramani Raj Chimaurya, Juhil Makwana, Siddharth Raut, Suhas Patil, and Aaroh Swarup.

Last but not least, I would like to thank my father, Mohammad Reza, my mother, Parvin, my sister, Tina, my grandparents, my uncle, Manouchehr, and all family members for teaching me one of the most important lessons to be learned about character, dignity, and integrity. They selflessly encouraged me to explore new directions in life and seek my own destiny. Without their sacrifice, endless support and blessing, this achievement would have been remained only a dream.

August 29, 2020

ABSTRACT

Development of a Structural Design Methodology for Cementitious
Sprayed Applied Pipe Linings in Gravity Storm
Water Conveyance Conduits

Amin Darabnoush Tehrani, Ph.D.,

The University of Texas at Arlington, 2020

Supervising Professor: Mohammad Najafi

Culverts are important components of the highway infrastructure. They form passageways through the embankment to convey storm water. Culverts are structurally designed to support superimposed earth loads or other fill materials as well as live loads. Corrugated metal pipes (CMPs) and reinforced concrete pipes (RCPs) are commonly used as culverts in the United States. Most of these culverts were installed four to five decades ago and have reached their design life. Spray applied pipe linings (SAPLs) are trenchless technology solutions for culvert rehabilitation that prevent further deterioration, such as corrosion, abrasion, etc., and can provide structural support for severely damaged host culverts and drainage structures. There is currently no available standard design methodology for SAPL culvert renewal methods. This dissertation presents the results of nine full-scale structural soil box tests including three control tests, three pipe arch culverts, and three circular culverts renewed with cementitious SAPL tests. The invert sections of

the corrugated metal pipe (CMP) samples were cut to simulate fully invert deteriorated culverts in service. The structural capacity of these pipe samples with and without SAPL were investigated. In addition, the feasibility of several design equations, applicable to a fully deteriorated culvert was investigated. Ultimately, a SAPL design equation was developed for circular and pipe arch culverts renewed with cementitious SAPL.

Table of Contents

ACKNOWLEDGEMENTS	i
ABSTRACT.....	iii
Table of Contents	v
Table of Figures	ix
List of Table.....	xxxv
CHAPTER 1. INTRODUCTION	1
1.1. Overview.....	1
1.2. Culverts	6
1.2.1. Culvert Structural Behavior	8
1.2.2. Corrugated Metal Pipes.....	14
1.2.3. Culvert Burial Configuration	17
1.2.4. Structural Design of CMP Culverts	20
1.3. Culvert Renewal Methods.....	31
1.3.1. Sliplining.....	32
1.3.2. Cured in Place Pipe (CIPP) Lining	33
1.3.3. Spiral Wound Lining.....	35
1.3.4. Fold and Form lining (Close-fit).....	36

1.3.5. Spray Applied Pipe Lining (SAPL)	37
1.4. Objectives	60
1.5. Methodology	60
1.6. Contributions to the Body of Knowledge	62
CHAPTER 2. LITERATURE REVIEW	63
2.1. Soil-pipe Testing.....	63
2.1.1. Field Testing Method.....	63
2.1.2. Laboratory Testing Method	69
2.1.3. Hybrid Testing Method.....	75
2.1.4. Applicable Load Rate in a Soil-Pipe Testing.....	77
2.2. SAPL Renewed Pipe Testing.....	78
2.3. Applicable Design Equations for SAPLs.....	81
2.3.1. CIPP Design Methodology	82
2.3.2. Flexible Pipe Design Methodology.....	86
2.3.3. Other Analytical Approaches.....	88
CHAPTER 3. EXPERIMENTAL PROGRAM.....	89
3.1. Overview	89
3.2. Experimental Test Design and Setup Preparation	91
3.2.1. Soil Box Requirements and Preparation	92
3.2.2. Test Burial Configuration	96

3.2.3.	CMP Samples.....	102
3.2.4.	Pipe Installation and Embedment.....	105
3.2.5.	Load Pads.....	106
3.2.6.	Instrumentation	108
3.2.7.	Test Operation and Load Rate	119
3.3.	Control Test Details	120
3.4.	SAPL Renewed Test Details.....	125
3.4.1.	Cementitious SAPL Details	130
3.4.2.	CMP Samples Preparation	133
3.4.3.	SAPL Installation.....	136
3.4.4.	SAPL Mechanical Properties Testing Samples.....	141
3.4.5.	SAPL Visual Inspection and Internal Instrumentation	145
3.4.6.	SAPL Thickness Measurement.....	153
CHAPTER 4. RESULTS AND DISCUSSIONS.....		154
4.1.	Overview.....	154
4.2.	Soil Box Testing Results.....	154
4.2.1.	Control Test Results.....	154
4.2.2.	SAPL Renewed Invert-cut Pipe Arch CMP Test Results	183
4.2.3.	SAPL Renewed Invert-cut Pipe Circular Test Results.....	236

CHAPTER 5. CONCLUSIONS, LIMITATIONS, AND RECOMMENDATIONS FOR FUTURE RESEARCH	303
5.1. Summary	303
5.2. Conclusions.....	303
5.3. Limitations and Recommendations for Future Research.....	307
APPENDIX A. Load Pad Design	309
APPENDIX B. Compaction Measurement.....	313
APPENDIX C. GeoCast© Data Sheet.....	317
APPENDIX D. Compressive Strength Test Results.....	319
APPENDIX E. Thickness Measurement Results.....	321
APPENDIX F. Crown Crack Width Measurement for Circular CMP Samples.....	323
APPENDIX G. Gallery of Soil Box Test Pictures.....	347
REFERENCES	377
BIOGRAPHY	391

Table of Figures

Figure 1-1. ASCE’s report card on the US infrastructure (ASCE 2017).....	2
Figure 1-2. A 17-year old 84 in. culvert failure in Maryland, USA (ACPA 2008).....	2
Figure 1-3. Culvert failure in South Dakota (ACPA 2008).....	3
Figure 1-4. A 96 in. culvert failure in Hickory, North Carolina (ACPA 2008).....	4
Figure 1-5. Failure of a 4-year old HDPE culvert (ACPA 2008).	4
Figure 1-6. Different shapes of culverts: (a) closed conduits, and (b) open-bottom conduits (FHWA 2012).	7
Figure 1-7. Culvert response: (a) Terminology for a culvert cross section, (b) flexible culvert, and (c) rigid culvert behavior.....	8
Figure 1-8. Flexible and stiff springs representing (a) soil-rigid, and (b) soil-flexible pipes (Moser and Folkman 2008).....	10
Figure 1-9. Comparison of positive projection conduits for (a) rigid, and (b) flexible pipe (CVWD 2013).....	11
Figure 1-10. Common failure modes of rigid culverts.	12
Figure 1-11. Common flexible culverts failure modes	13
Figure 1-12. Fully invert deteriorated CMP culvert (FHWA 2012).....	15
Figure 1-13. Corrugated metal pipe types: a) helical, b) annular, and c) spiral rib CMP (PCPIPE 2016).	17
Figure 1-14. Typical burial configuration of a pipe in trench.....	19

Figure 1-15. Pipe cross section showing how voids are generated if the soil is not deliberately placed in the haunch area.....	19
Figure 1-16. Minimum Cover Orientation (AASHTO 2017).....	20
Figure 1-17. Combined H-20 highway live load and dead load is a minimum at about 5 ft of cover. Live load is applied through a pavement of 1 ft thick (NCSPA 2008).....	23
Figure 1-18. Railroad live load, cooper E 80, combined with dead load is a minimum at about 12 ft. Live load is applied through three 2 × 8 ft areas on 5 ft centers (NCSPA 2008).....	23
Figure 1-19. Free body diagram of a circular pipe subjected to vertical load.	25
Figure 1-20. The pressure on a pipe-arch varies with location and radius being greatest at the corners (American Iron and Steel Institute 1999).....	27
Figure 1-21. Common trenchless technology culvert renewal methods.....	31
Figure 1-22. Culvert renewal using sliplining method (photo credit: pomonapipelineproducts.com).	33
Figure 1-23. CIPP curing using UV light (photo credit: ohm-advisors.com).....	34
Figure 1-24. Spirally wound liner installation (Wagener and E. Leageid 2014).....	35
Figure 1-25. Fold and form pipe lining (photo credit: agru.at): (a) folded thermoplastic liner, and (b) inserted folded liner.....	36
Figure 1-26. Hand spray polyurethane SAPL: (a) before renewal, and (b) after renewal (Kohankar Kouchesfehane 2020).	39
Figure 1-27. Material property comparison for all three major polymeric SAPL material (Curran 2016).	40

Figure 1-28. Centrifugal spray cast machine for cementitious SAPL: (top) schematic of the required equipment (Caltrans 2002) and (bottom) renewed culvert with a cementitious SAPL(credit: CentriPipe).....	42
Figure 1-29. Conversion of fly ash into geopolymers/concrete (Singh et al. 2015).....	44
Figure 1-30. Macro Fibers: Polypropylene Fibers, (b) Fiberglass, (c) Polyolefin Fibers and (d) Steel Fibers.....	45
Figure 1-31. Micro-Fibers: (a) Acrylic Fiber, (b) Alkali Resistant (AR) Glass Fiber, (c) PVA Fiber, and (d) Alkali Resistant Glass Scrim.....	45
Figure 1-32. Different size fibers bridge different crack width (Kohankar Kouchesfehane et al. 2019).	46
Figure 1-33. Numerical analysis of a pipe subjected to vertical downward loading according to three-edge bearing test configuration (Darabnoush Tehrani 2016).	47
Figure 1-34. Different types of mesh reinforcements: (a) hexagonal iron mesh, (b) woven polypropylene, (c) woven Nylon 66, (d) expanded metal mesh, (e) basalt mesh grid, and (f) basalt mesh placed into wet concrete prior to final layer's placement.....	49
Figure 1-35. 6×2-in CMP renewed with SAPL: (a & d) followed corrugation with shortfall at the sloped surface, and (b & c) filled corrugation pattern.	51
Figure 1-36. Hydraulic capacity comparison of SAPL renewed CMPs with a bare CMP.....	53
Figure 1-37. Transformed-section with the same neutral axis for: (a) filled corrugation, and (b) following corrugations.....	57
Figure 1-38. Cracking moment capacity of renewed CMP with SAPL at the crown.....	59

Figure 1-39. Cracking moment improvement by filling the corrugation compared with following corrugation pattern of the renewed CMP with SAPL.....	59
Figure 1-40. Design methodology development methodology.....	61
Figure 2-1. Pipe installation and testing method (Chaallal et al. 2014).....	66
Figure 2-2. Field pipe testing using soil dead load (Liu et al. 2016)	67
Figure 2-3. Test culvert, truck and the layout of the truck position over the culvert (Liu et al. 2020).	68
Figure 2-4. Cross-section of the culvert tested (Kunecki and Kubica 2004).....	71
Figure 2-5. View of trench backfills: (a) first configuration; (b) second configuration (Tafreshi et al. 2012)	72
Figure 2-6. Helical invert-cut CMP buried inside a trench:(a) laboratory testing method in an open-air facility, (b) full invert-cut CMP, (c) partially invert-cut CMP, and (d) invert-paved CMP.	76
Figure 2-7. Load carrying capacity of the RCPs renewed with different liner materials.	80
Figure 2-8. Schematic pattern of external loads on a culvert in fully deteriorated CIPP design equation: (left) hydrostatic pressure,(middle) live load pressure, and (right) soil pressure (credit: CUIRE).	84
Figure 3-1. CUIRE’s laboratory located at the UTA’s Civil.....	90
Figure 3-2. CUIRE soil box: (a) before steel frame installation, and (b) after installation of the 330-kips actuator and steel reaction frame.	90

Figure 3-3. Soil box schematic design: (a) proposed soil box, and (b) proposed burial configuration in the soil box. 93

Figure 3-4. Soil box test configuration: (a) 2D schematic plan view of the soil box layout including partition walls and three testing pipe samples, and (b) 3D schematic cross-sectional view of a pipe sample in one of the soil box cells, separated by wooden partition walls. 94

Figure 3-5. Soil box preparation: (a) schematic plan view of soil box including partition walls and three testing pipe samples, and (b) wooden walls construction to divide the soil box into four separate sections..... 95

Figure 3-6. Soil box ventilation: (a) schematic design, and (b) constructed ventilation system. . 96

Figure 3-7. Foundation compaction: (a) schematic illustration of soil compaction, (b) soil compaction using a 4,496 lbs vibratory plate compactor. 97

Figure 3-8. Embedment soil characteristics: a) soil sieve analysis, and b) standard Proctor test. 98

Figure 3-9. Test setup and burial configuration for: (a) circular CMPs, and (b) for pipe arch CMPs..... 99

Figure 3-10. Modes of operation of nuclear density gauge (photo credit: multiquip.com)..... 101

Figure 3-11. In-situ soil compaction measurement: (a) sand cone test, and (b) nuclear density gauge. 101

Figure 3-12. Intact and invert-cut CMP samples: (a) transportation to laboratory facility, and (b) storage area. 104

Figure 3-13. Pipe installation and preparation before backfilling: (a) bedding layer leveling process, (b) pipe positioning and installation, and (c) gap sealing using plywood, Styrofoam, and duct tape.....	106
Figure 3-14. Steel load pads.....	107
Figure 3-15. Pressure sensors: (a) 3D cross sectional view, and (b) 3D view of pressure cell locations around the CMP, (c) Geokon 4800 series earth pressure cell, and (d) Geokon data acquisition system.....	109
Figure 3-16. Mechanical sensors, used to measure pipe deflection: (a) Micro-Epsilon WPS-500-MK30-P10 cable displacement sensor, and (b) Omega LD 650 LVDT.....	110
Figure 3-17. DIC displacement measurement: (a) schematic diagram of the basic DIC principles, and (b) a DSLR Cannon Rebel T5i.....	112
Figure 3-18. Pipe sample monitoring in real time during the test at front view, crown and West springline.....	113
Figure 3-19. Strain gauges: (a) installed locations around the circular CMPs, (b) installed locations around the pipe arch CMPs, (c) C2A-06-250LW-120 uniaxial strain gauge, (d) installed strain gauge on the exterior surface of a CMP coated with air drying M-Coat D.	115
Figure 3-20. Strain gauges configuration and details: (a) schematic profile view at the crown for the bare CMP, (b) schematic profile view at the crown for SAPL renewed CMP, (c) installed strain gauges outside of the bare CMP, and (d) installed strain gauges inside the SAPL renewed CMP.	116
Figure 3-21. Experimental test instrumentation setup: (a) pipe sample inner instrumentation, (b) data acquisition systems, and (c) instrumentation central control station setup.....	118

Figure 3-22. Load pad level investigation prior to the loading to assure the load will apply uniformly..... 120

Figure 3-23. Control test CMP samples: (a) intact circular CMP, (b) invert-cut pipe arch CMP, (c) invert-cut circular CMP, (d) detachable invert section layout, and (e) invert cut section with detachable fasteners. 121

Figure 3-24. Control test configuration: (a) plan view, (b) cross sectional view of the circular pipe sample; (c) profile view of the aligned pipe samples in the soil-box; (d) cross sectional view of the arch pipe sample; (e) averaged water content and compaction rate distribution at different layers. 122

Figure 3-25. Test setup configuration for all three cells: (a) during CMP installation, (b) during embedment, and (c) filled hunch area with poorly graded sand without compaction. 123

Figure 3-26. Control test series averaged moisture content and compaction rate contour-plot for different burial layers..... 124

Figure 3-27. DIC result for the circular invert-cut pipe sample movement due to the invert section detachment..... 125

Figure 3-28. Plan view of the detachable invert mechanism for SAPL renewed CMPs during the SAPL installation..... 126

Figure 3-29. Pipe installation: (a) Longitudinal configuration of pipe arch CMPs in the soil box, (b) a pipe arch CMP with end sealing, and (c) a pipe arch CMP sample with detachable invert and end-strip section. 127

Figure 3-30. The pipe arch CMPs’ burial configuration: (top) plan view, (middle) profile view of the aligned pipe arch CMPs in the soil-box, and (bottom) cross sectional view of the pipe arch CMP. 128

Figure 3-31. The CMPs’ burial configuration: (top) plan view, (middle) profile view of the aligned CMPs in the soil-box, and (bottom) cross sectional view of the CMP. 129

Figure 3-32. The contour-plot of the averaged values for moisture content and compaction rate in 8 in. lifts measurement for: (a) circular CMPs renewed with SAPL, and (b) pipe arch CMPs renewed with SAPL. 130

Figure 3-33. GeoCast© mortar with its micro fibers. 131

Figure 3-34. XRD Analysis Results on: (a) new, and (b) 15 year old cement liner material (Henning 2020). 132

Figure 3-35. GeoCast© material delivery to CUIRE facility. 133

Figure 3-36. End-strip detachment: (a) end-strip preparation, (b) end-strip before SAPL installation, end-strip detachment after SAPL installation. 134

Figure 3-37. Implementation of bonding agent into the SAPL mix to increase adhesion of the SAPL to the smooth metallic surface. 135

Figure 3-38. Cementitious SAPL installation equipment including: (a) portable mortar mixer, water tank, and (b) rotor-stator pump. 136

Figure 3-39. Cementitious SAPL installation on: (a) pipe arch, and (b) on circular CMPs. 138

Figure 3-40. Cementitious SAPL Installation: (a) pipe arch CMP with un-sprayed invert section for applicator’s movement, (b) completed installation on pipe arch CMPs, and (c) SAPL installation on circular CMPs with bottom half finished and top half unfinished surfaces..... 138

Figure 3-41. End gaps cleaning to prevent SAPL attachment to the wooden partition walls: (a) duct tape removal to clean the gap, and (b) clear gap between the renewed CMP and the end wall..... 139

Figure 3-42. Thickness measurement using a depth gauge at the time of SAPL installation..... 140

Figure 3-43. Cementitious SAPL renewal of fully invert deteriorated CMPs: (a) pipe arch CMP before SAPL application, (b) pipe arch CMP after SAPL application, (c) circular CMP before SAPL application, and (b) circular CMP after SAPL application. 141

Figure 3-44. SAPL casting method into the cylinders: (left) spray-cast, and (right) hand-cast method..... 142

Figure 3-45. Mechanical properties testing samples: (a) compressive testing cylinders molds, (b) mold preparation, and (c) sample storage at a curing room..... 144

Figure 3-46. Geopolymer mortar compressive testing samples: (a) a sample capped with a sulfur capping compound which is perfectly levelled, and (b) testing specimens after 7 days of curing. 145

Figure 3-47. Crack width measurement using DIP for 3-in. thick cementitious SAPL on an invert-cut pipe arch CMP at: (a) invert, and (b) crown..... 146

Figure 3-48. Crack width measurement using DIP for 2-in. thick cementitious SAPL on an invert-cut pipe arch CMP at: (a) invert, and (b) crown..... 147

Figure 3-49. Crack width measurement using DIP for 1-in. thick cementitious SAPL on an invert-cut pipe arch CMP at: (a) invert, (b) crown, and (c) East haunch area.	148
Figure 3-50. Crack width measurement using DIP for 3-in. thick cementitious SAPL on an invert-cut circular CMP at: (a) crown, (b) East haunch area, and (c) West haunch area.	150
Figure 3-51. Crack width measurement using DIP for 2-in. thick cementitious SAPL on an invert-cut circular CMP at: (a) West haunch area, (b) West shoulder area.	151
Figure 3-52. Crack width measurement using DIP for 1-in. thick cementitious SAPL on an invert-cut circular CMP for: (a) circumferential East springline crack, (b) longitudinal crack at crown, (c) East haunch area, (d) West springline and, (e) invert.....	152
Figure 3-53. SAPL thickness measurement: (a) measurements in circumferential direction on circular and, (b) pipe arch SAPL samples, (c) measurements in longitudinal direction on circular and, (d) pipe arch SAPL samples.....	153
Figure 4-1. Intact CMP with local buckling at the crown location.....	156
Figure 4-2. Intact CMP static live load: (top) load-time and, (bottom) load-soil displacement graphs.....	157
Figure 4-3. Earth pressure cell results for the intact CMP with respect to: (top) time, and (bottom) crown displacement.	158
Figure 4-4. Mechanical sensors result for the intact CMP.....	159
Figure 4-5. Strain gauges reading for the intact CMP.	159
Figure 4-6. Pipe profiling using DIC for the intact circular CMP.	160

Figure 4-7. Load vs. displacement of the soil surface, crown, springline, and shoulder of the intact CMP due to the applied static load.	161
Figure 4-8. Load vs. pressure for the intact CMP.....	161
Figure 4-9. Invert-cut pipe arch CMP: (a) free body diagram, (b) haunch area under the pipe (after exhumation), (c) local buckling at the crown, and (d) invert uplift due to the vertical load at the crown.....	163
Figure 4-10. Invert-cut pipe arch CMP static live load: (top) load-time and, (bottom) load-soil displacement graphs.....	165
Figure 4-11. Earth pressure cell results for the invert-cut pipe arch CMP with respect to: (top) time, and (bottom) crown displacement.....	166
Figure 4-12. Mechanical sensors results for the invert cut pipe arch CMP.....	167
Figure 4-13. Strain gauges reading for the invert-cut pipe arch CMP.....	167
Figure 4-14. Pipe profiling using DIC for the invert-cut pipe arch CMP.....	168
Figure 4-15. DIC method verification with mechanical sensors for invert-cut pipe arch CMP.	169
Figure 4-16. Load vs. displacement of the soil surface, crown, springline, and shoulder of the invert-cut pipe arch CMP due to the applied static load.	169
Figure 4-17. Load vs. pressure for the invert-cut pipe arch CMP	170
Figure 4-18. Invert-cut circular CMP: (a) free body diagram, (b) CMP deflection at end of the test, (c) invert section before loading, and (d) invert section after loading.	172
Figure 4-19. Invert-cut circular CMP static live load: (top) load-time and, (bottom) load-soil displacement graphs.....	174

Figure 4-20. Earth pressure cell results for the invert-cut circular CMP with respect to: (top) time, and (bottom) crown displacement.....	175
Figure 4-21. Mechanical sensors result for invert-cut circular CMP.....	176
Figure 4-22. Strain gauges reading for the invert-cut circular CMP.	176
Figure 4-23. Pipe profiling using DIC for the invert-cut circular CMP.	177
Figure 4-24. DIC method verification with mechanical sensors for invert-cut circular CMP. ..	178
Figure 4-25. Load vs. displacement of the soil surface, crown, springline, and shoulder of the bare invert-cut pipe arch CMP due to the applied static load.	178
Figure 4-26. Load vs. pressure for the invert-cut circular CMP.....	179
Figure 4-27. Soil settlement results for the invert-cut arch, invert-cut circular, and intact circular pipes due to the applied load.....	180
Figure 4-28. Soil settlement results for the invert-cut arch, invert-cut circular, and intact circular pipes due to the applied pressure on the soil surface.....	181
Figure 4-29. Soil settlement results for the invert-cut arch, invert-cut circular, and intact circular pipes due to the applied pressure at top of the pipe samples.	182
Figure 4-30. Load vs. applied pressure at crown: (1) AASHTO H20 truck service load, and (2) equivalent service load on the invert-cut circular CMP.....	183
Figure 4-31. Pipe arch CMP behavior due to the vertical load, where the red boxes show the soil support under the pipe on the west haunch area and the blue boxes illustrates the pipe upward movement.....	184

Figure 4-32. Invert-cut pipe arch renewed with 3 in. cementitious SAPL: (a) before loading, (b) after loading, (c) after unloading, and (d) delamination in the West springline. 186

Figure 4-33. Invert-cut pipe arch CMP renewed with 3-in. thick cementitious SAPL subjected to static live load: (top) load-time and, (bottom) load-soil displacement graphs. 188

Figure 4-34. Earth pressure cell results for the 3-in. thick SAPL renewed invert-cut pipe arch CMP with respect to: (top) time, and (bottom) crown displacement..... 189

Figure 4-35. Mechanical sensors result for 3-in. thick SAPL renewed invert-cut pipe arch CMP. 190

Figure 4-36. Strain gauges reading for the 3-in. thick SAPL renewed invert-cut pipe arch CMP. 190

Figure 4-37. Pipe profiling using DIC for the 3-in. thick SAPL renewed invert-cut pipe arch CMP. 191

Figure 4-38. DIC method verification with mechanical sensors for the 3-in. thick SAPL renewed invert-cut pipe arch CMP..... 192

Figure 4-39. Load vs. displacement of the soil surface, crown, springline, and shoulder of the 3-in. thick SAPL renewed invert-cut pipe arch CMP due to the applied static load. 192

Figure 4-40. Load vs. pressure for the 3-in. thick SAPL renewed invert-cut pipe arch CMP.... 193

Figure 4-41. Visual inspection of the 3-in. thick SAPL renewed pipe arch CMP: (top) cracked SAPL, and (b) crack pattern schematic, where black represents the shrinkage cracks, red represents the cracks due to the load, and gray area represents delaminated area..... 194

Figure 4-42. New circumferential cracks on 3-in. thick SAPL renewed pipe arch CMP at: (a) West, (b) East, and (c) invert locations.....	195
Figure 4-43. Widened longitudinal shrinkage cracks due to load for 3-in. thick SAPL renewed pipe arch CMP at: (a) invert, and (b) crown locations.....	196
Figure 4-44. Thickness measurement for the 3-in. thick cementitious SAPL.....	197
Figure 4-45. Invert-cut pipe arch renewed with 2 in. cementitious SAPL: (a) before loading, and (b) after loading.....	199
Figure 4-46. Invert-cut pipe arch CMP renewed with 2-in. thick cementitious SAPL subjected to static live load: (top) load-time and, (bottom) load-soil displacement graphs	201
Figure 4-47. Earth pressure cell results for the 2-in. thick SAPL renewed invert-cut pipe arch CMP with respect to: (top) time, and (bottom) crown displacement.....	202
Figure 4-48. Mechanical sensors result for 2-in. thick SAPL renewed invert-cut pipe arch CMP.	203
Figure 4-49. Strain gauges reading for 2-in. thick SAPL renewed invert-cut pipe arch CMP... ..	203
Figure 4-50. Pipe profiling using DIC for the 2-in. thick SAPL renewed invert-cut pipe arch CMP.....	204
Figure 4-51. DIC method verification with mechanical sensors for the 2-in. thick SAPL renewed invert-cut pipe arch CMP.....	205
Figure 4-52. Load vs. displacement of the soil surface, crown, springline, and shoulder of the 2-in. thick SAPL renewed invert-cut pipe arch CMP due to the applied static load.	205
Figure 4-53. Load vs. pressure for the 2-in. thick SAPL renewed invert-cut pipe arch CMP....	206

Figure 4-54. Visual inspection of the 2-in. thick SAPL renewed pipe arch CMP: (a) cracked SAPL on the East side of the invert, (b) cracked SAPL on the West side of the invert, and (bottom) crack pattern schematic, where black represents the shrinkage cracks and red represents the cracks due to the load..... 207

Figure 4-55. Longitudinal cracks at the crown of the 2-in. thick SAPL renewed invert-cut pipe arch CMP: (top) center of the crown, and (bottom) north side of the crown. 208

Figure 4-56. Longitudinal cracks at the invert of the 2-in. thick SAPL renewed invert-cut pipe arch CMP: (top) existed shrinkage crack, and (bottom) newly generated crack due to load. 209

Figure 4-57. Circumferential cracks of the 2-in. thick SAPL renewed invert-cut pipe arch CMP at: (top) West and (bottom) East springline and haunch area. 210

Figure 4-58. Thickness measurement for the 2-in. thick cementitious SAPL 211

Figure 4-59. Invert-cut pipe arch renewed with 1 in. cementitious SAPL: (a) before loading, where the East haunch had a shrinkage crack, and (b) after loading, where the shrinkage crack is closed. 213

Figure 4-60. Invert-cut pipe arch CMP renewed with 1-in. thick cementitious SAPL subjected to static live load: (top) load-time and, (bottom) load-soil displacement graphs 215

Figure 4-61. Earth pressure cell results for the 1-in. thick SAPL renewed invert-cut pipe arch CMP with respect to: (top) time, and (bottom) crown displacement..... 216

Figure 4-62. Mechanical sensors result for 1-in. thick SAPL renewed invert-cut pipe arch CMP. 217

Figure 4-63. Strain gauges reading for 1-in. thick SAPL renewed invert-cut pipe arch CMP... 217

Figure 4-64. Pipe profiling using DIC for the 1-in. thick SAPL	218
Figure 4-65. DIC method verification with mechanical sensors for the 1-in. thick SAPL renewed invert-cut pipe arch CMP.....	219
Figure 4-66. Load vs. displacement of the soil surface, crown, springline, and shoulder of the 1-in. thick SAPL renewed invert-cut pipe arch CMP due to the applied static load.	219
Figure 4-67. Load vs. pressure for the 1-in. thick SAPL renewed invert-cut pipe arch CMP....	220
Figure 4-68. Visual inspection of the 1-in. thick SAPL renewed pipe arch CMP: (top) cracked SAPL on the invert, and (bottom) crack pattern schematic, where black represents the shrinkage cracks and red represents the cracks due to the load.	222
Figure 4-69. Invert cracks of the 1-in. thick SAPL renewed invert-cut pipe arch CMP: (top) circumferential and (bottom) longitudinal.	223
Figure 4-70. Longitudinal cracks on the crown of the 1-in. thick SAPL renewed invert-cut pipe arch CMP at: (top) center of the pipe and (bottom) north side of the pipe.....	224
Figure 4-71. Thickness measurement for the 1-in. thick cementitious SAPL renewed pipe arch CMP.	225
Figure 4-72. Load vs. soil settlement comparison graph.	228
Figure 4-73. Load vs. crown displacement comparison graph	228
Figure 4-74. Load vs. springline displacement comparison graph.	229
Figure 4-75. Load vs. pressure comparison graph.....	229
Figure 4-76. Proposed equation for thickness calculation of SAPL renewed pipe arch CMP based on ultimate load.....	230

Figure 4-77. Box plot for the cube samples taken from SAPL batch sprayed on pipe arch CMPs	232
Figure 4-78. Box plot for the 3 × 6 cylinder samples taken from SAPL batch sprayed on pipe arch CMPs: (top) spray cast, (bottom) hand cast.	233
Figure 4-79. Box plot for the 4 × 8 cylinder samples taken from SAPL batch sprayed on pipe arch CMPs: (top) spray cast, (bottom) hand cast.	234
Figure 4-80. Box plot for the 6 × 12 cylinder samples taken from SAPL batch sprayed on pipe arch CMPs.....	235
Figure 4-81. Bar chart results for: (a) 7 days, and (b) 28 days samples.	235
Figure 4-82. Compression and tension zones of a circular pipe subjected to a vertical load	236
Figure 4-83. Invert-cut circular CMP renewed with 3 in. cementitious SAPL: (a) before loading, and (b) after loading.....	238
Figure 4-84. Invert-cut circular CMP renewed with 3-in. thick cementitious SAPL subjected to static live load: (top) load-time and, (bottom) load-soil displacement graphs.	240
Figure 4-85. Earth pressure cell results for the 3-in. thick SAPL renewed invert-cut circular CMP with respect to: (top) time, and (bottom) crown displacement.	241
Figure 4-86. Mechanical sensors result for 3-in. thick SAPL renewed invert-cut circular CMP.	242
Figure 4-87. Strain gauge result for 3-in. thick SAPL renewed invert-cut circular CMP.	242
Figure 4-88. Pipe profiling using DIC for the 3-in. thick SAPL renewed invert-cut circular CMP.	243

Figure 4-89. DIC method verification with mechanical sensors for the 3-in. thick SAPL renewed invert-cut circular CMP.	244
Figure 4-90. Load vs. displacement of the soil surface, crown, springline, and shoulder of the 3-in. thick SAPL renewed invert-cut circular CMP due to the applied static load.	244
Figure 4-91. Crack width measurement for the crown location at during the applied live load on the soil surface for the 3-in. thick SAPL renewed invert-cut circular CMP.	245
Figure 4-92. Load vs. pressure for the 3-in. thick SAPL renewed invert-cut circular CMP.	246
Figure 4-93. Visual inspection of the 3-in. thick SAPL renewed circular CMP: (top) cracked SAPL after the test, and (b) crack pattern schematic, where black represents the shrinkage cracks, and red represents the generated cracks due to the load.	247
Figure 4-94. Crack closure at the West haunch area in the 3-in. thick SAPL renewed circular CMP: (a) before, and (b) after loading.	248
Figure 4-95. Circumferential cracks on 3-in. thick SAPL renewed invert-cut circular CMP at: (a) West side, (b) South East side, and (c) North East side of the pipe.	250
Figure 4-96. Longitudinal cracks on 3-in. thick SAPL renewed invert-cut circular CMP at: (top) West side, (b) East side of the invert section.	251
Figure 4-97. Longitudinal cracks on 3-in. thick SAPL renewed invert-cut circular CMP at: (top) center, (b) South side of the crown section.	252
Figure 4-98. Thickness measurement for the 3-in. thick cementitious SAPL renewed circular CMP.	253

Figure 4-99. Invert-cut circular CMP renewed with 2 in. cementitious SAPL: (a) before loading, and (b) after loading..... 255

Figure 4-100. Invert-cut circular CMP renewed with 2-in. thick cementitious SAPL subjected to static live load: (top) load-time and, (bottom) load-soil displacement graphs. 257

Figure 4-101. Earth pressure cell results for the 2-in. thick SAPL renewed invert-cut circular CMP with respect to: (top) time, and (bottom) crown displacement..... 258

Figure 4-102. Mechanical sensors result for 2-in. thick SAPL renewed invert-cut circular CMP. 259

Figure 4-103. Strain gauges result for 2-in. thick SAPL renewed invert-cut circular CMP..... 259

Figure 4-104. Pipe profiling using DIC for the 2-in. thick SAPL renewed invert-cut circular CMP. 260

Figure 4-105. DIC method verification with mechanical sensors for the 2-in. thick SAPL renewed invert-cut circular CMP..... 261

Figure 4-106. Load vs. displacement of the soil surface, crown, springline, and shoulder of the 2-in. thick SAPL renewed invert-cut circular CMP due to the applied static load. 261

Figure 4-107. Crack width measurement for the crown location at during the applied live load on the soil surface for the 2-in. thick SAPL renewed invert-cut circular CMP..... 262

Figure 4-108. Load vs. pressure for the 2-in. thick SAPL renewed invert-cut circular CMP. 263

Figure 4-109. Visual inspection of the 2-in. thick SAPL renewed circular CMP: (top) cracked SAPL after the test, and (b) crack pattern schematic, where black represents the shrinkage cracks, and red represents the generated cracks due to the load. 264

Figure 4-110. Circumferential cracks on 2-in. thick SAPL renewed invert-cut circular CMP at: (top) West side, and (bottom) East side of the pipe.....	266
Figure 4-111. Longitudinal cracks on 2-in. thick SAPL renewed invert-cut circular CMP at: (top) East side, and (bottom) West side of the pipe.....	267
Figure 4-112. Longitudinal cracks on 2-in. thick SAPL renewed invert-cut circular CMP at: (top) East side, and (bottom) West side of the invert gaps.....	268
Figure 4-113. Longitudinal crack at the center of the pipe for 2-in. thick SAPL renewed invert-cut circular CMP.....	269
Figure 4-114. Thickness measurement for the 2-in. thick cementitious SAPL.....	270
Figure 4-115. Invert-cut circular CMP renewed with 1 in. cementitious SAPL: (a) before loading, and (b) after loading.....	272
Figure 4-116. Invert-cut circular CMP renewed with 1-in. thick cementitious SAPL subjected to static live load: (top) load-time and, (bottom) load-soil displacement graphs.	274
Figure 4-117. Earth pressure cell results for the 1-in. thick SAPL renewed invert-cut circular CMP with respect to: (top) time, and (bottom) crown displacement.....	275
Figure 4-118. Mechanical sensors result for 1-in. thick SAPL renewed invert-cut circular CMP.	276
Figure 4-119. Strain gauges result for 1-in. thick SAPL renewed invert-cut circular CMP.....	276
Figure 4-120. Pipe profiling using DIC for the 1-in. thick SAPL renewed invert-cut circular CMP.....	277

Figure 4-121. DIC method verification with mechanical sensors for the 1-in. thick SAPL renewed invert-cut circular CMP.....	278
Figure 4-122. Load vs. displacement of the soil surface, crown, springline, and shoulder of the 1-in. thick SAPL renewed invert-cut circular CMP due to the applied static load.....	278
Figure 4-123. Crack width measurement for the crown location at during the applied live load on the soil surface for the 1-in. thick SAPL renewed invert-cut circular CMP.....	279
Figure 4-124. Load vs. pressure for the 1-in. thick SAPL renewed invert-cut circular CMP. ...	280
Figure 4-125. Visual inspection of the 1-in. thick SAPL renewed circular CMP: (top) cracked SAPL after the test, and (b) crack pattern schematic, where black represents the shrinkage cracks, and red represents the generated cracks due to the load.....	281
Figure 4-126. Cracks on 1-in. thick SAPL renewed invert-cut circular CMP: (a) circumferential crack at East, (b) longitudinal crack on West haunch, and (c) East haunch area.	283
Figure 4-127. Longitudinal cracks on the crown of 1-in. thick SAPL renewed invert-cut circular CMP at: (top) North side, and (bottom) center of the pipe.....	284
Figure 4-128. Longitudinal cracks on the invert of 1-in. thick SAPL renewed invert-cut circular CMP at: (top) West, and (bottom) East of the invert-cut gap.....	285
Figure 4-129. Gap closure at the West springline: (a) before, and (b) after the test.....	286
Figure 4-130. Thickness measurement for the 1-in. thick cementitious SAPL renewed circular CMP.....	287
Figure 4-131. Load vs. crown displacement comparison graph.	289
Figure 4-132. Load vs. springline displacement comparison graph.	290

Figure 4-133. Load vs. soil surface settlement comparison graph.	290
Figure 4-134. Load vs. pressure comparison graph.	291
Figure 4-135. Cube samples taken from SAPL batch sprayed on circular CMPs: (top) broken cube samples with 45-degree failure planes, and (bottom) box plot of the results.	294
Figure 4-136. Box plot for the 3 × 6-cylinder samples taken from SAPL batch sprayed on circular CMPs: (top) spray cast, (bottom) hand cast.	295
Figure 4-137. Box plot for the 4 × 8 cylinder samples taken from SAPL batch sprayed on circular CMPs: (top) spray cast, (bottom) hand cast.	296
Figure 4-138. Box plot for the 6 × 12-cylinder samples taken from SAPL batch sprayed on circular CMPs.	297
Figure 4-139. Bar chart results for: (a) 7 days, and (b) 28 days samples.	297
Figure 4-140. Test result comparison with different available equations.	299
Figure 4-141. Test result comparison with adapted modified-AASHTO equation.	301
Figure 4-142. Residual analysis for the test result and the adopted AASHTO equation.	302
Figure 5-1. SAPL improvement on fully deteriorated CMPs: (top) pipe arch, (bottom) circular.	306
Figure F-1. Crack width measurement on the crown of the 1 in. SAPL renewed circular CMP at the beginning of the test.	323
Figure F-2. Crack width measurement on the crown of the 1 in. SAPL renewed circular CMP at the load 10.4 kips.	324

Figure F-3. Crack width measurement on the crown of the 1 in. SAPL renewed circular CMP at the load 26.45 kips.	325
Figure F-4. Crack width measurement on the crown of the 1 in. SAPL renewed circular CMP at the load 39.1 kips.	326
Figure F-5. Crack width measurement on the crown of the 1 in. SAPL renewed circular CMP at the load 45.2 kips.	327
Figure F-6. Crack width measurement on the crown of the 1 in. SAPL renewed circular CMP at the load 58.5 kips.	328
Figure F-7. Crack width measurement on the crown of the 1 in. SAPL renewed circular CMP at the load 71.7 kips.	329
Figure F-8. Crack width measurement on the crown of the 1 in. SAPL renewed circular CMP at the end of the test.	330
Figure F-9. Crack width measurement on the crown of the 2 in. SAPL renewed circular CMP at the beginning of the test.	331
Figure F-10. Crack width measurement on the crown of the 2 in. SAPL renewed circular CMP at the load 14 kips.	332
Figure F-11. Crack width measurement on the crown of the 2 in. SAPL renewed circular CMP at the load 33.92 kips.	333
Figure F-12. Crack width measurement on the crown of the 2 in. SAPL renewed circular CMP at the load 52.6 kips.	334

Figure F-13. Crack width measurement on the crown of the 2 in. SAPL renewed circular CMP at the load 67.6 kips.	335
Figure F-14. Crack width measurement on the crown of the 2 in. SAPL renewed circular CMP at the load 81.2 kips.	336
Figure F-15. Crack width measurement on the crown of the 2 in. SAPL renewed circular CMP at the load 85.3 kips.	337
Figure F-16. Crack width measurement on the crown of the 2 in. SAPL renewed circular CMP at the end of the test.	338
Figure F-17. Crack width measurement on the crown of the 3 in. SAPL renewed circular CMP at the beginning of the test.	339
Figure F-18. Crack width measurement on the crown of the 3 in. SAPL renewed circular CMP at the load of 15.6 kips.	340
Figure F-19. Crack width measurement on the crown of the 3 in. SAPL renewed circular CMP at the load of 30.2 kips.	341
Figure F-20. Crack width measurement on the crown of the 3 in. SAPL renewed circular CMP at the load of 59.5 kips.	342
Figure F-21. Crack width measurement on the crown of the 3 in. SAPL renewed circular CMP at the load of 84 kips.	343
Figure F-22. Crack width measurement on the crown of the 3 in. SAPL renewed circular CMP at the load of 93.8 kips.	344

Figure F-23. Crack width measurement on the crown of the 3 in. SAPL renewed circular CMP at the load of 109.2 kips.....	345
Figure F-24. Crack width measurement on the crown of the 3 in. SAPL renewed circular CMP at the end of the test.	346
Figure G-1. CMP delivery, donated by Contech Engineering Solutions.....	347
Figure G-2. CMP unloading and storage	348
Figure G-3. Partition wall construction and soil box preparation.....	349
Figure G-4. Soil box preparation	350
Figure G-5. Foundation Preparation using SP soil	351
Figure G-6. Foundation compaction, leveling, and scratching	352
Figure G-7. Foundation and pipe’s top leveling check.....	353
Figure G-8. Pipe installation.....	354
Figure G-9. CMP installation.....	355
Figure G-10. Pipe-wall gap sealing.	356
Figure G-11. Pipe preparation.....	357
Figure G-12. Outside strain gauge installation	358
Figure G-13. Strain gauge physical protection.	359
Figure G-14.PVC duct to protect the strain gauges wires.	360
Figure G-15. Soil material handling.	361
Figure G-16. Soil placement inside soil box.....	362

Figure G-17. Soil placement using casting bucket.	363
Figure G-18. Surface leveling and earth pressure cell installation.	364
Figure G-19. Aggregate top surface leveling.....	365
Figure G-20. Standard Cement vendor on site.....	365
Figure G-21. Wet geopolymer mortar.	366
Figure G-22. Cementitious SAPL mixing and pumping.	367
Figure G-23. SAPL Spraying and surface finishing.	368
Figure G-24. Spray applied lining installation.....	369
Figure G-25. Spraying and troweling.	370
Figure G-26. MTS hydraulic actuator applying a static load over the soil surface.	371
Figure G-27. Load pad penetration in to the soil at the end of test.....	372
Figure G-28. Longitudinal cracks on the circular CMP at: (left) crown, and (right) invert of the SAPL.....	373
Figure G-29. Crack opening at the crown location of the 3-in. thick circular SAPL renewed CMP at the end of the test.	374
Figure G-30. Longitudinal cracks at the both gaps of the invert-cut section.....	375

List of Table

Table 1-1. Common CMP profiles in North America (PCPIPE 2016).....	16
Table 1-2. Highway and railway loads on culverts (American Iron and Steel Institute 1999).....	22
Table 1-3. Volume fraction of fibers (Ramakrishnan et al. 1998).....	48
Table 1-4. Manning’s coefficients for gravity conduits (American Iron and Steel Institute 1999).	54
Table 1-5. Manning’s coefficients for CMP conduits (American Iron and Steel Institute 1999).	54
Table 3-1. List of experimental tests and testing samples details.....	91
Table 3-2. Pipe samples’ geometric details (NCSPA 2008).....	102
Table 3-3. Compressive testing samples for pipe arch CMPs renewed with cementitious SAPL.	143
Table 3-4. Compressive testing samples for circular CMPs renewed with cementitious SAPL	143
Table 4-1. Pipe arch CMP test results.....	226
Table 4-2. Circular CMP test results.....	288
Table 4-3. T-Test results.	302
Table D-1. Pipe arch CMP’s SAPL batch.	319
Table D-2. Circular CMP’s SAPL batch.	320
Table E-1. Pipe arch CMPs renewed with SAPL	321
Table E-2. Circular CMPs renewed with SAPL	322

CHAPTER 1. INTRODUCTION

1.1. Overview

Drainage infrastructure, including storm sewers and culverts, are an integral part of the United State Departments of Transportation (DOTs) as well as municipalities' assets that routinely require inspection, maintenance, repair, and renewal (Najafi et al. 2008). The U.S. department of homeland security's memorandum on "*Identification of Essential Critical Infrastructure Workers During COVID-19 Response*," states maintaining and repairing drainage infrastructure systems are essentials to continue infrastructure viability, which has significant impacts on people lives, economy and national security (Cybersecurity & Infrastructure Security Agency 2020). According to the federal highway administration (FHWA), the United States has approximately 4.12 million miles (6.63 million kilometers) of roadways, making it the largest in the world with millions of culverts hidden underneath. Culverts are important components of the highway infrastructure (Najafi and Gokhale 2005). The recent American society of civil engineering (ASCE) assessment on the United States' infrastructure, shown in Figure 1-1, reveals the poor grade "D" for the wastewater conveyance system, which raised the concern and the attention of the decision makers to this \$1.2 trillion asset value (ASCE 2017). Many of these culverts were installed four to five decades ago and have reached their design life. Culverts' failures raise the issues of public safety and liability. According to the Water Infrastructure Network, America's water and wastewater systems require \$23 billion a year more than current investments to meet the national environmental and public health requirements as well as to replace the aging and failing infrastructure including culverts (Water Infrastructure Network 2001). Culvert failures sometimes happen suddenly and may cause potholes on the pavement or total failure of the roadway embankment. In Owing mills, Maryland a 17-year old culvert with 84 in. diameter, failed and

produced a 20 by 20 ft sinkhole (ACPA 2008). Figure 1-2 illustrates the failure of the culvert which was big enough to swallow a car.

AMERICA'S INFRASTRUCTURE G.P.A.			
AVIATION	D	PORTS	C
BRIDGES	C+	PUBLIC PARKS AND RECREATION	C-
DAMS	D	RAIL	C+
DRINKING WATER	D	ROADS	D
ENERGY	D+	SCHOOLS	D
HAZARDOUS WASTE	D	SOLID WASTE	B-
INLAND WATERWAYS	D-	TRANSIT	D
LEVEES	D-	WASTEWATER	D

Figure 1-1. ASCE's report card on the US infrastructure (ASCE 2017).

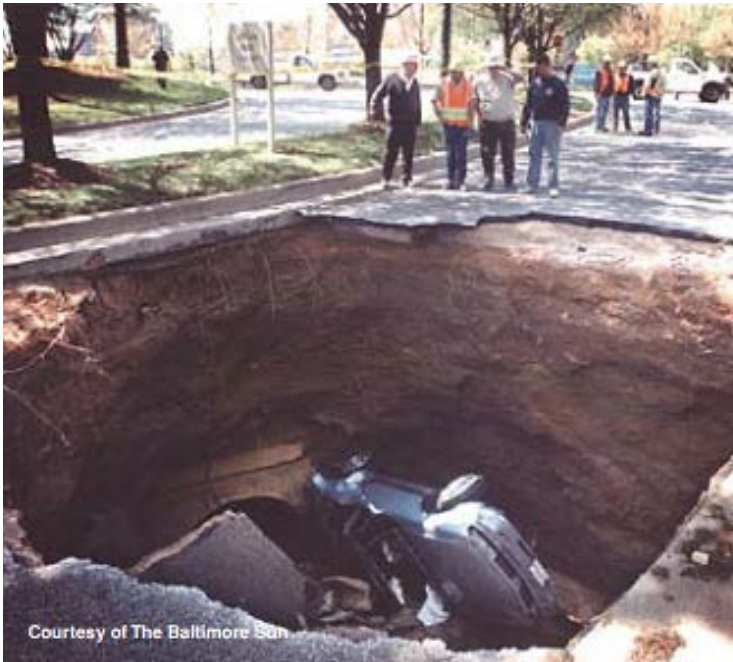


Figure 1-2. A 17-year old 84 in. culvert failure in Maryland, USA (ACPA 2008).

The failure of a 20-year old culvert with 84 in. diameter is shown in Figure 1-3. The culvert's collapse resulted in a sinkhole with approximately 75 ft wide, 250 ft long, and 25 ft depth. The culvert was replaced using open-cut method at the project cost of \$500,000.

The failure of a 30-year old 96 in. diameter CMP resulted in massive sinkhole in Hickory, North Carolina, as illustrated in Figure 1-4. Such a failure has a great impact on local businesses. In this case, the collapse of the culvert caused a local restaurant closure and affected the safety of U.S. Highway 70 and produced debate between the property owner, city and NCDOT as to liability and responsibility damage. The culverts, replacement and road repair cost near to \$1.5 million (ACPA 2008).



Figure 1-3. Culvert failure in South Dakota (ACPA 2008).



Figure 1-4. A 96 in. culvert failure in Hickory, North Carolina (ACPA 2008).

There are many more example of these aged culvert failures. However, culvert failure does not necessarily occur in old and aged pipes. Culverts routinely require inspection, maintenance and repair (Najafi et al. 2008). In Timonium, Maryland, a 4-year old 48 in. diameter high density polyethylene (HDPE) pipe collapsed near a large home improvement warehouse area as shown in Figure 1-5. The replacement and renewal of the collapsed culvert using open-cut method was \$500,000 (ACPA 2008).



Figure 1-5. Failure of a 4-year old HDPE culvert (ACPA 2008).

As a solution, the deteriorated culverts need to be repaired, renewed, or replaced (Wyant 2002). Culvert replacement can be done by open-cut method, which is usually costly as it is associated with indirect costs that typically left to be borne by the society as it involves traffic delays and detours (Ahmadi et al. 2020; Najafi 2013). Based on the type of work, this method is also called dig-and-install, dig-and-repair, or dig-and-replace. This method includes direct installation of culverts into open-cut trenches. Open-cut methods involve digging a trench along the length of the culvert, placing the culvert in the trench on suitable bedding materials and then backfilling with granular soil as specified by AASHTO or USCS. Open-cut method is more time-consuming and does not always yield the most cost-effective method of pipe renewal. In recent times, due to the understanding of the various social costs involved with open-cut, this method of renewal is being discouraged. Social costs include cost to public, environmental impacts, and damage to pavement and existing utilities and structures.

Culver repair, such as concrete invert paving, is the action of locally retrofitting the culvert to prevent further deterioration (Potter 1986). Renewal or rehabilitation of culverts is a trenchless technology practice to improve the current condition of culverts (Kohankar Kouchesfehni et al. 2019). It is more cost-effective, environmentally friendly, and low social impact solution compared to the replace or repair methods. Sliplining, cured in place pipe (CIPP) lining, and spray applied pipe lining (SAPL) are most common practice for culvert renewal (Najafi 2010; Najafi and Gokhale 2005; Syar et al. 2019). Among existing trenchless culvert renewal methods, spray-applied pipe linings (SAPLs) utilizes a special technology for renewing the old pipes and culverts using cementitious and polymeric materials for both partially and fully deteriorated culverts, such as corrugated metal pipes (CMP) and reinforced concrete pipes (RCP). However, as of today there is no design methodology or standard installation procedure for SAPL applications on deteriorated

CMP culverts (Syar et al. 2019). Manufacturers are utilizing different design methodologies, where some using the cured-in-place pipe (CIPP), ASTM F1216, methodology and others using various analytical design equations developed for other purposes. A gap in knowledge was identified and preliminary discussions for a research needs among the SAPL Technical Committee (SAPL-TC) members were formed. The development of practical spray applied structural culvert pipe linings could be of enormous benefit to the Departments of Transportation and municipalities. Such linings could be a key strategy in extending service life and managing the future burden expected from the aging network of culverts and storm sewers. Compared to other culvert rehabilitation systems, SAPLs promise greater cost effectiveness and less community disruptions.

1.2. Culverts

Culverts are buried structures that form passageways through the embankment to convey storm water. They are structurally designed to support superimposed earth loads or other fill materials as well as live loads (Al-Lami 2020; Darabnoush Tehrani et al. 2019). FHWA considers culverts as buried structures with span width less than 20 ft, either single or multiple barrel crossing (FHWA 2012). The service life of the pipe depends on many factors, such as pipe design, material properties, and installation.

Culverts are available in variety of shapes for both, closed and open-bottom conduits. The most common shapes of closed conduits are circular, box (i.e., rectangular), elliptical, and arch (FHWA 2012). However, the open-bottom culverts are mostly in arch configuration. Figure 1-6 illustrates the different shapes of culverts for both closed conduits and open-bottom conduits.

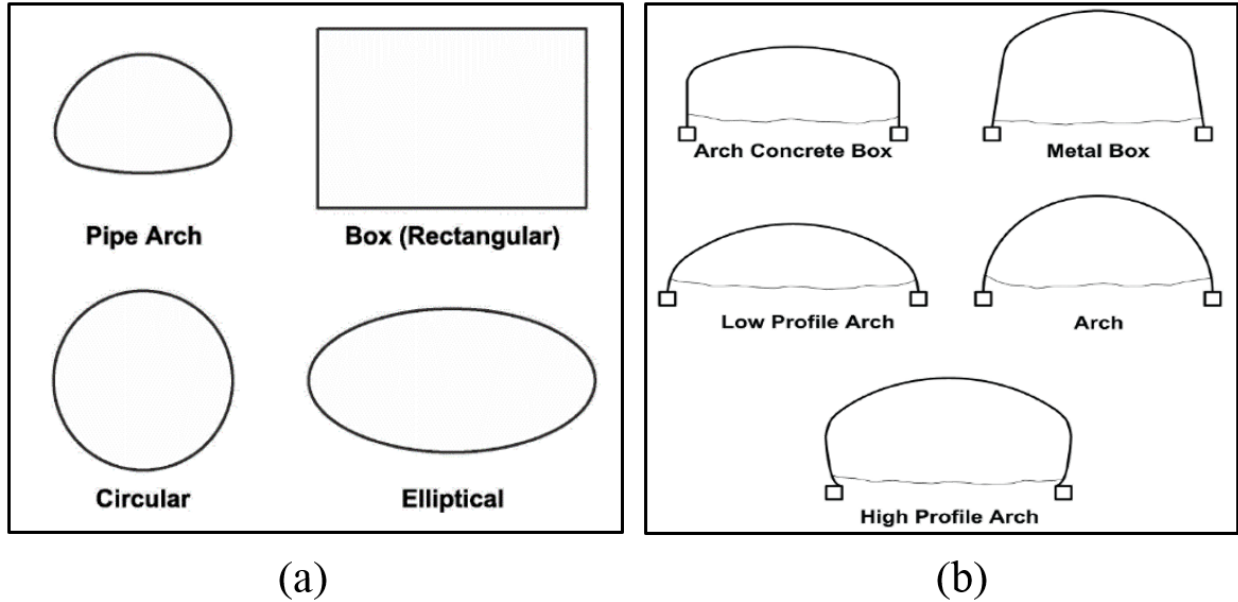


Figure 1-6. Different shapes of culverts: (a) closed conduits, and (b) open-bottom conduits (FHWA 2012).

There are many types of culvert materials used in the U.S. ranging from brittle to deformable materials such as concrete, vitrified clay, steel, plastic, etc. For a culvert production, such materials are selected due to their strength, stiffness, corrosion resistance, lightness, ease of fabrication, transportation, and installation (Kohankar Kouchesfehni et al. 2019). Material selection of a culverts is depended on required structural strength, hydraulic roughness (i.e., Manning's coefficient), durability, job site soil contamination and pH level, constructability, etc. In general, selection of a culvert, from both material and geometry prospective, for a roadway is depended on factors such as roadway profiles, channel characteristics, product availability, construction and maintenance costs, flood damage evaluations, considerable amount of debris or ice formation, and estimates of service life. The most common used culverts used in the United States are reinforced concrete (RCP), corrugated metal pipes (CMP), and plastic pipes (high-

density polyethylene (HDPE) or polyvinyl chloride (PVC))(Darabnoush Tehrani 2016; FHWA 2012).

1.2.1. Culvert Structural Behavior

In general, pipe shaped culverts (i.e., circular, arch, elliptical, etc.) can be structurally classified in two categories: flexible and rigid culverts (Moser and Folkman 2008; Watkins and Anderson 1999). A flexible culvert can deflect between 2~5% of its internal diameter (at crown) without structural distress (Kohankar Kouchesfehane et al. 2018; Kraus et al. 2014; Moser and Folkman 2008). According to the ASTM C822 the crown of a pipe is defined as the top or highest point and invert is the bottom or lowest point of the internal surface of the transverse cross section of a pipe (ASTM C822 2019). Springline is the points on the internal surface of the transverse cross section of a pipe intersected by the line of maximum horizontal dimension; or in box sections, the mid-height of the internal vertical wall. The invert, springline, crown, haunch, and shoulder locations of a pipe are illustrated in Figure 1-7 (a).

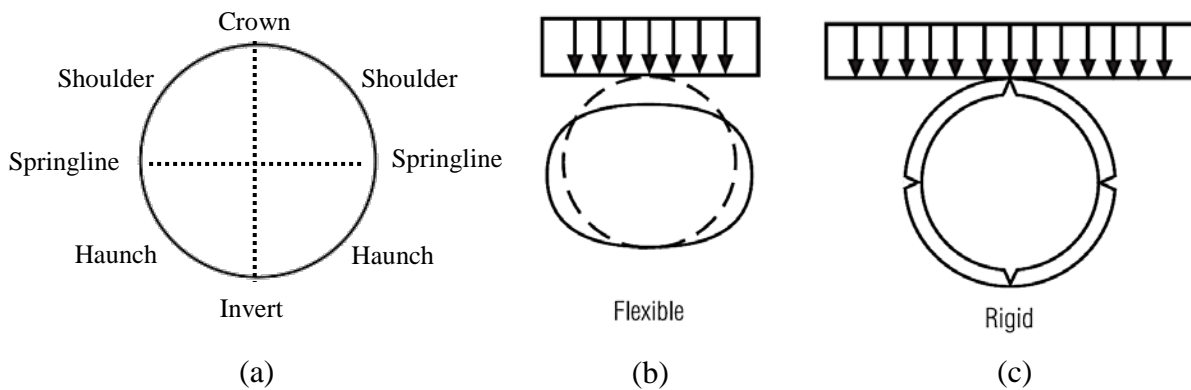


Figure 1-7. Culvert response: (a) Terminology for a culvert cross section, (b) flexible culvert, and (c) rigid culvert behavior.

Under the vertical load, a flexible culvert tends to deflect and as the result, develops passive soil support at the springline (i.e., horizontal sides of the pipe). Passive pressure is the condition that the culvert exerts a force on the soil in the vicinity. In addition to the passive pressure, the ring deflection mitigates a major portion of the load on the culvert, since the soil above the culvert takes more of the load in arching action over the culvert (Kohankar Kouchesfehni and Ghasemi 2013a; b; Whidden 2009). The failure of flexible culverts are usually due to wall buckling or inversion of crown or shoulder area (Watkins and Anderson 1999).

In contrast with a flexible culvert, a rigid culvert does not deflect enough to activate soil passive pressure. Therefore, the pipe's stability relies on its wall stiffness. In other words, rigid pipes are designed to transmit the vertical load through the pipe's wall to the foundation soil underneath. The failure of rigid pipes are usually due to cracking at crown and invert as well as outside of the springline (Darabnough Tehrani 2016; Kohankar Kouchesfehni et al. 2019).

Moser and Folkman (2008) stated that load on a rigid pipe is substantially more than that on a flexible pipe. They illustrated this discrepancy through an analogy between soil and pipe with springs, as illustrated in Figure 1-8. The three springs are hooked from top and bottom horizontally in a parallel configuration and are subjected to a vertical load (weight of an object), which represents soil and culvert stiffness. For the case of a rigid pipe, as shown in Figure 1-8 (a), an increased stiffness exhibited by spring 2 relative to springs 1 and 3, implies that the surrounding soil will deform more and the majority of the load will be carried by the culvert.

In case of a flexible culvert, more deflection occurs at the crown than the springline and consequently, the soil carries more load (Chapman et al. 2007; Moser and Folkman 2008). This reduction effect is sometimes referred as soil arching effect. However, the overall soil-pipe system performance is not only due to the arching effect. The embankment and installation conditions also

play as important role as the soil-culvert interaction system. This interaction is illustrated in Figure 1-9 for both rigid and flexible culverts. For a rigid culvert system, the soil prism on the side tends to settle relatively more than the central prism. This is due to the higher stiffness of the culvert buried under the central prism with respect to the soil on the side (i.e., side prism). Thereby, the shear forces generated due to the side prism movement are downward and cause a greater load on the culvert. This situation is opposite for flexible culverts, where the relative larger displacement of the central prism causes upward shear force and mitigates the load on the buried culvert (Moser and Folkman 2008). Similar upward shear force can also be generated in existence of a compressible material, such as poorly compacted soil or recycled scrap tire backfill material on top of a buried culvert, where the central prism due to the live load tends to be compressed and move downward (Mahgoub and El Naggar 2019).

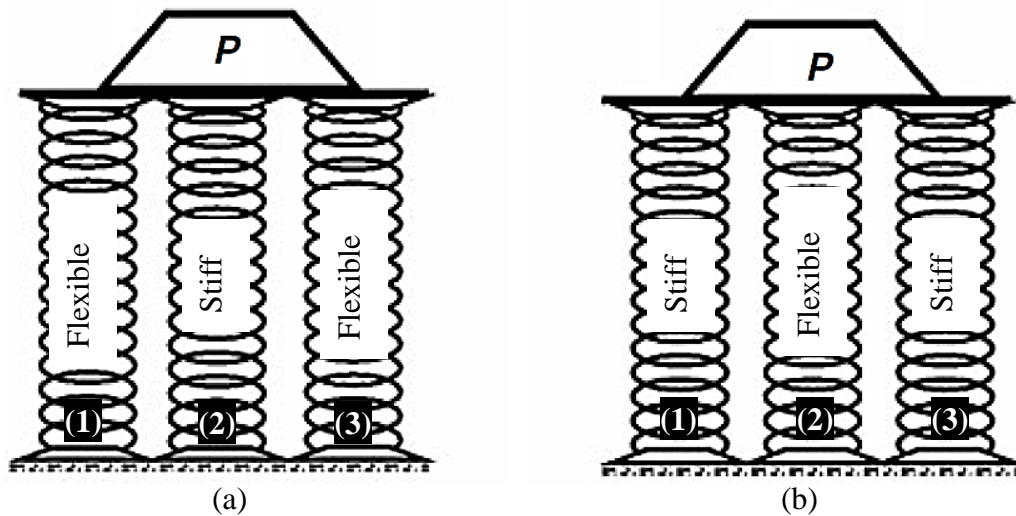


Figure 1-8. Flexible and stiff springs representing (a) soil-rigid, and (b) soil-flexible pipes (Moser and Folkman 2008).

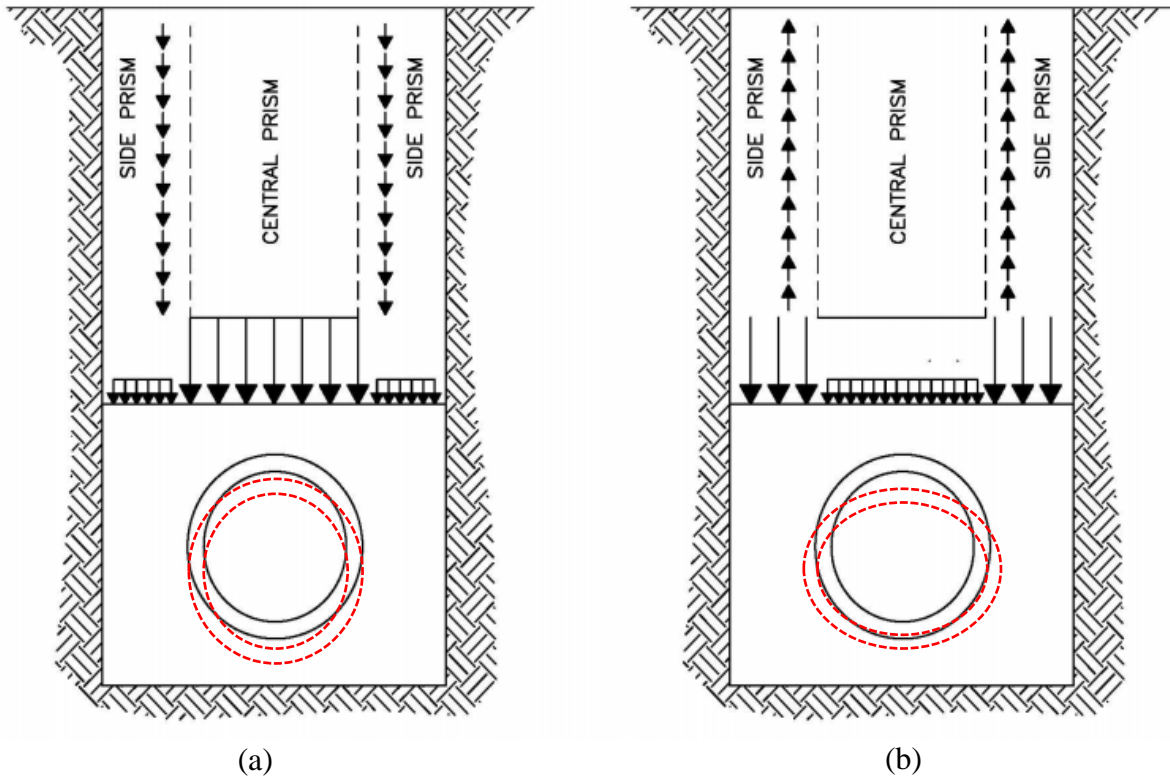


Figure 1-9. Comparison of positive projection conduits for (a) rigid, and (b) flexible pipe (CVWD 2013).

1.2.1.1. Circular Culverts Failure Modes

Rigid circular culverts have two general failure modes: wall crushing and three-hinge plastic formation. The wall crushing is more concerned when the culverts buried deeply underground and the effect of uniform dead load is more dominant than the applied live load (i.e., truck load). In this case, the whole culvert is subjected to the ring compression and most of the applied load is resisted by the pipe's thickness.

The three-hinge plastic formation occurs usually at the shallow cover culverts where the applied load cause bending of the crown, where in the case of rigid steel culverts it will cause

buckling of the crown, and in case of the reinforced concrete culverts it results in cracks at the crown location. Figure 1-10 illustrates the failure modes of a rigid culvert.

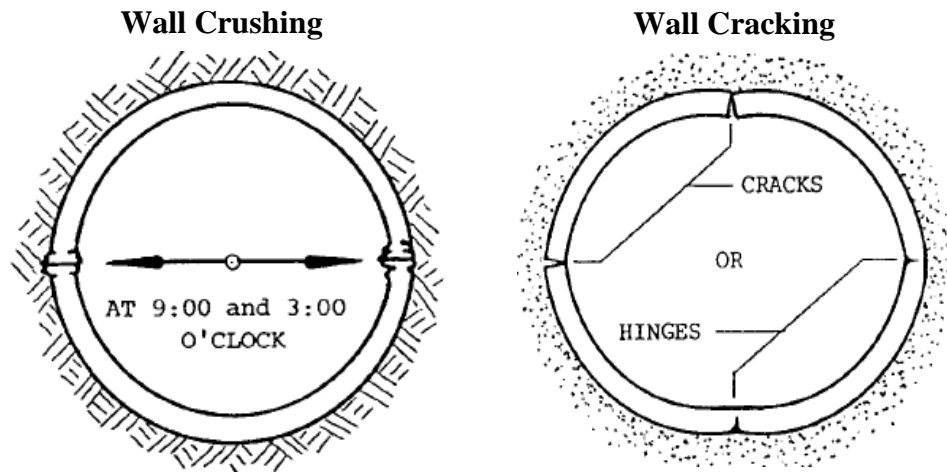


Figure 1-10. Common failure modes of rigid culverts.

Flexible culverts are usually designed to resist against five primary modes of failures. These failure modes are (1) wall buckling, (2) seams and joints separation, (3) elastic buckling, (4) inelastic buckling, and (5) excessive deflection or flattening, as illustrated in Figure 1-11 (Leonards and Stetkar 1978).

The wall buckling usually occurs when the compressive stress of the pipe section exceeds the yielding stress. The seams or joint separation occurs when the thrust force exceeds the seams or joint strength. Elastic buckling is a recoverable deformation which occurs within the pipe's elastic state of stress. The inelastic buckling and excessive deflection occurs do to plastic yielding under combined compressive and bending stresses.

The wall buckling, and seams or joint separation failure mode are comparatively easier to be prevented as magnitude of the circumferential thrust is relatively less sensitive to soil properties or pipe stiffness. However, bending stress, which plays an integral role in the other failure modes are more sensitive to both the above parameters. These failure modes can be proactively prevented by limiting the crown deflection during the service life (Leonards and Stetkar 1978).

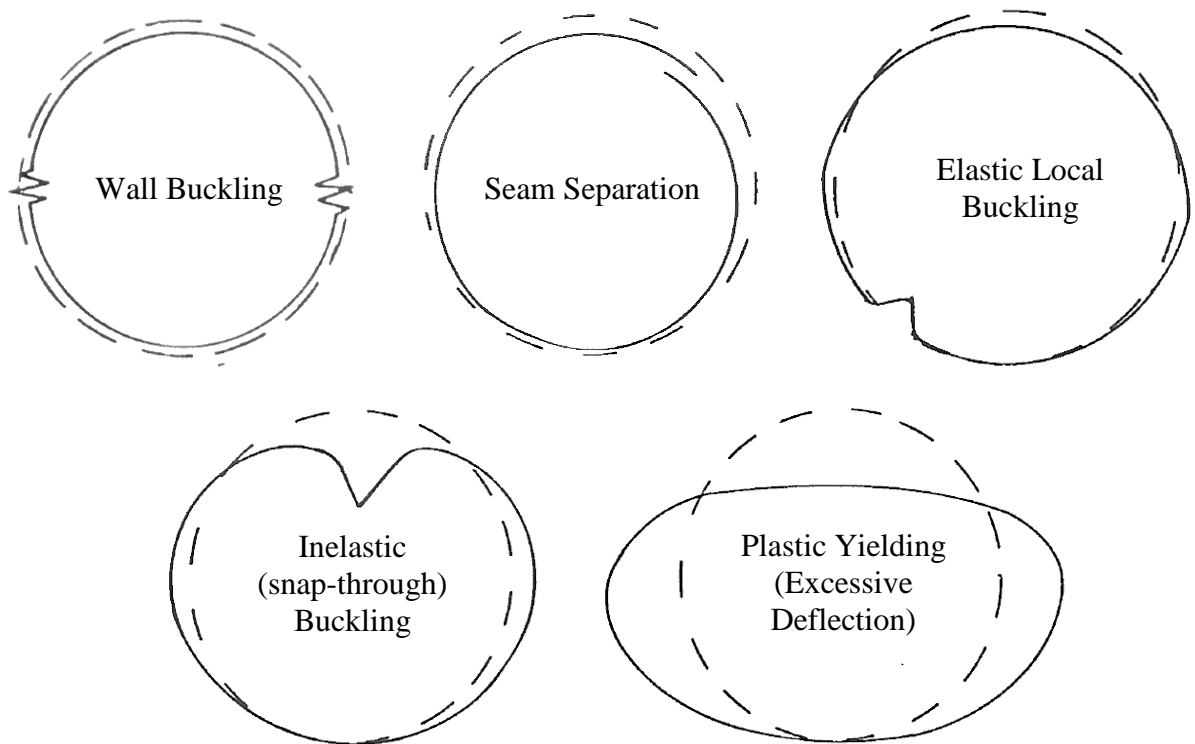


Figure 1-11. Common flexible culverts failure modes

There are generally three types of buckling of flexible culvert. Elastic buckling, local buckling, and inelastic buckling. Elastic buckling is recoverable deformation, initiated at stress levels below yield stress. There are two modes of elastic buckling; high mode and low mode. The high mode involves many small buckled sections distributed around the circumference. The low

mode buckling also involves the entire circumference but is characterized by a small number of larger buckled sections.

Local buckling is a localized bulge or crease involving one location in the culverts circumference, which is usually at the crown of the culvert. The snap-through buckle or inelastic buckling is initiated after portions of the conduit wall have undergone plastic yielding and generally occurs in a low buckling mode. The inelastic buckling involves a reversal of curvature or inversion in the conduit wall and could result in an instability if a sufficient fraction of the circumference is involved.

It is noteworthy that in accordance with currently accepted definitions, buckling is the development of a kink, wrinkle, bulge, or crease in the original shape of the culvert. The load at which buckling is initiated under ideal conditions is defined as the critical load. Likewise, the buckling load is the load at which induces the compressed element, or member to buckle.

1.2.2. Corrugated Metal Pipes

Corrugated metal pipe (CMPs) is invented in 1986 and is one of the most common types of flexible culverts used in the United States (NCSPA 2008). CMPs are cost-effective and are produced in wide range of diameters from 6 in. to 50ft. In general, the steel used in CMP contains the highest percentage, up to 96%, of recycled material. Versatility, cost-effectiveness, ease of production and handling of CMP, makes it an ideal choice to be used as culvert and drainage structures. However, they are exposed to abrasion and corrosion damages (Arnoult 1986; FHWA 2012). In many cases, CMP's inside degradation is due to the impingement of the suspending solid particles in the stream, which causes surface wear and removes the galvanic coating. Once the CMP's coating is removed, the bare metal rusts and this process continues until the whole invert

section is completely deteriorated, as illustrated in Figure 1-12. The speed of the deterioration can be directly affected by pH, amount of suspended solid particles, and temperature of the stream (Sargand et al. 2018).



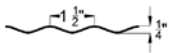
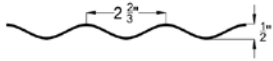
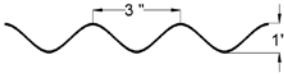
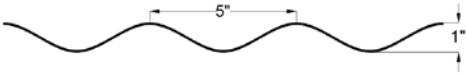
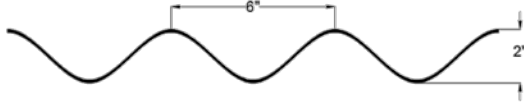
Figure 1-12. Fully invert deteriorated CMP culvert (FHWA 2012).

There are generally three types of CMPs: helical, spiral rib, and annular CMP (Darabnoush Tehrani et al. 2019). Helical CMP is a corrugated tube, fabricated with a tube-shaped shell in a spiral arrangement. Spiral rib CMP is similar to helical CMP, where the pipe is manufactured from a continuous metallic strips passed through a roll forming line that forms the external ribs, edges and joined by lock seaming (NCSPA 2017). While the annular CMP is usually fabricated from a bent hot-dip galvanized steel¹ sheets along their edges using bolts or rivets. Figure 1-13 illustrates

¹ The process of dipping fabricated steel into a kettle or vat containing molten zinc.

three CMP types of helical, annular and spiral rib corrugation profiles. Because of this corrugation profiles, in compare with the same thickness plane steel pipes, CMPs have higher hoop and bending strengths. Several CMP profiles have been used across the North America since its introduction in 1896, which are the $1\frac{1}{2}\times\frac{1}{4}$ in., $2\frac{2}{3}\times\frac{1}{2}$ in., 3×1 in., and 5×1 in. The CMP industry later added the 6×2 in. metal sheets for erecting pipe arch structures of sizes 61 in. by 55 in., and larger. From these available sizes, the most commonly encountered corrugation profiles today are the $2\frac{2}{3}\times\frac{1}{2}$ in., 3×1 in., and 6×2 in. Table 1-1 illustrates common CMP Profiles in the North America. The $2\frac{2}{3}\times\frac{1}{2}$ in. and 3×1 in. corrugation profiles may have a riveted construction (annular corrugations) or lock seam construction (helically wound corrugations), while the 6×2 -in. corrugation profile is made up by bolting standard panels together.

Table 1-1. Common CMP profiles in North America (PCPIPE 2016).

CMP Type	Corrugation Profile	Thickness
Helical and Annular		0.052" & 0.064"
		0.064" - 0.168"
		0.064" - 0.168"
		0.064" - 0.168"
Annular		0.1" - 0.168"

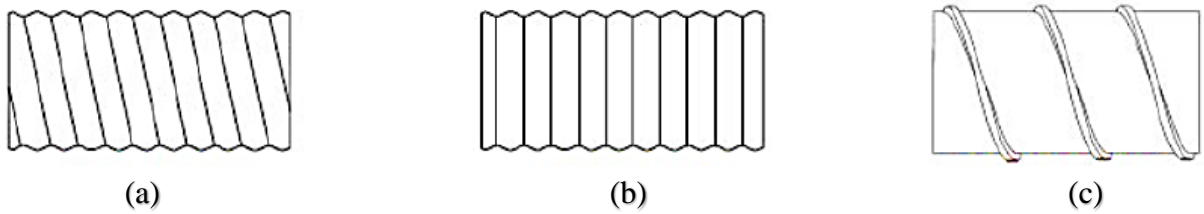


Figure 1-13. Corrugated metal pipe types: a) helical, b) annular, and c) spiral rib CMP (PCPIPE 2016).

1.2.3. Culvert Burial Configuration

A typical standard burial configuration of culverts consists of: foundation, bedding, haunch area, initial backfill (embedment), final backfill (cover) as illustrated in Figure 1-14 (Kohankar Kouchesfehiani et al. 2017; Moser and Folkman 2008; Watkins and Anderson 1999; Whidden 2009). The supporting soil beneath the culvert is generally known as the culvert foundation. The foundation provides a uniform support and a stable base to the culvert and should be designed to carry the full soil column above the culvert without appreciable settlement (Mai et al. 2018; NCSPA 2008; Syar et al. 2020). The culvert generally benefits from a foundation that has been naturally consolidated by the existing soil height. Where soft foundations need to be improved by over-excavating and rebuilding the foundation with compacted granular material used in embedment and backfill. The AASHTO LRFD bridge construction specifications Section 26, 26.5.2., provides standard installation process of foundation.

Bedding provides continuous support for the pipe at the required grade. The bedding should consist of an evenly graded, free flowing, granular material which is free of large stones or frozen material. This layer should not be compacted. The existence of this layer is essential to allow the pipe to settle and activate the haunch area (i.e., fill the voids). Due to the pipe curvature at the

haunch area, placement and compaction of the soil at this area is a challenging task. If the soil is not placed to fill the area, a void remains, which is unfavorable (Moser and Folkman 2008). According to the AASHTO LRFD Bridge Construction Specification, in order prevent the void formation, as shown in Figure 1-15, the bedding is necessary to be placed at top of the foundation with minimum of 4 in. of loose soil material (AASHTO 2017). Use of controlled low strength material (CLSM), also known as flow able fill, is an alternative to the use of bedding with the native soil (Takou et al. 2017). CLSM consists of a mixture of Portland cement, water, aggregate and sometimes fly ash with the strength less than 200 psi (1.3 MPa) and can be poured into the haunch area (Moser and Folkman 2008).

The purpose of haunch area is to provide the required side support without causing displacement from proper alignment. This layer should be placed and compacted similar to embedment and backfill. The backfill design and selection of culverts are similar to selection of a roadway embankment fill. The main differences in requirements are due to the fact that the culvert generates more lateral pressure than the earth within the embankment of a roadway without a buried structure (NCSPA 2008). The quality of backfills is characterized by the soil stiffness, which is depended on the level of the soil compaction. The best backfill materials are non-plastic sands and gravel (i.e., with negligible amount of clay and silt). Such soil characteristics can be found in GW, GP, GM, and SW soil in Unified Soil Classification System (USCS) and in A1, A2, and A3 soil material defined by AASHTO soil classification. For this layer, many governmental agencies like TxDOT (2014) or City of Dallas (2011) suggested compaction rate of 95% of standard Proctor dry density (SPDD), while AASTHO suggest minimum of 90% (AASHTO 2017). Compaction quality of the backfill is crucially important, especially for flexible culverts, as it provide the necessary support to pipe.

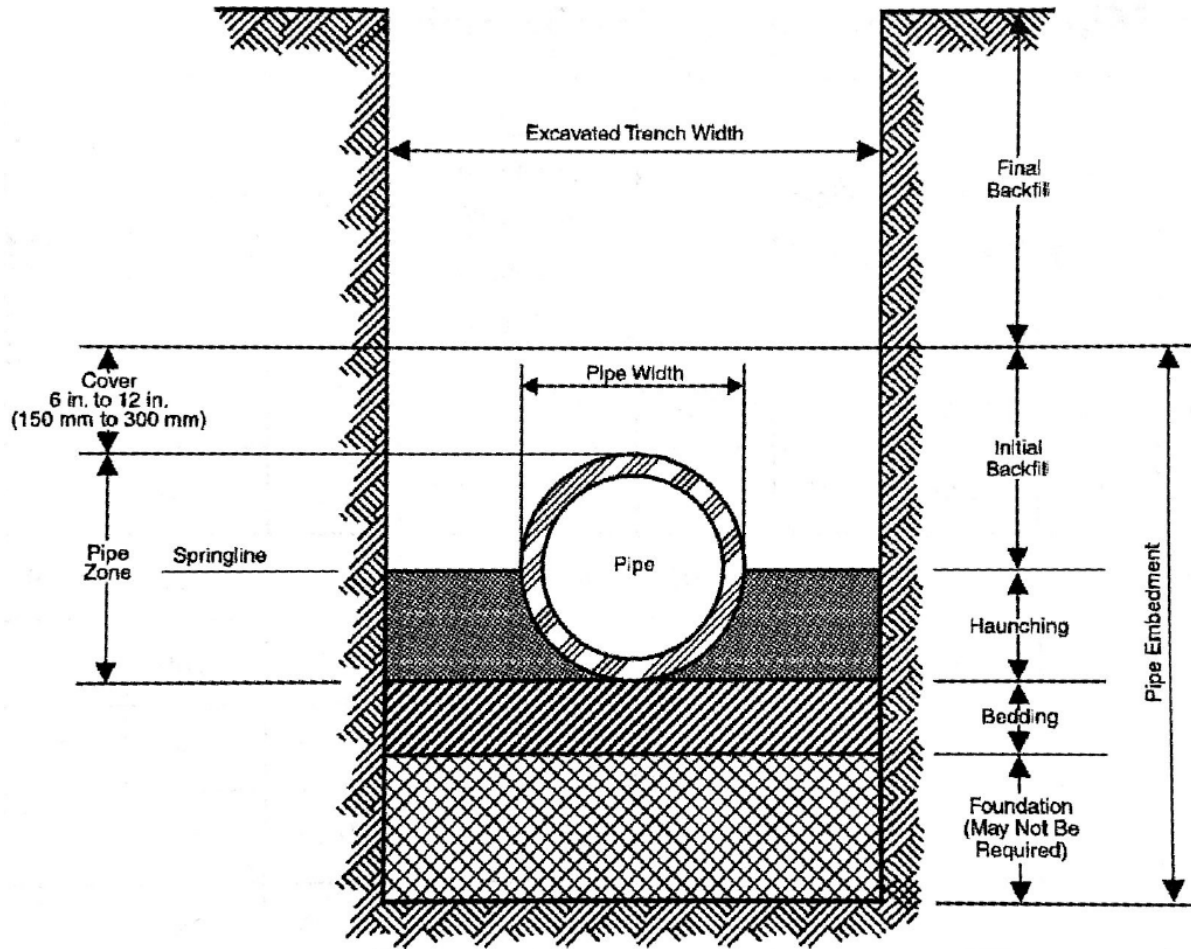


Figure 1-14. Typical burial configuration of a pipe in trench (Moser and Folkman 2008).

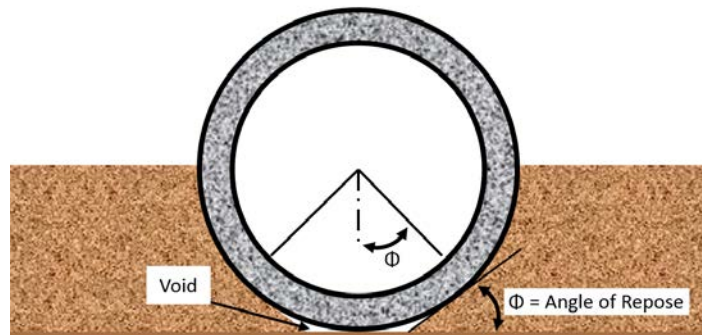


Figure 1-15. Pipe cross section showing how voids are generated if the soil is not deliberately placed in the haunch area.

CALTRANS recommends to use the minimum cover of span/5 or 2 ft (0.6 m) for the flexible pavement or unpaved surfaces, and minimum of span/5 or 1.2 ft (0.36 m) for rigid pavements. However, in many cases, different departments of transportation and AASHTO suggested a minimum cover of span/8 or 1 ft, including a well-compacted granular subbase and base course (AASHTO 2017; FDOT 2019). However, it should be noted that AASHTO considers flexible pavement excluded from cover height for flexible culverts and included rigid pavement into the cover height consideration as shown in Figure 1-16.

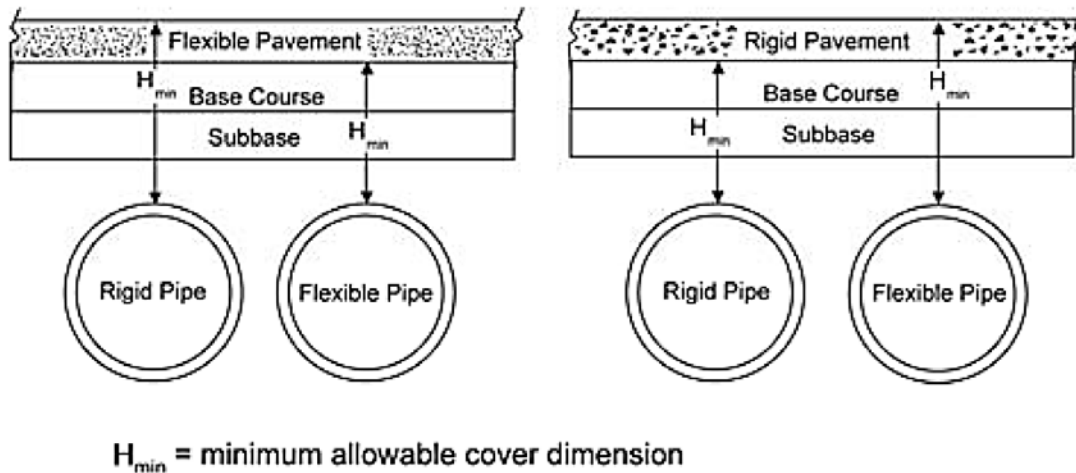


Figure 1-16. Minimum Cover Orientation (AASHTO 2017).

1.2.4. Structural Design of CMP Culverts

To design a culvert, first the required hydraulic capacity of the culvert should be calculated using the data collected from hydrology studies. Once the pipe geometry is determined for expected hydraulic flow, the structural design and burial configuration selection can be conducted.

The first consideration in structural design is the evaluation of the loads on the culvert. Underground conduits, such as culverts, are subject to two principal kinds of loads:

- a) dead loads developed by the backfill and stationary superimposed surface loads, and
- b) live loads exerted by the traffic over the culvert.

Once the loads were obtained, the CMP can be designed to adequately resist the applied loads. In general there are two design procedures for circular CMPs: American iron and Steel institute (AISI) and AASHTO LRFD method (AASHTO 2017; American Iron and Steel Institute 1999; Kang et al. 2008; NCSPA 2008).

1.2.4.1. AISI Method

The dead load is the soil prism over the culvert, where the unit pressure of this prism acting on the horizontal plane at top of the culvert is equal to:

$$DL = \gamma \cdot H. \quad (1)$$

Where γ is the unit weight of the soil (lb/ft³), and H is the height of fill over the culvert (ft).

The live loads are typically due to highway, railway, or construction traffic. Standard highway loadings are referred to as AASHTO H-20 and H-25 live loads, and standard railroad loadings are referred to as AREA E-80 live loads as presented in Table 1-2. National corrugated steel pipe association's (NCSPA) corrugated steel pipe design manual combined the results of the Table 1-2 with the calculated dead load pressure at various depths and presented in a chart as illustrated in Figure 1-17 and Figure 1-18. The charts modify the theoretical distribution of live

loads to the values compatible with observed performance of structures under relatively low covers.

Table 1-2. Highway and railway loads on culverts (American Iron and Steel Institute 1999)

Highway Loading			Railway E-80 Loading	
Depth of Cover (ft)	Load (psf)		Depth of Cover (ft)	Load (psf)
	H-20	H-25		
1	1800	2280	2	3800
2	800	1150	5	2400
3	600	720	8	1600
4	400	470	10	1100
5	250	330	12	800
6	200	240	15	600
7	175	180	20	300
8	100	140	30	100
9	-	110	-	-

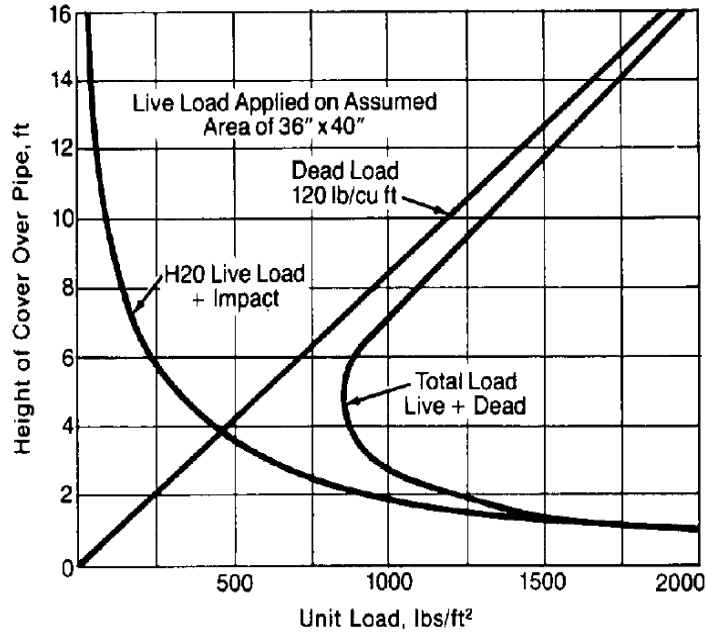


Figure 1-17. Combined H-20 highway live load and dead load is a minimum at about 5 ft of cover. Live load is applied through a pavement of 1 ft thick (NCSPA 2008).

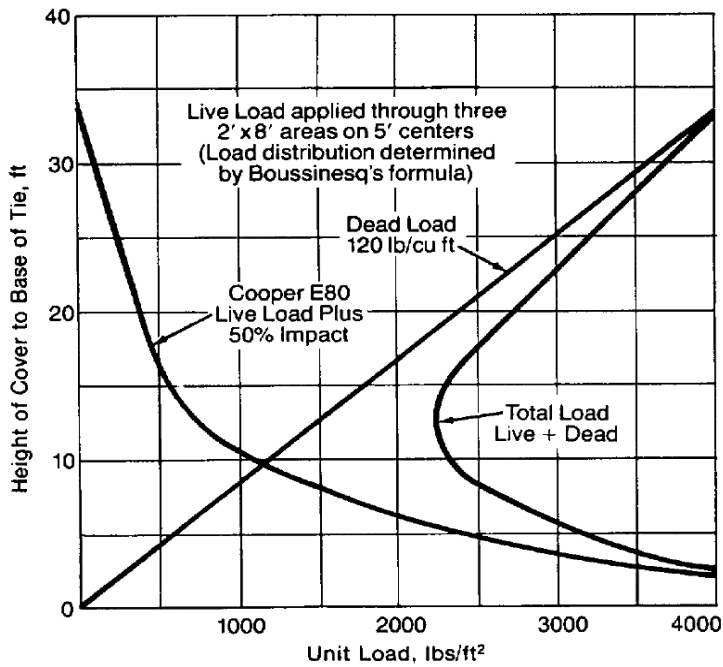


Figure 1-18. Railroad live load, cooper E 80, combined with dead load is a minimum at about 12 ft. Live load is applied through three 2 × 8 ft areas on 5 ft centers (NCSPA 2008).

When the height of cover is equal to or greater than the span or diameter of the CMP, the total load, which is the summation of the live and dead load, can be reduced by a factor of K to obtain the design pressure on the culvert. This factor, which is a function of soil density and is suggested by AASHTO T-99 or ASTM D98 to be taken as 0.86, 0.75, and 0.65 respectively for the 85, 90, and 95% of the standard density. If the height of cover is less than one pipe diameter, then the K factor should not be included in the design pressure calculation. The design pressure can be obtained as follow:

$$P_V = K \cdot (DL + LL), \text{ when } H \geq S, \quad (2)$$

$$P_V = (DL + LL), \text{ when } H < S, \quad (3)$$

where, the P_V is the design pressure (psf), K is load factor, DL is the dead load (psf), LL is the live load (psf), H is the height of cover (ft), and the S is the culvert span or diameter (ft). With the inherent flexibility of corrugated metal pipe (i.e., flexible culvert), the vertically directed total load pushes the springline of the pipe ring against the compacted fill material on the side and activates the passive earth pressure. Thus, the pipe ring is often assumed to be loaded by radial pressure. For circular culverts, the pressure around the periphery tends to be approximately equal, particularly at deep buried pipes where there is soil arching effect. For pipe-arch shapes, the pressure is approximately inversely proportional to the radius of curvature of the segments. Since the pressures at the corners of the pipe-arch culvert are greatest, the soil adjacent to them is subjected to the highest pressures. Figure 1-20 illustrates the pressure distribution around a pipe-arch. The soil in the corner areas at the springline must have sufficient bearing capacity to resist the applied pressure. Accordingly, the soil-bearing capacity may control the maximum allowable fill height for pipe arches.

In circular CMPs the radial pressures develop a compressive thrust in the pipe wall, and the pipe must have structural strength adequate for this purpose. Accordingly, the stress in the culvert wall may be determined and compared to recognized allowable values to prevent yielding, buckling, or seam failures. The compressive thrust in the culvert wall is equal to the radial pressure acting on the wall multiplied by the pipe radius or $C = P \times R$. The ring compression (i.e., thrust) is the force carried by the culvert material which in this case is steel. The ring compression is an axial force acting tangentially to the culvert wall as illustrated in Figure 1-19. For conventional structures in which the top arc approaches a semicircle, it is common to substitute half the span for the wall radius.

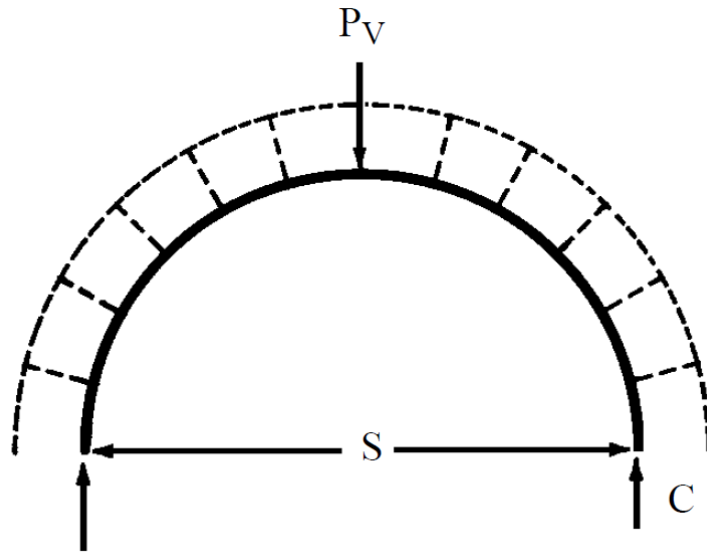


Figure 1-19. Free body diagram of a circular pipe subjected to vertical load.

The ring compression can be obtained as follows:

$$C = P_V \cdot \frac{S}{2}, \quad (4)$$

where, C is the ring compression (lb/ft), P_V is the design pressure (psf), and S is the span or diameter (ft). The ultimate compressive stress for corrugated metal structures with backfill compacted to 90% of SPDD and yield point of 33,000 psi is as follow:

$$f_b = f_y = 33,000 \text{ psi, when } \frac{D}{r} \leq 294 , \quad (5)$$

$$f_b = 275 - 558 \cdot 10^{-6} \times \left(\frac{D}{r}\right)^2 , \text{ when } 294 \leq \frac{D}{r} \leq 500 , \quad (6)$$

$$f_b = \frac{3.4 \cdot 10^7}{\left(\frac{D}{r}\right)^2} , \text{ when } \frac{D}{r} > 500 , \quad (7)$$

where, f_b is the ultimate compressive stress (psi), D is diameter or span (in.) r is radius of gyration (in.), and I is moment of inertia (in.⁴/ft). The design stress can be obtained by imposing a factor of safety of 2 to the ultimate compressive stress that yields:

$$f_c = \frac{f_b}{2}. \quad (8)$$

The required wall area (A) can be computed using the wall compression and design stress as follows:

$$A = \frac{C}{f_c}. \quad (9)$$

Additionally, the CMP should be stiff enough during the handling and installation without having undue care or bracing. The resultant flexibility factor, FF, limits the size of each combination of corrugation and metal thickness:

$$FF = \frac{D^2}{E \cdot I'} \quad (10)$$

where, E is modulus of elasticity (psi), D is the diameter or span (in.), I moment inertia of wall (in.⁴/in.).

The pipe-arch culvert poses special design problems not found in round or elliptical pipe. Pipe-arches generate corner pressures greater than the pressure in the fill that often becomes the practical limiting design factor rather than stress in the pipe wall. To calculate the corner pressure, the bending strength of the corrugated metal should be ignored and establish allowable loads based on the allowable pressure on the soil at the corners. Assuming zero moment strength of the pipe wall, ring compression, C , is the same at any point around the pipe-arch, and $C = P \times R$ at any point on the periphery. This means the normal pressure to the pipe-arch wall is inversely proportional to the wall radius. The corner pressure can be obtained as follows:

$$P_c = P_v \cdot \frac{R_t}{R_c}, \quad (11)$$

where, P_c is pressure acting on soil at corners (psf), P_v is the design pressure (psf), R_c is radius of corner (ft), and R_t is the radius at crown (ft).

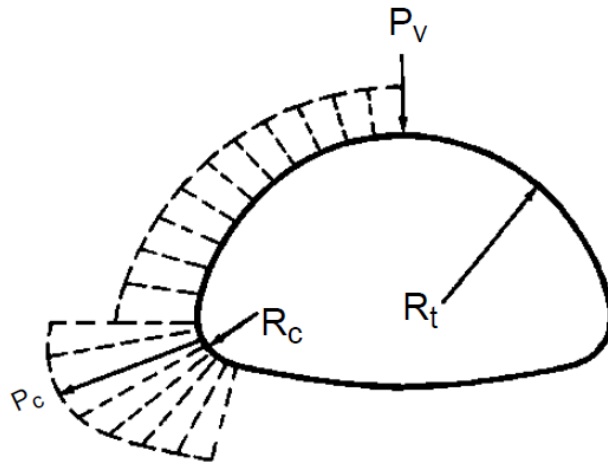


Figure 1-20. The pressure on a pipe-arch varies with location and radius being greatest at the corners (American Iron and Steel Institute 1999).

1.2.4.2. AASHTO LRFD Method

AASHTO LRFD bridge design specifications suggest live load calculation on the crown of culverts for H-20 truck with tire contact area of 10×20 in., or any other contact area sizes according to the section C3.6.1.2.5, using the 60-degree rule (i.e., 2:1 method) stress distribution approximation method found in many texts on soil mechanics and foundation design guidelines. In the 60-degree rule approximation method the pressure on top of the culvert can be calculated using following equation:

$$q_z = q_0 \cdot \frac{B \cdot L}{(B + z) \cdot (L + z)}, \quad (12)$$

where, q_z is the pressure at depth z (psf), z is the depth of cover (ft), B is the width of the loaded area (ft), L is the length of the loaded area (ft), q_0 is the applied pressure on the soil or pavement surface (psf). However, AASHTO requires inclusion of the dynamic load impact on the pressure calculation as the traffic passing over the culverts apply dynamic loads on the soil-culvert system. Therefore equation (12) yields to:

$$P_L = \frac{P \cdot \left(1 + \frac{IM}{100}\right) \cdot m}{A_{LL}}, \quad (13)$$

$$A_{LL} = l_w \cdot w_w, \quad (14)$$

$$IM = 33 \cdot [1 - 0.125 \cdot \text{minimum depth of cover}(ft)], \quad (15)$$

Where, A_{LL} is the rectangular area at depth H (ft^2), l_w and w_w are the live load patch length and width at depth H (ft) obtained by 2:1 rule, P is the live load applied at surface on all interacting

wheels (kip), P_L is the live load vertically applied on crown pressure (ksf), IM is the dynamic load allowance, and m is the multiple presence factor specified in section 3.6.1.1.2 of AASHTO LRFD.

By having the total load (i.e., live and dead loads) the factored thrust per unit length of wall can be calculated as follows

$$T_L = \frac{P_{FD}}{2} + \frac{P_{FL} \cdot C_L \cdot F_1}{2}, \quad (16)$$

in which:

$$C_L = l_w \leq S, \quad (17)$$

$$F_1 = \frac{0.75 \cdot S}{l_w} \geq F_{min}, \quad (18)$$

where, C_L is width of culvert on which live load is applied parallel to span (ft), l_w is live load patch length at depth H , S is culvert span (ft), T_L factored thrust per unit length (kip/ft), P_{FL} factored live load vertical crown pressure (ksf), and P_{FD} factored dead load vertical crown pressure with VAF taken as 1 and D_o taken as S (ksf). Vertical arching factor (VAF) is to reduce the earth load to account for the support provided by adjacent soil columns. The VAF can be calculated as follows:

$$VAF = 0.76 - 0.71 \left(\frac{S_h - 1.17}{S_h - 2.92} \right), \quad (19)$$

$$S_h = \phi s \cdot \frac{M_s \cdot R}{E_s \cdot A_s}, \quad (20)$$

$$R = \frac{ID}{2} + c, \quad (21)$$

where, S_h hoop stiffness factor, ϕ_s resistance factor for soil stiffness (taken as 0.9), M_s secant constrained soil modulus (psi), R effective radius of pipe, ID inside diameter of pipe (in.), c distance from inside diameter to neutral axis of pipe wall (in.), A_s section area of pipe wall, (in.²/in.), and E_s is modulus of elasticity of pipe (psi).

The wall resistance of the CMP culvert can be calculated using factored axial resistance (R_n) per unit of length of wall without consideration of buckling as follows:

$$R_n = \phi \cdot F_y \cdot A, \quad (22)$$

where, ϕ resistance factor, F_y yield strength of metal (ksi), and A wall area (in.²/ft).

The wall area, calculated using equation (22), shall be investigated for buckling. If $F_{cr} < F_y$, A shall be recalculated using F_{cr} in lieu of F_y as demonstrated below:

$$\text{if } S < \left(\frac{r}{k}\right) \cdot \sqrt{\frac{24 \cdot E_m}{F_u}}, \text{ then } f_{cr} = F_u - \frac{\left(\frac{F_u \cdot k \cdot S}{r}\right)^2}{48 \cdot E_m}, \quad (23)$$

$$\text{if } S > \left(\frac{r}{k}\right) \cdot \sqrt{\frac{24 \cdot E_m}{F_u}}, \text{ then } f_{cr} = \frac{12 \cdot E_m}{\left(\frac{k \cdot S}{r}\right)^2}, \quad (24)$$

where, S diameter of pipe or span of plate structure (in.), E_m modulus of elasticity of metal (ksi), F_u tensile strength of metal (ksi), f_{cr} critical buckling stress (ksi), r radius of gyration of corrugation (in.), k soil stiffness factor taken as 0.22.

Handling flexibility shall be indicated by a flexibility factor determined as:

$$FF = \frac{S^2}{E_m \cdot I} \quad (25)$$

1.3. Culvert Renewal Methods

The conventional method for construction, replacement, and repair of culverts has been trenching or open-cut. Trenchless technology or No-Dig culvert renewal method is a cost-effective and socially/environmentally friendly option to open-cut culvert replacement that can renew the pipes without digging or with minimize surface disruption. Generally, the main objective of a structural renewal is to delay further deterioration and be able to structurally renew the severely damaged culverts and drainage structures (Najafi 2016). Trenchless technology culvert renewal methods include sliplining (SL), cured-in-place pipe (CIPP), spiral wound lining, close fit pipe, and spray applied pipe lining (SAPL), as illustrated in Figure 1-21 (Najafi et al. 2008).

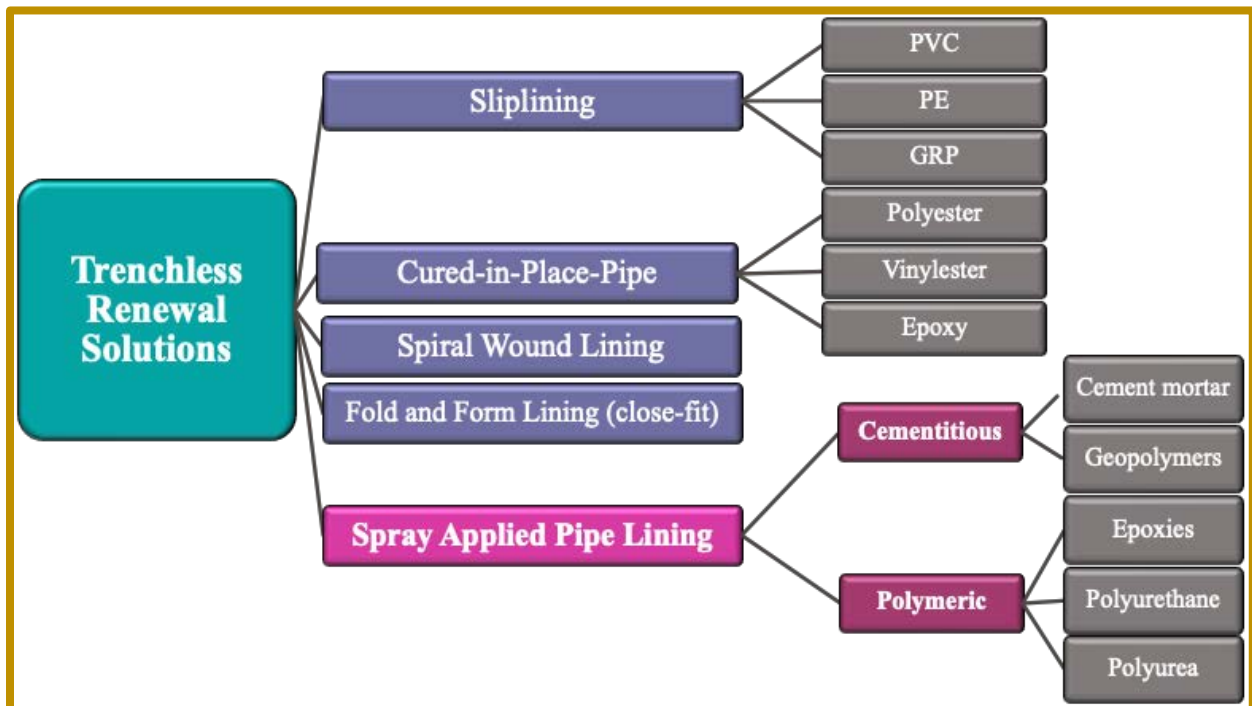


Figure 1-21. Common trenchless technology culvert renewal methods.

1.3.1. Sliplining

Sliplining culvert renewal method involves inserting a pipe liner of smaller diameter directly into a deteriorated culvert. Sliplining can be carried out using fiberglass pipes, polyethylene pipes, PVC pipes, reinforced concrete pipes, or steel pipe such as CMPs. Typical sliplining method includes; host pipe cleaning and preparation, slipline insertion, slipline joint connection (for segmental sliplining) or joint fusion (for continuous sliplining), and grouting the annular gaps (ASCE 2010).

Prior to the renewal of culvert with sliplining, it is important to inspect the culvert and remove any debris or obstruction that may interfere with the installation process. The existing flow inside the culvert should be prevented or diverted during the renewal process.

The slipliner pipe can be pushed using jacking methods or pulled through an open end. It is important to determine maximum allowable force to prevent liner wall buckling. After insertion, the annular gap between the existing culvert and slipliner is grouted with a cementitious material such as controlled low strength material (CLSM), low density cellular concrete (LDCC), or cellular grout with 100-150 psi compressive strength, to provide watertight seal and uniform support to the liner. Annular gap is the space between the outside diameter of the slipliner and the host culvert. Proper grouting help provide uniform support around the pipe, eliminates point load and minimized the effect of hydrostatic pressure. However, it is important not to use excessive grout pressure to avoid liner buckling. Culverts ranging from 18 to 160 in. can be sliplined (Wagener and E. Leagjeid 2014). Sliplining is one of the common method of culvert renewal. However, it reduces hydraulic capacity of the culvert as it will always have a smaller diameter than the existing host culvert.



Figure 1-22. Culvert renewal using sliplining method (photo credit: pomonapipelineproducts.com).

1.3.2. Cured in Place Pipe (CIPP) Lining

Cured in place pipe (CIPP) lining involves with the insertion of a felt or fiber tube saturated with polyester, vinylester or epoxy resin. CIPP was the first truly trenchless full pipeline renewal method, invented in 1970 in the United Kingdom. There are two methods of CIPP liners installation; pulled-in-place and inversion technique. ASTM F1216 outlines the standard practice for CIPP installation using inversion method and ASTM F1743 outlines standard CIPP installation using pulled-in-place method. CIPP can be carried out on pipes ranging from 4 to 120 in (Najafi 2013). The wall thickness of the CIPP can be designed pending on the installation process, applied loads, host pipe condition (partially or fully deteriorated condition as specified by the ASTM F1216), and physical properties of the finished CIPP laminate (ASCE 2010). To install the CIPP, the saturated fabric with thermosetting resin, is commonly inserted to the host pipe using inversion or pulled-in-place method and inflated by water or air pressure. To cure the resin and finish the

installation process, hot water, hot air, steam, or UV light can be used. However, a large majority of CIPP installed since 2008 has used the water pressure to insert the CIPP tube and heated water to cure the heat-initiated resin. For culverts if water is used to install and cure CIPP, the waste process water must either be pumped to an adjacent sanitary sewer system or hauled to a suitable deposit site to prevent environmental contamination. This additional cost of waste water transportation to the disposal location, may increase the cost of CIPP renewal method for rural area. In addition, if a metal culvert, such as CMP, have heavy corrosion or missing invert, the sharp edges must be trimmed voids need to be filled and smoothed prior to CIPP installation.



Figure 1-23. CIPP curing using UV light (photo credit: ohm-advisors.com).

1.3.3. Spiral Wound Lining

Spirally wound lining implements interlocking profile strips, mostly made from PVC and HDPE material to line a deteriorated culvert. Coiled, interlocking profile strips are fed through a winding machine, which mechanically forces the strips to interlock and form a smooth and continuous spirally wound lining system. During the interlocking process, a sealant is applied to each joint to form a watertight seam. Figure 1-24 illustrates the spirally wound liner installation, where the material is wound and snapped together and is forced into the existing culvert. However, this method similar to sliplining remains an annular gap with the host culvert, which needs to be filled with grout.



Figure 1-24. Spirally wound liner installation (Wagener and E. Leagjeid 2014).

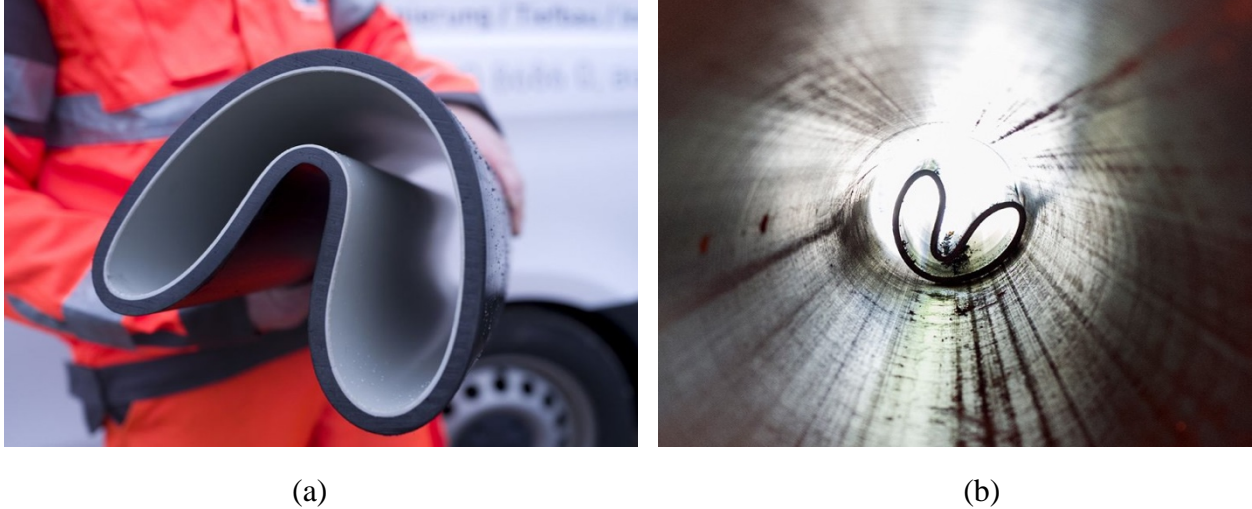


Figure 1-25. Fold and form pipe lining (photo credit: agru.at): (a) folded thermoplastic liner, and (b) inserted folded liner.

1.3.4. Fold and Form lining (Close-fit)

Close-fit lining, also sometimes referred to as modified sliplining, involves the insertion of a thermoplastic pipe (e.g. PVC, HDPE) with an outside diameter the same or slightly larger than the inside diameter of the host culvert. Because of such close-fit, the liner's cross section must be modified before insertion to the host culvert. The modified liner is winched into place and reformed to provide a close-fit with the host culvert as illustrated in Figure 1-25. To reform the liner, once the folded thermoplastic pipe was inserted into the host culvert, a flow-through plug is inserted into the liner at the boiler end and steam is sent through the liner to relax it from the axial forces of the insertion pull. Once the liner has dimensionally stabilized, it is cut to the length and hydrophilic gasket end seals are positioned if they are to be used. The liner is then plugged at both ends. Pressurized hot steam is then utilized to process the liner reform. The reformed liner conforms the exact geometry of the host culvert, for instance, if the host culvert is corrugated the close-fit liner will likewise become corrugated. It should be noted that, prior to the pipe insertion,

similar to other lining methods, the host pipe needs to be cleared and water flow must be stopped or diverted. Close-fit lining method is more appropriate for culverts with diameter lower than 30 in. The structural design of fold and form lining are in accordance with the ASTM F1216.

1.3.5. Spray Applied Pipe Lining (SAPL)

Application of the SAPLs protects the culvert from further corrosion and abrasion deterioration of the culvert and improves its structural and hydraulic performance as well as their design life (Darabnoush Tehrani et al. 2019, 2020a; Moore and García 2015a). Spray applied pipe lining (SAPL) application dates back to 1930s, which is the pioneer technique for pipe renewal (Ellison et al. 2010). SAPL applies layers of liner on the interior surface of the host pipe to provide corrosion protection and structural capacity enhancement. It can be sprayed by hand or a spin-caster machine. SAPLs can be cementitious such as cement mortar and geopolymers, or polymeric material including epoxy, polyurethane, and polyurea. SAPLs have many advantages over other lining methods. It does not leave annular gaps and conforms the host culvert geometry. SAPL is one continuous length of liner without joints or weak points. Hydraulic capacity of the culvert can be maintained or improved with its smooth and uniform surface (Darabnoush Tehrani et al. 2019). Thickness of the SAPL and the quality of the SAPL material provide the greatest flexibility for design consideration. SAPL also has lower construction cost and footprint than other methods. For instance, in compare with sliplining which requires heavy vehicles to transport the slipline segments, hydraulic jacks or backhoe to slipline the liner, SAPL only requires a portable ordinary air compressor and a medium size mixer that all can be installed on a small truck. In compare with CIPP, it does not need large amount of pressurized water to install the liner and boiling systems to

cure the liner. SAPLs are cost effective, environmentally friendly, chemical resistant, and can be rapidly installed.

1.3.5.1. Polymeric SAPLs

Polymeric SAPL is developed in 1970s (Ellison et al. 2010). Initially, it was based on 100% solid elastomeric polyurethane. In mid-1990s 100 percent solids rigid polyurethane coatings was developed, which was able to form a 3-D cross-linked structure, resulted in a superior resistance to chemicals, water penetration, and high temperatures (Matthews et al. 2012). Polymeric SAPLs can be applied through a spin caster machine or hand spray. There are three types of polymeric SAPL available for pipe and culvert renewal; polyurea, polyurea, polyethylene, and epoxy, as illustrated in Figure 1-21. Epoxies are widely use as corrosion protection coating for metal applications. They have excellent corrosion and chemical resistance and can perfectly adhere to the metallic surface. However, epoxies are not flexible and can crack in the applications that involve substrate movement, and as a result they may not be suitable for flexible pipes, where the pipe can deflect up to the allowable deflection limit.

Polyurea, provides high degree of chemical resistance and is able to cure rapidly (i.e., about 5 to 15 seconds) as its speed of reaction is extremely fast (Howarth 2003). It does not need for a catalyst or heat, even at low temperatures (down to -°20 C). In compare with other polymeric SAPLs, polyurea has less volatile organic compounds (VOC) to smell and breathe during the installation process. At the time of installation, polyurea is insensitive to moisture and does not form blisters when it is exposed to.

Polyurethane is solvent-based consisted of two-component (2K) coating systems. It can be formulated to achieve a very flexible or very rigid polyurethane coating material. In compare with other polymeric SAPLs, polyurethane can achieve higher structural capacity. However, it in most cases, it is sensitive to moisture at the time of installation and may form blisters or a soft foam. It became available to the market of pipeline renewal in 1990 and has been used for manhole and pipe renewal since then. Figure 1-26 illustrates polyurethane SAPL application inside a pipe arch.

The characteristics of all polymeric SAPLs are provided in Figure 1-27. Currently, many departments of transportation (DOTs) have already approved polymeric coatings for rehabilitation of culverts in the United States, such as Ohio DOT, Virginia DOT, Florida DOT, etc.



Figure 1-26. Hand spray polyurethane SAPL: (a) before renewal, and (b) after renewal (Kohankar Kouchesfehni 2020).

Item	Product Performance on Steel Surface				Material
	1 = Poor	2 = Fair	3 = Good	4 = Best	
Adhesion	Blue	Blue			Polyurea
	Yellow	Yellow	Yellow		Polyurethane
	Green	Green	Green	Green	Epoxy
Impact	Blue	Blue	Blue	Blue	Polyurea
	Yellow	Yellow	Yellow		Polyurethane
	Green				Epoxy
Application Temperature	Blue	Blue	Blue	Blue	Polyurea
	Yellow	Yellow	Yellow		Polyurethane
	Green				Epoxy
Corrosion Resistance	Blue	Blue			Polyurea
	Yellow	Yellow	Yellow		Polyurethane
	Green	Green	Green	Green	Epoxy
Chemical Resistance	Blue	Blue			Polyurea
	Yellow	Yellow			Polyurethane
	Green	Green	Green	Green	Epoxy
Abrasion Resistance	Blue	Blue	Blue	Blue	Polyurea
	Yellow	Yellow	Yellow	Yellow	Polyurethane
	Green	Green			Epoxy
Curing Time	Blue	Blue	Blue	Blue	Polyurea
	Yellow	Yellow	Yellow		Polyurethane
	Green	Green			Epoxy
Flexibility	Blue	Blue	Blue	Blue	Polyurea
	Yellow	Yellow	Yellow	Yellow	Polyurethane
	Green				Epoxy
Weatherability	Blue	Blue	Blue		Polyurea
	Yellow	Yellow	Yellow	Yellow	Polyurethane
	Green				Epoxy

Figure 1-27. Material property comparison for all three major polymeric SAPL material (Curran 2016).

1.3.5.2. Cementitious SAPLs

Cementitious SAPL is the oldest method to line culverts. There are three methodologies for cementitious SAPL: centrifugally casting in place, pumping and troweling on, and shotcreting (ASCE 2010). Centrifugally casting, which is the most new and accepted method, applies the cementitious liner by an air powered rotating nozzle for a designed thickness. The thickness of the applied mortar is controlled by the speed of a vehicle or the installation crew that pulls the centrifugally casting machine (Wagener and E. Leagjeid 2014). Figure 1-28 illustrates cementitious SAPL installation using centrifugally casting machine. The cementitious SAPLs typically start at pipes around 36 in. (i.e., man entry size pipes) in diameter. The minimum finished thickness of these SAPLs are usually between 1 and 1.5 in., dependent on the conservatism of the design engineer or pipe owner (Royer and Iseley 2017). Generally, there are two types of cementitious SAPL: cement mortar and geopolymer SAPL. Conventional cement mortar SAPLs are economical but provide relatively poor corrosion protection than polymeric SAPL in corrosive environment (Matthews et al. 2012; Walker and Guan 1997). One of the possible reasons could be due to the higher void ratio of cementitious SAPL in compare with polymeric (i.e., polyurethane, polyurea, and epoxy) liners. However, they provide extra strength to the culvert by increasing the rigidity of the renewed pipe system.

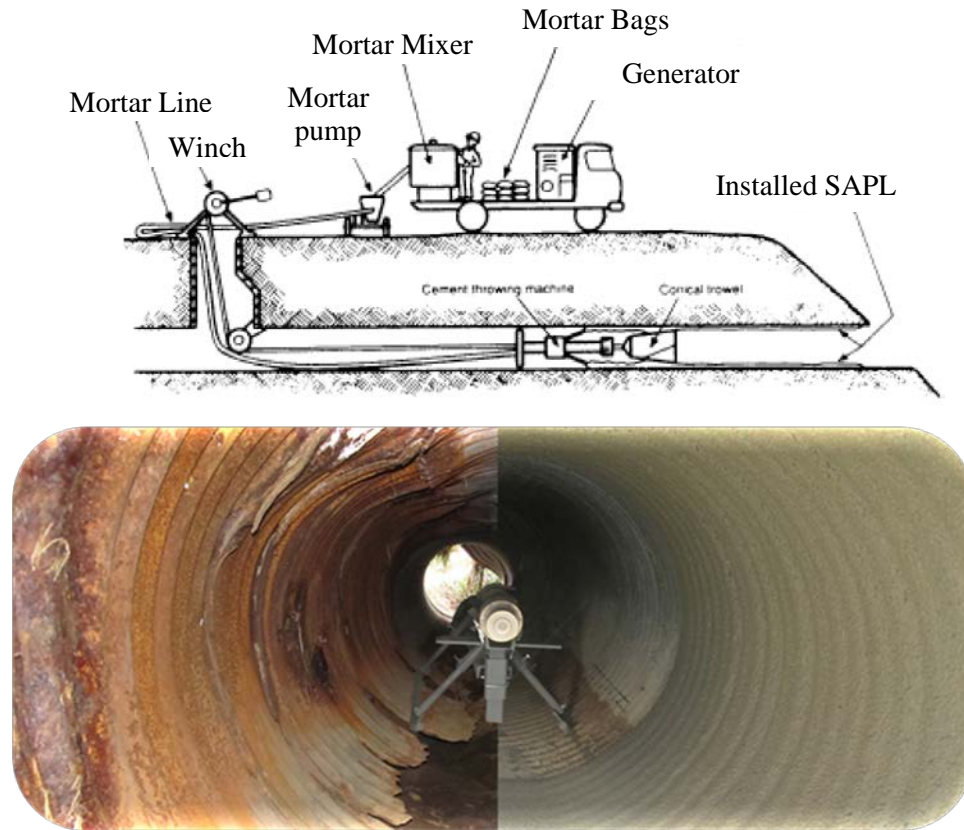
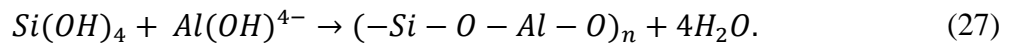
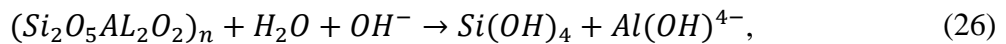


Figure 1-28. Centrifugal spray cast machine for cementitious SAPL: (top) schematic of the required equipment (Caltrans 2002) and (bottom) renewed culvert with a cementitious SAPL(credit: CentriPipe)

In contrast to the cement mortar SAPL, geopolymer SAPL has higher chemical resistance, enhanced resistance to fire, lower shrinkage, lower creep and less CO₂ emissions (Park et al. 2016; Royer and Iseley 2017). In compared with traditional Portland cement mortar, geopolymers provide also a better physical properties such as compressive and tensile strengths (Davidovits 1991, 2015). The term “geopolymer” was originally applied to three dimensional aluminosilicate materials formed by condensation of a solid aluminosilicate source such as metakaolin with an alkali silicate solution under highly alkaline conditions (Brew and Mackenzie 2007; Davidovits 2015). Geopolymer is achieved by the reaction of aluminosilicate materials such as fly ash,

metakaoline, silica fume, slag, rice-husk ash, or red mud with highly alkaline solutions such as hydroxides or silicates (Okoye et al. 2016). Unlike Portland cement mortar SAPL, geopolymer SAPL do not require calcium-silicate-hydrate (C-S-H) gel for matrix formation and strength but utilize the polycondensation of silica and alumina precursors to achieve the required strength. In the past recent years, a considerable amount of research studies on geopolymer cement has being carried out to elucidate the mechanism of formation, strength development and durability of geopolymers. Under highly alkaline conditions, polymerization takes place when reactive aluminosilicates are rapidly dissolved and free tetrahedral units such as $[\text{SiO}_4]^-$ and $[\text{AlO}_4]^-$ are released in solution (Singh et al. 2015). The tetrahedral units are alternatively linked to polymeric precursor by sharing the atom of oxygen, therefore forming polymeric Si–O–Al–O bonds. The following reactions occur during geopolymerisation:



During dissolution, this process releases water that is normally consumed. The expelled water from the geopolymer during the reaction add workability to the mixture at the time of casting. This is in contrast with ordinary Portland cement mixture's chemical reaction of water during the hydration process. Using different aluminosilicate sources (i.e., fly ash, slag, etc.) in geopolymer may provide different chemical properties. For instance, fly ash-based geopolymer are generally stronger and durable than Metakaolin-based geopolymer. While Metakaolin-based geopolymer can be manufactured constantly with predictable properties during both preparation and development (Singh et al. 2015). The slag-based geopolymers is considered to have greater acid

resistance and higher early strength. Figure 1-29 illustrates a schematic on formation of fly ash-based geopolymers.

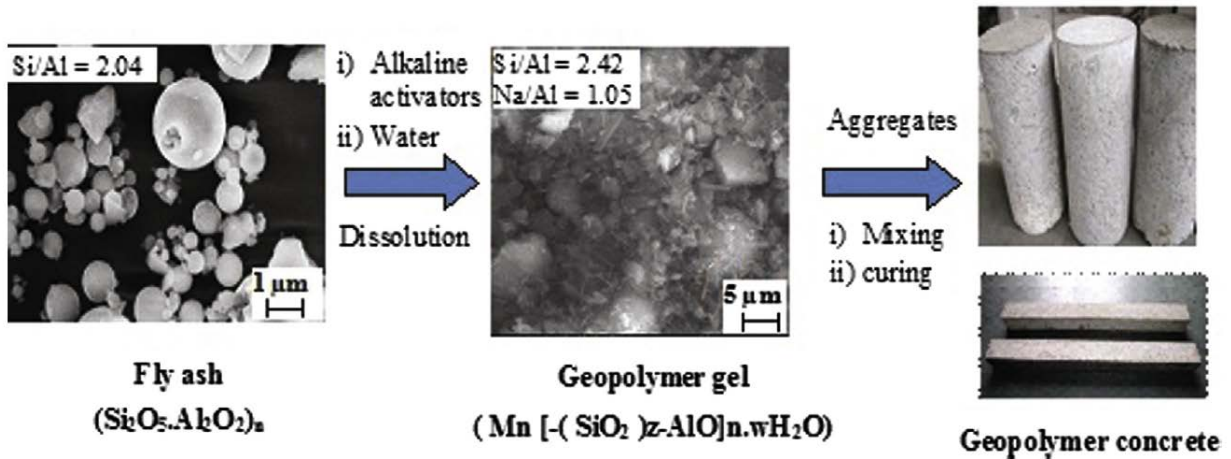


Figure 1-29. Conversion of fly ash into geopolymers/concrete (Singh et al. 2015).

1.3.5.3. Fiber Reinforced Cementitious SAPL

The cementitious SAPLs have brittle behavior and are commonly crack due to shrinkage, stress concentration and their low tensile strength (Banthia et al. 2014; Kohankar Kouchesfehni et al. 2019). These cracks are mostly in micro-level size and distributed all over the cementitious SAPL. Under an applied load, these distributed micro-cracks propagate further and form a larger crack (i.e., macro-level size). With progression of the applied load, the width of the macro-cracks can become wider and make the liner's condition critical, which may increase the probability of the liner structural failure. In addition, macro-cracks increase the chance of host pipe corrosion, freeze and thaw damage, liner's spalling and discoloration. To prevent macro-crack formation, and increase the mechanical properties of SAPL, Kohankar Kouchesfehni suggests to use fiber reinforcement in cementitious SAPL (Kohankar Kouchesfehni et al. 2019). Addition of fibers can limit the formation and further propagation of micro-cracks. The fibers can be selected from

different materials such as steel, carbon, polypropylene, polyester, nylon, glass and cellulose fibers in two major categories of micro and macro sizes. The applicable fibers to be used in a cementitious SAPL are illustrated in Figure 1-30 and Figure 1-31. The existence of fibers in a cement matrix reinforce the cementitious composite material due to their snitching effect (Darabnough Tehrani 2016). The existence of the fibers add resistance to the SAPL against crack opening by bridging the cracks, as illustrated in Figure 1-32. Furthermore, the fibers can enhance the bond strength between the host pipe and the cementitious SAPL material (Dawood and Ramli 2011; Iucolano et al. 2013; Zanotti et al. 2014).

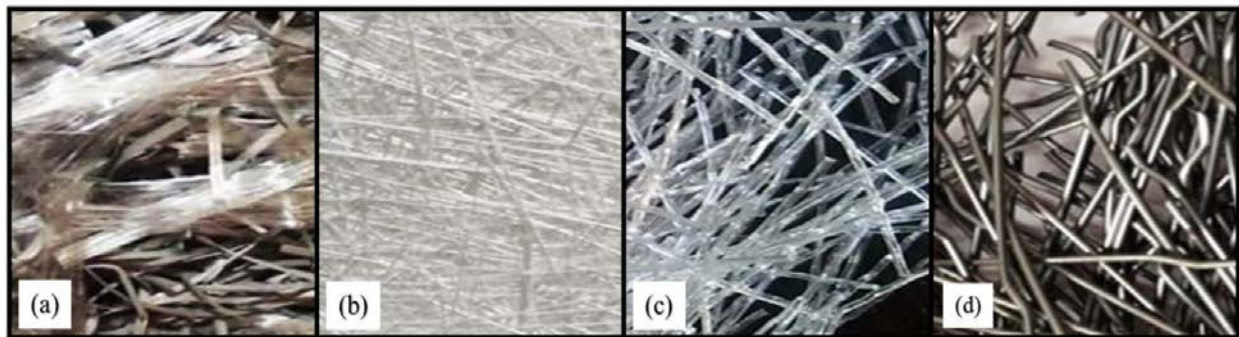


Figure 1-30. Macro Fibers: Polypropylene Fibers, (b) Fiberglass, (c) Polyolefin Fibers and (d) Steel Fibers.

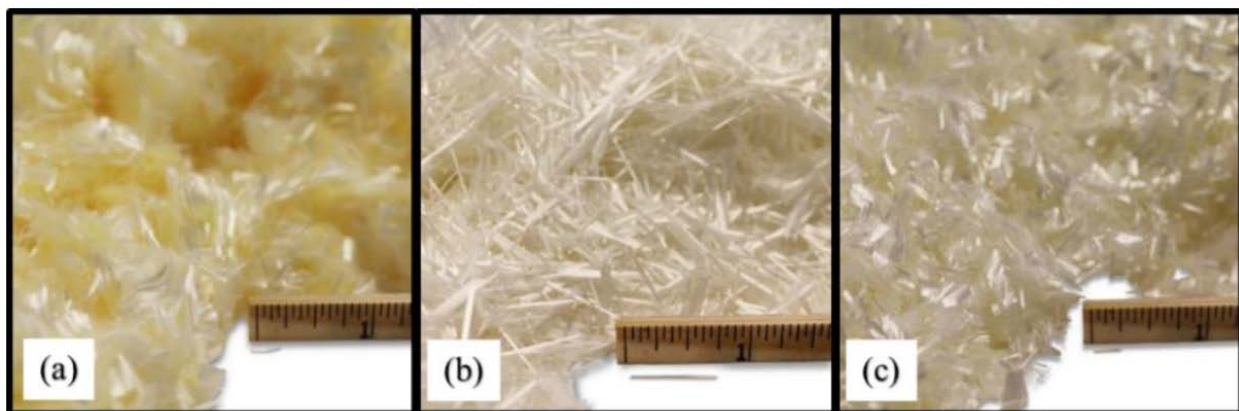


Figure 1-31. Micro-Fibers: (a) Acrylic Fiber, (b) Alkali Resistant (AR) Glass Fiber, (c) PVA Fiber, and (d) Alkali Resistant Glass Scrim.

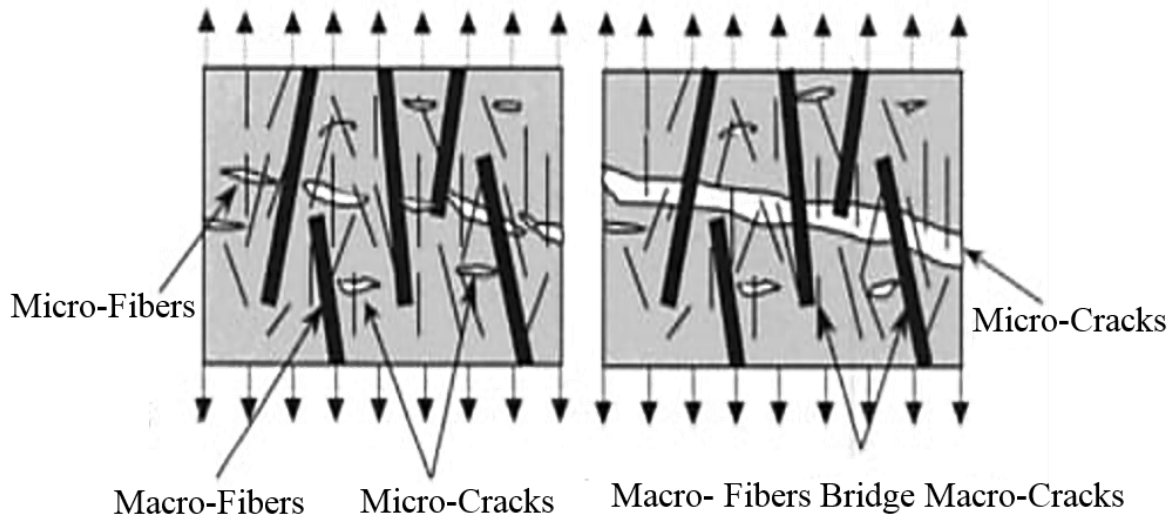


Figure 1-32. Different size fibers bridge different crack width (Kohankar Kouchesfehni et al. 2019).

A pipe subjected to a vertical load experiences tension forces at the interior surface of crown and invert, and the exterior surface of springline, as illustrated in Figure 1-33. Likewise, a cementitious SAPL in a renewed pipe is prone to crack at crown and invert, when subjected to external vertical loads such as live or dead load. Although, the host pipe acts as a reinforcement at the exterior surface of SAPL, it cannot provide any resistance to the interior surface of the crown and invert, and yet the system is susceptible to crack at those locations. Therefore, inclusion of fiber reinforcements in the cementitious SAPL mortar strengthens the matrix against cracking at the crown and invert.

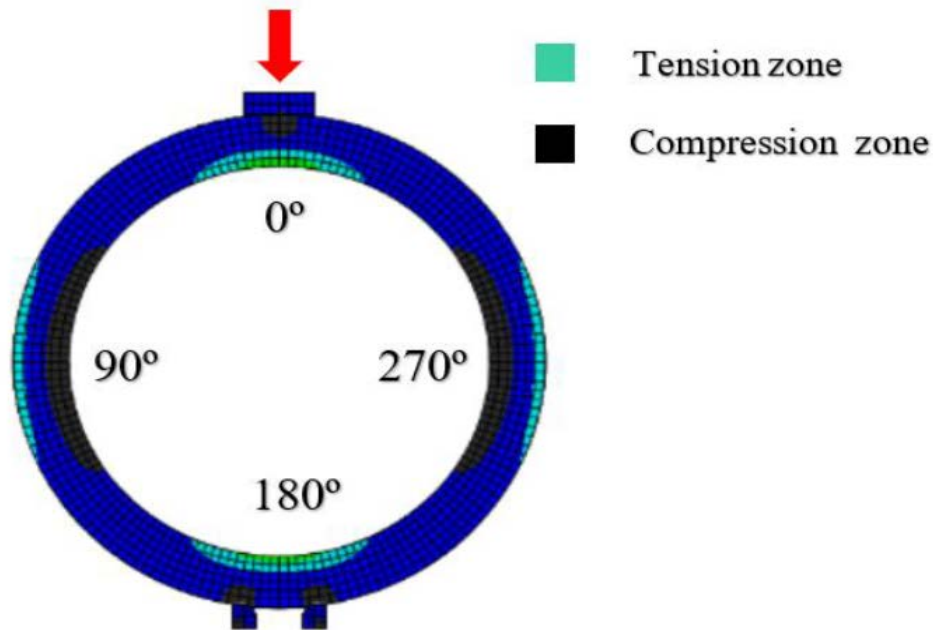


Figure 1-33. Numerical analysis of a pipe subjected to vertical downward loading according to three-edge bearing test configuration (Darabnoush Tehrani 2016).

In thin-shelled SAPLs, selection of fiber reinforcement must consider the fiber's length so that the fibers can fit within the thickness of the liner, which are usually ranging from 1 to 3 in. Depending on the volume fraction, fibers can increase the flexural strength of a fiber reinforced mortar by 25%-55% in compare to conventional Portland cement mortar (Roesler and Gaedicke 2004). To maintain the SAPL workability, the volume fraction should not exceed 3% of the cement mortar (Luk 2001; Ramakrishnan et al. 1998). Table 1-3 presents the suggested volume fraction of fibers. A medium volume fraction (i.e., 1 - 3 %) can increase the post crack load-carrying capacity for both tensile and flexural. In addition, it enhances shrinkage crack resistance, durability, energy absorption, toughness, and impact resistance of SAPLs.

Table 1-3. Volume fraction of fibers (Ramakrishnan et al. 1998)

Fiber Addition	Percentage (%) of Total Volume of Concrete
High	3 - 12
Intermediate	1 - 3
Low	0.1 - 1

1.3.5.4. Mesh Reinforced Cementitious SAPL

As an alternative to fiber reinforced SAPLs, mesh reinforcement can be used to fortify the cementitious SAPL and weak zones (i.e., crown and invert). Generally, there are two types of mesh that are currently used; welded wire mesh, non-metallic mesh, and basalt mesh reinforcements. The welded wire mesh is used by many DOT's to minimize age dependent cracking in the slabs which are not subjected to structural loading (ACI318.2-14). Welded wire mesh reinforcements are fabricated from cross laid wires welded at the cross-passed points. The minimum over for metallic mesh reinforcements is 1 in. Non-metallic mesh is significantly more flexible than metallic meshes. The typical non-metallic meshes are polypropylene and Nylon 66. A recent study conducted by Rahman et al. showed that the Nylon 66 increased the rupture modulus of mortar plate samples about 200 psi more than polypropylene and metallic meshes (Rahman et al. 2013). Basalt is a kind of inorganic fiber made by the extrusion of melted basalt rock. This type of mesh has better tensile strength, and greater failure strain than other types of meshes.

Basalt reinforcement mesh geo-grid is available in different sizes with epoxy coatings for cementitious composites. They can be stronger than steel wires of comparable size, lighter and

easier to install. Basalt reinforcement mesh geo-grid does not rust or corrode or cause cracking and does not conduct electricity or induce electric fields. Furthermore, basalt mesh has a good resistance to chemical attack, impact load, and fire with less poisonous fumes. Therefore, basalt mesh has a good potential to be a replacement for glass, steel, and carbon fibers in many construction applications. The advantage of using a basalt mesh over a polymeric mesh for reinforcement of the SAPL is that it is not affected by high or low temperatures as the polymeric meshes. In addition, due to their volcanic origins, they can bond quite well to the cementitious SAPLs.

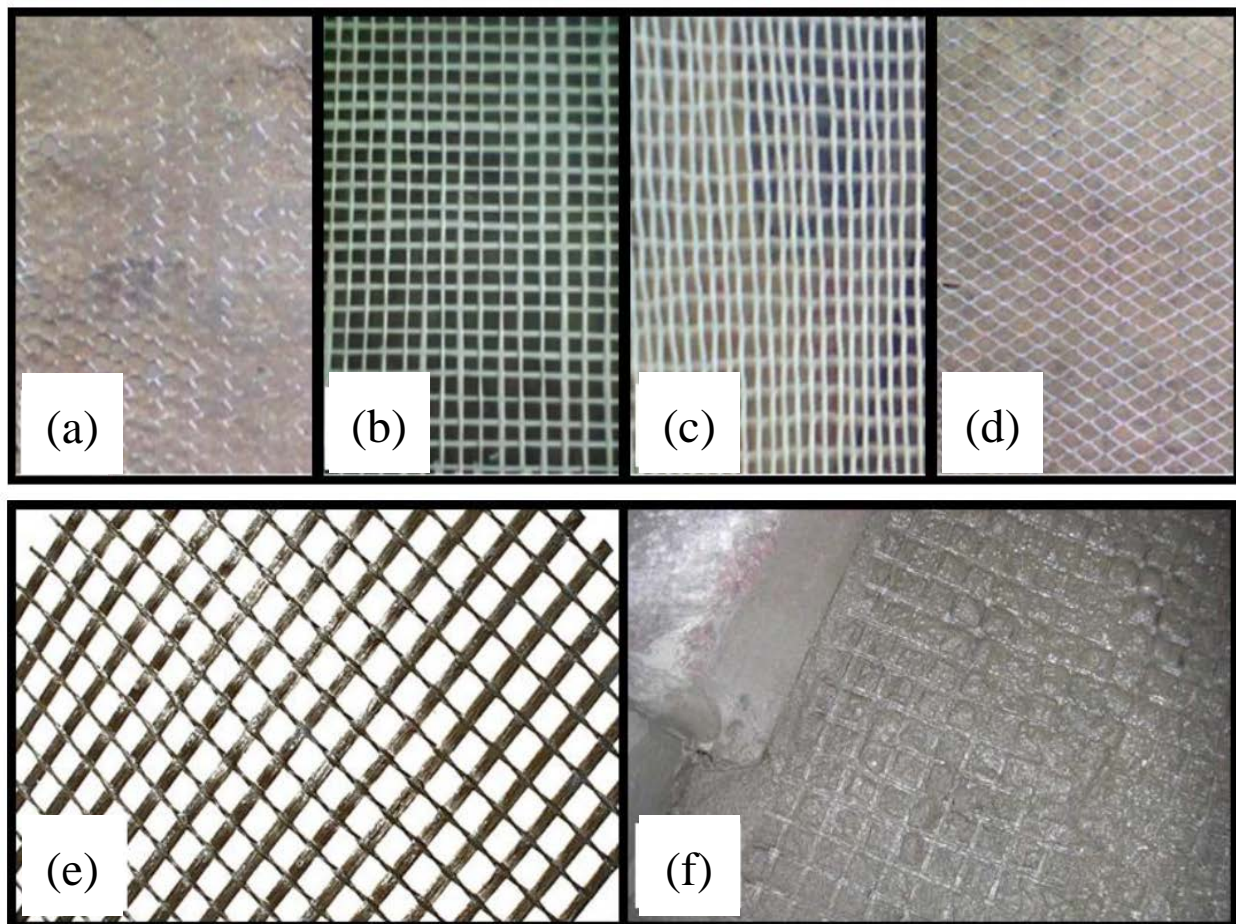


Figure 1-34. Different types of mesh reinforcements: (a) hexagonal iron mesh, (b) woven polypropylene, (c) woven Nylon 66, (d) expanded metal mesh, (e) basalt mesh grid, and (f) basalt mesh placed into wet concrete prior to final layer's placement.

1.3.5.5. SAPL Installation Options

The cementitious SAPLs typically are installed on culverts with 36 in. diameter and larger. The cementitious SAPL can be applied on CMPs by either filling or following the corrugations, as illustrated in Figure 1-35. The minimum finished thickness of these SAPLs are usually between 0.50 and 1.0-in., dependent on the conservatism of the design engineer or pipe owner. However, considering these minimum values, for a pipe having a low corrugation depth, such as $2\frac{2}{3}\times\frac{1}{2}$ in., it is not practical to follow shallow corrugation for any thickness of liner. Therefore, for shallow corrugation profiles, filling the corrugations would be unavoidable for all three installation methodologies.

For larger corrugation profiles, such as 6×2 in., using the following corrugation pattern saves a significant amount of material on these CMPs, which makes the vendors to take a serious consideration of this alternative. However, a graphical analysis of the lining process shows that using a spin-caster pulled at a constant rate of speed through such a pipe and applying the liners perpendicularly to the crest surface, would result in a shortfall of approximately 27% on the sloped surfaces of the corrugation section (see Figure 1-35). Therefore, the sloped section of the corrugations always receives lesser amount of SAPL than what is prescribed and consequently this section is more vulnerable to crack. To compensate this, an increase of thickness to the crest of the corrugations is needed (i.e., increasing the thickness of liner 30% more). For the pump-trowel and shotcrete installation methodologies, more controls need to be used on the sloped surfaces, but this puts too many expectations on the installer and the quality assurance inspection process itself to assure that the specified thickness can be "uniformly" applied.

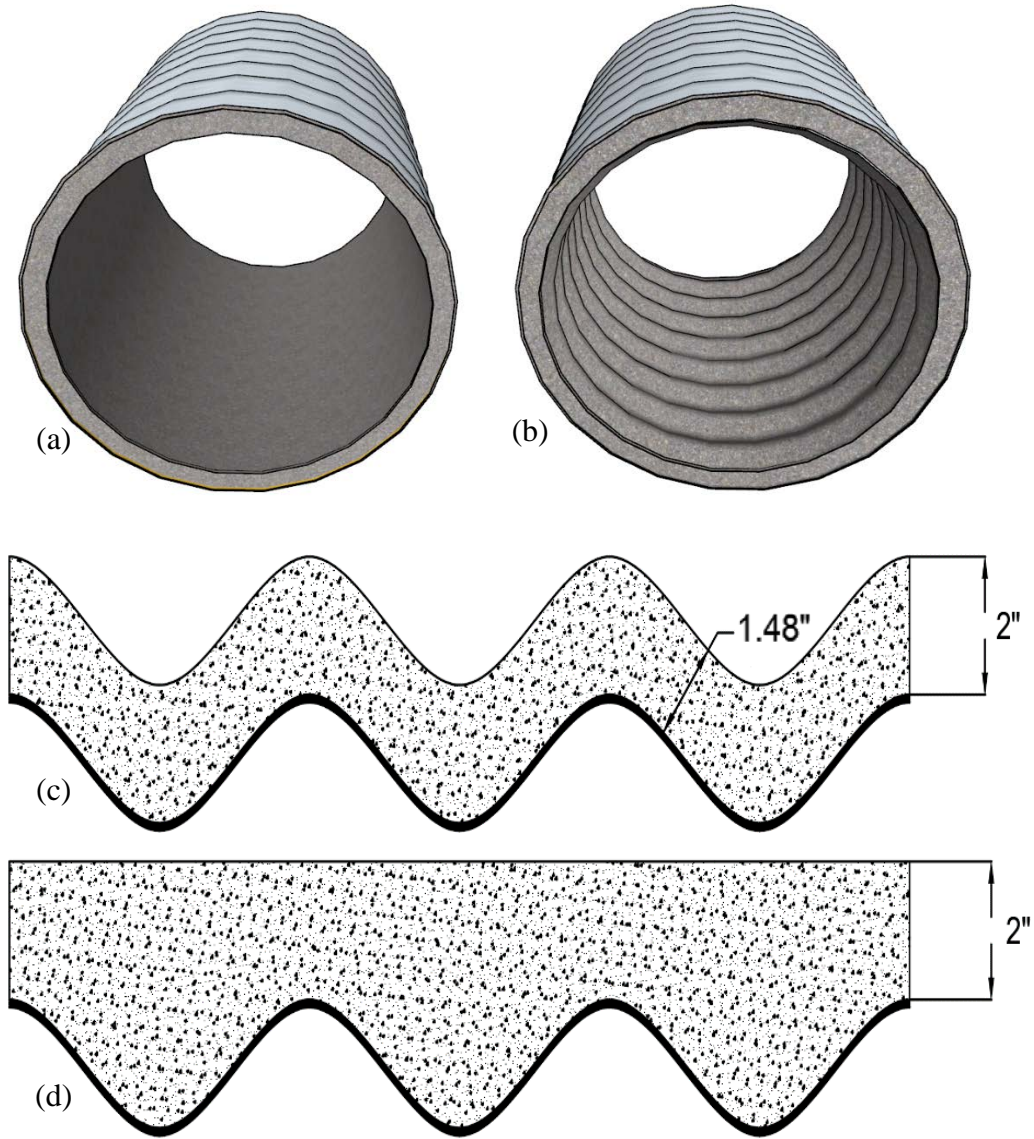


Figure 1-35. 6×2-in CMP renewed with SAPL: (a & d) followed corrugation with shortfall at the sloped surface, and (b & c) filled corrugation pattern.

1.3.5.5.1. Hydraulic Efficiency

In addition to the impracticality of following the corrugation for shallow profiles, stated above, there is hydraulic requirements for the SAPL renewed culvert. The Manning's coefficients

value for the "follow the corrugation profile" versus "filling the corrugation profile" produces a significant difference in the hydraulic capacity of the culverts, when in outlet control.

In gravity conduits (i.e., culvert) the moving force of the flow is provided by gravity. However, the friction between the flow and the culvert losses the flow energy. The Manning equation is the most commonly used equation governing gravity conduits, which is an empirical approach. The equation takes into the account the channel velocity, conduit roughness, flow area, and channel's slope. The Manning's formula is written as:

$$Q = V \cdot A = \frac{K \cdot A \cdot R^{2/3} \cdot S^{1/2}}{n}, \quad (28)$$

where, Q (ft³/s) is flow rate, A (ft²) is cross-sectional area of flow, V (ft/s) is velocity, R (ft) is hydraulic radius, S (ft/ft) is slope of channel, K is the unit constant (i.e., 1 for SI and 1.49 for Imperial units), and n is the Manning's roughness coefficient.

While the purpose of the culvert renewal with cementitious SAPL is to provide durability and longevity to the existing culverts at a minimum wall thickness, other performance parameters, such as hydraulic capacity, should be maintained or improved as well. Having two same size CMP culvert with the same flow area, pipe slope, and hydraulic radius, causes the Manning roughness coefficient, to play an integral role for hydraulic capacity of the pipe. Therefore, filling or following the corrugations with SAPL directly effects the hydraulic efficiency of the renewed CMP culvert.

Figure 1-36 illustrates hydraulic comparison of 2 2/3×1/2, 3×1, and 5×1 in. annular CMPs, renewed with both filled and followed corrugation pattern cementitious SAPL versus the bare CMP. The slop of the culvert, and diameter of CMPs were assumed 0.01 (ft/ft) and 60 in.

respectively. The Manning's coefficient of bare CMPs were selected from Table 1-5, and the Manning's coefficient of SAPL renewed CMPs with filled corrugation condition were assumed to be the same as a concrete pipe with the averaged coefficient of 0.013, selected from Table 1-4. In addition, the Manning's coefficient of SAPL renewed CMPs with followed corrugation pattern condition were assumed to be same as the host CMP. It is noteworthy that these assumptions were made due to the lack of any information regarding the Manning's coefficient of cementitious SAPL.

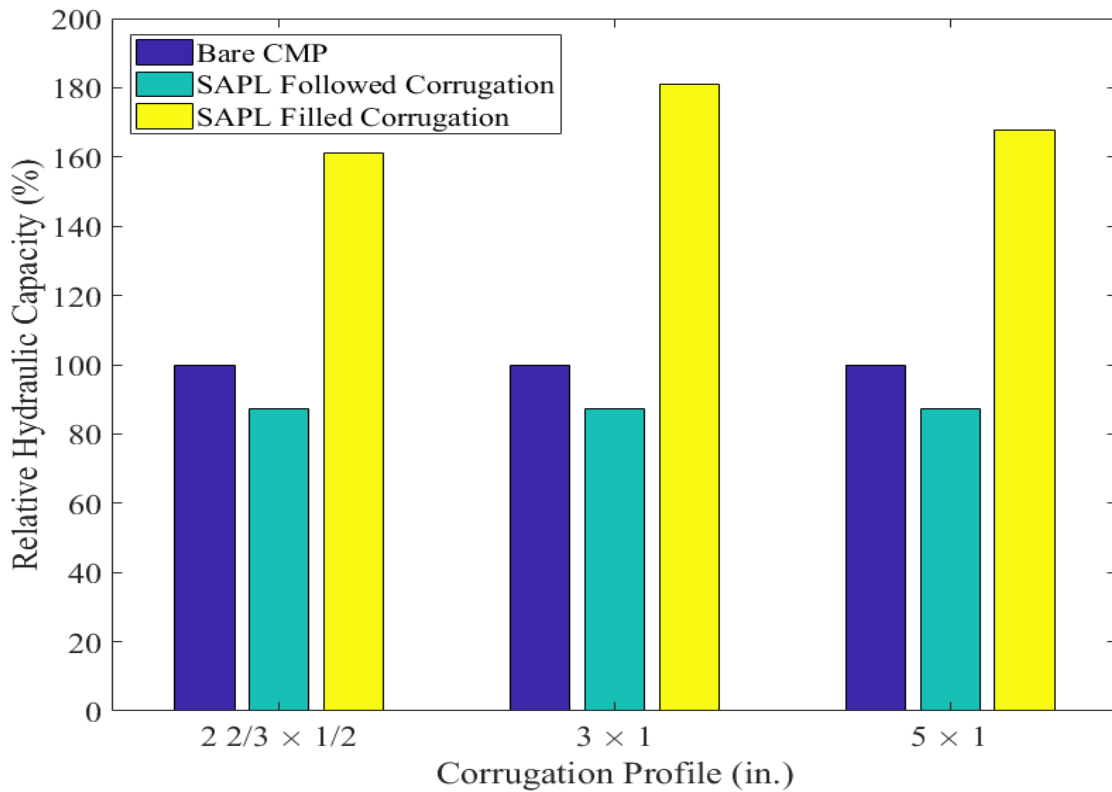


Figure 1-36. Hydraulic capacity comparison of SAPL renewed CMPs with a bare CMP.

Table 1-4. Manning’s coefficients for gravity conduits (American Iron and Steel Institute 1999).

Conduit Material	Manning’s Coefficient (n)
Asbestos-cement	0.011 - 0.015
Brick	0.013 - 0.017
Cast iron pipe with cement lined & seal coated	0.011 - 0.015
Concrete (monolithic)	
Smooth forms	0.01 - 0.014
Rough forms	0.015 - 0.017
Concrete pipe	0.011 - 0.015
Verified clay	
Pipes	0.011 – 0.015
Liner plates	0.013 – 0.017

Table 1-5. Manning’s coefficients for CMP conduits (American Iron and Steel Institute 1999).

Corrugation	Annular 2 ² / ₃ in.	Helical													
		1 ¹ / ₂ × 1 ¹ / ₄ in.		2 ² / ₃ × 1 ¹ / ₂ in.											
Flowing	Diameters	8 in.	10 in.	12 in.	15 in.	18 in.	24 in.	30 in.	36 in.	42 in.	48 in.	54 in. and larger			
Full Unpaved	0.024	0.012	0.014	0.011	0.012	0.013	0.015	0.017	0.018	0.019	0.020	0.021			
Full 25% Paved	0.021						0.014	0.016	0.017	0.018	0.020	0.019			
Part Full Unpaved	0.027			0.012	0.013	0.015	0.017	0.019	0.020	0.021	0.022	0.022			
Flowing	Pipe-Arch				17×13	21×15	28×20	35×24	42×29	49×33	57×38	64×43 and larger			
Full Unpaved	0.026				0.013	0.014	0.016	0.018	0.019	0.020	0.021	0.022			
Part Full	0.029				0.018	0.019	0.021	0.023	0.024	0.025	0.025	0.026			
	Annular 3×1 in.	Helical													
		3×1 in.													
Flowing	Diameters								36 in.	42 in.	48 in.	54 in.	60 in.	66 in.	72 in.
Full Unpaved	0.027								0.022	0.022	0.023	0.023	0.024	0.025	0.026
25% Paved	0.023								0.019	0.019	0.020	0.020	0.021	0.022	0.022
	Annular 5×1 in.	Helical													
		5×1 in.													
Flowing	Diameters										48 in.	54 in.	60 in.	66 in.	72 in.
Full Unpaved	0.025										0.022	0.022	0.023	0.024	0.024
25% Paved	0.022										0.019	0.019	0.020	0.021	0.022
All Pipe with Smooth Interior		All Diameters 0.012													

The hydraulic comparison of the filled versus following corrugation pattern of SAP, illustrated in Figure 1-36, showed that the action of filling the corrugation increases the hydraulic capacity of the renewed culvert as filling the rough corrugations always resulted in lower Manning's coefficient which can increase the hydraulic capacity up to 80%. While following the corrugation pattern will always result in lower hydraulic capacity as the reduced diameter effect the flow discharge rate. Thus, if preservation of the existing culvert's hydraulic capacity is indeed a design consideration for the DOTs, then filling of the corrugations and then applying the liner thickness is a recommended alternative, when the structure is in outlet control.

In addition to the higher hydraulic efficiency of the filled corrugation with SAPL, a smooth surface profile can produce a lowered tendency to catch debris (i.e., tree limbs) as it is moved through the pipe barrel. Moreover, smooth surface brings protection against impact damage from large rocks and boulders as they pass through the culvert. Therefore, filling the corrugations reduces abrasion and provides better corrosion coverage over any protruding CMP assembly hardware, i.e. bolts and rivets. To achieve a minimum cover thickness in the valley area basically demands filling the valley area.

1.3.5.5.2. Structural Efficiency

A concrete pipe under vertical loading has two modes of failure: beam failure (i.e., longitudinal bending) and ring failure. It is already proven that the ring failure is most dominant situation (Bazant and Cao 1987). Concrete pipe ring failure occurs due to the crack initiation from inside of the crown and invert. Secondary cracks later initiate outside of the spring lines (see Figure 1-33). Due to the soil loading and boundary conditions, these pipe's regions are subjected to tension stresses and generally concrete is much weaker in tension than compression. Darabnough Tehrani (2016) studied the standard ASTM-C76 reinforced concrete pipes' behavior under the

three-edge bearing test (TBT) configuration using experimental testing and finite element analysis. He also studied the effect of one layer of reinforcements at different locations in pipe thickness. Both experimental tests and FEM analysis showed the more reinforcement get closer to the outer surface of the pipe, the more improvement goes to the pipe ultimate strength, but weakens the pipe against service load cracking at the crown and invert. Likewise, under the assumption of perfect bonding (i.e., composite behavior), a renewed CMP with cementitious SAPL has a steel reinforcement at the outer surface that helps with ultimate strength but cannot support the SAPL for service load cracking at the crown and invert. Therefore, the effect of filling or following the corrugation pattern of SAPL can be another factor to increase the structural efficiency of the renewed CMP with cementitious SAPL. To achieve this goal, the cracking moment at the crown of 30 different combination of all corrugation profiles, demonstrated in Table 1-1, for different thicknesses of 0.5, 1, and 2 in. SAPL thickness have been calculated. The cracking moment of composite cross section can be obtained as follows:

$$M_{cr} = \frac{I_c \cdot f_r}{y_t}, \quad (29)$$

where, f_r (psi) is the modulus of rupture, y_t (in.) is the distance from the neutral axis to the extreme fiber in tension, and I_c (in.⁴) is the moment of inertia with respect to the neutral axis. However, in the composite sections, such as CMP renewed with cementitious SAPL, instead of I_c , the transformed-section's moment of inertia should be calculated. Where, the cross-section of a composite component, made of different materials, is transferred to an equivalent cross-section of one material. It is noteworthy, that in the transformed-section method, the neutral axis of composite and transformed section should be the same to provide same moment-resisting capacity. To transform a section, the modular ratio should be computed and multiplied by the area of the

stronger material, i.e. CMP in this case, and the material will be replaced with the weaker material of equivalent area. The modular ratio for the CMP-SAPL is defined as follows:

$$n = \frac{E_{CMP}}{E_{SAPL}}, \quad (30)$$

where, E_{CMP} (psi) and E_{SAPL} (psi) are the elastic modulus of the CMP and SAPL respectively. Figure 1-37 illustrates the transformed-section for CMP-SAPL for both filled and followed condition.

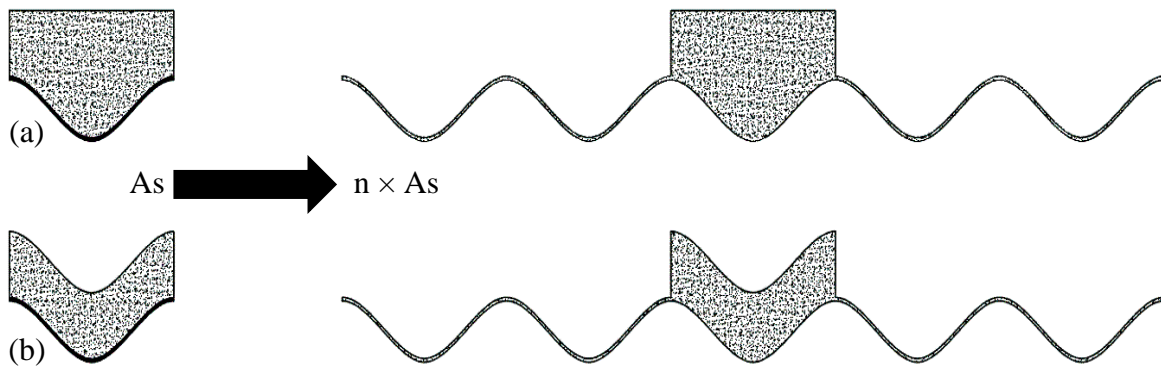


Figure 1-37. Transformed-section with the same neutral axis for: (a) filled corrugation, and (b) followed corrugations.

In this study the elastic modulus of the galvanized CMP and cementitious SAPL is considered as 29,010,000 and 5,802,000 psi, respectively. Also, the modulus of rupture for the SAPL is considered 1,000 psi. These material properties might vary from one manufacturer to another. Knowing the modular ratio, the moment of inertia and the distance of the neutral axis to the extreme fiber at tension surface, (i.e. inner surface of the SAPL), for the transformed-section have been calculated using AutoCAD 2019. Figure 1-38 illustrates the cracking moment capacity of 30 combinations of different SAPL thicknesses for filled and followed different corrugation

patterns. The results show that filling the corrugation can significantly enhance the cracking moment capacity of CMP-SAPL composite sections. The difference is more evident in the deeper corrugation profile sections, such as 6×2 in. In some cases (e.g. 3×1 in. corrugation profile), following the corrugation pattern will result in lower cracking capacity than one size smaller corrugation (i.e., 2⅔×½ in. corrugation profile) with filled pattern. Figure 1-39 shows the cracking moment capacity improvement by filling the corrugation in compare with followed corrugation pattern in different profiles. The results also show that in the deeper profiles, (e.g. 6×2), the effect of filling the corrugation is much more significant than the smaller corrugations such as 1½×¼.

In addition to the cracking moment capacity enhancement, since the pipe's ring stiffness is directly proportional to the section's moment of inertia, filling the corrugation is also beneficial to increase the ring stiffness. However, this is under the assumption of perfect bonding between the SAPL and the host pipe (i.e. composite section). If the bond is loose or gone, then the compound section moment of inertia should be calculated, which provides lesser value for ring stiffness.

The pipe's ring stiffness can be calculated as follows:

$$Rs = \frac{EI}{D^3}, \quad (31)$$

where, E (psi) is elastic moment, I (in.⁴) is moment of inertia of the pipe's cross section, and D (ft) is the diameter.

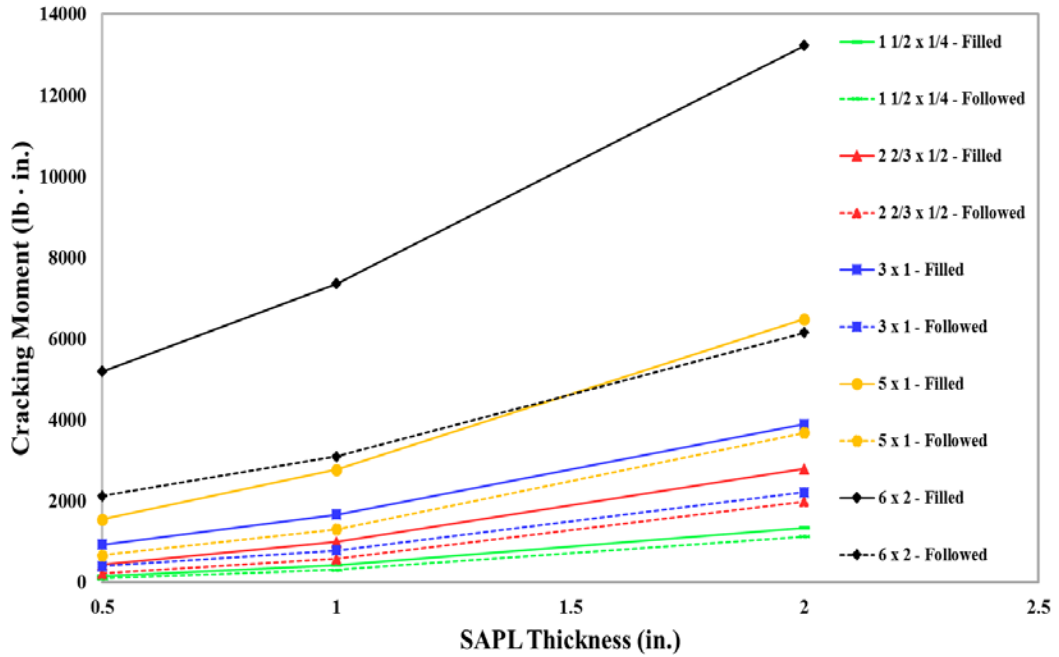


Figure 1-38. Cracking moment capacity of renewed CMP with SAPL at the crown.

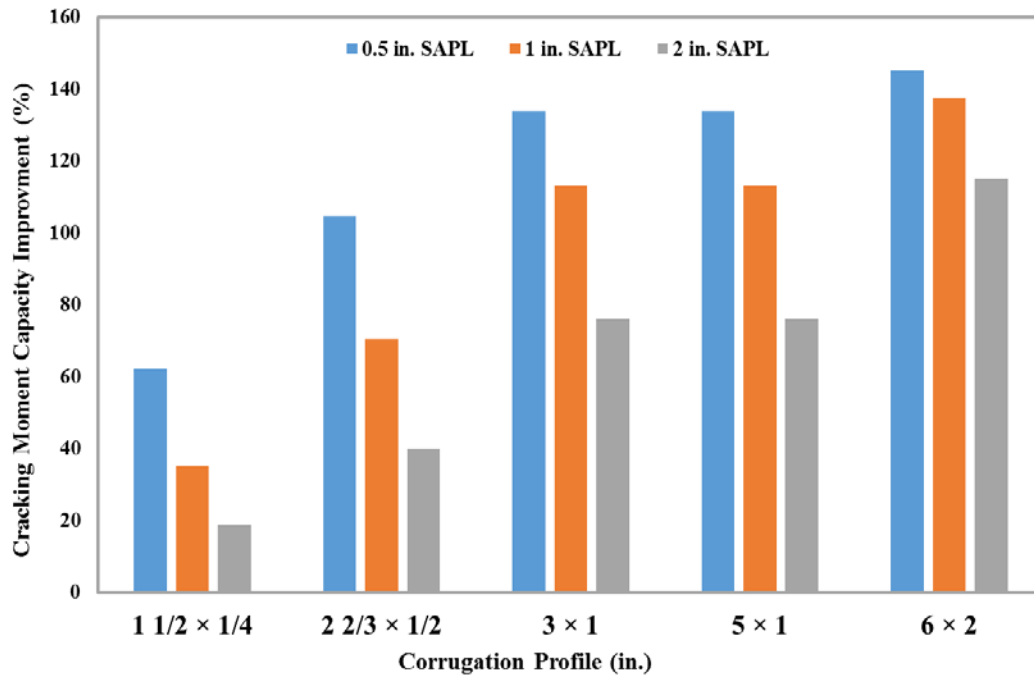


Figure 1-39. Cracking moment improvement by filling the corrugation compared with following corrugation pattern of the renewed CMP with SAPL.

1.4. Objectives

The objectives of this study are:

- a) to examine the performance of invert-cut circular and arch CMP culverts renewed with a commercially available cementitious SAPL through a series of full-scale laboratory soil box testing,
- b) to compare the renewed CMPs with a same size invert-cut bare (unlined) CMPs,
- c) to observe failure modes and cracking pattern of CMPs renewed with cementitious SAPL during the applied static load,
- d) to investigate the feasibility of cementitious SAPL application as a fully structural renewal method
- e) to investigate the applicability of currently available design equations for cementitious SAPLs, and
- f) to propose a design methodology for CMP renewal using cementitious SAPL.

1.5. Methodology

Since December 2017, a group of researchers at the Center for Underground Infrastructure Research and Education (CUIRE) at the University of Texas at Arlington have been conducting a comprehensive study to develop structural design methodologies for polymeric and cementitious spray applied pipe linings (SAPLs). The research program was developed by the U.S. National Cooperative Highway Research Program (NCHRP) sponsored by seven US DOTs of DelDOT, FDOT, MnDOT, NCDOT, NYSDOT, Ohio DOT (lead of the project), and PennDOT. The program includes five sets of full-scale soil-pipe structural testing (Darabnough Tehrani et al.

2020a; Syar et al. 2019). To investigate the soil-pipe structural capacity, the CMPs were backfilled with SP soil and buried under 2 ft of soil cover. A monotonic displacement-control static load was applied through a rigid 20 × 40 in. steel load pad over the crown of the pipes.

The obtained results from the experimental tests including deflection magnitude, force, and strain values will be compared from the results obtained from the available base equations (i.e., potential equations), presented in the section 2.3. The result comparison may result in three scenarios where (1) both data are perfectly match, which in this case, no new equation is needed to be developed, (2) both data are slightly match that requires moderated equation modification, and (3) both data are completely in a different trend, then a new equation must be developed.

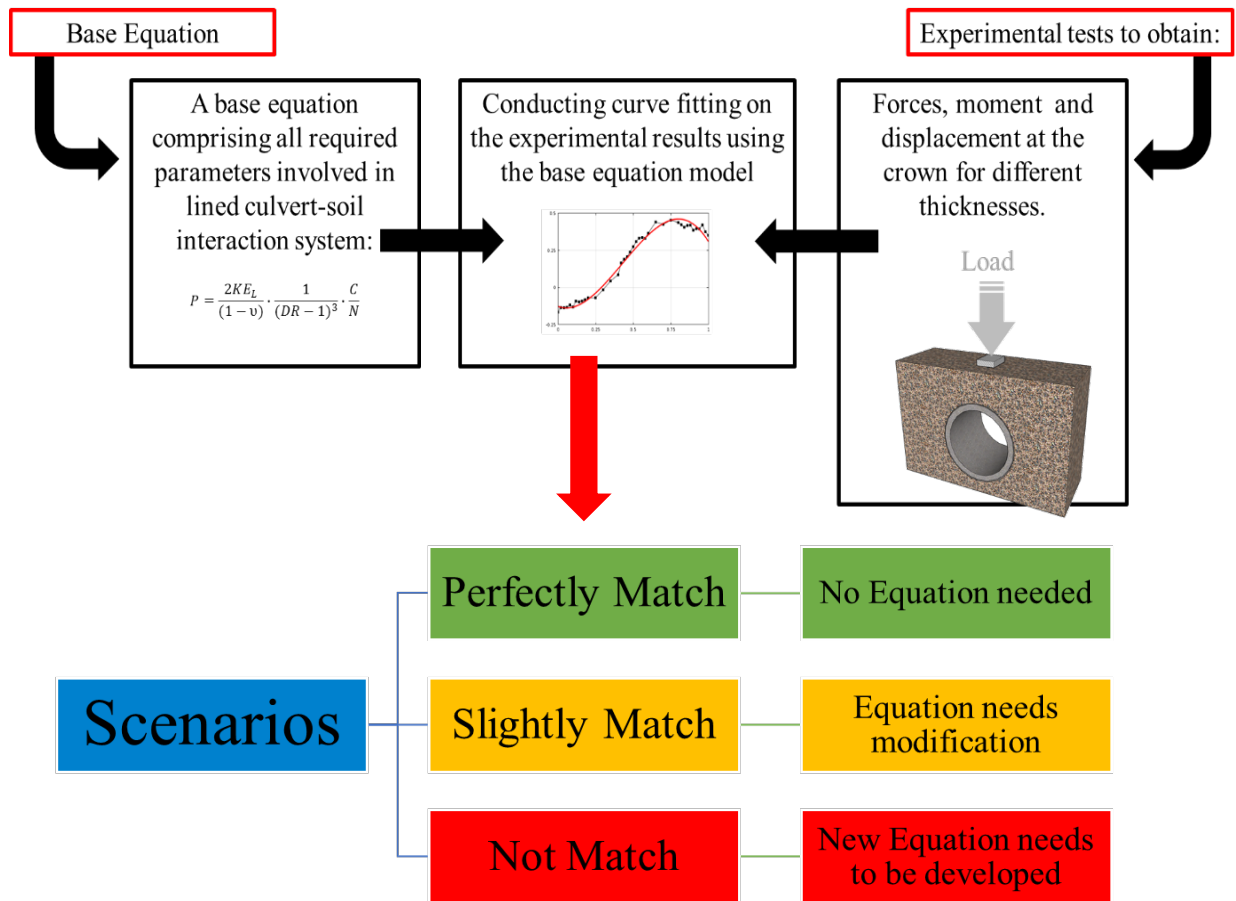


Figure 1-40. Design methodology development methodology.

1.6. Contributions to the Body of Knowledge

Previous studies have tested partially deteriorated renewed CMPs with SAPL, however, behavior of a fully invert-cut CMP (to simulate a fully deteriorated condition) renewed for cementitious SAPL for both circular and arch shapes were not studied before. This study compared behavior of cementitious SAPL with bare CMPs (control test) in shallow cover condition.

The major contributions to body of knowledge in this study are summarized below:

- Structural evaluation of invert-cut CMP, renewed with cementitious SAPL for both arch and circular shape.
- Comparison of structural behavior of cementitious SAPL-renewed CMP with bare CMPs.
- Development of proposed structural design equations for both circular and arch CMP.
- Evaluation of SAPL installation methods, and provided related recommendations based on different analyses.
- Comparison of the load bearing capacity of circular and arch CMPs.
- Pipe profiling method development using DIC.
- Soil-structure testing method development.
- SAPL material evaluation.

CHAPTER 2. LITERATURE REVIEW

2.1. Soil-pipe Testing

Generally, there are two common types of soil-pipe testing methods: field testing and laboratory testing. However, there is a third testing method which is a combination of both laboratory and field testing method. Selection of each method depends on the logistics, equipment, scale of the pipe sample, and the test requirements (Darabnoush Tehrani et al. 2020c).

2.1.1. Field Testing Method

Field testing is usually conducted by digging a trench and placing the pipe sample in field and backfilling to a required cover height or testing an existing pipe in service by passing or placing a weight on top of the pipe sample (Chaallal et al. 2014; Mahgoub and El Naggar 2019; Wang et al. 2016). The term “weight” in here refers to the weight of the soil or any designated objects, like concrete blocks that applies load on the soil-pipe system (Nehdi et al. 2016).

Pocock et al. (1980) studied on the effect of static and rolling wheel loads on shallow buried 4 in. steel pipe using experimental testing. The center of pipes was selected for instrumentation, to eliminate possible end effects. The pipes were installed in field with 2 ft soil cover, clay, and 0.3 ft of flexible pavement. The loading was applied using four vehicles with different weight and axle spacing loaded with concrete blocks. For the static loading, the rear axle of vehicles was positioned on the pipe for several minutes (the duration is not mentioned). For the rolling wheel loading, the vehicles were drove at the speed of 10, 20, and 30 mph. The test result showed that the static loading produces higher strain at pipes.

Sargand et al. conducted an experimental study to evaluate time-dependent deflection of thermoplastic pipes under deep burial cover (Sargand et al. 2001a). The pipes were buried 40 ft (12.2 m) deep and backfilled with Ohio Department of Transportation (ODOT) 304 at 96 percent compaction. The pipes' deflections were measured due to the weight of soil over the pipes. To measure the applied pressure at different depth of soil, earth pressure cells were used. It was observed that the higher pressure would be applied over the crown of the pipes at deeper depth (Sargand et al. 2001b).

Arockiasamy et al. (2006) carried out field testing on flexible pipes under live load application for 36 in. HDPE, PVC, steel, and aluminum pipes. The burial depths were 1.5, 3, and 6 ft using SP-SM backfill material. The backfill compaction rate was 95%. The loading was carried out using two different trucks; the tandem dump truck and the FDOT truck. Both were loaded with concrete blocks based on the required axle loads. The loading rate, which in this case means the speed of the truck to be positioned on the pipe, is not mentioned. Therefore, it is assumed that the loading of the pipe from zero to reaching the maximum load (40.7 kips) is relatively fast. The paper concluded that all pipes had vertical deflection less than 5%, which is required by AASHTO. It was also observed that deeper buried pipes had fewer deflections, which indicates that the live load dominates the dead load on pipe deflection.

Yeau et al. (2009) carried out in situ testing on 39 in. large corrugated metal culverts in Ohio under static and dynamic loadings. The objective of the testing was to evaluate culverts under loading of either the standard HS20-44 truck or ODOT buried structure research truck (BUSRET) with total weight of 63 kips. For static load tests, the truck was positioned over the culverts to ten static load cases. The ten loads comprising of placing front load and rear center load at predefined locations of A, B, C, D, and E. Then, each culvert was tested by passing a truck at the speed of 5,

10, 15, 20, 30, and 40 mph. As a consequence of field testing, there is no record of the loading rate. The study showed that the maximum deflection was nearly zero for deep culverts with backfill height more than 13 ft. Also, the maximum dynamic loading was approximately 30% less than corresponding deflection for static truck loading. A detailed parametric study on the effect of static and dynamic load of the buried culverts have been conducted by Alzabeebee et al. through a robust numerical modelling and verified the results (Alzabeebee et al. 2018).

Rakitin evaluated the performance of a 70 in. reinforced concrete pipe (RCP) under a car, medium truck and heavy truck loads (Rakitin 2010; Rakitin and Xu 2014). The vehicles were passing slowly on top of the pipe. The RCP was buried under 3 to 13 ft soil covers. The study concluded that deeper soil cover reduces the influence of the traffic load, which is in conformity with AASHTO specifications. In addition to that, the pipe would experience the most unfavorable conditions when the heaviest axle of the traffic vehicle was located directly above the pipe crown.

Chaallal et al. studied on field test performance of buried flexible pipes under live truck loads (Chaallal et al. 2014). The specimens comprising of 36 in. HDPE, PVC, steel, and aluminum pipes under burial depth of 1.5, 3, and 6 ft. It was reported that the backfill compaction rate was 95%. The loading was conducted using the tandem dump truck (design highway load HS-20 truck) and the FDOT truck. Both were loaded with concrete blocks based on the required axle loads. The loading rate, which in this case means the speed of the truck to be positioned on the pipe, is not mentioned. Therefore, it is assumed that the loading of the pipe from zero to reaching the maximum load (40.7 kips) is relatively fast. The results showed that the HDPE and PVC pipes' vertical deflection were double the horizontal diameter change, while in the steel and aluminum pipes the differences were negligible. In general, the vertical and horizontal diameter changes for 3 and 6 ft

burial depth were very smaller than pipes with 1.5 ft soil cover. The pressure cells also showed that the deeper the pipe the less pressure transfers to the pipe.



Figure 2-1. Pipe installation and testing method (Chaallal et al. 2014)

Liu et al. evaluated structural performance of two corrugated metal pipes (CMPs) with 4 ft (1.2 m) diameter, but different corrugation profiles buried under 13 ft (4 m) of soil cover through field testing conditions (Liu et al. 2016). The test was carried out by excavating the initial ground surface, then placing the pipes and backfilling up to the required height. In this test, the deflection of pipes was measured against the placement of different layers of soil cover, in the absence of any other external load on the pipes. The study concluded that larger deformation of the flexible pipe makes the interaction of soil and pipes evident, which reduces the vertical pressure of backfill soil on the pipes.



Figure 2-2. Field pipe testing using soil dead load (Liu et al. 2016)

Takou et al. (2017) measured pipe deflection during embedment and backfilling of a 108 in. (2.7 m) diameter steel pipe with controlled low-strength material (CLSM) and compacted native soil. In the study, the only load that was applied on the pipe was the weight of the backfill material. In similar studies, however, a vehicle (mostly trucks) with a specified weight and wheel size is used rather than loading via concrete blocks or soil weight (Mahgoub and El Naggar 2019; Rakitin and Xu 2014). In many cases, the selection of the vehicles and their weights are based on roadway design standards like AASHTO LRFD Bridge Design Specifications (2017).

Sargand et al. (2018) conducted field testing of a shallow cover severely deteriorated arch CMP at Coopermill Road in Muskingum County, Ohio. Asphalt concrete pavement was applied on the half of the pipe sample's invert as a repair method and the other half was left unpaved. Static loading was applied at the top of the paved and unpaved pipe sample sections respectively. The test results showed that the unpaved section was subjected to higher transverse strain at the crown compared to the paved section, while transverse strain difference at the springline was inconsequential. Moreover, despite the advanced level of deterioration, both sections of the culvert carried significant load capacity. For untreated section the plastic limit of the steel was exceeded

at the crown with the load of 60-kip. It should be noted that, due to different levels of water exfiltration, soil strength around different locations of the pipe sample may not have been the same and level of CMP's deterioration might not have been the same along the culvert.

Liu et al. (2020) conducted field testing on an open-bottom low profile arch CMP with the span of 122 in. and rise of 51.96 in. The culvert had cover depth of 17.71 in. The load was applied using a dump truck with tandem rear axles and total load of 59.5 kips. The objective of the study was to evaluate different deflection measurement systems including fiber-optic strain sensors, digital image correlation (DIC) method, total station, and Lidar optical sensor. To measure the culverts' deflection, the truck's rear wheel pairs were positioned over the culvert at different locations as illustrated in Figure 2-3. The study concluded that the applied live load was not distributed evenly in the longitudinal direction and was reduced by 50% at a distance of 17.7 in., longitudinally from the wheel pairs. It was also observed that the highest vertical displacement can be achieved when one truck wheel pair was positioned directly above the crown of the culvert.

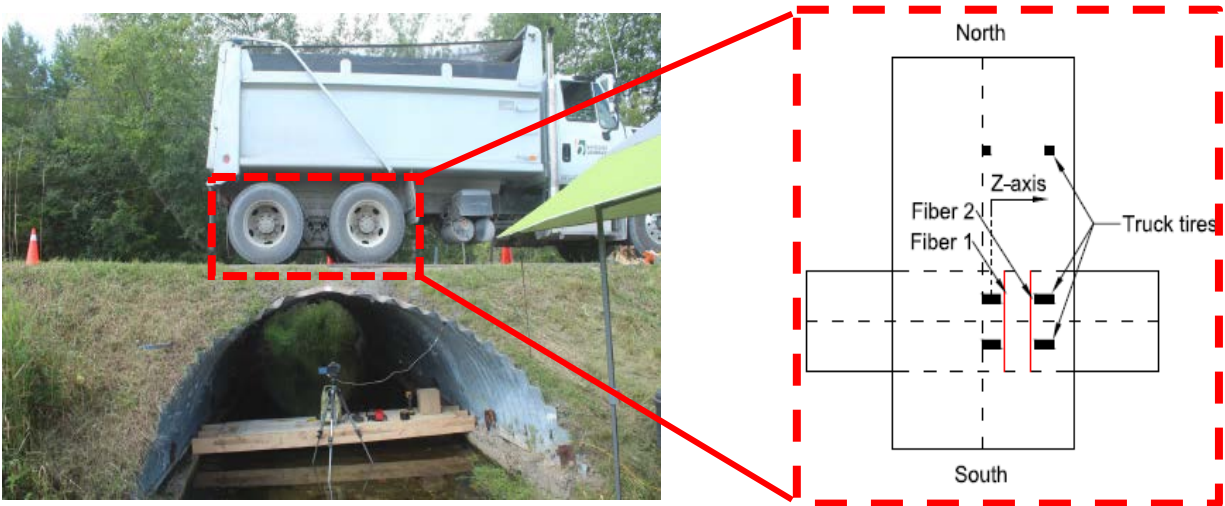


Figure 2-3. Test culvert, truck and the layout of the truck position over the culvert (Liu et al. 2020).

In case of the field test method and in the absence of a hydraulic actuator, there is no recording of load rate and it can be assumed that the load is being applied continuously and in a short period of time since the maximum load will be applied once the weight/truck is located on top the pipe. This is one of the biggest disadvantage of field test method, as the loading increment and its rate cannot be controlled. In addition, other parameters, such as soil moisture content, and ambient temperature are out of control. Nearly in all field testing cases, to prevent damage to the truck and instrumentations, these tests are not designed to fail the soil-pipe structure.

2.1.2. Laboratory Testing Method

Laboratory test method is to carry out the tests under the laboratory condition using a hydraulic actuator, which provides more control on the load rate, type of the applied load, soil moisture content, etc. (Becerril García and Moore 2015; Khatri et al. 2015; Kunecki and Kubica 2004). There are two methods to control the loading: force-control and displacement-control. In the force-control method, the actuator applies a prescribed load increment at a certain amount of time (e.g., 300 lb/min). While, in the displacement-control method, the actuator applies prescribed displacement increment at a unit of time (e.g., 0.05 in./min) (Darabnoush Tehrani 2016; Sivaselvan et al. 2007; Syar et al. 2020). Displacement-control is utilized more frequently when the post failure behavior of the testing sample is important to be monitored (Ghahremannejad and Abolmaali 2018). Both methods can be applied in two loading regimes: incremental loading, and continuous loading. In incremental loading regime, the load is applied incrementally and held for few minutes after each increments to stabilize the soil (Al-Naddaf et al. 2018; Becerril García and Moore 2015; Munro et al. 2009). This technique is more appropriate for a soil type containing clay particles, where delayed soil settlement, consolidation or stabilization is concerned. In contrast,

continuous loading regime applies the load non-stop until a prescribed load/displacement value or specimen structural failure is attained. It is noteworthy that the continuous loading regime is being widely used for structural evaluation of pipes, such as three edge bearing test or parallel plate test method (ASTM-C497 2003; ASTM D2412 2018).

In general, laboratory testing provides more control on different parameters affecting on the test. Although it has numerous advantageous over the field testing, it is not without limitation or unfavorable effects of laboratory testing condition. Barchman et al. (2000) have studied the effect of rigid walls on small pipe behavior and it was observed that the walls of the test facility can attract much of the load being placed on the ground surface if the effects of friction are not properly mitigated. As a solution, Tognon et al. (1999) was suggested the implementation of polyethylene sheeting and lubrication to lower the angle of friction down to 5°. The following studies are some of the related laboratory testing of soil-pipe systems.

Trautmann et al. (1986) conducted experimental testing to evaluate uplift force-displacement response of buried pipe during vertical ground movement. The study objectives aimed to evaluate how the force-displacement behavior varies with soil density and H/D, and to characterize the force-displacement behavior in terms of a mathematical function. The testing apparatus utilizes hydraulic actuator. The pipe sample had 4 in. diameter. The backfill was Cornell filter sand having coefficient of uniformity of 2.6 and effective grain size of 0.078 in. The loading type was static at the average displacement rate of 0.78 in./min.

Kunecki and Kubica (2004) conducted full-scaled laboratory test on arch CMP under standardized railroad loading condition. The pipe had 9.8 ft span, 7.9 ft height and 47.5 ft length with the soil cover of 2.6 ft. The backfill had well-graded material with maximum grain size of 1.2 in. at 97% compaction rate. The load was applied through two hydraulic actuators on a steel plate,

according to railway loads UIC 71 for Europe, as shown in Figure 3-2. A static pressure of 10.13 psi (128.59 Kips/load pad area) were applied in three steps comprising dynamic load factor, according to European Standards, at the duration of 20 minutes. Therefore, the load rate that was applied was 0.166 psi/min (2.14 kips/min). The result comparison of experimental tests and FEM modeling showed good agreement. However, the axial stresses in the structure were higher than numerical model.

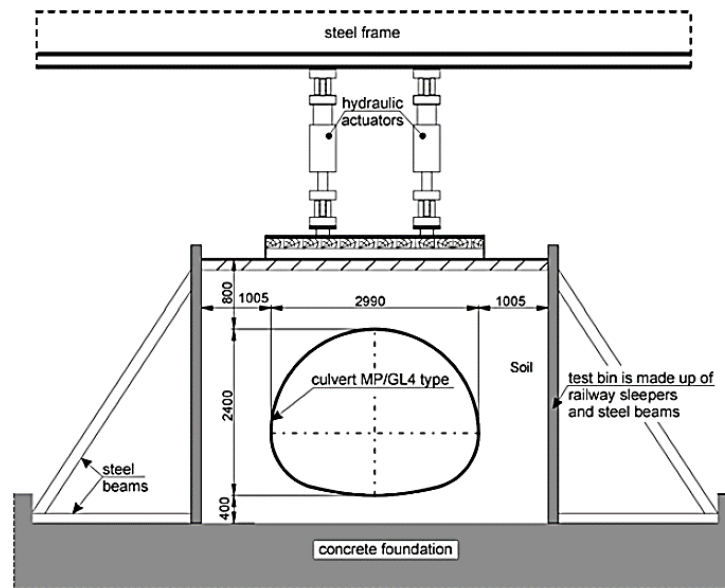


Figure 2-4. Cross-section of the culvert tested (Kunecki and Kubica 2004).

Tafreshi et al. (2012) investigated the effect of rubber-soil backfill on buried pipe subjected to cyclic loading. A 6 in. Polymeric unplasticized PVC drainage pipe was used as a testing pipe specimen with soil cover of 12.6 in. A hand operated hydraulic jack was used to apply dynamic load (cyclic load) through a circular plate. Two sets of tests were carried out; the first set includes one cycle of loading up to the maximum attainable pressure, as illustrated in Figure 2-5. The loading was incrementally applied up to the maximum attainable pressure (in that test, 114 psi) and unloading was incrementally as well. Each load increment was maintained constant to stabilize

the soil surface. The second set, the maximum applied pressure were divided to four stages of 31, 60, 89, and 114 psi to simulate the light to heavy traffic loading (Tavakoli Mehrjardi et al. 2012). For each stage loading and unloading were applied until the maximum pressure reached. However, the duration of each hold and loading rate was not reported. The research concluded that the rubber soil mixtures exhibit significant initial deformation under loading. Also using rubber- soil mixture without soil cap is disadvantageous regarding pipe responses.

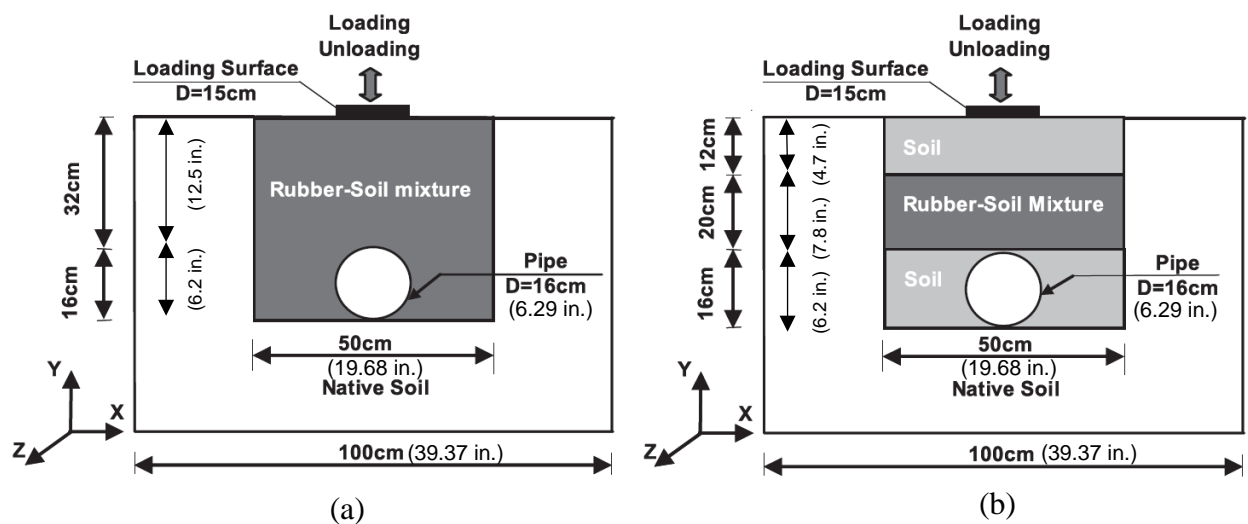


Figure 2-5. View of trench backfills: (a) first configuration; (b) second configuration (Tafreshi et al. 2012)

Mai et al. (2013) conducted experimental study on two deteriorated 71-in. CMPs. The pipe samples had different level of deterioration. They were corroded and perforated along both side of the invert. Both CMPs had bitumen asbestos protective coating, which was removed prior to the testing. The pipe samples were embedded with well-graded sandy gravel soil with 95% of the maximum dry unit weight achieved in a standard Proctor test. The CMPs were backfilled and tested with two different cover-depth of 2 and 3 ft using single axle and tandem load configuration. The result showed that higher deflection occurs at lower cover with single axle loading

configuration. In addition, despite the pipes were loaded several times under different conditions, which caused irrecoverable deformations, they were able to take the full-service load 38.22 kips in tandem configuration.

Han et al. (2016) carried out laboratory testing on steel reinforced HDPE pipes under shallow soil cover using geosynthetic grids between different soil layers. The pipe sample had 2 ft (0.6 m) diameter and was buried under 2 ft of soil cover. Polyethylene sheets were placed on the walls of the soil box to minimize the friction between the walls and the soil. Two different backfill material was used. A poorly graded from Kansas River sand based on the Unified Soil Classification System, with mean particle size of 0.02 in., and crush stone aggregate were used as the backfill materials. A clayey soil type was used for trench soil, representing native soil in field. A 9-in. thick layer of well graded aggregate was used to simulate base coarse layer of pavement. The compaction rate for the bedding and base coarse layers were 70 and 95% respectively. The objective of the test was to investigate the benefits of geosynthetic grids to the protection of shallow cover buried pipes under cyclic and static loading. The study concluded that the effectiveness of the geosynthetic material was influenced by the stiffness of the backfill. In other words, the bearing capacity of the backfill directly affects the soil-pipe bearing capacity.

Regier et al. (2016) applied static loading in an incremental force-control method on a horizontal-ellipse CMP a span of 5.2 ft and rise of 4.4 ft. The ellipse CMP was buried under 1.5 ft and 3 ft of soil cover. The load was applied through a tandem axle load configuration, where the load pads, also known as wheel pads, were placed at shoulder area. The test result showed that the maximum deflection of the CMP occurs under the load pad area and this effect is inversely proportional to the height of soil cover. Due to the asymmetric local buckling in the CMP's shoulders at the ultimate stage, i.e., end of the test, it can be implied that the load pads were not

tightly attached to the actuator. The CMP was buckled through formation of three plastic-hinge failure mechanism. Plastic hinges are yielded zones in a structural element, when the maximum bending capacity is reached (Gere and Timoshenko 1998).

Tetreault et al. (2018) have continued Regier et al. (2016) study using the same test setup with the same size horizontal ellipse CMP buried under 1.5 ft (0.45 m) of soil cover. The invert of the pipe was corroded using an accelerated corrosion technique and then was rehabilitated using a concrete paved invert method. The comparison between the corroded CMP and the intact CMP, which have been presented by Regier et al. (2016), showed that there seemed to be no impact on the structural behavior of both pipes as the pipes had similar stiffness. However, paving the invert did improve structural performance of the rehabilitated CMP in compared with the corroded CMP.

Mahgoub and El Naggar (2020) conducted a laboratory testing on an upright 88×108×70 in. rigid steel soil box. Four circular helical CMPs with 23.6 in. diameter. The CMPs were backfilled with tire-derived aggregate (RDA) in four different backfill envelop configurations. The CMPs were instrumented with mechanical sensors including LVDTs and strain gauges. The strain gauges were installed at 45° intervals circumferentially. For the foundation and embedment, a poorly graded sand, known as concrete sand, was used. The study concluded that using a TDA layer around the culvert (but not underneath) reduced the culvert deformation during backfilling by around 80% of that observed with conventional backfill materials (i.e., without TDA). In addition, it was observed that the use of TDA around the whole culvert down to the invert resulted in greater deformation and stresses than was the case for culverts with a layer of TDA only above the crown or down to the spring lines. The larger deformation of the CMP was due to the utilization of a TDA layer around the whole culvert resulted in less confinement, thus allowing greater deformation and consequently higher stresses.

2.1.3. Hybrid Testing Method

The synopsis presented above categorized soil-pipe test methods into two general categories of field test and laboratory test methods. However, there are some studies that do not exist in these categories. For instance, Masada carried out field and laboratory testing on an intact, a deteriorated invert, and an invert paved 60 in. circular CMPs (Masada 2017b; Masada et al. 2020). The field test was conducted on a CMP in service that unlike the common field test methods which use a truck to apply the load, they used a portable hydraulic actuator for loading and concrete blocks to provide a support to the hydraulic jacks. In the same study, a series of laboratory testing were conducted on an open air facility using steel reaction frame, where the test sample (a circular CMP) was buried inside a trench, excavated inside a native soil, similar to the field test method, as illustrated in Figure 2-6 (a). The laboratory testing included four full-scale tests of 13-ft long circular CMPs with 60 in. diameter. The first test sample were an intact CMP (i.e., unmodified) to be used as a baseline performance for the other tests. The second test, was conducted on an invert-cut CMP with the middle third of the invert removed. The third test was conducted on a fully invert-cut CMP, paved with mesh concrete according to the Ohio DOT's requirement. The fourth test included a partially invert-cut CMP, paved with rebar reinforced concrete. The load was applied through a 68 × 108 in. load pad. The study concluded that the failure mode of the intact CMP was wall buckling at the springline location. The load was applied incrementally until the pipe failure at the load of 923 kips.

Partially removing the invert section reduced the ultimate load carrying capacity for 37%. During the test, a separation of pipe sample's helical interlocking seems separation was observed at 81% of the ultimate load carrying capacity of 667 kips. The invert-cut CMP, repaired with mesh reinforced concrete had 13% lower capacity than the intact CMP and failed at the load of 800 kips.

Eventfully, the structural capacity of the invert-cut CMPs repaired with welded # 4 rebars and concrete was as same as the intact CMP. However, it should be considered that none of the tested CMP samples had a fully removed invert. The remaining invert sections partially maintained the resistance to ring compression and played an important role in the CMP's stability and load carrying capacity. While, there are still many culverts in service with fully invert section gone and their structural behavior and load carrying capacity are yet unknown.

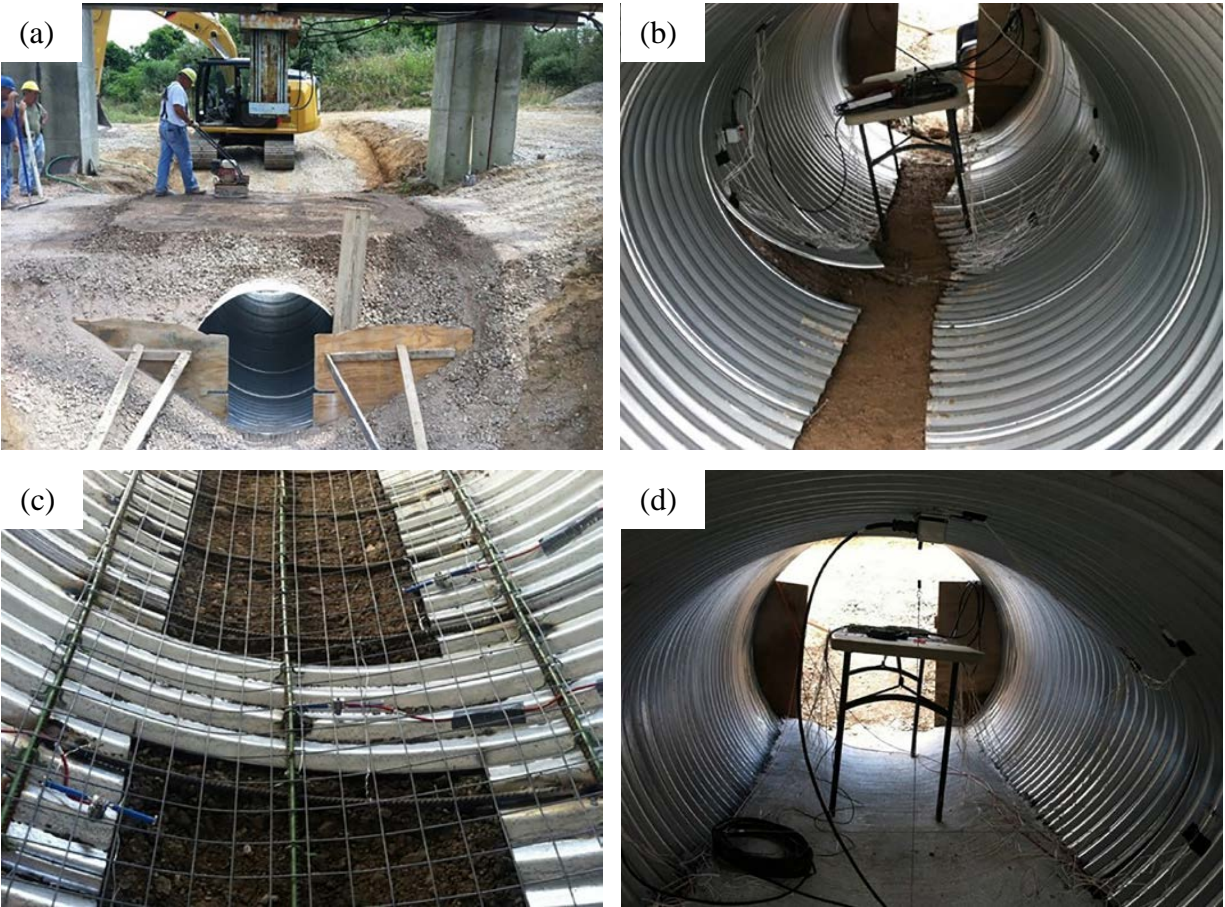


Figure 2-6. Helical invert-cut CMP buried inside a trench:(a) laboratory testing method in an open-air facility, (b) full invert-cut CMP, (c) partially invert-cut CMP, and (d) invert-paved CMP.

A similar open air laboratory testing method has been carried out by Bian et al., where a concrete pipe was tested using a hydraulic actuator on an open air soil box facility (Bian et al. 2012). The arch shape culvert was buried and tested under 1.6, 4.9, and 11.5 ft of granular soil cover. It is found that the vertical deformation of the granular fill is almost proportional to the load intensity. In addition, the vertical deformation of the granular fill increases with increasing cover depth under the same loading configuration.

Sharma et al. (2011) conducted a structural testing on two 73.7 in. diameter steel pipe in laboratory condition. However, in the absence of a hydraulic actuator, soil weight was used to apply a surcharge load on the pipe samples. To achieve this goal, pipes were placed into a soil box and was backfilled under 10 ft of granular soil. The applied pressure, stresses, and pipe deflection were monitored during the 9 weeks testing period (Sharma 2013). The controlled condition of the laboratory enabled the research team to carry out this relative long-time testing.

2.1.4. Applicable Load Rate in a Soil-Pipe Testing

The synopsis of similar studies, presented above, discusses laboratory testing condition. However, in many similar studies, particularly when it is in displacement control, the load rate is not reported.

Lougheed (2008) used 0.039 in./min for testing a buried deep corrugated large-span arch culvert in an incremental regime where the displacement is applied at a predefined increment and held for a known period before exerting the next increment. ASTM D2412 suggests 0.5 in./min for testing flexible pipes, such as CMPs, under the parallel-plate testing configuration (ASTM-D2412 2018). However, Schluter and Shade (1999) studied the effect of load rate on the parallel-

plate testing and suggested 0.05 in./min instead of 0.5 in./min and stated that the 0.5 in./min does not ASTM D 2414 deflection rate does not relate to the real world behavior of pipes. Similar study has been done by Sargand and Hazen (1998) for plastic pipes and a rate between 0.01 to 0.06 in./min is suggested. In addition to the suggested load rates for flexible pipes, ASTM D1633 suggests 0.05 in./min loading rate for testing compressive strength of soil-cement cylinders (ASTM D1633 2013). Therefore, a reasonable load rate value should be within the range of the numbers in agreement with soil and pipe testing values.

2.2. SAPL Renewed Pipe Testing

The Army Corps of Engineers released the results of their field study on the performance of concrete-lined corrugated metal pipe (CLCMP) for use as an alternative to reinforced concrete pipe in November of 1986. Approximately 12,000 linear feet of concrete-lined pipe were inspected during their 15-month long study. Essentially, all were relatively new installations (less than two years old) with the concrete lining installed at the manufacturing plant. The only exception to this was a 26-year old installation that had the concrete lining installed in the field. The pipe manufacturer was ARMCO. The objective of this evaluation was to verify the manufacturer's claims, that this product offered the hydraulic efficiency of concrete pipe and the structural efficiency of corrugated metal pipe. All these pipes had the valleys of the corrugations filled and a specified minimum lining of 0.375-in. over the crests of the corrugations; but the actual minimum thickness was found to usually be 0.750 in. The result of this study led to development of the ASTM A979 - Concrete Pavements and Linings Installed in Corrugated Steel Structures in the Field standard. It was recommended in this standard to fill the corrugation valleys with concrete

lining (ASTM A979 2003). The result of the Army Corps study showed that the concrete liner increased the load bearing capacity of the pipes.

Walker and Guan conducted a set of material property tests and reviewed the performance of five primary materials of sprayed liners used in North America (Walker and Guan 1997). The spray applied liners were including 100% solids rigid polyurethane, 100% solids epoxy, solvent amine-based epoxy, 100% solids elastomeric polyurethane and cement mortar lining for the internal renewal of potable water steel pipes. The study concluded that in compare with the other tested liner materials, the 100% solids polyurethane had a better performance to be used in potable water steel pipe.

Szafran and Matusiak (2017) studied the structural behavior of concrete and reinforced concrete pipes renewed from inside and outside surfaces with polyurea SAPL through the three-edge bearing test. The study observed that the application polyurea SAPL membrane in two layers (the thickness is unknown) on both surfaces increased the compressive capacity of the pipe samples by 21.9%. Authors stated further research is needed to explore the performance of polyurea SAPL in the existence of soil-pipe interaction system.

Entezarmahdi (2015) conducted structural evaluation on 17 reinforced concrete pipes (RCPs), renewed with epoxy lining and tested through three-edge bearing test. The pipe samples had 24 in. inside diameter and were selected from class II category of the ASTM C76 (2015). Different types of liners including epoxy, polyurethane, multi structural liners with modified pleurae and foam, cementitious, and resin impregnated cured-in-place lining (CIPP) were applied on different layers and thicknesses. All the utilized spray applied liner materials increased the bearing capacity of the RCPs ranging from 45 to 133%. The results presented in Figure 2-7 show significant increase in renewed RCP structural capacity.

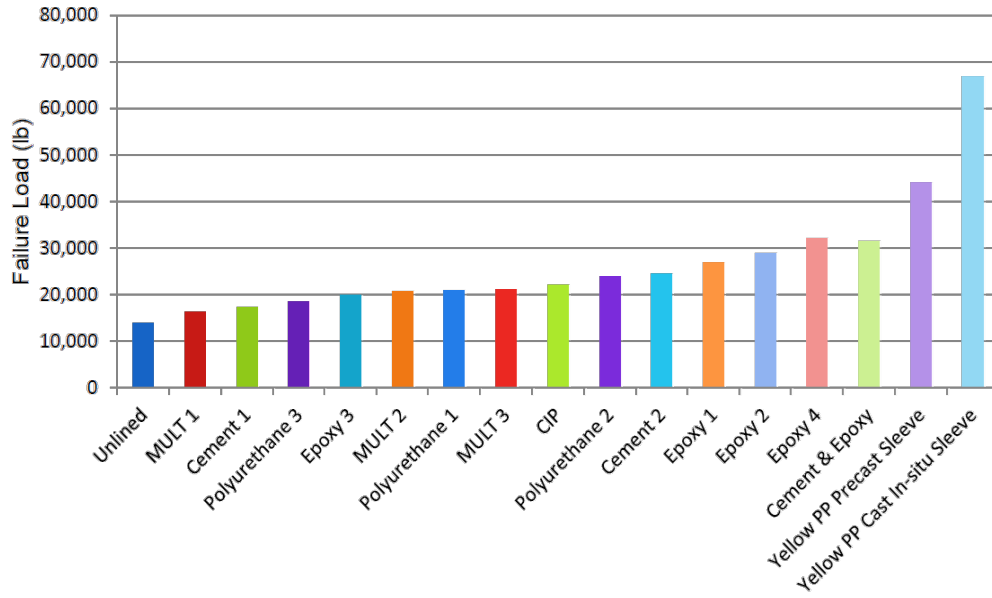


Figure 2-7. Load carrying capacity of the RCPs renewed with different liner materials.

Royer and Iseley conducted a series of laboratory testing on geopolymer SAPL renewed pipe samples through the three-edge bearing test (Royer and Iseley 2017). The geopolymer SAPL was applied inside CMP, RCP, and cardboard with three diameters of 24, 36 and 48 in. The SAPL was installed using a spincast machine into each of the pipe samples to a predetermined thickness that was scaled as the pipe’s diameter increased. Some samples were pre-loaded to reach 12% ovality prior to the SAPL application. The experimental program included SAPL thickness ranging from 0.66 to 2.66 in. The study concluded that minimum thickness of 1 in. is required for the pipes smaller than 54 in. diameter.

García and Moore (2015) conducted laboratory testing to evaluate the performance of deteriorated helical corrugated metal pipes renewed with cementitious spray applied liners under deferent burial depths and truck axles. The CMP diameters were 47 in. and were corroded at the invert location with some perforations at hunch area. The pipe samples were buried at the 47.2 in. and 82.6 in (4 ft and 8 ft) cover depths using poorly graded sandy gravel (GP-SP) backfill material.

The culverts samples were renewed with geopolymer (i.e., cementitious) non-ceramic liner at 3 and 2 in. thickness respectively. The installation was conducted using a spin caster spray machine that applies the liner by the cementitious liner by an air powered rotating nozzle. The results showed that no sign of failure was observed in the rehabilitated pipelines. The pipe, with thicker liner showed stiffer response to the live load. Load reduction effect of the cover depth was evident on the deeper cover.

Moore and García (2015) studied the ultimate strength of two deteriorated metal culverts renewed with cementitious SAPL. The specimen size and burial configuration is same as their previous study (García and Moore 2015). However, the load was applied until the failure of the system was achieved. The load-control loading regime was applied and consequently, the post failure behavior of the system was not obtained. The results showed that the liner increased the ultimate bearing capacity of the deteriorated culverts. The sample 1 with 2 in. of SAPL failed at 200 kips and the sample 2 with 3 in. of SAPL failed at 260 kips in tandem axle configuration. It was noted that the thickness of the SAPL was not the same everywhere, and its variation at some location was almost two times greater than the designed thickness.

2.3. Applicable Design Equations for SAPLs

Currently, no standardized structural design methodology existed for the spray applied pipe lining. Inevitably, manufacturers are utilizing different design methodologies with some using the cured-in-place pipe (CIPP), ASTM F1216 methodology and others using various classical analytical structural design equations developed for other purposes or conditions.

2.3.1. CIPP Design Methodology

The ASTM F1216 outlines two sets of equations for partially and fully deteriorated host culverts. According to the ASTM F1216 definitions, a partially deteriorated culvert may have displaced joints, cracks or corrosion, but is structurally able to support all soil and surface loads. In this case the existing culvert is intended to provide structural support over the full circumference of the liner. In this case, the liner (i.e., CIPP) will be designed to withstand uniform hydrostatic pressure only. On the contrary, a fully deteriorated culvert has insufficient strength to support all soil and surface loads. A fully deteriorated pipe is characterized by severe corrosion, missing pipe, crushed pipe, longitudinal cracks, and severely deformed pipe. In this case, the liner is designed as a pipe able to withstand all hydrostatic, soil, and live loads that may exist in the liner-soil system with adequate soil support.

The ASTM F1216 design equation for partially deteriorated culverts is derived from the basic buckling theory of a free ring, developed by Bresse in 1866 (Omara 1997). In this theory the critical buckling pressure (P_{cr}) of a free-standing circular ring under external hydrostatic pressure is expressed as follows:

$$P_{cr} = \frac{3 \cdot E \cdot I}{r^3}, \quad (32)$$

where, E is the modulus of elasticity, I is the moment of inertial of the ring's cross sections, and r is the mean radius of the ring. The equation was further developed by Bryan in 1888, where the term $(1 - \nu^2)$ were added to the equation to account for the plane strain condition of the infinitely long pipe. In addition, since $I = bt^3/12$, the equation yielded to:

$$P_{cr} = \frac{2 \cdot E}{(1 - \nu^2)} \cdot \left(\frac{t}{D}\right)^3, \quad (33)$$

where, ν is the Poisson's ratio, t is the mean thickness, and D is the mean diameter of the pipe.

Timoshenko in 1961 further developed the equation as follows, which is the basis for designing CIPP for partially deteriorated culverts:

$$P_{cr} = \frac{2KE_L}{(1 - \nu^2)} \cdot \frac{1}{(DR - 1)^3}, \quad (34)$$

where, the $DR = OD/t$, in which the OD is the outside diameter of the pipe.

The currently available, equation, has included, safety factor, ovality reduction factor, enhancement factor and replacement of the long-term modulus of elasticity instead of the short-term modulus to consider creep of the plastic entity of CIPP material. The CIPP design equation for the partially deteriorated culverts are as follows (Najafi and Gokhale 2005):

$$P_w = \frac{2KE_L}{(1 - \nu^2)} \cdot \frac{1}{(DR - 1)^3} \cdot \frac{C}{N} \quad (35)$$

where, P_w is the critical ground water pressure, K is the enhancement factor, E_L is long-term (time corrected) modulus of elasticity, C is ovality reduction coefficient, and N is the safety factor. By substituting the $DR = OD/t$ into the equation (35) and solve the equation for t , the following equation yields:

$$t = \frac{OD}{\left(\frac{2 \cdot K \cdot E_L \cdot C}{P_w \cdot N(1 - \nu^2)}\right)^{1/3} + 1} \quad (36)$$

The current design practice for CIPP design on a fully deteriorated host culvert, presented in the ASTM F1216, is adopted from the AWWA C950 that has included ovality reduction factor.

The AWWA C950 equation was a modified version of an equation developed by Luscher (1966) to predict the buckling pressure of buried flexible pipes (Omara 1997). Thus, this equation uses the buckling failure as design criterion. The ASTM F1216 design equation for a fully deteriorated includes hydrostatic, soil and live loads on the host culvert, as illustrated in Figure 2-8.

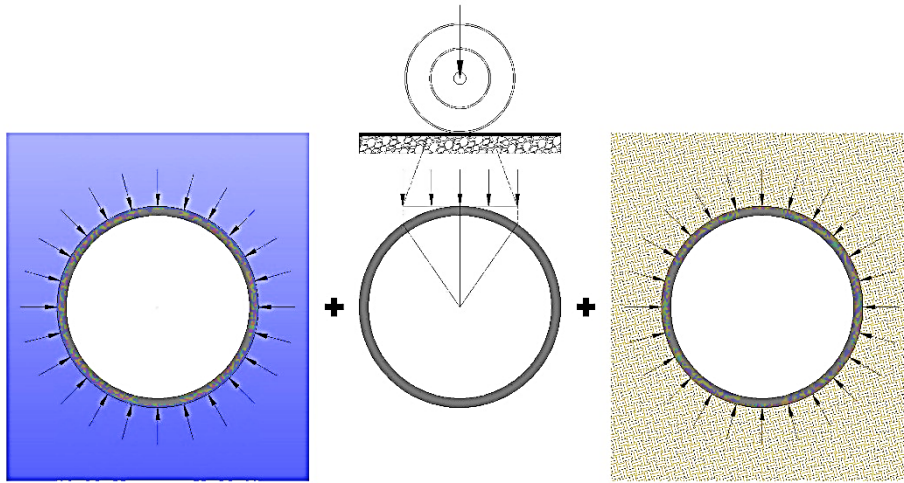


Figure 2-8. Schematic pattern of external loads on a culvert in fully deteriorated CIPP design equation: (left) hydrostatic pressure, (middle) live load pressure, and (right) soil pressure (credit: CUIRE).

The CIPP design equation for fully deteriorated culvert is as follows:

$$q_t = \frac{1}{N} \cdot \left[32 \cdot R_w \cdot B' \cdot E'_s \cdot C \cdot \left(\frac{E_L \cdot I}{D^3} \right) \right]^{0.5}, \quad (37)$$

where, q_t is the total pressure on the pipe, R_w is the water buoyancy factor, B' is coefficient of elastic support, and E'_s modulus of soil reaction.

Modified AWWA C950 formula specifies CIPP to have a minimum 50% of required stiffness (EI/D_o^3), which is 0.093 in. In the following equation this means that for the fully deteriorated culvert design, the liner with a flexural modulus of elasticity $E = 350,000$ psi would

have a dimension ratio equal to 67. If the liner's stiffness is too low, the wall thickness must be increased accordingly to ensure that the following design condition is met:

$$\frac{E \cdot I}{OD^3} = \frac{E}{12 \cdot (DR)^3} \geq 0.093, \quad (38)$$

In the equation (37), the moment of inertia (I) can be substituted with $t^3/12$, and the equation can be solved for t as follows:

$$t = 0.721 \cdot OD \cdot \left(\frac{(N \cdot q_t)^2}{C \cdot E_L \cdot R_w \cdot B' \cdot E'} \right)^{1/3}. \quad (39)$$

It should be noted that in fully deteriorated condition, the host culvert has lost its ring and bending stiffness and is prone to collapse. In this condition, the liner is designed to resist groundwater pressure, soil pressure and traffic loads. The likelihood of this condition is assumed to be a function of the condition of the culvert at the time of lining. However, some researchers studied that in the majority of practical situations, the amount of the load that transfers to the liner is negligible as the lining process effectively locks in the existing equilibrium of fully deteriorated culverts (Falter 1996; Gumbel 2001; Thepot 2000). According to the Gumbel (1998) for fully deteriorated host pipe condition, the ASTM F1216 overestimates the transferred soil load to the liner and considers the liner as a direct buried culvert, which is too conservative. While, if the host culvert may continue deteriorating even after the application of the liner, the more accurate methodology to be considered is more similar to the tunnel lining (Schrock and Gumbel 1997).

2.3.2. Flexible Pipe Design Methodology

Marston (1913) is generally recognized as the first researcher who brought some engineering insight to the design and analysis of underground conduit (Omara 1997). Prior to that time, pipes and conduits were installed with limited structural design. Marston was the first researcher who recognized that the loading on an underground structure is dependent on the soil-structure interaction. Marston's theory assumes that the dead load on the underground conduit is due to a prism of soil whose movement is relative to the adjacent soil. The movements imposed the load on the conduit. Therefore, the theory takes the relative deflection of the pipe and the settlement of the soil into account. Based on Marston's theory, Spangler estimated the amount of uniformly distributed load at the top of the pipe with the assumption that a uniform pressure is applied over part of the bottom, depending upon the bedding angle. It was also assumed that the horizontal pressure on each side would be proportional to the deflection of the pipe into the soil (Moser and Folkman 2008). Through analysis, he derived the well-known Iowa formula, in which the constant of proportionality was called the modulus of passive resistance of the soil. The preliminary Iowa formula was:

$$\Delta x = \Delta y = \frac{D_L \cdot K \cdot W_c \cdot R^3}{E \cdot I + 0.061 \cdot e \cdot R^4}, \quad (40)$$

where, Δx is horizontal deflection or change in diameter, Δy is vertical deflection or change in diameter, D_L is deflection lag factor, K is bedding constant, W_c is the Marston's load per unit length of the pipe, R is the mean radius, E is the modulus of elasticity, I is the moment of inertia, and e is the modulus of soil passive resistance.

The Spangler's Iowa formula assumes the pipe has the same vertical and horizontal deflection. However, it is well recognized that the vertical deflection is always greater than the

horizontal deformation. In addition, Watkins in 1985 have conducted a comprehensive analysis on the modulus of passive resistance, which indicated that "e" could not possibly be a true property of the soil in that its units are not those of a true modulus. As the result of the study, the modified Iowa formula was proposed as follows:

$$\Delta y = \frac{D_L \cdot K \cdot W_c \cdot R^3}{E \cdot I + 0.061 \cdot E' \cdot R^3}, \quad (41)$$

where the E' is the modulus of soil reaction. Several research efforts have attempted to measure the modulus of soil reaction E' that remained unsuccessful. The most useful method to measure the modulus of soil reaction is through a back-calculation of the Iowa formula for a known pipe deflection and load values. Nowadays, the E' is available in different sources such as AASHTO, ASTM standards, text books etc., (AASHTO 2017; Moser and Folkman 2008; Watkins and Anderson 1999).

AASHTO LRFD bridge design specifications' section 12 requires a modified version of the Spangler's Iowa formula for design of thermoplastic pipes. The AASHTO's equation for total deflection calculation for predicting flexural deflection in combination with the expression for circumferential shortening, is presented as:

$$\Delta_t = \frac{K_B \cdot (D_L \cdot P_{sp} + C_L \cdot P_L) \cdot D_o}{1000 \cdot (E_p \cdot I_p / R^3 + 0.061 \cdot M_s)} + \varepsilon_{sc} \cdot D, \quad (42)$$

where, ε_{sc} service compressive strain, D_L deflection lag factor, K_B bedding coefficient, P_{sp} soil prism pressure evaluated at pipe springline, C_L live load coefficient, P_L live load pressure, D_o outside diameter of pipe, E_p short- or long-term modulus of pipe material, R radius from center of pipe to centroid of pipe profile (i.e., mean radius), D diameter to centroid of pipe profile (i.e.,

mean radius), I_p moment of inertia of pipe profile per unit length of pipe, and M_s secant constrained soil modulus.

2.3.3. Other Analytical Approaches

2.3.3.1. Watkins's Equation

Watkins developed a crack propagation model which provides a thickness based on required crack width. The developed design equation is derived base on mechanical analysis of thin-wall rings with symmetrical loads. The proposed equation is:

$$t = \sqrt{\frac{7.0464 \cdot P \cdot r^2}{w_{fr} \cdot E}}, \quad (43)$$

where, P is the vertical pressure being applied to the horizontal soil plane at the top of the pipe, w_{fr} is the allowable crack opening width, r mean pipe radius, and E is the modulus of elasticity.

2.3.3.2. Roark's Equation

Roark developed an equation for a thin tube under uniformly lateral external pressure which is based on the case outlined in Table 15.2 case 19b of Roark's formulas for stress and strain book written by Young and Budynas (1989). The equation is presented below:

$$t = \sqrt[2.5]{\left(\frac{q_t \cdot L \cdot r^{1.5} \cdot (1 - \nu^2)^{0.75}}{0.807 \cdot E}\right)}, \quad (44)$$

where q_t is the external pressure, L is the distance of fixed end, ν is Poisson's ratio, E is elastic modulus, and r is the mean radius of the pipe.

CHAPTER 3. EXPERIMENTAL PROGRAM

3.1. Overview

As a main part of the study on the “*structural design methodology for spray applied pipe lining (SAPLs) in gravity storm water conveyance conduits,*” pipe samples were tested in the soil box located at the Center for Underground Infrastructure Research and Education (CUIRE) laboratory at the University of Texas at Arlington (UTA), as shown in Figure 3-1. The CUIRE soil box is 25 ft long 12 ft wide and 10 ft deep. The soil box is equipped with a 330-kips MTS actuator installed on a steel reaction frame designed for this type of experimental project. The CUIRE soil box is illustrated in Figure 3-2.

The experimental testing program consisted of five sets of full scale laboratory tests including (1) control test, (2) circular CMPs renewed with polymeric SAPL, (3) pipe arch CMPs renewed with polymeric SAPL, (4) circular CMPs renewed with cementitious SAPL, and (5) pipe arch CMPs renewed with cementitious SAPL. This dissertation only includes the results of control test, and both circular and pipe arch cementitious SAPL test series.

The control test consisted of one intact circular CMP, one invert-cut circular CMP, and one invert cut pipe arch CMP. The circular and pipe arch cementitious SAPL test series consisted of three separate invert-cut CMP samples each, renewed with 1, 2, and 3-in. thick cementitious SAPL. To acquire the structural capacity of the liners, the invert section of the CMPs were cut and detached after backfilling. Therefore, no ring compression was existed in the pipe sample and the load was resisted by the SAPL only. Table 3-1 lists the tests sequence with its specifications.



Figure 3-1. CUIRE's laboratory located at the UTA's Civil Engineering Laboratory Building (CELB).



(a)



(b)

Figure 3-2. CUIRE soil box: (a) before steel frame installation, and (b) after installation of the 330-kips actuator and steel reaction frame.

Table 3-1. List of experimental tests and testing samples details

Test Name	Test Number	CMP Shape	Invert-cut	Liner type	Liner Thickness (in.)
Control Test	1	Circular	No	N/A	N/A
	2	Arch	Yes	N/A	N/A
	3	Circular	Yes	N/A	N/A
Circular Cementitious	4	Arch	Yes	Geopolymer	1
	5	Arch	Yes	Geopolymer	2
	6	Arch	Yes	Geopolymer	3
Arch Cementitious	7	Circular	Yes	Geopolymer	1
	8	Circular	Yes	Geopolymer	2
	9	Circular	Yes	Geopolymer	3

3.2. Experimental Test Design and Setup Preparation

According to literature review presented in CHAPTER 2, a laboratory test setup was designed to meet the requirements of such a structural testing of a soil-culvert system. This section

discusses the soil box and test setup preparation, test burial configuration, load pad design, and required instrumentation.

3.2.1. Soil Box Requirements and Preparation

The term soil box commonly refers to a rigid testing pit such that the pipe sample is embedded and backfilled inside for testing. It should include rigid walls and floor that restrain the box volume change during the test. The advantage of testing in a soil box is that it allows effective simulation of loads on the buried pipe under different conditions with respect to soil, load, and buried depth (Kraus et al. 2014). The height of the box should be at least twice of diameter larger than the testing sample to provide enough space for a standard burial configuration, specified in section 1.2.3, to encompass soil foundation, bedding, and minimum soil cover. The width of the box should be minimum of one-half diameter or 3 ft (0.9 m), whichever is less, to permit adequate compaction of backfill material and prevent the rigid wall effect on the soil-pipe interaction system (CALTRANS 2000). If the soil box is constructed under the ground level, there is possibility of infiltration of ground water, which can affect the moisture content of embedment material (Sharma 2013). To prevent such an issue, it is suggested to construct the soil box floor inclined and use minimum of 6-in. (150 mm) thick highly compacted poorly graded gravel (PG) with no fine material, such as washed P-gravel, to level the floor and allow water movement to the lowest level of the soil box. A sump pump is needed at the deepest corner of the soil box to dewater the excessive infiltrated water during the testing setup preparation. The sump pump should be placed inside a perforated compartment to be secured from the soil ingress to its motor and transmit the water out of the soil box through a small diameter drainage pipe. A layer of thick polyethylene sheets can be used between the PG and fill material (i.e., embedment and bedding). Existence of these polyethylene sheets are highly beneficial since they prevent testing fill material (i.e.,

embedment and bedding) mixture and moisture content exchange with the PG soil underneath. Polyethylene sheets should be placed on the walls of the box to minimize the friction between the wall and soil (Khatri et al. 2015; Mai et al. 2018; Tognon et al. 1999). It is also suggested to use lubrications between the sheets and rigid wall. The schematic design of such as soil box is illustrated in Figure 3-3.

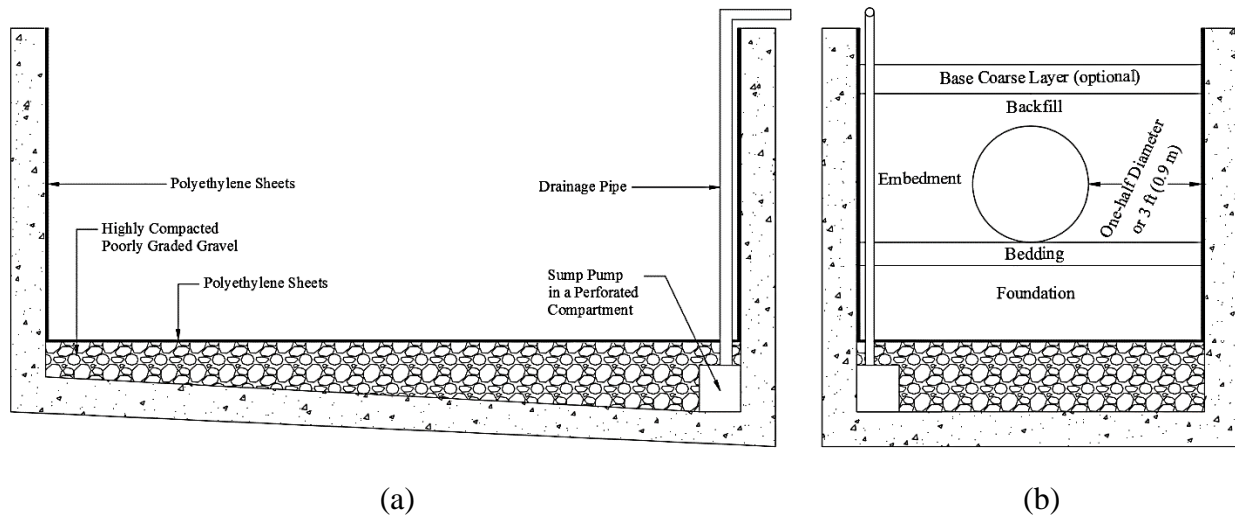


Figure 3-3. Soil box schematic design: (a) proposed soil box, and (b) proposed burial configuration in the soil box.

In this study, the soil box was prepared as stated above. To minimize the experiments' setup time and for ease of SAPL installation for each set of tests, it was decided to place three CMP testing samples longitudinally along each other in the soil box, as depicted in Figure 3-4. To accomplish that goal, the soil box interior space was divided into four sections; one for entrance and three for pipe samples. Figure 3-5 illustrates construction of wooden walls on top of the compacted gravel layer to provide the separated testing cells. A 40 × 30 in. opening at the center of each wall was improvised to provide access to the inside of each CMP. All the wooden walls and soil box concrete walls were lubricated and covered with polyethylene sheets.

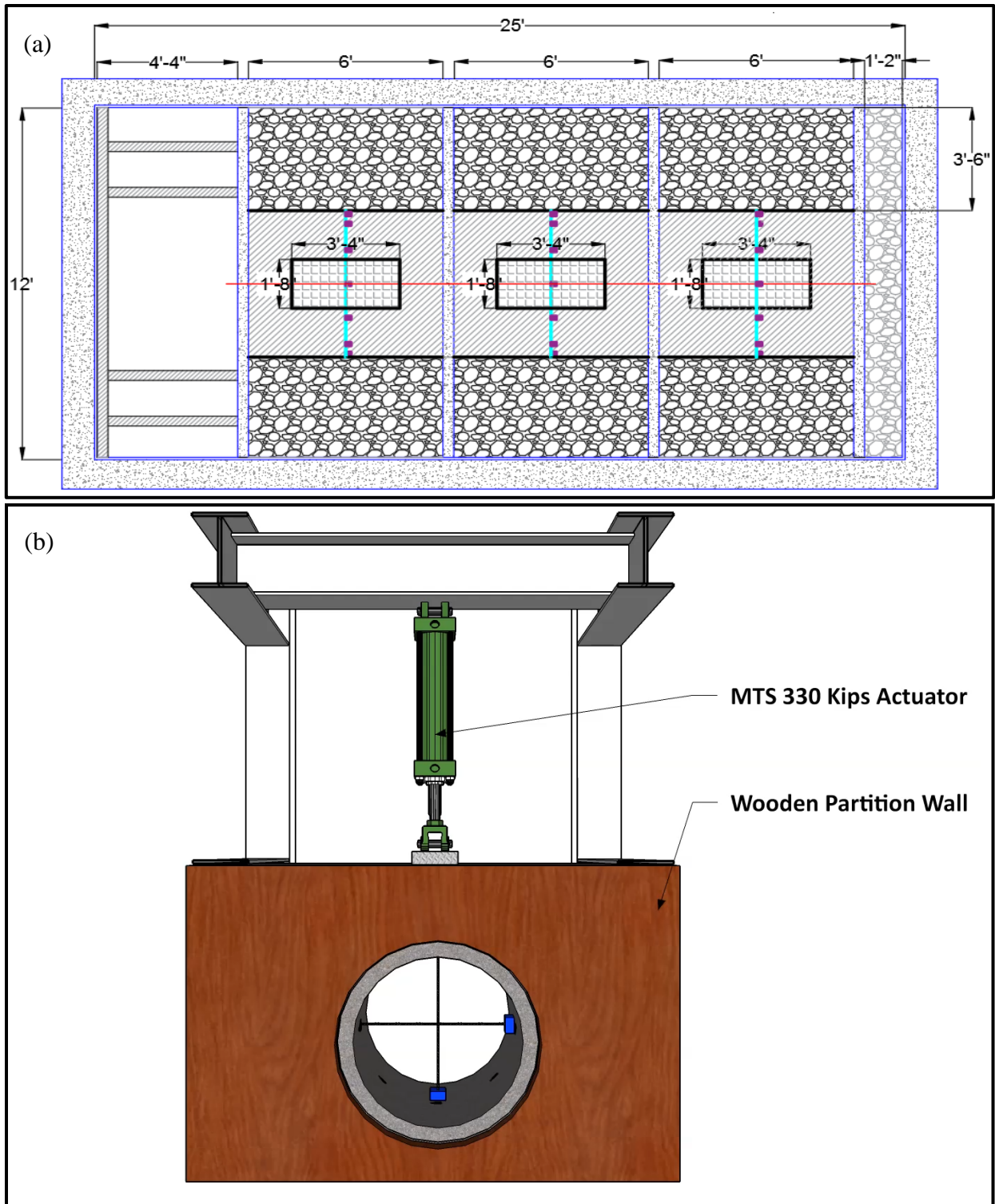


Figure 3-4. Soil box test configuration: (a) 2D schematic plan view of the soil box layout including partition walls and three testing pipe samples, and (b) 3D schematic cross-sectional view of a pipe sample in one of the soil box cells, separated by wooden partition walls.

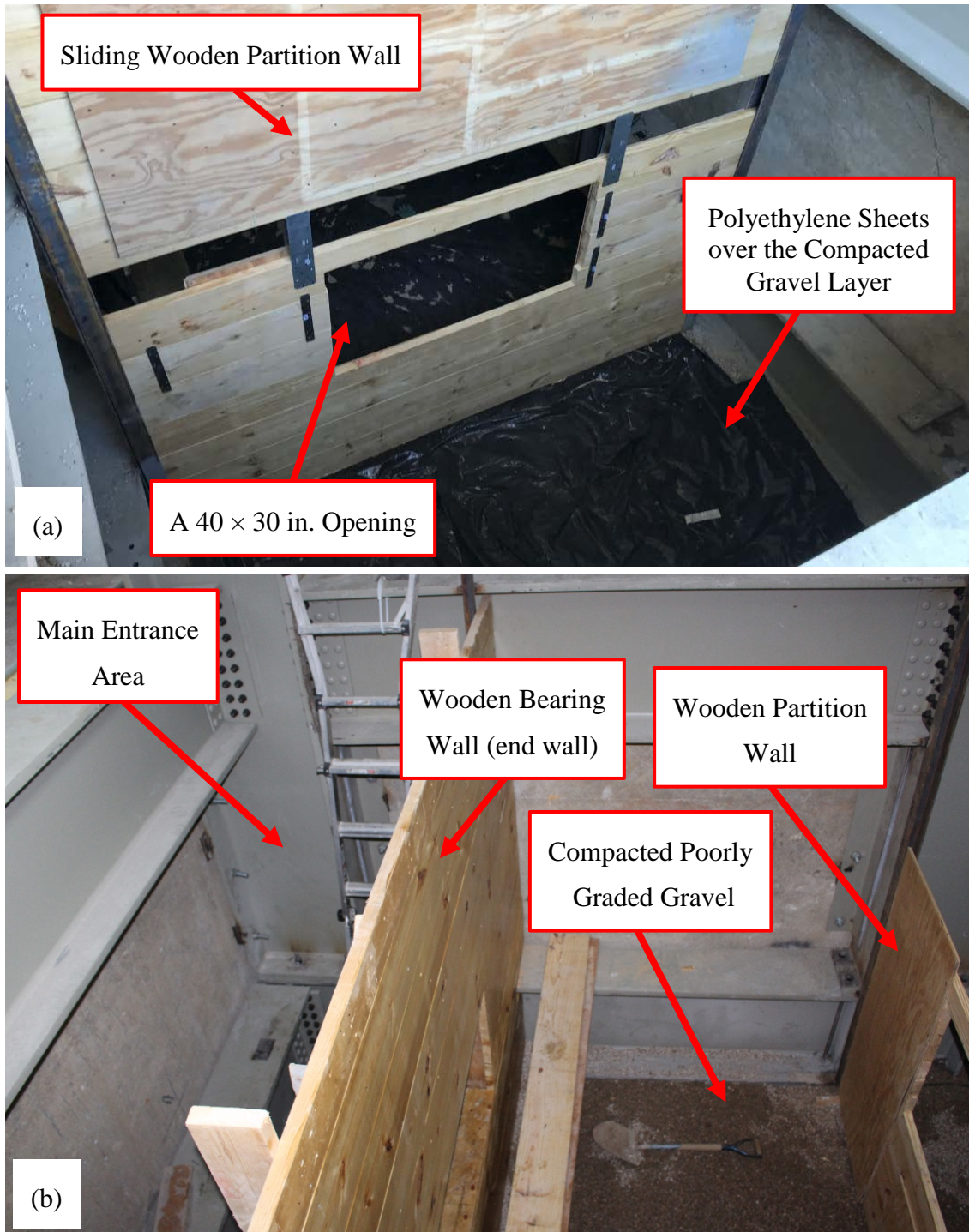


Figure 3-5. Soil box preparation: (a) schematic plan view of soil box including partition walls and three testing pipe samples, and (b) wooden walls construction to divide the soil box into four separate sections.

Placement of the CMPs along each other in the soil with only one opening would raise the safety concerns for the research team and SAPL installer crew inside the pipes. Therefore, a ventilation system was designed by the author to allow air circulation inside the CMPs through a network of PVC pipes and a vacuum pump. Figure 3-6 illustrates the ventilation PVC pipes installed at the south side of the soil box. The vacuum pump was installed at the end of the PVC pipe on the top of the soil box at the time of SAPL installation or instrumentation inside the CMPs.

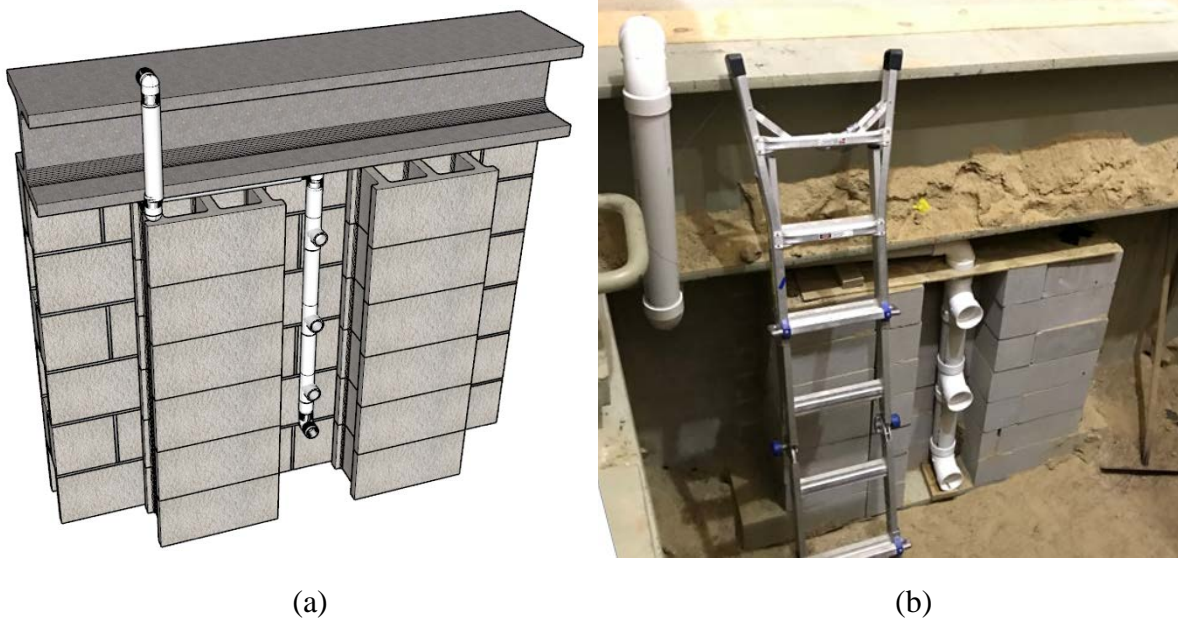


Figure 3-6. Soil box ventilation: (a) schematic design, and (b) constructed ventilation system.

3.2.2. Test Burial Configuration

Burial configuration of culverts depends on the type of the culvert and the test requirements. In general, as discussed in section 1.2.3, a burial configuration of a culvert consists of: foundation, bedding, embedment, backfill and cover (Moser and Folkman 2008; Watkins and Anderson 1999; Whidden 2009). A foundation is suggested to be utilized with the highly

compacted material, same as trench or embedment for at least 1ft (0.3 m) for small diameter and 2 ft (0.6 m) for large diameter pipes (Mai et al. 2018; Syar et al. 2020). Use of this layer is suggested to mitigate the rigid response of the concrete slab on the bottom of soil box.

In this study, two passes of a plate vibratory compactor with 4,496 lbs. compaction force were carried out at every 8 in. lift to archive approximately 93% of the maximum standard Proctor dry density (SPDD), as illustrated in Figure 3-7. Since the pipe arch samples had a lower rise than the circular pipes, the soil level at the top for the pipe samples would become different. This would raise the concern that due to the limited actuator stroke length, in the absent of the invert section, the ultimate load bearing capacity of pipe arch CMPs would not be achieved at the full stroke range. Therefore, the foundation of the pipe arch samples was increased until their crown reached the same level of the crown of the circular CMPs. The foundation layer was placed using a 20 in. of well compacted poorly graded sand (SP) for circular CMPs, and 33 in. of SP soil for pipe arch CMPs.

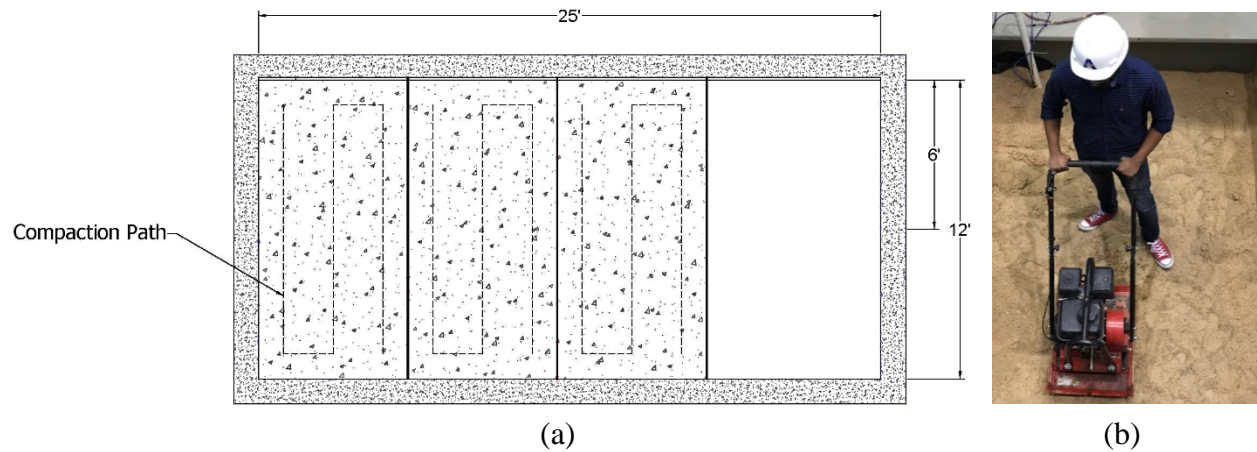


Figure 3-7. Foundation compaction: (a) schematic illustration of soil compaction, (b) soil compaction using a 4,496 lbs vibratory plate compactor.

For the foundation, loose bedding, embedment, and one ft of backfill, a poorly graded sand (SP), known as concrete sand, was selected according to the unified soil classification system (USCS). Similar sand was used in the same application by other researchers (Mahgoub and El Naggar 2020). A particle size distribution curve was prepared according to the ASTM D6913 through sieve analysis which is illustrated Figure 3-8 (a). In addition, standard proctor compaction test was conducted to obtain the SPDD of the soil, illustrated in Figure 3-8 (b). The proctor test showed the maximum unit weight of the SP soil was 115 pcf. Moreover, it showed for this type of soil that has negligible amount of silt and clay, the soil sample's density did not significantly change with the alteration of the moisture content (Berney and Smith 2008). Therefore, during the soil placement in the soil box, no attempt was conducted to control the soil's water content to achieve the maximum SPDD.

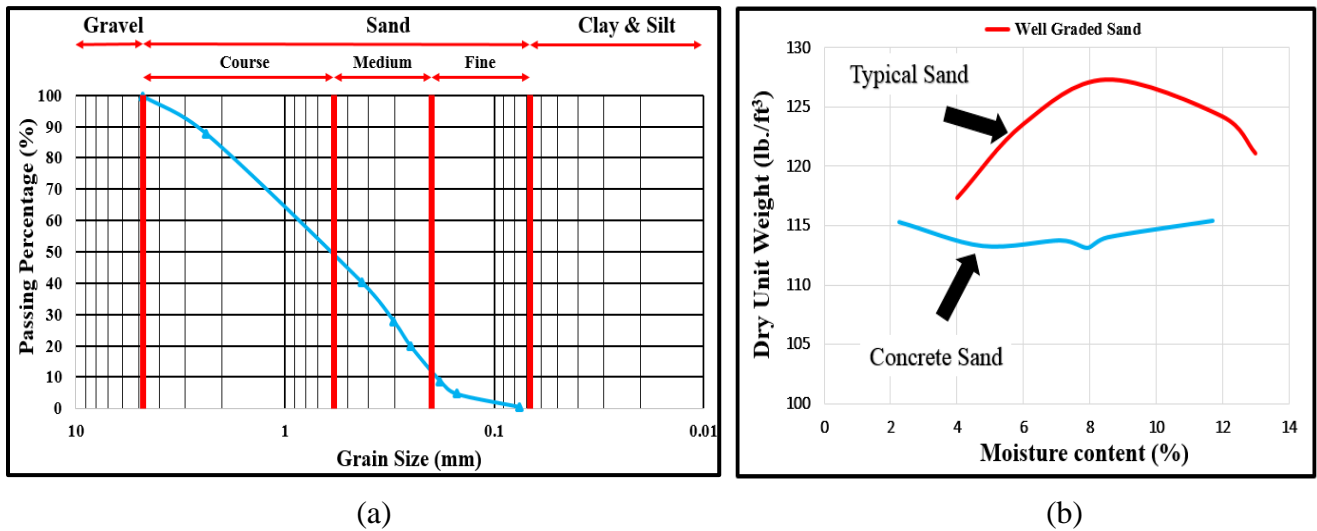


Figure 3-8. Embedment soil characteristics: a) soil sieve analysis, and b) standard Proctor test.

Figure 3-9 (a) and (b) illustrates the CMPs burial configuration in the soil box. Once the foundation was placed and compacted, a 4-in. layer of loose soil was placed at each cell. This loose

bedding layer would allow the pipe sample to settle properly and to provide even bedding conditions. In addition, this layer was to represent loosened soil in the field under the pipe sample's invert, as a result of stream passage in the absence of the invert section (i.e., fully corroded invert). To consider a worst installation scenario, where the contractor does not compact the soil as expected, the compaction rate of 85% of SPDD was selected for embedment and the one ft SP soil backfill as specified by AASHTO (2017). In some soil material including the concrete sand, the 85% compaction value can be achieved by only dumping and spreading the soil. In-situ compaction measurement using nuclear density gauge showed the 85% compaction rate of SP soil can be achieved by dumping only. Therefore, no attempt was made to compact the soil embankment. The soil was placed and spread out at 8 in. lifts. The water content and the compaction rate of the soil was measured at each layer using a nuclear density meter. Since the objective of these tests were to obtain the ultimate load bearing capacity in the field, a one ft (304.8 mm) layer of aggregates with maximum particle size of 1.75 in. (44.5 mm), known as TxDOT 247 grade 1 type D aggregates, was placed on top of the backfill layer to prevent immature soil failure prior to the pipe sample failure. This layer is representative of the base course as a part of culvert's cover in the field (Khatri et al. 2015).

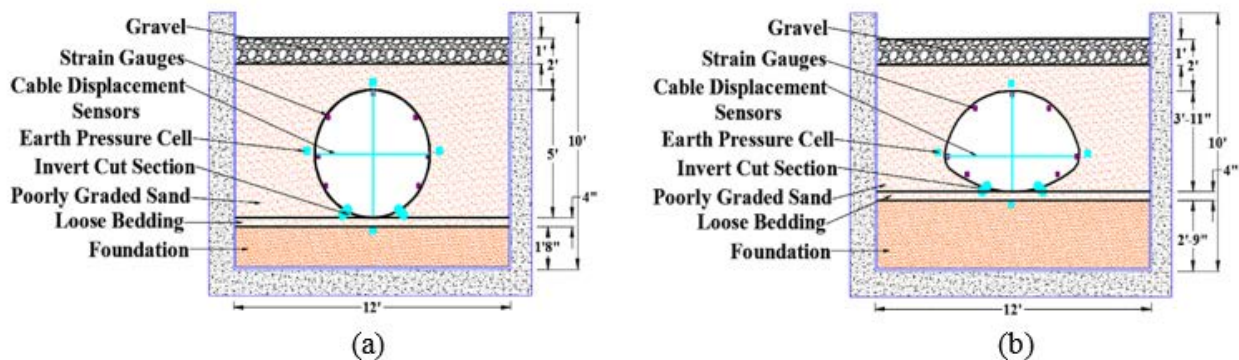


Figure 3-9. Test setup and burial configuration for: (a) circular CMPs, and (b) for pipe arch CMPs.

3.2.2.1. Soil Compaction Measurement

There are various methods of soil field compaction measurements. ASTM D2167, ASTM D1556, and ASTM D6780 detail field compaction measurement using rubber balloon method, sand cone method, and time domain reflectometry (TDR) method respectively. However, since the SP soil used in this study is cohesionless, the rubber balloon and sand cone methods were not applicable. In addition, due to the complexity of TDR calibration, relatively longer measurement duration, and lack of service provider it was decided not to use this method. Therefore, the alternative field compaction measurement method was implementation of nuclear density gauge as specified in the ASTM D6938.

Nuclear density gauge is fairly accurate non-destructive measurement method for soil density and moisture content in shallow depths, which have been used widely in the similar soil-culvert evaluation studies (Moore and García 2015a; Regier et al. 2018). It consists of a probe that emits a cloud of particles of radioactive isotope (i.e., usually ¹³⁷ Cesium) and detector sensors that receives the transmitted isotopes passed through the soil material. Depending on the mode of use, the gauge can be configured for both invasive (direct transmission mode) and non-invasive (backscatter mode), as illustrated in Figure 3-10. For direct transmission, a small hole needs to be made in the test surface, either through drilling or by pushing the gauge's rod into the soil. This would increase the possibility of loose materials falling into the hole, which can affect the accuracy of the readings. Hence, backscatter mode might be more suitable as it is non-invasive.

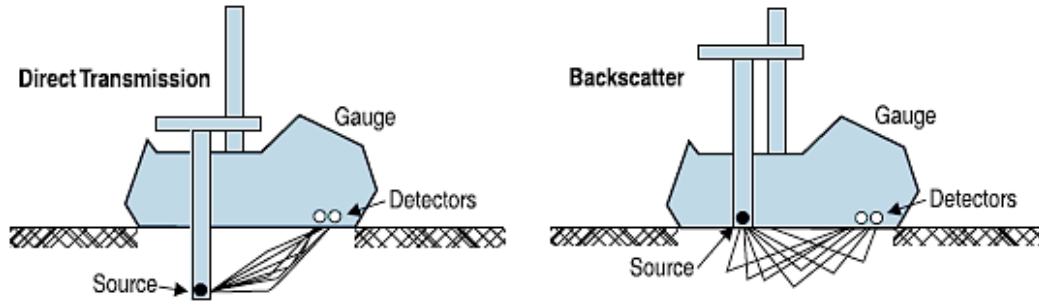


Figure 3-10. Modes of operation of nuclear density gauge (photo credit: multiquip.com).

In this study, soil compaction and moisture content of foundation, embedment, and embankment were measured at each lift using a nuclear density gauge, where two certified vendors, HVJ Associate and D&S Engineering Labs, were collaborated with the research team. For each lift, four measurements were conducted on both sides of the pipe samples, and the averaged values were reported. It should be noted that the sand cone method was also tested, however, as it was expected the method did not provide an accurate measurement. Figure 3-11 illustrates both sand cone and nuclear density gauge in the soil box.

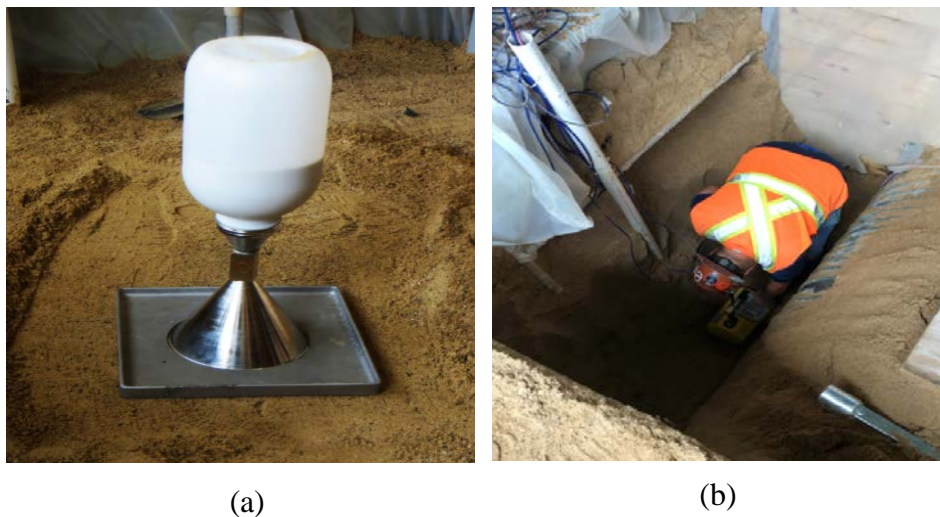
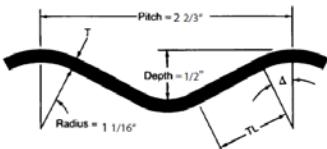


Figure 3-11. In-situ soil compaction measurement: (a) sand cone test, and (b) nuclear density gauge.

3.2.3. CMP Samples

Total of 9 annular corrugated metal pipe (CMP) samples were used in this study; five circular and four arch CMPs. The circular CMP samples had an internal diameter of 60 in., and the pipe arch CMP samples had a span of 71 in. and a rise of 47 in. (119.3 cm). All CMP samples were 6-ft long with a corrugation pitch length of $2 \times \frac{2}{3}$ in. and gauge 12 thickness, fabricated from bent hot-dip galvanized steel sheets along their edges fastened by rivets. The geometric details of the CMP profile are provided in Table 3-2. The CMP samples' steel were in compliance with the ASTM A796 (Contech 2019), with the minimum yield strength (f_y) of 33 ksi, a minimum tensile strength (f_u) of 45 ksi, and a Young's modulus of 29,000 ksi. The yield strain of $1,138 \mu\epsilon$ was calculated using the elastic stress-strain relationship.

Table 3-2. Pipe samples' geometric details (NCSPA 2008).

Thickness	Uncoated Thickness	Area of Section (A)	Tangent Length (TL)	Tangent Angle (Δ)	Moment of Inertia (I)	Section Modulus (S)	Radius of Gyration (r)	
(in.)	(in.)	(in. ² /ft)	(in.)	(Degree)	(in. ⁴ /in.)	(in. ³ /ft)	(in.)	
0.109	0.1046	1.356	0.740	27.11	0.0034	0.1360	0.1741	

For a culvert in field condition, the invert deterioration is a slow process and occurs in several years. As a result of this long corrosion process, the soil pipe system is stabilized and does not induce significant culverts geometry change. To simulate a culvert with entirely deteriorated invert section condition, an 18-in. (45.7 cm) wide strip of invert-cut pipe samples were entirely cut. This value has been calculated based on observations that usually one-third of wetted perimeter CMPs are more vulnerable to severe corrosion (Masada 2017). Furthermore, this value is in conformity with the middle bedding section as specified in AASHTO (2017). In order to maintain the CMPs original geometry during the installation and burial, the invert-cut section was left bolted to the CMPs' main body using angle sections and wood spacers. This detachable mechanism made the invert section's removal possible after burial of the CMP samples. The detachable invert section was specifically designed to withstand handling and installation forces as specified in the ASTM A796. Once the CMPs were installed and embedded, the invert sections were disassembled. Details of the detachable invert-cut section for the control tests and SAPL renewed samples were different which is discussed in sections 3.3, and 3.4. Figure 3-12 illustrates CMP samples prepared for this study.



Figure 3-12. Intact and invert-cut CMP samples: (a) transportation to laboratory facility, and (b) storage area.

3.2.4. Pipe Installation and Embedment

To install the CMPs in the soil box as detailed in Figure 3-9, where the CMPs should be placed at the center of the cells, the parameters of each CMPs were measured and the crown, springline, and invert were located and marked accurately. In addition, the center of the partition walls was located and entirely marked to be used as benchmark for pipe installation location. The existence of these marks was essentially important since the CMPs' invert was cut. Thus, the pipe samples were no longer an ordinary pipe and it was crucial to position the center of the invert-cut section on the center of the soil box cell. Prior to the CMPs installation, the 4-in. loos bedding soil was perfectly leveled in every direction to provide even and uniform substratum.

Once the CMPs were positioned in their location, the gap between both pipes and the partition wall were covered with a flexible thin plywood and Styrofoam rolls to prevent soil ingress inside the CMPs. The plywood and the Styrofoam was wrapped around the CMPs and were attached to the pipe using duct tape. The bedding leveling, pipe positioning and gap sealing are illustrated in Figure 3-13.

After CMPs placement, positioning, and gap sealing inside the cells, the hunch area was filled with the SP soil to prevent pipe rolling during instrumentation and backfilling process. Attempts were made to fill the annular gap at the haunch area, illustrated in Figure 1-15, using shovel and light hand compaction. Once the CMPs were stable in the location, the outside surface of CMPs were instrumented with strain gauges. The strain gauges' wires were clustered and attached to the valley of the pipes' corrugation and protected with both aluminum and duct tapes. To pass the wires through the soil a small duct was used to eliminate friction between wires and the soil.

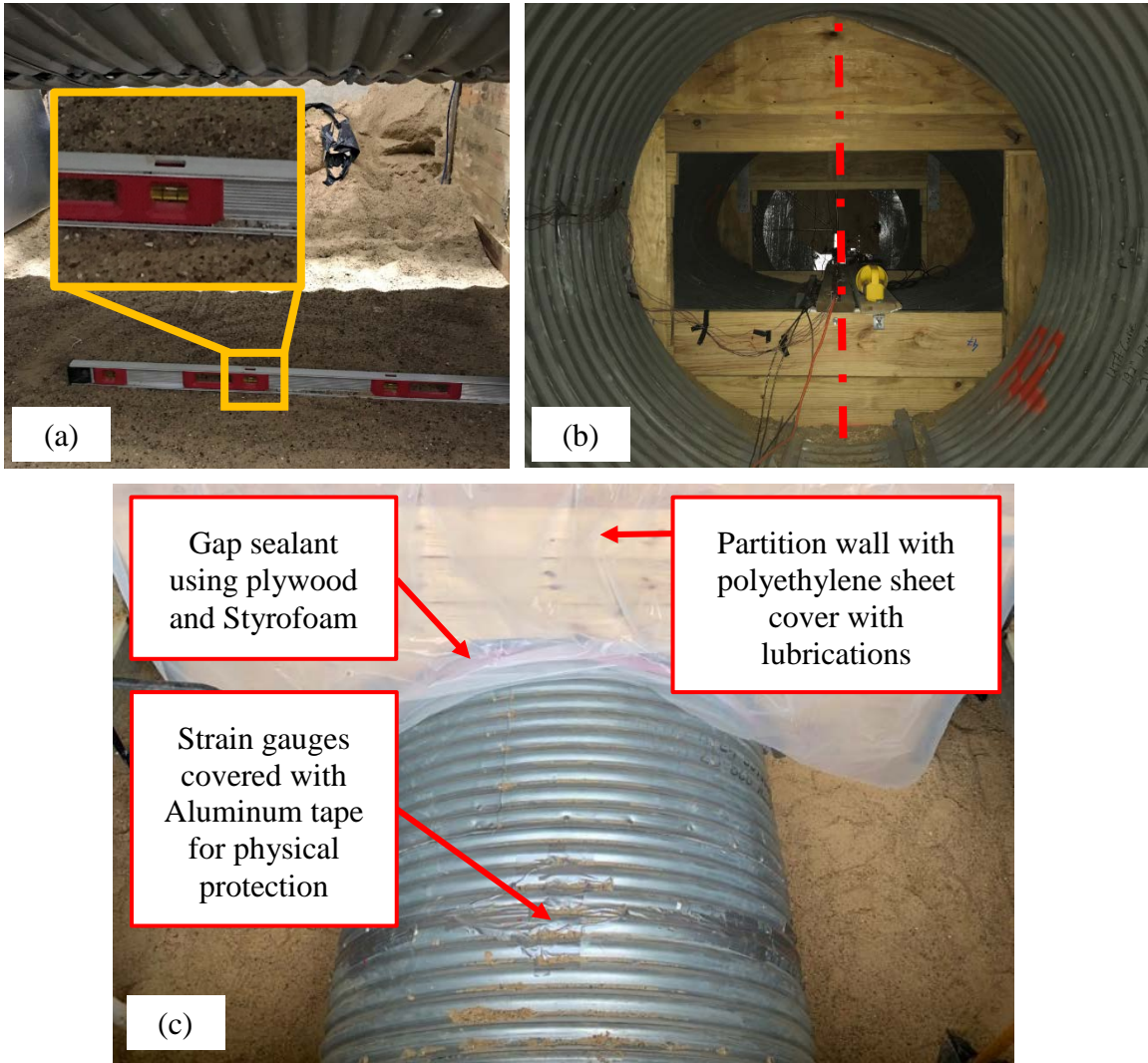


Figure 3-13. Pipe installation and preparation before backfilling: (a) bedding layer leveling process, (b) pipe positioning and installation, and (c) gap sealing using plywood, Styrofoam, and duct tape.

3.2.5. Load Pads

According to AASHTO LRFD bridge design specifications, the load through a vehicle on the culvert cover will be transferred as a uniform stress over a rectangular area equal to the contact area of the wheels, as discussed in section 1.2.4.2. In this study two different load pads were used;

3.2.6. Instrumentation

Experimental structural testing of soil-culvert system generally includes load and pressure measurement system, pipe internal deflection measurement system, and pipe stress measurement instrumentation (Kohankar Kouchesfehni et al. 2020; Moore and García 2015b).

3.2.6.1. Earth Pressure Cells

Earth pressure cells and load cells are widely used for measurement of the applied load and pressure on the soil surface and inside the soil (Arockiasamy et al. 2006; Chaallal et al. 2014; Moore and García 2015a; Tetreault et al. 2018). Earth pressure cells such as Geokon 4800 series or similar models are suitable sensors, which can be placed inside the soil on the top, sides and bottom of the pipe to measure the applied pressure at different depths and directions (GEOKON 2019; Khatri et al. 2015). However, to avoid any point load on the earth pressure cells, it is suggested not to attach the pressure cells directly along the pipe surface and embed it with at least 4 in. (70 mm) distance away from the pipe since the pressure cells are generally required to be in contact with uniform soil on both sides. In this study, four Geokon 4800 series earth pressure cells were installed around each pipe samples at the locations; top, bottom, and both sides of the pipe sample with a 4 in. distance from the outer surface of the CMPs, as illustrated in Figure 3-9 and Figure 3-15 (a) and (b). For the crown location, the pipes were backfilled up to 8 in. above top of the pipe samples. Then a small area with dimensions of the pressure cell were excavated for 8 in. to reach the pipe's top surface. After proper preparation and measurement, a 4 in. of soil were placed, hand compacted and flattened to provide smooth and even bedding for the pressure cell. Once the pressure cell was placed, another 4 in. of soil were placed on its top to reach the backfill surface. Similar procedure of backfilling-excavation-filling were conducted for the invert and side

pressure cells. The wires of the pressure cells were placed with a figure-eight configuration to prevent wire rupture due to any possible movement during the test.

The earth pressure cells were wired to a Geokon data acquisition system (DAQ), which digitalizes the transmitted analog signals from the earth pressure cells at the predefined sampling rate during the test. Figure 3-15 (c) and (d) show the soil pressure measuring device including earth pressure cell sensor and the data acquisition systems.

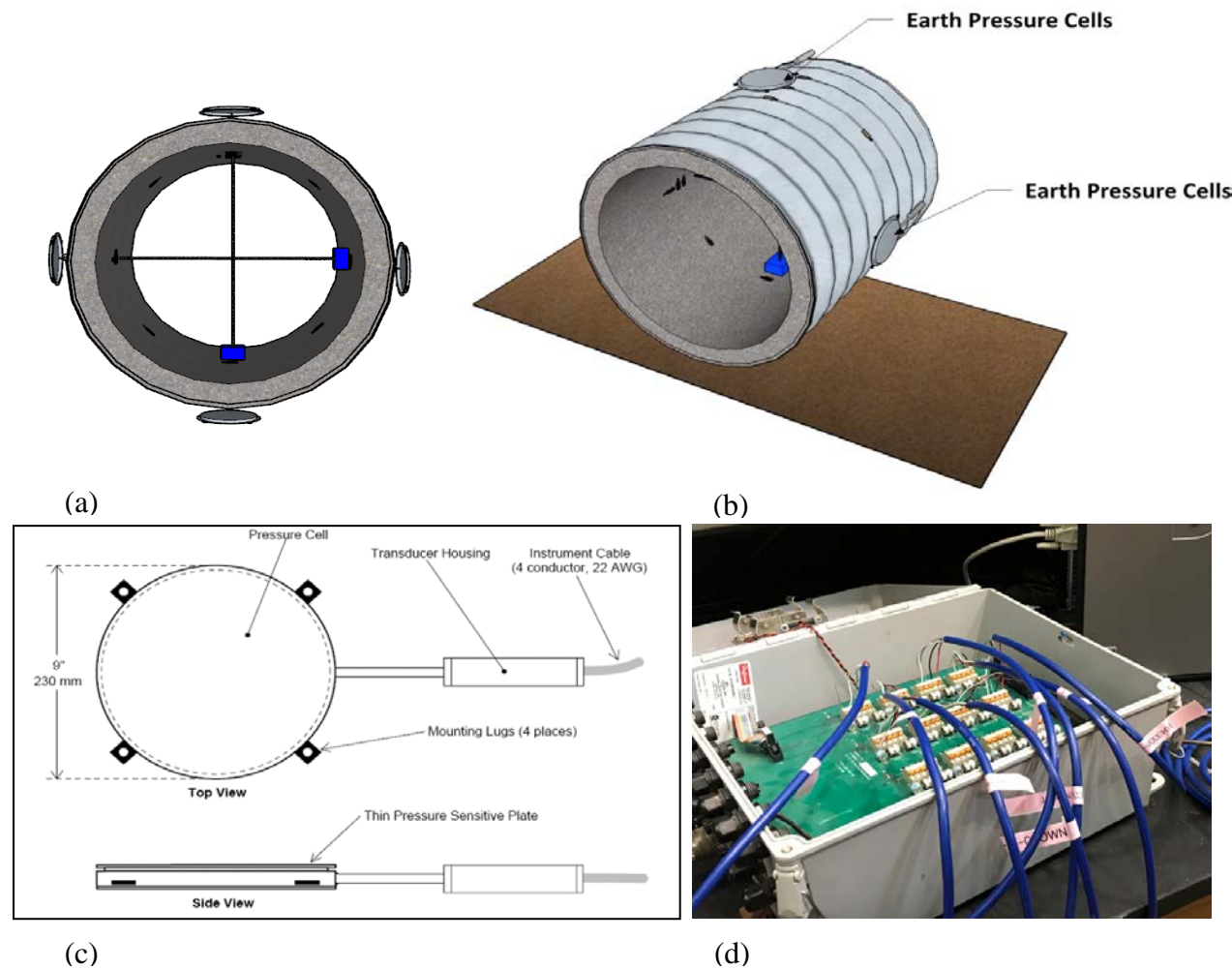


Figure 3-15. Pressure sensors: (a) 3D cross sectional view, and (b) 3D view of pressure cell locations around the CMP, (c) Geokon 4800 series earth pressure cell, and (d) Geokon data acquisition system.

3.2.6.2. Mechanical Sensors for Displacement Measurement

Internal deflection measurement of the culverts can be carried out using different sensors and techniques. Cable Displacement Sensors (CDSs) and Linear Variable Differential Transformers (LVDTs) are the most common sensors to measure the diameter change of pipe samples under dead and live loads (Masada 2017b; Tetreault et al. 2018). Implementation of LVDTs require a frame inside the pipes to hold the sensors, as shown in Figure 3-21 (a). The frame should not touch the testing specimen since it may affect the test results. The frame should be cantilevered inside the pipe to hold the sensors. CDS is more suitable option which does not require a holding frame. However, keeping the CDSs fully adhered to the testing pipe wall during such a destructive testing is challenging. In this study, Micro-Epsilon WPS-500-MK30-P10 CDS and Omega LD650 were used to measure pipe deflections in both horizontal and vertical directions (Micro-Epsilon 2019; OMEGA 2019).

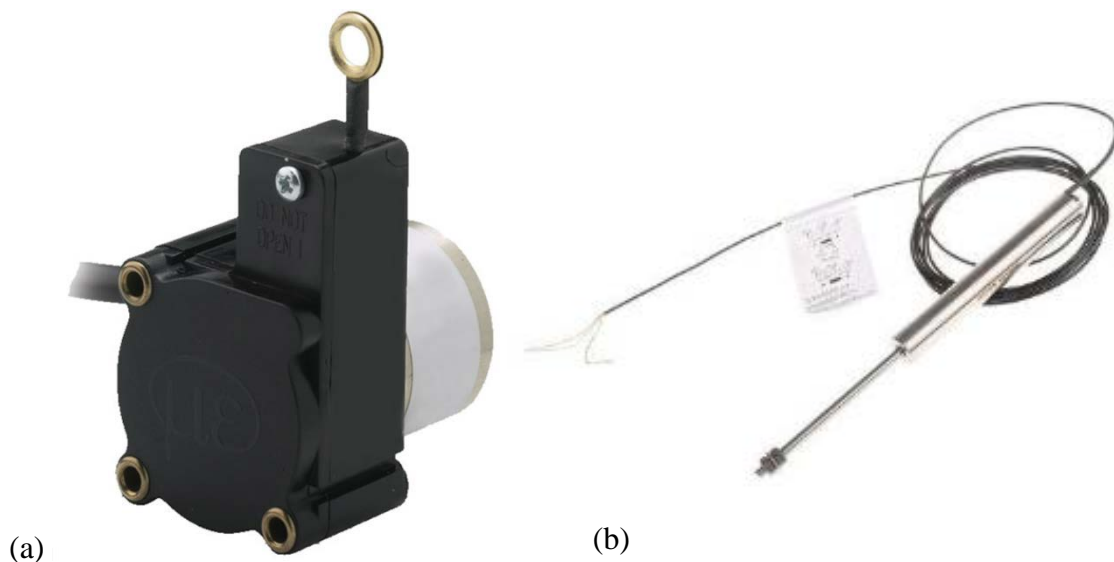


Figure 3-16. Mechanical sensors, used to measure pipe deflection: (a) Micro-Epsilon WPS-500-MK30-P10 cable displacement sensor, and (b) Omega LD 650 LVDT.

3.2.6.3. Digital Image Correlation (DIC) Method

Digital image correlation (DIC) is an inexpensive optical-numerical measurement technique that is a suitable alternative to the conventionally used mechanical sensors, such as LVDTs and CDSs (Caporossi et al. 2018; Darabnoush Tehrani et al. 2020b). It can measure deflection and displacement as accurate as mechanical sensors. The main advantage of DIC is its ability to provide multipoint measurement inside the pipe in both vertical and horizontal direction which makes profiling of testing pipe samples at any stage of loading possible. In DIC, the digital image is converted to a gray-scale image, where the pixel intensity can vary from 0 (black) to 255 (white). An easier way is to convert the image to binary, where the pixels are either 0 (black) or 1 (white). In the converted images, the pre-event and post-event targets is registered to allow their location change to be measured in the unit of pixels, as illustrated in Figure 3-17 (a). However, in order to calculate the displacement, a length unit should be assigned to the pixels (e.g. 1 pixel = 0.0001 in.) to correlate the target movements in a required length unit (i.e., in. or mm). This correlation value varies based on the location of camera and its resolution. Therefore, DIC requires calibration every time that the camera or target is moved in out of plane direction.

DIC is a fully remote measurement system, however, there are two basic requirements to conduct accurate deflection measurement using DIC; existence of the target points and a scale reference. If the displacement measurement of a point is the goal, then a high contrast target should be installed in that point and be registered as the monitoring object, which is also called a region of interest (ROI). If the displacement/deformation of an area is the interest, then a random spackled pattern should be applied on the ROI surface. The existence the target is essentially required since identifying the correspondence between single pixels in two images with large number of pixels (ex., 18 Megapixels) is almost impossible.

In this study, an 18 Megapixel digital single lens reflex (DSLR) Canon Rebel T5i camera was utilized for the pipe sample profiling during the tests using digital image correlation (DIC) technique, as illustrated in Figure 3-17 (b). To achieve this goal, multiple rigid DIC targets were installed on the crest of the pipe corrugation at the center of the pipe samples (i.e. in the same plane) circumferentially at an average of 2-in. spacing. The targets' spacing at the crown location, however, was about 1 in. since it was expected to observe cracks or local buckling at that location and therefore, more data points were required. In general, the more the target points, the more the profile resolution. To optimize the targets' size, a sensitivity analysis was conducted prior to the installation. The result showed, with respect to the laboratory lighting condition, camera resolution and the camera's distance from the targets, a black dot with a diameter of 0.1 to 0.25 in. (i.e., about 10 to 20 pixels) would be ideal for this application. The targets were designed with the high contrast colors, i.e. black and white, and were installed in a ring configuration at the center of the pipe samples to measure the pipe profile change during the tests. In 2D DIC, it is essential to place the camera perfectly straight (i.e., perpendicular) towards the measuring plane (Ham and Darabnoush Tehrani 2019). Therefore, extra exercise should be practiced to level the camera with respect to the ground and the pipe's cross section plane. The DIC targets installed inside a testing pipe sample is illustrated in Figure 3-21 (a).

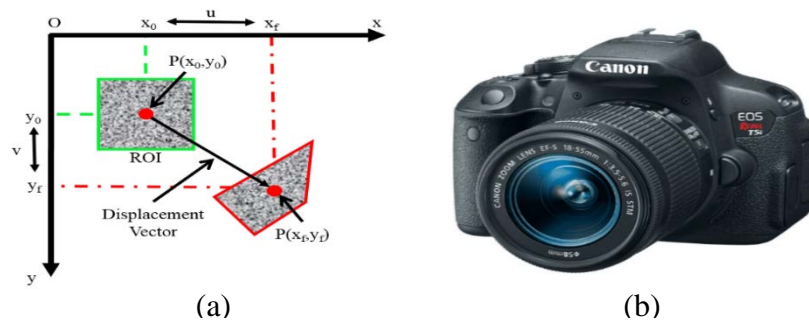


Figure 3-17. DIC displacement measurement: (a) schematic diagram of the basic DIC principles, and (b) a DSLR Canon Rebel T5i.

In addition to the DIC method, the digital cameras were used to monitor the pipes during the tests in real time. Aside from the camera, used for pipe profiling, two other cameras were installed on the instrumentation's wooden frame to monitor the crack initiation and its propagation at the crown and West springline, as illustrated in Figure 3-18. The cameras were connected to a 42 in. LCD TV, located in the instrumentation central control station, through USB-2 cables.

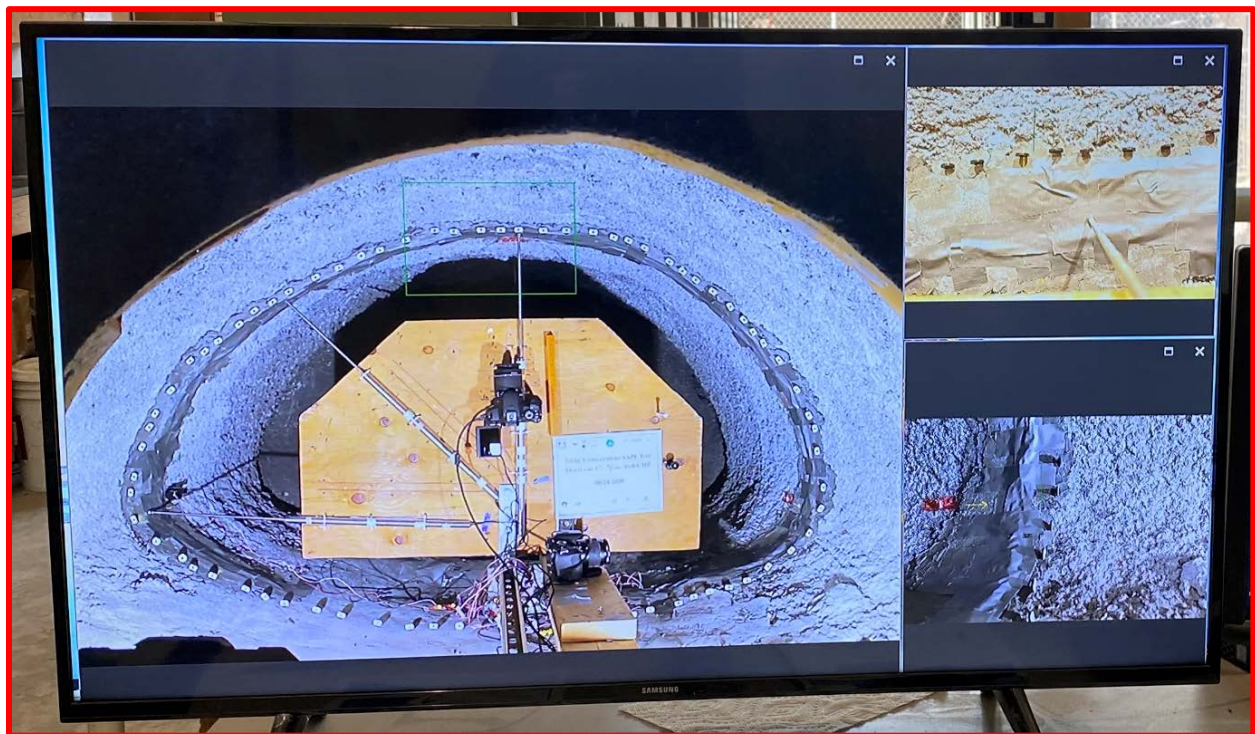


Figure 3-18. Pipe sample monitoring in real time during the test at front view, crown and West springline.

3.2.6.4. Strain Gauges

The stress analysis of the pipe samples due to the loading was carried out using strain gauges. They were installed circumferentially, in both inside and outside of the pipe surfaces. Several study suggested to implement strain gauges at crown, shoulder, haunch and invert of the testing pipe (Bryden et al. 2015; Sargand et al. 2001b; Syar et al. 2020). Prior to the strain gauge installation, the galvanic coating on the pipe samples at that location was removed and the surface was prepared according to the manufacturer recommendation. For cementitious SAPL renewed samples, the Micro Measurement M-bond adhesive resin and M-bond type 10 curing compound were used on the porous and rough cementitious surface to fill the pores and provide an even base for the strain gauge installation. Implementation of this compound minimizes the gauge reading errors due to the surface roughness. Once the gauges were installed, the Micro Measurement air drying M-Coat D was applied to protect gauges from moisture and electrical leakage. In addition, two layers of physical protection were provided by attaching M-Coat FA Aluminum foil tape and M-Coat FN Neoprene rubber sheets to protect gauges form abrasive soil particles movement. The wires were passed through a small duct in order to release the stress stemming from the soil surrounding the wires. In this study, the total of 16 Micro Measurement C2A-06-250LW-120 uniaxial strain gauges were installed in two layers (i.e., inside and outside) in the hoop direction around each pipe samples, in middle section, at 45 degree intervals, as illustrated in Figure 3-19.

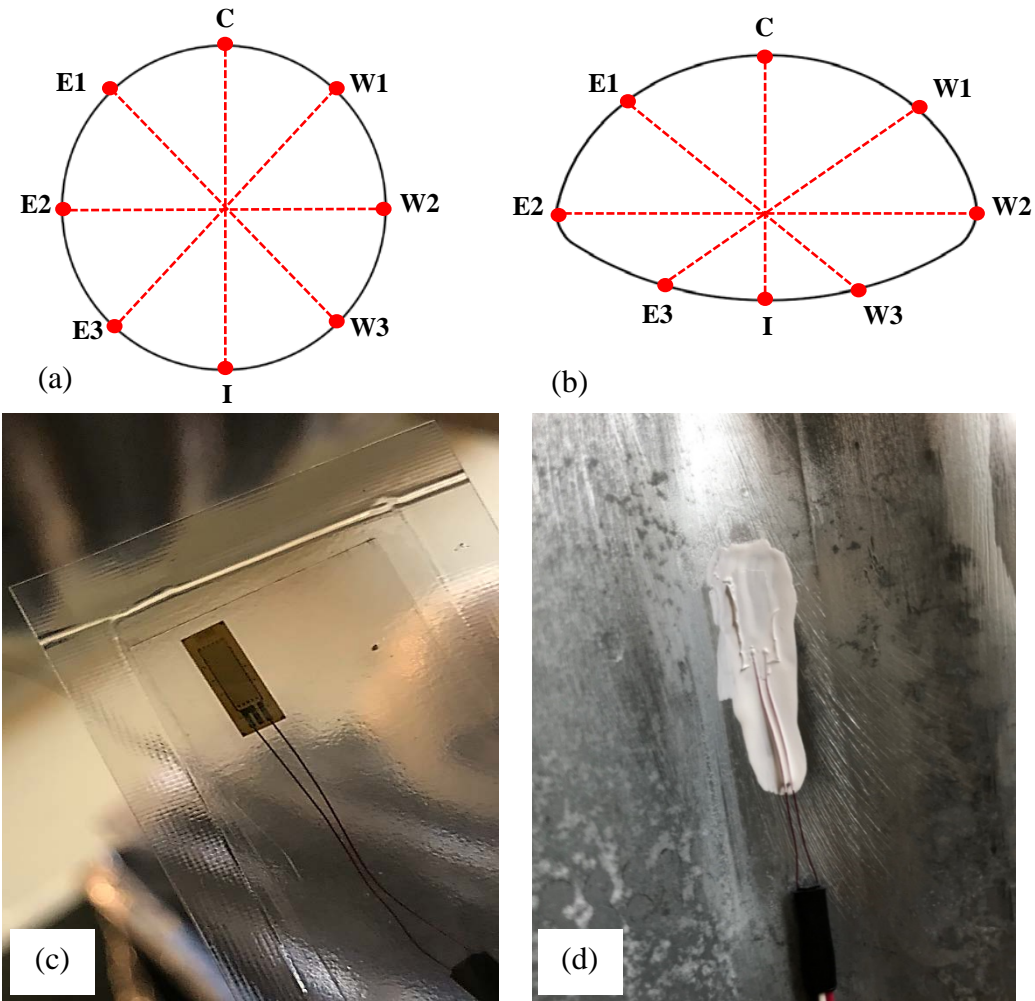


Figure 3-19. Strain gauges: (a) installed locations around the circular CMPs, (b) installed locations around the pipe arch CMPs, (c) C2A-06-250LW-120 uniaxial strain gauge, (d) installed strain gauge on the exterior surface of a CMP coated with air drying M-Coat D.

For the control test set, the strain gauges were installed on the outside surface of the CMPs on both crest and valley of the corrugation, as illustrated in Figure 3-20 (a) and (c). For the SAPL renewed CMPs, the gauges were installed on the outside surface of the CMP at crest of the corrugation and on the inside surface of the SAPL as illustrated in Figure 3-20 (b) and (d).

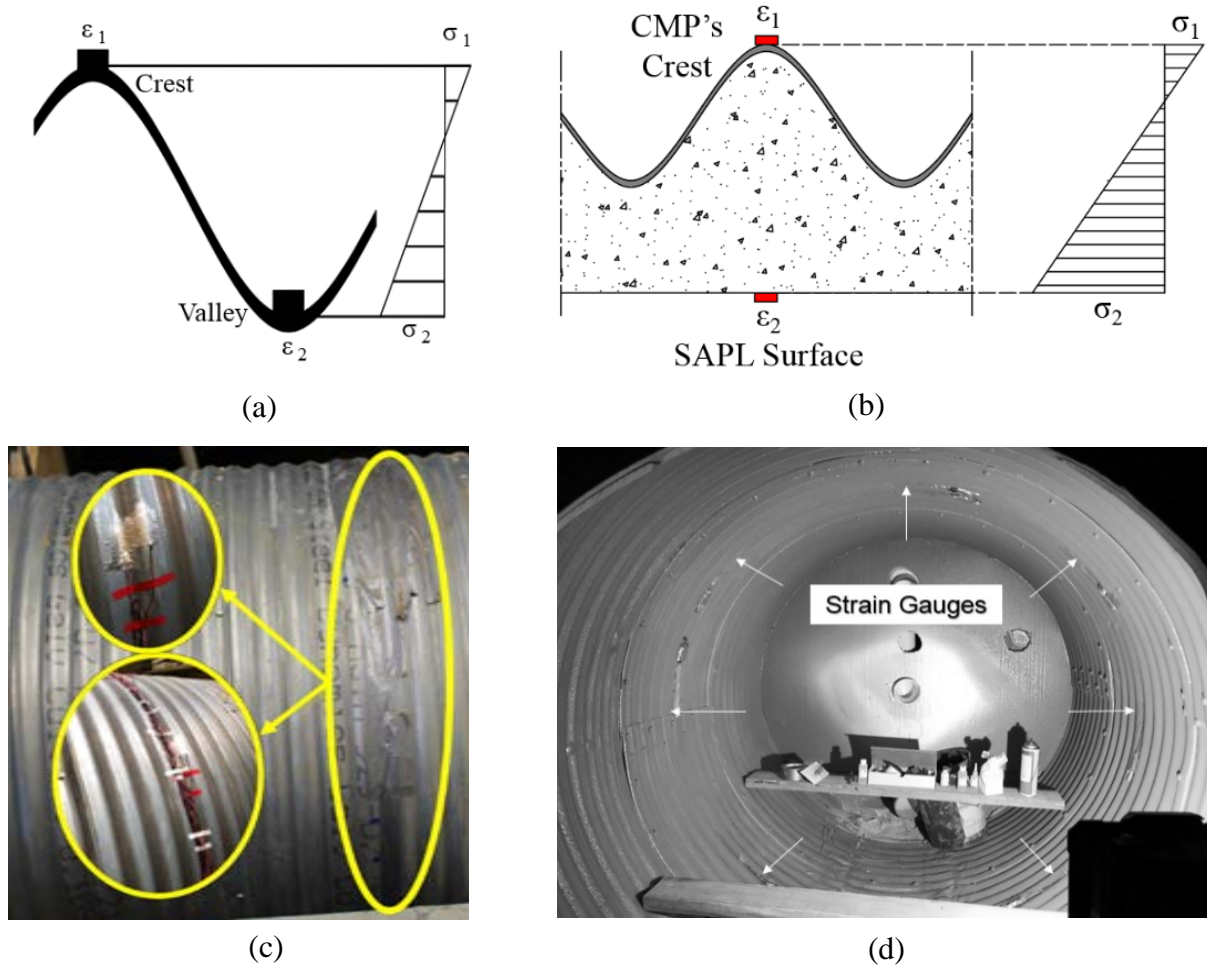


Figure 3-20. Strain gauges configuration and details: (a) schematic profile view at the crown for the bare CMP, (b) schematic profile view at the crown for SAPL renewed CMP, (c) installed strain gauges outside of the bare CMP, and (d) installed strain gauges inside the SAPL renewed CMP.

For the control test set the strain gauges were installed in both crest and valley to obtain the thrust force and bending moment. The circumferential thrust force is calculated using the average strain from the crest and valley at each point according to equations (45) and (46)

$$\varepsilon_{ave} = \frac{(\varepsilon_1 + \varepsilon_2)}{2}, \quad (45)$$

$$N = \varepsilon_{ave} EA, \quad (46)$$

where, N is the thrust force per unit of length, ε_{ave} is the average strain, ε_1 is the strain on the outer corrugation crest, ε_2 is the strain at the outer corrugation valley, E is the Young's modulus, and A is the cross sectional area of the CMP's wall per unit of length.

The local bending moment of the pipe sample was obtained by calculating the curvature at each point using the equations (47) and (48) respectively (Regier et al. 2016):

$$\kappa = \left(\frac{\varepsilon_1 - \varepsilon_2}{h} \right), \quad (47)$$

$$M = -EI\kappa, \quad (48)$$

where, κ is the local curvature, h is the height of the corrugation, I is the moment of inertia, and M is the bending moment per unit of length. It should be noted that equations (45) to (48) are only valid in the elastic regions.

The experimental test instrumentation setup and the control station are illustrated in illustrated in Figure 3-21 (a).

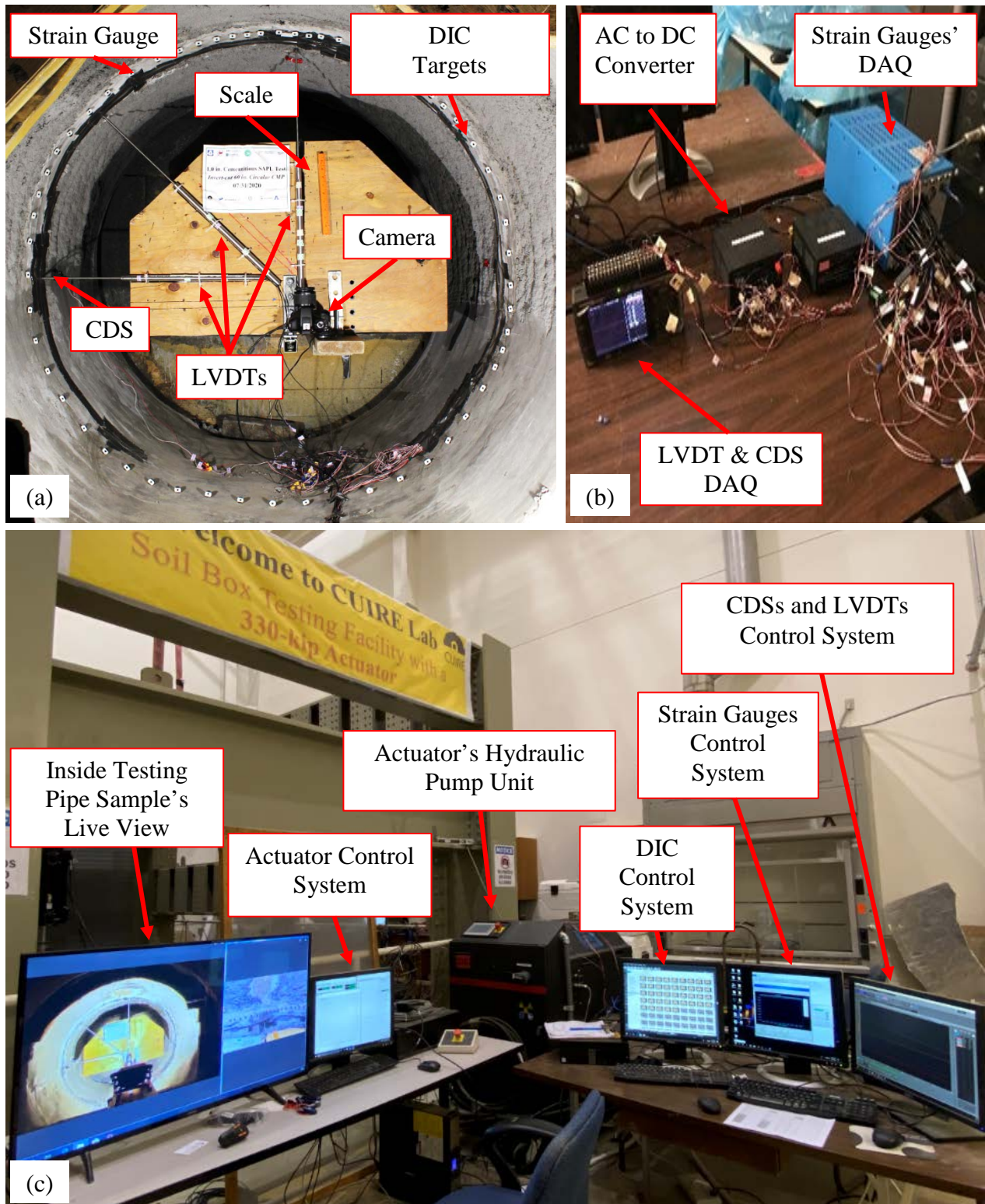


Figure 3-21. Experimental test instrumentation setup: (a) pipe sample inner instrumentation, (b) data acquisition systems, and (c) instrumentation central control station setup.

3.2.7. Test Operation and Load Rate

A continuous static load was applied to the soil using a MTS 330-kip hydraulic actuator attached to a reaction frame located at the CUIRE Laboratory at the University of Texas at Arlington. The static loading regime was chosen in this set of tests since it has higher impact on the pipe sample deformation (Yeau et al. 2009). The load was applied through the rigid load pad, as detailed in section 3.2.5, through the displacement-control procedure. The displacement-control method was chosen due to its advantage for obtaining the post-peak softening behavior of the specimens and it was applied by controlling the movement rate of the actuator's stroke at a certain defined rate. Choosing an appropriate load rate and loading method for these tests was one of the main challenges since in the similar studies they are not reported.

In this study the value 0.03 in./min was selected to be continuously applied to reach the failure and post failure of the soil-culvert system. The 0.03 in./min was selected based on the discussion in section 2.1.4. In comparison, to prevent soil lagged deformation and settlement, Masada (Masada 2017a) and Regier et al. (Regier et al. 2016) applied an incremental manner. However, the poorly graded sand (SP) was chosen in this study had no silt and clay, which makes it insensitive to time dependent deformations. Moreover, the loading speed is slow enough to compensate the lagged settlement effect. Therefore, continuous loading was selected for this study. Prior to applying the load, actuators swivels were locked at top and bottom to prevent any possible rotation due to possible uneven deformation soil-pipe structure under the load pad. In addition, the soil and load pad surface level were checked prior to the loading to assure the load is applied uniformly, as illustrated in Figure 3-22.

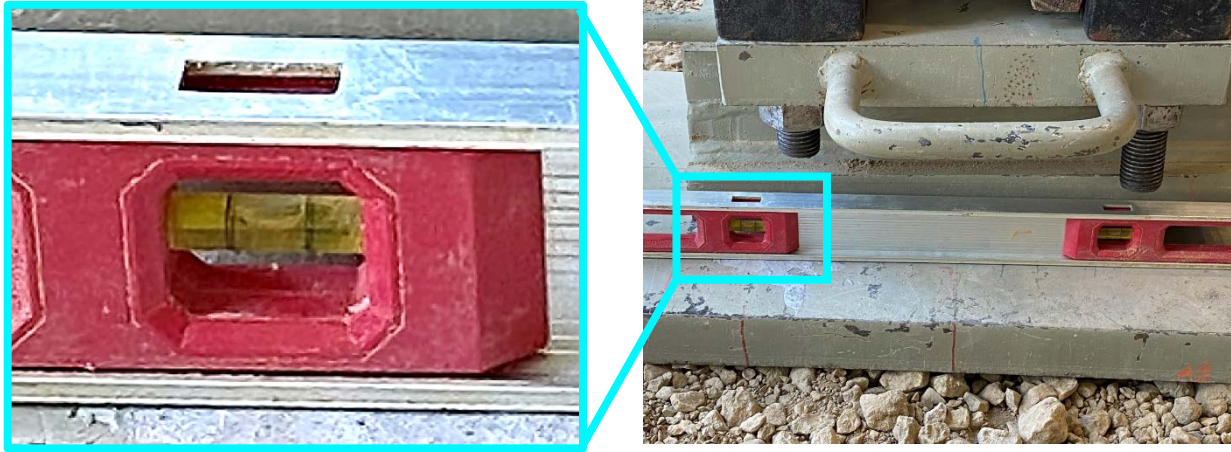


Figure 3-22. Load pad level investigation prior to the loading to assure the load will apply uniformly.

3.3. Control Test Details

The control tests consist three unlined CMPs including one intact circular CMP, one invert-cut pipe arch CMP, and one invert-cut circular CMP. To simulate fully invert deteriorated culvert, an 18-in. wide strip of the invert section of the invert-cut CMP samples were cut and were connected to the main body of the CMPs through bolts, wooden spacers and angle sections. The reason for implementation of such a detachable invert mechanism was to provide the same geometry similar to the intact CMP sample at the time of pipe installation and backfill. In addition, cutting the buried CMPs inside in such a confined area was challenging. Figure 3-23 illustrates the CMP samples and the detachable invert mechanism used in the control test.

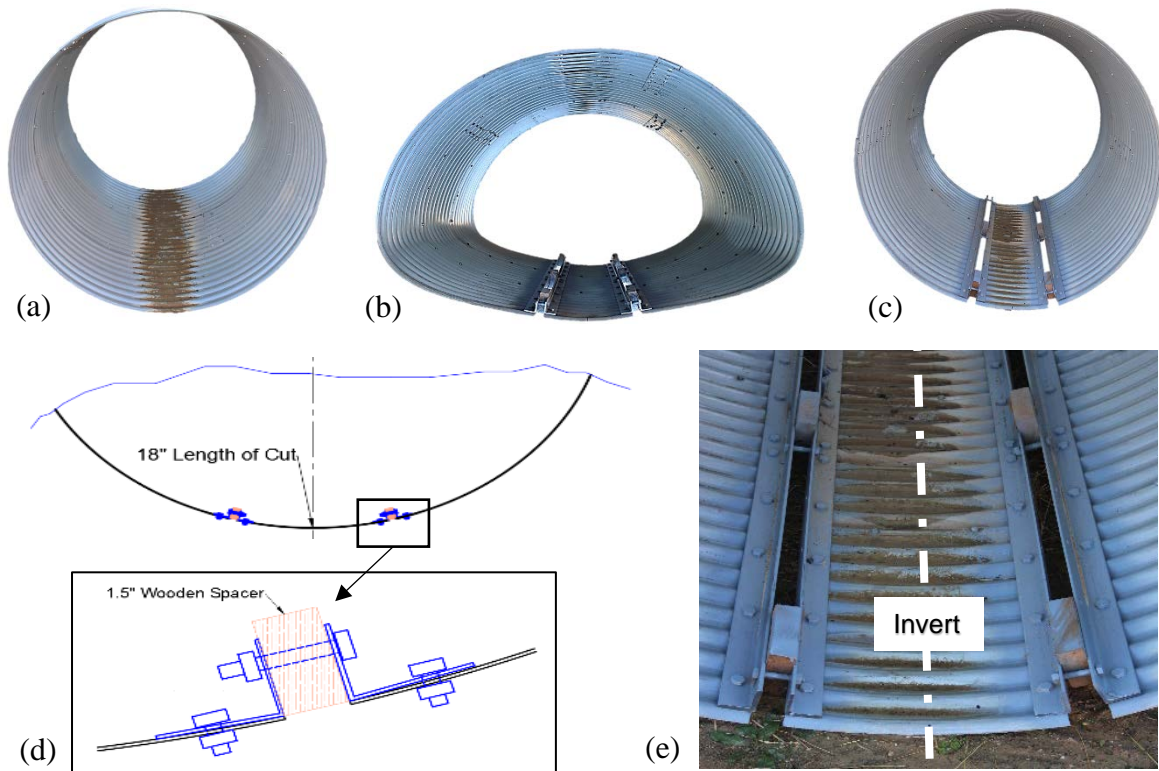


Figure 3-23. Control test CMP samples: (a) intact circular CMP, (b) invert-cut pipe arch CMP, (c) invert-cut circular CMP, (d) detachable invert section layout, and (e) invert cut section with detachable fasteners.

The CMPs were installed in the soil box and backfilled as elaborated in section 3.2.4. The control test layout is presented in Figure 3-24, where the south cell was assigned to the intact circular CMP sample. The invert-cut pipe arch CMP was installed in the middle cell and the invert-cut circular CMP was installed in the north cell. Control test pipe installation inside the soil box is illustrated in Figure 3-25. Due to the lower rise of the arch CMP, the foundation depth of the middle cell was increased for 13 in. to obtain same crown elevation for all three pipes.

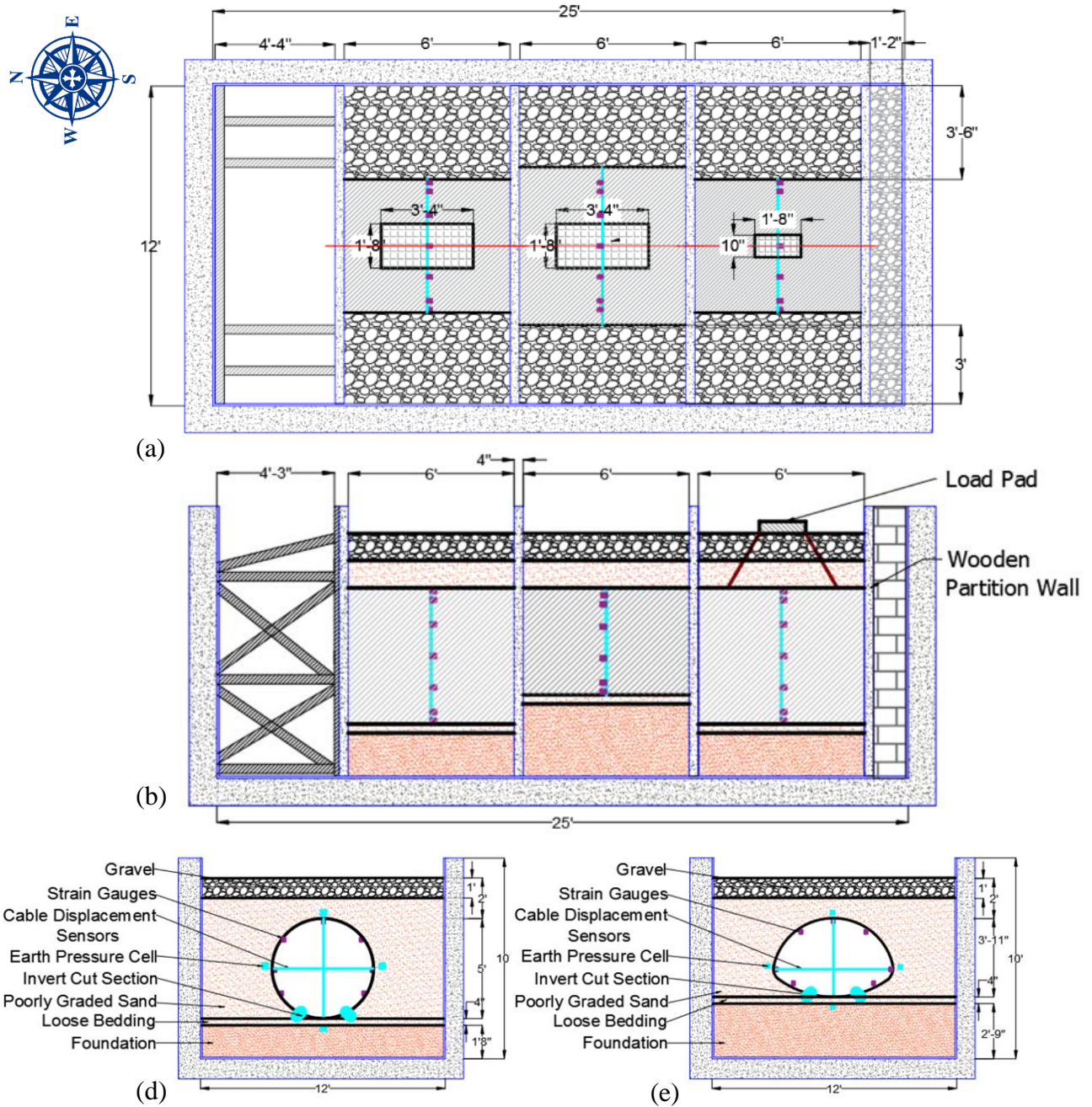


Figure 3-24. Control test configuration: (a) plan view, (b) cross sectional view of the circular pipe sample; (c) profile view of the aligned pipe samples in the soil-box; (d) cross sectional view of the arch pipe sample; (e) averaged water content and compaction rate distribution at different layers.



Figure 3-25. Test setup configuration for all three cells: (a) during CMP installation, (b) during embedment, and (c) filled hunch area with poorly graded sand without compaction.

During the soil placement inside the soil box, the compaction rate and moisture content were measured at every lift of foundation and backfill. For each lift, two measurements were conducted on each side of the pipes. The measured compaction rate and moisture content values are presented in [Compaction Measurement](#). Figure 3-26 illustrates the averaged values for all three cells at each lift through a contour plot.

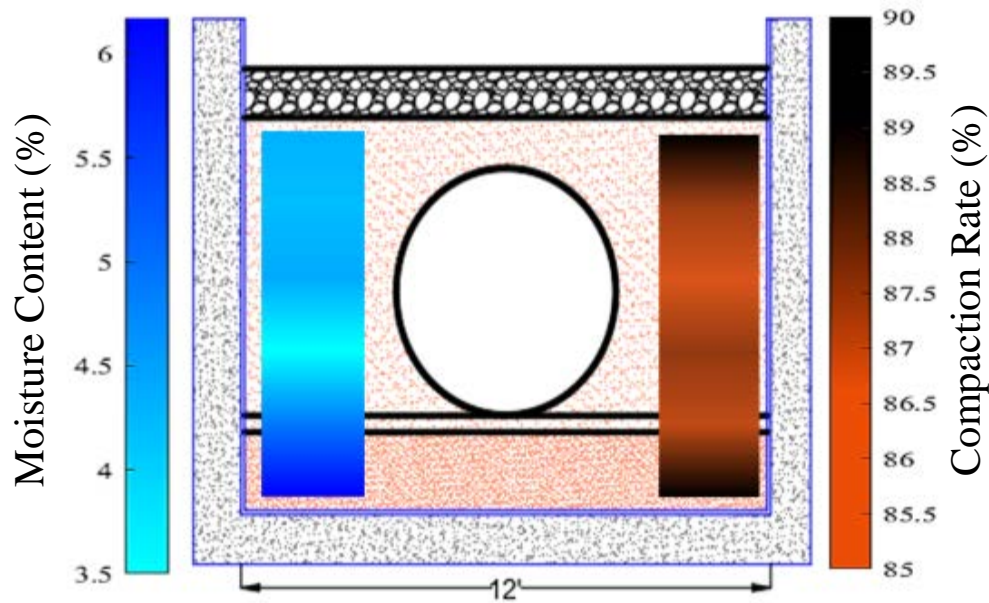


Figure 3-26. Control test series averaged moisture content and compaction rate contour-plot for different burial layers.

Prior to the loading, the invert sections were detached and taken out of the pipe samples. However, once the cut section was detached the CMPs moved and squeezed due to the active soil pressure to the sides of the pipe samples. The pipe samples were measured before and after invert detachment using a laser distance measurement tool with 0.06 in. accuracy. The result shows the pipe arch sample has moved for 2.23 in. downward at the crown and 5.24 in. inward at the springline. The amount of horizontal movement for the circular CMP, however, was smaller. The measurement showed the pipe sample moved 3.1 in. vertically and 3 in. horizontally. The reason could have been due to the fact that the invert of the arch pipe sample was almost flat and once the ring compression was gone after the detachment, the bottom of the CMP was slipped on the soil surface underneath. While, for the circular pipe sample, due to the sharp angle of the pipe at the hunch area, CMP slightly penetrated into the soil and was prevented from further movement. Using

DIC to detect circular pipe sample's movement before and after invert detachment revealed that the pipe sample was rotated clockwise approximately 0.45 in., as it is illustrated in Figure 3-27.

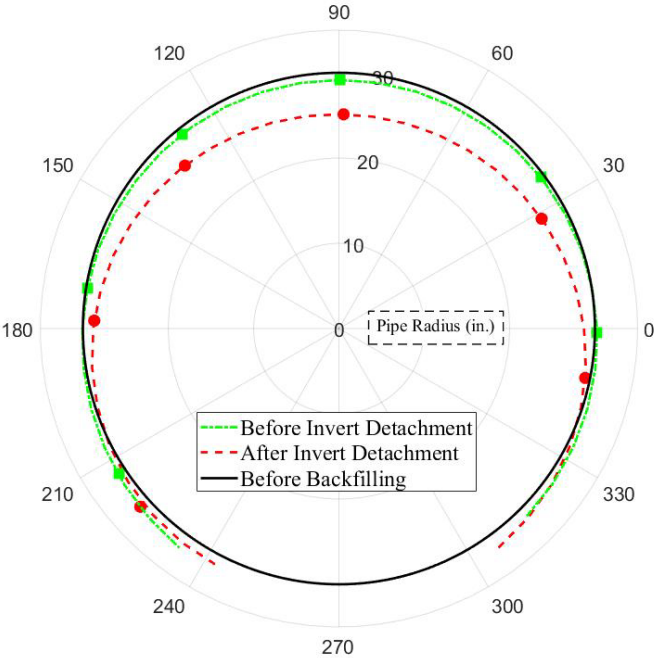


Figure 3-27. DIC result for the circular invert-cut pipe sample movement due to the invert section detachment.

3.4. SAPL Renewed Test Details

Three 47 in. × 71 in. pipe arch and three 60 in. CMPs with corrugation profile of $2\frac{2}{3} \times 1\frac{1}{2}$ in. and gauge 12 thickness were used for this sets of tests. The invert of all the CMP samples were cut as outlined in section 3.3. However, similar to the control test, after the invert-cut section detachment, the movement of CMPs due to the soil load was a major concern, and in that case the pipe would not have the exact same geometry at the time of SAPL installation. Furthermore, since a culvert in field condition is usually longer than the testing samples in this study, there is a larger

friction resistance between the soil and culvert in field that prevents culvert movement in a shallow cover configuration. Therefore, in order to have the same CMPs geometry for all SAPL renewed pipe samples, two narrow strips with 3 in. width at both ends of the invert-cut section were kept bolted to hold the CMPs' geometry. Once the SAPL was installed and cured, the 3 in. end-strips were removed to eliminate ring stiffness of the host pipe (i.e., CMP) and maximize the applied force on the liner to address the objective of the presented study for investigation of whether the SAPL is fully structural or not. Figure 3-28 shows a plan view of the detachable invert section for SAPL renewed CMP samples, where at the stage (1) the invert is bolted to the CMP's body during backfilling. Once the backfilling task was completed and the soil-pipe system was stabilized, in the stage (2) the middle detachable invert section was removed. In the stage (3) the cementitious SAPL was installed inside the CMP and in the stage (4) after full curing of the SPSL, the remaining invert section was unbolted to eliminate the ring stiffness of the host pipe (i.e., fully deteriorated pipe condition).

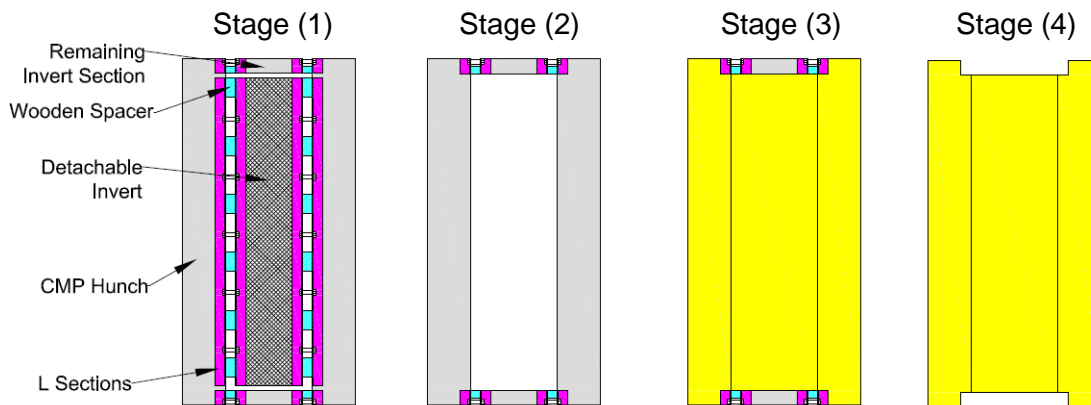


Figure 3-28. Plan view of the detachable invert mechanism for SAPL renewed CMPs during the SAPL installation.

The CMPs were installed in the soil box and backfilled with the similar procedure of the control test. The CMPs renewed with the cementitious SAPL test layout is presented in Figure 3-30 and Figure 3-31, where the south cell was assigned to the invert-cut CMP sample renewed with 3 in. cementitious SAPL. The middle and north cell were assigned to the invert-cut CMP renewed with 2 and 1 in. cementitious SAPL respectively. The pipe arch CMPs installation inside the soil box are illustrated in Figure 3-29.

During the soil placement inside the soil box, the compaction rate and moisture content were measured at every lift of foundation and backfill. For each lift, two measurements were conducted on each side of the pipes. Figure 3-32 illustrates the averaged values for all three cells at each lift through a contour-plot.

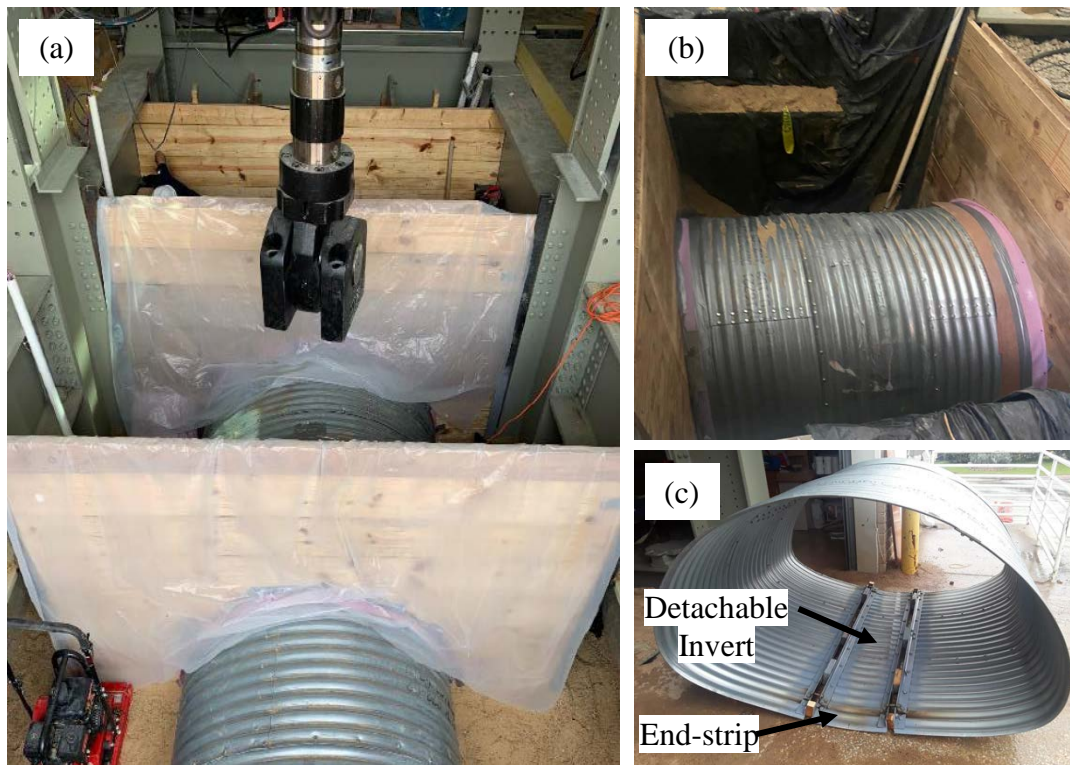


Figure 3-29. Pipe installation: (a) Longitudinal configuration of pipe arch CMPs in the soil box, (b) a pipe arch CMP with end sealing, and (c) a pipe arch CMP sample with detachable invert and end-strip section.

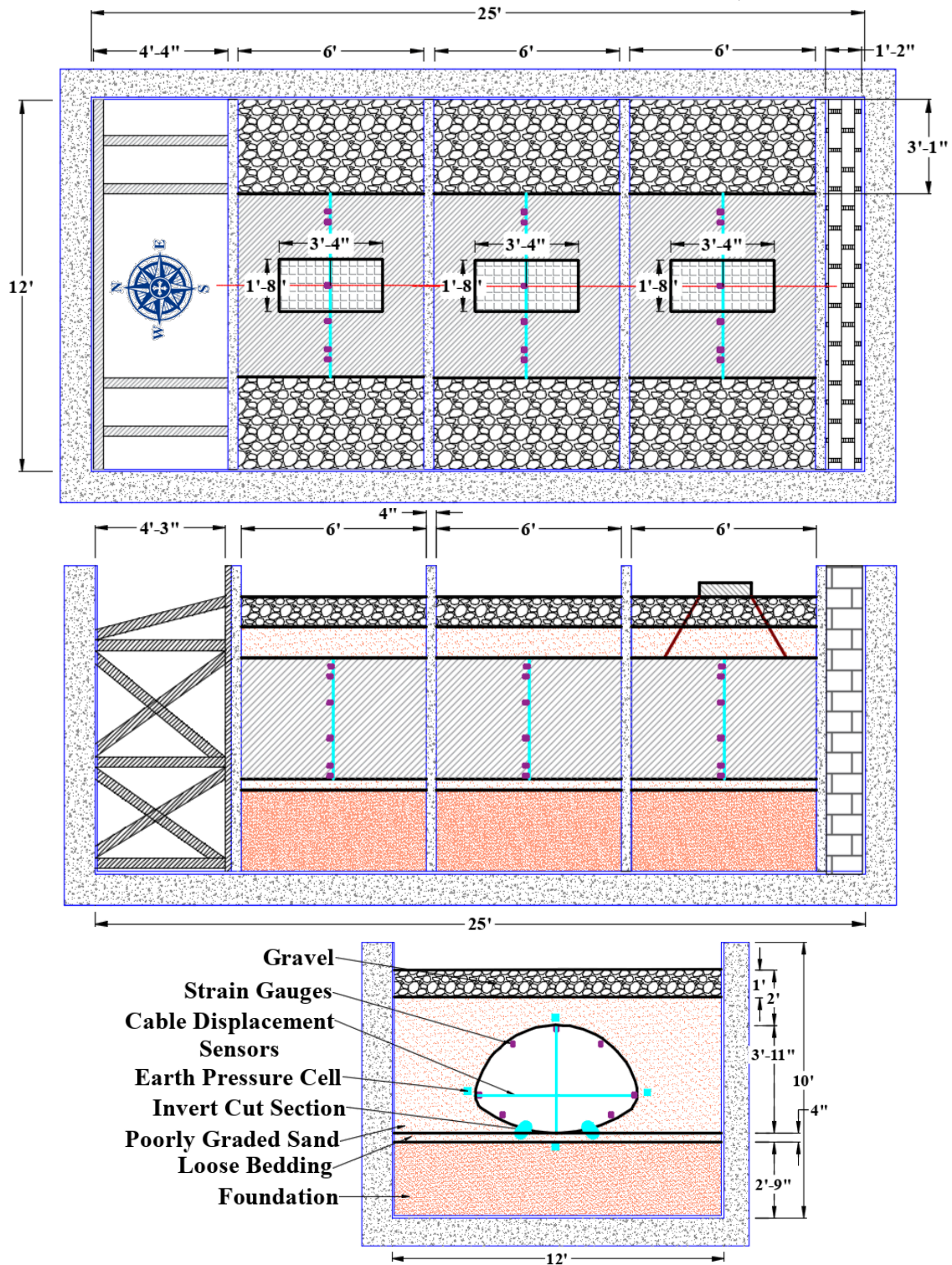


Figure 3-30. The pipe arch CMPs' burial configuration: (top) plan view, (middle) profile view of the aligned pipe arch CMPs in the soil-box, and (bottom) cross sectional view of the pipe arch CMP.

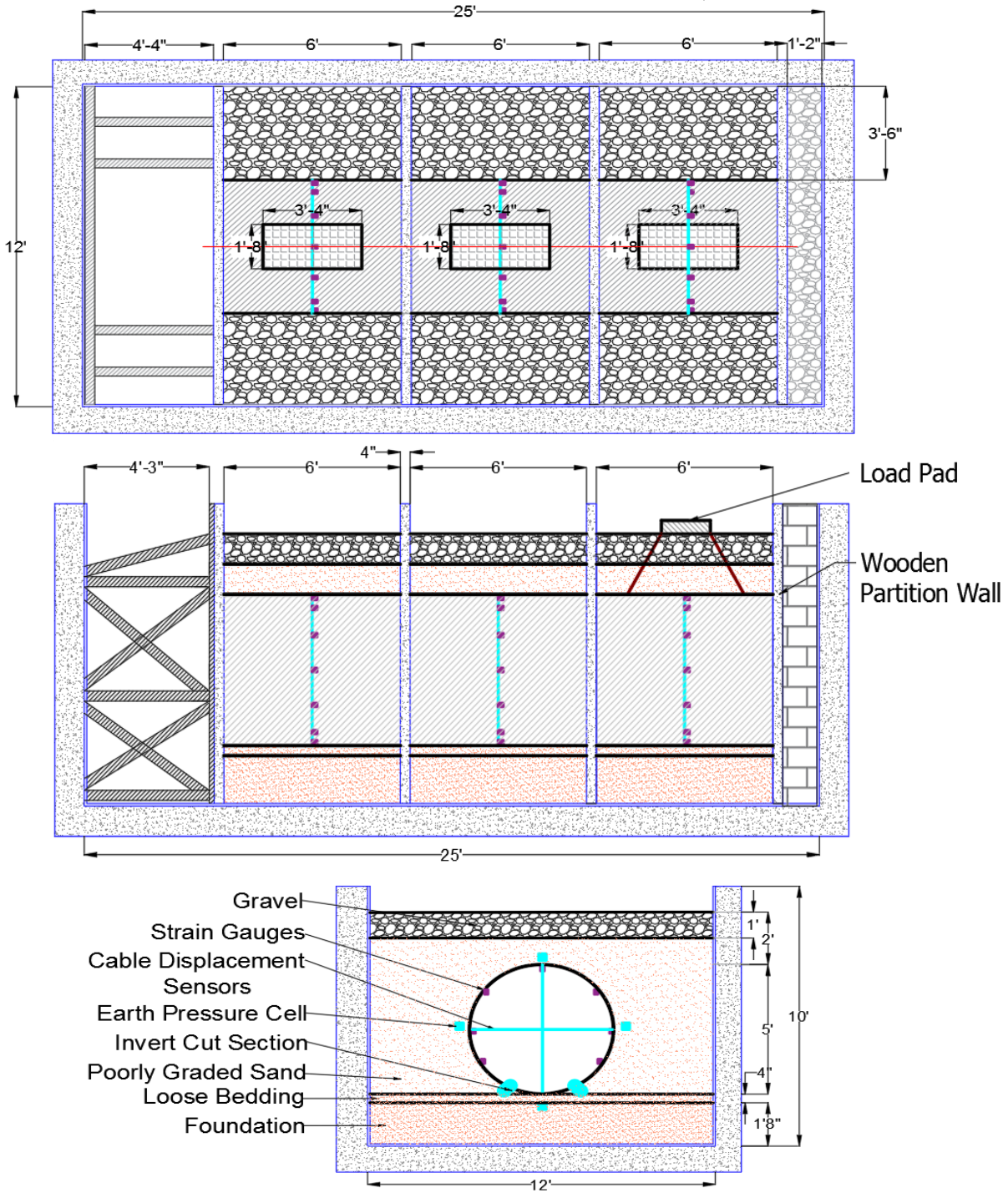


Figure 3-31. The CMPs' burial configuration: (top) plan view, (middle) profile view of the aligned CMPs in the soil-box, and (bottom) cross sectional view of the CMP.

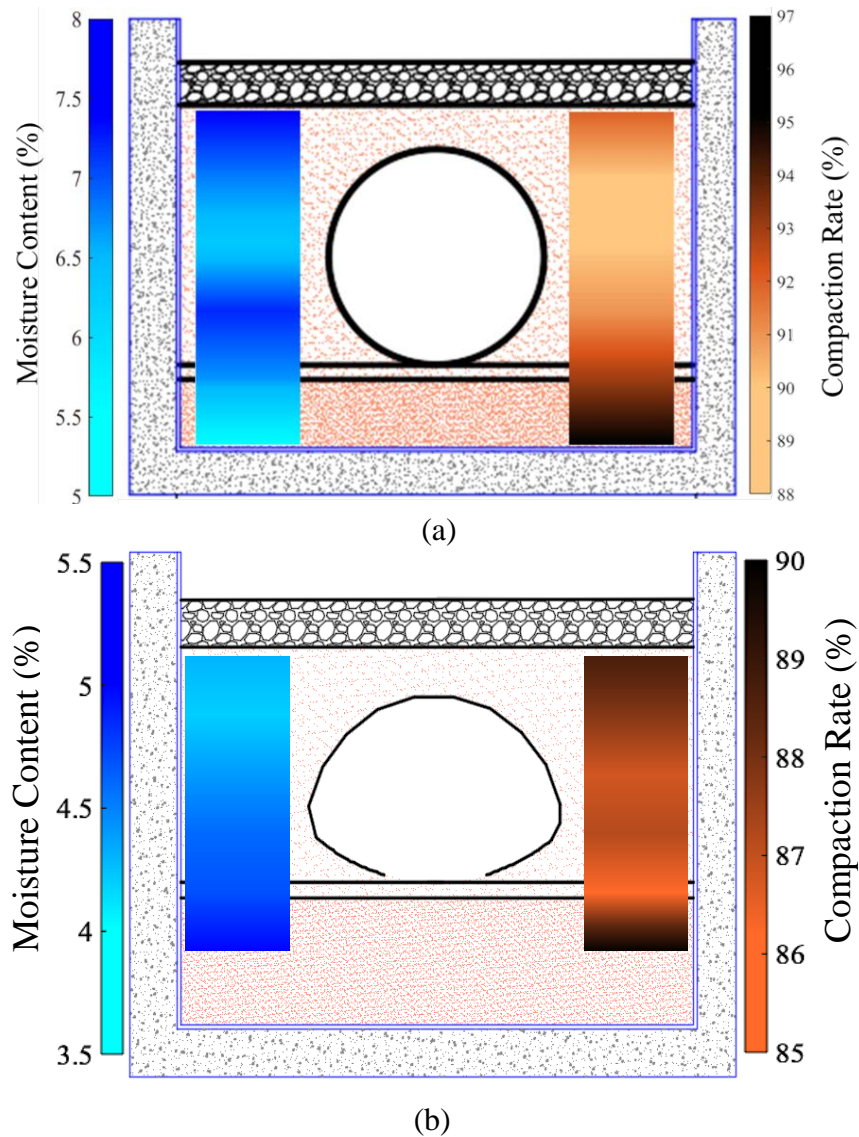


Figure 3-32. The contour-plot of the averaged values for moisture content and compaction rate in 8 in. lifts measurement for: (a) circular CMPs renewed with SAPL, and (b) pipe arch CMPs renewed with SAPL.

3.4.1. Cementitious SAPL Details

In this study the Standard Cement Materials' GeoCast© geopolymer mortar was used to renew the fully invert deteriorated pipe arch and circular CMPs. GeoCast© is designed to be used for concrete and corrugated metal culvert renewal as well as main sewers and stormwater drainage

systems. GeoCast© stops water infiltration, increase structural capacity of the deteriorated culvert, and prevents undercutting of pipe beddings. The source materials used in GeoCast© are microsilica silicon (Si) and aluminum (Al) as specified in 1.3.5.2. GeoCast© also includes micro polypropylene fibers to minimize shrinkage of the geopolymer mortar as discussed in section 1.3.5.3. Figure 3-33 illustrates the GeoCast© mortar, at initial setting stage (i.e., before hardening), with the micro fibers, used to rehabilitate the fully invert deteriorated (i.e., invert-cut) CMPs.



Figure 3-33. GeoCast© mortar with its micro fibers.

Recent x-ray diffraction (XRD) examination on core samples taken from sewer service manholes renewed with GeoCast©, showed the geopolymer samples are in good condition even after 15 years of aging in such a corrosive environment (Henning 2020). The constituents in the liner matrix are identified through XRD analyses, which are illustrated in Figure 3-34. The analyses showed that the 15-year aging period did not affect the liner and GeoCast© was still in a good condition.

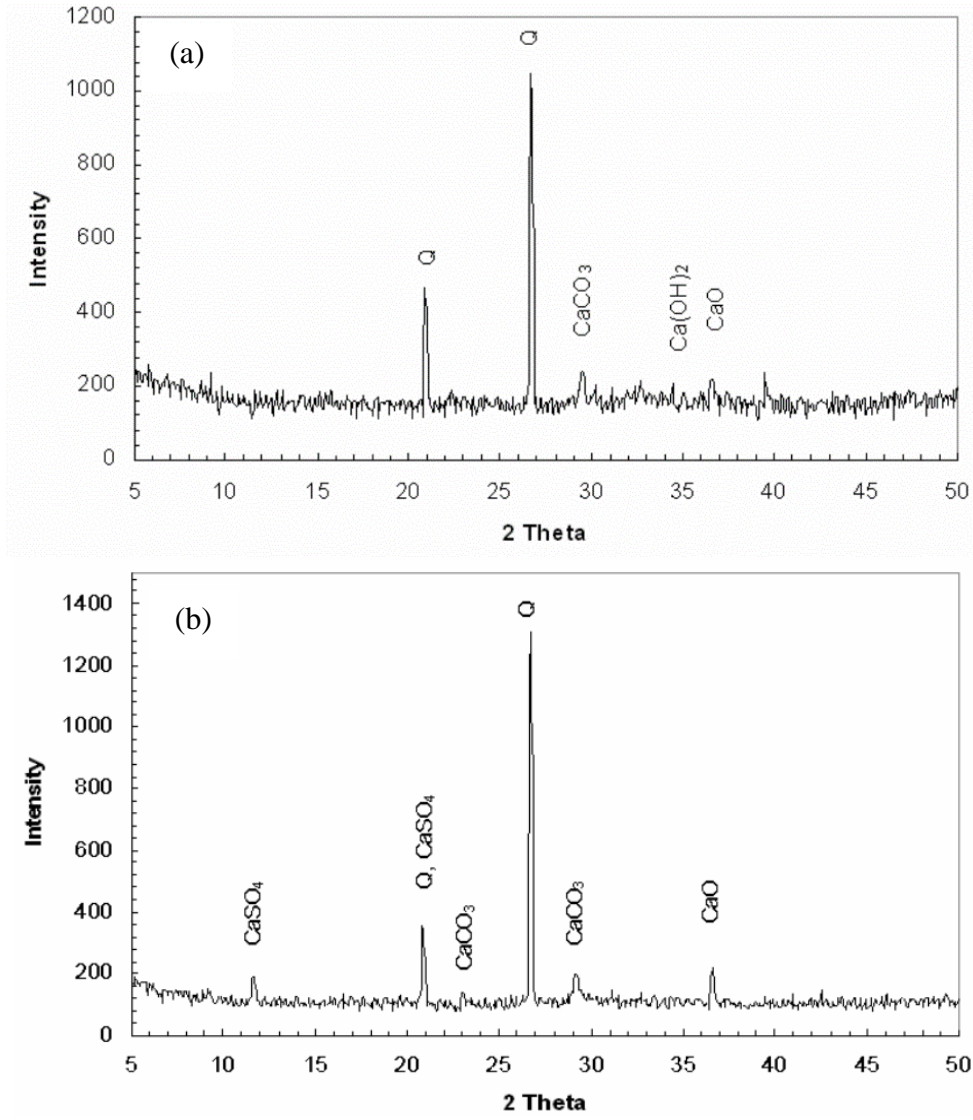


Figure 3-34. XRD Analysis Results on: (a) new, and (b) 15 year old cement liner material (Henning 2020).

The total number of 168 bags of GeoCast© ready mix were delivered to the CUIRE facility on Jun 2020. Each bag contained 75 lb of ready mix geopolymer, suitable for 0.68 cubic ft. The bages were store in an storage room protected form precipitations and sun light.



Figure 3-35. GeoCast© material delivery to CUIRE facility.

3.4.2. CMP Samples Preparation

The CMP samples were prepared for SAPL installation. The invert-cut section was unbolted and the angle sections were removed completely. However, since the SAPL cannot be sprayed on soil material, the unbolted invert section was left in place to be as bas for SAPL on the invert area. The 2 in. gaps between the detached invert and the main body of CMP were filled with Styrofoam, as shown in Figure 3-36 (a).

In this test it was essential to make sure the pipes and SAPL are both completely separated from the portion walls and there is no structural resistance coming from the attachment of the pipe and walls. In addition, since the inverts' end-strips were needed to be removed after hardening of the SAPL, it was crucial to keep them protected from being sprayed. Therefore, to acquire these

requirements, the gaps between the wooden partition walls and both ends of the CMPs as well as the invert's end-strips were covered with duct tape to be protected from SAPL application, as shown in Figure 3-36 (b).



Figure 3-36. End-strip detachment: (a) end-strip preparation, (b) end-strip before SAPL installation, end-strip detachment after SAPL installation.

SAPL installation on a deteriorated culvert requires cleaning and surface preparation. A common procedure is to implement sand blast or high-pressure water blast at minimum 4000 psi pressure on the interior surface of the culverts to remove, dirt, mud and rust from the CMP surface. However, since the pipe samples were used in this study were brand new pipe and were free of

surface rust or long exposure to dust and dirt, power wash and sand blast was not required. On the contrast, since they were brand new CMPs, the bonding of the cementitious SAPL to such a smooth metallic surface was a major concern. Lack of proper bonding between the SAPL and the CMP, especially on thicker thicknesses, would raise the probability of SAPL falling and detachment from the host pipe. To prevent such an issue the vendor utilized a mixture of the SAPL material with the CSI Concrete Bonder II on the surface of CMPs. The CSI Concrete Bonder II is a film forming, non re-emulsifiable liquid bonding agent and polymer modifier, which is designed to improve the adhesive and physical properties of most cementitious materials including geopolymer. Figure 3-37 illustrates concrete bonder agent detail and its utilization on the CMPs interior surface.

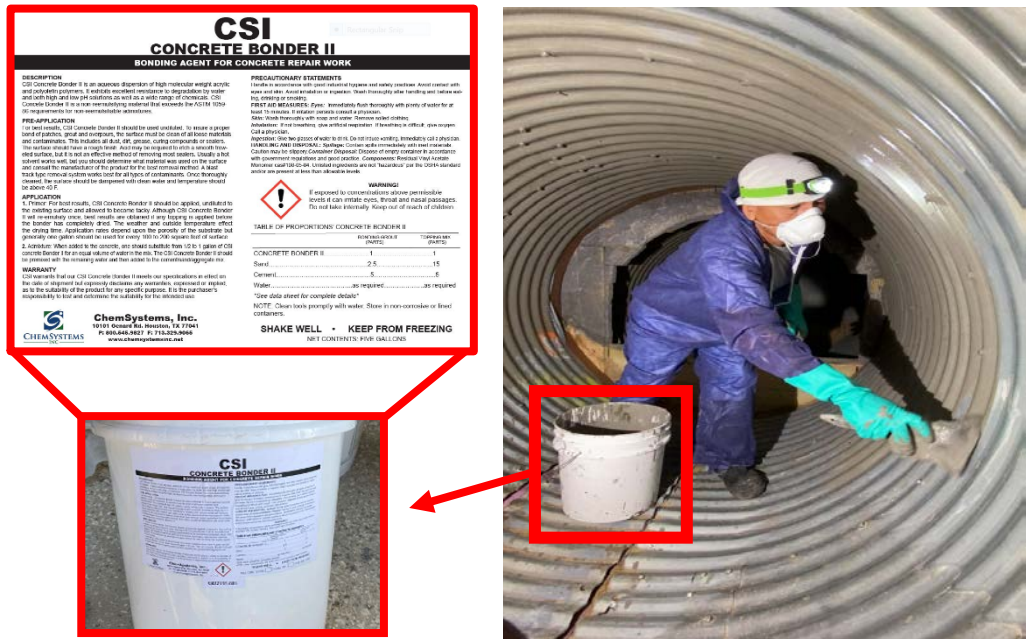


Figure 3-37. Implementation of bonding agent into the SAPL mix to increase adhesion of the SAPL to the smooth metallic surface.

3.4.3. SAPL Installation

The cementitious SAPL installation requires field equipment including a portable gas-powered engine mortar mixer, gas-powered engine rotor-stator pump, a water tank, and, if required, spinecaster machine and a portable air compressor. The Standard Cement vendor had all the required equipment mounted on a trailer connected to a medium size truck. Due to the existence of the soil box and the large steel frame that limited the access to the laboratory inside, placement of the rotor-stator pump near the mortar mixer was not possible. Therefore, except the rotor-stator pump, all other equipment was kept outside. To transport the mixed geopolymer mortar to the rotor-stator pump, a wheelbarrow was used, and the mortar was poured inside the pump using a shovel as illustrated in Figure 3-38.



Figure 3-38. Cementitious SAPL installation equipment including: (a) portable mortar mixer, water tank, and (b) rotor-stator pump.

Each bag of geopolymer was mixed with half a gallon of water and half a gallon of concrete bonder agent and then it was pumped inside the CMPs at the pressure of 60 psi. To install the required thicknesses of 1, 2, and 3 in., for circular CMPs a total of 83 bags, and for the pipe arch CMPs 85 bags of geopolymer cement were used. The SAPL vendor utilized hand spray method to apply the liner in both arch pipe and circular CMPs, as illustrated in Figure 3-39. The SAPL was first sprayed to fill the CMP's corrugation, as discussed section 1.3.5.5. Once the corrugations were filled, the pipes were sprayed for 1 in. thickness above the corrugation's crest. At this point, they allowed the material to rest for about an hour before they apply the second 1-in. thick layer for the CMPs with design thickness of 2 and 3 in. Similar procedure was carried out until all pipe samples reached their own required design thicknesses. During the installation process, as illustrated in Figure 3-40 (a), the invert of the CMPs were left unsprayed to allow the applicators move freely without disturbing the liner. Once the SAPL installation of the CMPs' main body were completed, the invert sections were filled and the surface of the bottom half section (i.e., from springline to springline) of the pipes were finished by troweling. The top half section was left untreated as it would raise the risk of SAPL falling and detachment from the CMP (shown in Figure 3-40 (c)). Once the SAPL installation was completed, the duct tapes, attached on the gaps between the CMPs and wooden partition walls were removed to prevent hardened over-sprayed material make contact between the walls and renewed CMPs (see Figure 3-41).

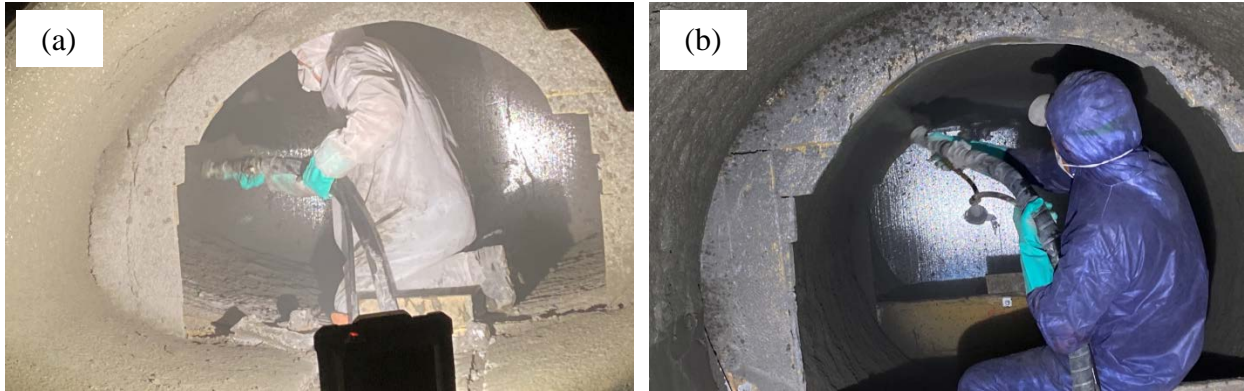


Figure 3-39. Cementitious SAPL installation on: (a) pipe arch, and (b) on circular CMPs.

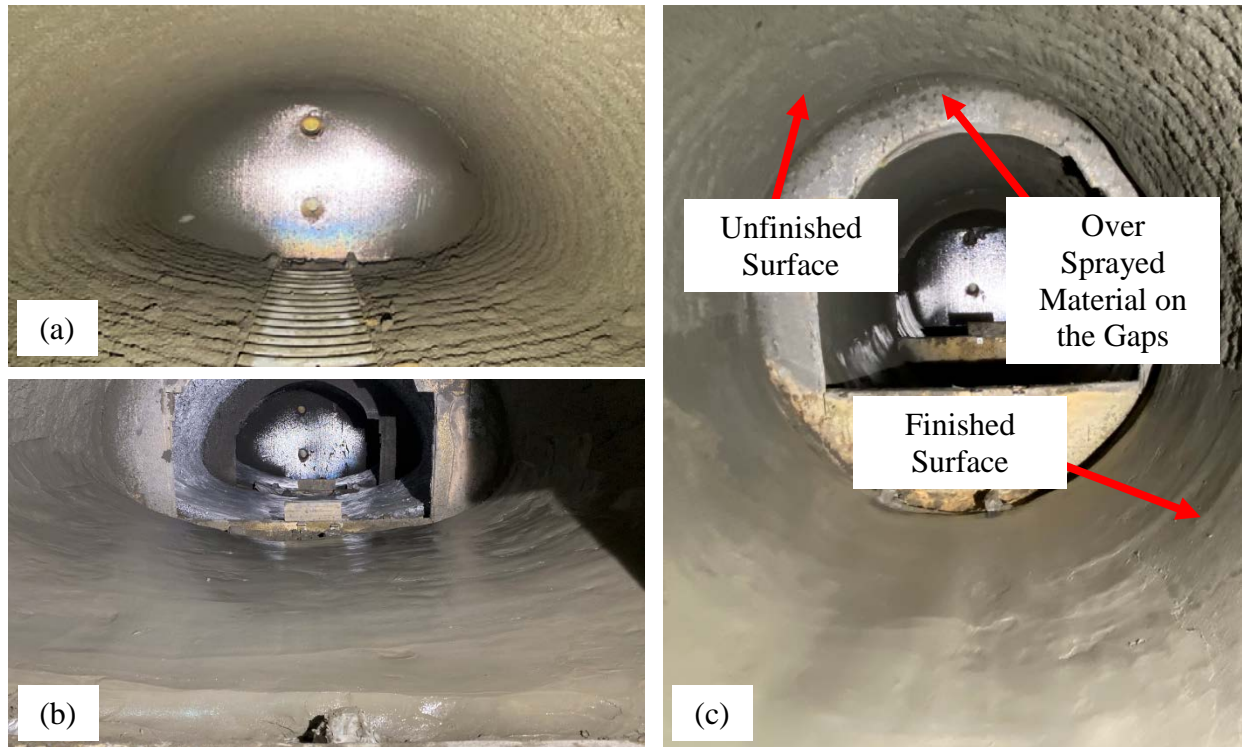


Figure 3-40. Cementitious SAPL Installation: (a) pipe arch CMP with un-sprayed invert section for applicator's movement, (b) completed installation on pipe arch CMPs, and (c) SAPL installation on circular CMPs with bottom half finished and top half unfinished surfaces.

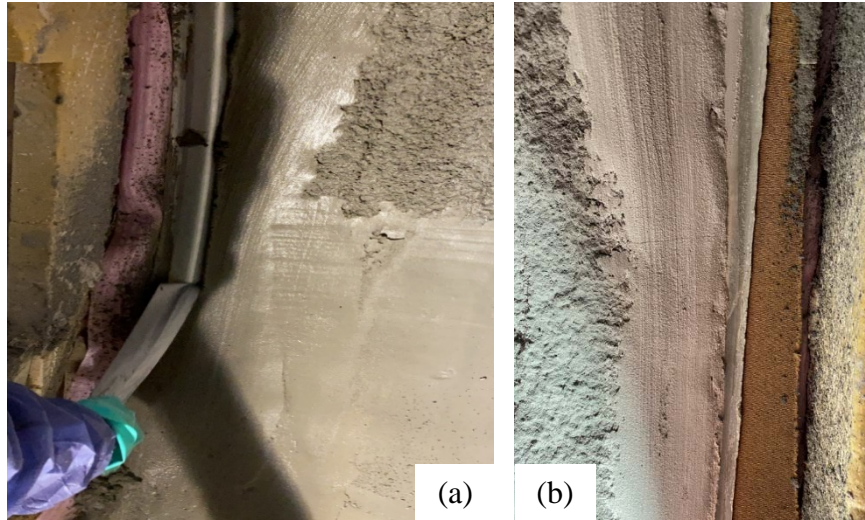


Figure 3-41. End gaps cleaning to prevent SAPL attachment to the wooden partition walls: (a) duct tape removal to clean the gap, and (b) clear gap between the renewed CMP and the end wall.

During the installation, the thickness of the SAPL was checked continuously using a depth gauge, illustrated in the Figure 3-42. The measurements were conducted over the crest of the corrugation to inform the SAPL applicator with the applied thickness. If the thickness is less than the designed thickness more material will be applied. However, if the applied thickness is more than required thickness, then the excessive amount will not be removed.



Figure 3-42. Thickness measurement using a depth gauge at the time of SAPL installation.

Once the installation procedure was completely carried out, the CMPs entrance area and the ventilation pipes were sealed to accelerate the curing process. It is noteworthy that for the invert-cut pipe arch CMPs, a concrete curing compound was applied on the top surface of SAPL. The whitish color of the compound is evident in the Figure 3-43 (b). However, for the circular CMPs, the vendor decided not to use the compound.

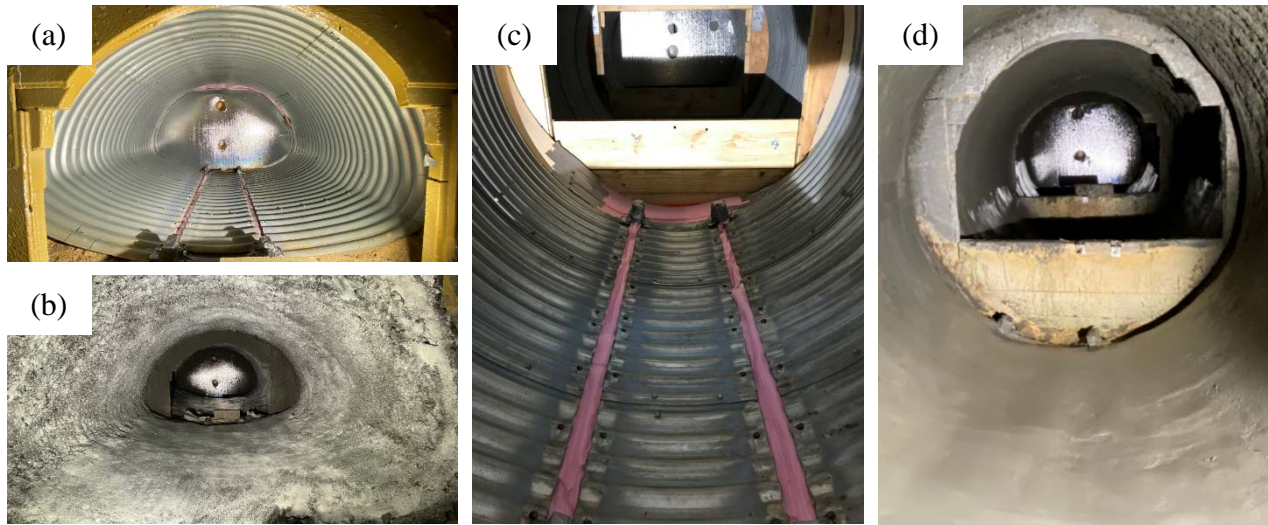


Figure 3-43. Cementitious SAPL renewal of fully invert deteriorated CMPs: (a) pipe arch CMP before SAPL application, (b) pipe arch CMP after SAPL application, (c) circular CMP before SAPL application, and (d) circular CMP after SAPL application.

3.4.4. SAPL Mechanical Properties Testing Samples

In order to measure compressive strength of the applied cementitious SAPL, 38 samples were taken from the same batch of SAPL installed on the pipe arch CMPs. Likewise, 41 samples were taken for the circular CMPs' SAPL batch. The samples include cubes and cylinders in different sizes, which were allocated to be tested at 24 hours, 7 and 28 days of curing. The cylinder samples were taken using both hand and spray cast method, as illustrated in Figure 3-44. The sampling details and their quantity for pipe arch and circular CMP test series are presented in Table 3-3 and Table 3-4 respectively. Although majority of the molds were brand new, they were washed and prepared prior to the SAPL casting. The molds were prepared with a mold release agent 24 hour before casting the SAPL, as illustrated in Figure 3-45 (a) and (b).

The cylinder and cube samples were casted, prepared, and tested in accordance with the ASTM C39 and ASTM C109 respectively. The samples were demolded and transported to a curing

room 24 hour after the casting, as illustrated in Figure 3-45 (c). The 24 hours samples were capped and tested right after the demolding process.



Figure 3-44. SAPL casting method into the cylinders: (left) spray-cast, and (right) hand-cast method.

Table 3-3. Compressive testing samples for pipe arch CMPs renewed with cementitious SAPL.

Specimen Type	Specimen Size (in.)	Casting Date	Curing Time			Casting Type
			24 Hours	7 Days	28 Days	
Cube	2×2	6/13/2020	0	5	4	Hand
Cylinder	3×6		0	2	2	Hand
Cylinder	3×6		0	2	2	Sprayed
Cylinder	4×8		4	3	3	Sprayed
Cylinder	4×8		0	3	3	Hand
Cylinder	6×12		0	2	3	Sprayed
Total	-		-	4	17	17

Table 3-4. Compressive testing samples for circular CMPs renewed with cementitious SAPL

Specimen Type	Specimen Size (in.)	Casting Date	Curing Time			Casting Type
			24 Hours	7 Days	28 Days	
Cube	2×2	7/18/2020	3	3	3	Hand
Cylinder	3×6		0	2	2	Hand
Cylinder	3×6		0	2	2	Sprayed
Cylinder	4×8		3	3	3	Sprayed
Cylinder	4×8		3	3	3	Hand
Cylinder	6×12		0	3	3	Sprayed
Total	-		-	9	16	16



Figure 3-45. Mechanical properties testing samples: (a) compressive testing cylinders molds, (b) mold preparation, and (c) sample storage at a curing room.

Both ends of the samples were capped using a sulfur capping material as specified in its corresponding ASTM standard. Extra care was made to have both sides of the cylinder perfectly leveled. The specimens were tested using a hydraulic actuator with 400 kips capacity of compression. Figure 3-46 illustrates geopolymer cylinders capped with sulfur material.

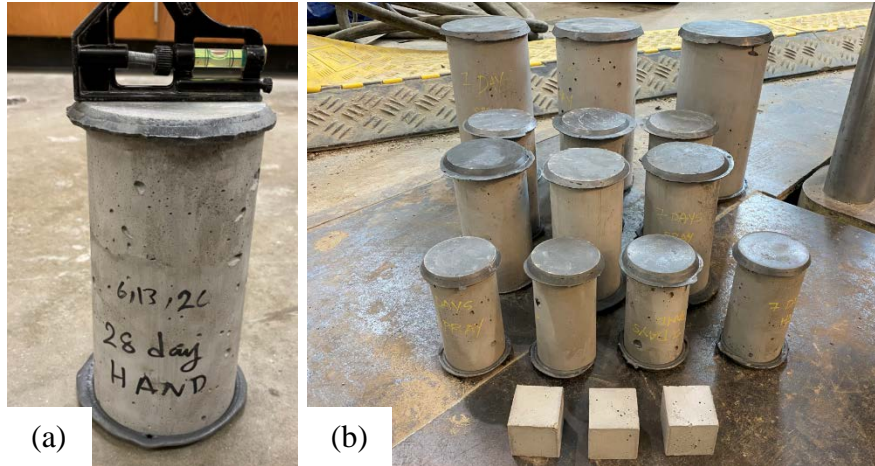


Figure 3-46. Geopolymer mortar compressive testing samples: (a) a sample capped with a sulfur capping compound which is perfectly levelled, and (b) testing specimens after 7 days of curing.

3.4.5. SAPL Visual Inspection and Internal Instrumentation

The CMPs' SAPL were allowed to cure for three continuous days. On the fourth day, the entrance sealing was removed, and the research team was allowed to enter the SAPL renewed CMPs for visual inspection and internal instrumentation.

3.4.5.1. Pipe Arch CMPs Renewed with Cementitious SAPL

The visual inspection of the SAPL renewed pipe arch CMPs showed that all three liners had shrinkage cracks at multiple locations, mostly, in longitudinal direction. The crack width was measured using a digital image processing (DIP) method. To conduct the DIP measurement the digital camera was located perfectly perpendicular to the crack plane.

The 3-in. thick cementitious SAPL, located at the south cell (see Figure 3-30), had a longitudinal crack throughout the invert at the invert-cut gap area. The averaged crack opening was 0.023 in. A 24-in. long longitudinal crack was observed at the crown from south side towards

the center of the pipe. The averaged crack width was 0.016 in. Figure 3-47 illustrates DIP crack width measurement for the crown and invert locations.

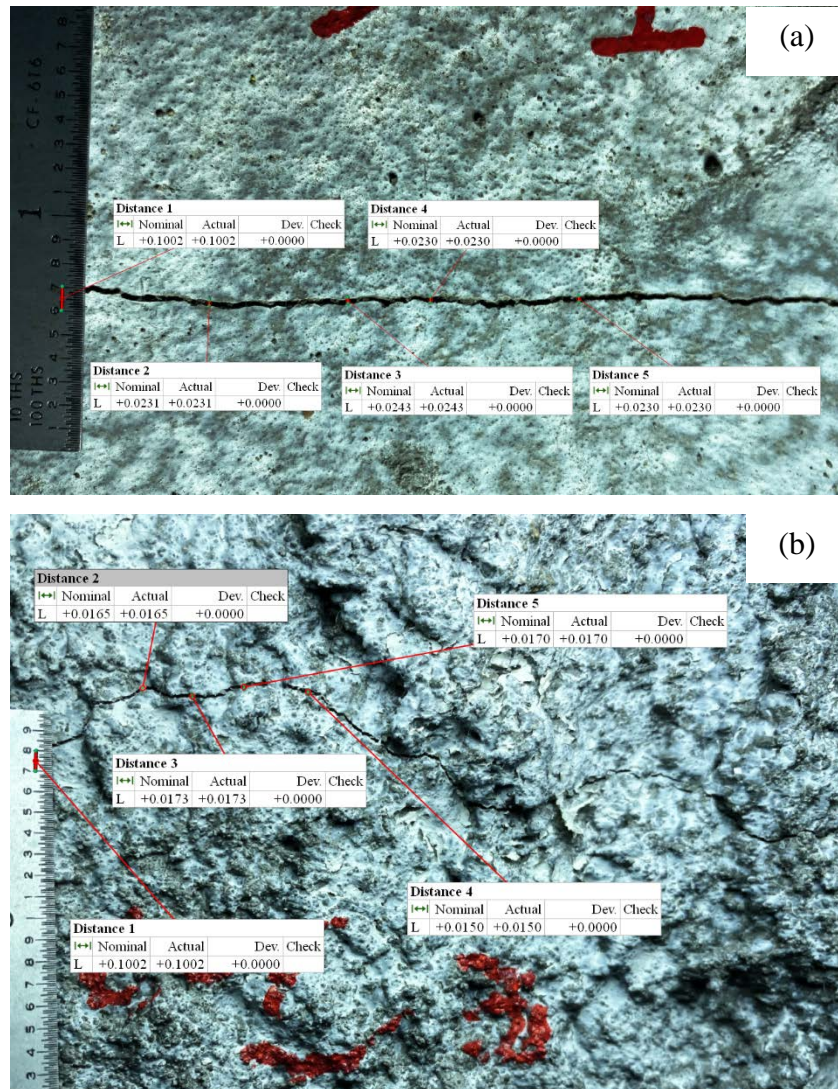


Figure 3-47. Crack width measurement using DIP for 3-in. thick cementitious SAPL on an invert-cut pipe arch CMP at: (a) invert, and (b) crown

The 2-in. thick cementitious SAPL, located at the middle cell, had a longitudinal crack throughout the invert at the invert-cut gap area. The averaged crack opening was 0.0325 in. A full

length long longitudinal crack was observed at the crown the pipe. The averaged crack width was 0.0214 in. Figure 3-48 illustrates DIP crack width measurement for the crown and invert locations.

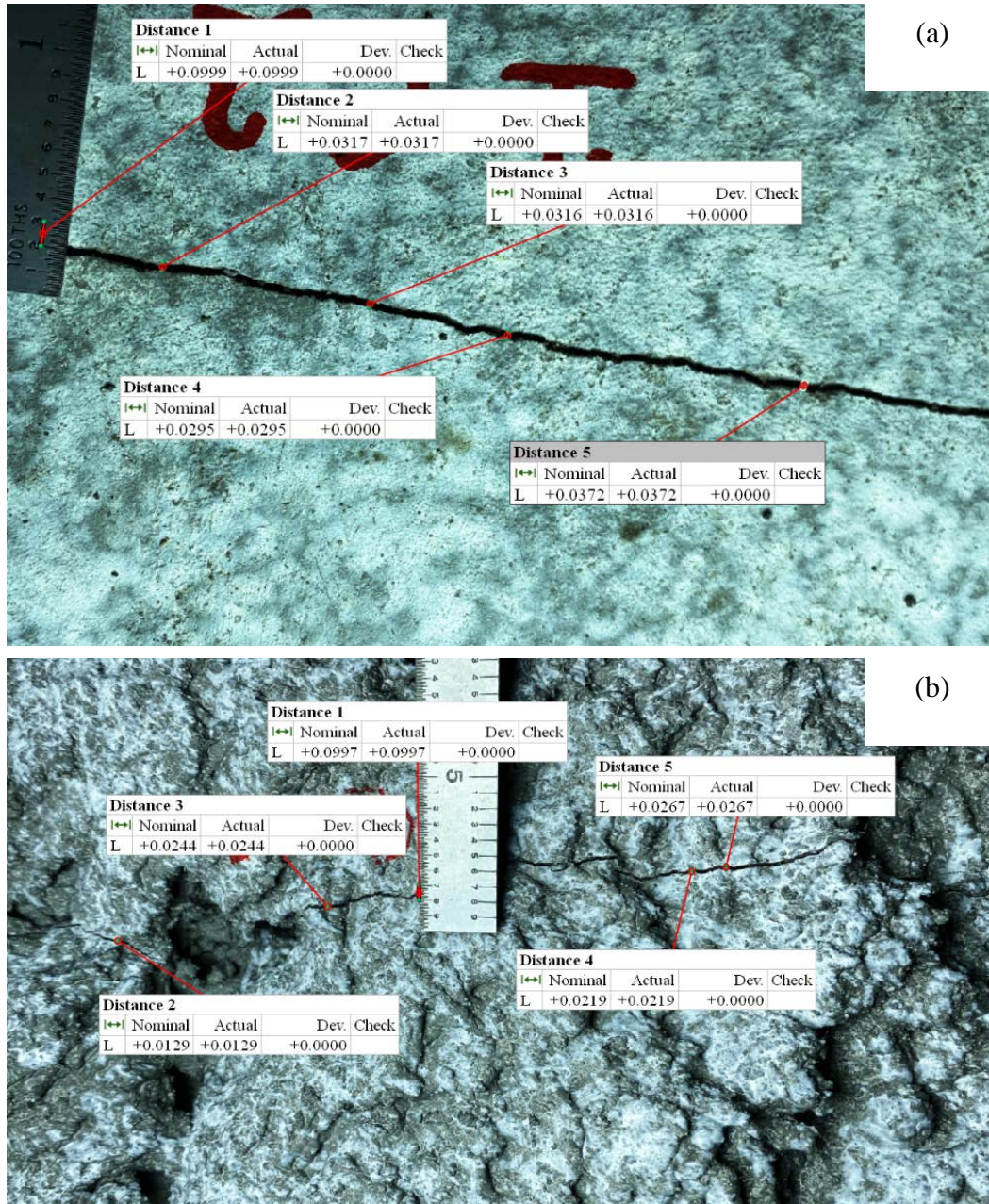


Figure 3-48. Crack width measurement using DIP for 2-in. thick cementitious SAPL on an invert-cut pipe arch CMP at: (a) invert, and (b) crown

The 1-in. thick cementitious SAPL, located at the north cell, had a longitudinal crack throughout the invert at the invert-cut gap area. The averaged crack opening was 0.0376 in. A full length long longitudinal crack was observed at the crown the pipe. The averaged crack width was 0.0091 in. In addition, a full length longitudinal crack was also observed on the East (see Figure 3-30) haunch area. The average crack width was 0.0103 in. Figure 3-49 illustrates DIP crack width measurement for the crown, invert, and East haunch area.

Other than the aforementioned cracks in the SAPL renewed pipe arch CMPs, no other crack was observed.

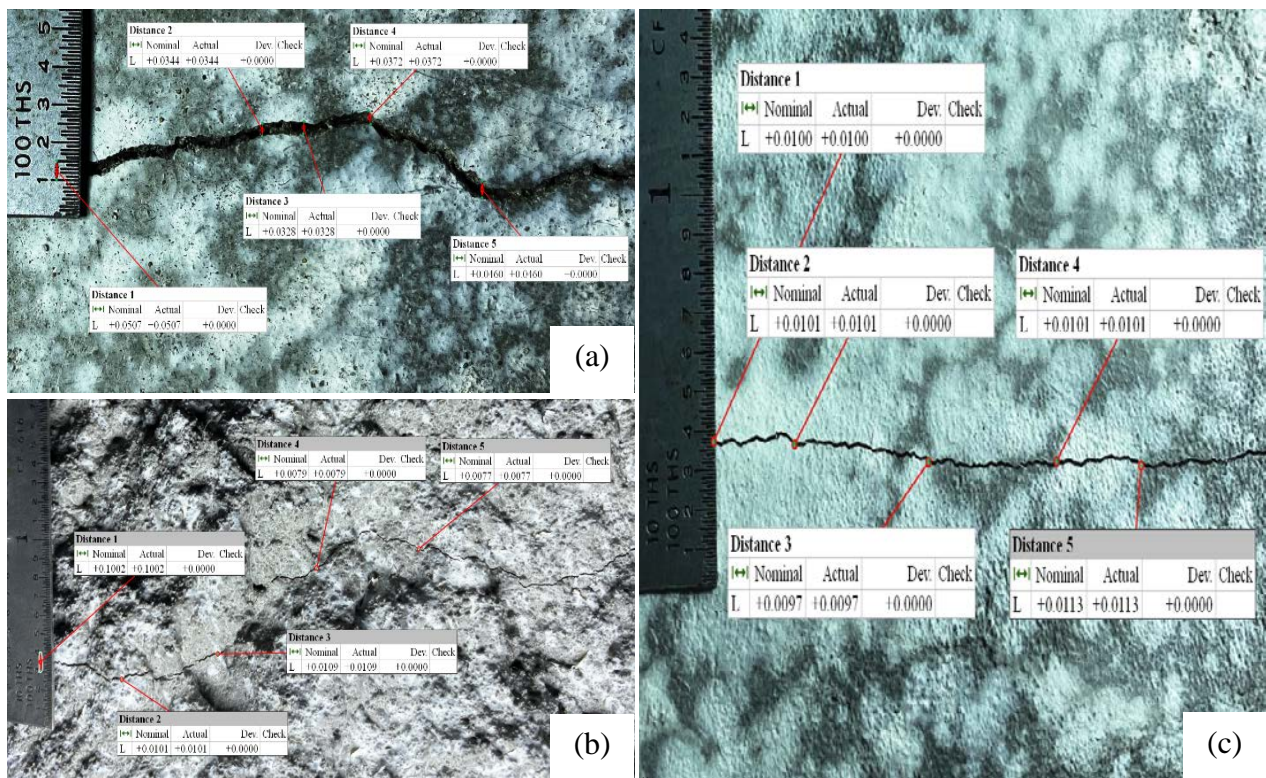


Figure 3-49. Crack width measurement using DIP for 1-in. thick cementitious SAPL on an invert-cut pipe arch CMP at: (a) invert, (b) crown, and (c) East haunch area.

3.4.5.2. Circular CMPs Renewed with Cementitious SAPL

The visual inspection of the SAPL renewed circular CMPs showed that all three liners had shrinkage cracks at multiple locations, mostly, in longitudinal direction. In general, the crack widths were much smaller than the pipe arch samples that could be due to the curing compound that was not applied on the circular SAPL renewed CMPs. The crack width was measured using a digital image processing (DIP) method. To conduct the DIP measurement the digital camera was located perfectly perpendicular to the crack plane.

The 3-in. thick cementitious SAPL, located at the north cell, had a longitudinal crack throughout the crown. The averaged crack opening was 0.0204 in. A 40-in. long longitudinal crack was observed at the East haunch area from north side towards the center of the pipe. The averaged crack width was 0.0093 in. In addition, a 20 in. long longitudinal crack was observed at the West haunch area from north side towards the center of the pipe. The averaged crack width was 0.0045 in. Figure 3-50 illustrates DIP crack width measurement for the crown and East and West haunch area.

The 2-in. thick cementitious SAPL, located at the middle cell, had a longitudinal crack throughout the West haunch area. A 20-in. long crack was also observed on the West shoulder. The averaged crack opening for the West shoulder and haunch area were 0.01848 and 0.01228 in. respectively. No sign of crack at invert, crown or East locations were found. Figure 3-51 illustrates DIP crack width measurement for the West shoulder and haunch area locations.

The 1-in. thick cementitious SAPL, located at the north cell, had a longitudinal crack throughout the crown, a 30-in. long crack at the East haunch area, a 20-in. long crack at the invert location at the invert-cut gap location, a full pipe length crack at the West springline, and a 20-in.

long crack at the West shoulder area. The averaged crack widths for the crown, invert, East haunch area, West springline and West shoulder were 0.01286, 0.009, 0.0068, 0.0058, and 0.01282 in. respectively. In addition, a 20-in. circumferential crack was observed at the East springline with the averaged width of 0.0047 in. Figure 3-52 illustrates DIP crack width measurement for the crown, invert, East haunch area, West springline and West shoulder locations.

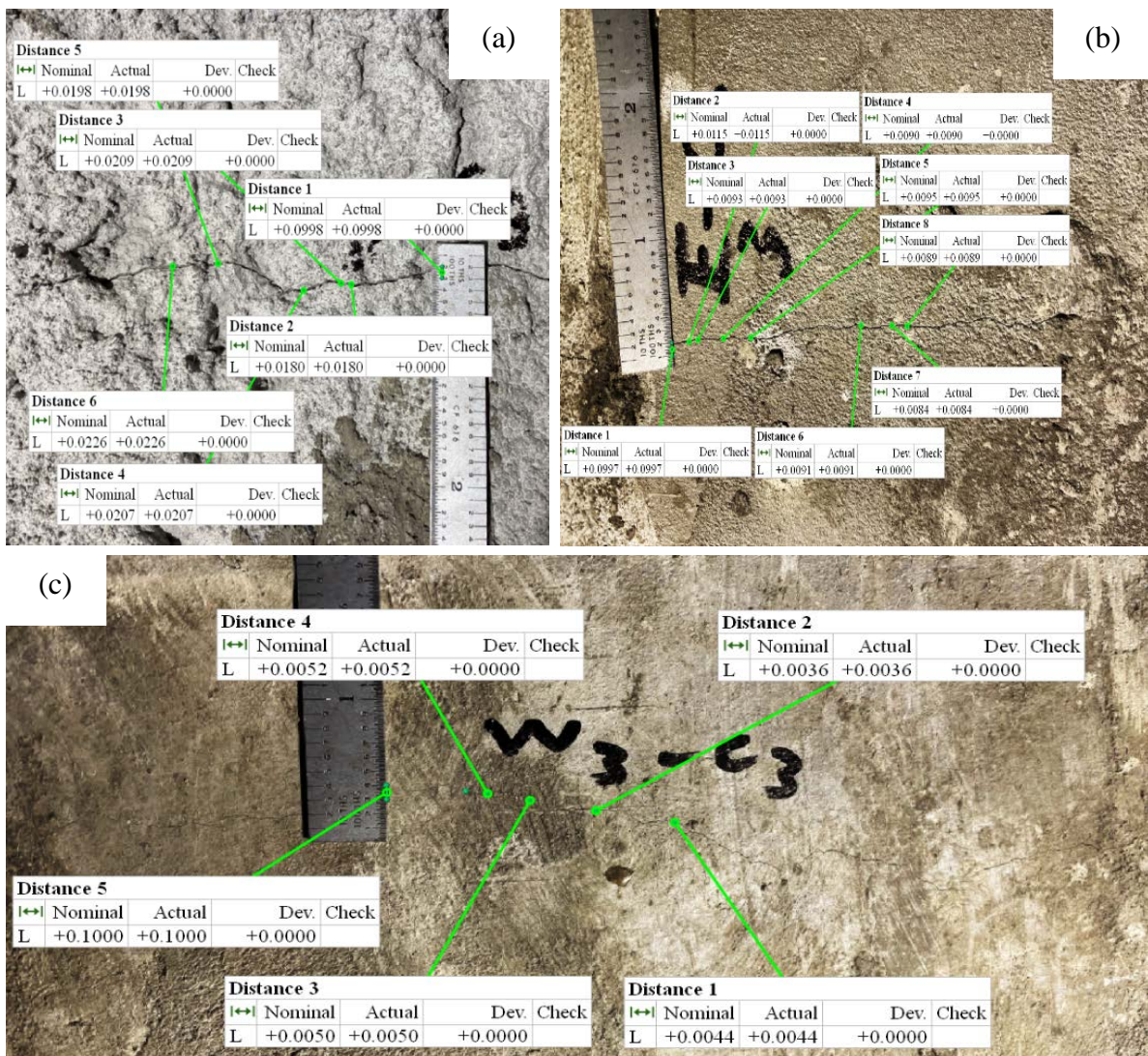
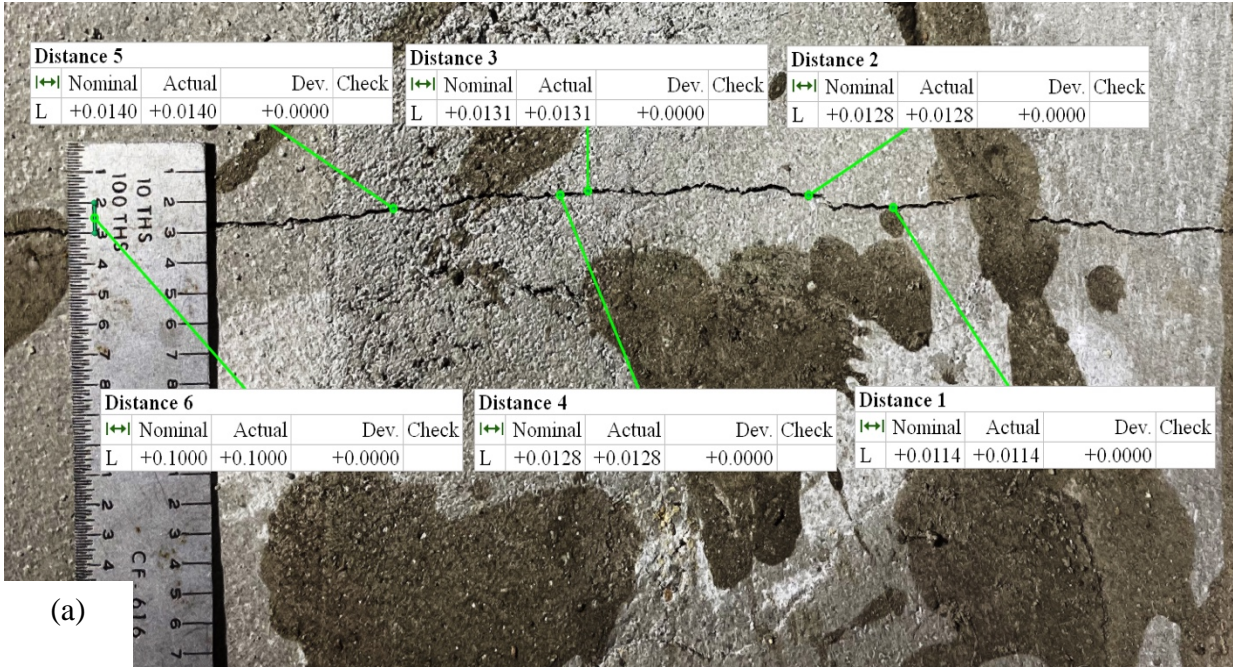
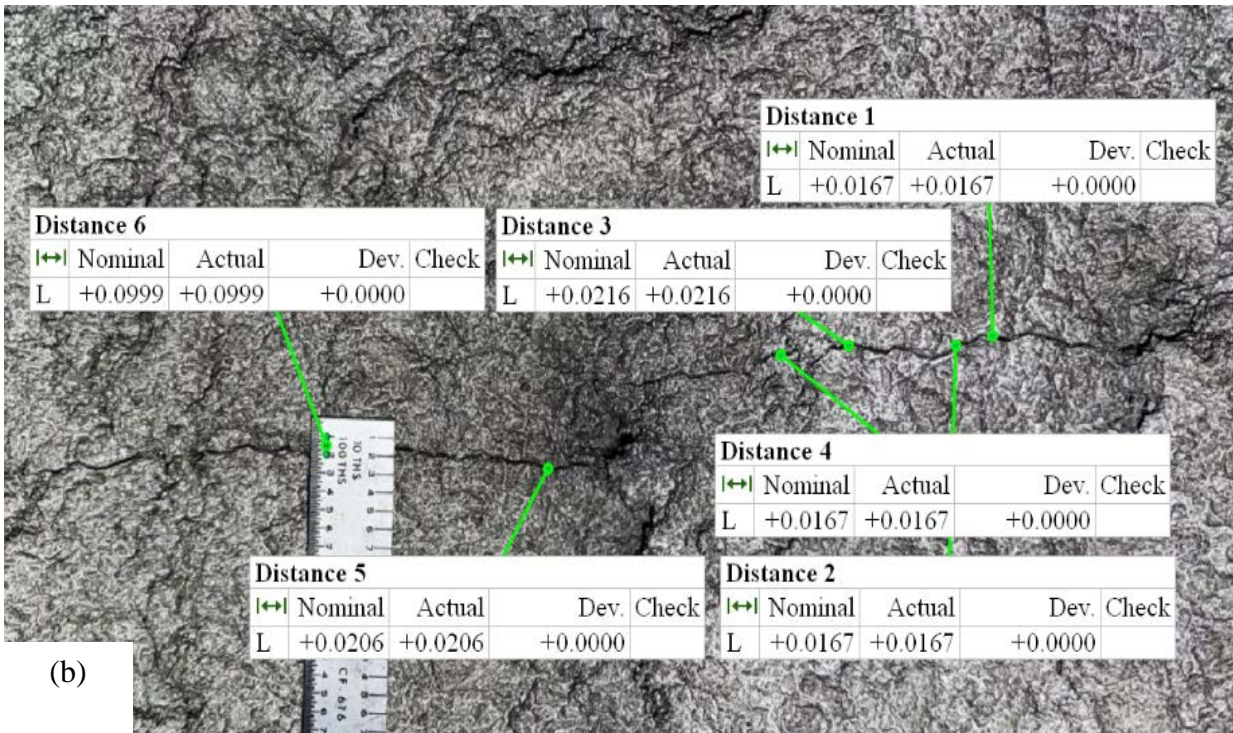


Figure 3-50. Crack width measurement using DIP for 3-in. thick cementitious SAPL on an invert-cut circular CMP at: (a) crown, (b) East haunch area, and (c) West haunch area.



(a)



(b)

Figure 3-51. Crack width measurement using DIP for 2-in. thick cementitious SAPL on an invert-cut circular CMP at: (a) West haunch area, (b) West shoulder area.

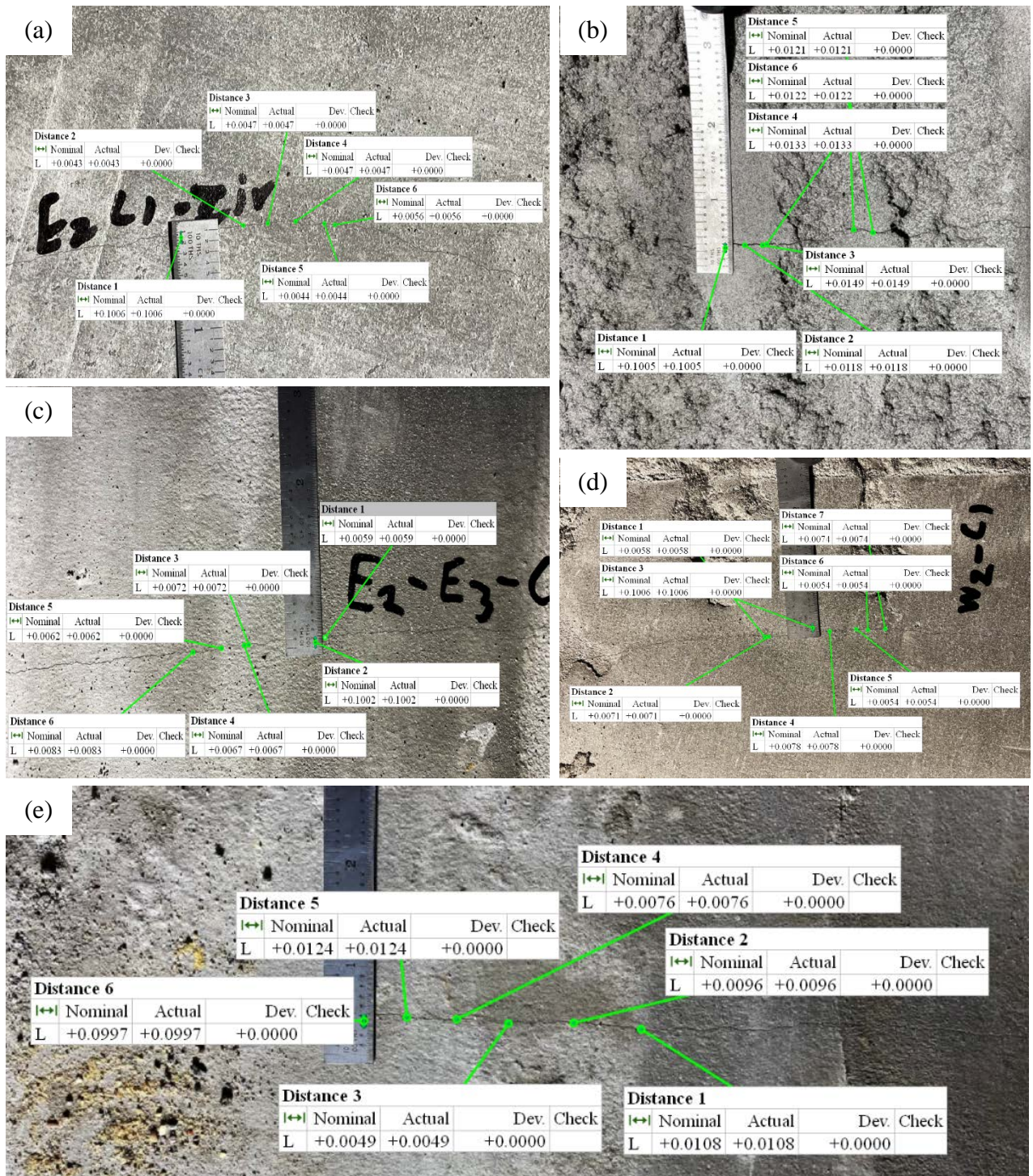


Figure 3-52. Crack width measurement using DIP for 1-in. thick cementitious SAPL on an invert-cut circular CMP for: (a) circumferential East springline crack, (b) longitudinal crack at crown, (c) East haunch area, (d) West springline and, (e) invert.

For both circular and pipe arch SAPL renewed CMPs, remaining invert section (i.e., 3 in. end-strips) were detached, four days after the installation. Aside from the existing shrinkage that is elaborated above, no new crack was observed as the result of end-strips removal. By removing the end-strips the ring compression of the host CMPs were completely eliminated and all the ring compressive force, due to live and dead loads, were resisted by the SAPL solely. Figure 3-36 (c) illustrates the removed end-strip four days after SAPL installation.

3.4.6. SAPL Thickness Measurement

To measure the installed SAPL thickness, after the structural testing of the soil-CMP system, the liners were drilled, and the depth of the holes were measured using a digital caliper. The thickness of the installed cementitious SAPL was measured longitudinally at three locations along the pipe length and in circumferential direction with 45° intervals. The measurements were conducted on the top of corrugation's crest. For each point, three measurements were conducted, and the averaged values were recorded. The measuring locations for both pipe arch and circular CMP samples are illustrated in Figure 3-53.

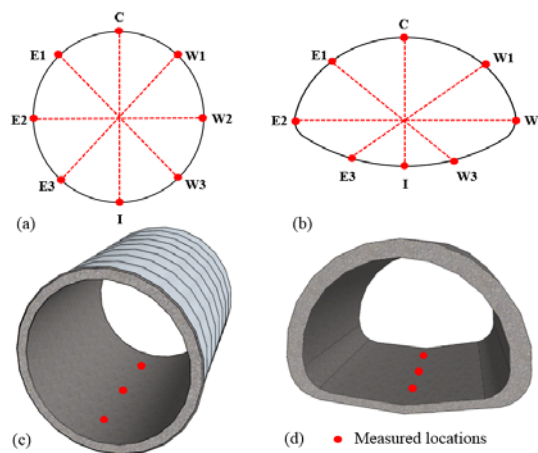


Figure 3-53. SAPL thickness measurement: (a) measurements in circumferential direction on circular and, (b) pipe arch SAPL samples, (c) measurements in longitudinal direction on circular and, (d) pipe arch SAPL samples.

CHAPTER 4. RESULTS AND DISCUSSIONS

4.1. Overview

This chapter presents the results of the soil box test sets, including control tests set, SAPL renewed invert-cut pipe arch CMP test set, and SAPL renewed invert-cut circular CMP test set. For each set of tests, the soil box test results and comparison with other test results, the results of thickness measurements, crack width measurement, and compressive strength test results are presented. In addition, this chapter covers investigation on the applicability of the available design equations, presented in section 2.3. Eventually, the proposed developed design equation is presented in this chapter.

4.2. Soil Box Testing Results

4.2.1. Control Test Results

As stated previously, for the intact CMP the 10×20 in. load pad size were used. However, for invert-cut CMPs, the pad size of 20×40 in. was used to prevent immature soil failure prior to the CMP failure, since it was expected that the weakened CMPs (i.e., invert-cut) deflect relatively larger than the intact and could not provide strong support for the soil. Therefore, the chance of soil failure was higher than the CMPs. Implementation of larger pad (i.e., 20×40 in.) however reduces the load pressure on the soil and resolves the concern. In all tests, load was applied continuously with a rate of 0.03 in./min. It should be noted that during the laboratory structural testing due to the harsh abrasive nature of the soil surrounding the pipes, some of the strain gauges were damaged during the soil placement and compaction. Hence, their results are not illustrated in their corresponding figures. In addition, the CDS located in the springline location was not

showing accurate results, therefore, the results of the CDS used in springline are not included in this study.

4.2.1.1. Intact CMP Test Results

The intact circular CMP was tested on July 7th, 2019, using the AASHTO H20 load pad size (i.e., 10 × 20 in.). The test duration was 7.48 hours, where the load was continuously applied until approximately 15% load drop of the ultimate load. The CMP sample failed at the load of 24.85 kips with 9.6 in. of soil settlement. The failure occurred due to the buckling of the crown through formation of three plastic hinges (shown in Figure 4-1). The soil-CMP system reached the AASHTO H20 service load (i.e., 16 kips) at 1.95 in. of soil settlement. Figure 4-2 illustrates the load and soil settlement graph, registered by the actuator's load cell and LDVT.

The earth pressure cell results registered the maximum pressure of 75.63 psi at the crown location. The maximum pressure applied on the invert, West and East locations were 0.935, 3.491, and 2.019 psi respectively. In this test, immature soil failure was observed the crown pressure of 48.11 psi and the surface load of 21.21 kips. At this load, the load pad punched into the soil and applied the load with less distributed area over the CMP culvert. Figure 4-3 illustrates earth pressure results for the intact CMP test with respect to time and CMP's crown deflection.

Figure 4-4 illustrates the results of the mechanical sensors. The results show that the pipe was subjected to 4.86 in. of crown deflection. In addition, the CMP had 0.3 in. of horizontal expansion in East location (i.e., full expansion of 0.6 in.). It should be noted that the crown CDS was detached from the crown due to the large buckling of the connection point, which is evident in the Figure 4-4.

The strain gauge results showed the intact CMP experienced a large strain at the crown and both shoulder locations that indicates the formation of a three-hinge plastic collapse mechanism (i.e., local buckling) at the crown. The corrugation crest at the crown location was the first that reached the steel yielding point (i.e., 1138 $\mu\epsilon$) at the load of 15.9 kips. The valley of the crown was the next location that reached yield point at the load of 19.02 kips. The West and East shoulder at the corrugation valley were also failed at the load of 24.28 and 22.87 (after CMP failure) kips respectively. Other locations did not reach the steel yield point.

The pipe profile before and after the applied load are illustrated in Figure 4-6. The results of the DIC are in an excellent conformity with the LVDT results. In this test, since the developed pipe profiling system using DIC was utilized to monitor the pipe's profile for the first time and it was in the preliminary stage, only half of the pipe with less number of data points were monitored.

The load-displacement values for soil surface, crown, springline, and shoulder of the intact CMP due to the applied static load is illustrates in Figure 4-7. The applied load on the soil surface versus its corresponding pressure at the crown of the CMP is illustrated Figure 4-8, where the recursive part of the graph represents drop in both pressure and load at the same time.



Figure 4-1. Intact CMP with local buckling at the crown location.

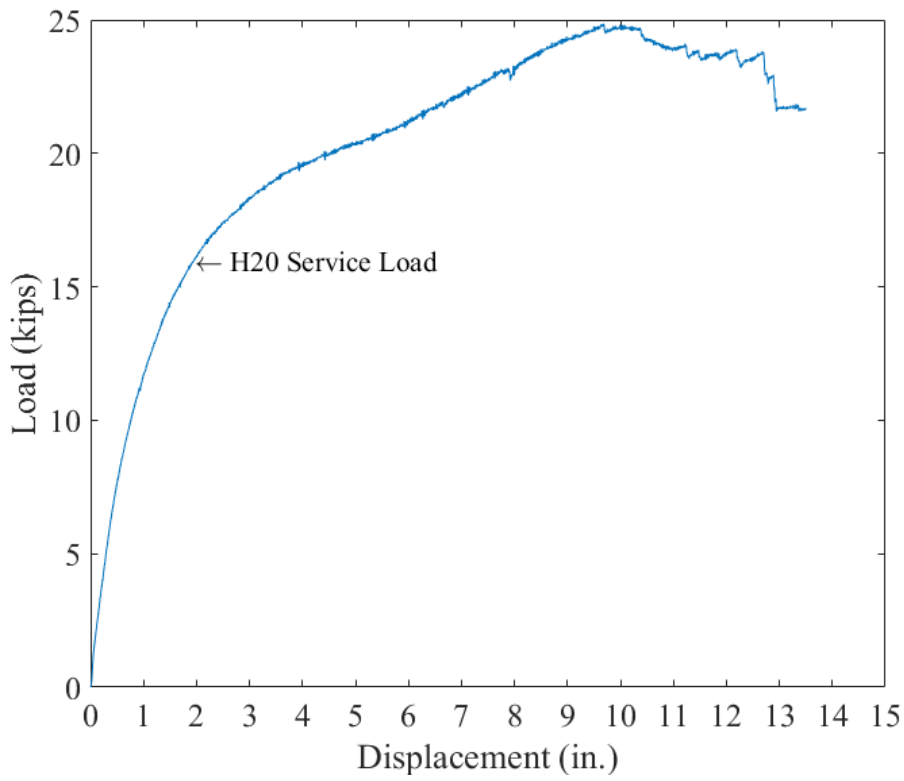
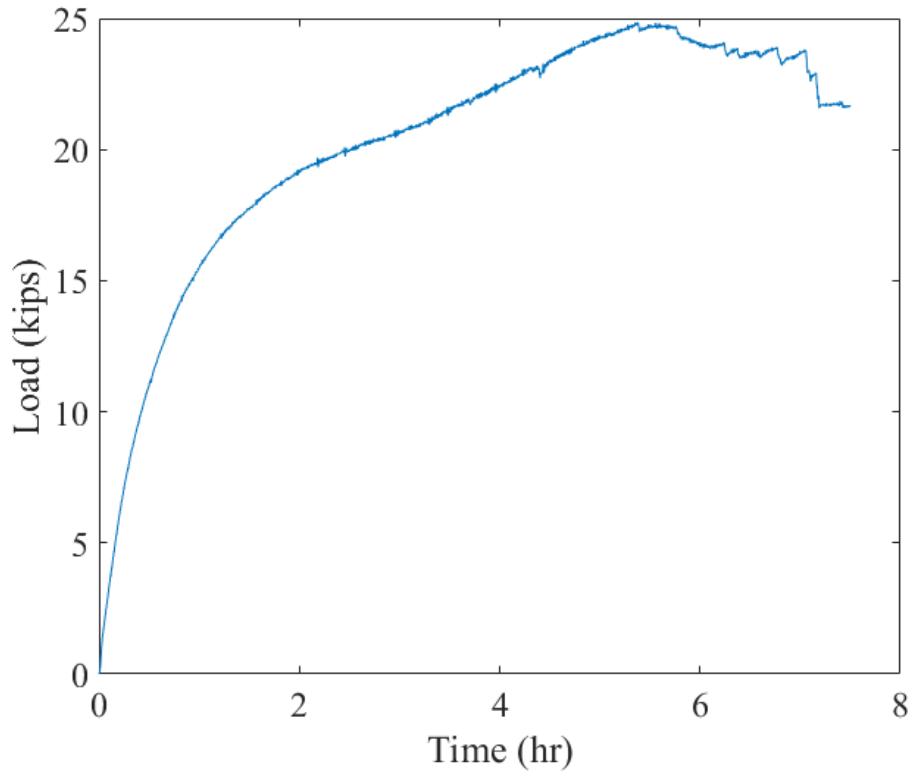


Figure 4-2. Intact CMP static live load: (top) load-time and, (bottom) load-soil displacement graphs.

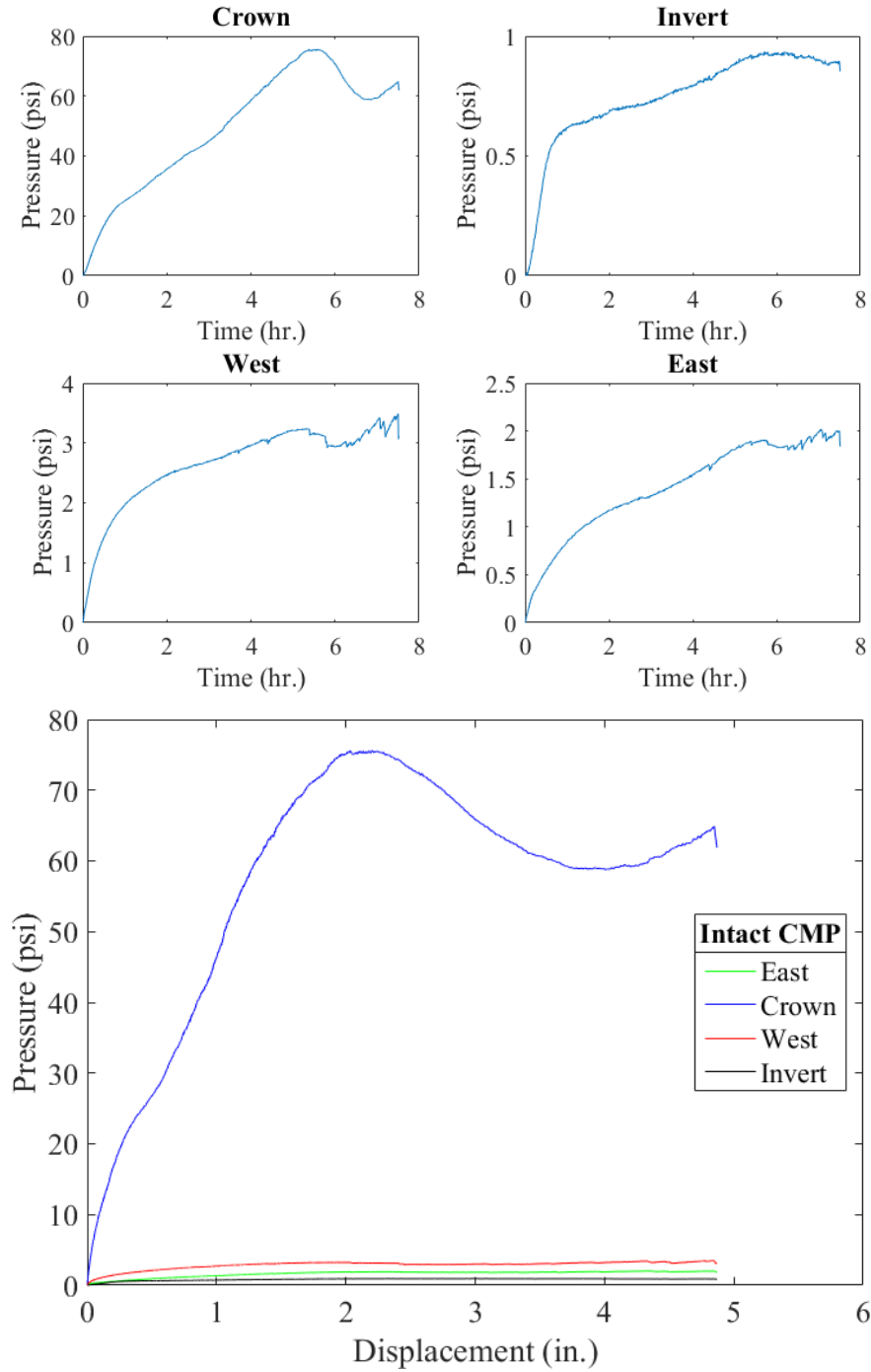


Figure 4-3. Earth pressure cell results for the intact CMP with respect to: (top) time, and (bottom) crown displacement.

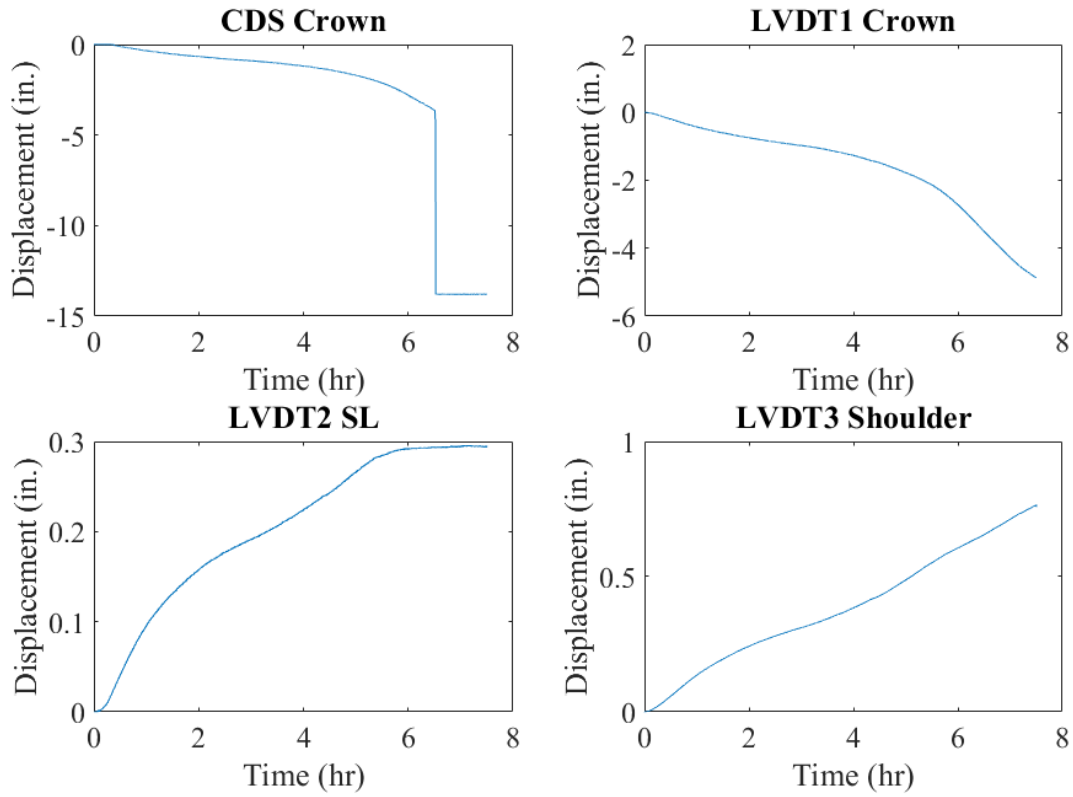


Figure 4-4. Mechanical sensors result for the intact CMP.

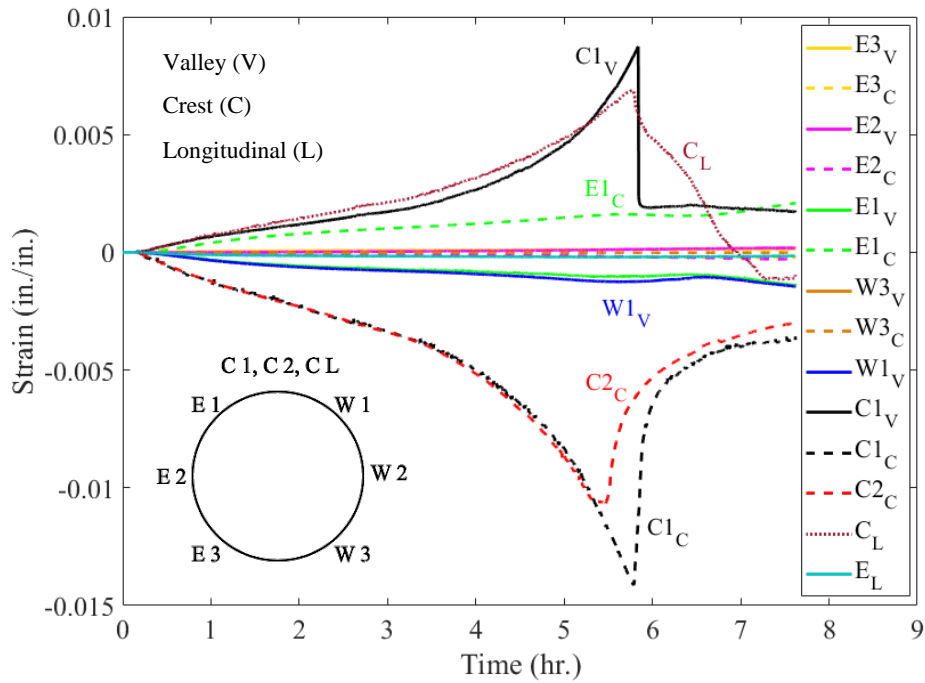


Figure 4-5. Strain gauges reading for the intact CMP.

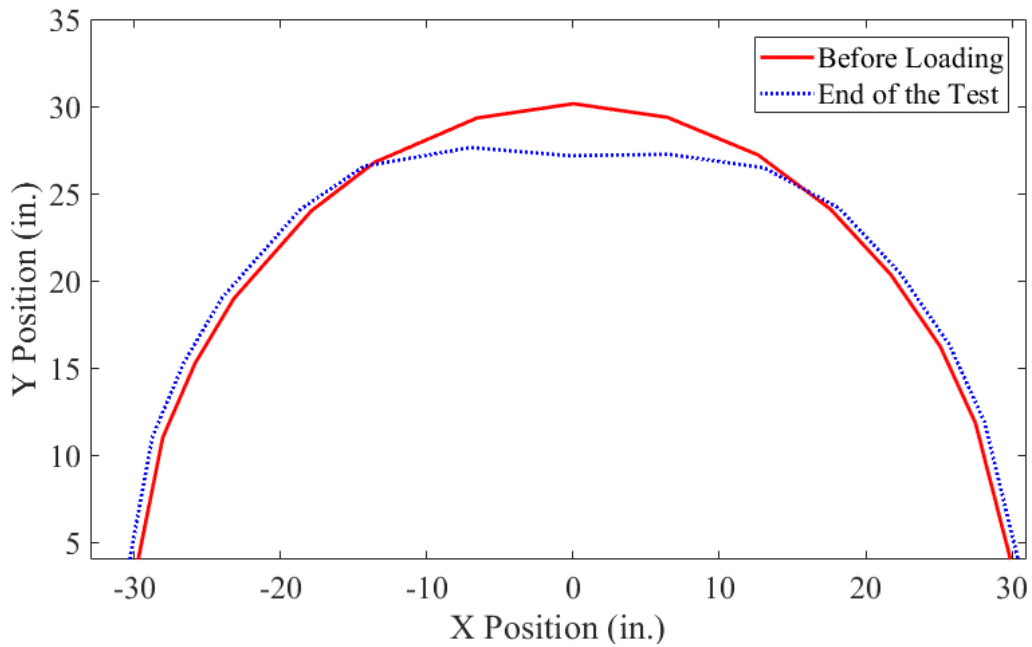
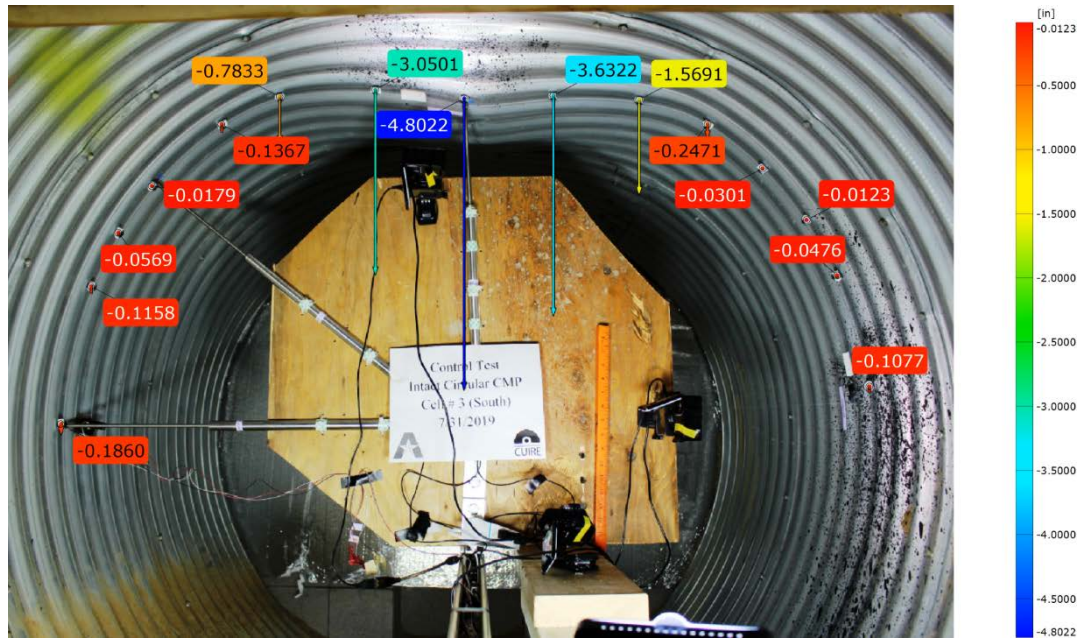


Figure 4-6. Pipe profiling using DIC for the intact circular CMP.

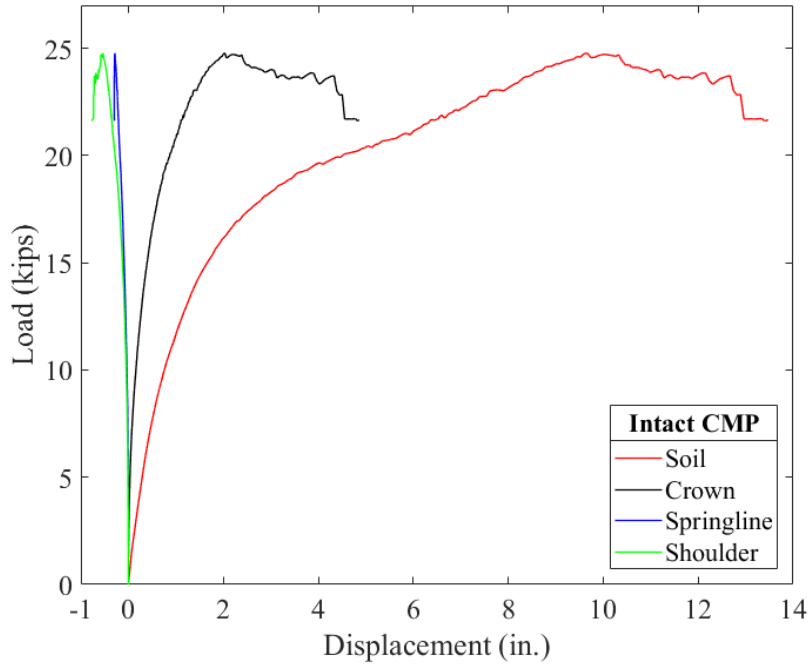


Figure 4-7. Load vs. displacement of the soil surface, crown, springline, and shoulder of the intact CMP due to the applied static load.

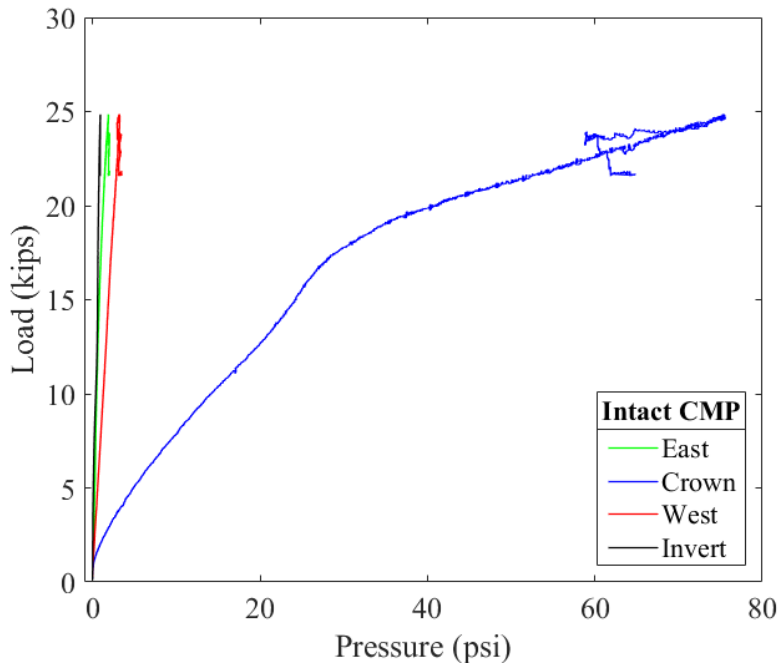


Figure 4-8. Load vs. pressure for the intact CMP

4.2.1.2. Invert-cut Pipe Arch CMP Test Results

The invert-cut pipe arch CMP was tested on August 8th, 2019, using the 20 × 40 in. load pad. The test duration was 5.6 hours. The CMP sample failed at the load of 26.98 kips with 6.57 in. of soil settlement. The failure occurred due to the buckling of the crown through formation of three plastic hinges similar to the intact CMP. However, since the load pad was larger than the pad used in the intact CMP test, the buckling area was larger than the intact CMP sample, as illustrated in Figure 4-9. Free body diagram of the invert-cut pipe arch CMP, illustrated in Figure 4-9 (a), shows vertical force at top of the pipe sample, generates positive moment that produces an upward forces in invert section, and consequently movement of the pipe sample at the free end of the invert section. This expected displacement was observed in the test, where a uniform displacement of approximately 2.2 in. was observed at the invert-cut section, as shown in Figure 4-9 (d). This upward movement generated a gap, which was previously misconceived as a result of soil erosion, while it possibly could be the combination of both. In addition, the test showed that pipe arch CMPs are more dependent on the haunch area rather than the invert. Figure 4-9 (b) illustrates the activated haunch area under the CMP, where the vertical load was transferred to the soil underneath. Figure 4-10 illustrates the load and soil settlement graph, registered by the actuator's load cell and LDVT.

The earth pressure cell results registered the maximum pressure of 14.23 psi at the crown location. Since this CMP had not invert section, no pressure was transferred on the bottom of the pipe. The maximum pressure applied on the West and East locations were 2.67, and 4.46 psi respectively. Figure 4-3 illustrates earth pressure results for the invert-cut pipe arch CMP test.

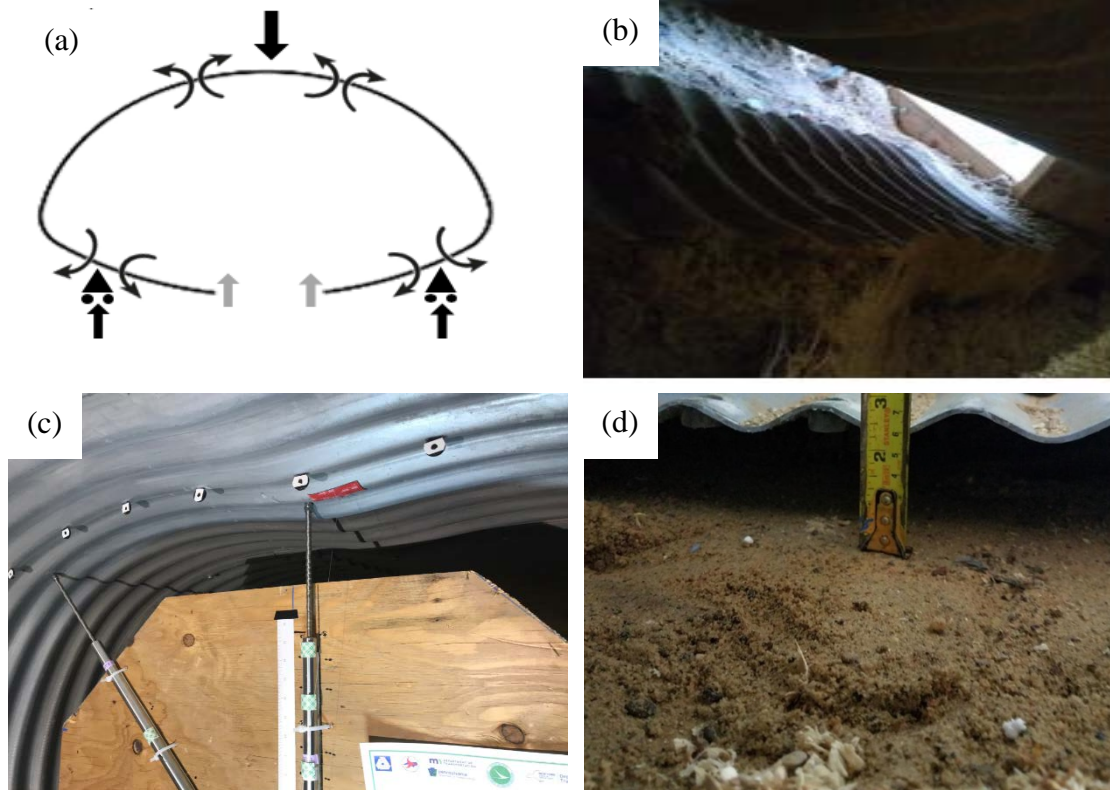


Figure 4-9. Invert-cut pipe arch CMP: (a) free body diagram, (b) haunch area under the pipe (after exhumation), (c) local buckling at the crown, and (d) invert uplift due to the vertical load at the crown.

Figure 4-12 illustrates the results of the mechanical sensors. The results show that the pipe was subjected to 8.165 in. of crown and 0.6 in. of springline deflection. The shoulder had 1.149 in. downward movement. At the end of the test once the load was released from the surface, the pipe's crown, and shoulder had reversal movement of 2 and 0.14 in. respectively.

The strain gauge results showed the invert-cut pipe arch CMP experienced a large strain at the crown and both shoulder locations that indicates the formation of a three-hinge plastic collapse mechanism (i.e., local buckling) at the crown. The corrugation crest at the crown location was the first that reached the steel yielding point (i.e., $1138 \mu\epsilon$) at the load of 17.21 kips. The valley of the crown was the next location that reached yield point at the load of 19.84 kips. The East and West

shoulder at the corrugation crest were also yielded at the load of 20.77 and 23.48 kips respectively. The East and West shoulder at the corrugation valley were also yielded at the load of 23.48 and 25.01 kips respectively. Other locations did not reach the steel yield point.

Figure 4-14 illustrates the pipe arch CMP profile before and after the static load. The pipe profile at end of the test clearly illustrates the crown buckling with three-hinge plastic failure mechanism. The comparison between the mechanical sensors and DIC are presented in Figure 4-15. The deflection results captured by the DIC method is in an excellent conformity with the mechanical sensors result that verifies the accuracy of the DIC profiling method.

The load-displacement values for soil surface, crown, springline, and shoulder of the invert-cut pipe arch CMP due to the applied static load is illustrates in Figure 4-16. In addition, Figure 4-17 illustrates the applied load on the soil surface versus its corresponding pressure at the crown of the invert-cut pipe arch CMP, where the recursive part of the graph represents drop in both pressure and load at the same time.

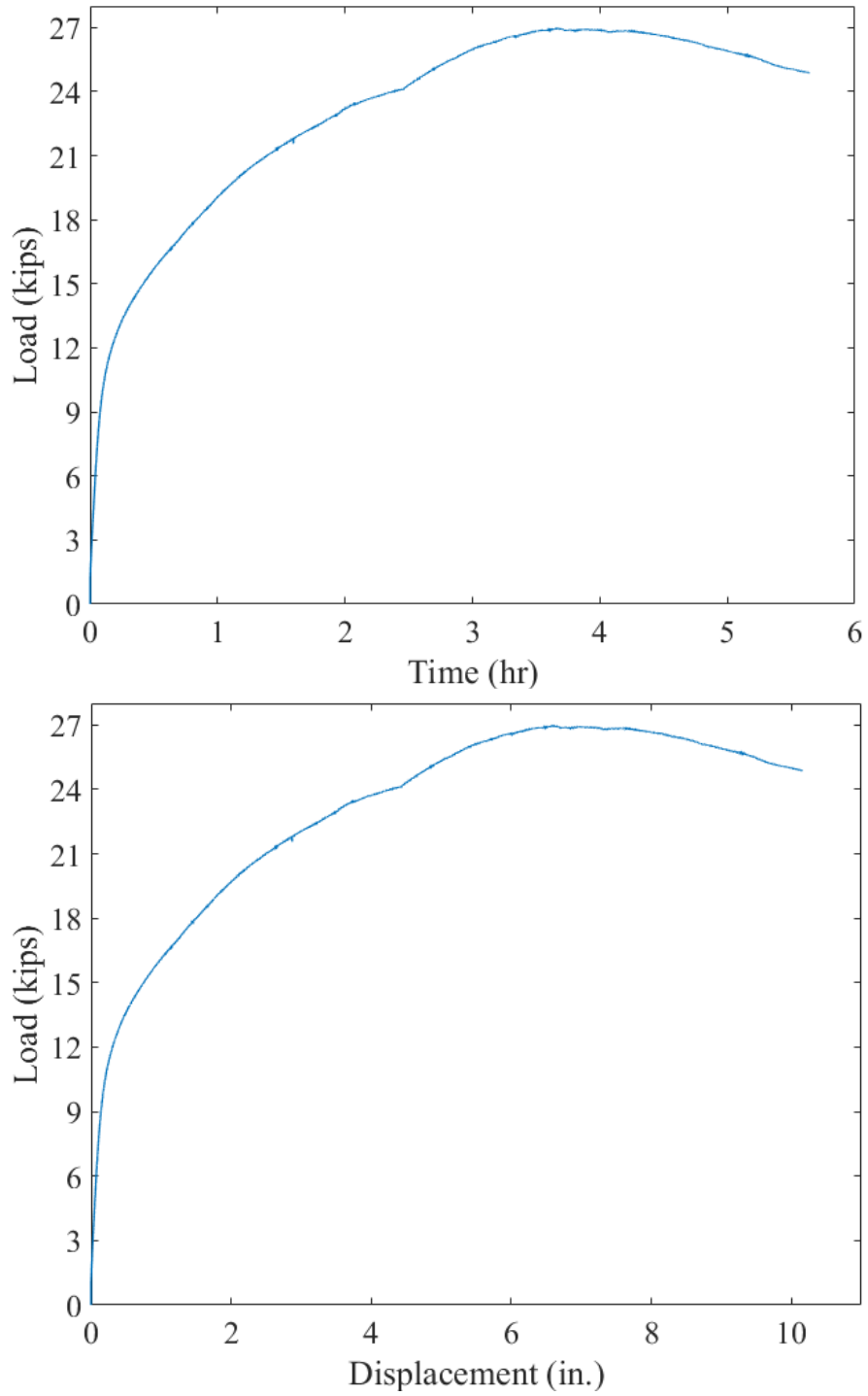


Figure 4-10. Invert-cut pipe arch CMP static live load: (top) load-time and, (bottom) load-soil displacement graphs.

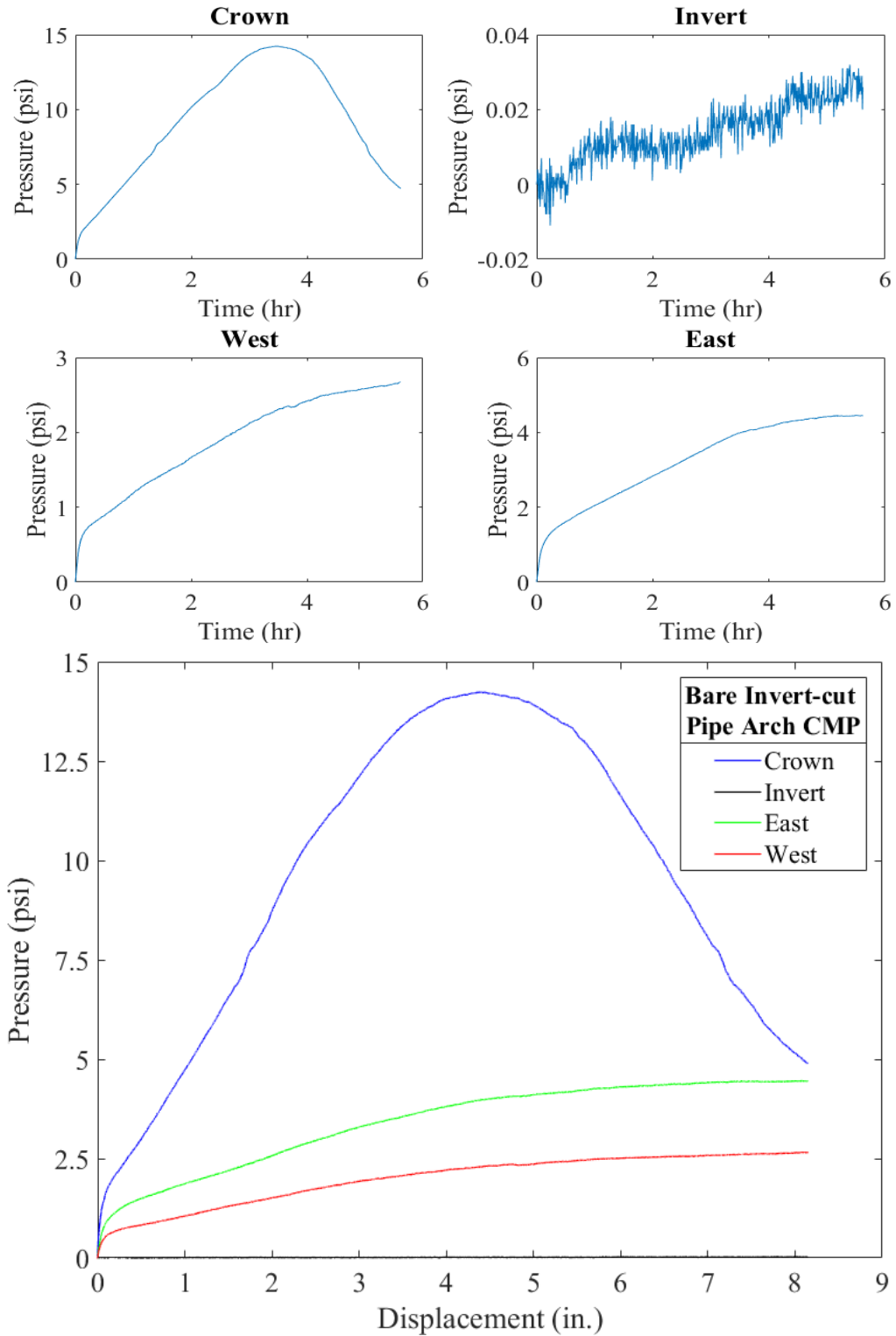


Figure 4-11. Earth pressure cell results for the invert-cut pipe arch CMP with respect to: (top) time, and (bottom) crown displacement.

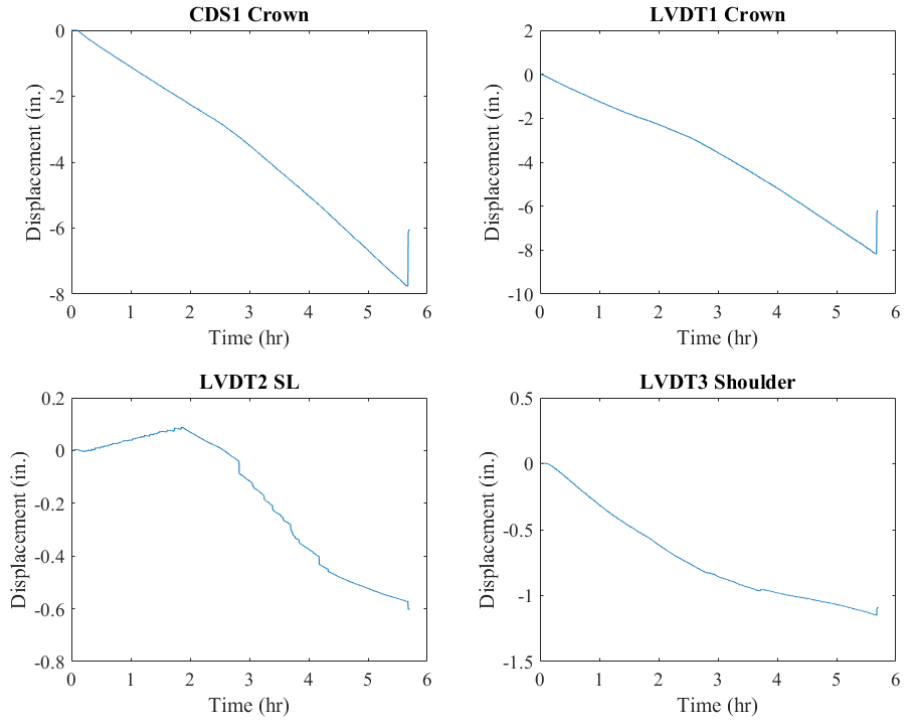


Figure 4-12. Mechanical sensors results for the invert cut pipe arch CMP.

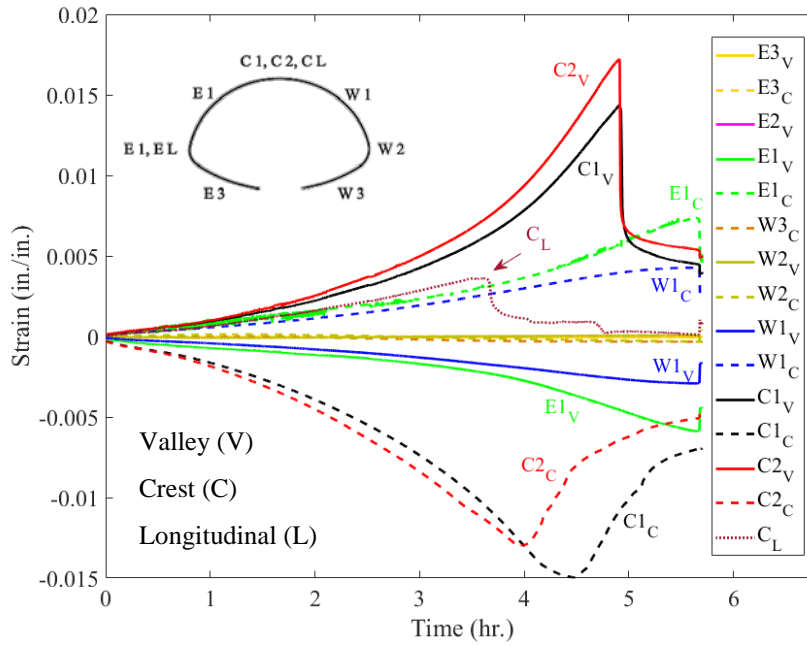


Figure 4-13. Strain gauges reading for the invert-cut pipe arch CMP.

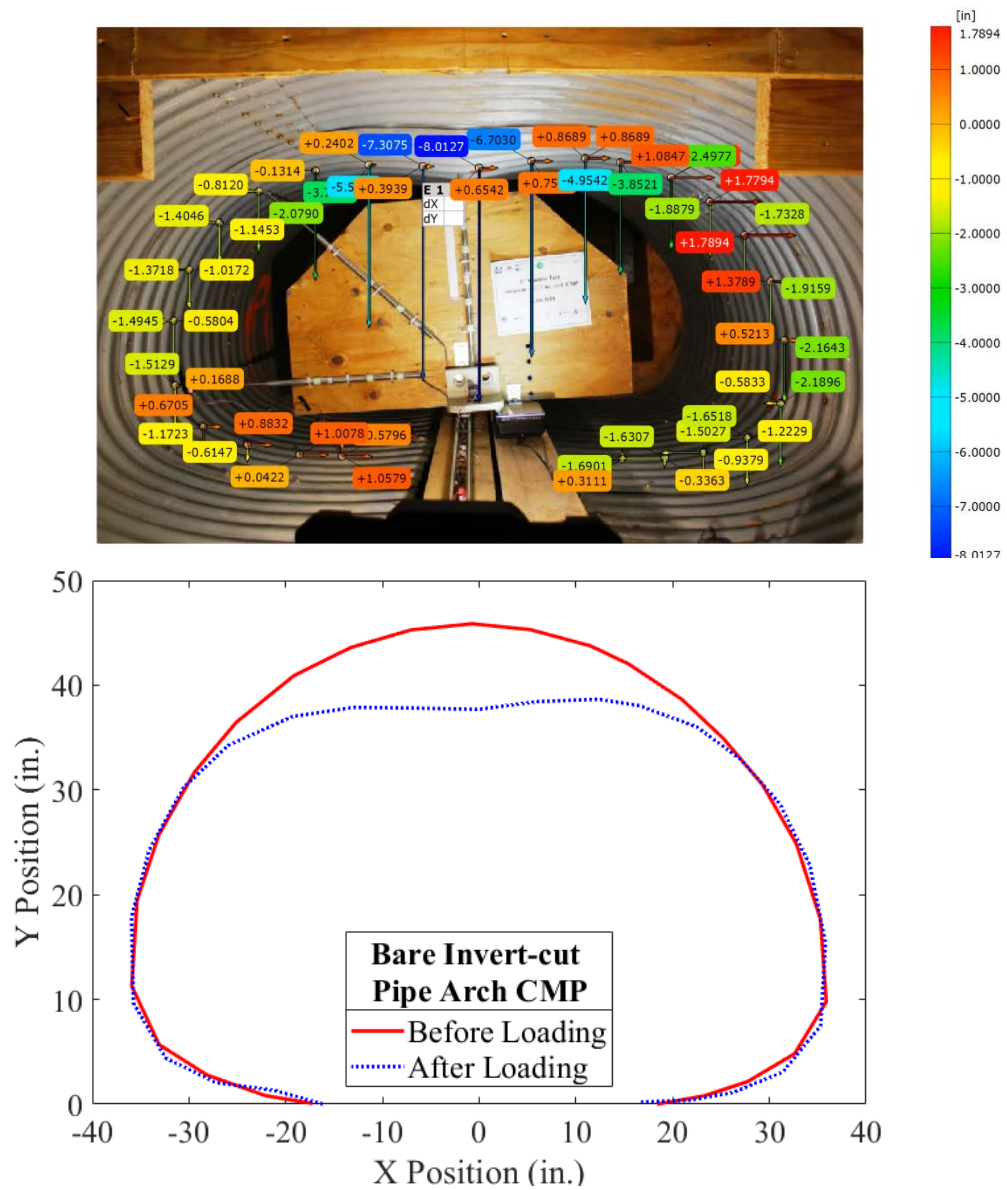


Figure 4-14. Pipe profiling using DIC for the invert-cut pipe arch CMP.

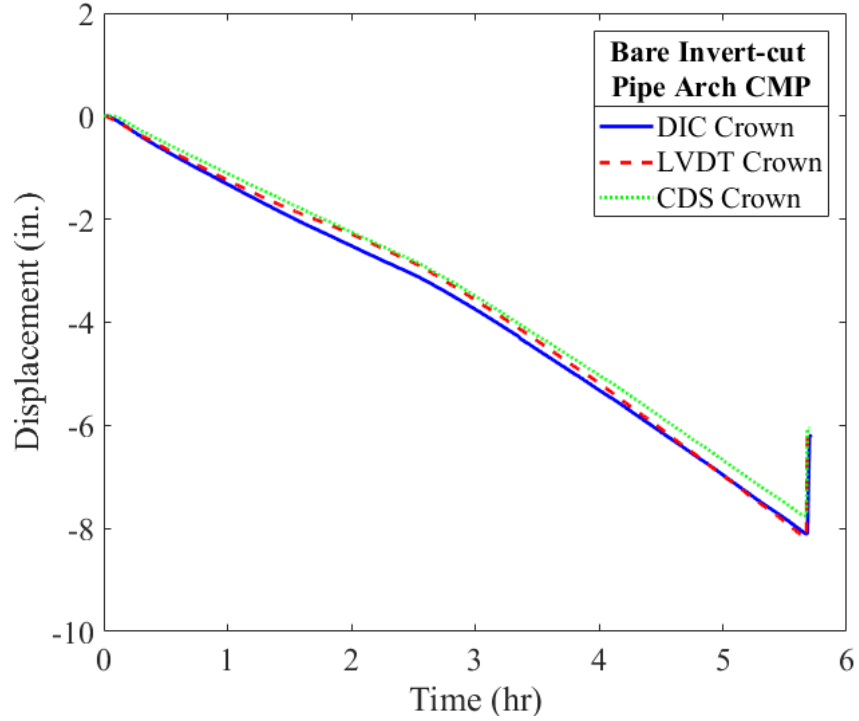


Figure 4-15. DIC method verification with mechanical sensors for invert-cut pipe arch CMP.

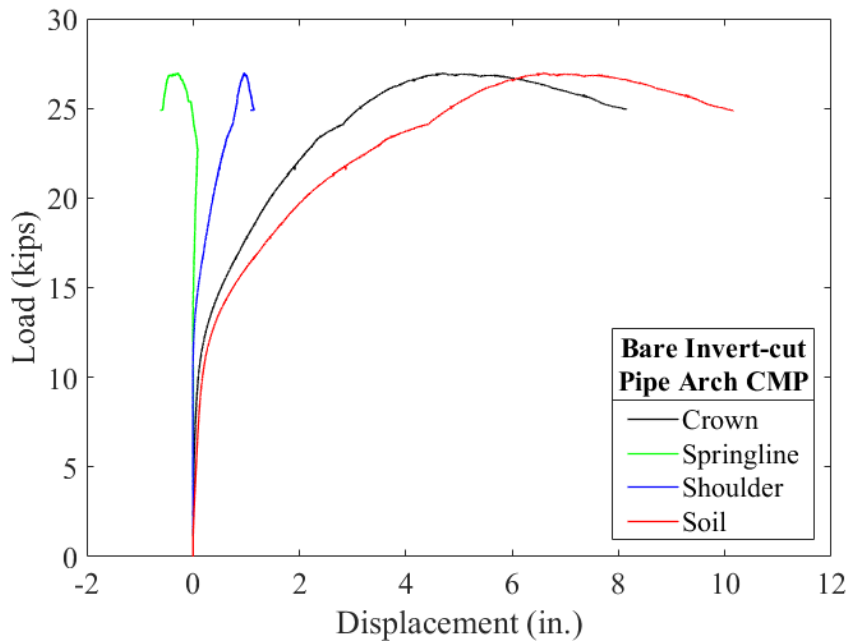


Figure 4-16. Load vs. displacement of the soil surface, crown, springline, and shoulder of the invert-cut pipe arch CMP due to the applied static load.

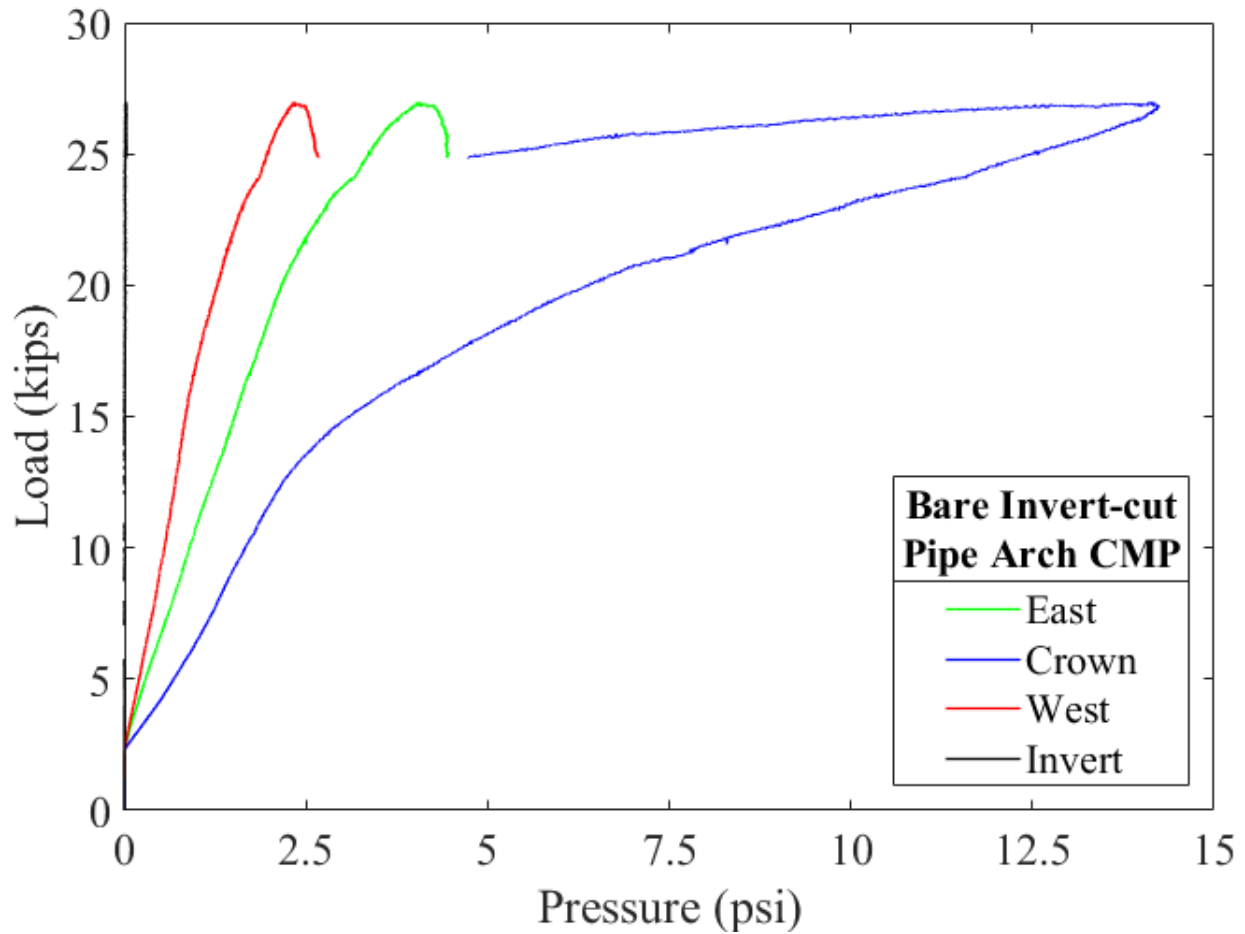


Figure 4-17. Load vs. pressure for the invert-cut pipe arch CMP

4.2.1.3. Invert-cut Circular CMP Test Results

The invert-cut circular CMP was tested on August 15th, 2019, using the 20 × 40 in. load pad. The test duration was 5.01 hours. The CMP sample failed at the load of 39.93 kips with 7.26 in. of soil settlement. Figure 4-19 illustrates the load and soil settlement graph, registered by the actuator’s load cell and LDVT. The CMP’s failure occurred due to the combination of local buckling of the crown and pipe geometry change due to the circumferential movement. Due to the

applied load, after about 5 kips of load that most likely the maximum friction resistance between the soil and CMP was reached, the pipe continuously moved circumferentially until both ends of the CMPs came to contact. At that point, the CMP's ring compression was recovered, and the pipe was able to resist the applied load. Figure 4-18 (a) illustrates the invert-cut circular CMP free body diagram and the movement mechanism. Figure 4-18 (b) shows closing the gap at the invert due to loading. This phenomenon can occur in the field at a slower pace, since usually there is pavement at top of the culvert that distributes the traffic loads and therefore, it takes more load to move the pipe circumferentially. In addition, due to external corrosion, the roughness and consequently the friction between the CMP and soil increases. Moreover, horizontal frictional resistance is a function of the length of the CMP, which is usually longer than the tested pipe samples in the laboratory. Therefore, longer CMP has higher circumferential resistance force that reduces the CMP's movement. This may increase the chance of local buckling occurrence even prior to the pipe circumferential movement.

The earth pressure cell results registered the maximum pressure of 29.95 psi at the crown location. Although the CMP had not the invert section (i.e., invert cut) and it was expected to observe no pressure transferred to the bottom of the pipe, it was observed that due to the invert-cut closure a 2.787 psi pressure was applied to the soil bellow the pipe. The maximum pressure applied on the West and East locations were 9.65, and 7.35 psi respectively. Figure 4-20 illustrates earth pressure results for the invert-cut circular test.

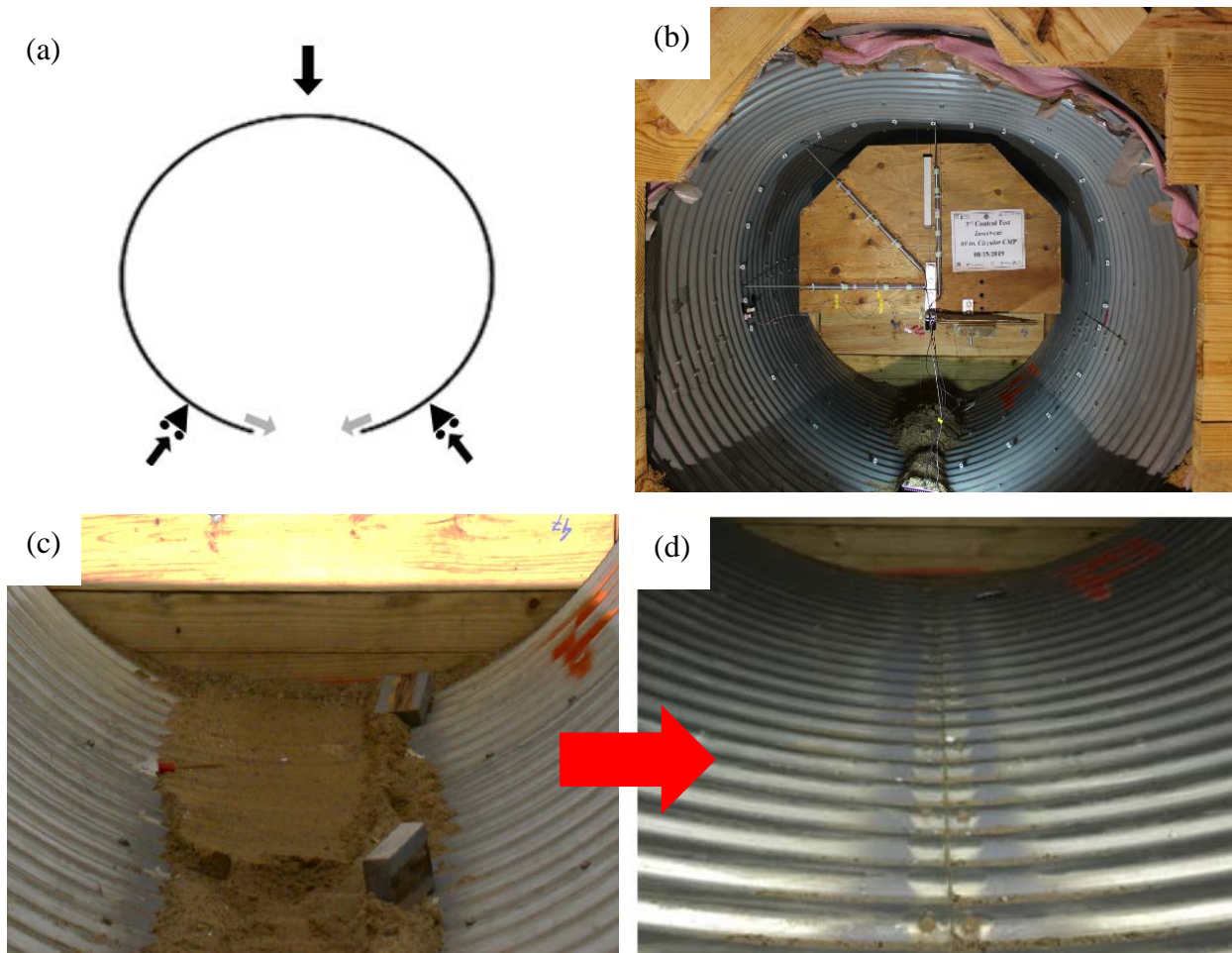


Figure 4-18. Invert-cut circular CMP: (a) free body diagram, (b) CMP deflection at end of the test, (c) invert section before loading, and (d) invert section after loading.

Figure 4-21 illustrates the results of the mechanical sensors. The results show that the pipe was subjected to 7.6 in. of crown and 0.1 in. of springline deflection. However, the deflection of the springline at the end of the test is not representative of the overall pipe horizontal deflection, as the CMP had circumferential movement as well. The shoulder had 1.875 in. downward movement. At the end of the test once the load was released from the surface, the pipe's crown, springline and shoulder had reversal movement of 1.08, 0.051, and 1.054 in. respectively.

The strain gauge results showed the invert-cut pipe arch CMP experienced a large strain at the both shoulder locations as well as the crown. The corrugation crest at the West shoulder location was the first that reached the steel yielding point (i.e., $1138 \mu\epsilon$) at the load of 22.28 kips. Then the crest of the crown was the next location that reached yield point at the load of 22.9 kips. The East shoulder at the corrugation crest were also yielded at the load of 25.27 kips. The East and West shoulder at the corrugation valley were both yielded at the load of 29.01 kips. The valley of the crown location eventually yielded at the load of 32.03 kips. Other locations did not reach the steel yield point. The strain gauges results are presented in Figure 4-22.

Figure 4-23 illustrates the pipe arch CMP profile before and after the static load. The pipe profile at end of the test clearly illustrates the crown flattening and CMP's circumferential movement. The comparison between the mechanical sensors and DIC are presented in Figure 4-24. The deflection results captured by the DIC method is in an excellent conformity with the mechanical sensors result that verifies the accuracy of the DIC profiling method.

The load-displacement values for soil surface, crown, springline, and shoulder of the invert-cut circular CMP due to the applied static load is illustrates in Figure 4-25. In addition, Figure 4-26 illustrates the applied load on the soil surface versus its corresponding pressure at the crown of the invert-cut circular CMP, where the recursive part of the graph represents drop in both pressure and load at the same time.

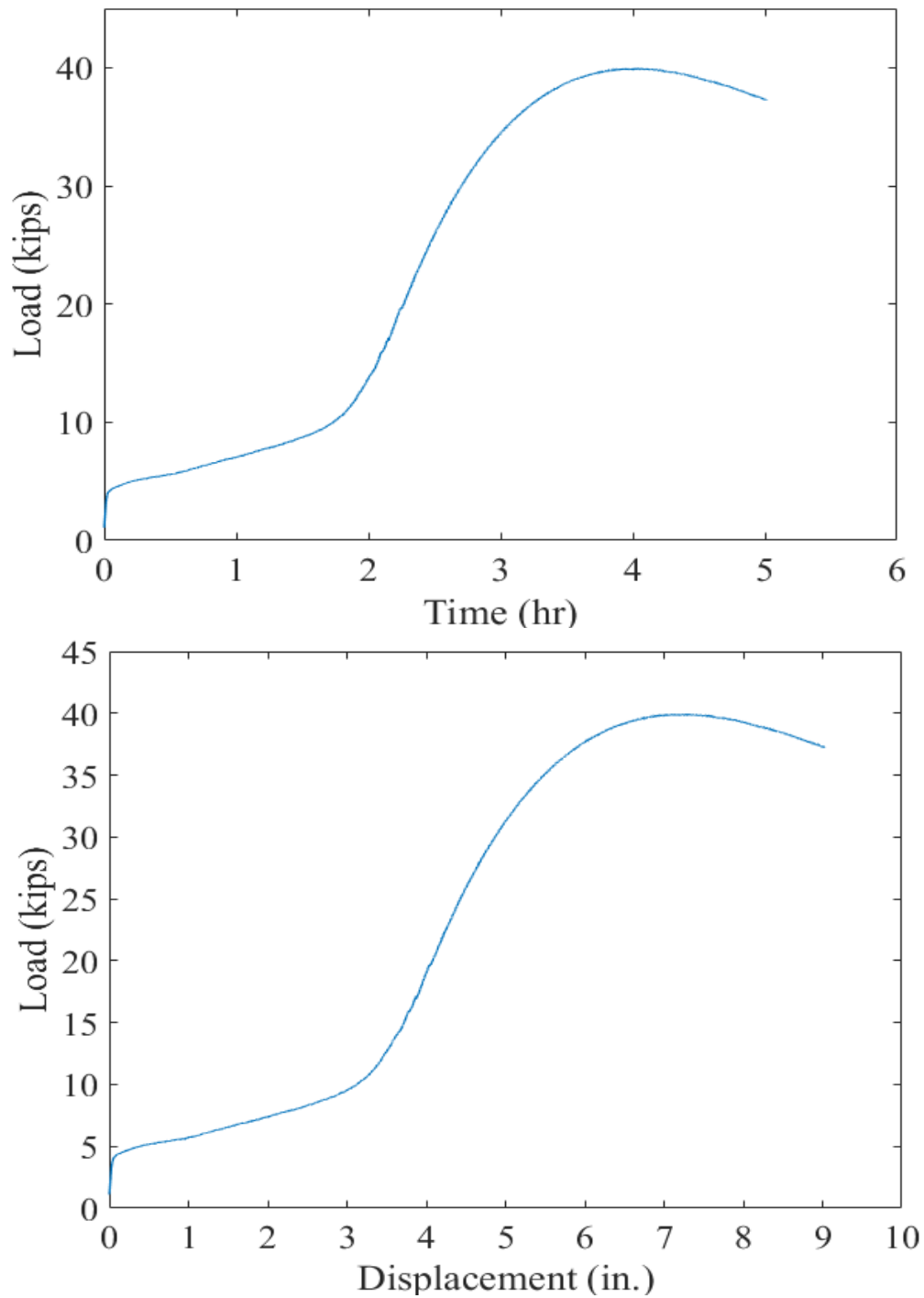


Figure 4-19. Invert-cut circular CMP static live load: (top) load-time and, (bottom) load-soil displacement graphs.

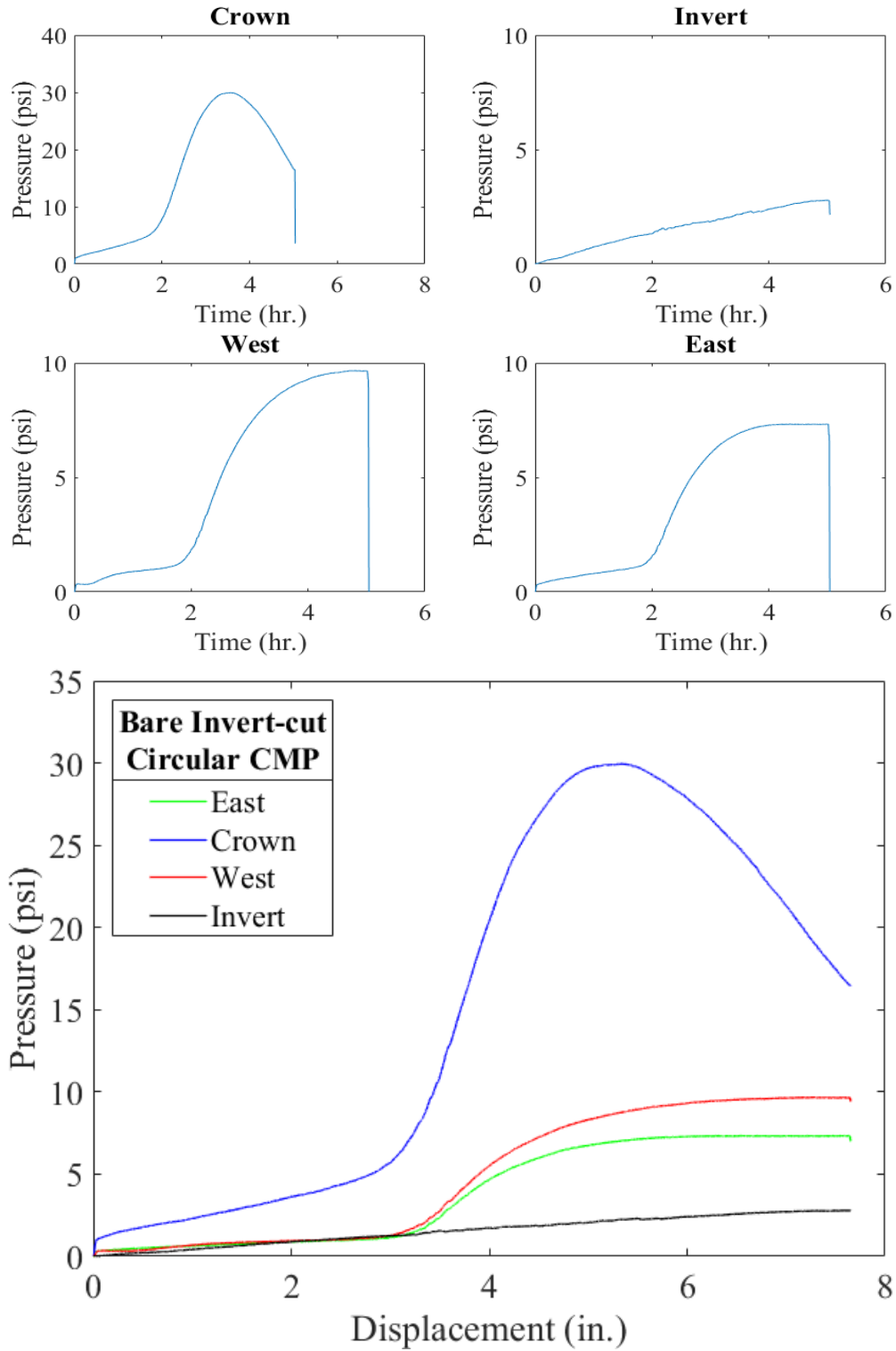


Figure 4-20. Earth pressure cell results for the invert-cut circular CMP with respect to: (top) time, and (bottom) crown displacement.

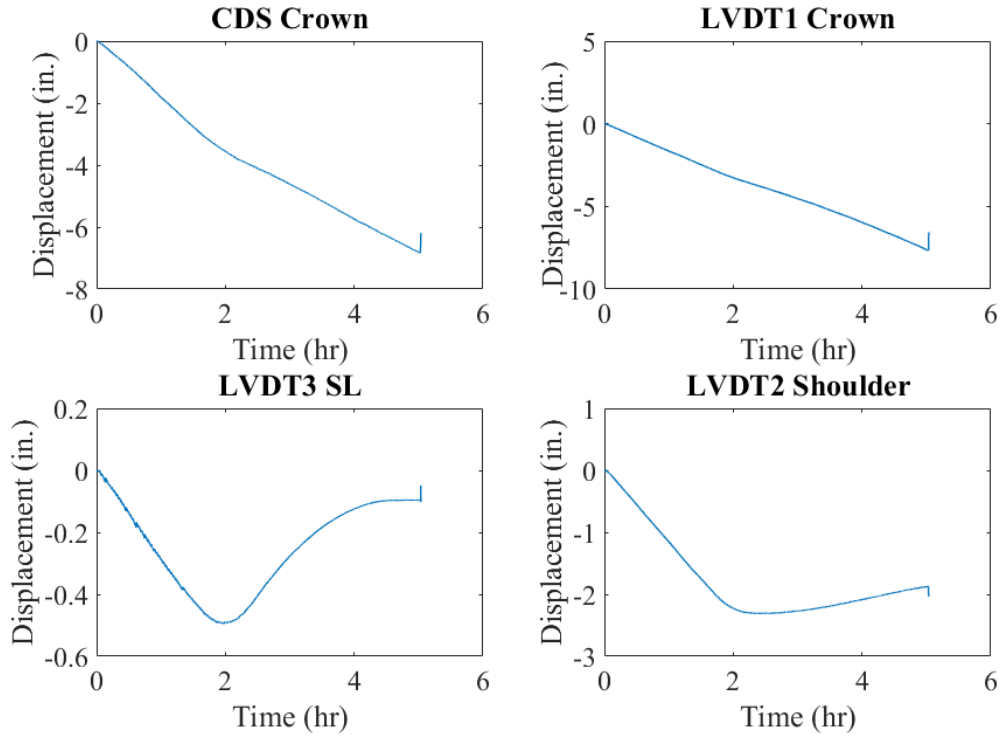


Figure 4-21. Mechanical sensors result for invert-cut circular CMP.

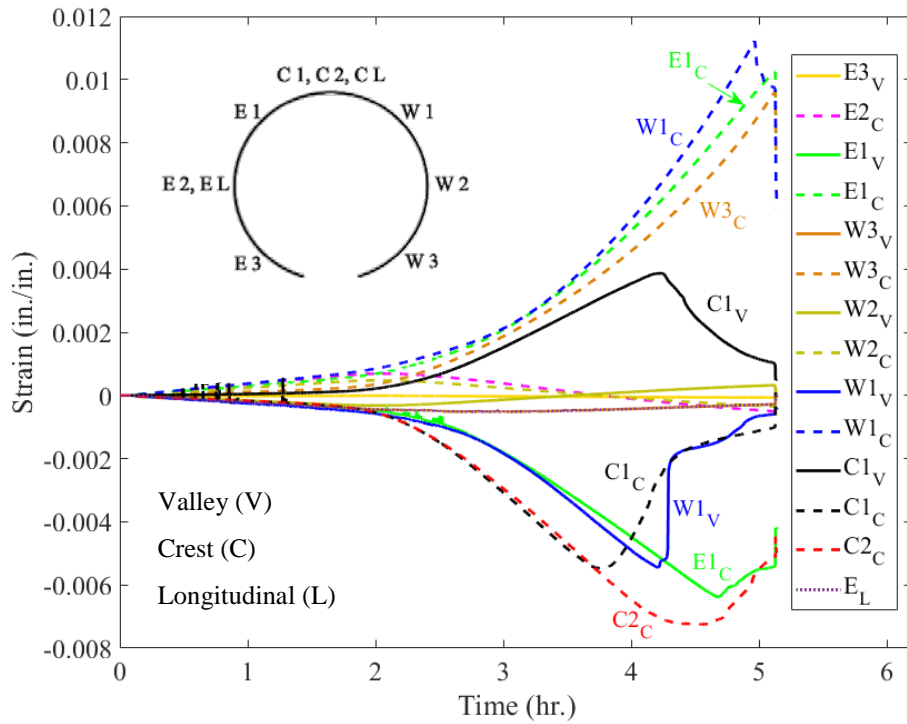


Figure 4-22. Strain gauges reading for the invert-cut circular CMP.

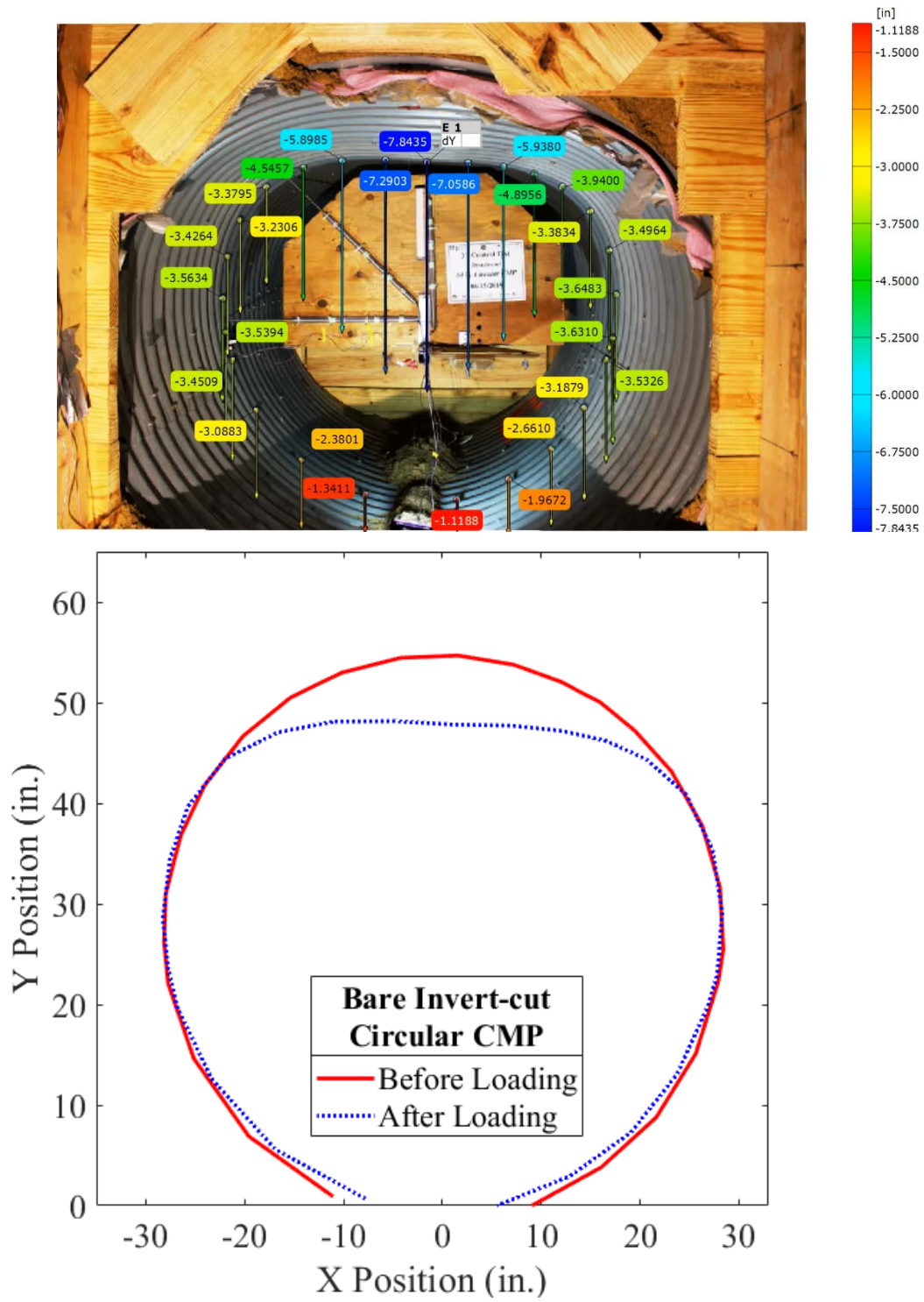


Figure 4-23. Pipe profiling using DIC for the invert-cut circular CMP.

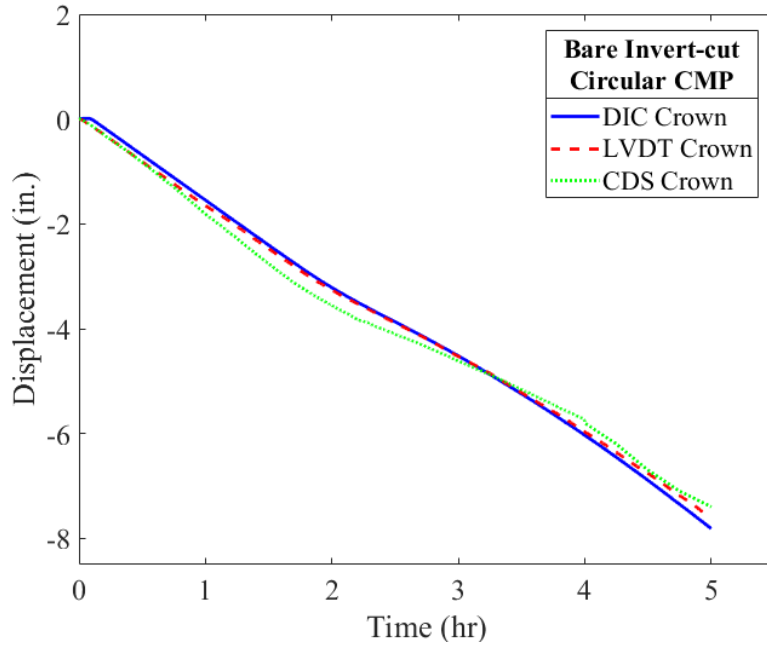


Figure 4-24. DIC method verification with mechanical sensors for invert-cut circular CMP.

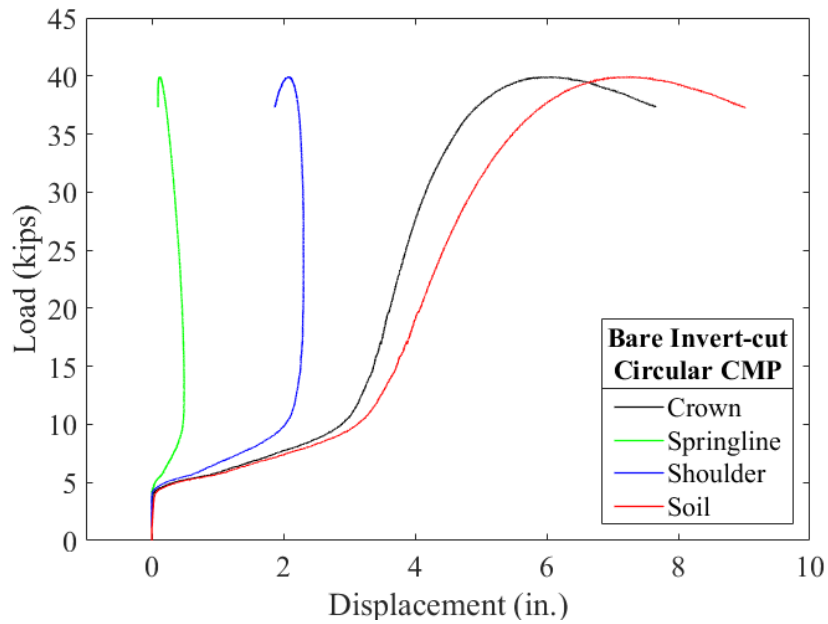


Figure 4-25. Load vs. displacement of the soil surface, crown, springline, and shoulder of the bare invert-cut pipe arch CMP due to the applied static load.

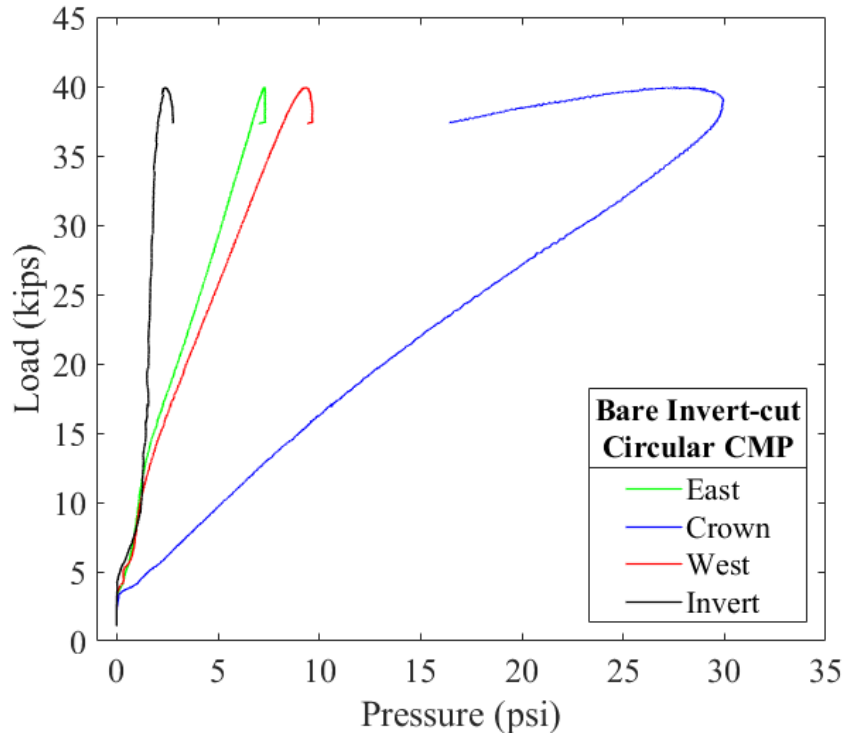


Figure 4-26. Load vs. pressure for the invert-cut circular CMP

4.2.1.4. Control Test Results Comparison

Figure 4-27 compares the soil-culvert load responses of bare (i.e., unlined) pipe arch and circular invert-cut CMPs with the intact circular CMP sample. The intact soil-CMP system, under the AASHTO H20 load pad size, showed stiff response to the live load up to 16 kips (i.e., AASHTO H20 service load) with approximately 1.95 in. of soil surface displacement, illustrated in Figure 4-27 by the notation ‘i’. However, after reaching the service load, soil-pipe system showed softened response to the load until the soil failure at the point (ii). Once the soil failed, pipe carried the load and caused stiffening of the system (iii) until the ultimate failure at the load of 24.8 kips (iv).

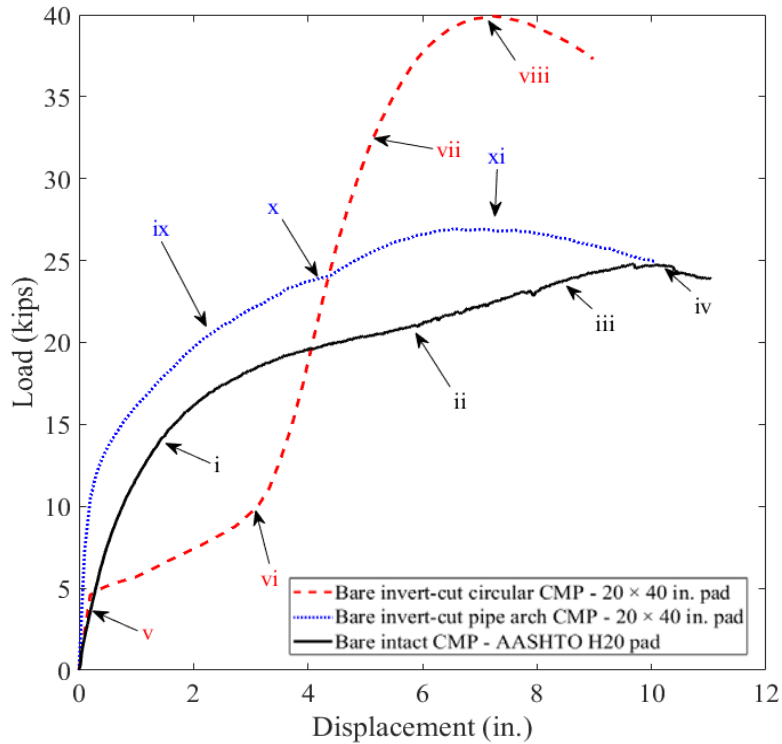


Figure 4-27. Soil settlement results for the invert-cut arch, invert-cut circular, and intact circular pipes due to the applied load

The invert-cut circular CMP sample, showed a different behavior under the static live load. The CMP initially had stiffer response (v), which is believed to be due to the friction resistance force of the soil-CMP system. Once the limit (i.e., 4.58 kips) was reached, the CMP did not show much resistance to the load and continuously deformed until both side of the cut section contacted each other and recovered the ring stiffness (vi). After this point, the system showed significantly stiffer response to the loading (vii) until the failure at the load of 39.9 kips with almost 7.22 in. soil displacement was reached (viii). The pipe arch CMP was able to maintain its stability by taking advantage of its arching shape in the absence of ring compression at no significant horizontal displacement (ix). This is due to the pipe sample’s low slope at the shoulder and large flat area at the invert of the CMP, which causes the applied vertical force to be resisted by the bottom of the

pipe sample. The pipe sample ultimately failed at 26.9 kips with 6.54 in. soil surface displacement. The structural failure mode of both pipe samples was local buckling at crown, which is the critical location right under the load pad, by formation of three-hinge plastic collapse mechanism.

Figure 4-28 and Figure 4-29 are presenting the applied pressure results from soil surface (i.e., under the load pad) and on top of the CMPs (i.e., over the crown). The effect of increasing the load pad size is explicitly evident on the CMPs response, where the smaller load pad resulted in higher pressure. As discussed in section 4.2.1.1, in the intact CMP test, the soil failed at the load of 21.21 kips that had corresponding surface and crown pressure of 105 and 47.5 psi respectively. While, in none of the invert-cut CMP test, the soil-pipe system reached that pressure in soil and the CMPs were failed sooner than the soil above. This implies increasing the load pad dimensions satisfied one of the test requirements to fail the CMP prior to the soil failure.

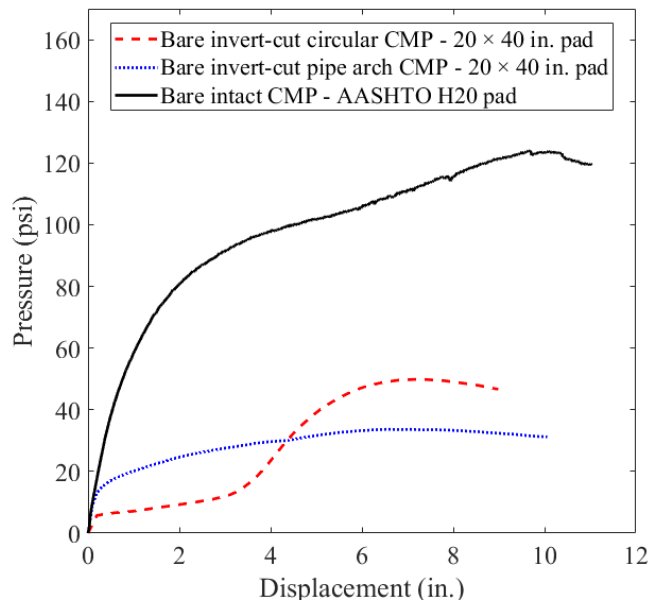


Figure 4-28. Soil settlement results for the invert-cut arch, invert-cut circular, and intact circular pipes due to the applied pressure on the soil surface

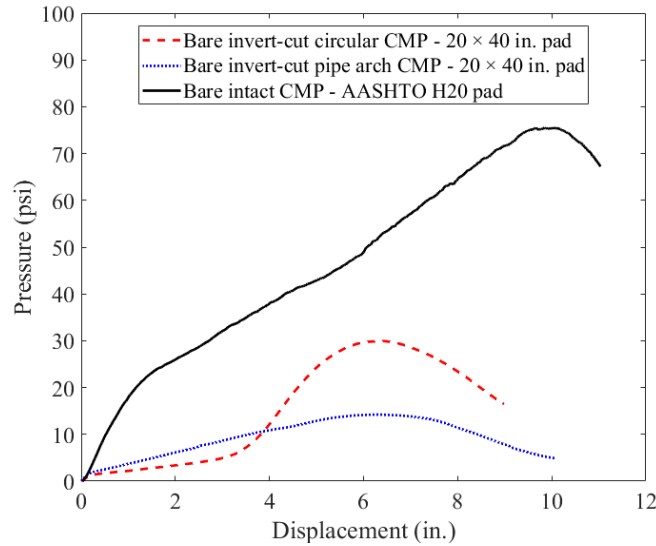


Figure 4-29. Soil settlement results for the invert-cut arch, invert-cut circular, and intact circular pipes due to the applied pressure at top of the pipe samples.

To investigate whether the invert-cut CMP samples have reached the AASHTO H20 service load, the load and pressure should be compared with intact CMP test results. However, since the invert-cut CMPs were tested with the larger diameter load pad, the direct load comparison of the load was not possible. However, the applied pressure at the crown registered by the earth pressure cell at the service load was selected as a baseline to compare the results and obtain an equivalent AASHTO service load. The comparison load-pressure graphs for top of the pipe samples (i.e., above crown) are illustrated in Figure 4-30 that shows that the intact CMP experienced 25.72 psi pressure at the service load of 16 kips, which is marked by “1” in Figure 4-30. The invert-cut pipe arch CMP could not reach the same pressure (i.e., 25.72 psi) and can be considered as in danger of collapse, if the pressure equivalent to the AASHTO H20 service load is applied. However, the invert-cut circular CMP sample reached the same pressure of 25.72 psi (177 kPa) at the load of 32 kips (142 kN), which is marked by “2” in Figure 4-30. This can be interpreted as the equivalent AASHTO H20 service load for the invert-cut circular CMP using 20

× 40 in. load pad size. Therefore, considering the pipe sample length, the frictional resistance factor, and the higher loading capacity of the circular pipe sample, they can lead to less risk of the circular CMP over the arch CMP in a fully deteriorated invert condition.

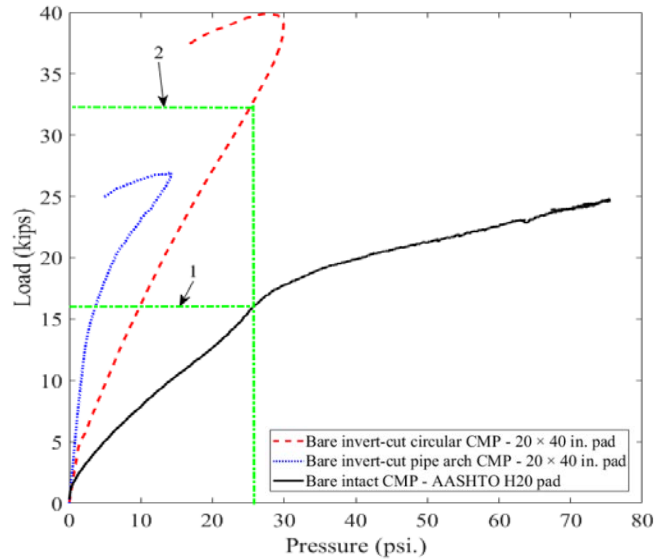


Figure 4-30. Load vs. applied pressure at crown: (1) AASHTO H20 truck service load, and (2) equivalent service load on the invert-cut circular CMP.

4.2.2. SAPL Renewed Invert-cut Pipe Arch CMP Test Results

The invert-cut pipe arch CMPs renewed with the cementitious SAPL were tested using the same load rate and load pad as invert-cut bare pipe arch CMPs specified in sections 4.2.1.2. Due to required time for test preparation, instrumentation and operation, conducting all the three tests of this set in one day was not possible. The first test was conducted on the 3-in. thick SAPL renewed pipe arch CMP after 7 days of curing. The 2 and 1-in. thick SAPL renewed pipe arch CMPs were conducted with a 2-day interval respectively. It is noteworthy that none of the existing shrinkage cracks, discussed in 3.4.5.1, were repaired before the loading and the soil-pipe systems were tested with existed cracks.

In general, due to the applied vertical load all three invert-cut pipe arch CMPs experienced a large crack width in both crown and invert. The crown is located right under the applied load that generates larger deformation than other sections of the CMP, which makes the crown susceptible to crack and buckle. The invert section also is susceptible to crack as the applied vertical load on the CMP generates a negative bending moment on the invert, which causes a relatively large uplift in the invert section. Due to this negative bending moment, the bottom of the pipe arch in the invert section does not receive any pressure, and therefore, the pressure reading at the invert of all three SAPL renewed pipe arch tests are zero. Figure 4-31 illustrates free body diagram of a SAPL renewed pipe arch, which is validated with the DIC results, that includes both positive and negative bending on the crown and invert of the pipe arch.

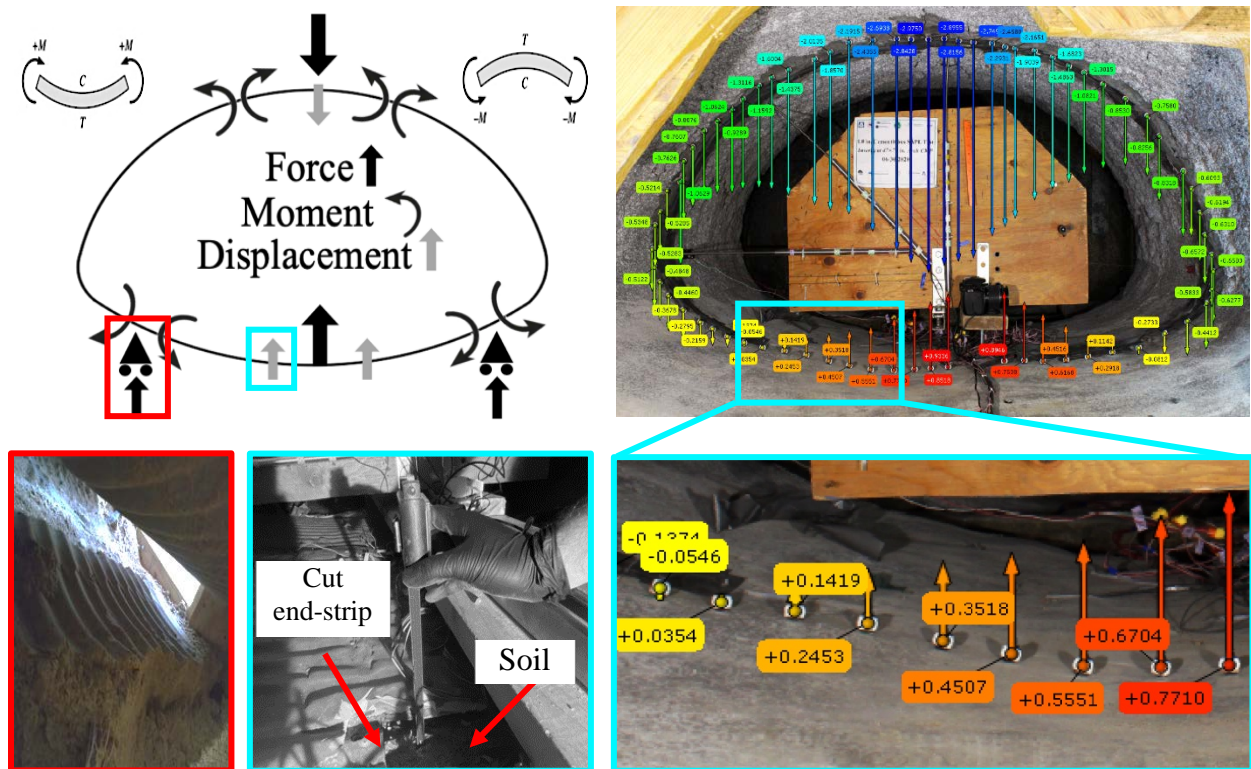


Figure 4-31. Pipe arch CMP behavior due to the vertical load, where the red boxes show the soil support under the pipe on the west haunch area and the blue boxes illustrates the pipe upward movement.

4.2.2.1. 3-in. Thick SAPL Sample

The 3-in. thick SAPL renewed invert-cut pipe arch CMP was tested on Jun 24th, 2020, using the 20 × 40 in. load pad. The test duration was 5.04 hours. During the test, due to the existence of shrinkage cracks no major drop in the load-displacement graphs was observed, and the cracks width were increasing with load progression. The SAPL renewed CMP sample failed at the load of 67.84 kips with 6.606 in. of soil settlement. The failure occurred due to the buckling and large deflection of the crown. Figure 4-32 (a) and (b) illustrate the test sample at before and after loading stage. Once the SAPL-CMP system was failed, the test was continued until about 15% load drop. Then the test was stopped, as further deflection would increase the chance of liner detachment and fall, which would damage the mechanical sensors and cameras inside the pipe. Once the load was released from the soil surface, the pipe had an upward movement and relaxed. However, this upward movement resulted in a large delamination from the West shoulder and springline which is illustrated in Figure 4-32 (c) and (d). Figure 4-33, also illustrates the load and soil settlement graph, registered by the actuator's load cell and LDVT.

The earth pressure cell results registered the maximum pressure of 93.32 psi at the crown location. The maximum pressure applied on the West and East locations were 4.37, and 4.59 psi respectively. Figure 4-34 illustrates earth pressure results for the invert-cut circular test.

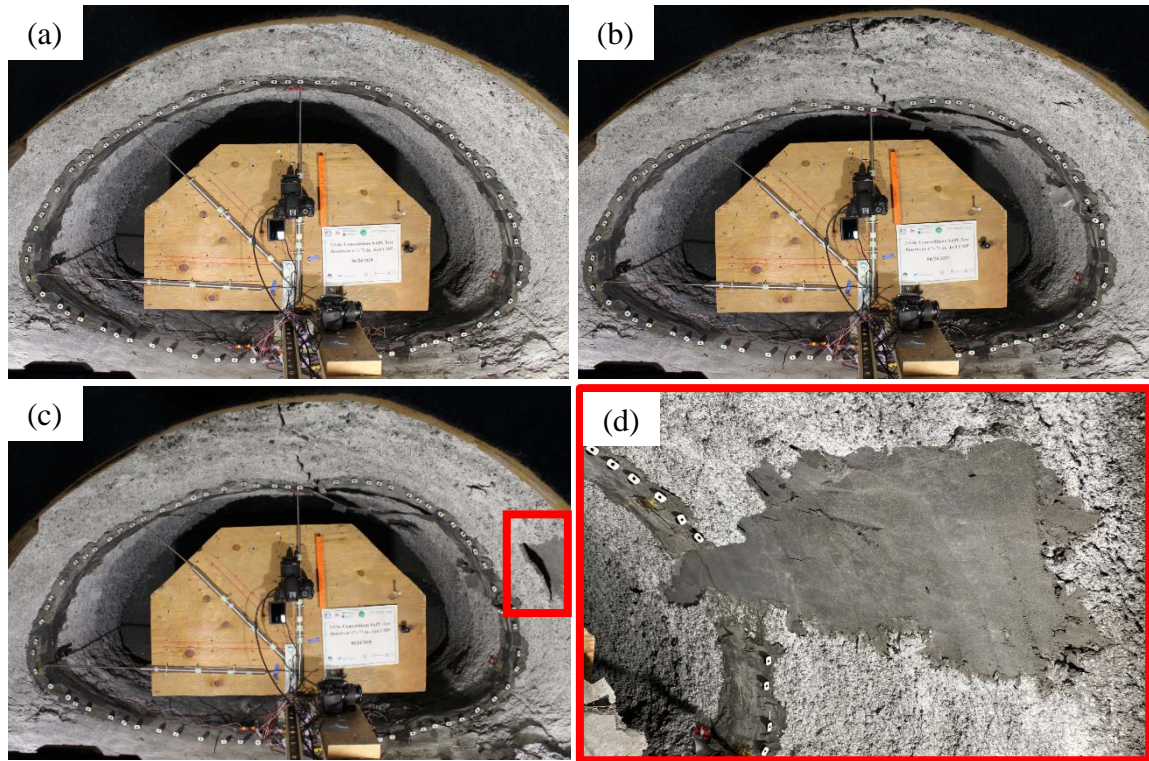


Figure 4-32. Invert-cut pipe arch renewed with 3 in. cementitious SAPL: (a) before loading, (b) after loading, (c) after unloading, and (d) delamination in the West springline.

Figure 4-35 illustrates the results of the mechanical sensors. The LVDT results show that the pipe was subjected to 4.224 in. of crown and 0.722 in. of springline deflection. The shoulder had 0.33 in. downward movement. The CDS showed 4.77 in. of crown movement, which is 0.546 in. higher than the LVDT's reading. This discrepancy is due to the fact that the LVDT could move along the SAPL surface as the liner was deflecting, while the CDS was glued to certain location. The result of the DIC is also closer to the CDS result for this experiment. At the end of the test once the load was released from the surface, the pipe's crown, and springline had reversal movement of 0.863 and 0.07 in. respectively.

The strain gauge results showed the invert-cut pipe arch CMP experienced a large strain at the crown and both shoulder locations as well as springline that indicates the formation of buckling

at the crown, as illustrated in Figure 4-36. The crown of the CMP was the first location that reached the steel yielding point (i.e., $1138 \mu\epsilon$) at the load of 35.22 kips. West shoulder at the CMP also yielded at 49.27 kips. Eventually, the East shoulder of the CMP yielded at the load of 60.38 kips, which was reached after the ultimate failure of the SAPL-CMP system. Other locations did not reach the steel yield point. The strain gauges on the SAPL surface showed that the cementitious liner cracked at the load of 15.79 kips, which resulted in a drop in strain reading of the springline and shoulder of the East and West (i.e., W3, W2, and E2) locations. At this load, a drop in the load-displacement graph (Figure 4-33) can be observed. The Figure 4-36 also illustrates a sudden strain reduction in the crown of the SAPL at the load of 26.12, which can be due to a crack at this location.

Figure 4-37 illustrates the 3-in. thick SAPL renewed pipe arch CMP profile before and after the static load. The pipe profile at end of the test clearly illustrates the crown flattening. In addition, the roughness and irregularity of the SAPL is explicitly evident in the profiling result. The comparison between the mechanical sensors and DIC are presented in Figure 4-38. The deflection results captured by the DIC method is in an excellent conformity with the CDS sensor.

The load-displacement values for soil surface, crown, springline, and shoulder of the 3-in. thick SAPL renewed pipe arch CMP due to the applied static load is illustrates in Figure 4-39. In addition, Figure 4-40 illustrates the applied load on the soil surface versus its corresponding pressure at the crown of the renewed pipe arch CMP, where the recursive part of the graph represents drop in both pressure and load at the same time.

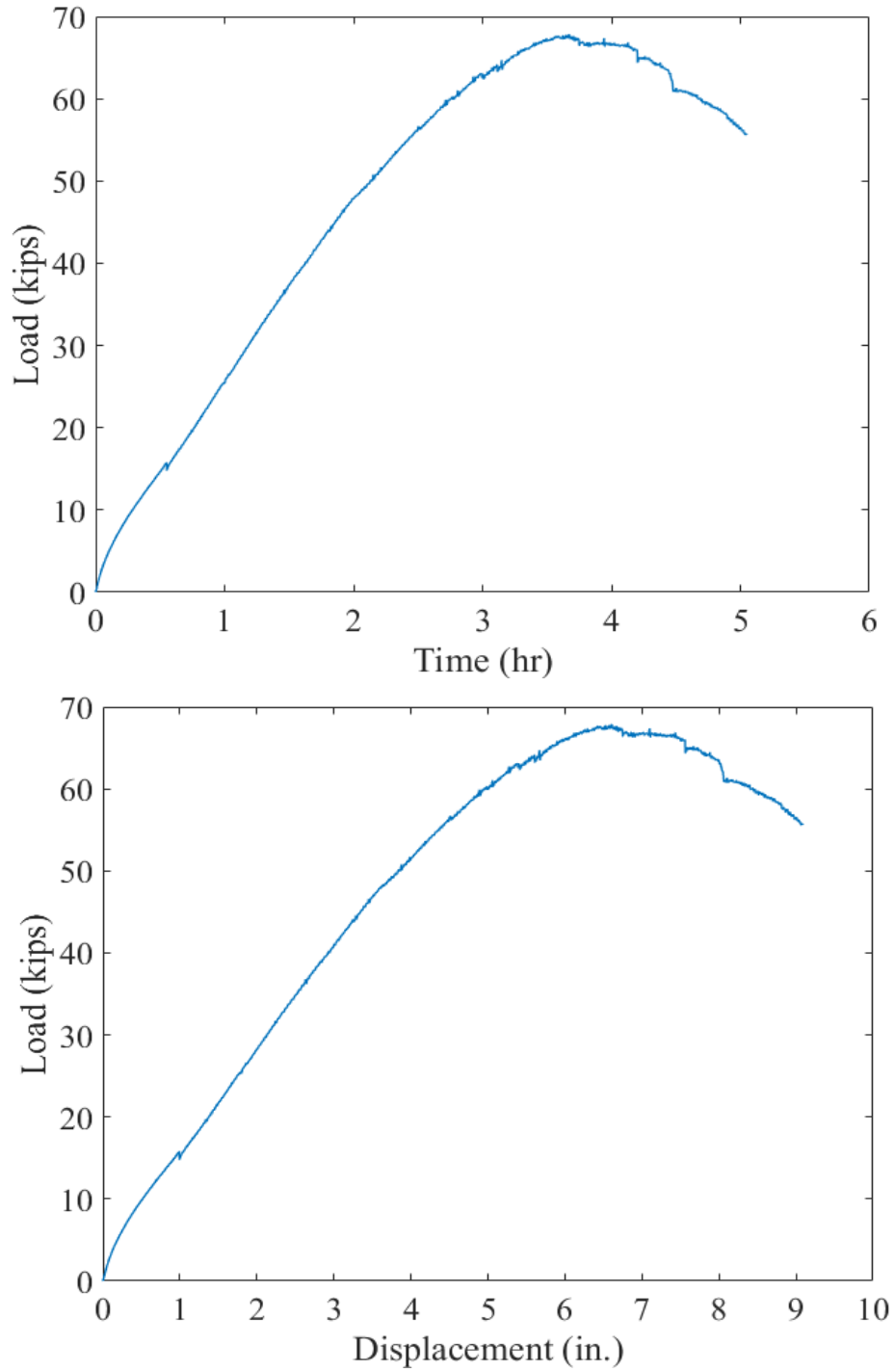


Figure 4-33. Invert-cut pipe arch CMP renewed with 3-in. thick cementitious SAPL subjected to static live load: (top) load-time and, (bottom) load-soil displacement graphs.

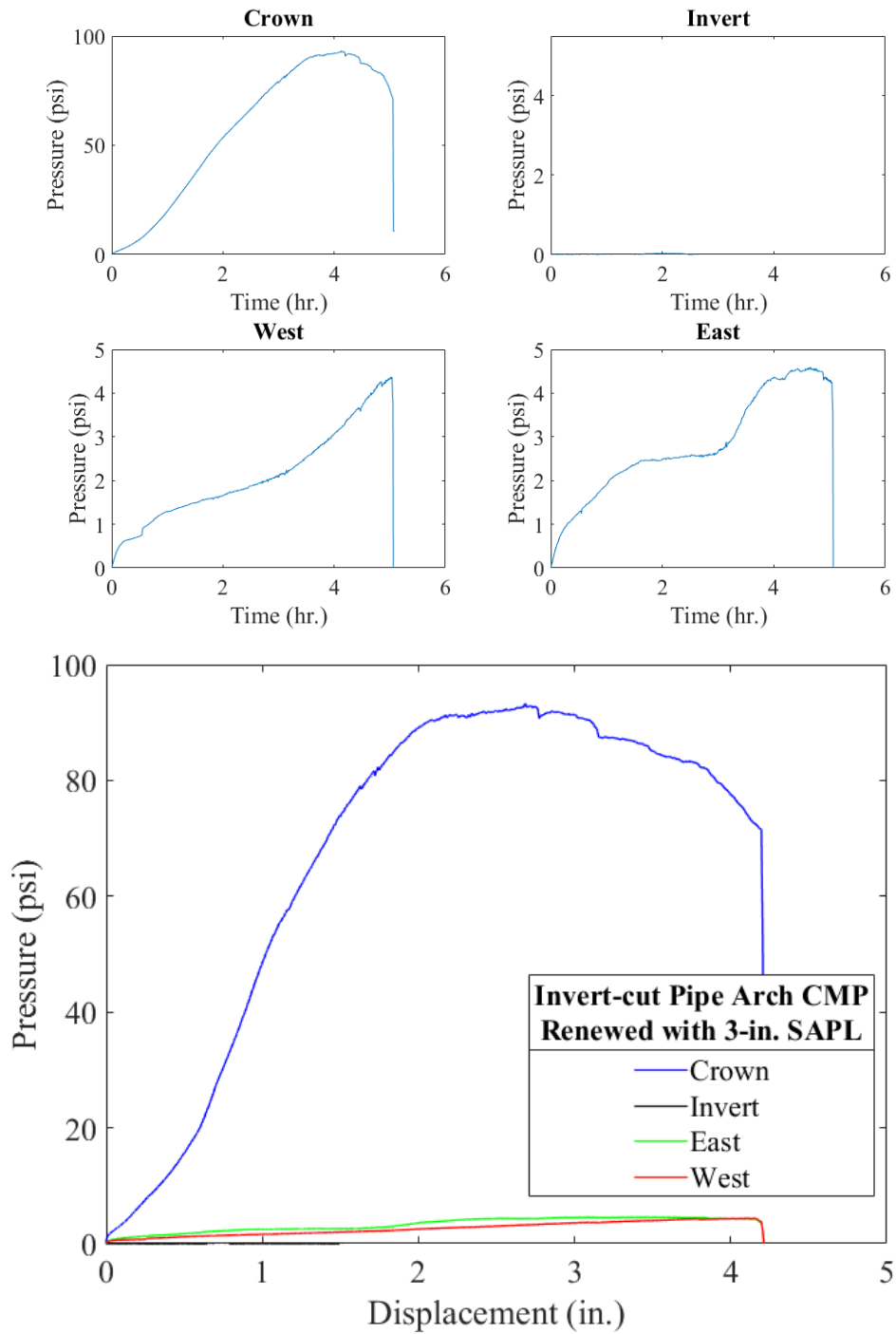


Figure 4-34. Earth pressure cell results for the 3-in. thick SAPL renewed invert-cut pipe arch CMP with respect to: (top) time, and (bottom) crown displacement.

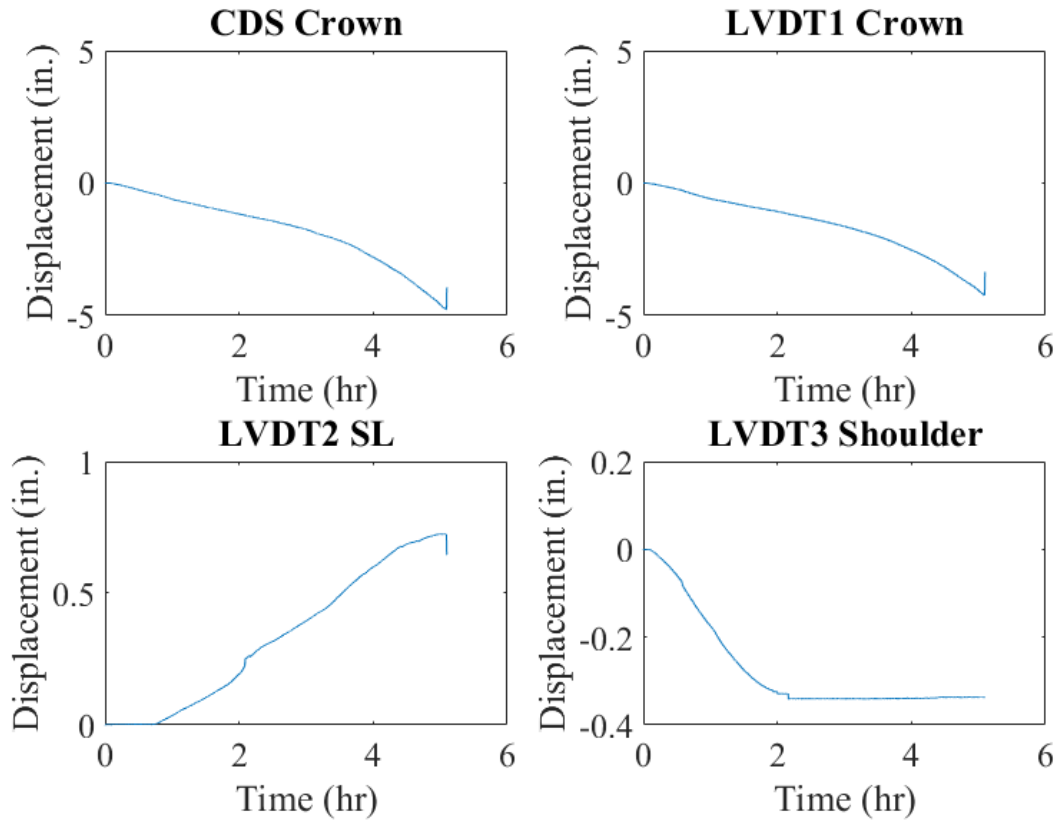


Figure 4-35. Mechanical sensors result for 3-in. thick SAPL renewed invert-cut pipe arch CMP.

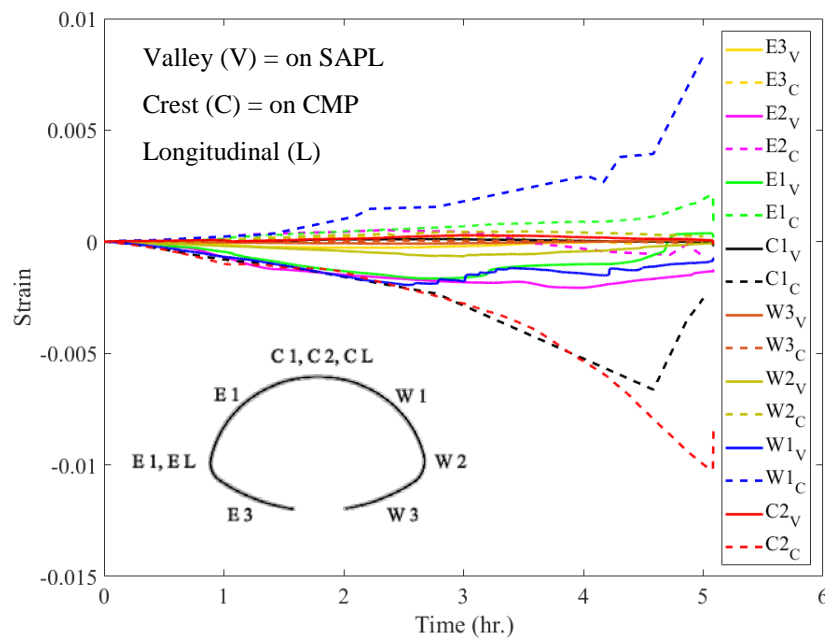


Figure 4-36. Strain gauges reading for the 3-in. thick SAPL renewed invert-cut pipe arch CMP.

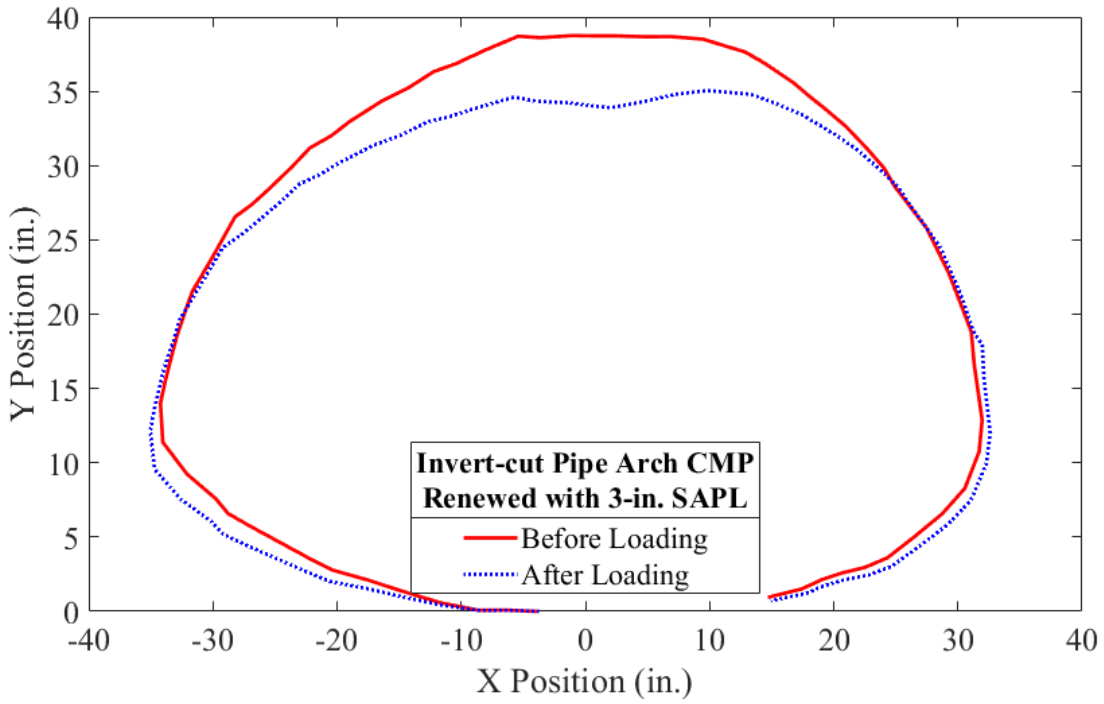
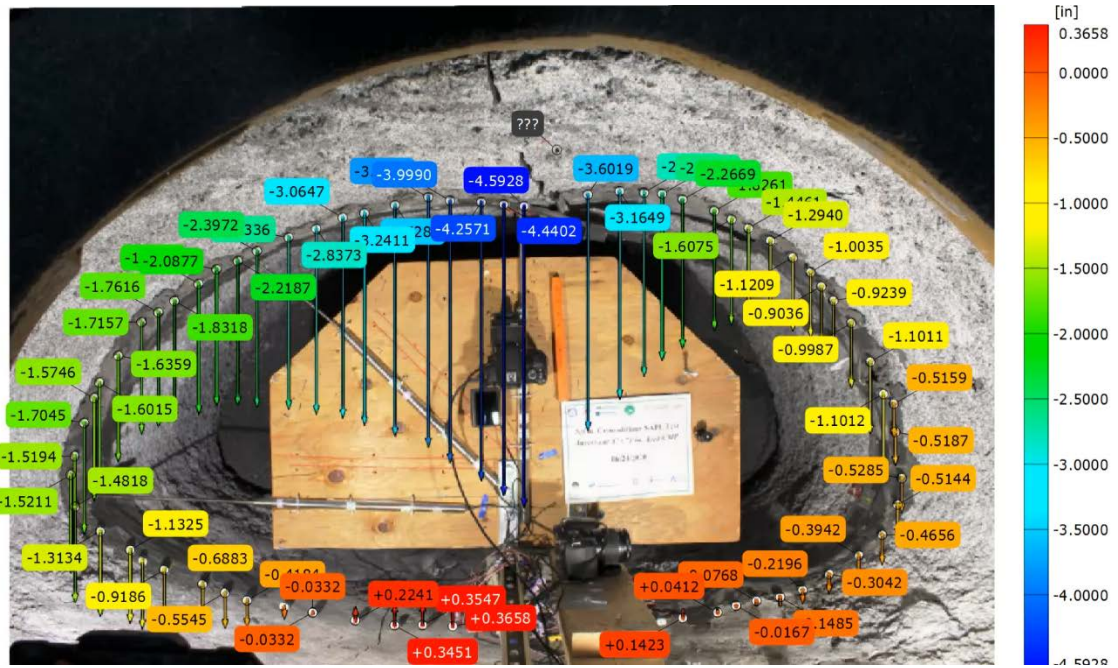


Figure 4-37. Pipe profiling using DIC for the 3-in. thick SAPL renewed invert-cut pipe arch CMP.

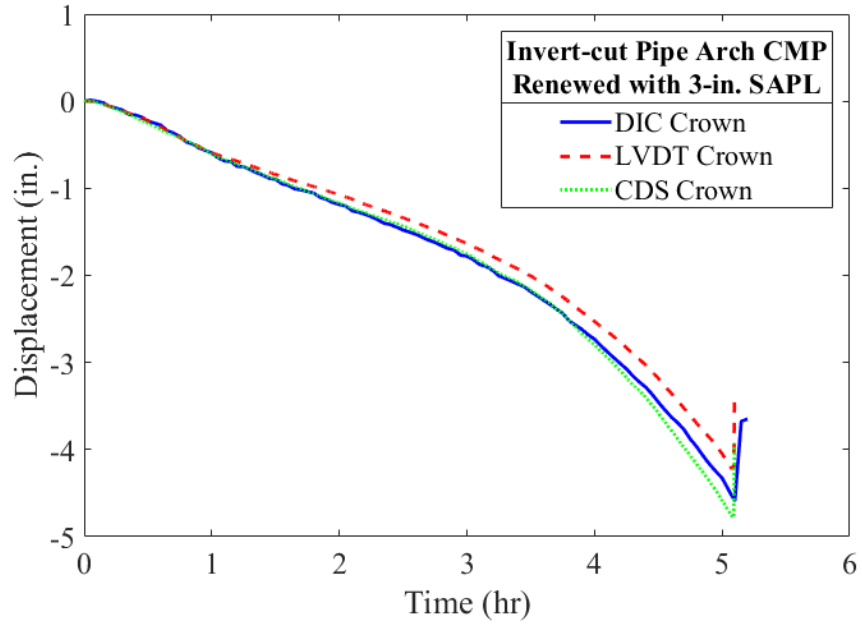


Figure 4-38. DIC method verification with mechanical sensors for the 3-in. thick SAPL renewed invert-cut pipe arch CMP.

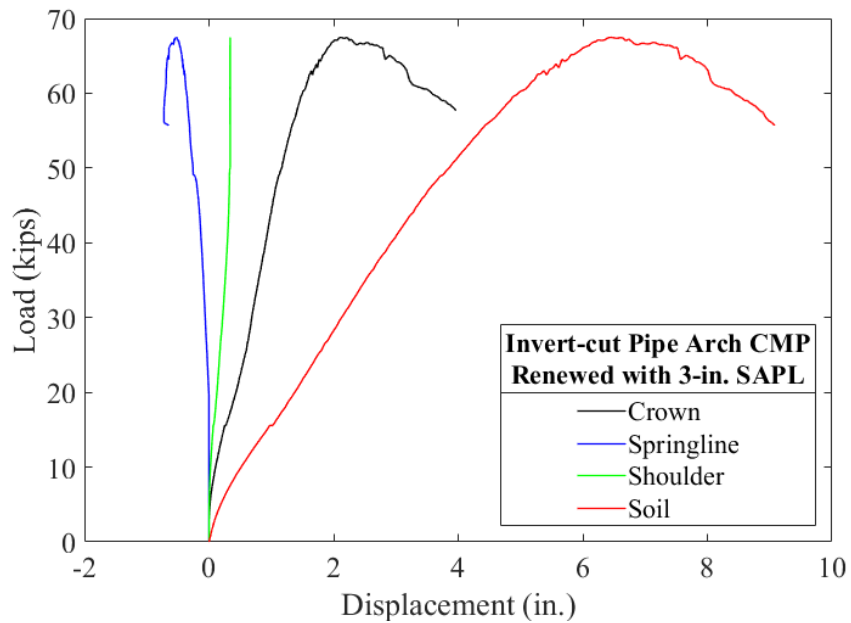


Figure 4-39. Load vs. displacement of the soil surface, crown, springline, and shoulder of the 3-in. thick SAPL renewed invert-cut pipe arch CMP due to the applied static load.

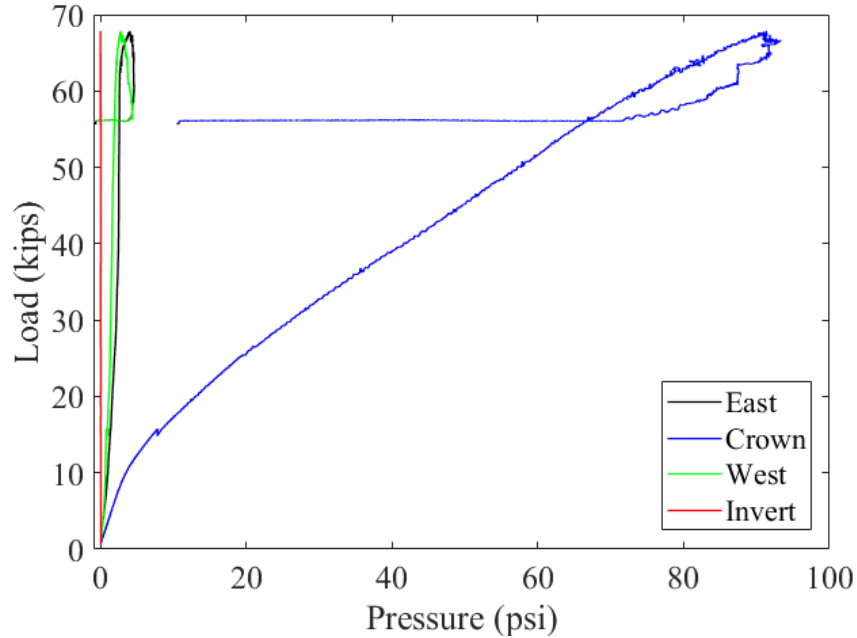


Figure 4-40. Load vs. pressure for the 3-in. thick SAPL renewed invert-cut pipe arch CMP.

4.2.2.1.1. Post Failure Crack Measurement

Visual inspection was conducted after unloading the pipe sample. The crack width for both load induced (i.e., new), and existed (i.e., shrinkage) cracks were measured using digital image processing (DIP) method. Figure 4-41 illustrates the cracked 3-in. thick SAPL and the schematic crack patterns due to the shrinkage and the applied load. The visual inspection revealed that due to the load circumferential cracks were generated at the West and East springline and were propagated toward the haunch area. The averaged crack width for West and East circumferential cracks were 0.0218 and 0.0303 in., respectively. In addition to that, a 20 in. long circumferential was detected on the East side of the invert with the averaged width of 0.0311 in.

Due to the applied load, the existing longitudinal shrinkage cracks at the invert and crown had widened. The averaged crack width of the invert and crown were 0.0673 and 0.1883 in. respectively. The cracks are illustrated in Figure 4-42 and Figure 4-43.

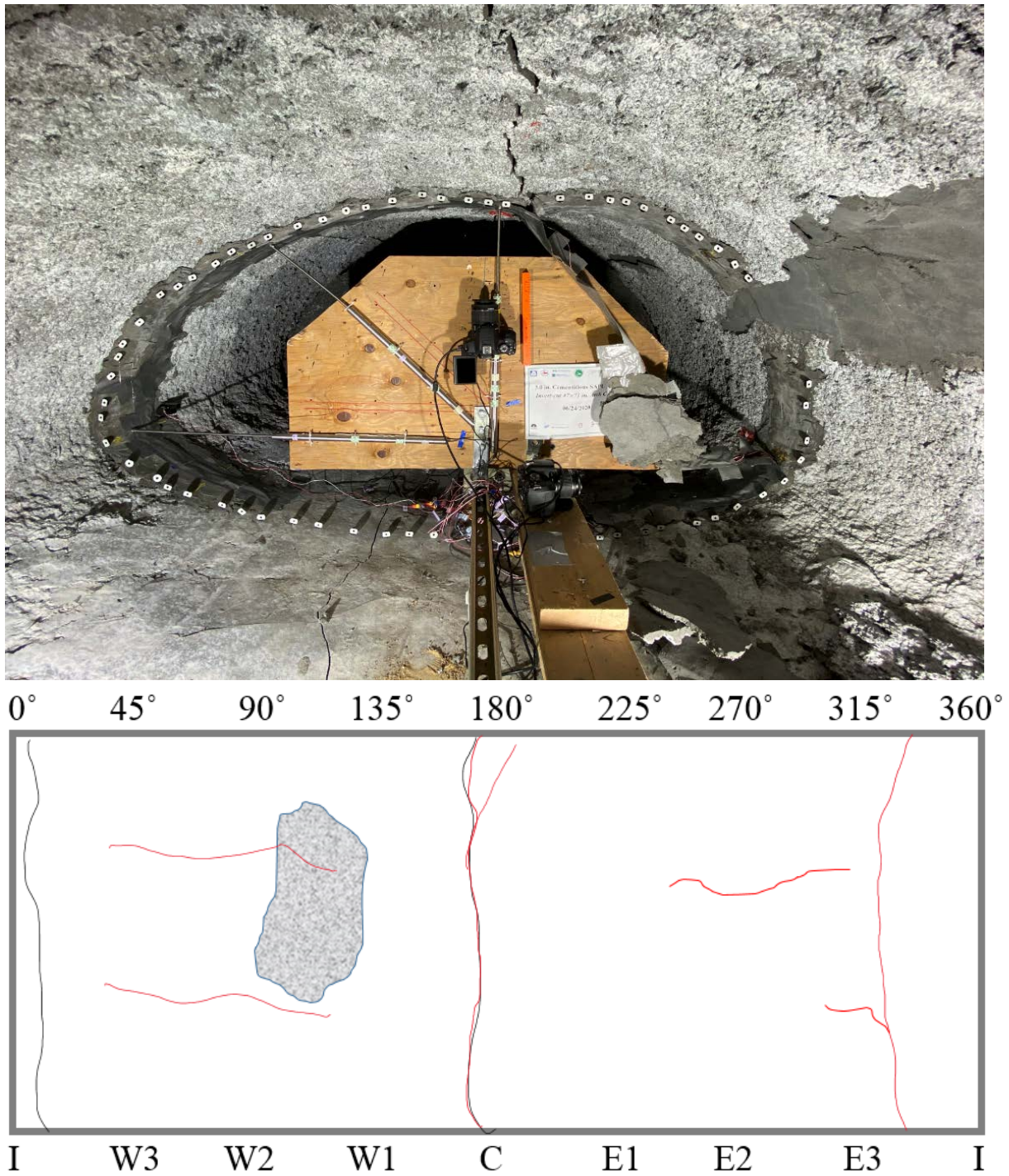


Figure 4-41. Visual inspection of the 3-in. thick SAPL renewed pipe arch CMP: (top) cracked SAPL, and (b) crack pattern schematic, where black represents the shrinkage cracks, red represents the cracks due to the load, and gray area represents delaminated area.

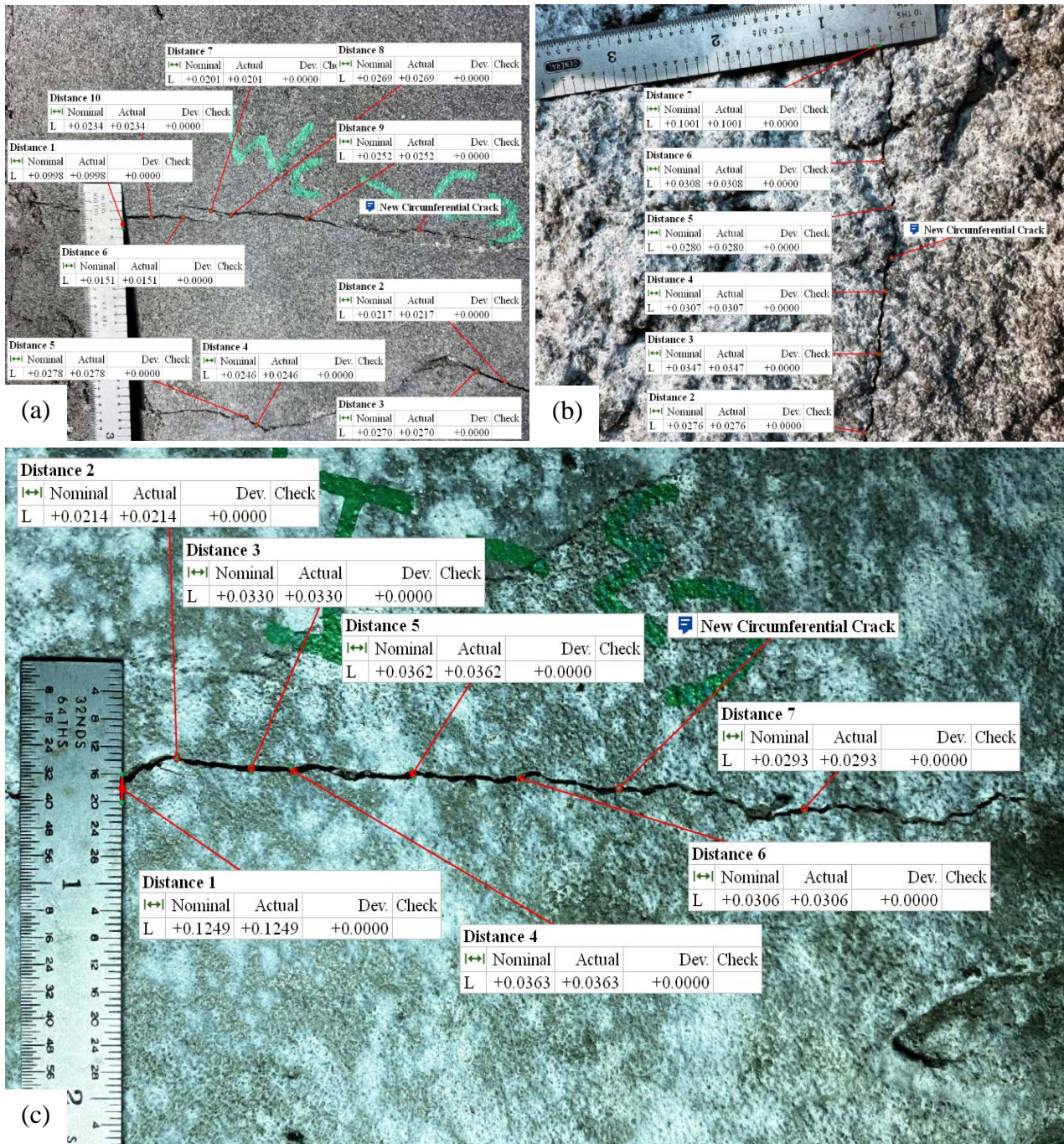


Figure 4-42. New circumferential cracks on 3-in. thick SAPL renewed pipe arch CMP at: (a) West, (b) East, and (c) invert locations.

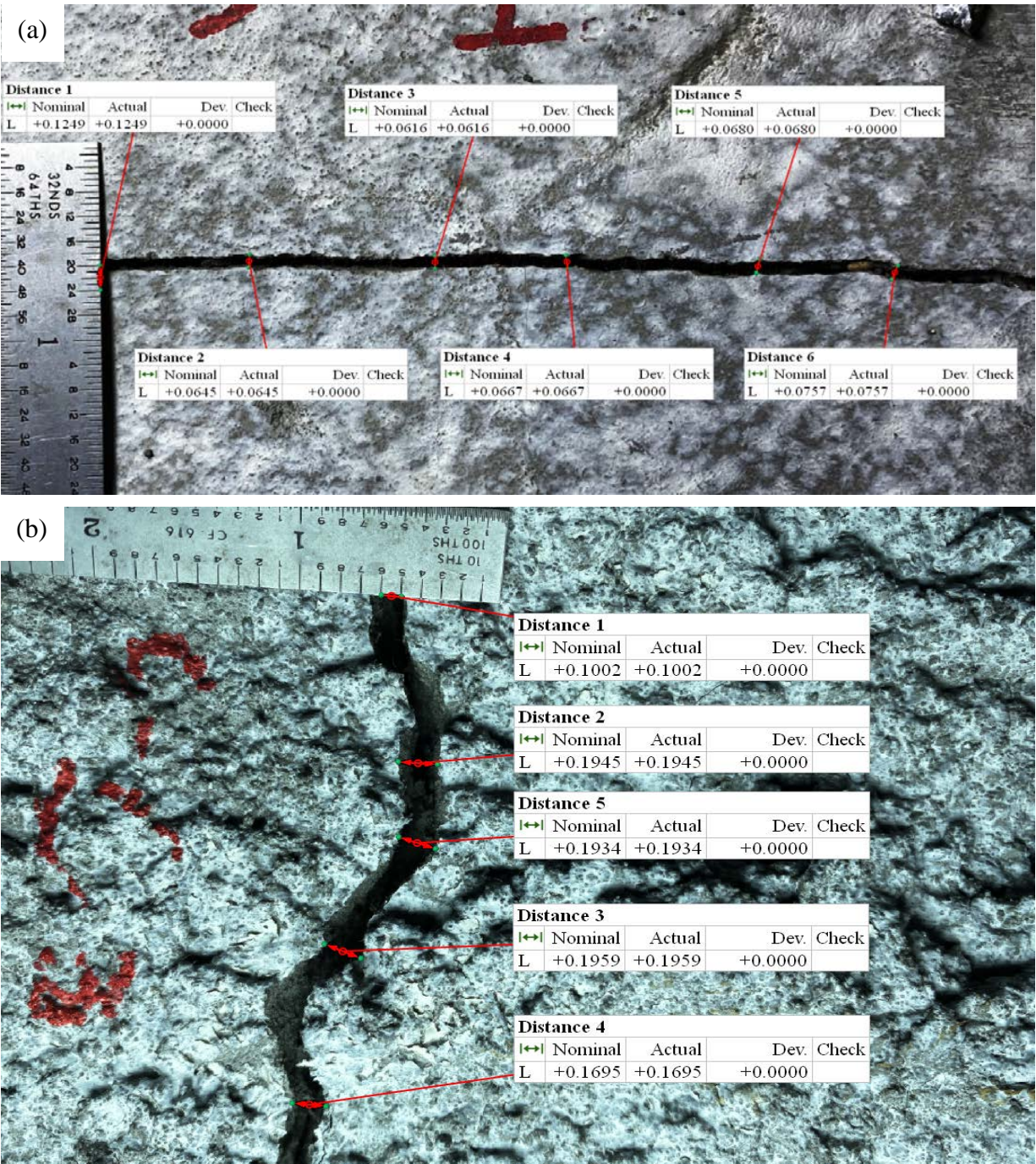


Figure 4-43. Widened longitudinal shrinkage cracks due to load for 3-in. thick SAPL renewed pipe arch CMP at: (a) invert, and (b) crown locations.

4.2.2.1.2. Thickness Measurement

The thickness of the 3-in. thick cementitious SAPL renewed pipe arch CMP were measured after the structural test and before exhumation as elaborated in section 3.4.6. The detailed result of the measurements are presented in APPENDIX E. Figure 4-44 illustrates the thickness measurements results for all three locations along the length of the pipe (i.e., north, center and south). The results showed that the liner's thickness varied from 2 to 3.4 in. The SAPL was thicker at the West springline and was thinner at crown and invert. In general, the averaged thickness was slightly lower than the required design thickness.

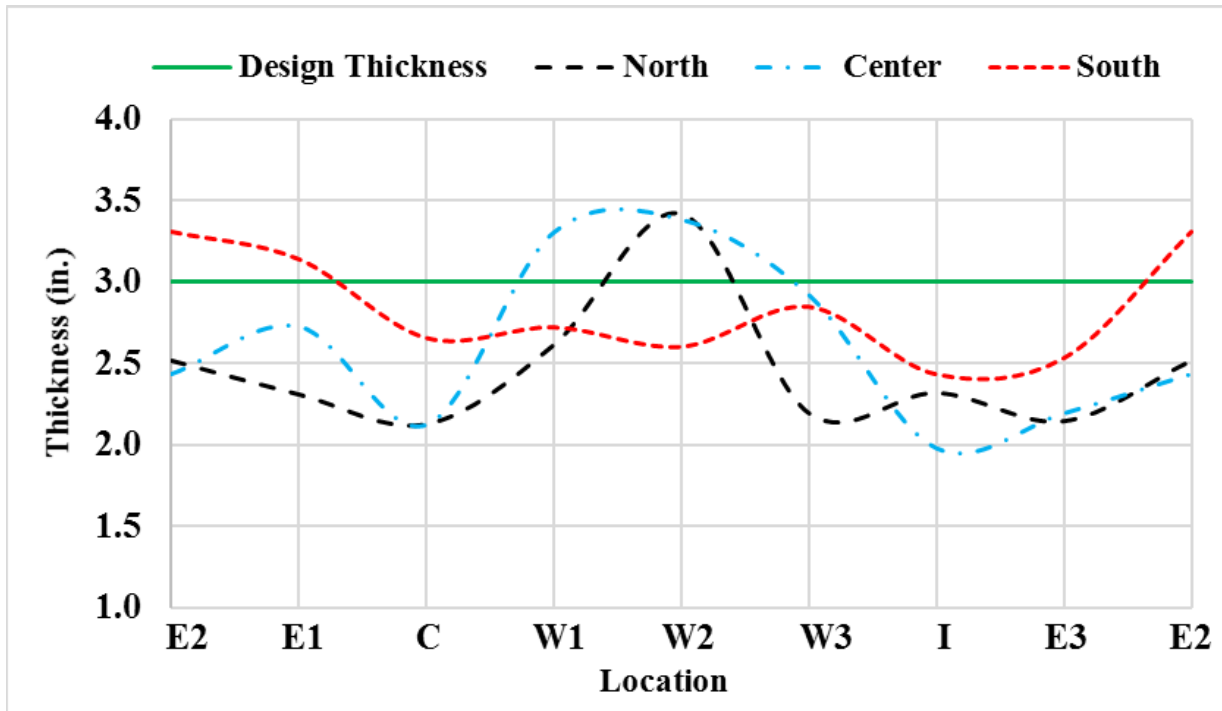


Figure 4-44. Thickness measurement for the 3-in. thick cementitious SAPL renewed pipe arch CMP.

4.2.2.2. 2-in. Thick SAPL Sample

The 2-in. thick SAPL renewed invert-cut pipe arch CMP was tested on Jun 26th, 2020, using the 20 × 40 in. load pad. The test duration was 5.48 hours. During the test, the first visible crack was observed on East side of invert section, at the load of 20 kips. The West side of the crown also cracked at the load of 21 kips at the soil displacement of 0.87 in. The existing cracks' (due to shrinkage) width were increasing with load progression. The SAPL renewed CMP sample failed at the load of 55.16 kips with 7.391 in. of soil settlement. The failure occurred due to the buckling and large deflection of the crown. Figure 4-45 (a) and (b) illustrate the test sample at before and after loading stage. Once the SAPL-CMP system was failed, the test was continued until about 20% load drop. Then the test was stopped, as further deflection would increase the chance of liner detachment and fall, which would damage the mechanical sensors and cameras inside the pipe. Once the load was released from the soil surface, the pipe had an upward movement and relaxed. At this stage, unlike the 3-in. thick sample, no delamination or spalling was observed. Figure 4-46 also illustrates the load and soil settlement graph, registered by the actuator's load cell and LDVT.

The earth pressure cell results registered the maximum pressure of 64.63 psi at the crown location. The maximum pressure applied on the West and East locations were 7.96, and 4.158 psi respectively. Figure 4-47 illustrates earth pressure results for the invert-cut circular test.

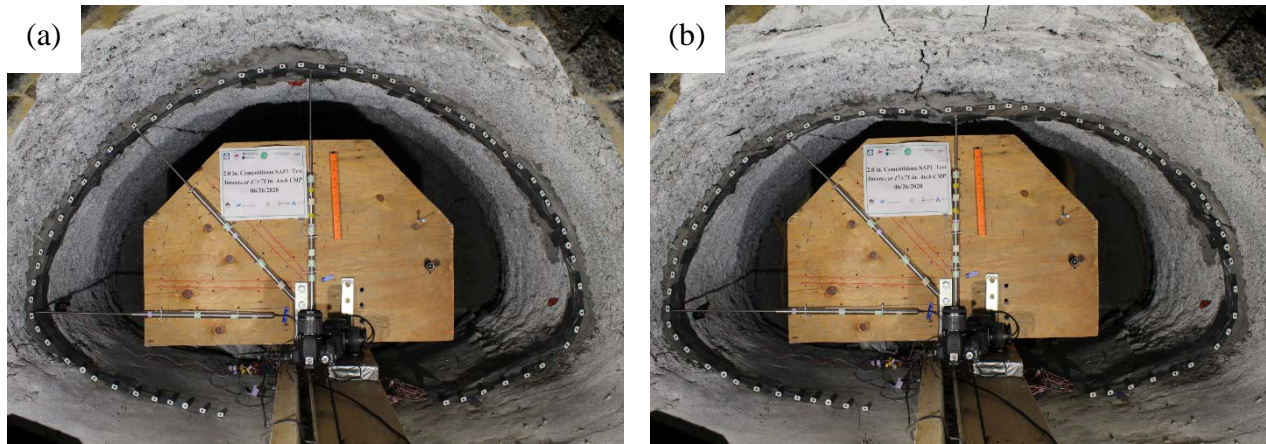


Figure 4-45. Invert-cut pipe arch renewed with 2 in. cementitious SAPL: (a) before loading, and (b) after loading.

Figure 4-48 illustrates the results of the mechanical sensors. The LVDT results show that the pipe was subjected to 5.819 in. of crown and 1.01 in. of springline deflection. The shoulder had 1.07 in. downward movement. The CDS showed an exact similar result as the crown LVDT. At the end of the test once the load was released from the surface, the pipe's crown, and springline had reversal movement of 1.048 and 0.068 in. respectively.

The strain gauge results showed the invert-cut pipe arch CMP experienced a large strain at the crown and both shoulder locations as well as springline that indicates the formation of buckling at the crown, as illustrated in Figure 4-49. The crown of the CMP was the first location that reached the steel yielding point (i.e., $1138 \mu\epsilon$) at the load of 32.35 kips. East shoulder of the CMP also yielded at 52.38 kips. Other locations of the CMP did not reach the steel yield point. The strain gauges on the SAPL surface of the showed that the cementitious liner cracked at the load of 14.59 kips. At this load, a small drop in the load-displacement graph (Figure 4-46) can be observed. The Figure 4-49 also illustrates a sudden strain reduction in both East and West shoulders of the SAPL at the load of 19.82, which can be due to a crack at this location.

Figure 4-50 illustrates the 2-in. thick SAPL renewed pipe arch CMP profile before and after the static load. The pipe profile at end of the test clearly illustrates the crown flattening. In addition, the roughness and irregularity of the SAPL is explicitly evident in the profiling result. The comparison between the mechanical sensors and DIC are presented in Figure 4-51. The deflection results captured by the DIC method is in an excellent conformity with the CDS sensor.

The load-displacement values for soil surface, crown, springline, and shoulder of the 2-in. thick SAPL renewed pipe arch CMP due to the applied static load is illustrates in Figure 4-52. In addition, Figure 4-53 illustrates the applied load on the soil surface versus its corresponding pressure at the crown of the renewed pipe arch CMP, where the recursive part of the graph represents drop in both pressure and load at the same time.

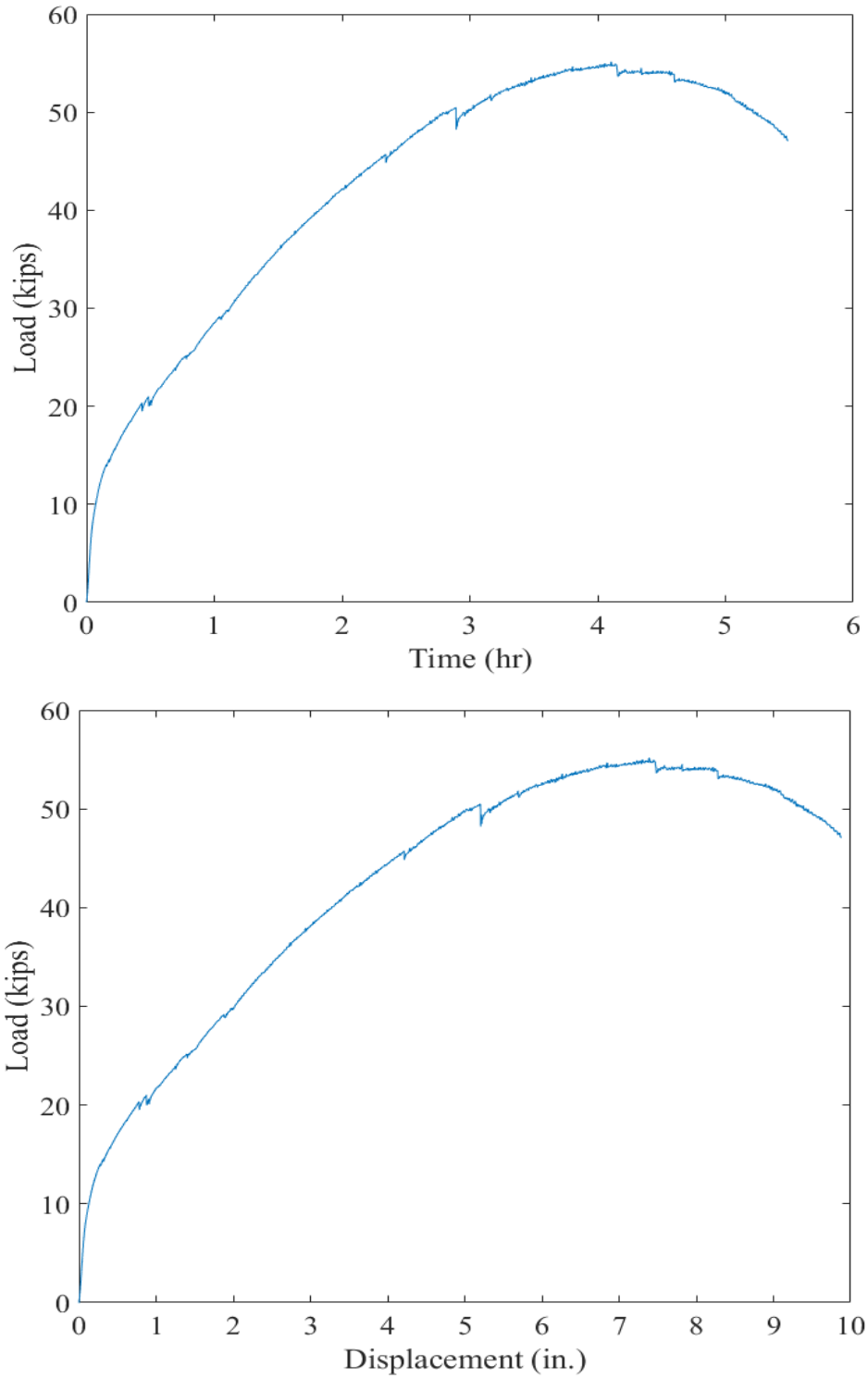


Figure 4-46. Invert-cut pipe arch CMP renewed with 2-in. thick cementitious SAPL subjected to static live load: (top) load-time and, (bottom) load-soil displacement graphs

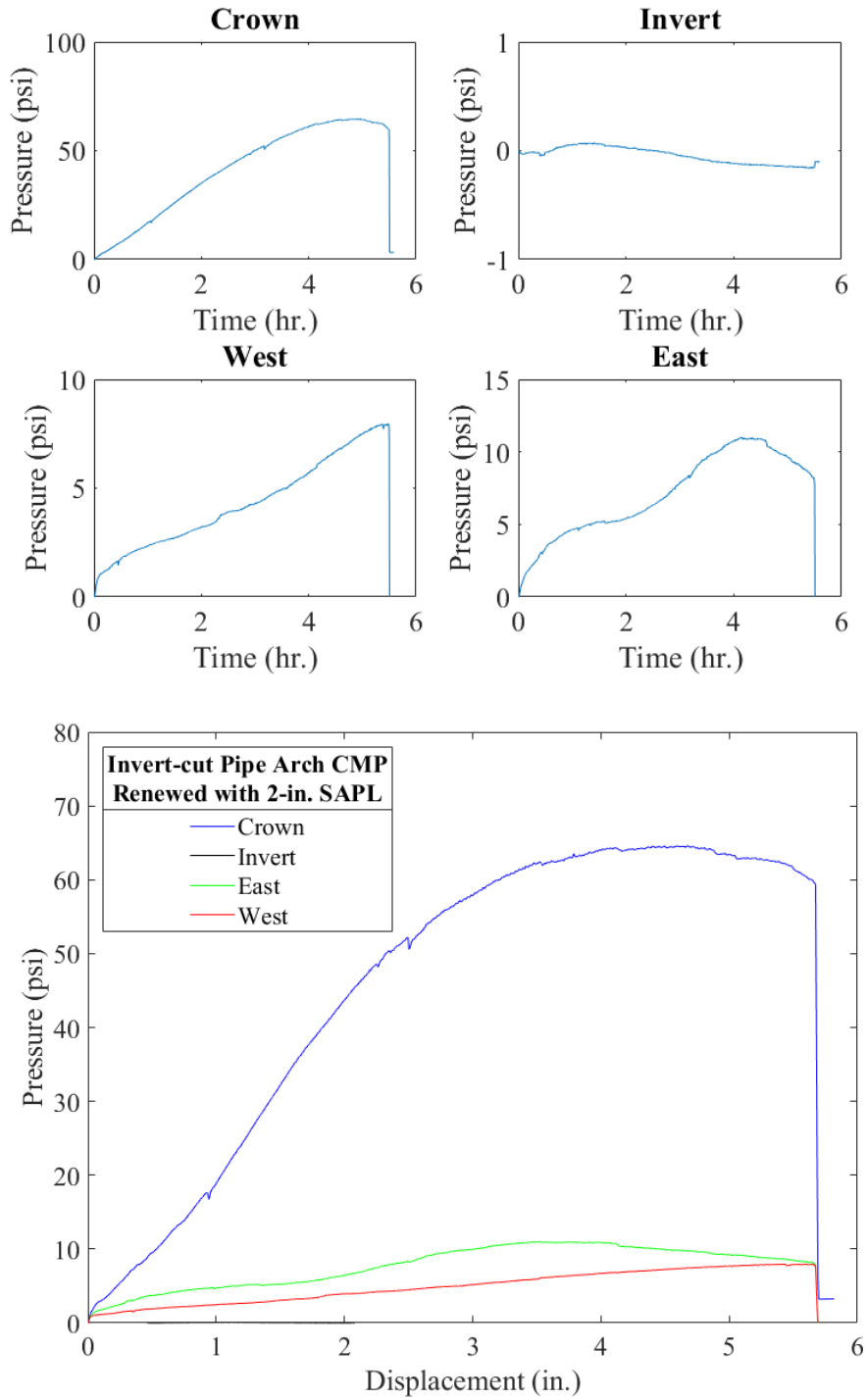


Figure 4-47. Earth pressure cell results for the 2-in. thick SAPL renewed invert-cut pipe arch CMP with respect to: (top) time, and (bottom) crown displacement.

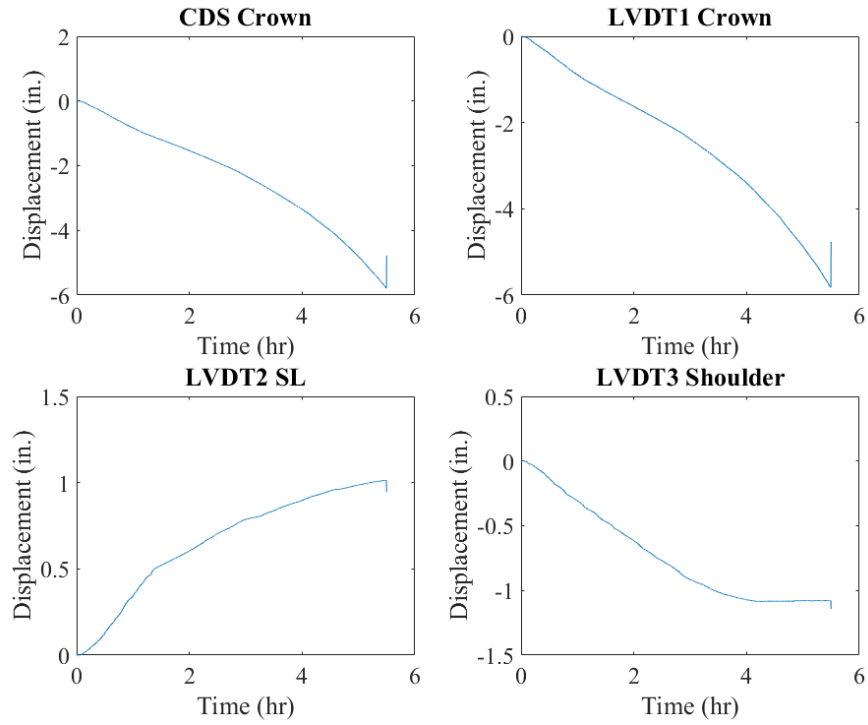


Figure 4-48. Mechanical sensors result for 2-in. thick SAPL renewed invert-cut pipe arch CMP.

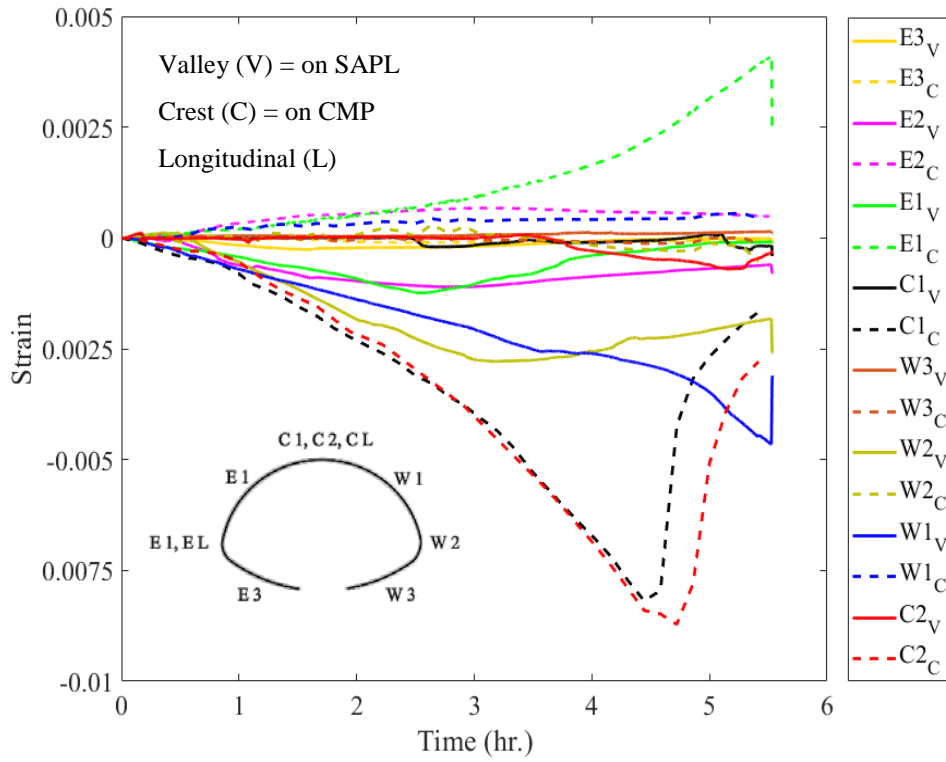


Figure 4-49. Strain gauges reading for 2-in. thick SAPL renewed invert-cut pipe arch CMP.

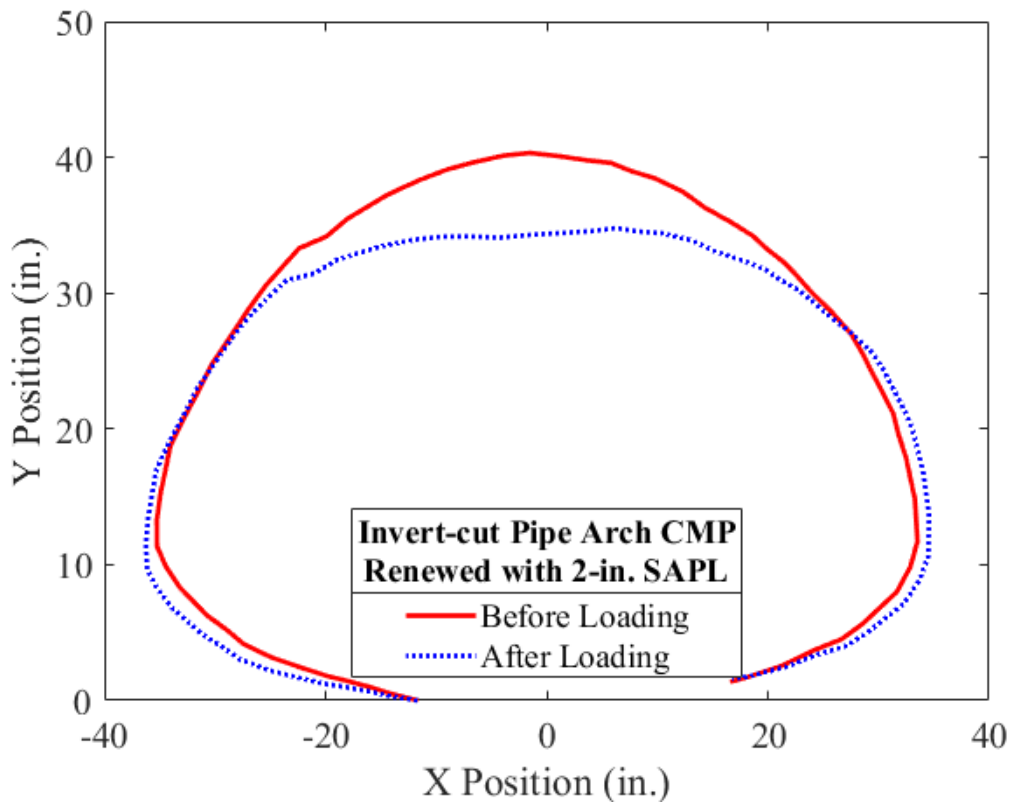
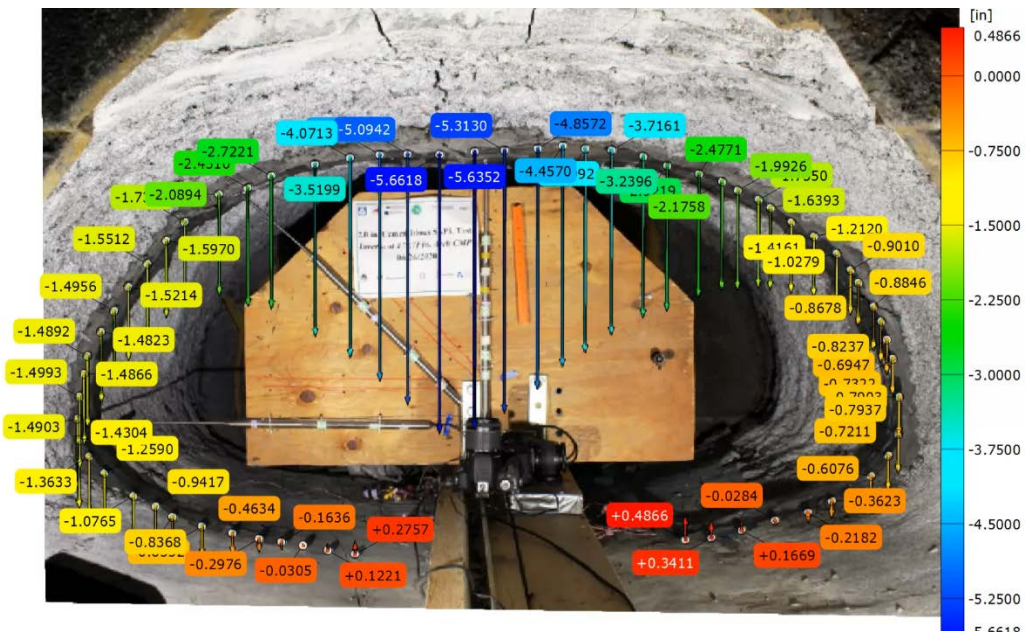


Figure 4-50. Pipe profiling using DIC for the 2-in. thick SAPL renewed invert-cut pipe arch CMP.

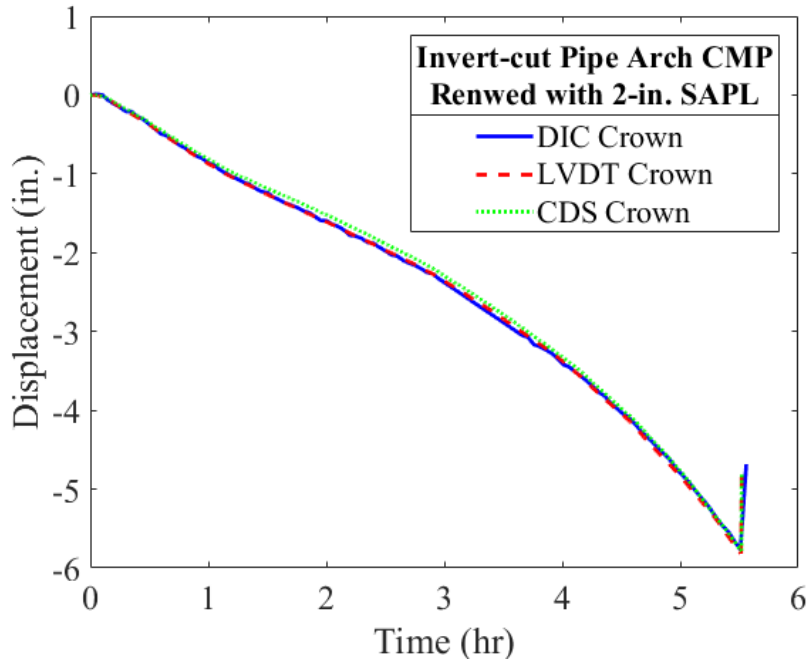


Figure 4-51. DIC method verification with mechanical sensors for the 2-in. thick SAPL renewed invert-cut pipe arch CMP.

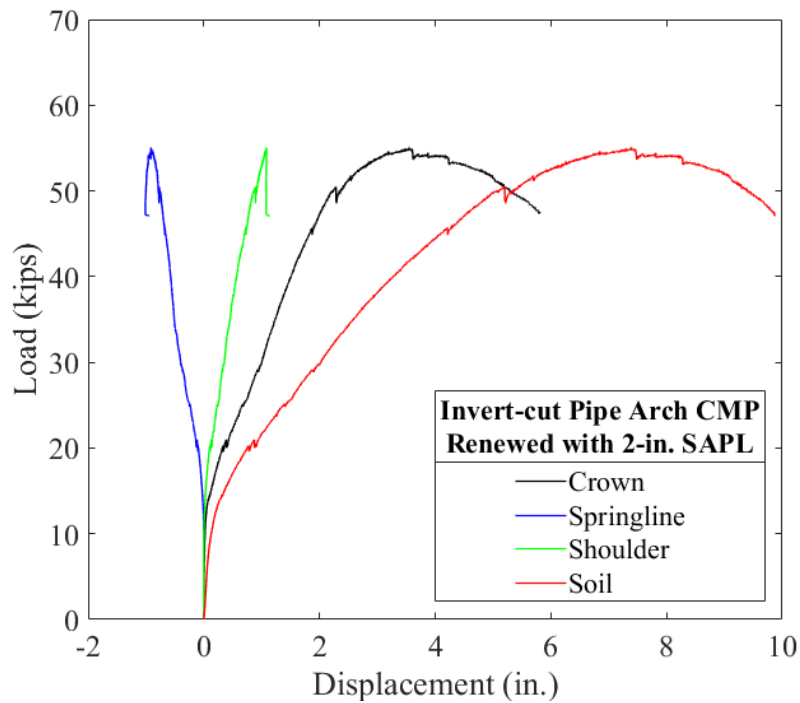


Figure 4-52. Load vs. displacement of the soil surface, crown, springline, and shoulder of the 2-in. thick SAPL renewed invert-cut pipe arch CMP due to the applied static load.

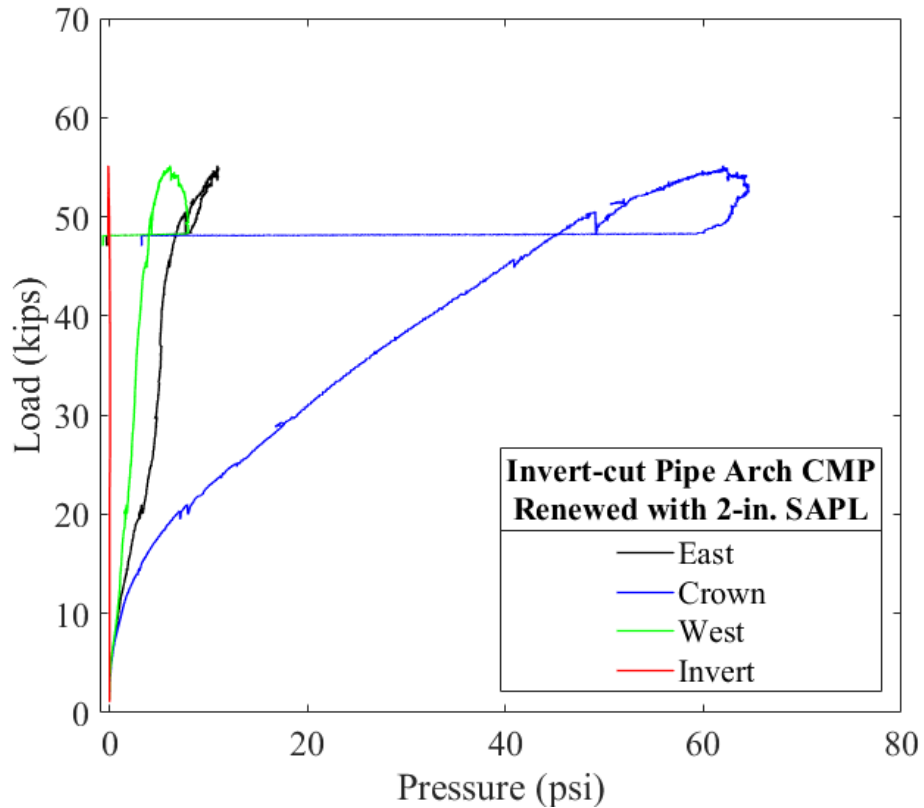


Figure 4-53. Load vs. pressure for the 2-in. thick SAPL renewed invert-cut pipe arch CMP.

4.2.2.2.1. Post Failure Crack Measurement

Visual inspection was conducted after unloading the pipe sample. The crack width for both load induced (i.e., new), and existed (i.e., shrinkage) cracks were measured using digital image processing (DIP) method. Figure 4-54 illustrates the cracked 2-in. thick SAPL at the invert location and the crack patterns schematic due to the shrinkage and the applied load. The visual inspection revealed that due to the load a longitudinal crack in invert, multiple longitudinal crack in crown, and multiple circumferential cracks in both haunch area of the East and West locations were created. The averaged width of the invert longitudinal crack, created by the load, was 0.0835 in. The existed longitudinal shrinkage crack, at the West side of the invert, after the loading had the

crack width of 0.1430 in. Few circumferential cracks around the invert were observed which had the average crack width of 0.0129 in. The averaged crack width for West and East circumferential cracks were 0.02256 and 0.02405 in., respectively. The existing longitudinal shrinkage cracks at the crown had widened. The crack had wider width at the center location and was thinner towards the end of the pipe. The averaged crack width of the crown at center and north side of the crown were 0.3443 and 0.1908 in. respectively. The cracks are illustrated in Figure 4-42 and Figure 4-43.

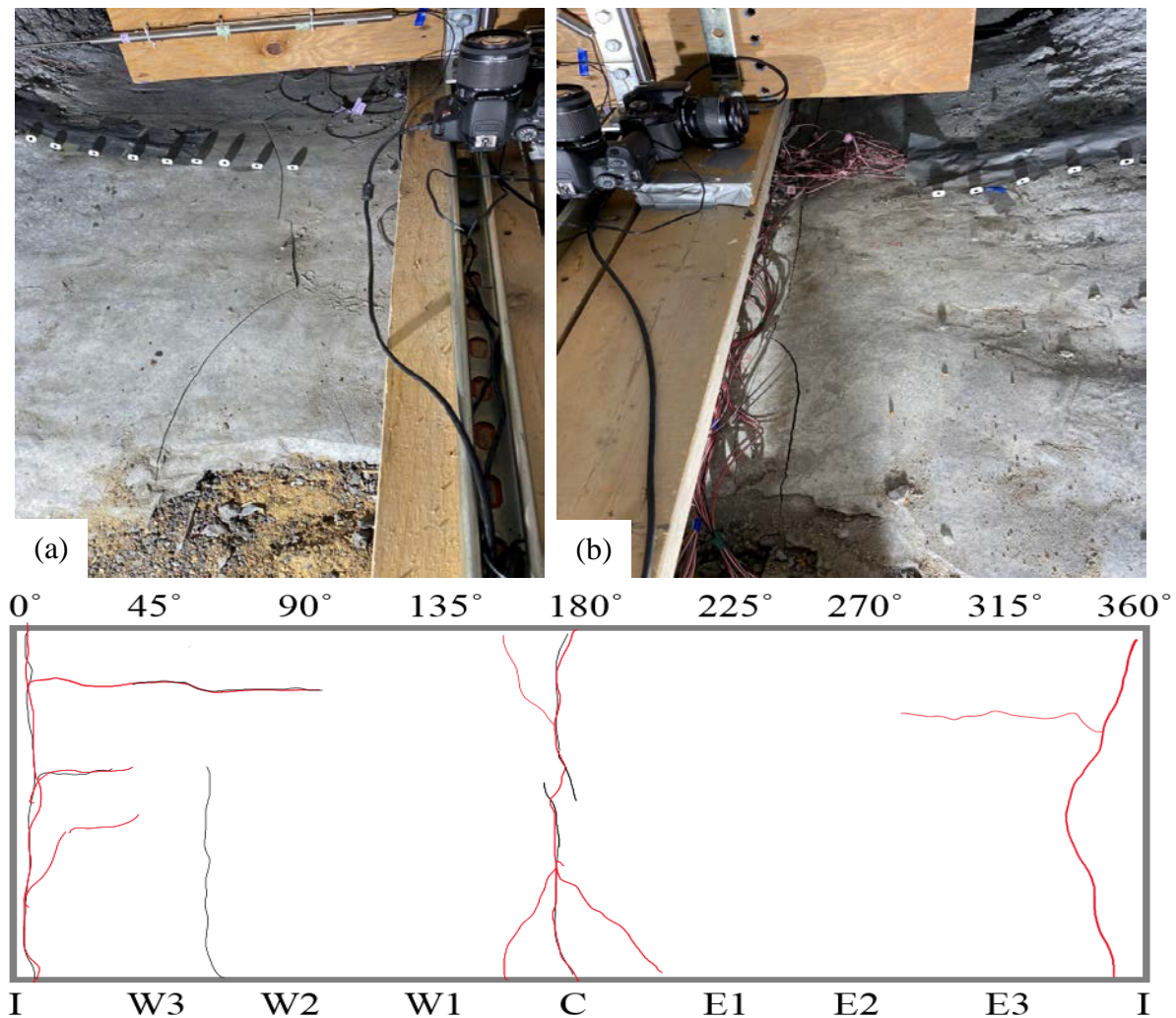


Figure 4-54. Visual inspection of the 2-in. thick SAPL renewed pipe arch CMP: (a) cracked SAPL on the East side of the invert, (b) cracked SAPL on the West side of the invert, and (bottom) crack pattern schematic, where black represents the shrinkage cracks and red represents the cracks due to the load.

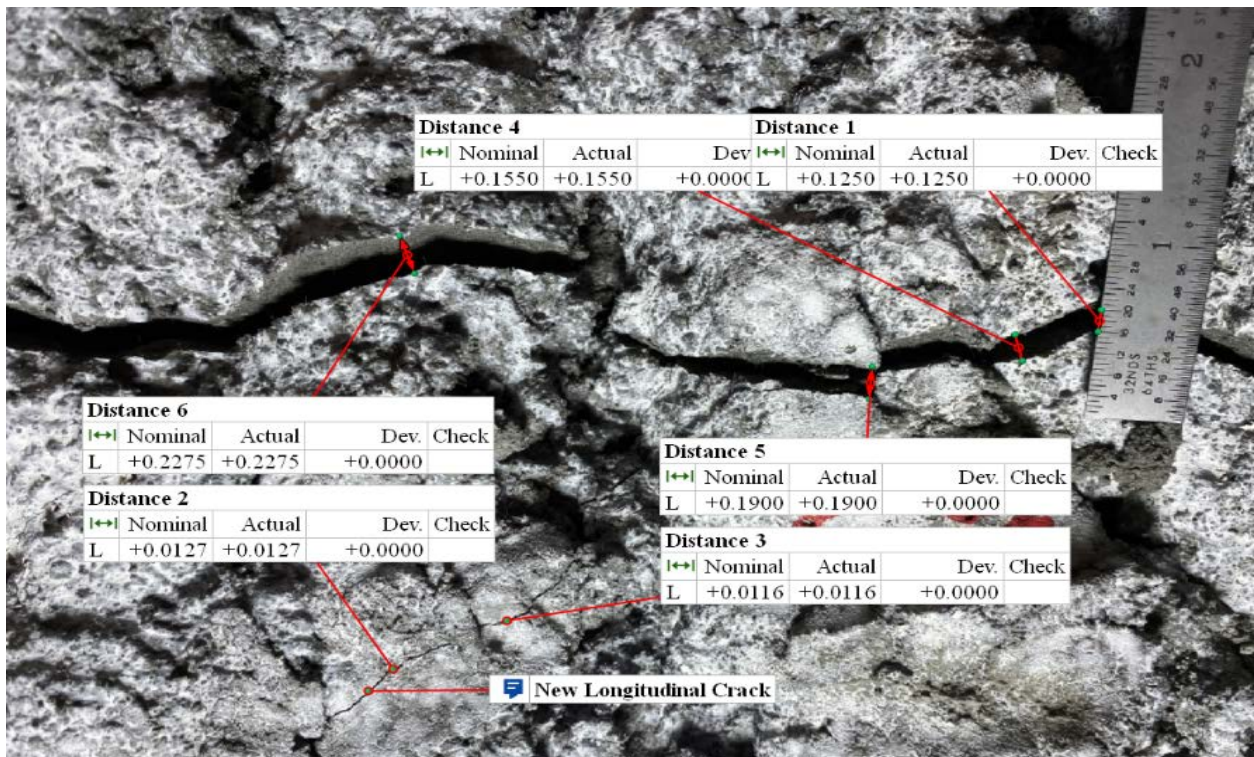
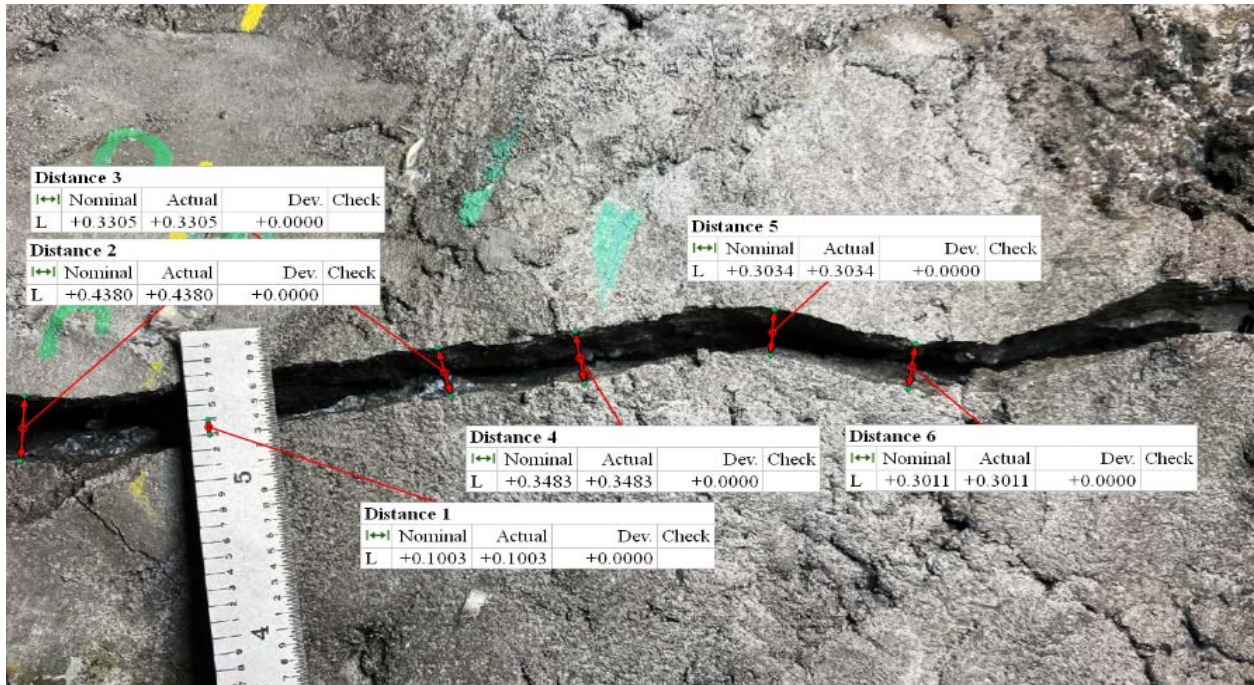


Figure 4-55. Longitudinal cracks at the crown of the 2-in. thick SAPL renewed invert-cut pipe arch CMP: (top) center of the crown, and (bottom) north side of the crown.

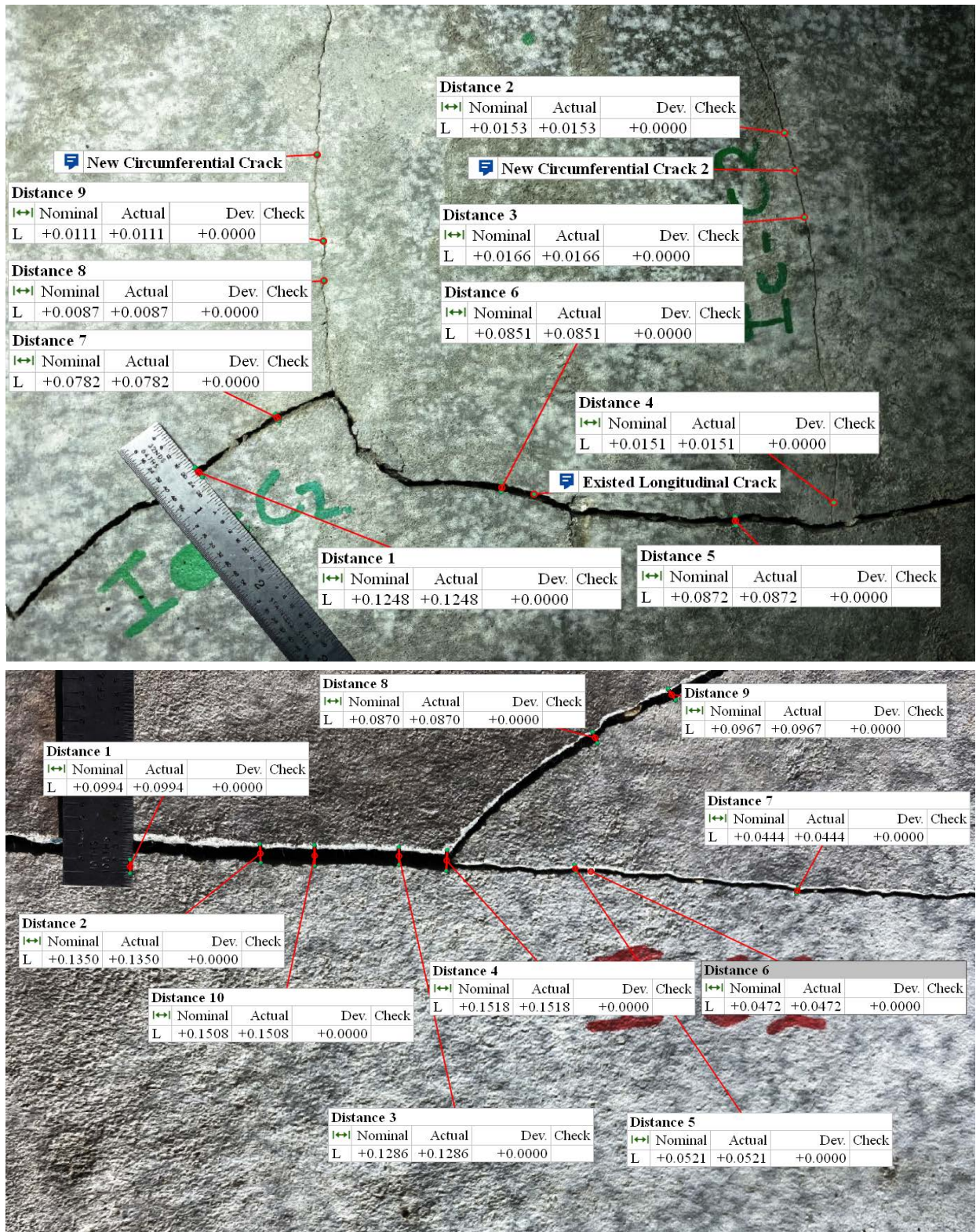


Figure 4-56. Longitudinal cracks at the invert of the 2-in. thick SAPL renewed invert-cut pipe arch CMP: (top) existed shrinkage crack, and (bottom) newly generated crack due to load.

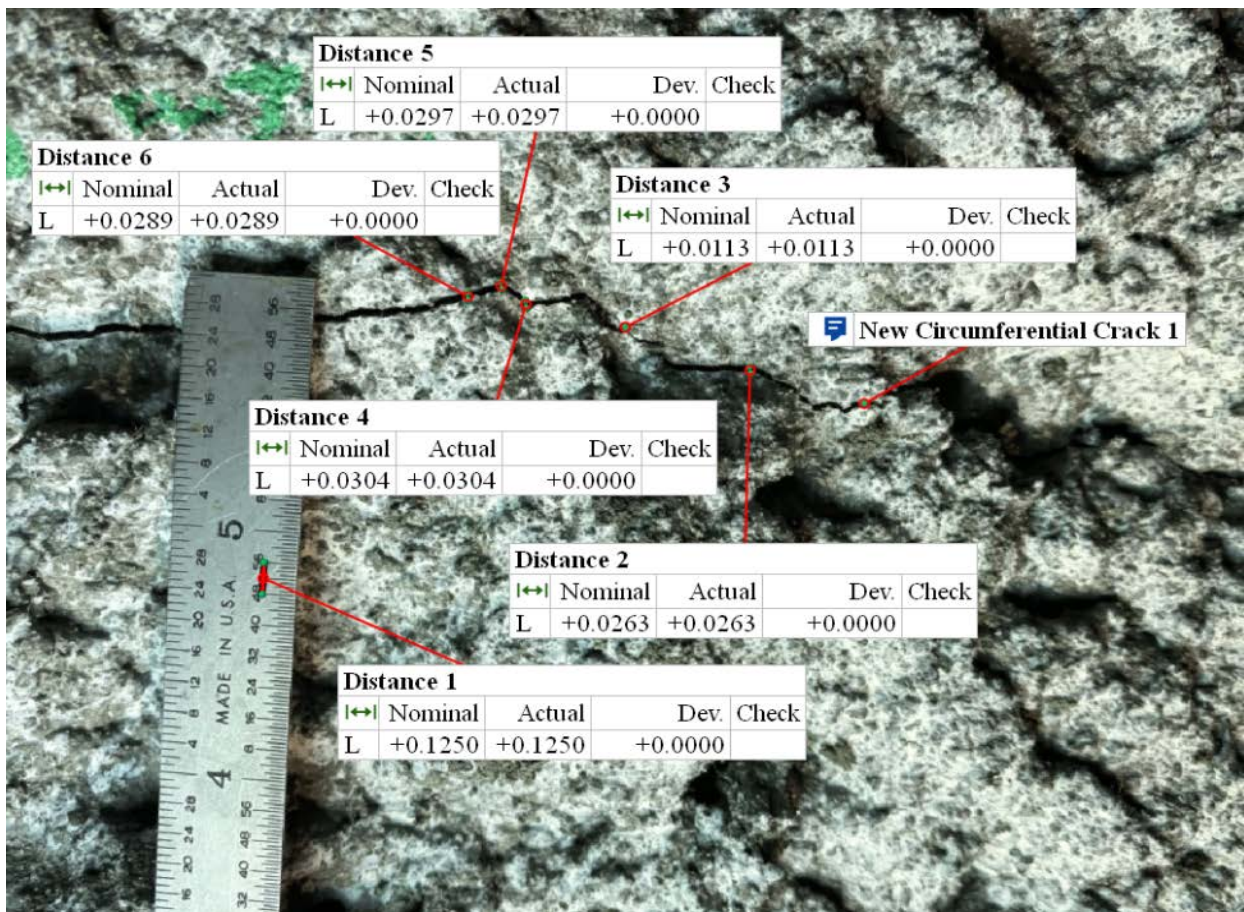
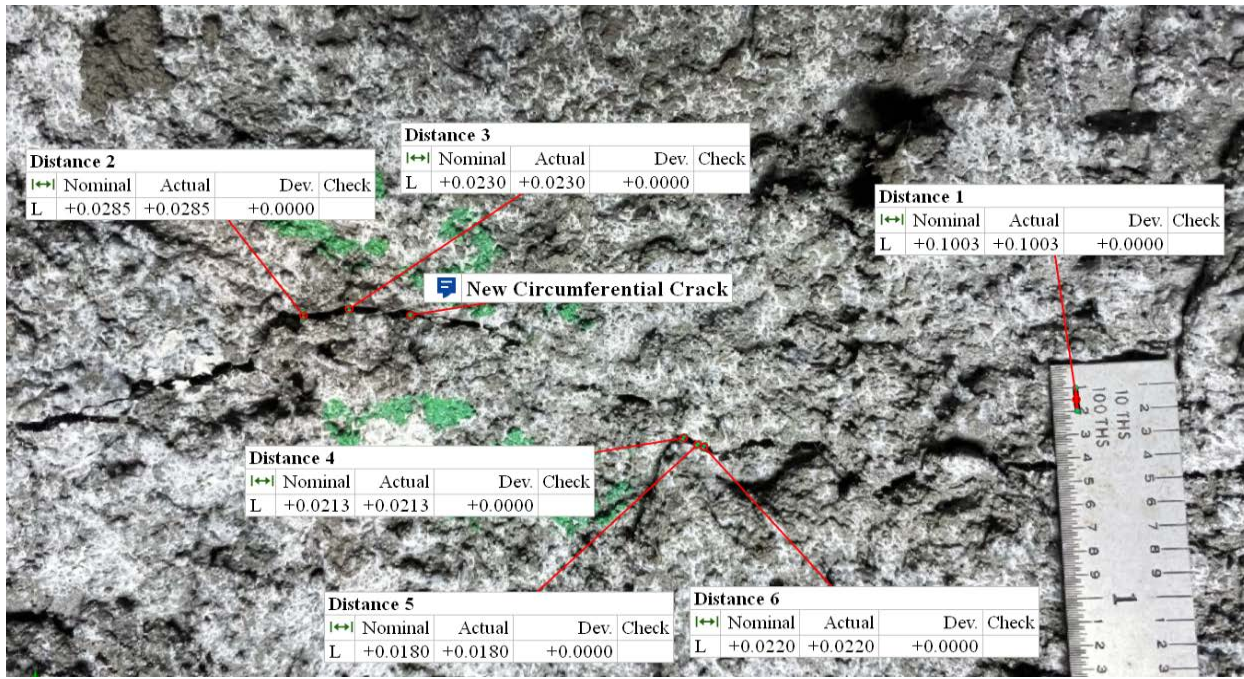


Figure 4-57. Circumferential cracks of the 2-in. thick SAPL renewed invert-cut pipe arch CMP at: (top) West and (bottom) East springline and haunch area.

4.2.2.2.2. Thickness Measurement

The thickness of the 2-in. thick cementitious SAPL renewed pipe arch CMP were measured after the structural test and before exhumation as elaborated in section 3.4.6. The detailed result of the measurements is presented in APPENDIX E. Figure 4-58 illustrates the thickness measurements results for all three locations along the length of the pipe (i.e., north, center and south). The results showed that the liner's thickness variation ranged from 1.6 to 2.2 in. The SAPL was more uniformly applied than the 3-in. thick pipe sample. The SAPL was generally thicker towards south side and was thinner towards south side of the CMP. In general, the averaged thickness was slightly lower than the required design thickness.

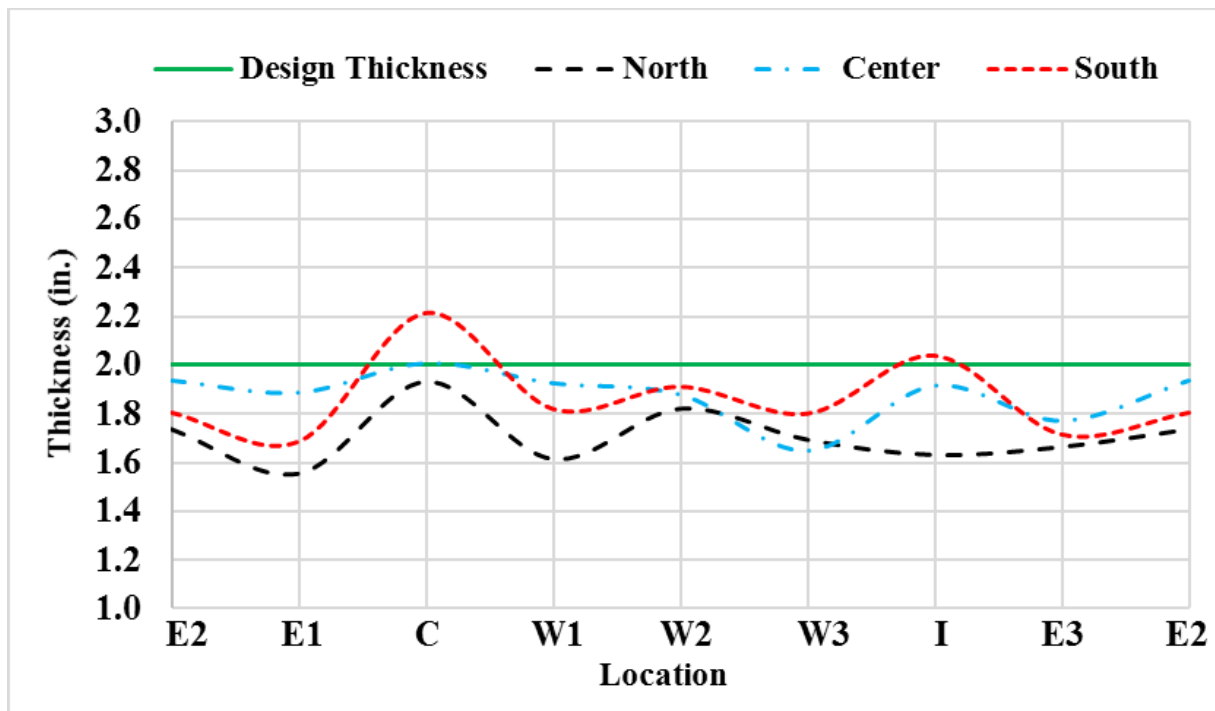


Figure 4-58. Thickness measurement for the 2-in. thick cementitious SAPL renewed pipe arch CMP.

4.2.2.3. 1-in. Thick SAPL Sample

The 1-in. thick SAPL renewed invert-cut pipe arch CMP was tested on Jun 30th, 2020, using the 20 × 40 in. load pad. The test duration was 2.9 hours. The SAPL renewed CMP sample failed at the load of 46.5 kips with 3.9 in. of soil settlement. The failure occurred due to the buckling and large deflection of the crown. In contrast with the 2 and 3 in. SAPL renewed pipe arch CMPs, where the SAPL experienced two full pipe length longitudinal cracks, the 1 in. SAPL had only a single crack in the invert section. In addition to that, in this test, the longitudinal shrinkage crack at the East haunch area was entirely closed at the end of the test. This implies that due to the applied vertical load, the haunch area near the springline was subjected to compression. Figure 4-59 (a) and (b) illustrate the test sample at before and after loading stage. Once the SAPL-CMP system was failed, the test was continued until about 20% load drop. Then the test was stopped, as further deflection would increase the chance of liner detachment and fall, which would damage the mechanical sensors and cameras inside the pipe. At this stage, a minor delamination at the East and West shoulders were observed. Figure 4-60 also illustrates the load and soil settlement graph, registered by the actuator's load cell and LDVT.

The earth pressure cell results registered the maximum pressure of 62.88 psi at the crown location. The maximum pressure applied on the West and East locations were 5.014, and 3.253 psi respectively. Figure 4-61 illustrates earth pressure results for the invert-cut circular test.

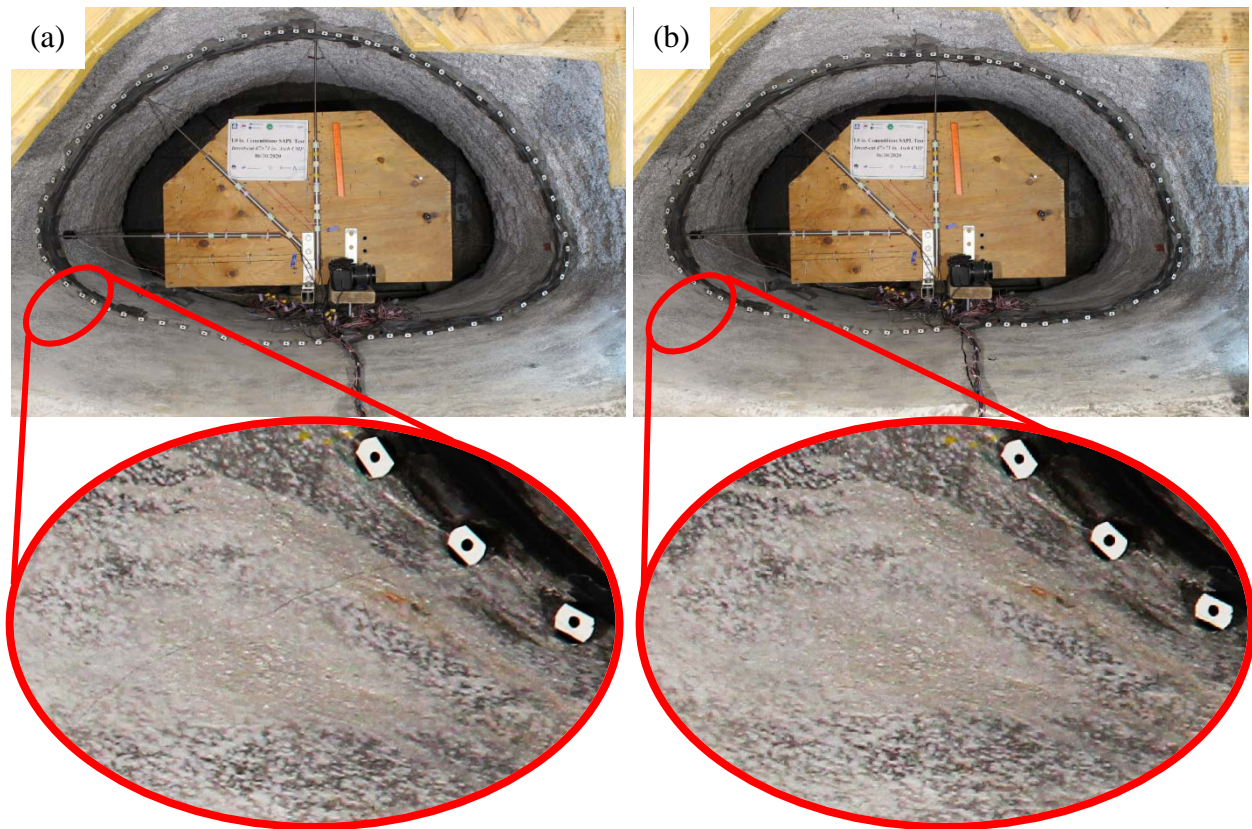


Figure 4-59. Invert-cut pipe arch renewed with 1 in. cementitious SAPL: (a) before loading, where the East haunch had a shrinkage crack, and (b) after loading, where the shrinkage crack is closed.

Figure 4-62 illustrates the results of the mechanical sensors. The LVDT results show that the pipe was subjected to 2.811 in. of crown and 0.602 in. of springline deflection. The shoulder had 0.53 in. downward movement. The CDS showed an exact similar result as the crown LVDT. At the end of the test once the load was released from the surface. Unlike the other SAPL renewed pipe arch CMPs, this pipe did not have a reversal movement.

The strain gauge results showed the SAPL cracked at the crown location at the loads of 9.5 and 12.64 kips. The West shoulder of the SAPL also cracked at the load of 12.64 kips, as illustrated in Figure 4-63. The crown of the CMP was the only location that reached the steel yielding point

(i.e., 1138 $\mu\epsilon$) at the load of 27.01 kips. At the time of SALP-CMP failure, strain drop is evident on the SAPL surface at the East shoulder and springline. In addition, negative strain value at these locations justifies the shrinkage crack closure as discussed above.

Figure 4-64 illustrates the 1-in. thick SAPL renewed pipe arch CMP profile before and after the static load. The pipe profile at end of the test clearly illustrates the pipe's ovality. In addition, the roughness and irregularity of the SAPL is explicitly evident in the profiling result. The comparison between the mechanical sensors and DIC are presented in Figure 4-65, which shows an excellent conformity with the CDS sensor.

The load-displacement values for soil surface, crown, springline, and shoulder of the 1-in. thick SAPL renewed pipe arch CMP due to the applied static load is illustrates in Figure 4-66. The applied load on the soil surface versus its corresponding pressure at the crown of the renewed pipe arch CMP are depicted in Figure 4-67, where the recursive part of the graph represents drop in both pressure and load at the same time.

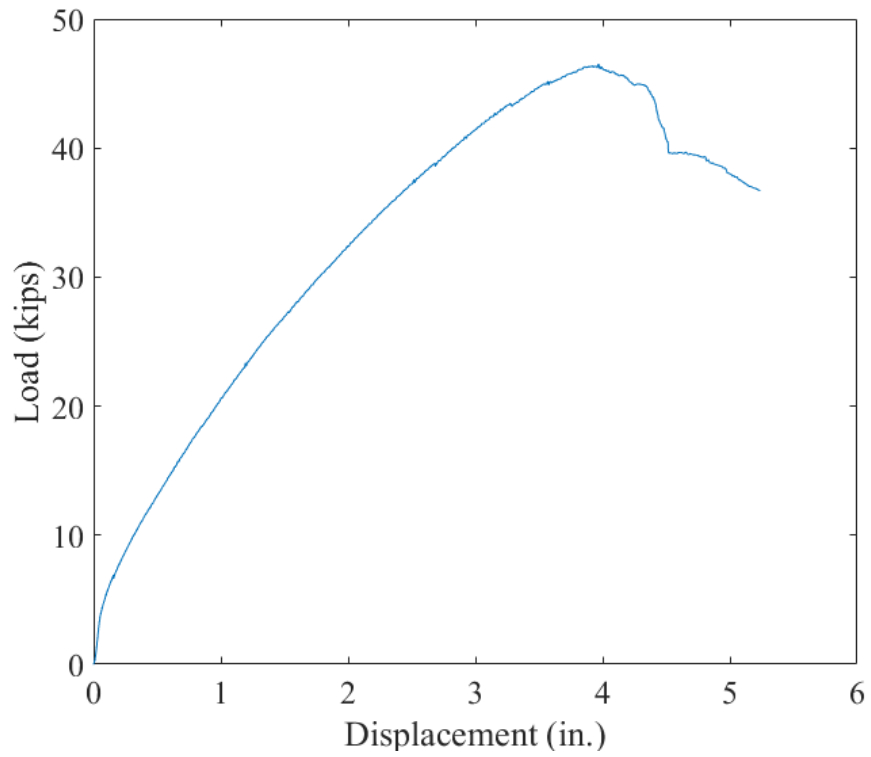
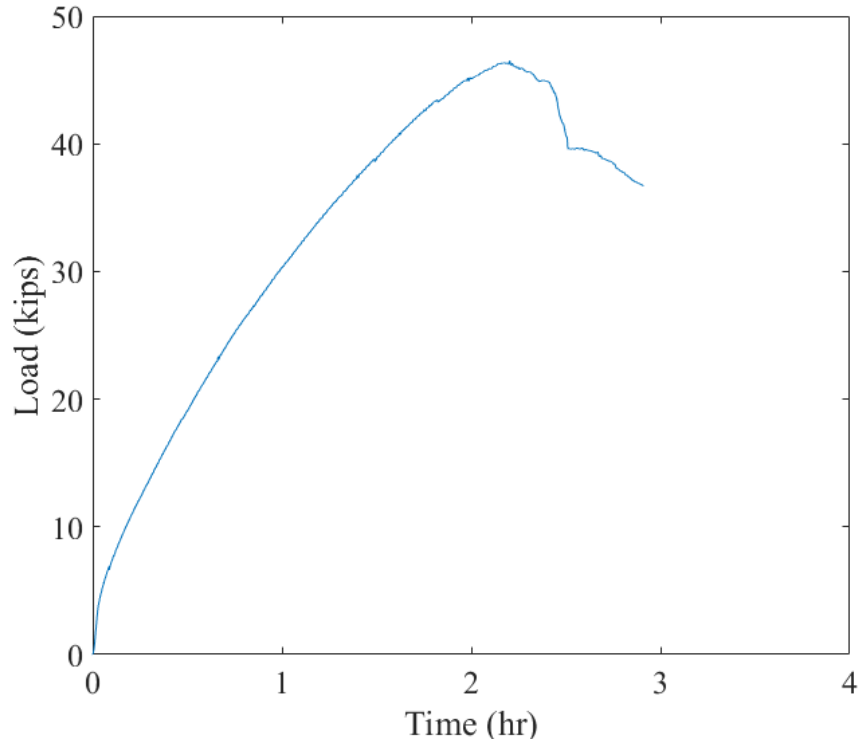


Figure 4-60. Invert-cut pipe arch CMP renewed with 1-in. thick cementitious SAPL subjected to static live load: (top) load-time and, (bottom) load-soil displacement graphs

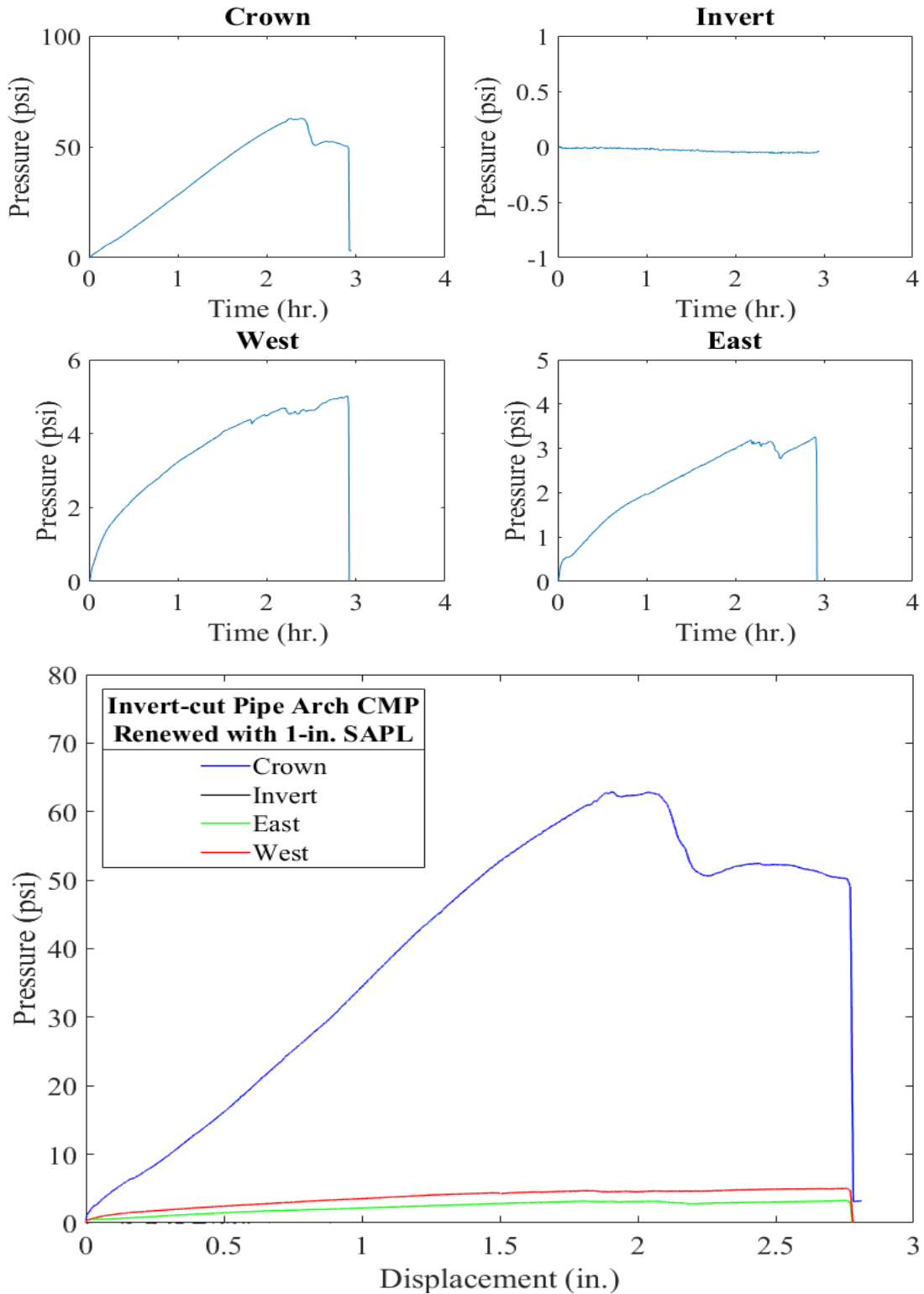


Figure 4-61. Earth pressure cell results for the 1-in. thick SAPL renewed invert-cut pipe arch CMP with respect to: (top) time, and (bottom) crown displacement.

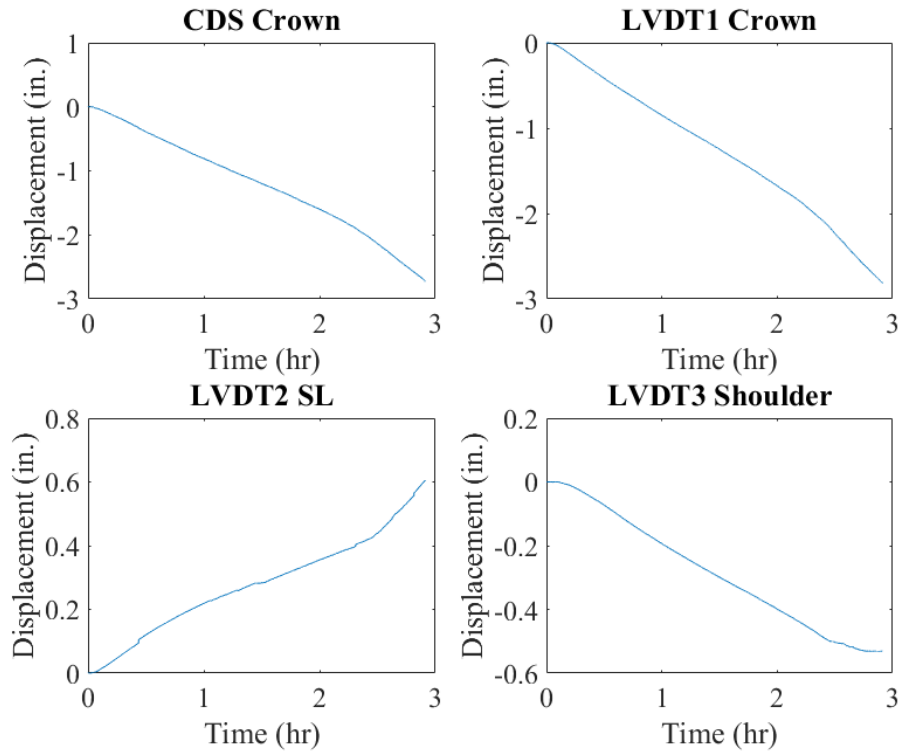


Figure 4-62. Mechanical sensors result for 1-in. thick SAPL renewed invert-cut pipe arch CMP.

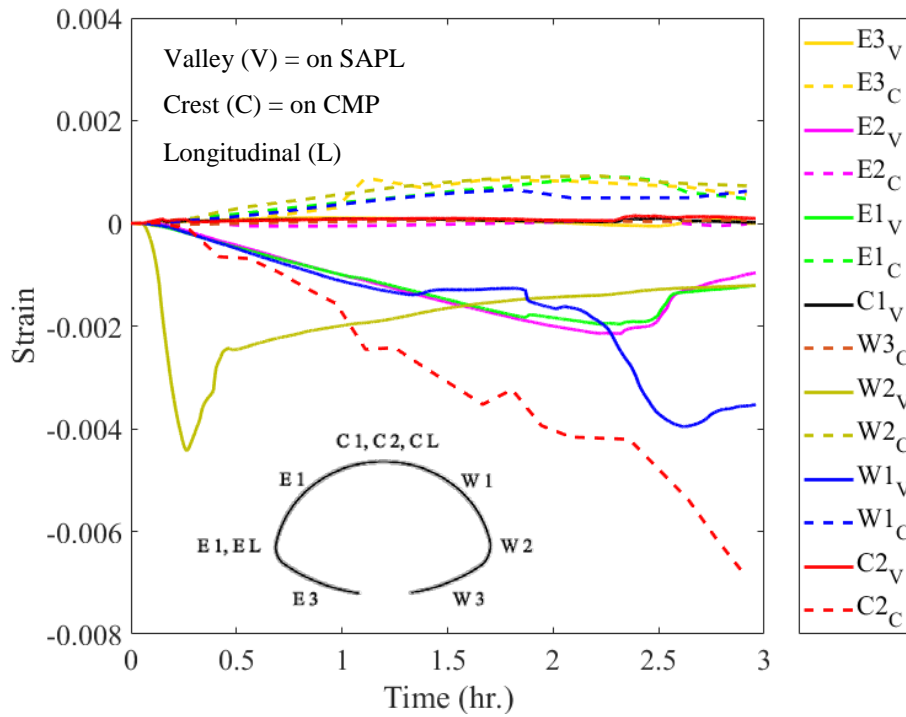


Figure 4-63. Strain gauges reading for 1-in. thick SAPL renewed invert-cut pipe arch CMP.

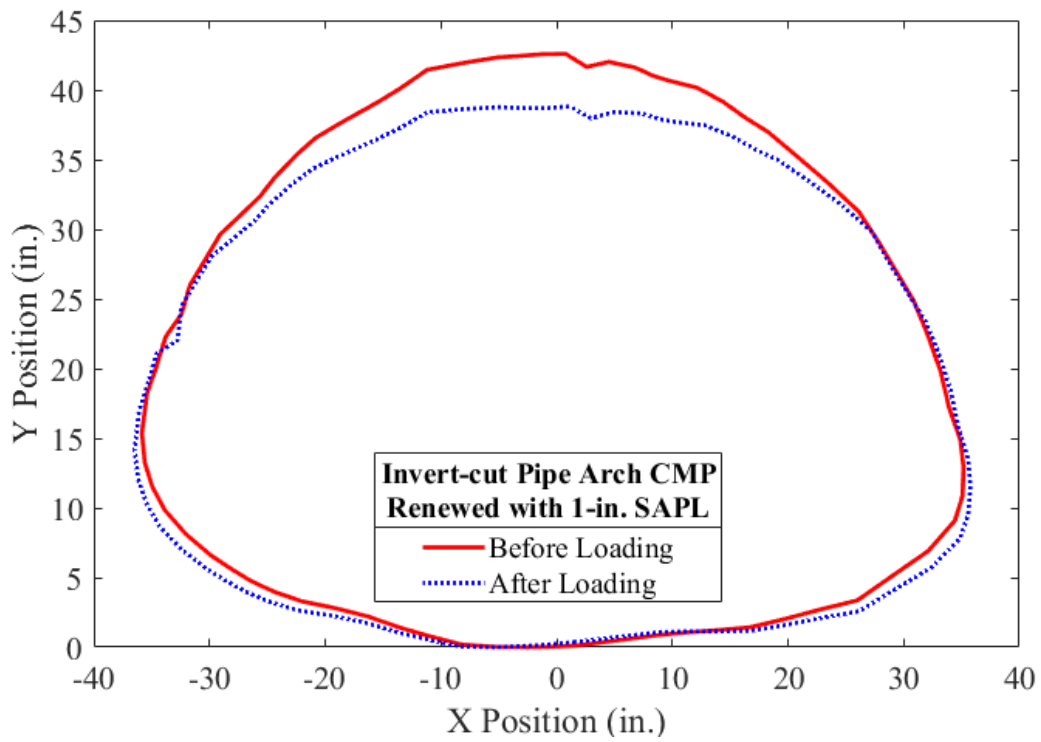
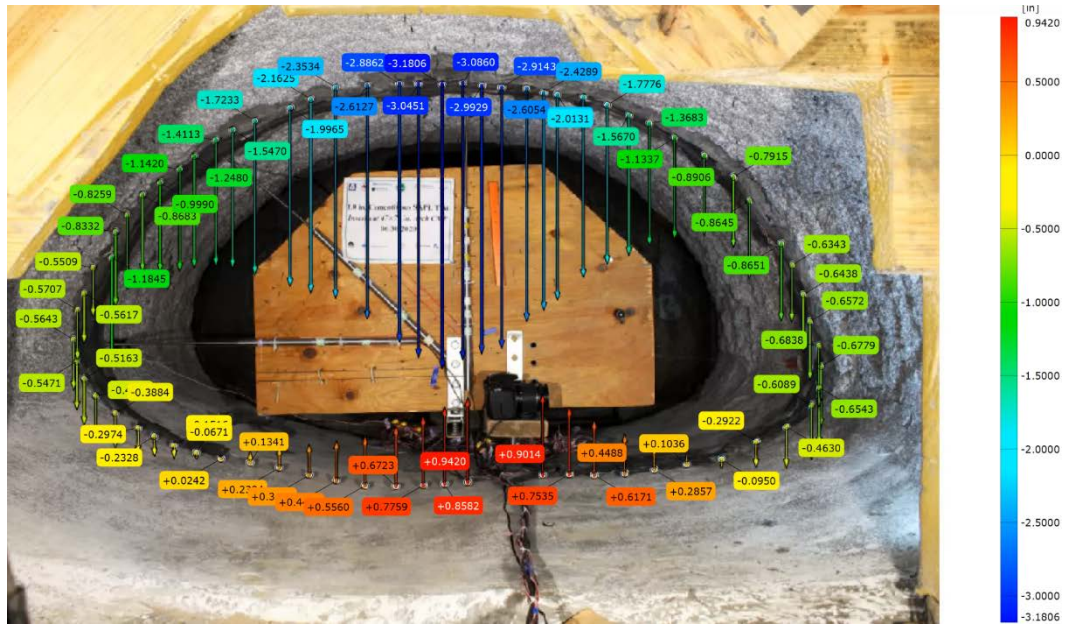


Figure 4-64. Pipe profiling using DIC for the 1-in. thick SAPL renewed invert-cut pipe arch CMP.

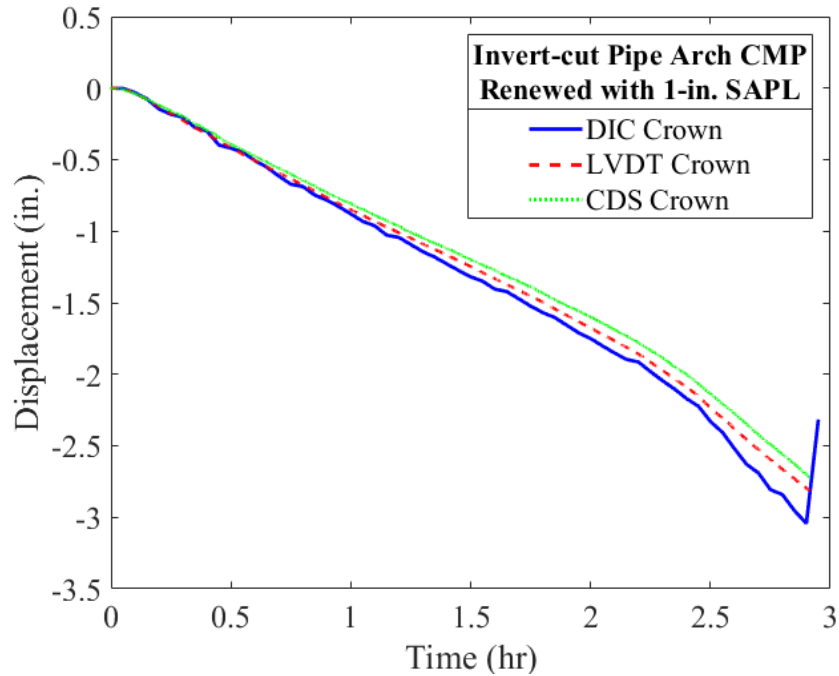


Figure 4-65. DIC method verification with mechanical sensors for the 1-in. thick SAPL renewed invert-cut pipe arch CMP.

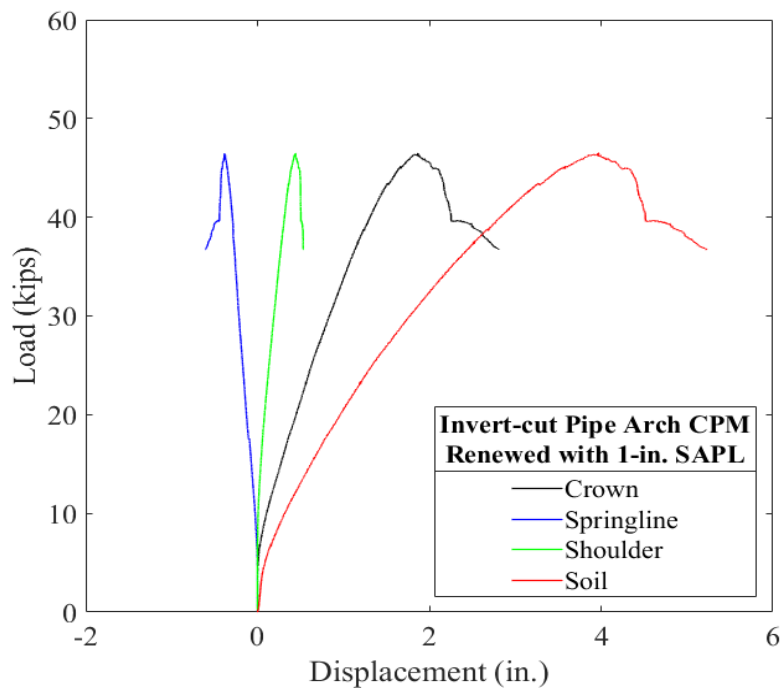


Figure 4-66. Load vs. displacement of the soil surface, crown, springline, and shoulder of the 1-in. thick SAPL renewed invert-cut pipe arch CMP due to the applied static load.

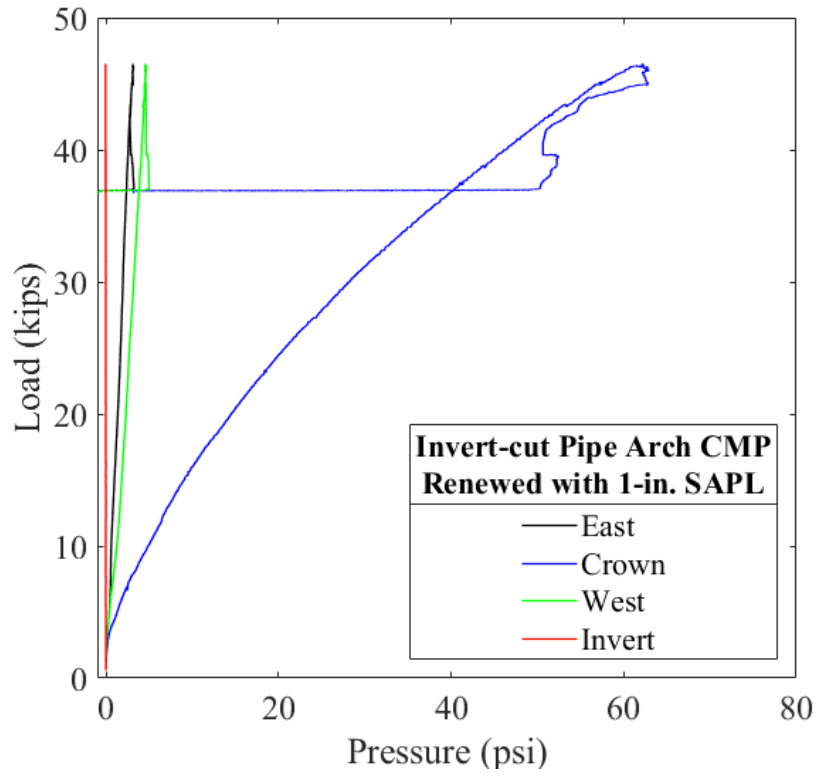


Figure 4-67. Load vs. pressure for the 1-in. thick SAPL renewed invert-cut pipe arch CMP.

4.2.2.3.1. Post Failure Crack Measurement

Visual inspection was conducted after unloading the pipe sample. The crack width for both load induced (i.e., new), and existed (i.e., shrinkage) cracks were measured using digital image processing (DIP) method. In this pipe, there were two major locations subjected to crack, which were at the crown and invert. There were multiple cracks formed on the crown which were divergent at the both ends of the pipe and convergent at center of the pipe. On the invert section, unlike the previous pipe samples, there was only one longitudinal crack propagated. Figure 4-68 illustrates the cracked 1-in. thick SAPL at the invert location, and the crack patterns schematic due to the shrinkage and the applied load. The visual inspection revealed that due to the load a longitudinal crack in invert, multiple longitudinal crack in crown, and multiple circumferential cracks in East haunch area were created. Figure 4-68 also shows two longitudinal cracks at the both springline locations. However, these were not actual longitudinal cracks, they were cracks due to delamination at the load removal stage. The averaged width of the invert longitudinal crack, created by the load, was 0.1545 in., which was the largest crack generated in the SAPL. The circumferential cracks on the invert had the average width of 0.0041 in., which is illustrated in Figure 4-69. The existed longitudinal shrinkage crack, at the East haunch area, was totally closed and disappeared as it was not visible with bare eyes, which is illustrated in Figure 4-59. The averaged crack width for crown location at the center and end of the pipe were 0.178 and 0.0732 in. respectively. The longitudinal cracks at the crown are depicted in Figure 4-70.

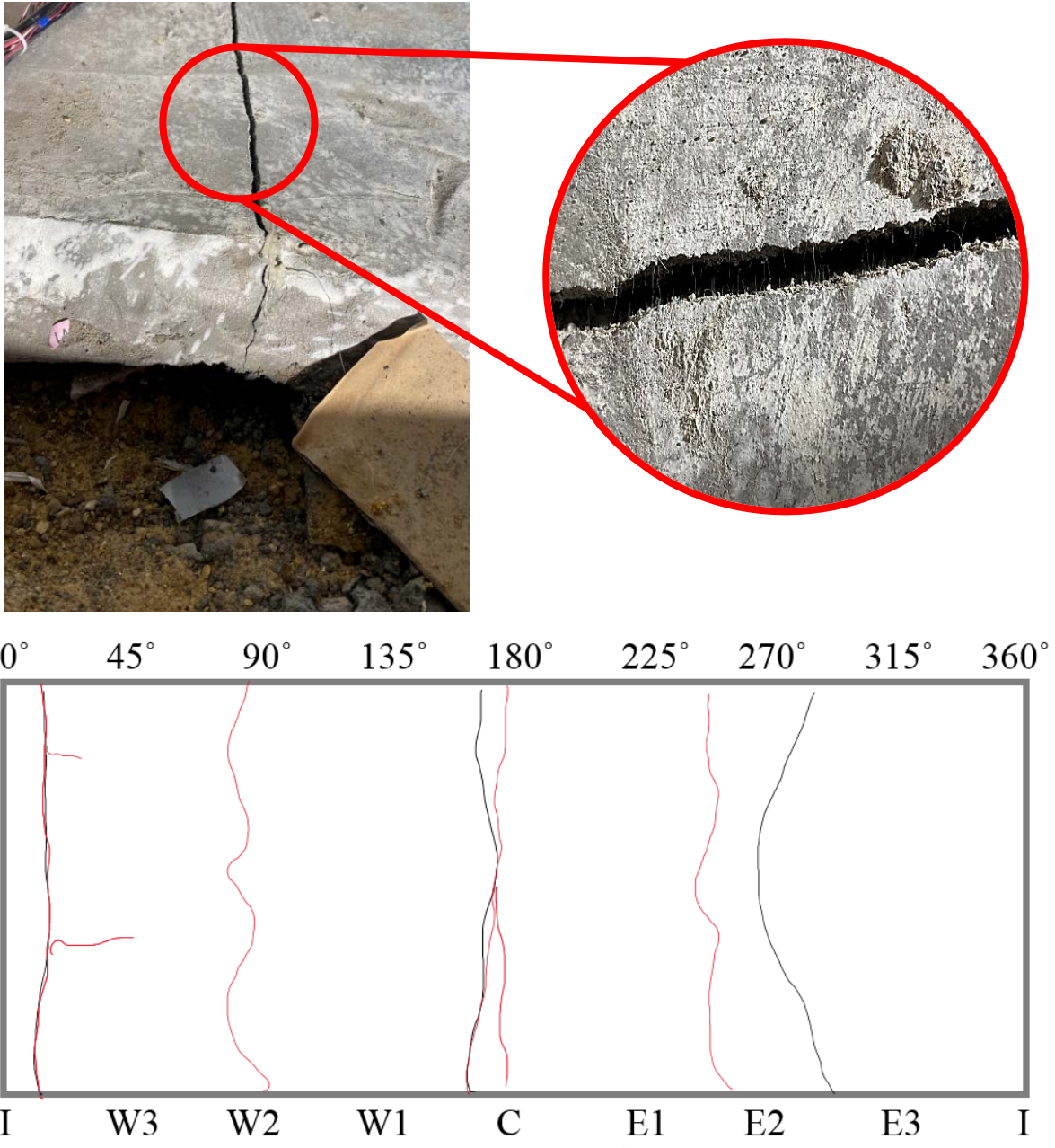


Figure 4-68. Visual inspection of the 1-in. thick SAPL renewed pipe arch CMP: (top) cracked SAPL on the invert, and (bottom) crack pattern schematic, where black represents the shrinkage cracks and red represents the cracks due to the load.

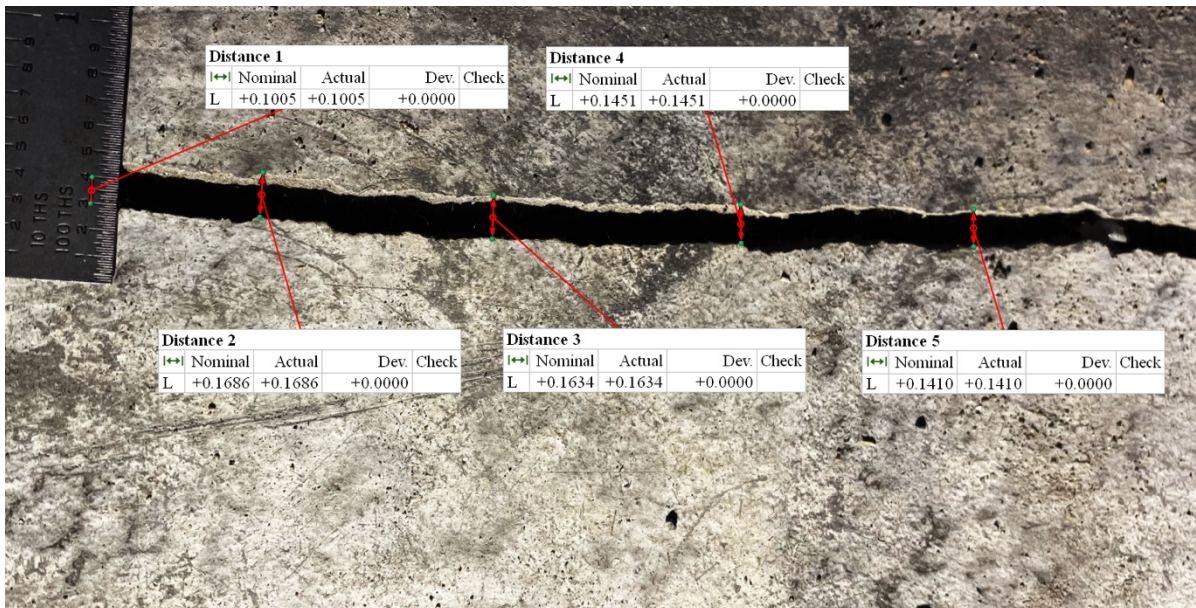
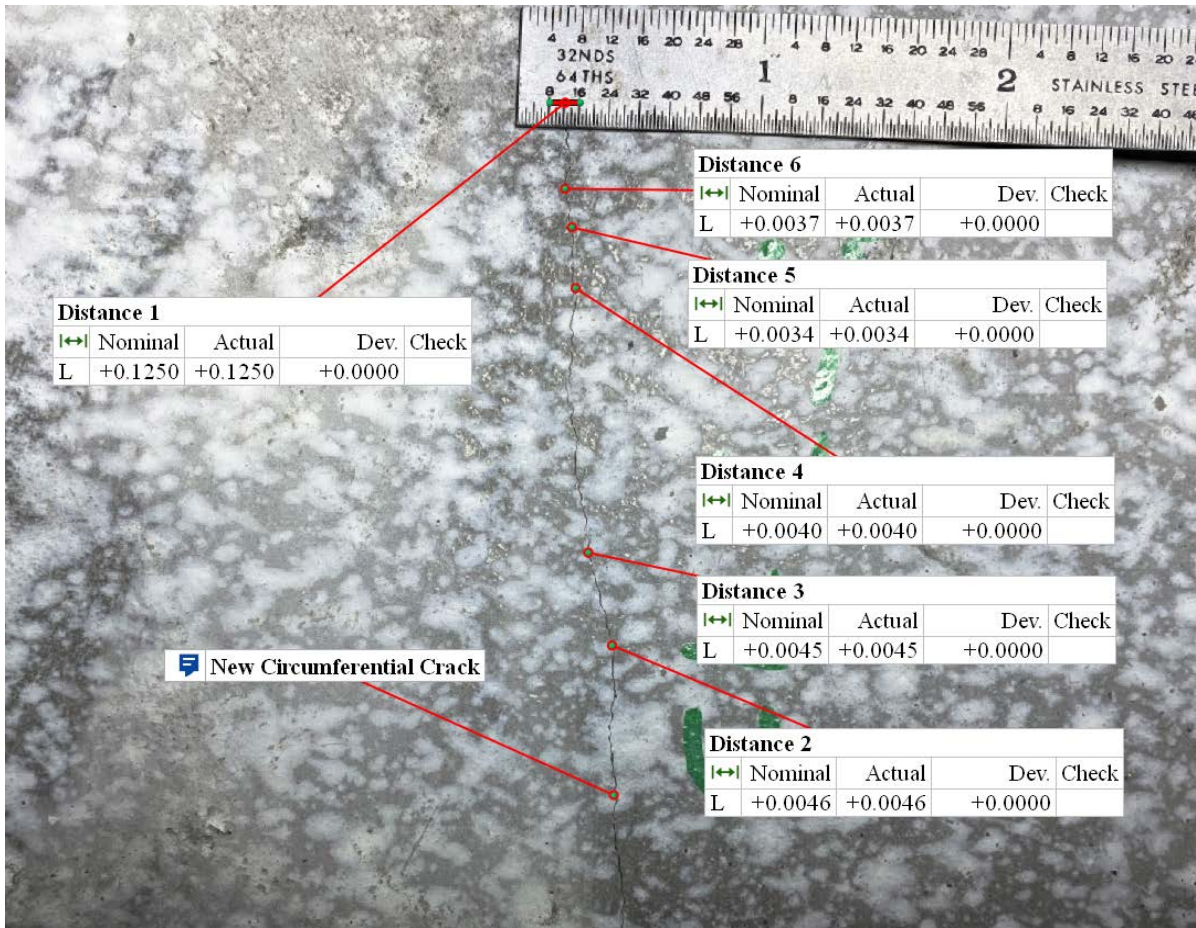


Figure 4-69. Invert cracks of the 1-in. thick SAPL renewed invert-cut pipe arch CMP: (top) circumferential and (bottom) longitudinal.

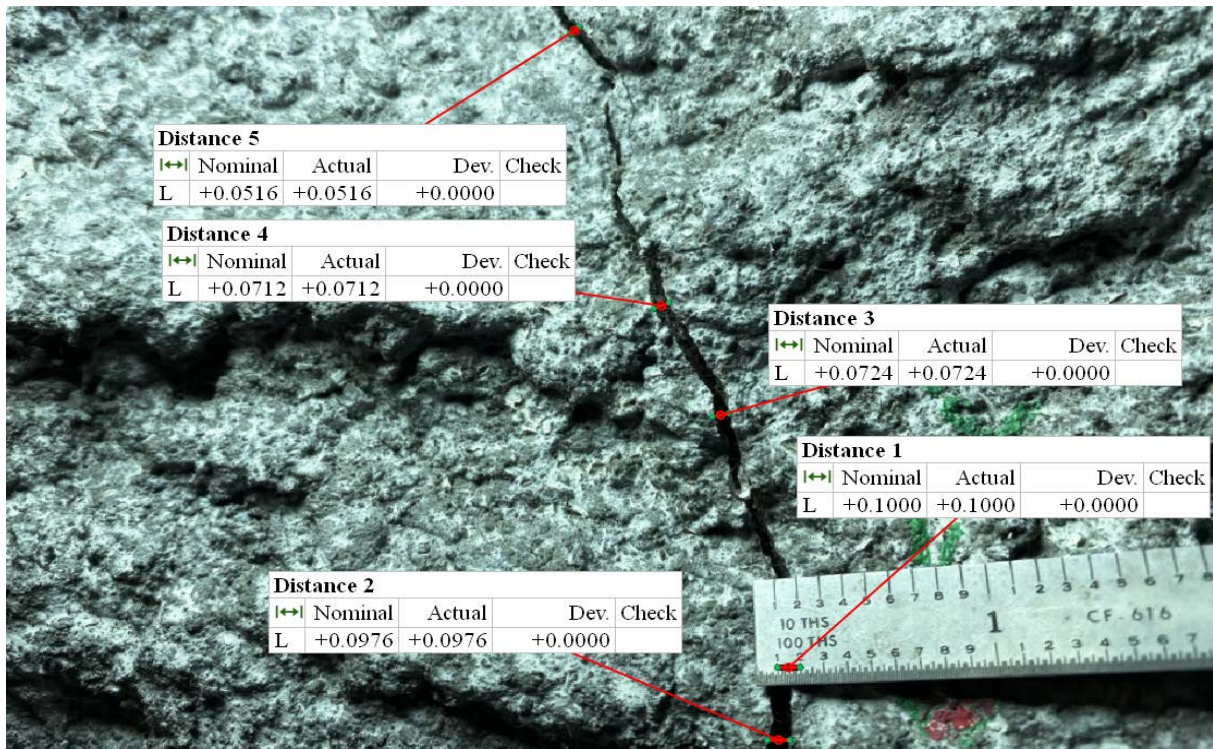
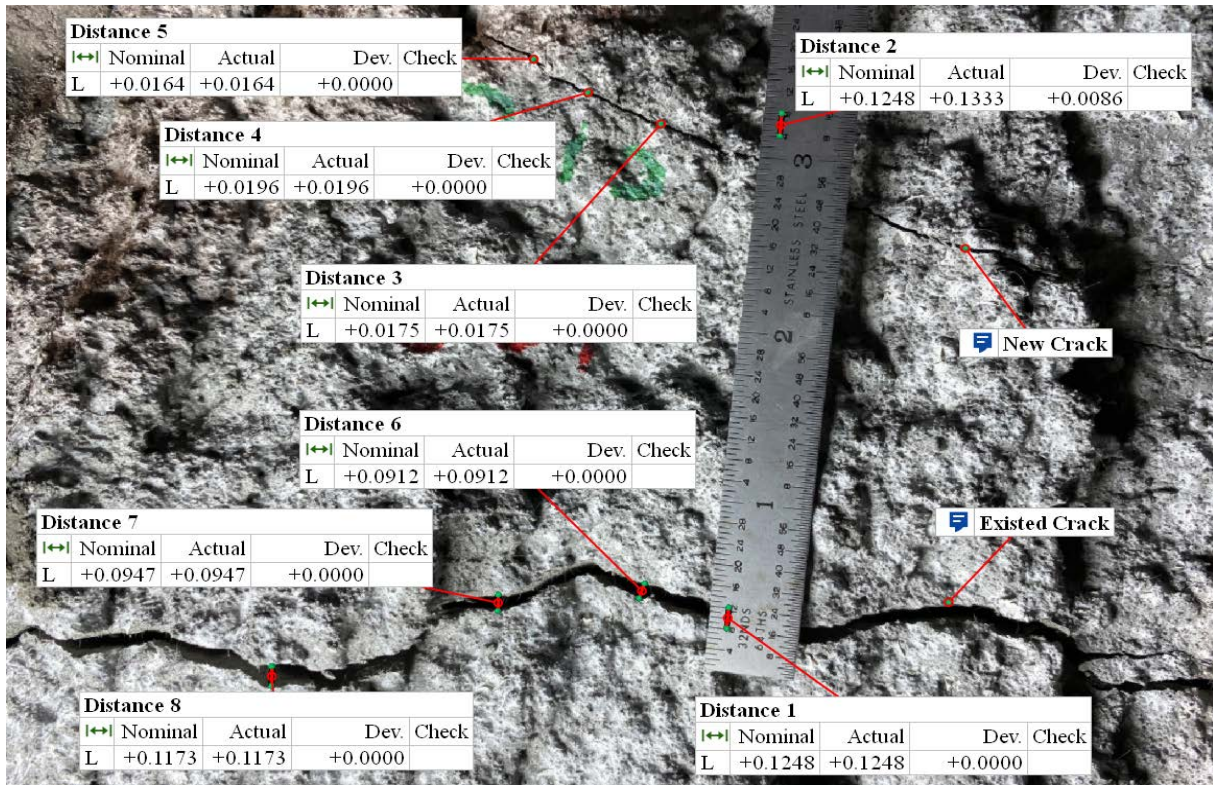


Figure 4-70. Longitudinal cracks on the crown of the 1-in. thick SAPL renewed invert-cut pipe arch CMP at: (top) center of the pipe and (bottom) north side of the pipe.

4.2.2.3.2. Thickness Measurement

The thickness of the 1-in. thick cementitious SAPL renewed pipe arch CMP were measured after the structural test and before exhumation as elaborated in section 3.4.6. The detailed result of the measurements are presented in APPENDIX E. Figure 4-71 illustrates the thickness measurements results for all three locations along the length of the pipe (i.e., north, center and south). The results showed that the liner's thickness variation ranged from 0.6 to 1.8 in. In compare with north and south location, the SAPL was generally thicker at center of the CMP. In general, for this pipe, the averaged thickness of the SAPL was about the required design thickness.

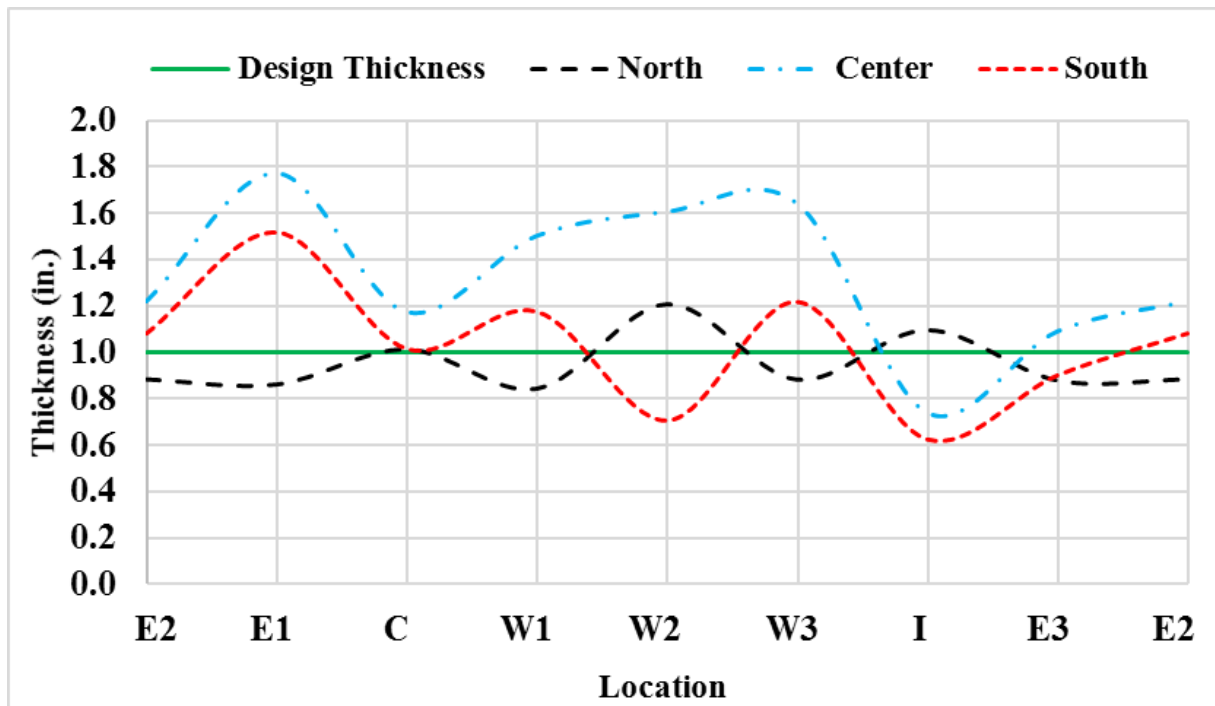


Figure 4-71. Thickness measurement for the 1-in. thick cementitious SAPL renewed pipe arch CMP.

4.2.2.4. Pipe Arch SAPL Result Comparison

Result comparison between the bare (i.e., unlined) invert-cut pipe arch CMP and SAPL renewed samples showed that application of 1, 2 and 3-in. thick cementitious SAPL on the invert-cut pipe arch CMPs have increased the load carrying capacity for 72.34, 104.4, and 151.44 % respectively. Table 4-1 presents the ultimate load results and the load carrying capacity enhancement using different SAPL thickness.

Table 4-1. Pipe arch CMP test results

Testing Pipe Samples	SAPL Material	Ultimate Load (Kips)	Improvement (%)
Bare Pipe Arch	-	26.98	-
1 in. Thick SAPL	Geopolymer	46.50	72.34
2 in. Thick SAPL	Geopolymer	55.16	104.4
3 in. Thick SAPL	Geopolymer	67.84	151.44

The comparison between the soil settlement at the time of soil-CMP failure with different SAPL thicknesses show that the application of SAPL increased the required soil settlement to achieve failure of the system. Figure 4-72 illustrates a graph presenting the load versus soil settlement for all pipe arch CMPs. The result also showed that the soil settlement value for the 2 and 3-in. thick SAPL at the time of failure is about the same. One of reasons could be due to the fact that the actual crown thickness of the both pipe samples are very close. However, it was observed that the crown displacement of the 2-in. thick pipe sample, presented in Figure 4-73, at the time of soil-CMP failure is higher than the both 1 and 3-in. thick pipe samples. The main reason of this behavior is yet unknown to the research team, however, one of the possible reasons could be due to the higher level of thickness variation and geometry irregularity of the 3 in.-thick SAPL,

illustrated in Figure 4-37. The result of horizontal diameter changes of different SAPL renewed thicknesses and the bare invert-cut pipe arch CMP is presented in Figure 4-74. Where the 2-in SAPL renewed CMP sample had the heights horizontal expansion.

Figure 4-75 illustrates the result of the applied static load on the soil surface versus the applied pressure over the crown of the pipe. The AASHTO H20 truck equivalent pressure, obtained from the intact CMP test (see Figure 4-30), is compared from the SAPL renewed pipe arch samples and it can be observed that, unlike the bare invert-cut pipe arch CMP, the SAPL renewed pipe arch samples could resist the equivalent AASHTO H20 truck pressure. The figure shows that the thicker the liner the higher load is required to fail the SAPL-CMP system. It can be concluded that all three thicknesses are sufficient for the AASHTO H20 truck load.

Figure 4-76 illustrates the results of the ultimate applied pressure over the crown of the renewed pipe arch CMPs versus the averaged installed SAPL thicknesses. A non-linear regression analysis was conducted on the experimental test results and the following equation is obtained:

$$P = 8.2968 \cdot t^2 - 8.7202 \cdot t + 57. \quad (49)$$

where, P is the applied live load pressure over the crown of the pipe and t is the SAPL thickness. The R^2 value of the equation is 0.9524, which can indicate an acceptable accuracy of the equation with the available data points. It should be noted that the equation is suggested to be only used for the SAPL thickness range from 0.5 to 3 in., as for the cementitious SAPL, installation of the thickness lower than 0.5 in. is not practical and for equations larger than 3 in., the risk of material falling from the host pipe is high. Therefore, for the SAPLs higher than 3 in. thickness it is highly recommended to use a mesh reinforcement, as described in section 1.3.5.4, which in that case the equation (49) will no longer govern.

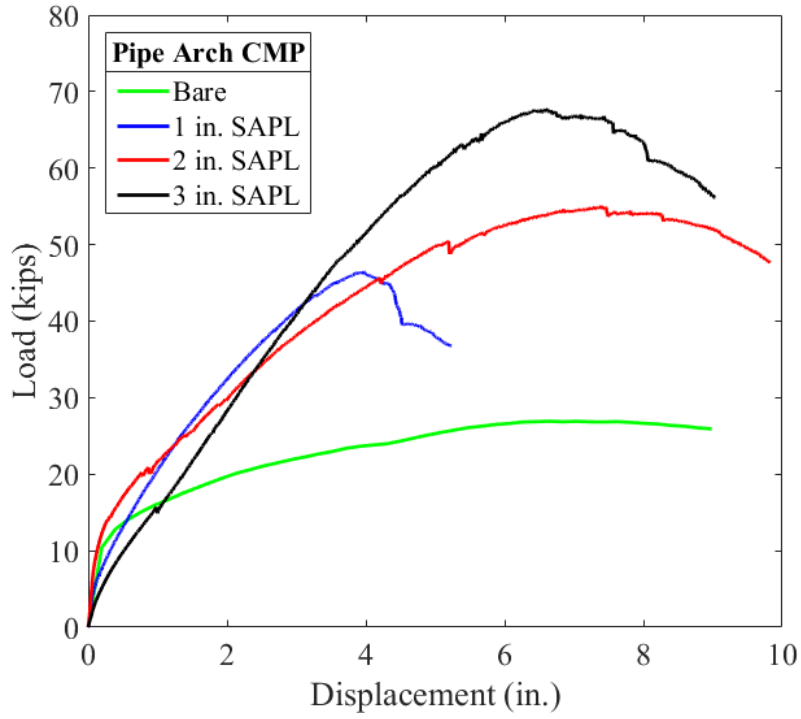


Figure 4-72. Load vs. soil settlement comparison graph.

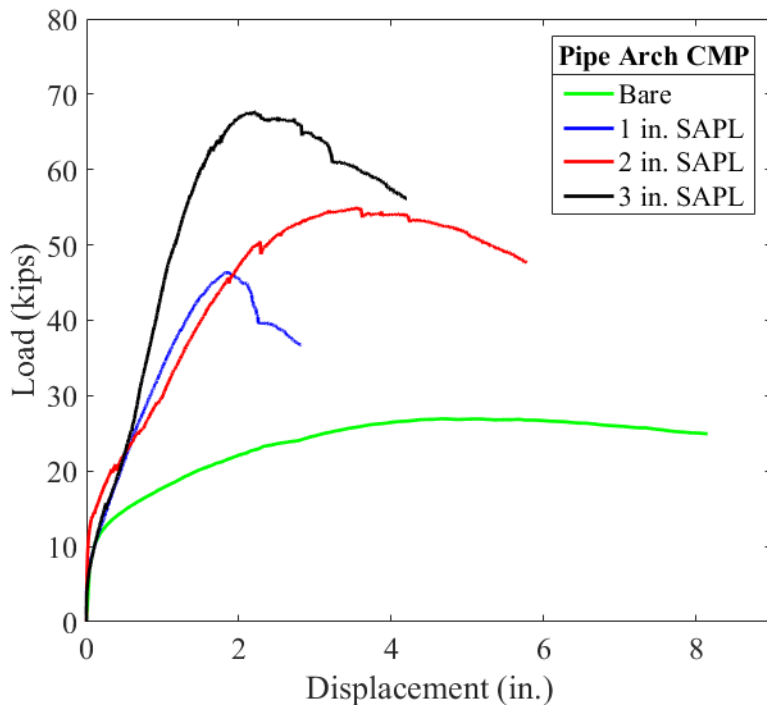


Figure 4-73. Load vs. crown displacement comparison graph

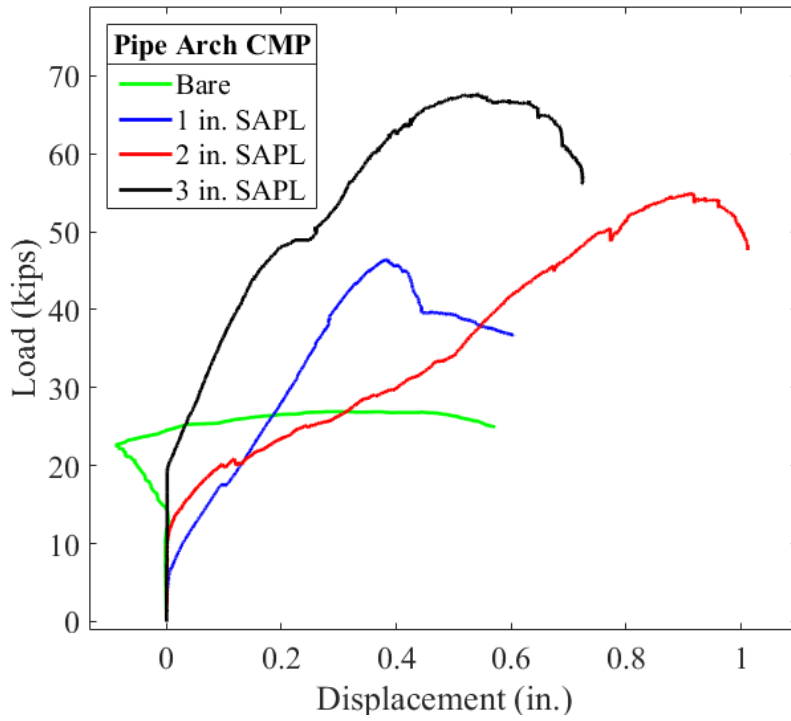


Figure 4-74. Load vs. springline displacement comparison graph.

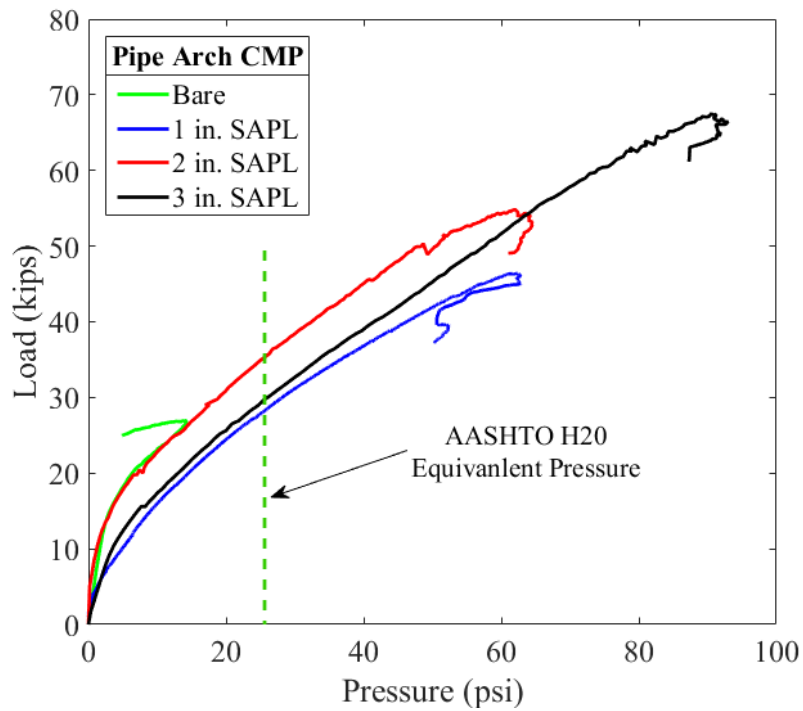


Figure 4-75. Load vs. pressure comparison graph.

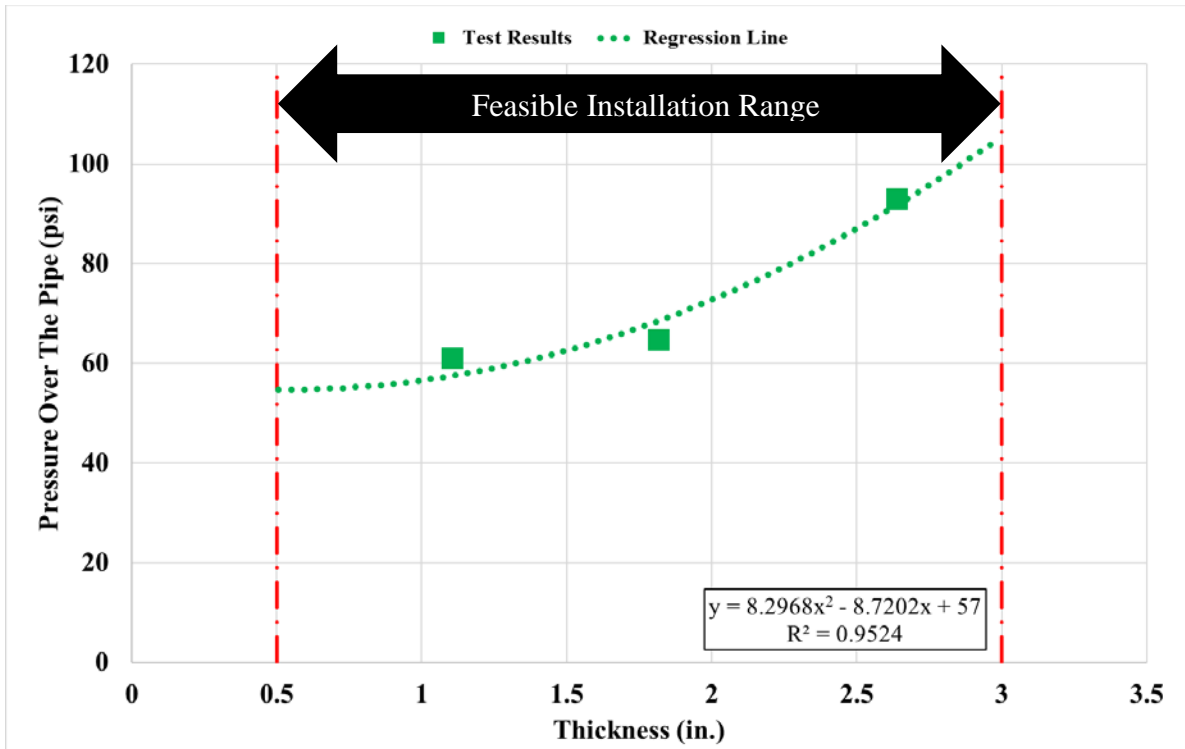


Figure 4-76. Proposed equation for thickness calculation of SAPL renewed pipe arch CMP based on ultimate load.

4.2.2.5. Mechanical Properties Test Result

The compressive strength of the samples was evaluated at 24 hours, 7 days, and 28 days. All the Detailed test results are presented in Compressive Strength Test Results.

The cube samples were tested according to the ASTM C109. The load was applied at the rate of 300 lb/sec, as described in the test guideline. Figure 4-77 illustrates the box plot of the cube samples result that shows the cubes were able to reach the compressive strength of 6431 psi within 28 days, which is 22% higher than the 7 days compressive strength.

All the cylinder samples were tested according to the ASTM C39 at the pressure rate of 30 psi/sec. The 3 × 6 in. spray-cast cylinder samples, were able to reach 4423 psi at the 28 days, which was 2008 psi less than the cubes' compressive strength at 28 days. The sprayed cylinders showed about 27% increase from 7 to 28 days of curing. The hand-cast cylinders showed relatively higher compressive strength than the spray-cast cylinders at 7-day curing period and relatively lower strength at the 28-day curing time. Figure 4-78 illustrates the box plot of the 3 × 6 in. samples test results.

The 4 × 8 in. spray-cast cylinder samples showed that the geopolymer was able to achieve 1959 psi compressive strength within 24 hours. The 7 and 28 days test specimens showed 2831, and 3506 psi respectively. The comparison between the results showed that the geopolymer could increase its strength for 78% during the 28 days of curing time. The hand-cast cylinders also showed similar results to the spray-cast samples. The results are presented in Figure 4-79.

The 6 × 12 in. spray-cast cylinder samples achieved 4009 psi at the end of 28 days curing time which was only 17% higher than the 7 day cured samples. The results of the 6 × 12 in. samples are illustrated in Figure 4-80.

The results from all different specimens are compared for both 7 and 28 days curing time and are presented in Figure 4-81. The result comparison illustrates that in the absence of large aggregates the smaller samples could result in higher compressive strength. In addition, the lower compressive strength of larger samples revealed that although the geopolymer was reinforced with micro fibers, the fibers could not contribute to the compressive strength. The total average compressive strength value for all the specimens at 7 and 28 days were 3653 and 4312 psi respectively.

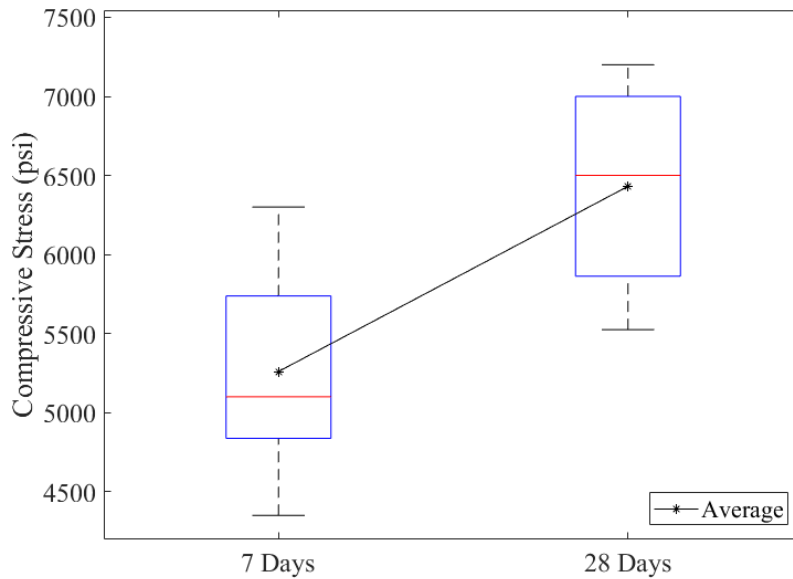


Figure 4-77. Box plot for the cube samples taken from SAPL batch sprayed on pipe arch CMPs

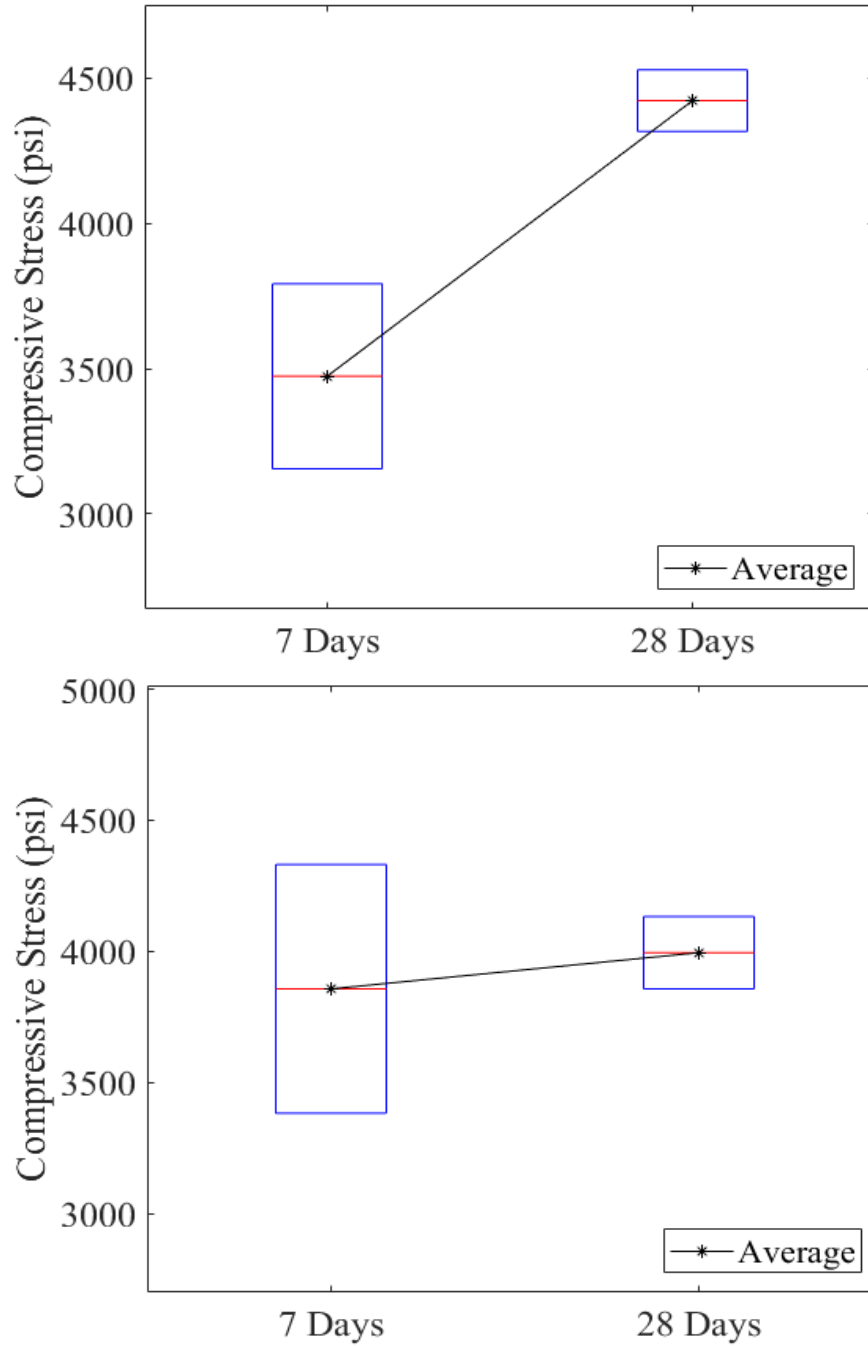


Figure 4-78. Box plot for the 3×6 cylinder samples taken from SAPL batch sprayed on pipe arch CMPs: (top) spray cast, (bottom) hand cast.

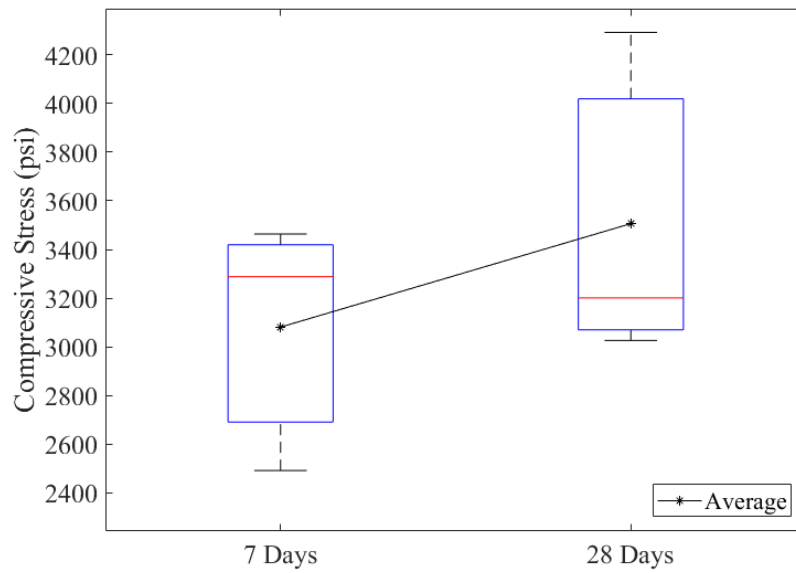
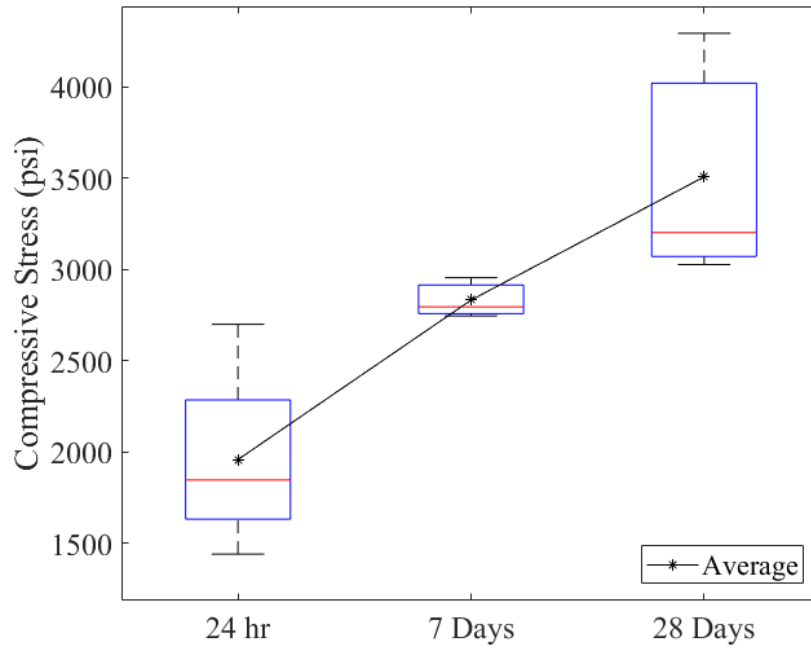


Figure 4-79. Box plot for the 4 × 8 cylinder samples taken from SAPL batch sprayed on pipe arch CMPs: (top) spray cast, (bottom) hand cast.

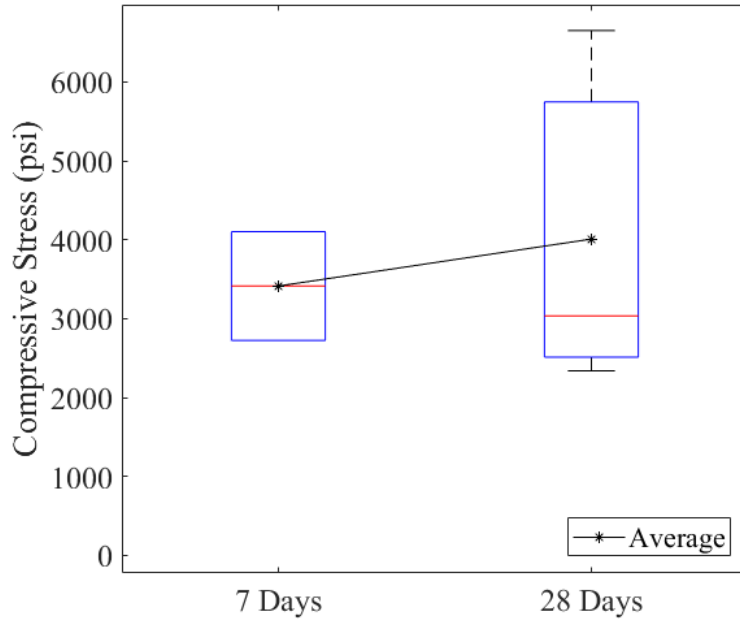


Figure 4-80. Box plot for the 6 × 12 cylinder samples taken from SAPL batch sprayed on pipe arch CMPs

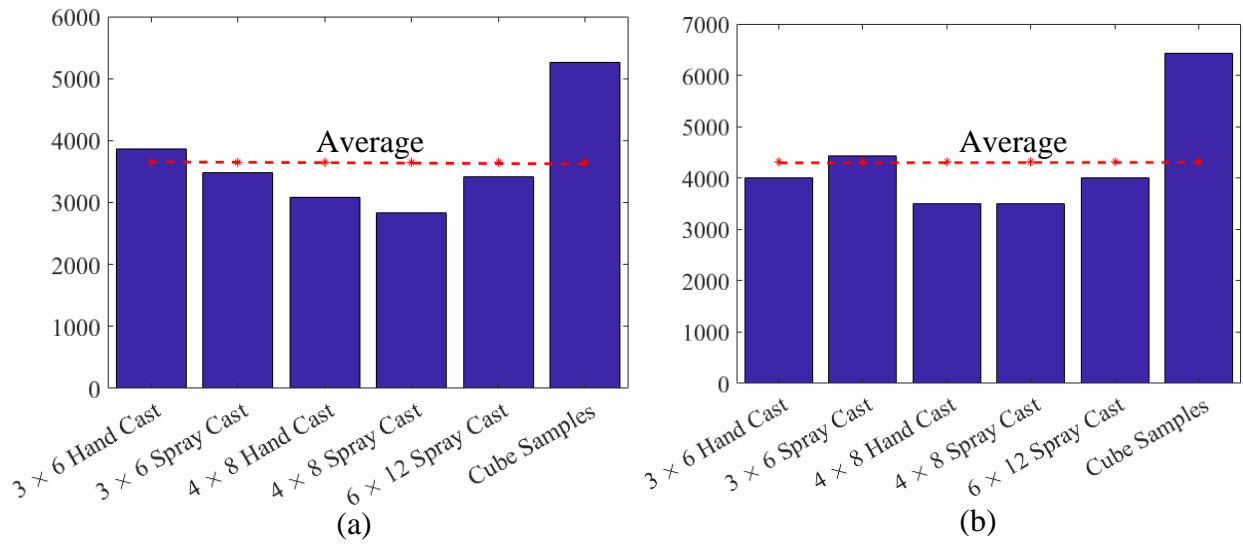


Figure 4-81. Bar chart results for: (a) 7 days, and (b) 28 days samples.

4.2.3. SAPL Renewed Invert-cut Pipe Circular Test Results

The invert-cut circular CMPs renewed with the cementitious SAPL were tested using the same load rate and load pad as specified in sections 4.2.1.3. Due to required time for test preparation, instrumentation and operation, conducting all the three tests of this set in one day was not possible. The first test was conducted on the 3-in. thick SAPL renewed circular CMP after 7 days of curing. The 2 and 1-in. thick SAPL renewed circular CMPs were conducted with a 2-day interval respectively. It is noteworthy that none of the existing shrinkage cracks, discussed in 3.4.5.2, were repaired before the loading and the soil-pipe systems were tested with existed cracks.

In general, a circular pipe subjected to vertical load will experience tension in the crown, invert and both exterior surfaces of the springline, as illustrated in Figure 4-82. In conformity to the expected cracking locations in the tension zones, it was observed in all three tested SAPL renewed circular CMPs that the majority of the cracks formed crown, invert (at the invert-cut's gaps) and in the transition zones at shoulders and haunches area.

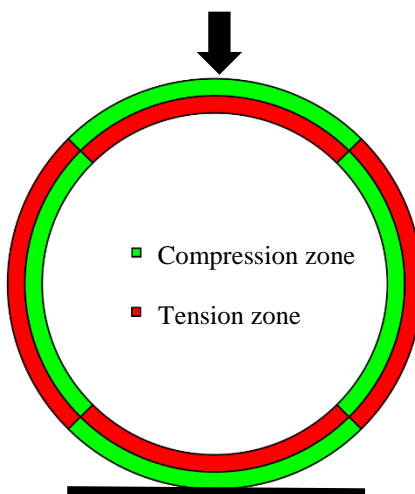


Figure 4-82. Compression and tension zones of a circular pipe subjected to a vertical load

4.2.3.1. 3-in. Thick SAPL Sample

The 3-in. thick SAPL renewed invert-cut circular CMP was tested on July 27th, 2020, using the 20 × 40 in. load pad. The test duration was 5.97 hours. During the test, due to the existence of shrinkage cracks no major drop in the load-displacement graphs was observed, and the cracks width were increased with the load progression. The SAPL renewed CMP sample failed at the load of 109.7 kips with 10.83 in. of soil settlement. The failure occurred due to the large deflection and cracking of the crown. Figure 4-83 (a) and (b) illustrate the test sample at before and after loading stage. Once the SAPL-CMP system was failed, the test was continued until about 20% load drop. Then the test was terminated, as further deflection would increase the chance of liner detachment and fall, which would damage the mechanical sensors and cameras inside the pipe. Once the load was released from the soil surface, the pipe had an upward movement and relaxed. Figure 4-84, also illustrates the load and soil settlement graph, registered by the actuator's load cell and LDVT.

The earth pressure cell results registered the maximum pressure of 106.8 psi at the crown location. The maximum pressure applied on the West and East locations were 23.17, and 16.51 psi respectively. Figure 4-85 illustrates earth pressure results for the invert-cut circular test. It also shows that the pressure one was dropped after 106 psi. At this pressure, the corresponding surface load and pressure, were 92 kips and 115 psi. Similar to the intact CMP discussed in section 4.2.1.1, at this surface pressure the soil cover is most likely failed.

Figure 4-86 illustrates the results of the mechanical sensors. The LVDT results show that the pipe was subjected to 4.356 in. of crown and 1.683 in. of springline deflection. The shoulder had 0.469 in. downward movement. The CDS showed an exact similar result (4.348) as the crown LVDT. At the end of the test once the load was released from the surface. Once the load was

released from the soil-pipe system, a reversal movement in crown and springline for 0.77 and 0.106 in. respectively, were observed.

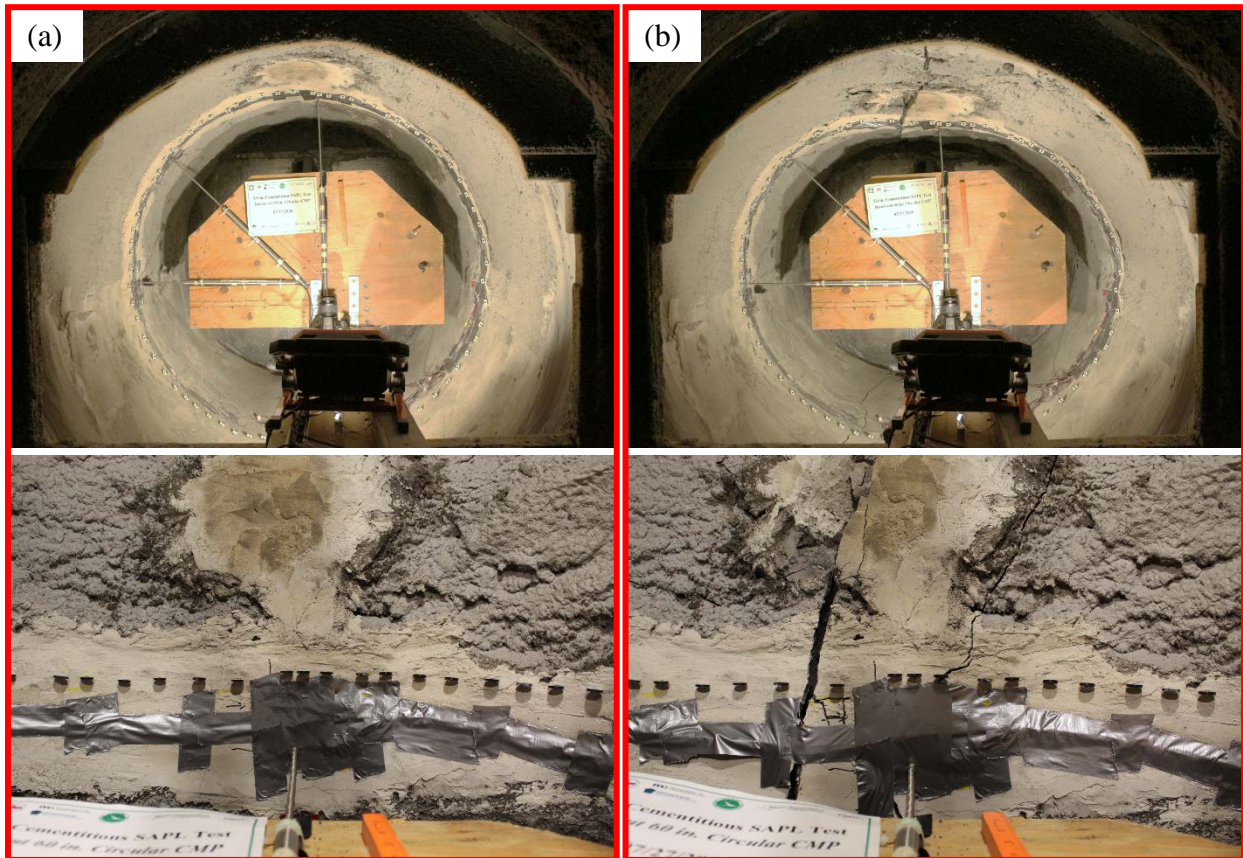


Figure 4-83. Invert-cut circular CMP renewed with 3 in. cementitious SAPL: (a) before loading, and (b) after loading.

The strain gauge results showed the SAPL was cracked at the invert on the West side of the invert at the load of 18.71 kips. In addition to that the East side of the invert is most likely cracked at the load of 30 kips as at this load all the strain gauges show a drop in their reading, while they did not show stress relaxation that implies somewhere in the liner is cracked other than installed strain gauges locations. Live monitoring of the SAPL using digital camera revealed that at this load the invert section is cracked. In addition to that, the East haunch cracked at 33 kips.

Due to the harsh and abrasive nature of the soil, the both strain gauges installed at the crown of CMP were damaged and were unable to measure the strain. At the load of 92 kips, which failed the soil cover on top of the CMP, a rise in all strain values were observed. After this point, the East shoulder and springline reached the steel yielding point (i.e., 1138 $\mu\epsilon$). No other location in the CMP reached the yield point.

Figure 4-88 illustrates the 3-in. thick SAPL renewed circular CMP profile before and after the applied static load. The pipe profile at end of the test clearly illustrates the pipe's ovality. In addition, the roughness and irregularity of the SAPL is explicitly evident in the profiling result. The comparison between the mechanical sensors and DIC are presented in Figure 4-89, which shows an excellent conformity with the CDS sensor.

The load-displacement values for soil surface, crown, springline, and shoulder of the 3-in. thick SAPL renewed circular CMP due to the applied static load is illustrates in Figure 4-90. The applied load on the soil surface versus its corresponding pressure at the crown of the renewed circular CMP are depicted in Figure 4-92, where the recursive part of the graph represents drop in both pressure and load at the same time.

During the load, the width of the crack on the crown was monitored using DIP method. Figure 4-91 illustrates the crack width different stage of the applied load on the soil surface. The result show that the pipe at the time of failure (i.e., stage 7) had the averaged 0.3528 in. crack width. This value is about 13 times higher than the crack width before load application (i.e., stage 1). The crack width at the time of failure was further increased by 36.6% in the stage 8, where the test was terminated. The DIP results and pictures for the crown's crack measurement of the circular CMPs are provided in APPENDIX F.

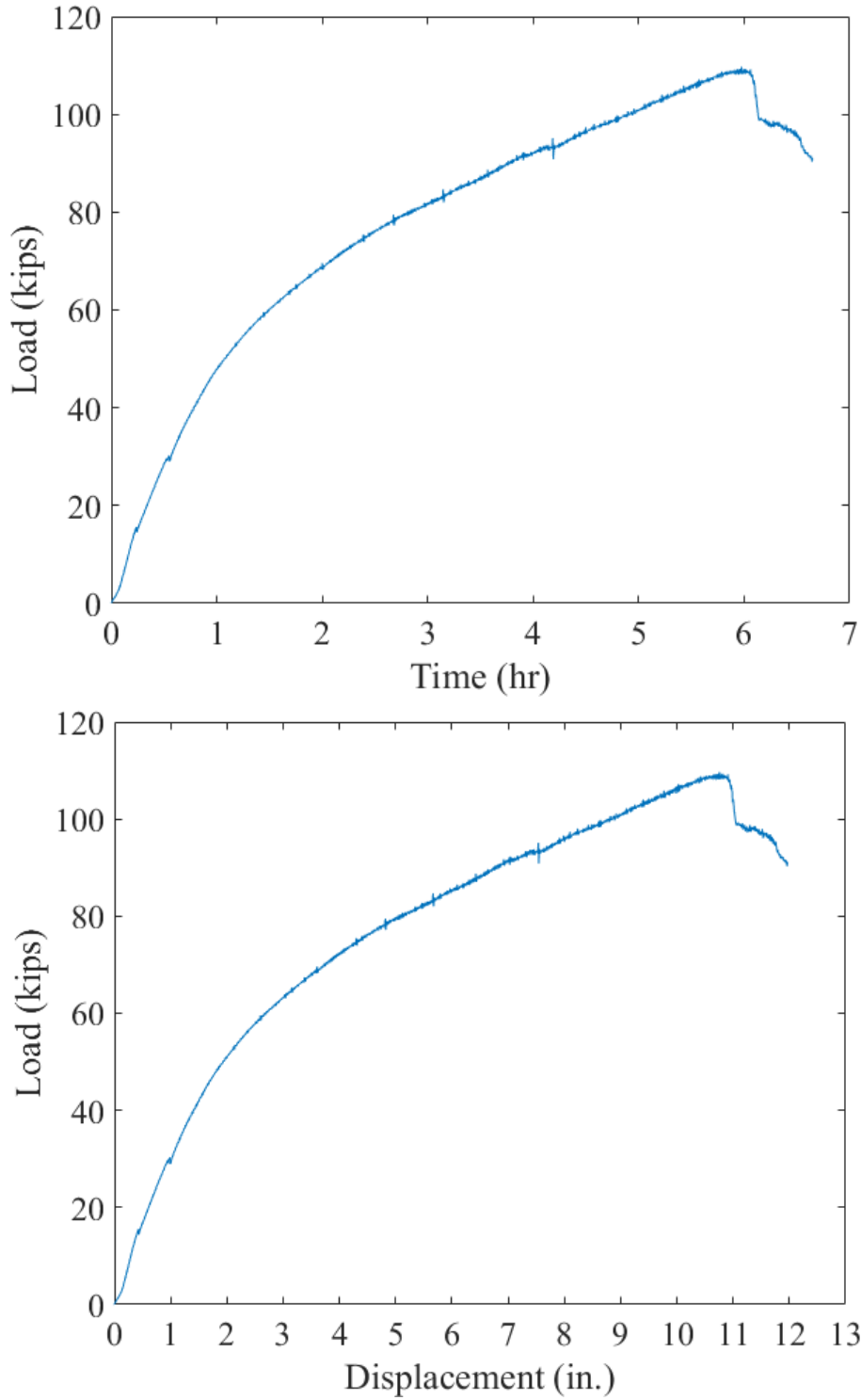


Figure 4-84. Invert-cut circular CMP renewed with 3-in. thick cementitious SAPL subjected to static live load: (top) load-time and, (bottom) load-soil displacement graphs.

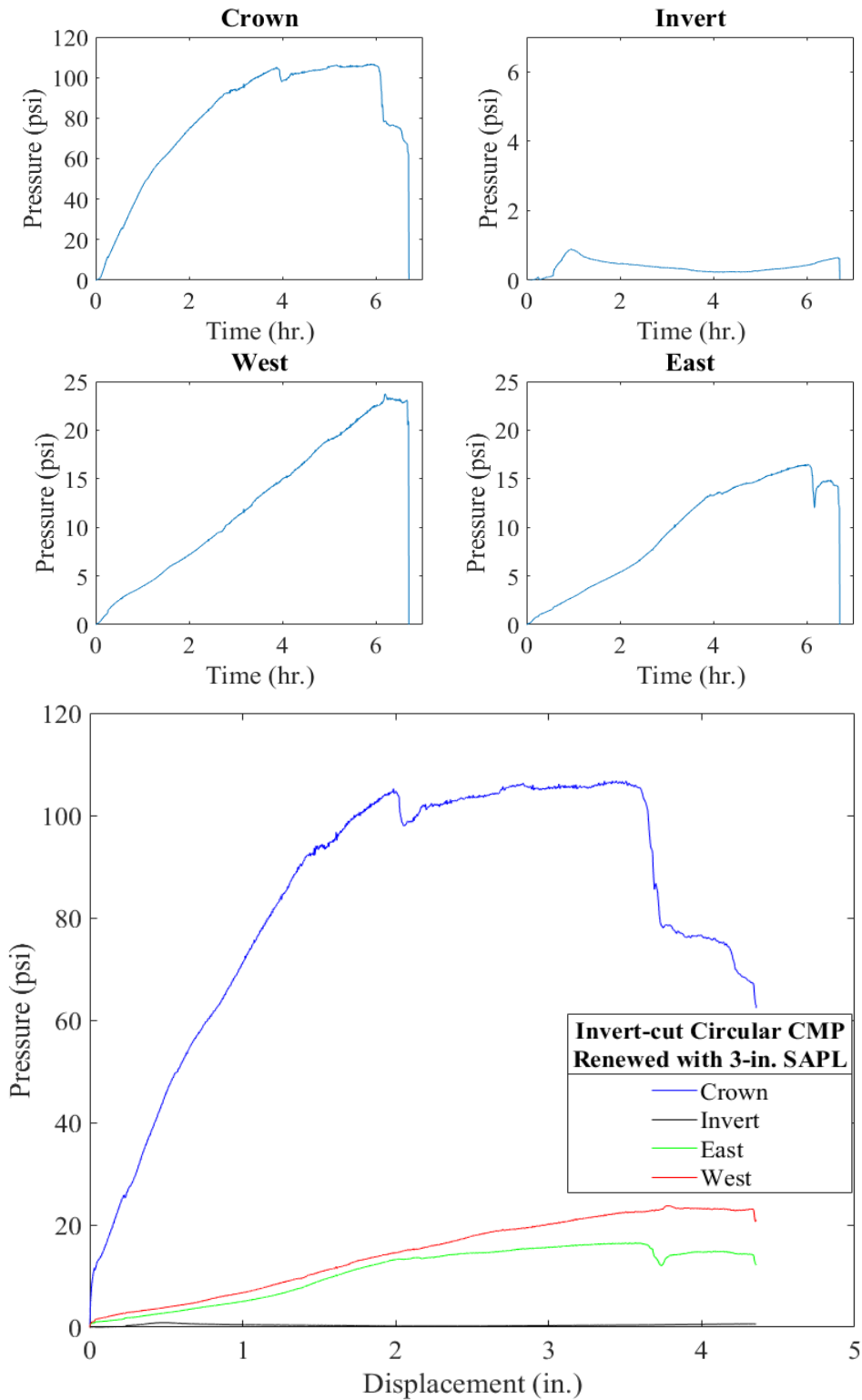


Figure 4-85. Earth pressure cell results for the 3-in. thick SAPL renewed invert-cut circular CMP with respect to: (top) time, and (bottom) crown displacement.

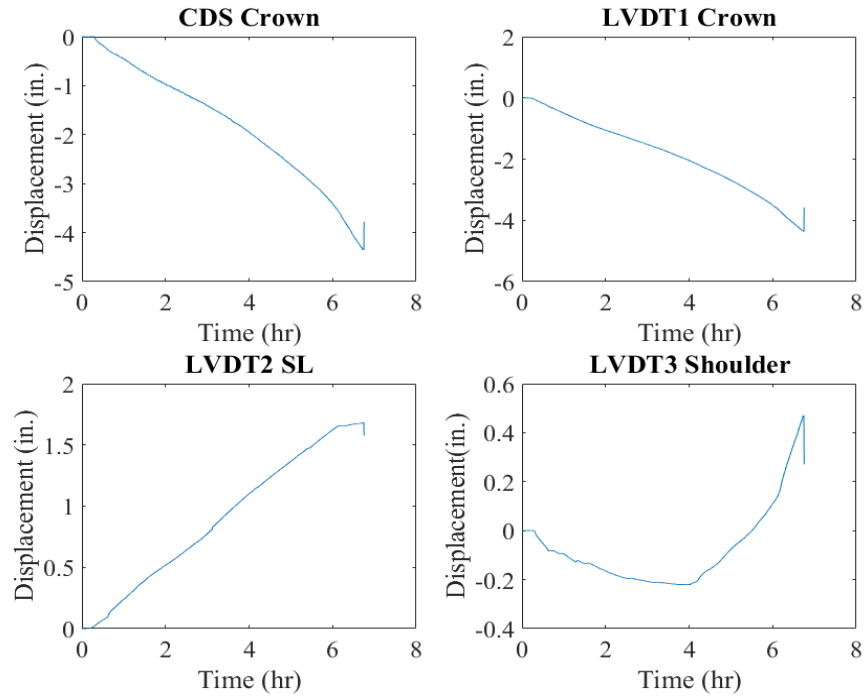


Figure 4-86. Mechanical sensors result for 3-in. thick SAPL renewed invert-cut circular CMP.

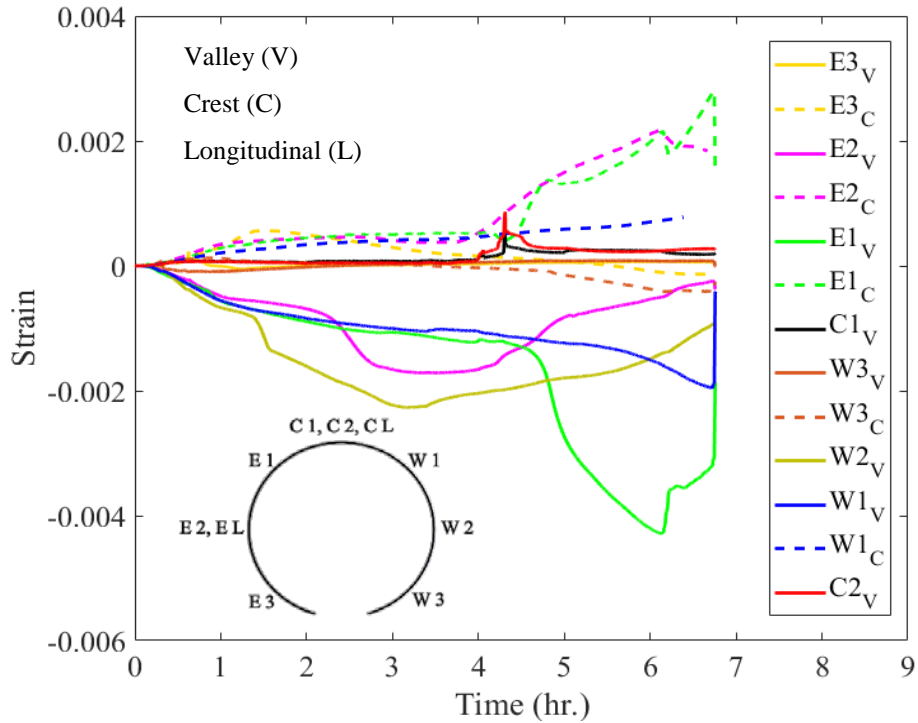


Figure 4-87. Strain gauge result for 3-in. thick SAPL renewed invert-cut circular CMP.

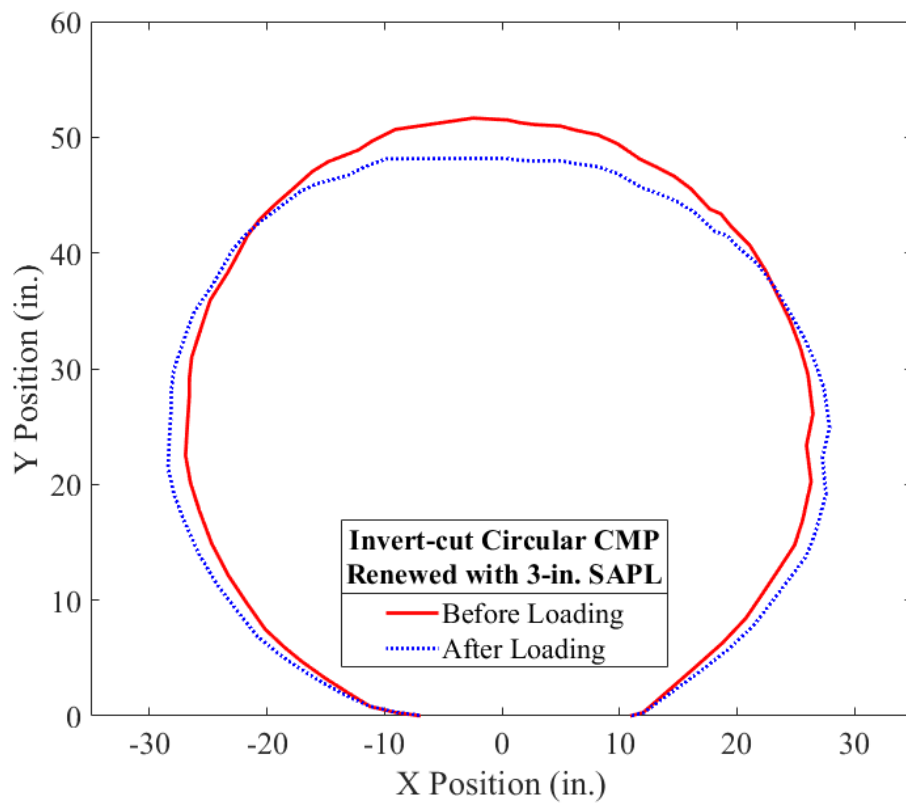
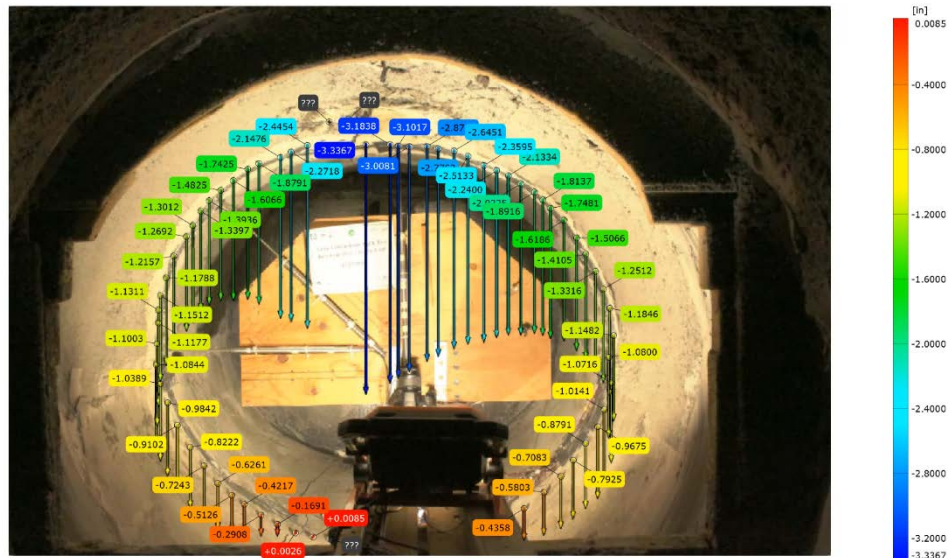


Figure 4-88. Pipe profiling using DIC for the 3-in. thick SAPL renewed invert-cut circular CMP.

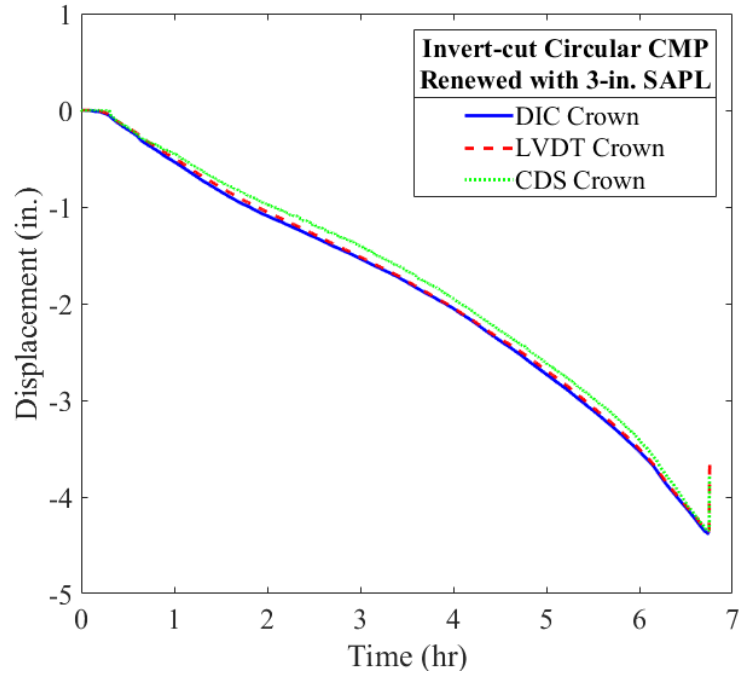


Figure 4-89. DIC method verification with mechanical sensors for the 3-in. thick SAPL renewed invert-cut circular CMP.

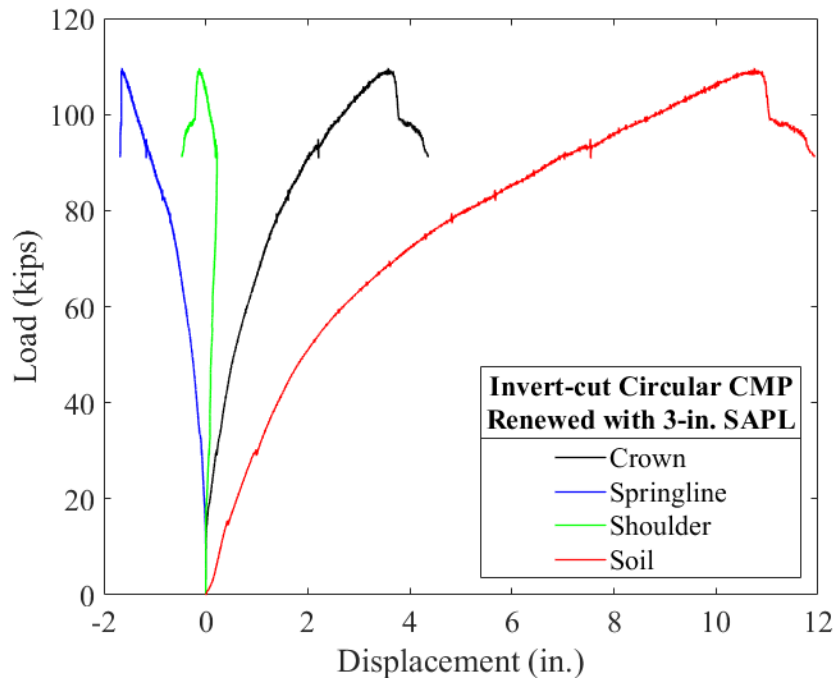


Figure 4-90. Load vs. displacement of the soil surface, crown, springline, and shoulder of the 3-in. thick SAPL renewed invert-cut circular CMP due to the applied static load.

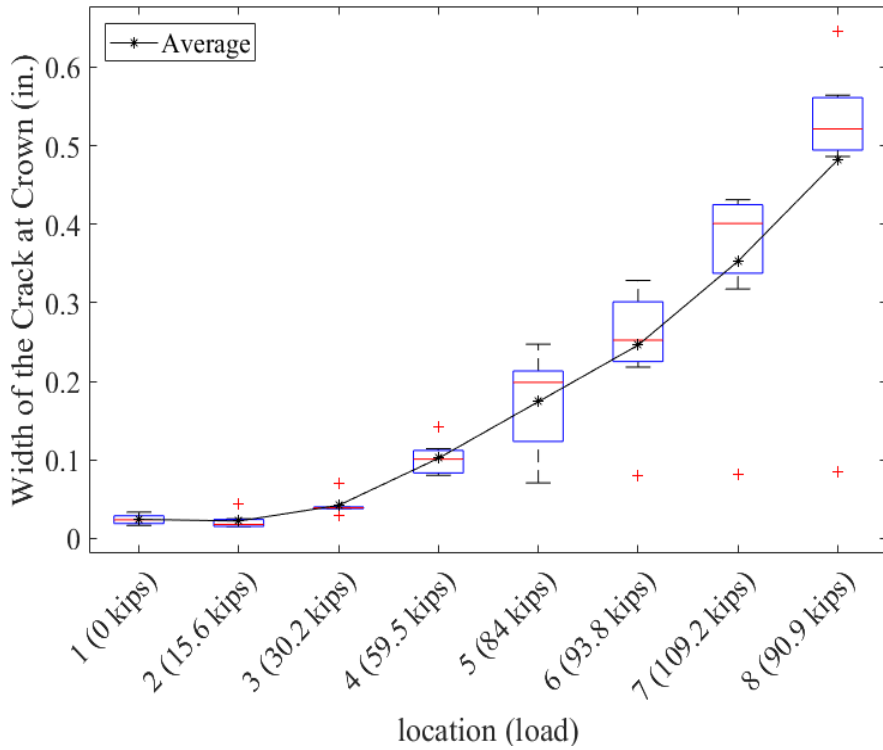
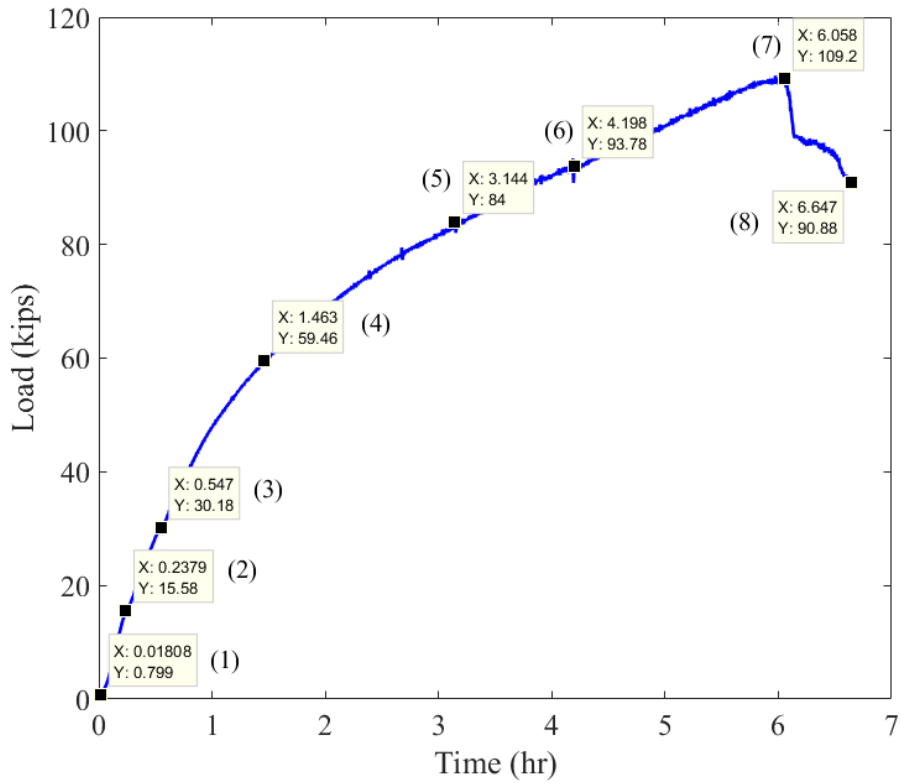


Figure 4-91. Crack width measurement for the crown location at during the applied live load on the soil surface for the 3-in. thick SAPL renewed invert-cut circular CMP.

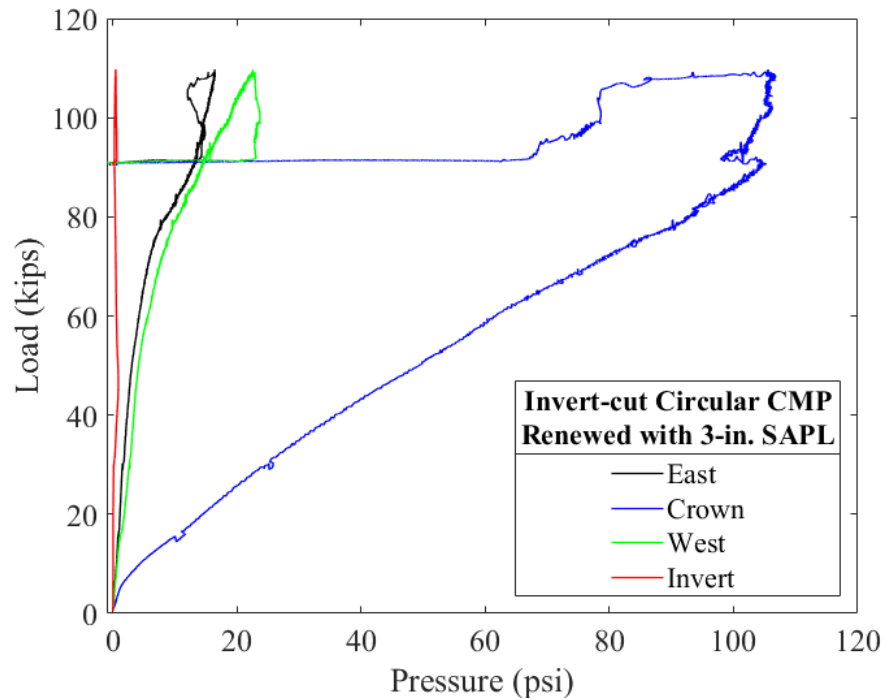


Figure 4-92. Load vs. pressure for the 3-in. thick SAPL renewed invert-cut circular CMP.

4.2.3.1.1. Post Failure Crack Measurement

Visual inspection was conducted after the test and crack width measurement were carried out using DIP method. Figure 4-93 (a) illustrates the 3-in. SAPL renewed invert-cut circular CMP and Figure 4-93 (b) shows the crack pattern schematic inside the pipe. Due to the vertical load, three major longitudinal cracks were formed inside the pipe; one on crown and two on the gaps between the invert-cut sections. In addition, two circumferential cracks were observed on both East and West side of the pipe. The circumferential cracks were propagated from shoulder to the haunch area.



0° 45° 90° 135° 180° 225° 270° 315° 360°



I W3 W2 W1 C E1 E2 E3 I

Figure 4-93. Visual inspection of the 3-in. thick SAPL renewed circular CMP: (top) cracked SAPL after the test, and (b) crack pattern schematic, where black represents the shrinkage cracks, and red represents the generated cracks due to the load.

The existed longitudinal shrinkage cracks at both East and West haunch area, shown in Figure 4-93 (b), were closed out entirely. During the experiment, due to the applied vertical load, the haunches sections were subjected to compressive force which is evident in the strain gauges results presented in Figure 4-87. The applied compressive force cause crack closure at both sides of the pipe, which was not visible with naked eyes. Figure 4-94 illustrates the longitudinal crack closure at the West haunch of the SAPL, which shows that no sign of longitudinal crack after loading the SAPL-CMP system.

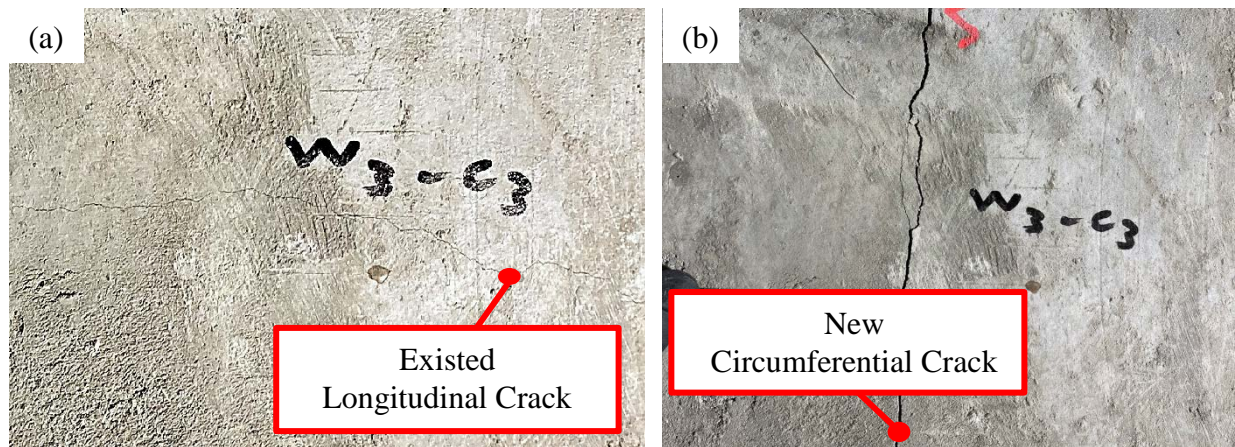


Figure 4-94. Crack closure at the West haunch area in the 3-in. thick SAPL renewed circular CMP: (a) before, and (b) after loading.

The averaged measured circumferential crack width at end of the test for the West and both East locations were 0.0336, 0.0386, and 0.0309 in. respectively, which shows that the generated circumferential cracks had an average crack width of 0.034 in. The DIP measurements for circumferential cracks are illustrated in Figure 4-95.

The longitudinal cracks on the invert locations are illustrated in Figure 4-96. The averaged crack width on the East gap of the invert-cut section was 0.165 in. This value for the West gap was 0.157 in. which is 0.01 in. smaller than the East crack.

The longitudinal cracks on the crown location are illustrated in Figure 4-97. The measurements were conducted at the center of the pipe and 15 in. offset towards the north location. The measurement showed that the crack width was about four times higher the center of the pipe. The crack width for the center and north side of the pipe were 0.4573 and 0.1306 in. respectively.

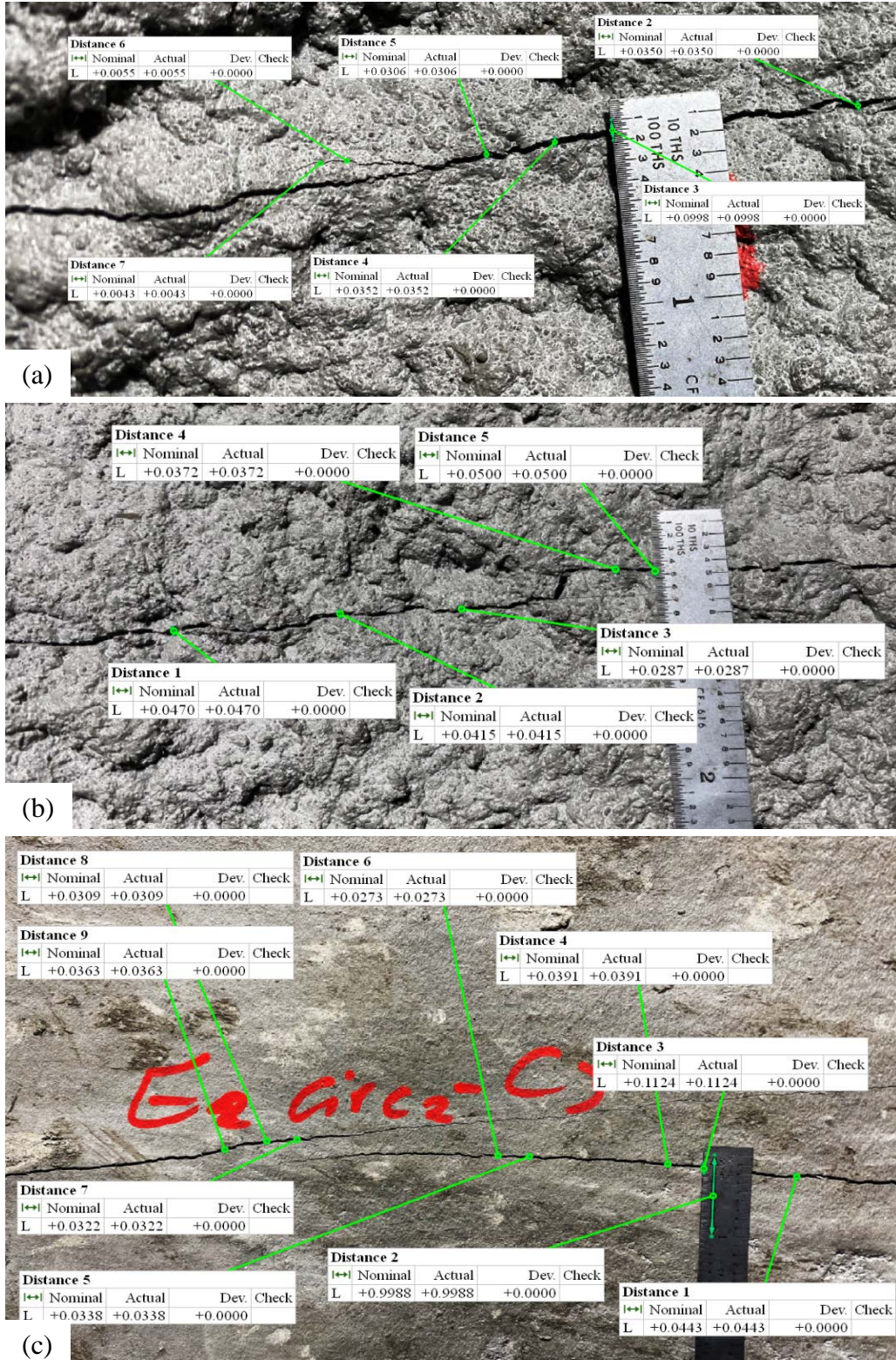


Figure 4-95. Circumferential cracks on 3-in. thick SAPL renewed invert-cut circular CMP at: (a) West side, (b) South East side, and (c) North East side of the pipe.

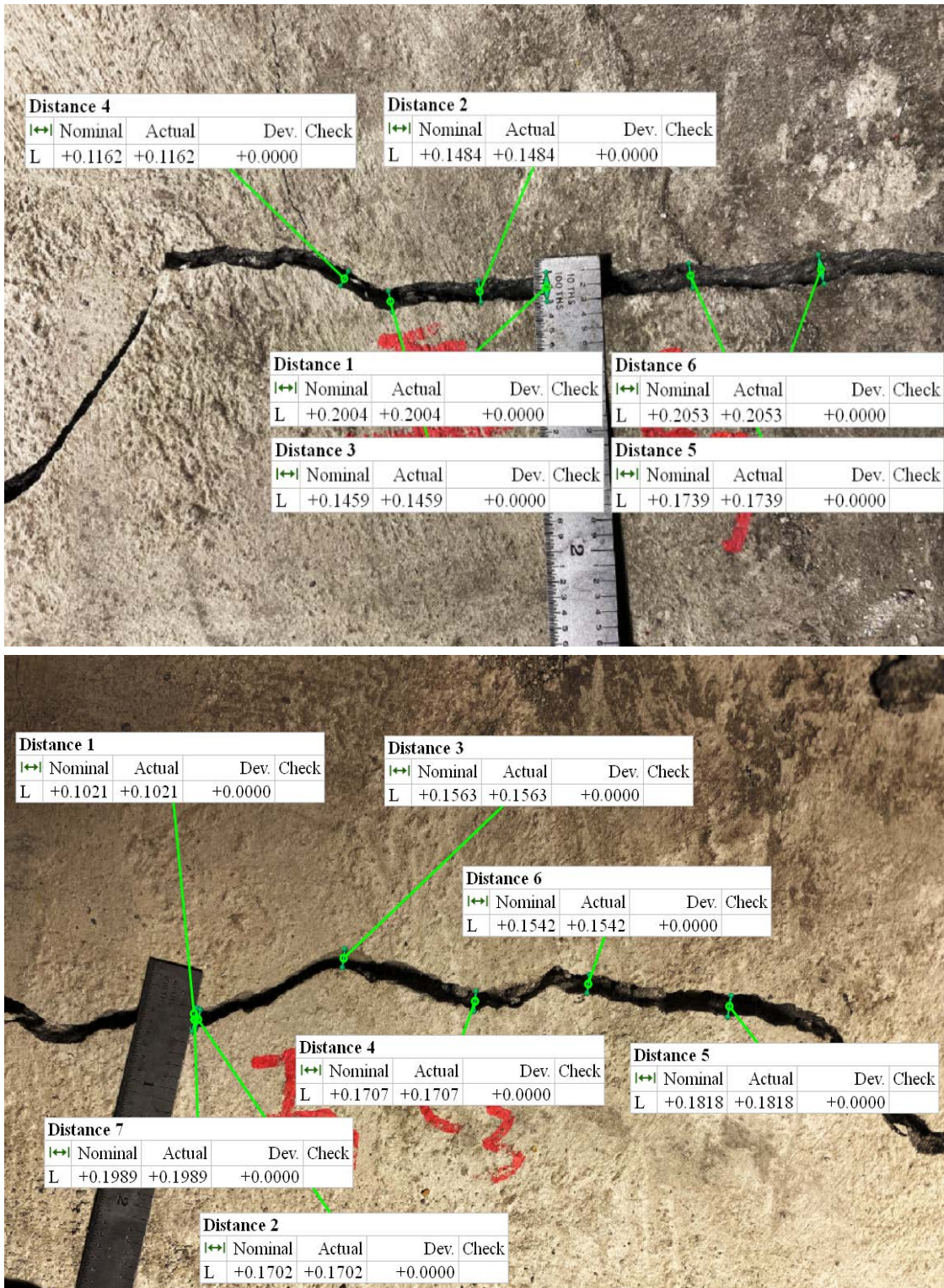


Figure 4-96. Longitudinal cracks on 3-in. thick SAPL renewed invert-cut circular CMP at: (top) West side, (b) East side of the invert section.

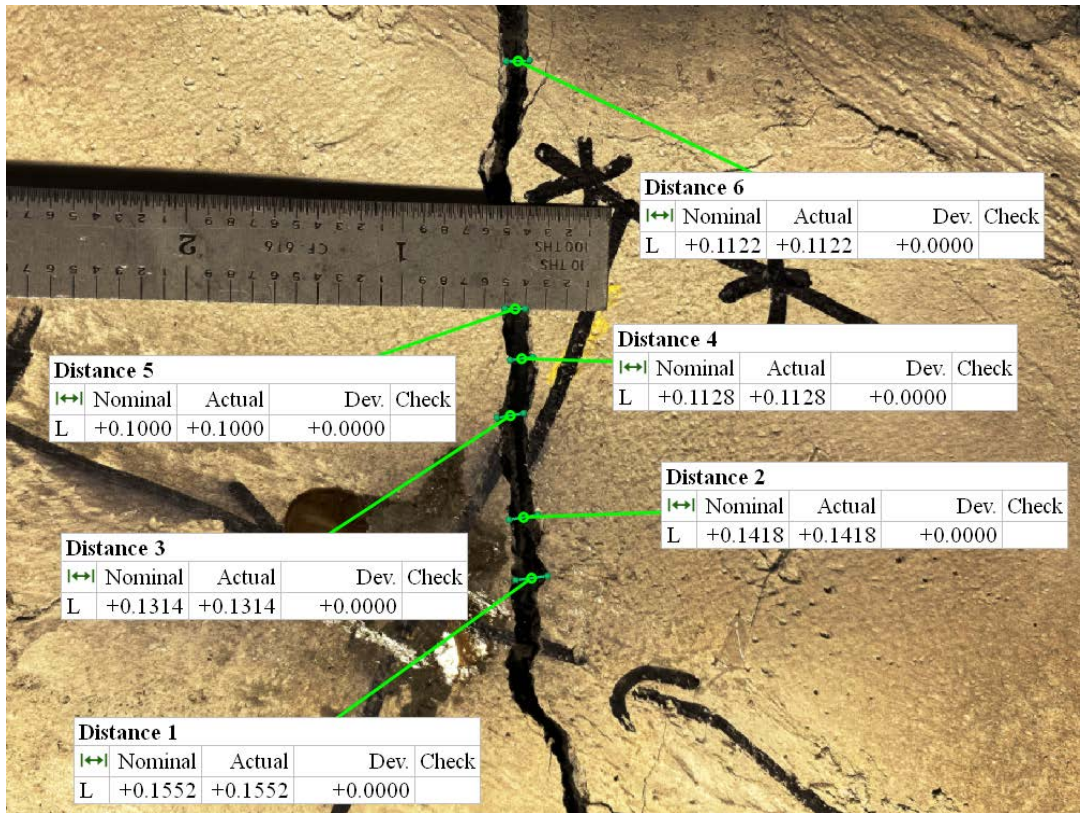
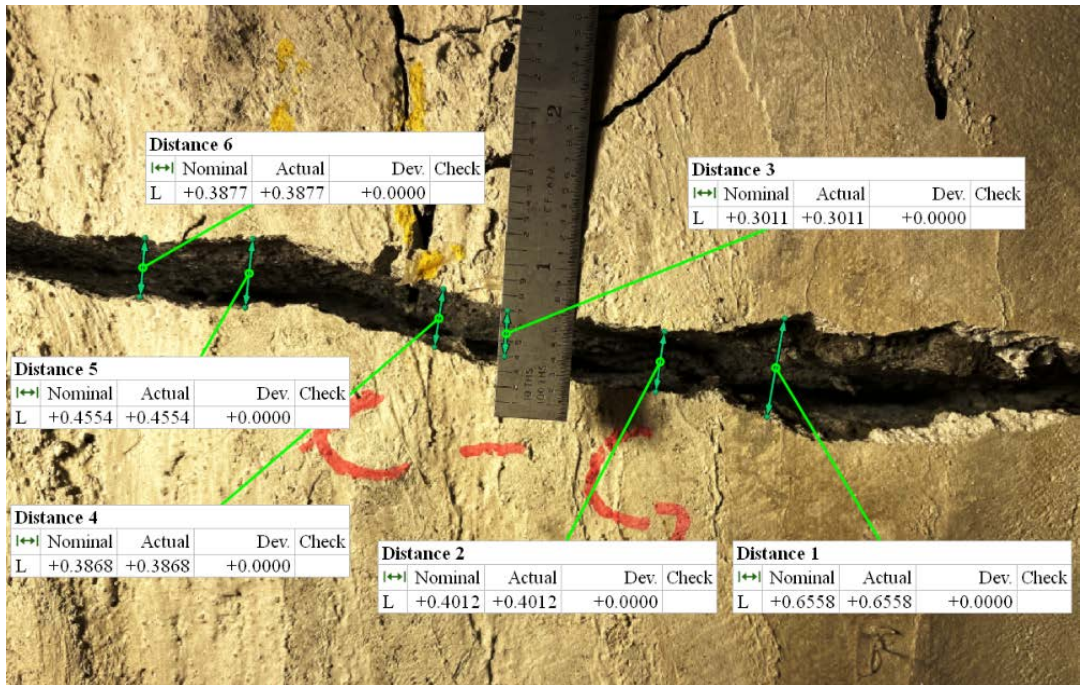


Figure 4-97. Longitudinal cracks on 3-in. thick SAPL renewed invert-cut circular CMP at: (top) center, (b) South side of the crown section.

4.2.3.1.2. Thickness Measurement

The thickness of the 3-in. thick cementitious SAPL renewed circular CMP were measured after the structural test and before exhumation as elaborated in section 3.4.6. The detailed result of the measurements is presented in Thickness Measurement Results. Figure 4-98 illustrates the thickness measurements results for all three locations along the length of the pipe (i.e., north, center and south). The results showed that the liner's thickness variation ranged from 1.5 to 3.6 in, which emphasizes on the superiority of centrifugal casting machine overt the hand sprayed method to provide uniform thickness in large thicknesses. The applied thickness was generally either higher or about the design thickness on the crown and both shoulder locations. However, the applied thickness was lower at the haunches and invert area. One of the possible reasons could be due to the troweling and finishing the surface of the half bottom portion of the pipe (i.e., from springline to springline) that either compressed or reduced the finished thickness.

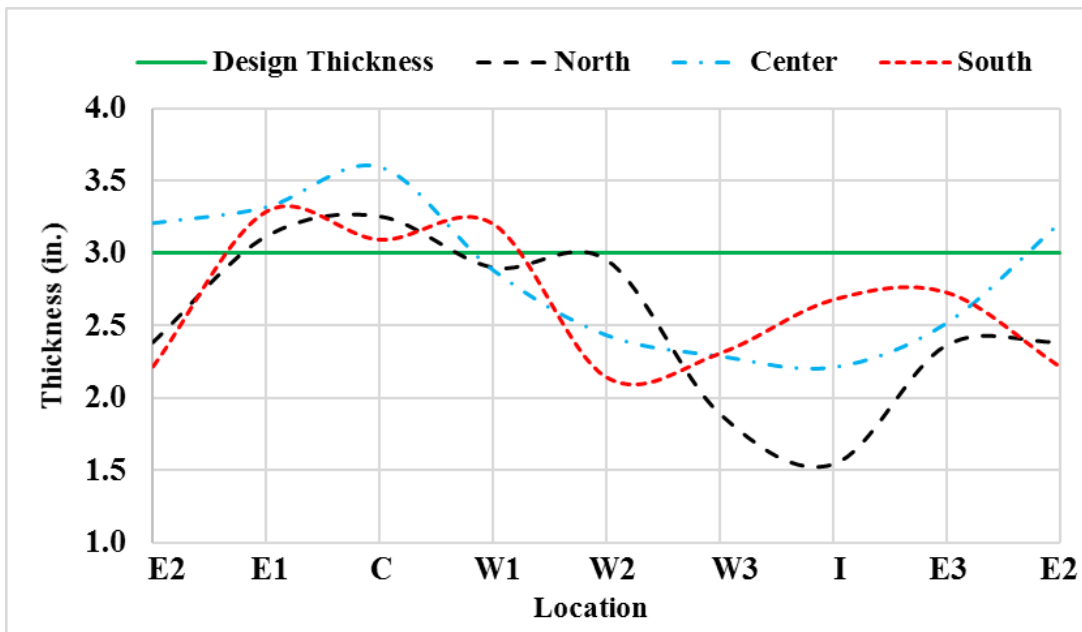


Figure 4-98. Thickness measurement for the 3-in. thick cementitious SAPL renewed circular CMP.

4.2.3.2. 2-in. Thick SAPL Sample

The 2-in. thick SAPL renewed invert-cut circular CMP was tested on July 29th, 2020, using the 20 × 40 in. load pad. The test duration was 6.38 hours. In this pipe sample, unlike the 3-in. thick sample, there was not shrinkage crack existed in the crown. The SAPL renewed CMP sample cracked at the crown in 14 kips of load and failed at the load of 85.42 kips with 8.5 in. of soil settlement. The failure occurred due to the large deflection and cracking of the crown. Figure 4-99 (a) and (b) illustrate the test sample at before and after loading stage. Once the SAPL-CMP system was failed, the test was continued until about 20% load drop. Then the test was terminated, as further deflection would increase the chance of liner detachment and fall, which would damage the mechanical sensors and cameras inside the pipe. Once the load was released from the soil surface, the pipe had an upward movement and relaxed. Figure 4-100, also illustrates the load and soil settlement graph, registered by the actuator's load cell and LDVT.

The earth pressure cell results registered the maximum pressure of 116.3 psi at the crown location, which was 10 psi higher than the 3 in. SAPL renewed sample. Once the ultimate load was reached, the earth pressure sensors failed to capture data thereafter. However, since the pressure was about to drop after the yield point and it occurred at the time of load drop registered by the actuator's load cell, it can be implied that the 116.3 psi was the maximum pressure that the pipe experienced over the crown. In addition, the value 116.3 is larger than the maximum surface pressure, which is 106.8 psi. The most probable reason could be due to the possible soil failure at the 80 kips of load which forms a prism-like failure plane under the pad and applies the load under a smaller surface that resulted in higher pressure reading of the earth pressure cell on top of the pipe. The maximum pressure applied on the West and East locations of the CMP were 10.2, and 5.93 psi respectively. Figure 4-101 illustrates earth pressure results for the invert-cut circular test.

Figure 4-102 illustrates the results of the mechanical sensors. The LVDT results show that the pipe was subjected to 4.727 in. of crown and 1.357 in. of springline deflection. The shoulder had 0.0566 in. downward movement. The CDS showed a similar result (4.589) as the crown LVDT. At the end of the test once the load was released from the surface a reversal movement in crown and springline for 0.159 and 0.0869 in. respectively, were observed.

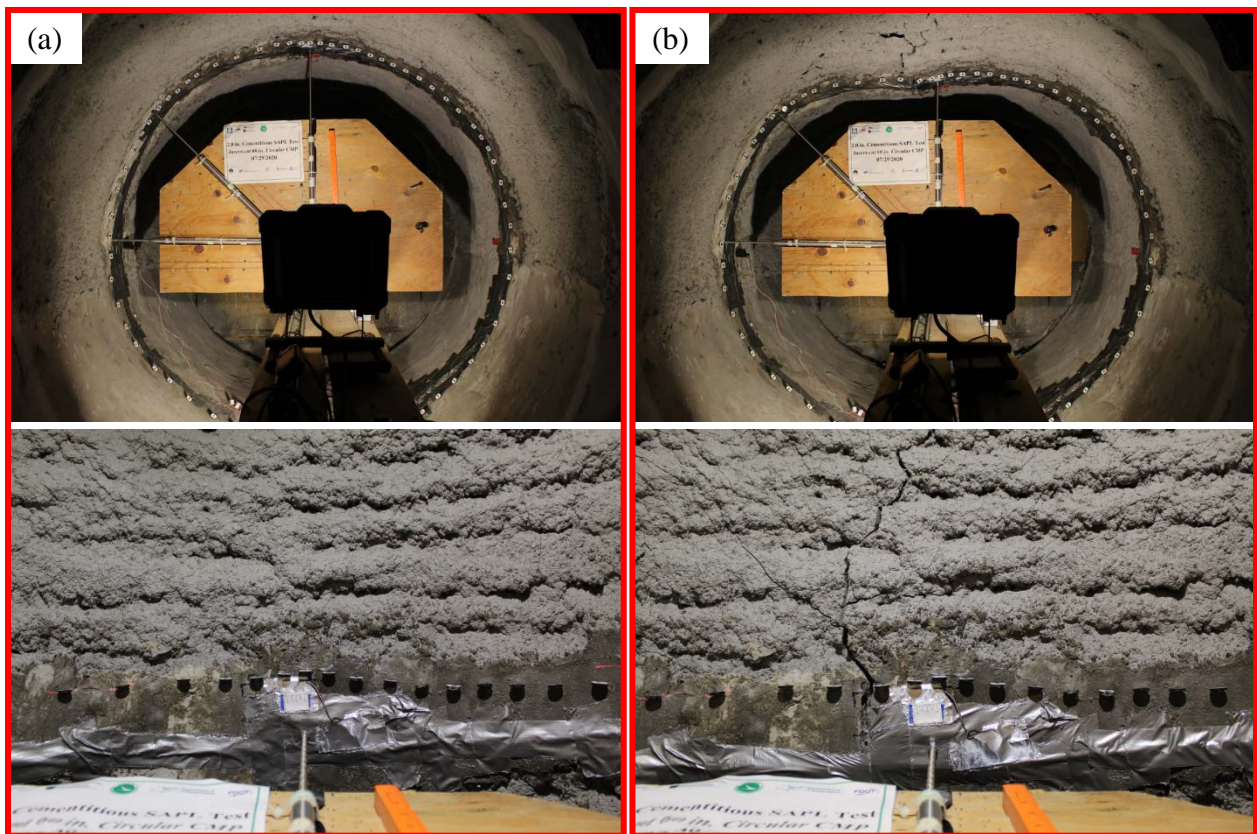


Figure 4-99. Invert-cut circular CMP renewed with 2 in. cementitious SAPL: (a) before loading, and (b) after loading.

The strain gauge results showed the SAPL was cracked at the invert on the crown with 14 kips of load. The West haunch (W3) experience a tensile strain at the load of 36.55 kips and it was subjected to compressive strain afterwards. This shows that the W3 location, illustrated Figure 4-103, is located on the transition zone as depicted in Figure 4-82. The crown of the CMP was the

first location that reached the steel yielding point (i.e., $1138 \mu\epsilon$) at the vertical load of 36.2 kips. The East springline and shoulder also yielded at 63.36, and 67.88 kips respectively. The West Shoulder of the CMP also yielded at 79.73 kips. No other location in the CMP reached the yield point.

Figure 4-104 illustrates the 2-in. thick SAPL renewed circular CMP profile before and after the applied static load. The pipe profile at end of the test clearly illustrates the pipe's ovality. In addition, the roughness and irregularity of the SAPL is explicitly evident in the profiling result. The comparison between the mechanical sensors and DIC are presented in Figure 4-105, which shows an excellent conformity with the CDS sensor.

The load-displacement values for soil surface, crown, springline, and shoulder of the 2-in. thick SAPL renewed circular CMP due to the applied static load is illustrates in Figure 4-106. The applied load on the soil surface versus its corresponding pressure at the crown of the renewed circular CMP are depicted in Figure 4-108, where the recursive part of the graph represents drop in both pressure and load at the same time.

During the load, the width of the crack on the crown was monitored using DIP method. Figure 4-107 illustrates the crack width different stage of the applied load on the soil surface. The first crack formed on the crown at the load of 14 kips. The averaged crack width at this load was 0.01557 in. The SAPL at the time of failure (i.e., stage 7) had the averaged 0.1405 in. crack width. This value is about 9 times higher than the crack width at the time of formation (i.e., stage 2). The crack width at the time of failure was further increased by 87.68% in the stage 8, where the test was terminated. The DIP results and pictures for the crown's crack measurement of the circular CMPs are provided in Crown Crack Width Measurement for Circular CMP Samples.

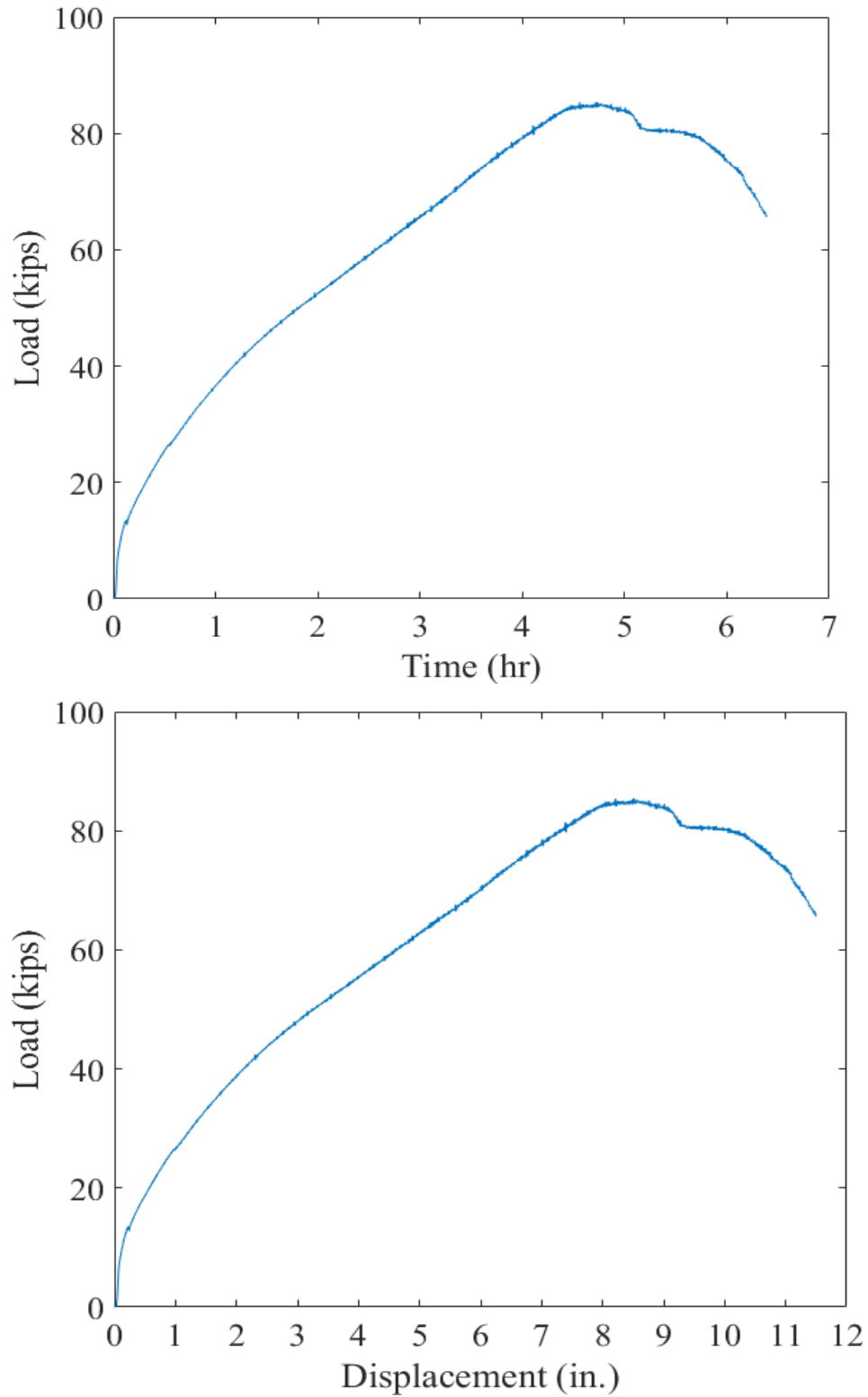


Figure 4-100. Invert-cut circular CMP renewed with 2-in. thick cementitious SAPL subjected to static live load: (top) load-time and, (bottom) load-soil displacement graphs.

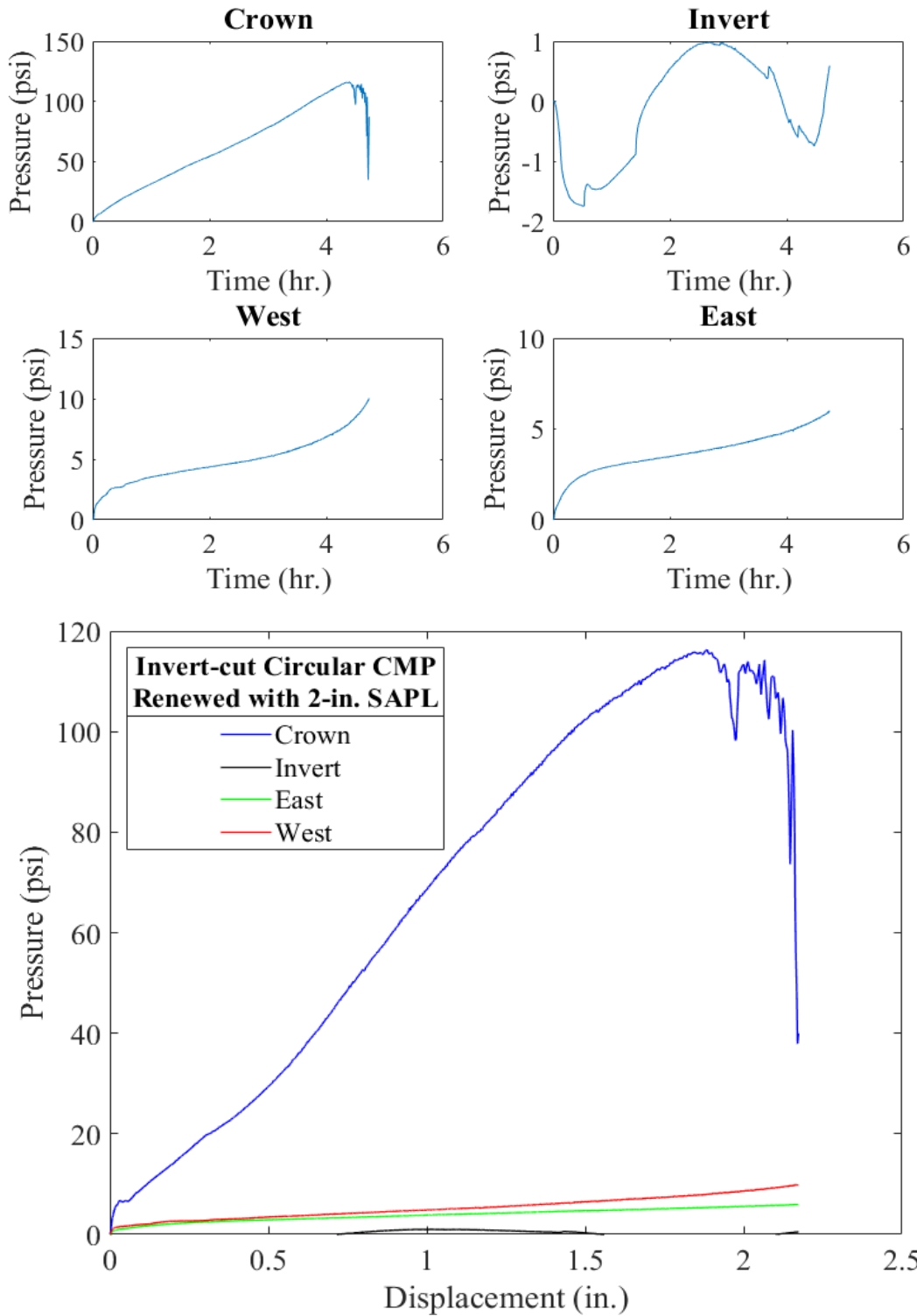


Figure 4-101. Earth pressure cell results for the 2-in. thick SAPL renewed invert-cut circular CMP with respect to: (top) time, and (bottom) crown displacement.

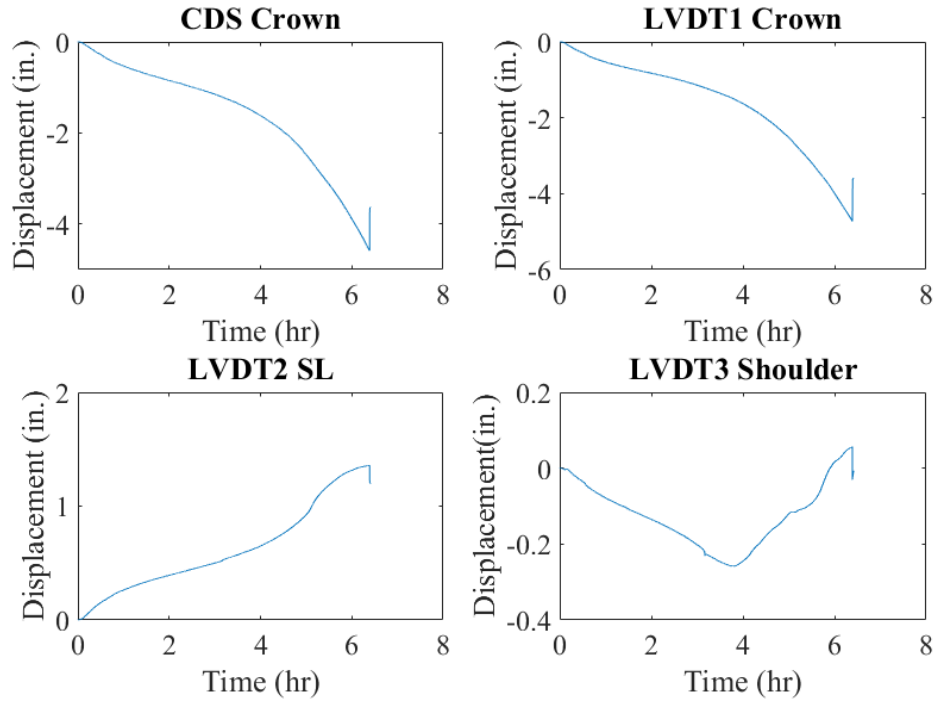


Figure 4-102. Mechanical sensors result for 2-in. thick SAPL renewed invert-cut circular CMP.

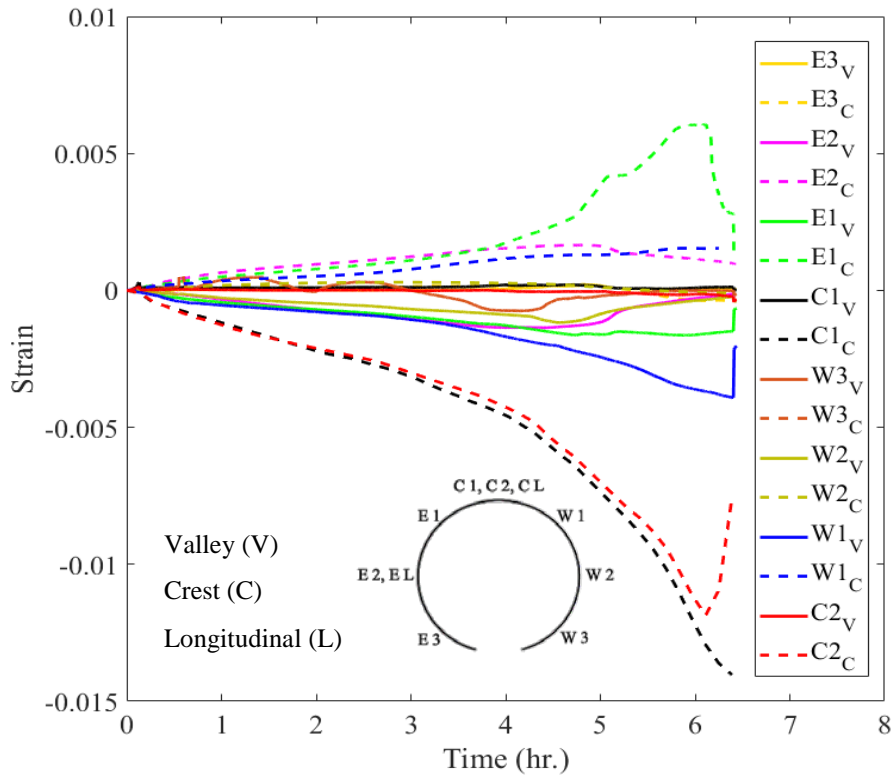
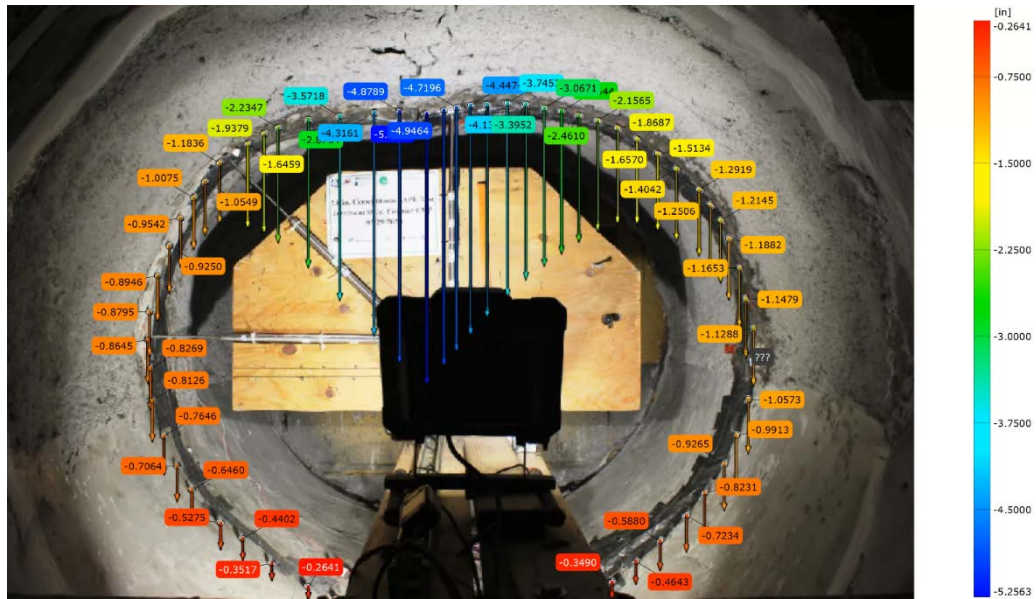


Figure 4-103. Strain gauges result for 2-in. thick SAPL renewed invert-cut circular CMP.



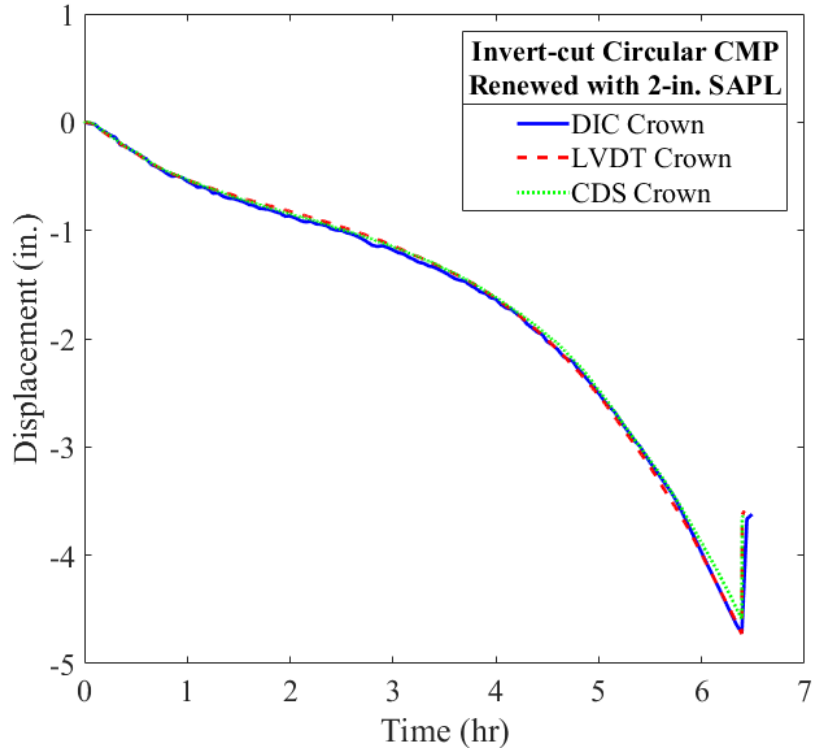


Figure 4-105. DIC method verification with mechanical sensors for the 2-in. thick SAPL renewed invert-cut circular CMP.

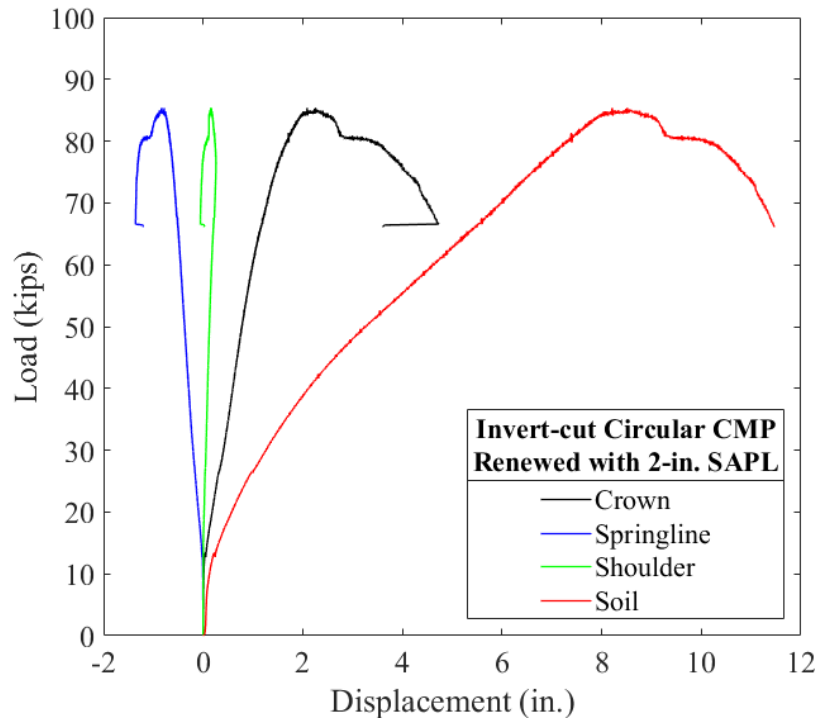


Figure 4-106. Load vs. displacement of the soil surface, crown, springline, and shoulder of the 2-in. thick SAPL renewed invert-cut circular CMP due to the applied static load.

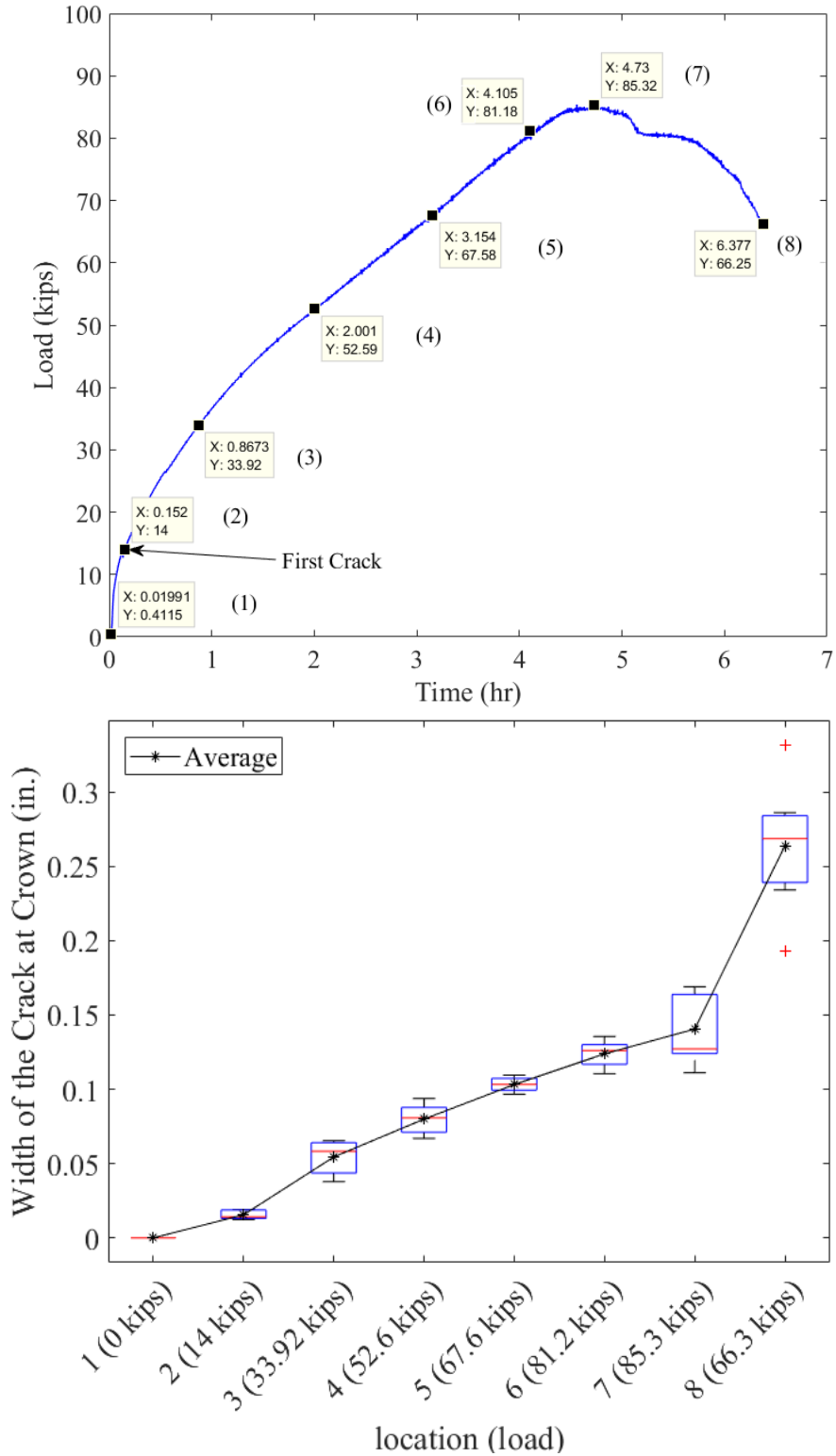


Figure 4-107. Crack width measurement for the crown location at during the applied live load on the soil surface for the 2-in. thick SAPL renewed invert-cut circular CMP.

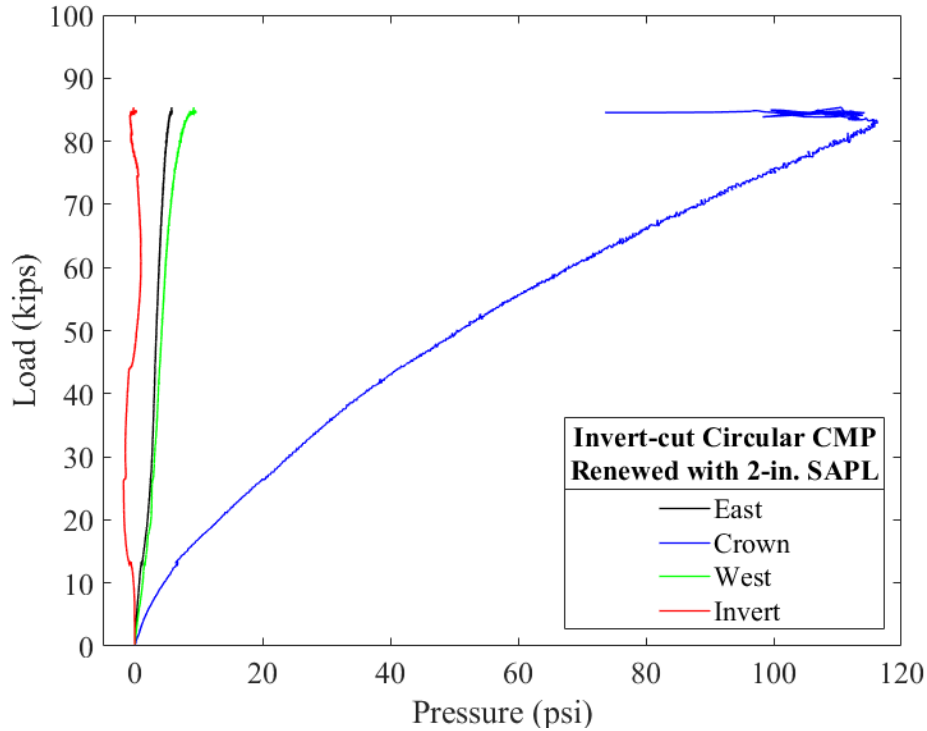


Figure 4-108. Load vs. pressure for the 2-in. thick SAPL renewed invert-cut circular CMP.

4.2.3.2.1. Post Failure Crack Measurement

Visual inspection was conducted after the test and crack width measurement were carried out using DIP method. Figure 4-109 (a) illustrates the 2-in. SAPL renewed invert-cut circular CMP and Figure 4-109 (b) shows the crack pattern schematic inside the pipe. Similar to the 3-in. SAPL renewed invert-cut circular CMP sample, three major longitudinal cracks were observed on the invert and crown of the SAPL. In addition, two circumferential cracks were observed on both East and West side of the pipe. The circumferential cracks were propagated from shoulder to the haunch area. However, in the contrast with the 3-in. thick sample, the longitudinal cracks on the haunch area did not close out, and the section remained cracked.

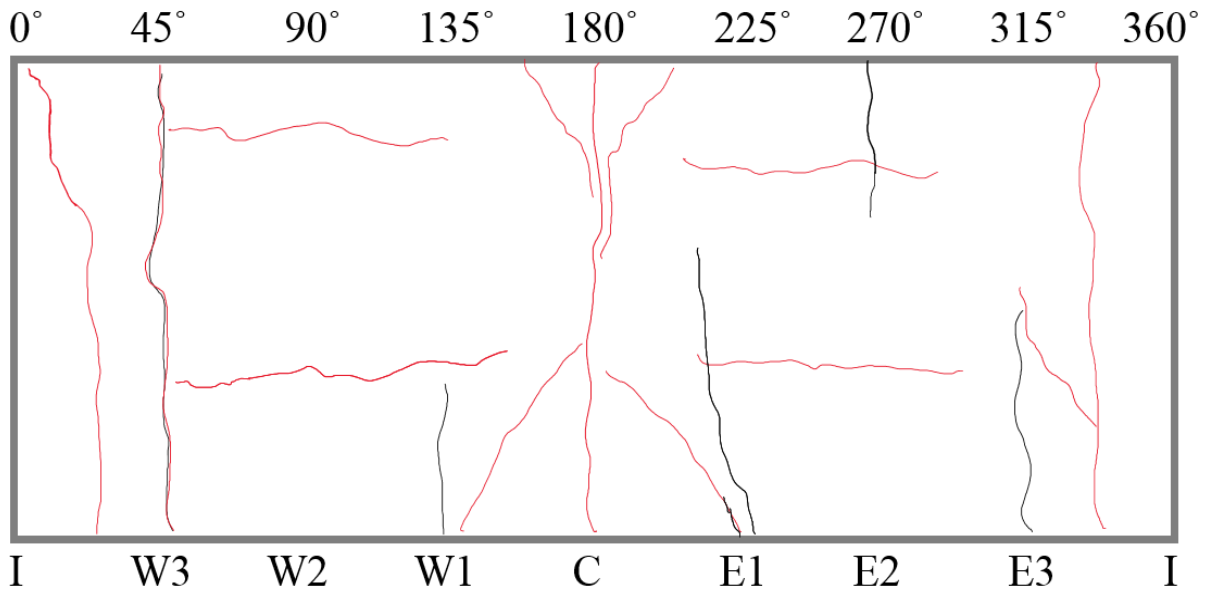


Figure 4-109. Visual inspection of the 2-in. thick SAPL renewed circular CMP: (top) cracked SAPL after the test, and (b) crack pattern schematic, where black represents the shrinkage cracks, and red represents the generated cracks due to the load.

The averaged measured circumferential crack width at end of the test for the West and East locations were 0.0267, and 0.0329 in. respectively. The DIP measurements for circumferential cracks are illustrated in Figure 4-110.

The longitudinal cracks at the East and West haunch area had the averaged width of 0.01934 and 0.0055 in, as illustrated in Figure 4-111. The West haunch longitudinal crack was existed before the load application, where the crack width was 0.01228 in. Therefore, the vertical load reduced the crack width for about 55%.

The longitudinal cracks on the invert locations are illustrated in Figure 4-112. The averaged crack width on the East gap of the invert-cut section was 0.03 in. This value for the West gap was 0.0601 in. which is 0.03 in. larger than the East crack.

The longitudinal cracks on the crown location are illustrated in Figure 4-113. The measurements were conducted at the center of the pipe. The measurement showed that the crack width was about seven times higher the invert crack of the pipe. The crack width for the crown at the center of the pipe was 0.4210 in. respectively.

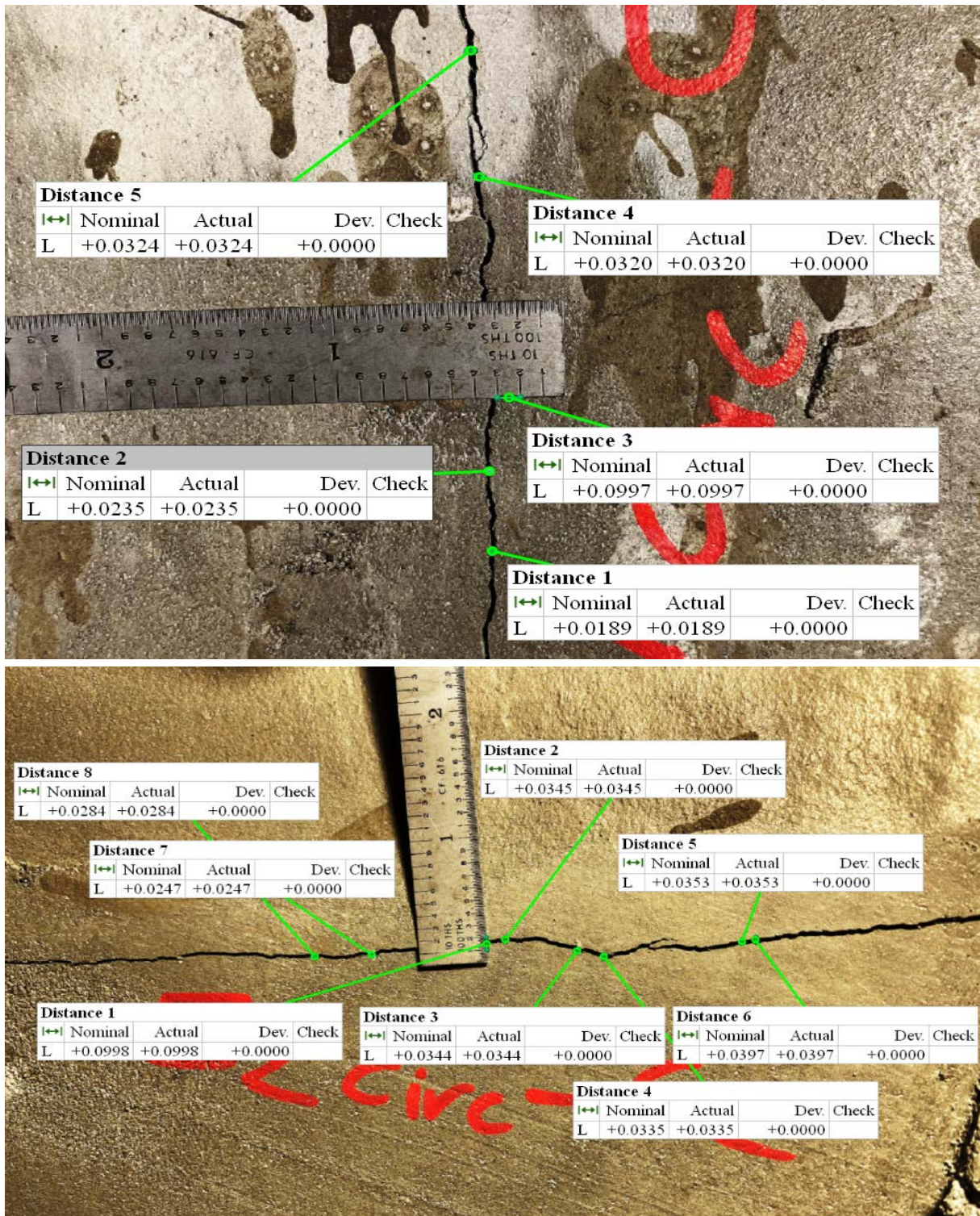


Figure 4-110. Circumferential cracks on 2-in. thick SAPL renewed invert-cut circular CMP at: (top) West side, and (bottom) East side of the pipe.

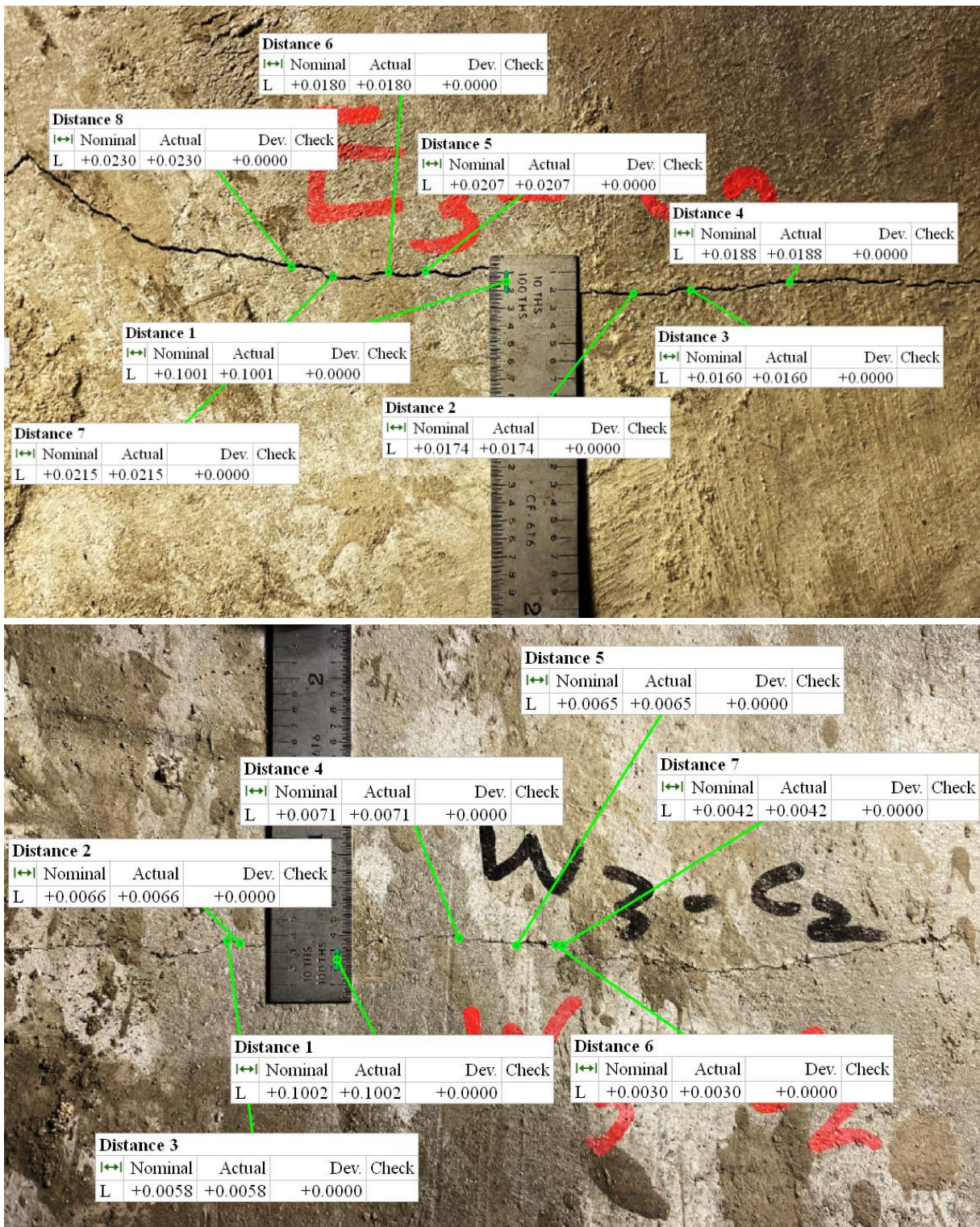


Figure 4-111. Longitudinal cracks on 2-in. thick SAPL renewed invert-cut circular CMP at: (top) East side, and (bottom) West side of the pipe.

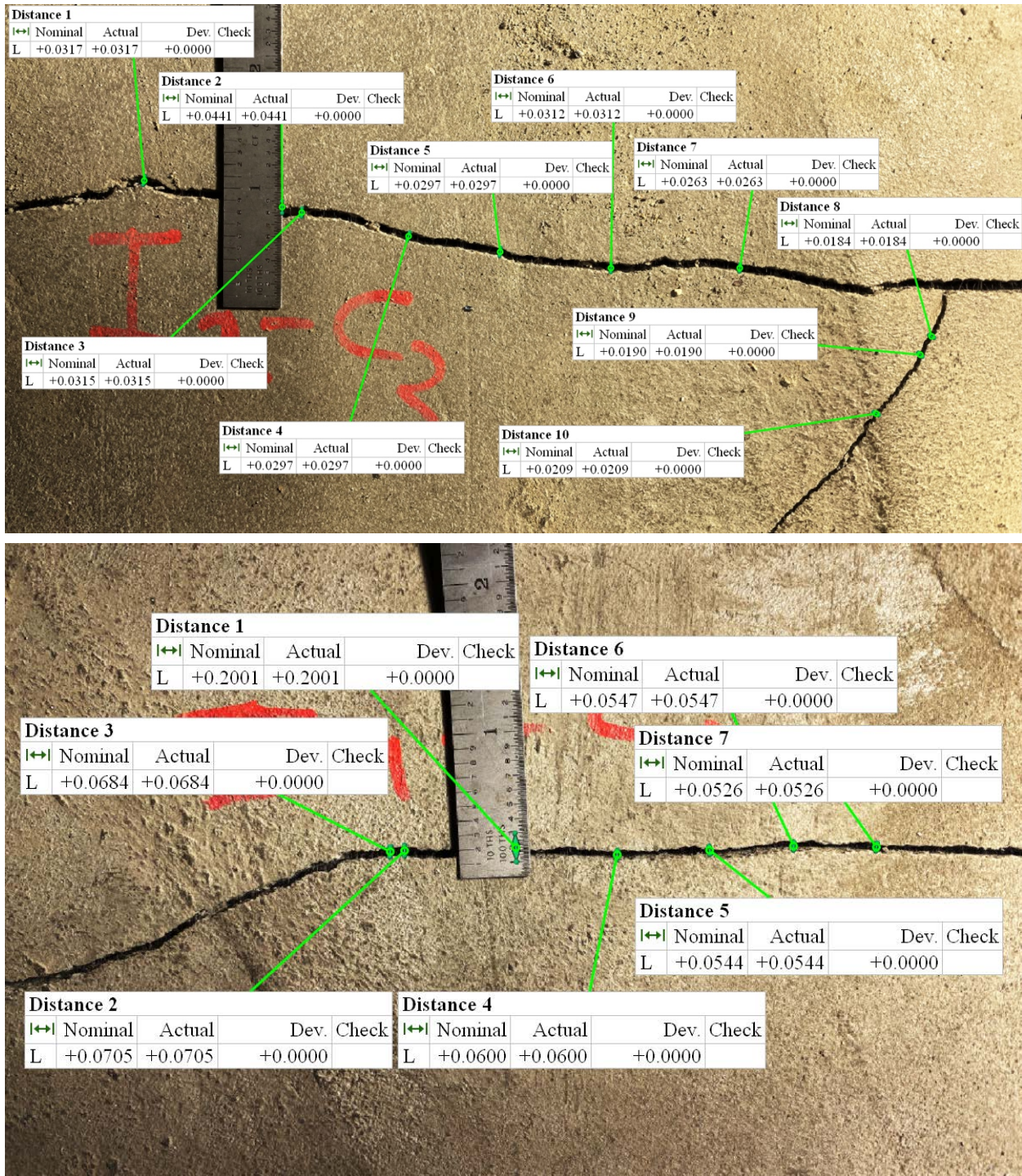


Figure 4-112. Longitudinal cracks on 2-in. thick SAPL renewed invert-cut circular CMP at: (top) East side, and (bottom) West side of the invert gaps.

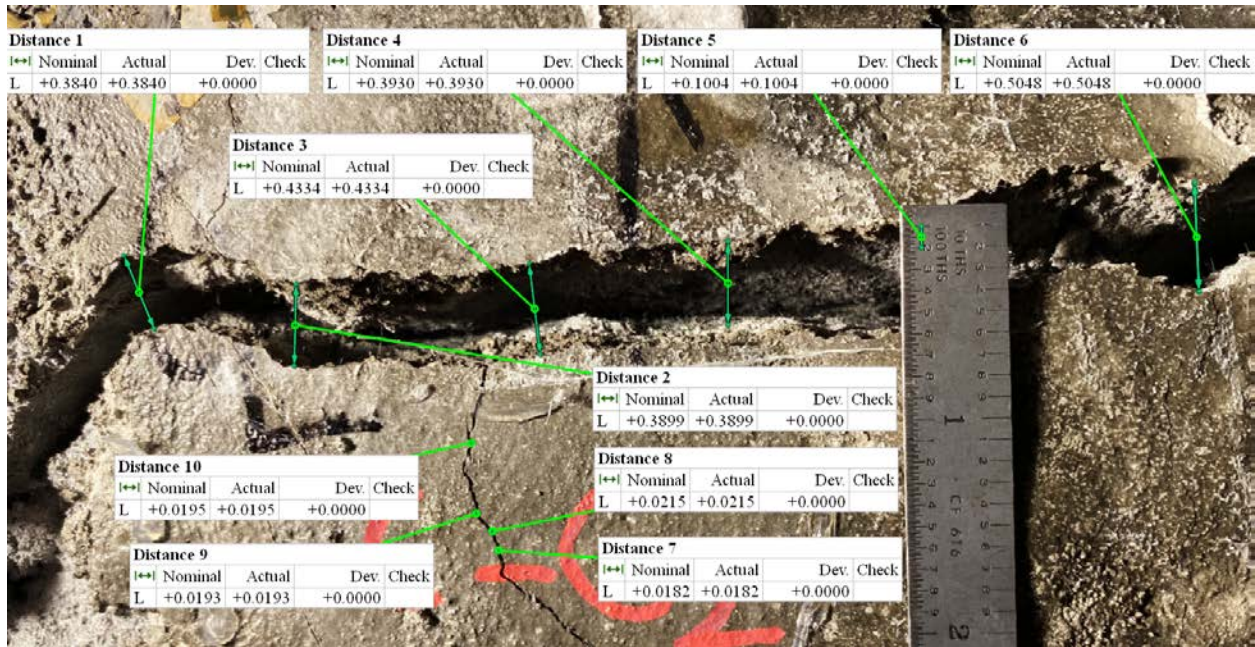


Figure 4-113. Longitudinal crack at the center of the pipe for 2-in. thick SAPL renewed invert-cut circular CMP.

4.2.3.2.2. Thickness Measurement

The thickness of the 2-in. thick cementitious SAPL renewed circular CMP were measured after the structural test and before exhumation as elaborated in section 3.4.6. The detailed result of the measurements is presented in APPENDIX E. Figure 4-114 illustrates the thickness measurements results for all three locations along the length of the pipe (i.e., north, center and south). The results showed that the liner's thickness variation ranged from 1.5 to 2.6 in. Except the West springline, the applied thickness was generally either higher or about the design thickness in all sections of the pipe. Similar to the 3-in thick SAPL, the applied SAPL was thicker on the crown and both shoulders, which can be due to the importance of this section that entices the attention of the applicator to this section more than the other locations.

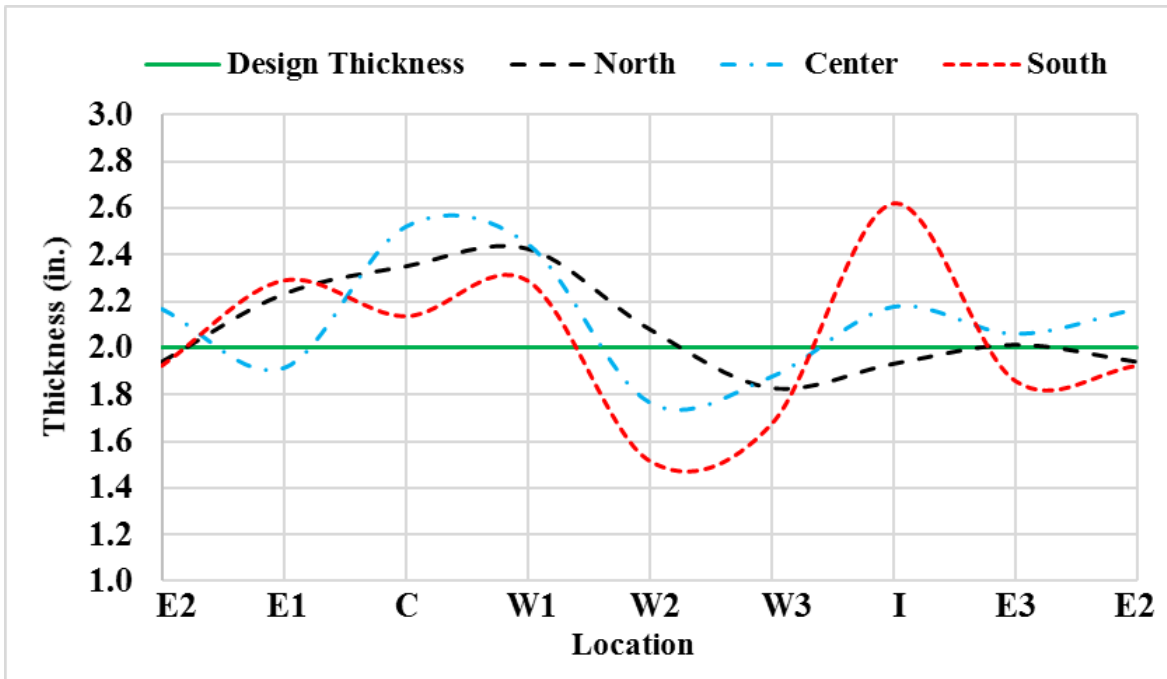


Figure 4-114. Thickness measurement for the 2-in. thick cementitious SAPL renewed circular CMP.

4.2.3.3. 1-in. Thick SAPL Sample

The 1-in. thick SAPL renewed invert-cut circular CMP was tested on July 31th, 2020, using the 20 × 40 in. load pad. The test duration was 5.283 hours. In this pipe sample, unlike the 3-in. thick sample, there was not shrinkage crack existed in the crown. The SAPL renewed CMP sample cracked at the crown in 10 kips of load and failed at the load of 71.76 kips with 8.05 in. of soil settlement. The failure occurred due to the large deflection and multiple cracks at the crown location. Figure 4-115 (a) and (b) illustrate the test sample in before and after loading stage. Once the SAPL-CMP system was failed, the test was continued until about 20% load drop. Then the test was terminated, as further deflection would increase the chance of liner detachment and fall, which would damage the mechanical sensors and cameras inside the pipe. Once the load was released from the soil surface, the pipe had an upward movement and relaxed. Figure 4-116, also illustrates the load and soil settlement graph, registered by the actuator's load cell and LDVT.

The earth pressure cell results registered the maximum pressure of 102.2 psi at the crown location, which was 14 psi lower than the 2 in. SAPL renewed sample. The maximum pressure applied on the West and East locations of the CMP were 8.66, and 10.93 psi, respectively. In this test, immature soil failure was not observed. Figure 4-117 illustrates earth pressure results for the invert-cut circular test.

Figure 4-118 illustrates the results of the mechanical sensors including LVDT and CDS. The LVDT results show that the pipe was subjected to 3.889 in. of crown and 1.1133 in. of springline deflection. The shoulder had 0.055 in. downward movement. The CDS showed a similar result (3.862) as the crown LVDT. At the end of the test, once the load was released from the soil-pipe system, a reversal movement in crown and springline for 1.07 and 0.1582 in. were observed.

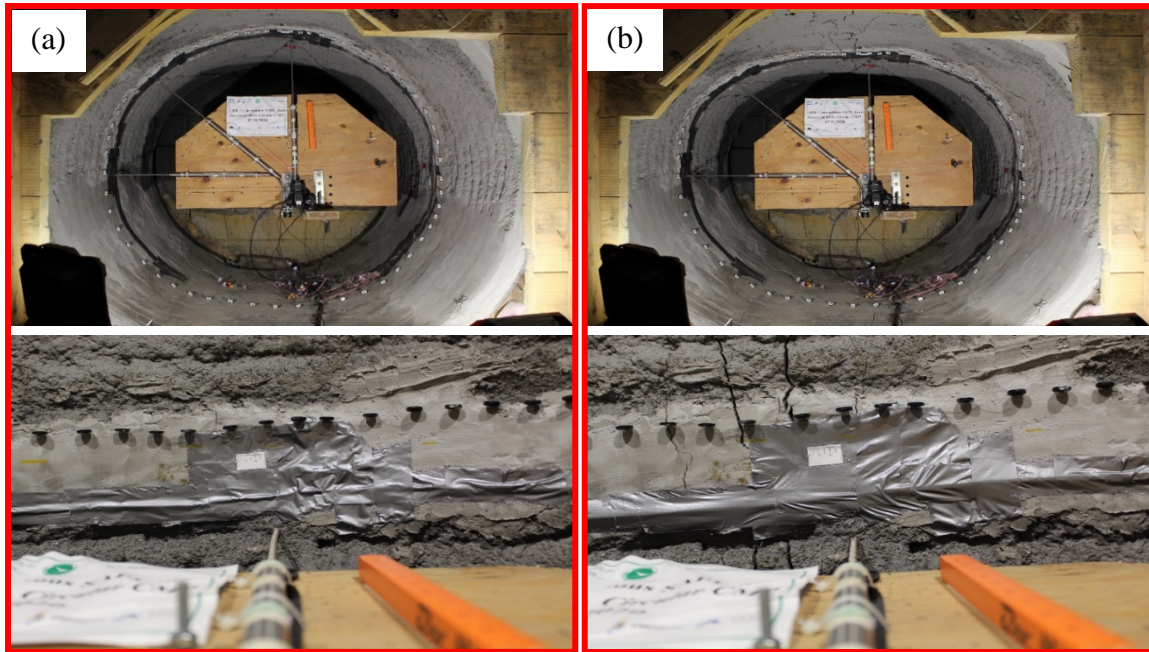


Figure 4-115. Invert-cut circular CMP renewed with 1 in. cementitious SAPL: (a) before loading, and (b) after loading.

The strain measurement results of the CMP and SAPL are presented in Figure 4-119. The strain gauge results showed the SAPL was cracked at the crown with 10.42 kips of load. The West haunch (W3) were cracked at the load of 18.84 kips which increased the tensile strain value of the host pipe's (i.e., CMP) West haunch area. Similar situation also occurred for the East haunch of the SAPL, which cracked with 22.74 kips of load. It is noteworthy that from the strain gauge results, cracking load estimation of the invert section were not possible. The crown of the CMP was the first location that reached the steel yielding point (i.e., $1138 \mu\epsilon$) at the vertical load of 20.52 kips. The West haunch was the next location that yielded at the load of 38.99 kips. Eventually, East shoulder was the last location that yielded at the load of 66.95 kips. It should be noted that in this test the strain gauge sensors at the locations W1 and W2 were damaged.

Figure 4-120 illustrates the 1-in. thick SAPL renewed circular CMP profile before and after the applied static load. The pipe profile at end of the test clearly illustrates the pipe's ovality. In

addition, the roughness and irregularity of the SAPL is explicitly evident in the profiling result. The comparison between the mechanical sensors and DIC are presented in Figure 4-121, which shows an excellent conformity with the CDS sensor.

The load-displacement values for soil surface, crown, springline, and shoulder of the 1-in. thick SAPL renewed circular CMP due to the applied static load is illustrates in Figure 4-122. The applied load on the soil surface versus its corresponding pressure at the crown of the renewed circular CMP are depicted in Figure 4-123, where the recursive part of the graph represents drop in both pressure and load at the same time.

During the loading process, width of the crack formed on the crown SAPL was monitored using DIP method. Figure 4-123 illustrates the crack width different stage of the applied load on the soil surface. The first coherent longitudinal crack formed on the crown at the load of 10 kips. The averaged crack width at this load was 0.01767 in. The SAPL at the time of failure (i.e., stage 7) had the averaged 0.1336 in. crack width. Direct comparison between the failure crack (i.e., stage 7) and the existed shrinkage crack at stage 1, shows the crack was widened 997%. The crack width at the time of failure was further increased by 13.92% at the stage 8, where the test was terminated. The DIP results and pictures for the crown's crack measurement of the circular CMPs are provided in Crown Crack Width Measurement for Circular CMP Samples.

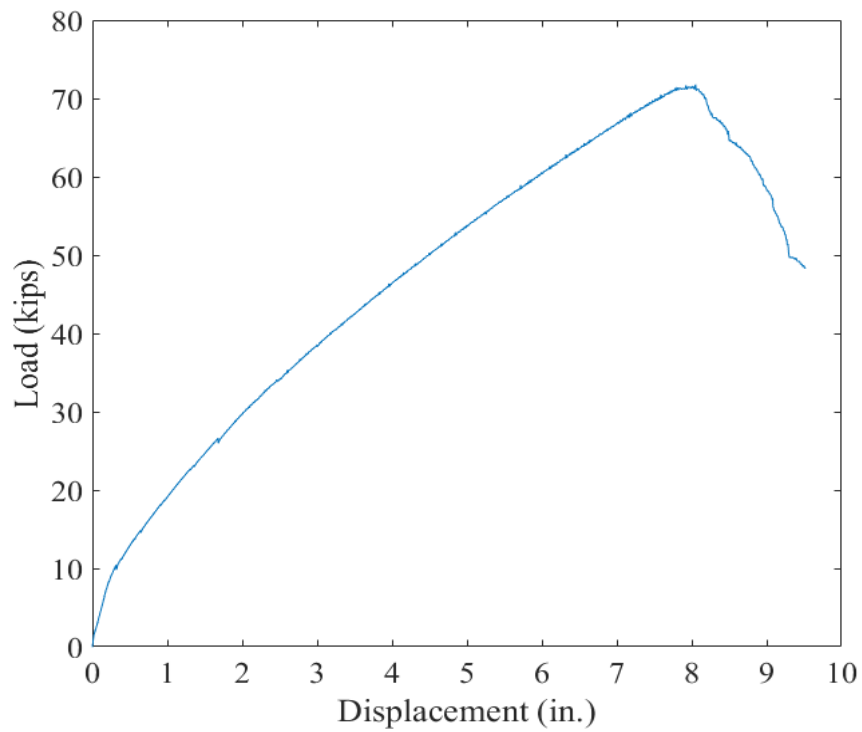
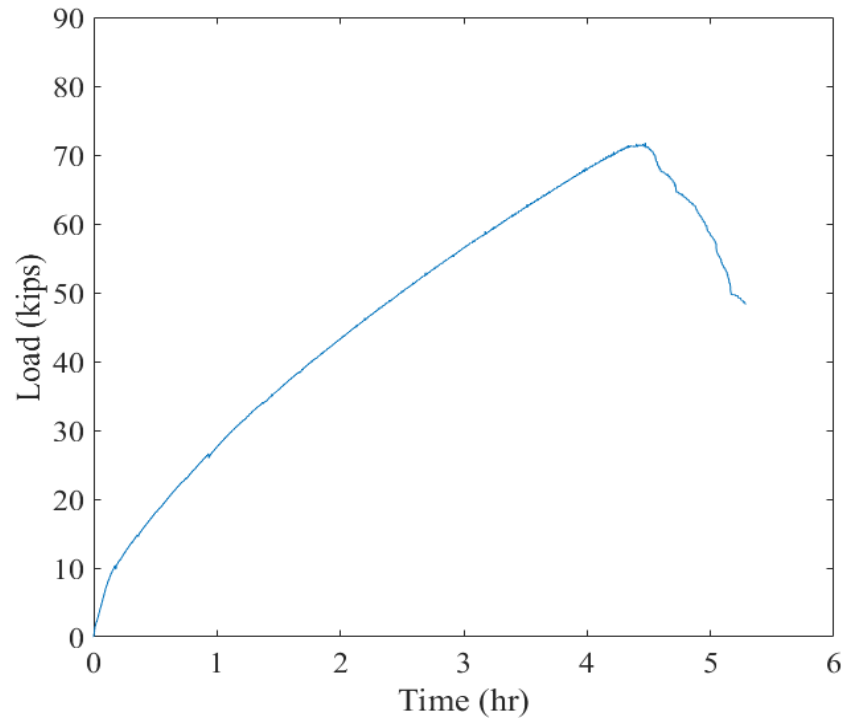


Figure 4-116. Invert-cut circular CMP renewed with 1-in. thick cementitious SAPL subjected to static live load: (top) load-time and, (bottom) load-soil displacement graphs.

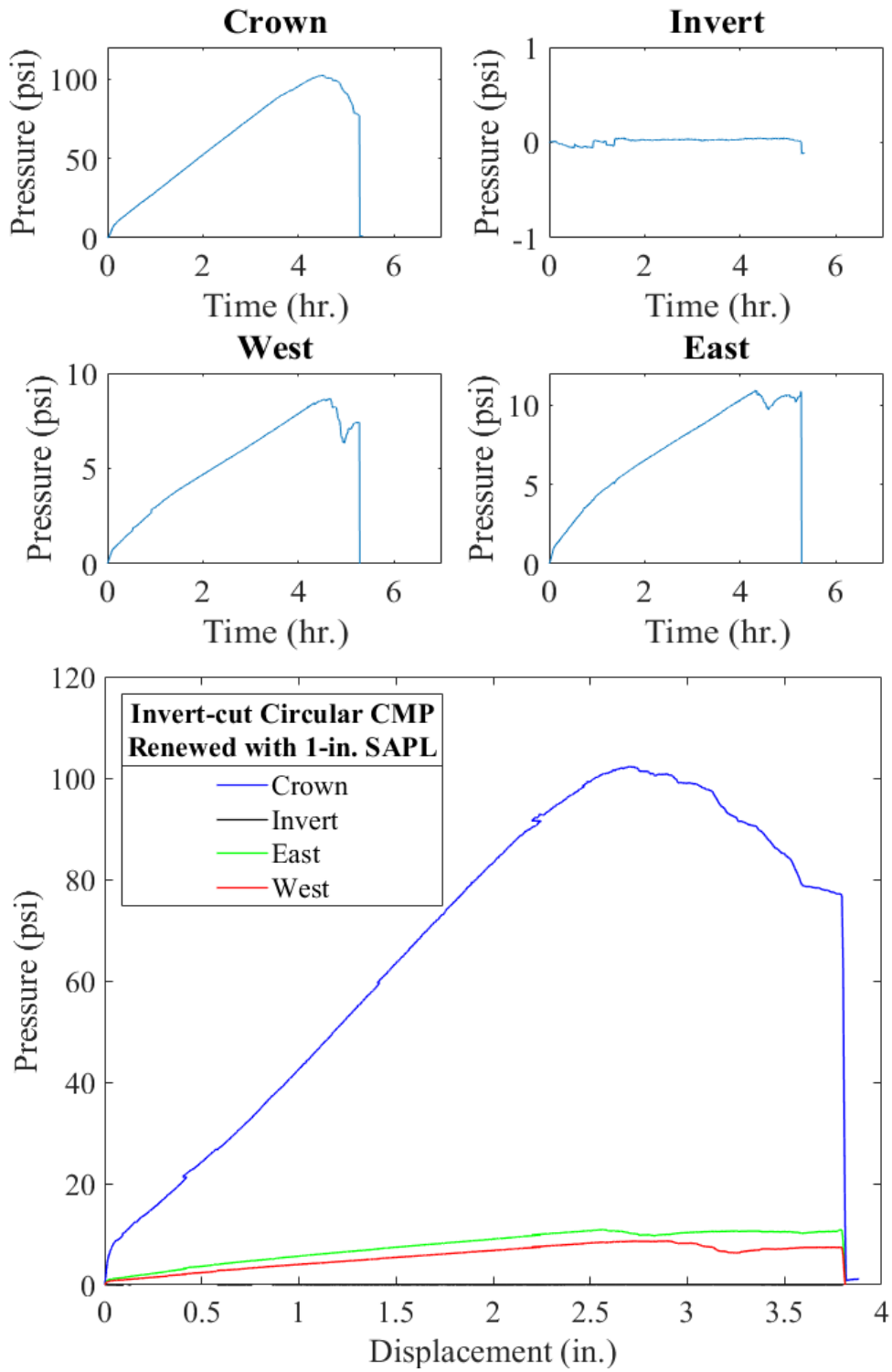


Figure 4-117. Earth pressure cell results for the 1-in. thick SAPL renewed invert-cut circular CMP with respect to: (top) time, and (bottom) crown displacement.

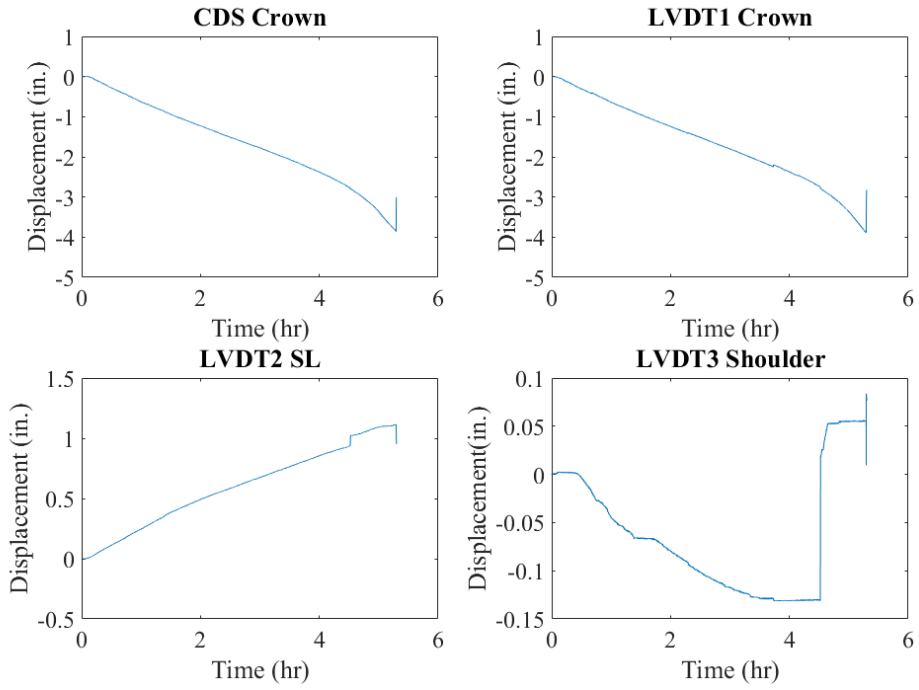


Figure 4-118. Mechanical sensors result for 1-in. thick SAPL renewed invert-cut circular CMP.

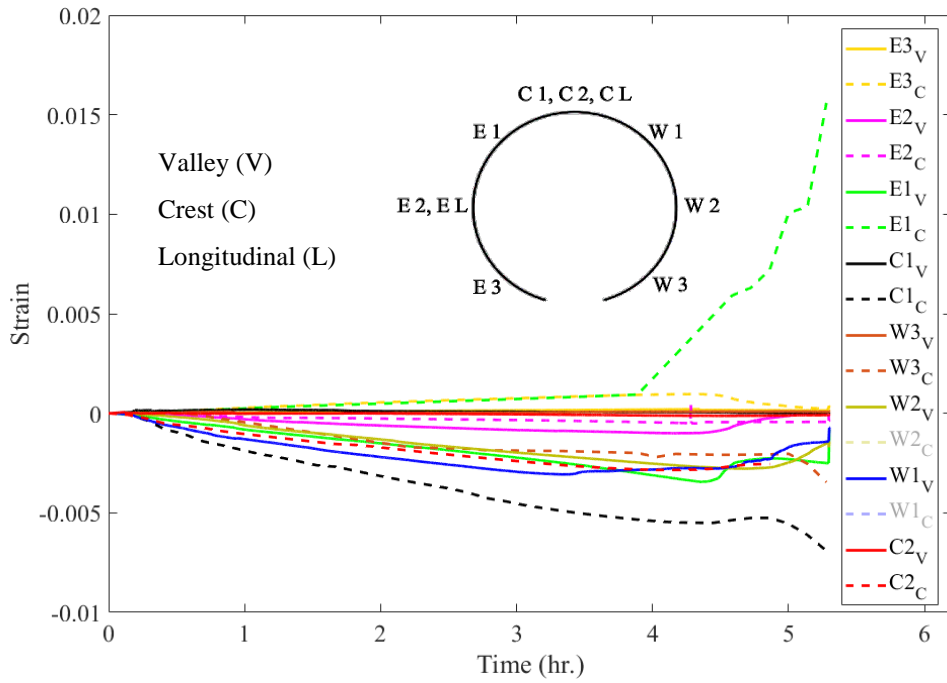


Figure 4-119. Strain gauges result for 1-in. thick SAPL renewed invert-cut circular CMP.

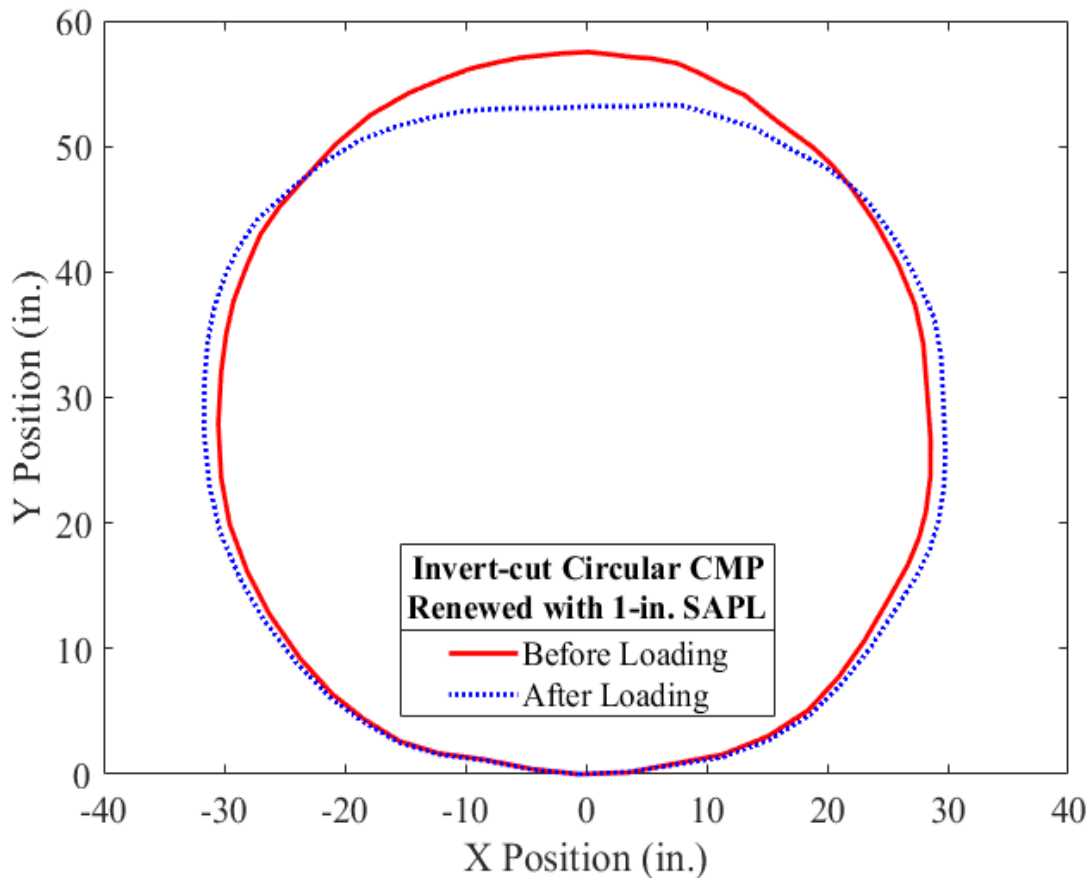
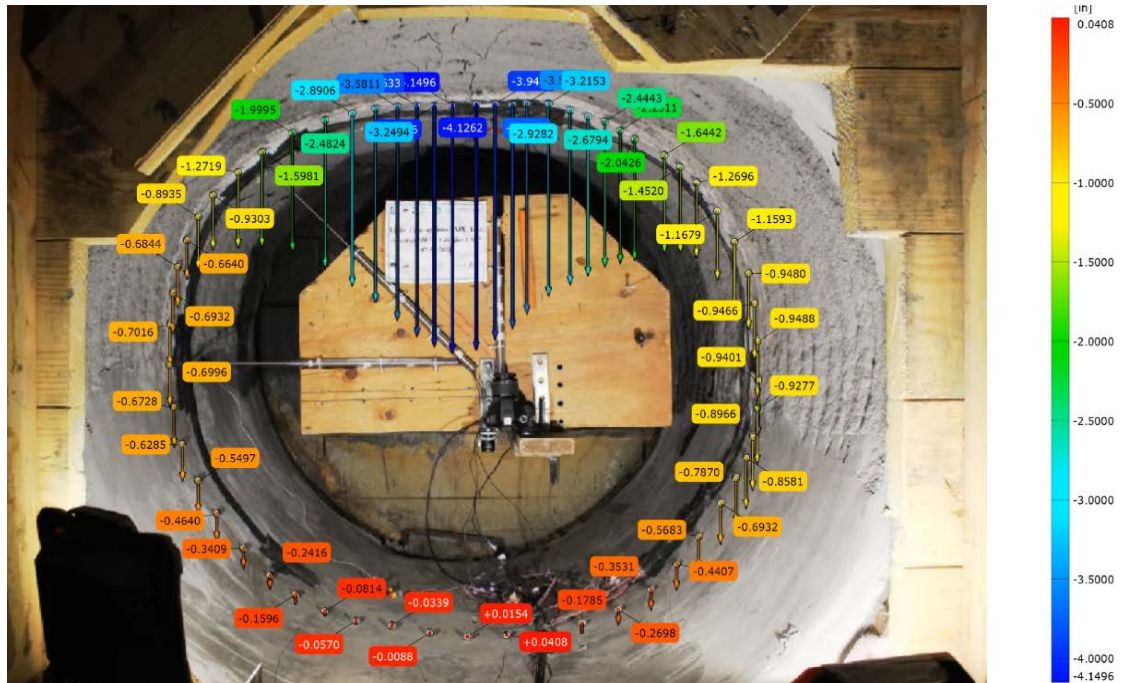


Figure 4-120. Pipe profiling using DIC for the 1-in. thick SAPL renewed invert-cut circular CMP.

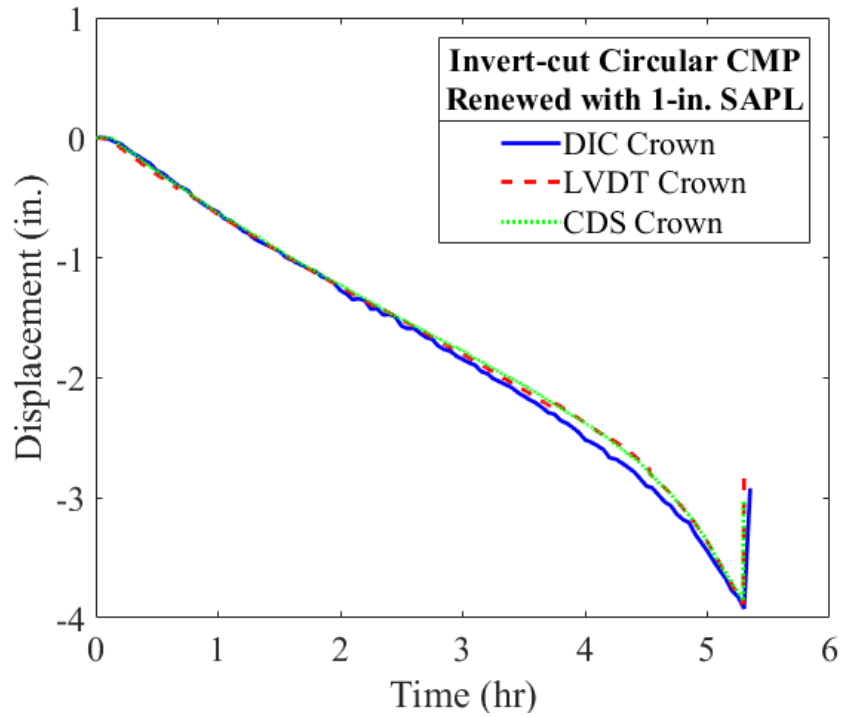


Figure 4-121. DIC method verification with mechanical sensors for the 1-in. thick SAPL renewed invert-cut circular CMP.

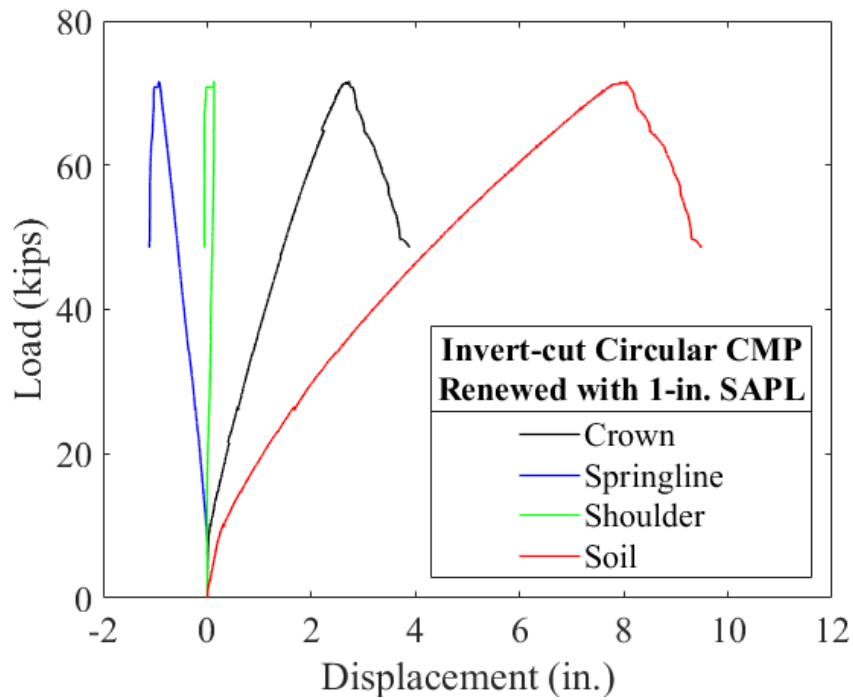


Figure 4-122. Load vs. displacement of the soil surface, crown, springline, and shoulder of the 1-in. thick SAPL renewed invert-cut circular CMP due to the applied static load.

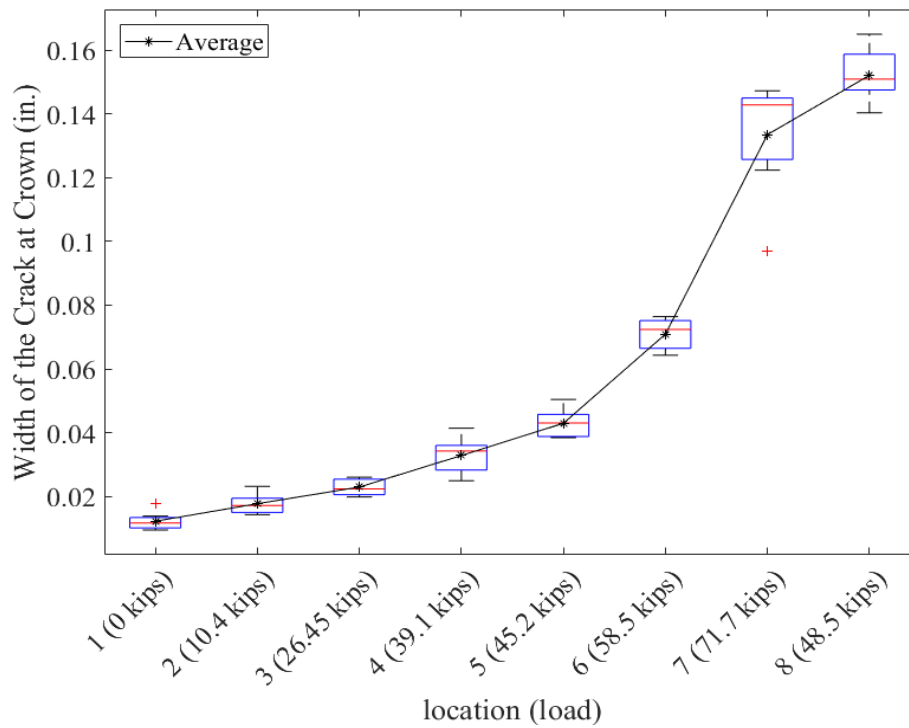
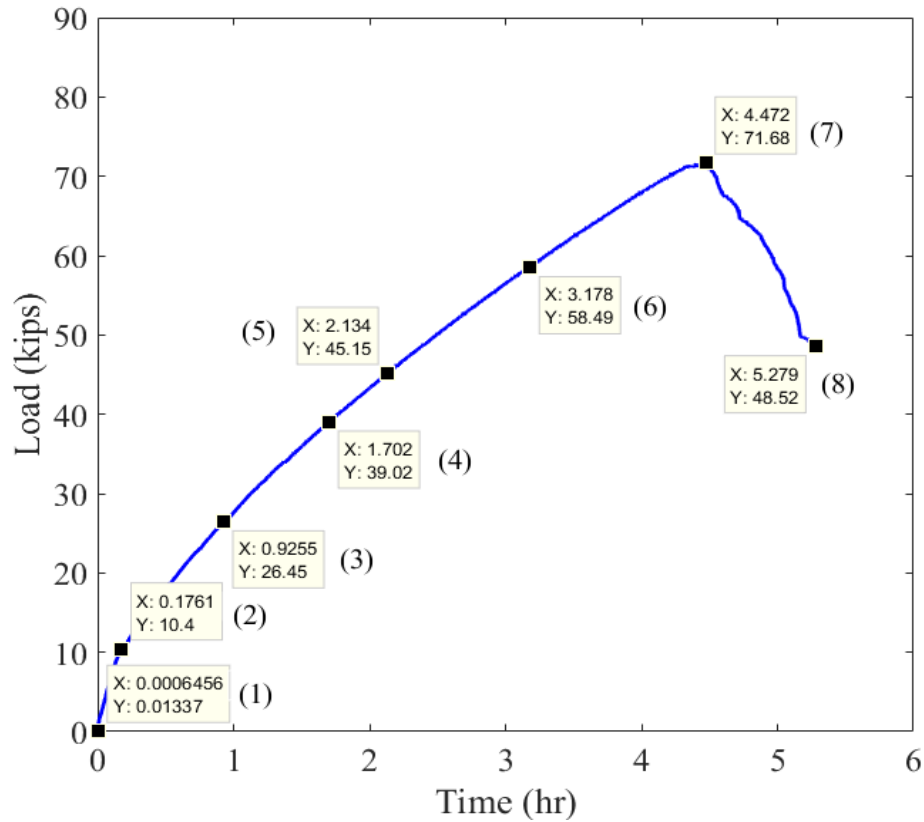


Figure 4-123. Crack width measurement for the crown location at during the applied live load on the soil surface for the 1-in. thick SAPL renewed invert-cut circular CMP.

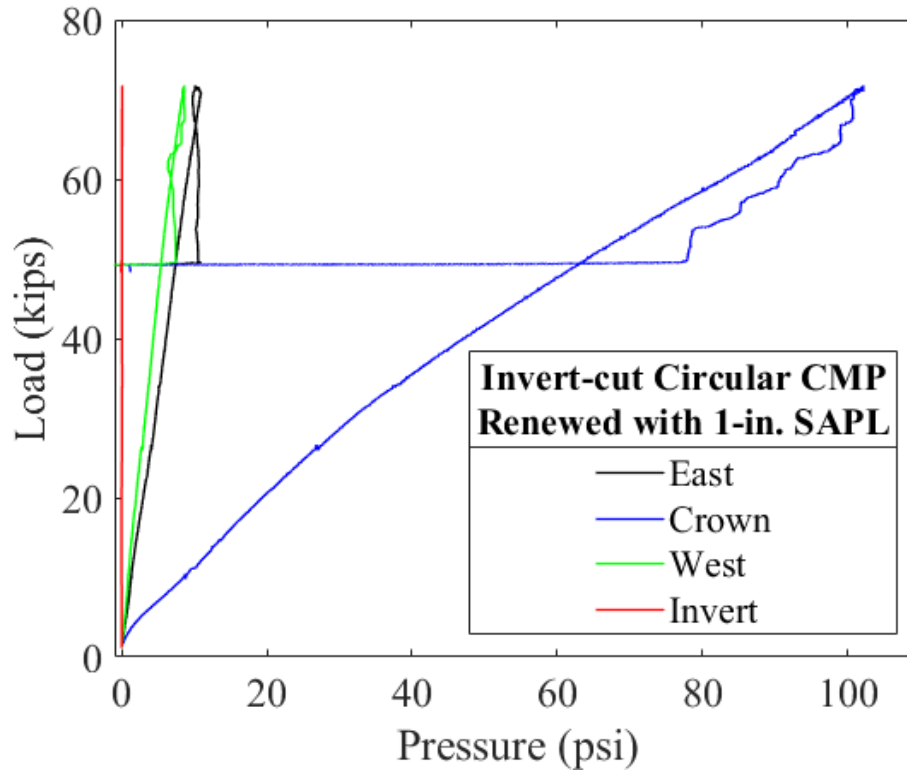


Figure 4-124. Load vs. pressure for the 1-in. thick SAPL renewed invert-cut circular CMP.

4.2.3.3.1. Post Failure Crack Measurement

Visual inspection was conducted after the test and crack width measurement were carried out using DIP method. Figure 4-125 (a) illustrates the 1-in. SAPL renewed invert-cut circular CMP and Figure 4-125 (a) shows the crack pattern schematic inside the pipe. Similar to the 3-in. SAPL renewed invert-cut circular CMP sample, three major longitudinal cracks were observed at the end of the test on the invert and crown of the SAPL. In addition, circumferential cracks were observed on both East and West side of the pipe. The circumferential cracks were propagated from shoulder to the haunch area. Furthermore, similar to the 3-in. thick sample, the longitudinal cracks on the springline area close out completely after SAPL-CMP loading, as shown in Figure 4-129.

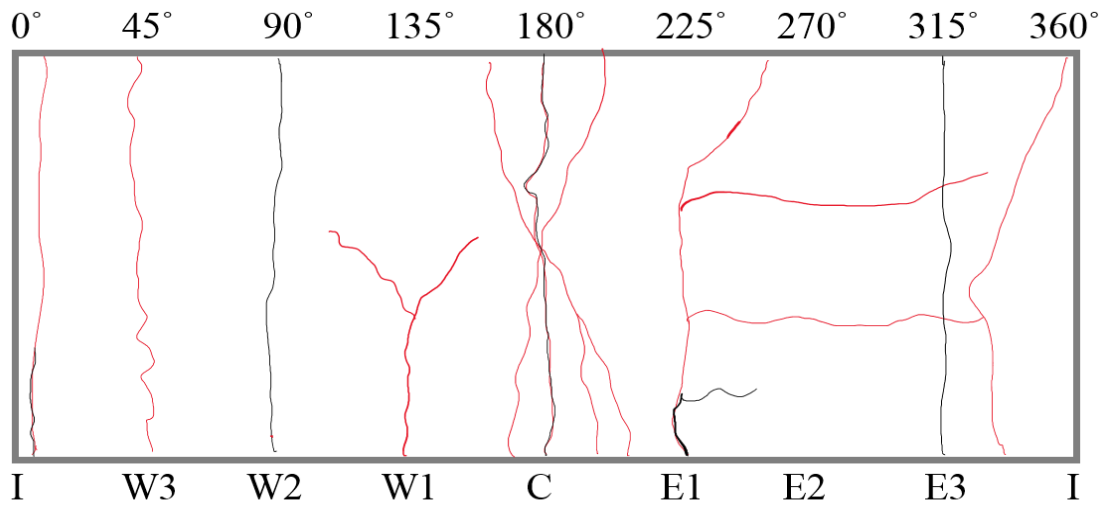


Figure 4-125. Visual inspection of the 1-in. thick SAPL renewed circular CMP: (top) cracked SAPL after the test, and (b) crack pattern schematic, where black represents the shrinkage cracks, and red represents the generated cracks due to the load.

The averaged measured circumferential crack width at end of the test for the East location were 0.0062 in. respectively. The DIP measurements for circumferential cracks are illustrated in Figure 4-126 (a).

The longitudinal cracks at the East and West haunch area had the averaged width of 0.0193 and 0.1051 in, as illustrated in Figure 4-126 (b) and (c). The existed longitudinal crack on the West and East springline before the load application, completely closed out so that they were not visible by unaided eyes. The reason of this gap closure was due to the compressive force applied on the inner surface of the springline zone, as illustrated in Figure 4-82. Figure 4-129 also illustrates the gap closure at the West springline.

The longitudinal cracks on the crown location were measured at two locations in the center and North end of the CMPs. The result of the measurements is presented in Figure 4-127. The crack width for the crown at the North end and center of the pipe were 0.0688, 0.1522 in. respectively. The measurement showed that the crack width at the center of the pipe was about 2.2 times higher than the end of the pipe.

The longitudinal cracks on the invert locations are illustrated in Figure 4-128. The averaged crack width on the East gap of the invert-cut section was 0.0303 in. This value for the West gap was 0.0843 in. which is 0.054 in. larger than the East crack.

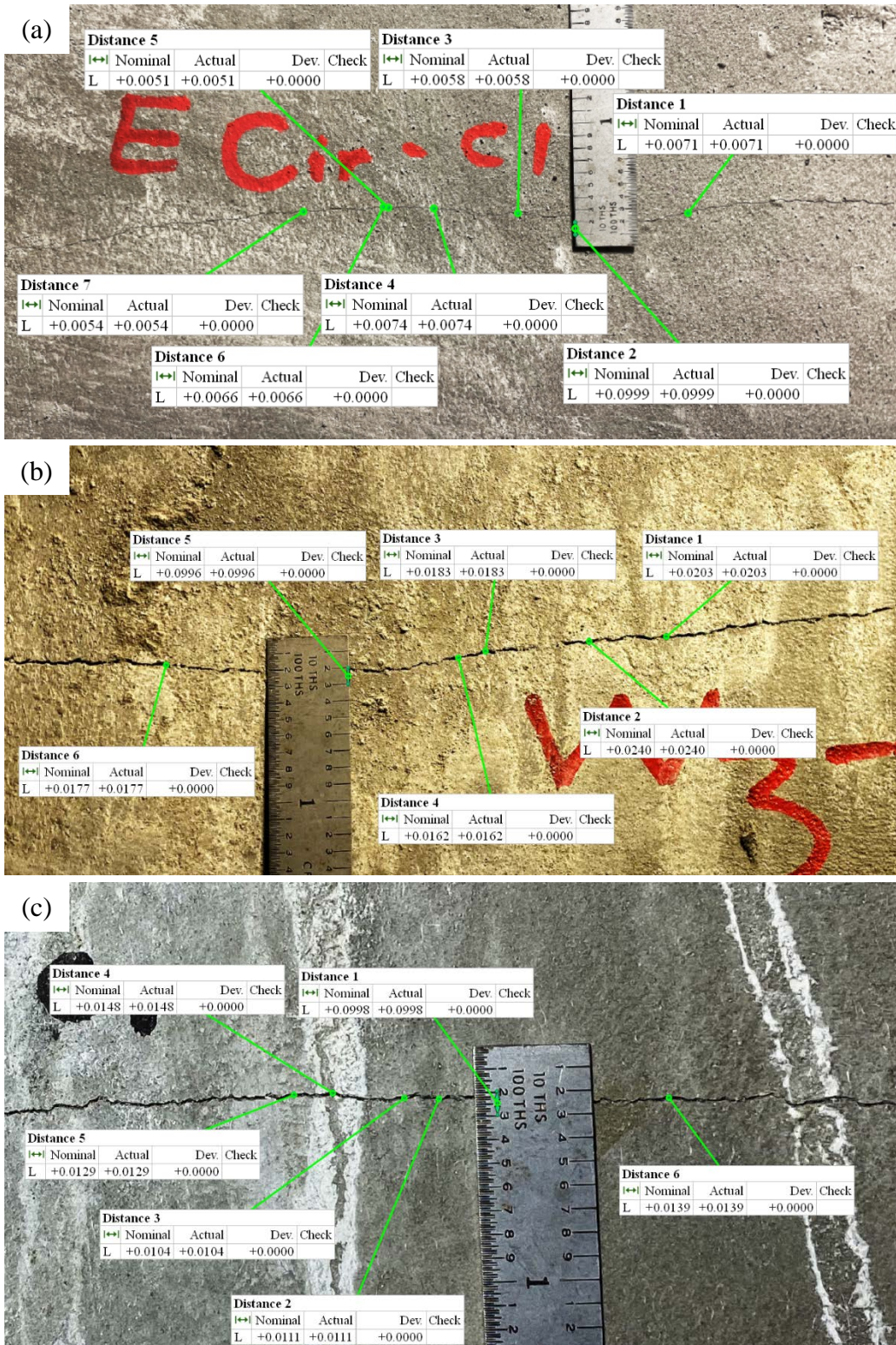


Figure 4-126. Cracks on 1-in. thick SAPL renewed invert-cut circular CMP: (a) circumferential crack at East, (b) longitudinal crack on West haunch, and (c) East haunch area.

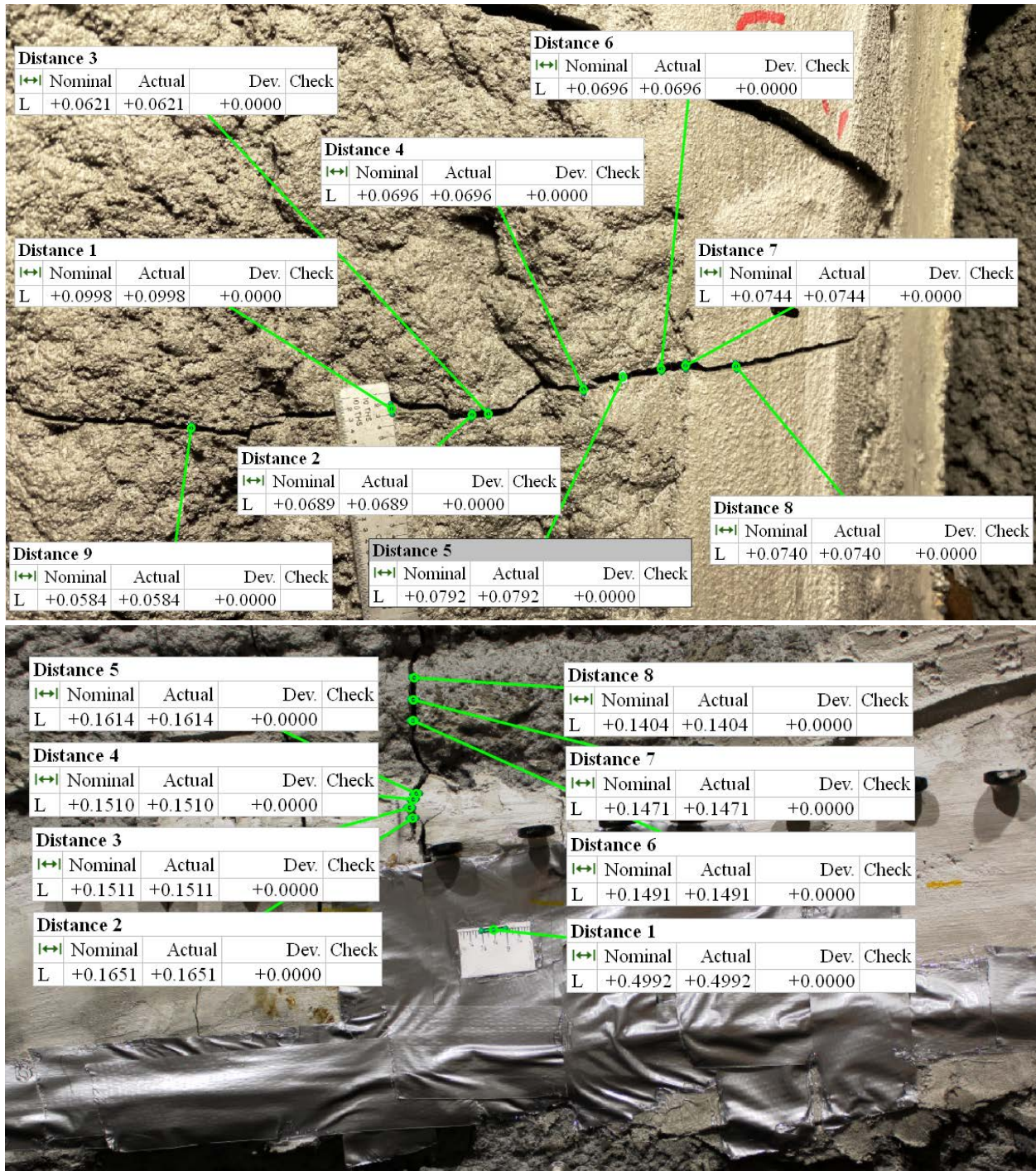


Figure 4-127. Longitudinal cracks on the crown of 1-in. thick SAPL renewed invert-cut circular CMP at: (top) North side, and (bottom) center of the pipe.

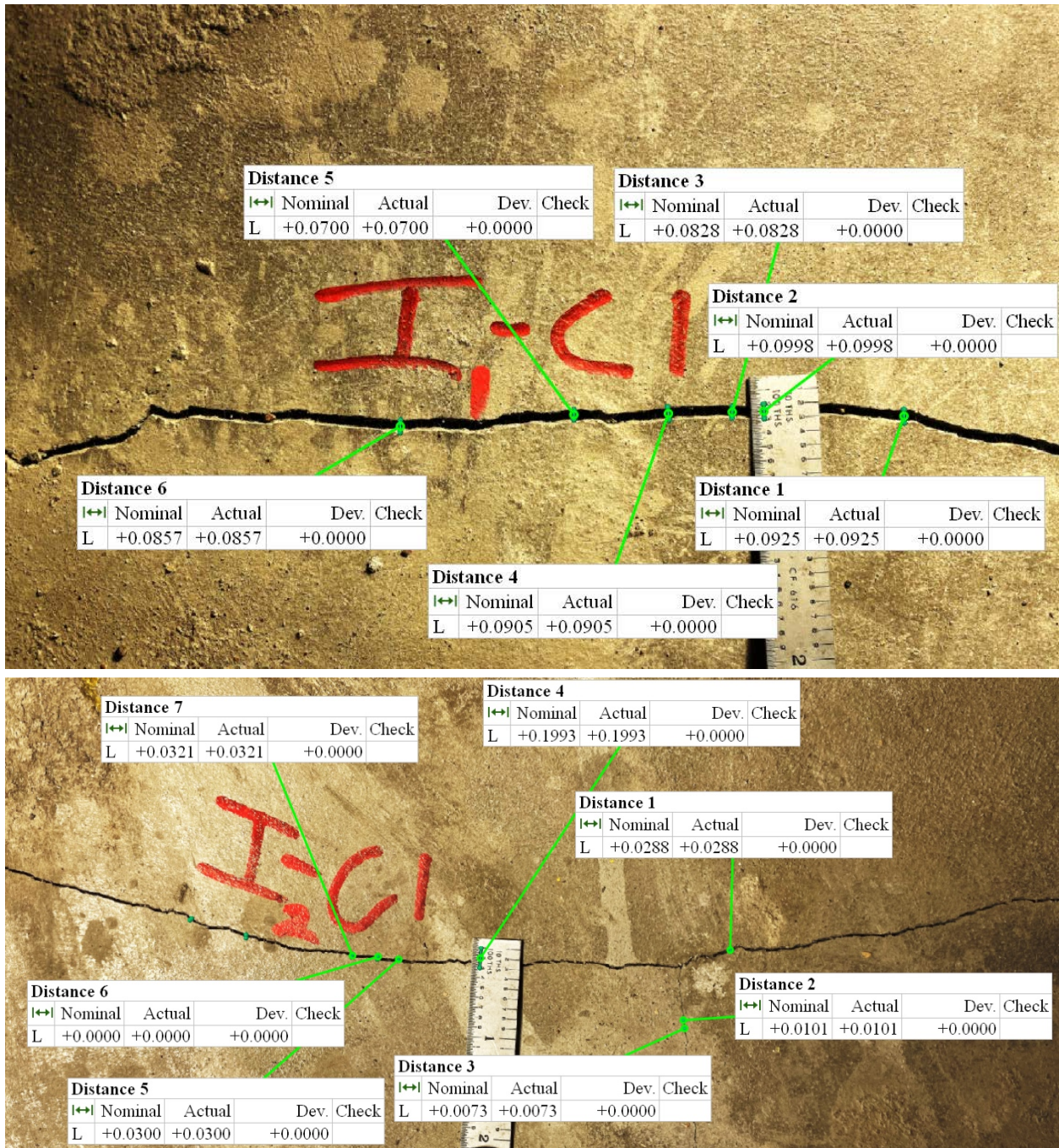


Figure 4-128. Longitudinal cracks on the invert of 1-in. thick SAPL renewed invert-cut circular CMP at: (top) West, and (bottom) East of the invert-cut gap.

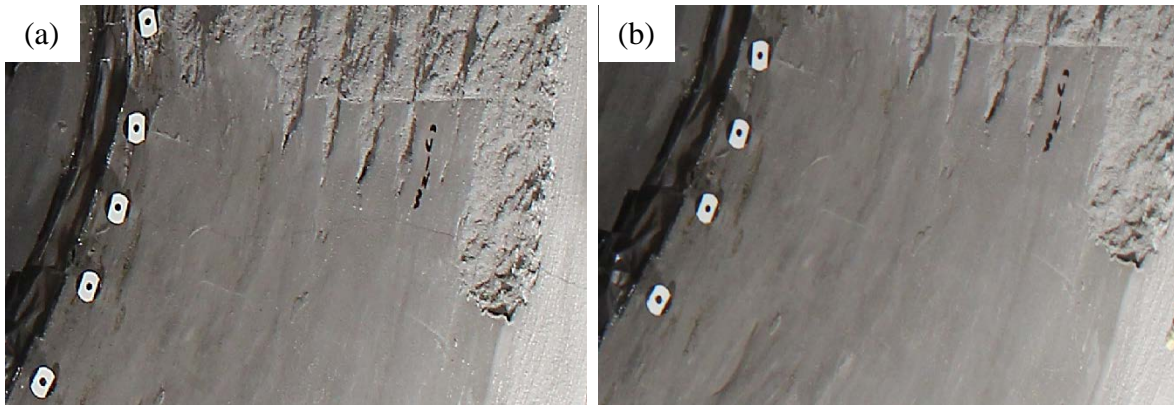


Figure 4-129. Gap closure at the West springline: (a) before, and (b) after the test.

4.2.3.3.2. Thickness Measurement

The thickness of the 2-in. thick cementitious SAPL renewed circular CMP were measured after the structural test and before exhumation as elaborated in section 3.4.6. The detailed result of the measurements is presented in Thickness Measurement Results. Figure 4-130 illustrates the thickness measurements results for all three locations along the length of the pipe (i.e., north, center and south). The results showed that the liner's thickness variation ranged from 0.4 to 1.6 in. The applied thickness on the center ring of the pipes was more uniformly applied in compare with North and South rings. At this section, the thickness alteration was ranging from 1.1 to 1.6 in., which were all above the required thickness. The South ring had the similar condition, except the West springline which had 0.3 in. less than the required thickness. The North ring, had the largest thickness variation inside the 1-in thick renewed CMP. In general, the half upper section of the pipe in the North ring had a thickness less than the designed thickness (i.e., 1 in.).

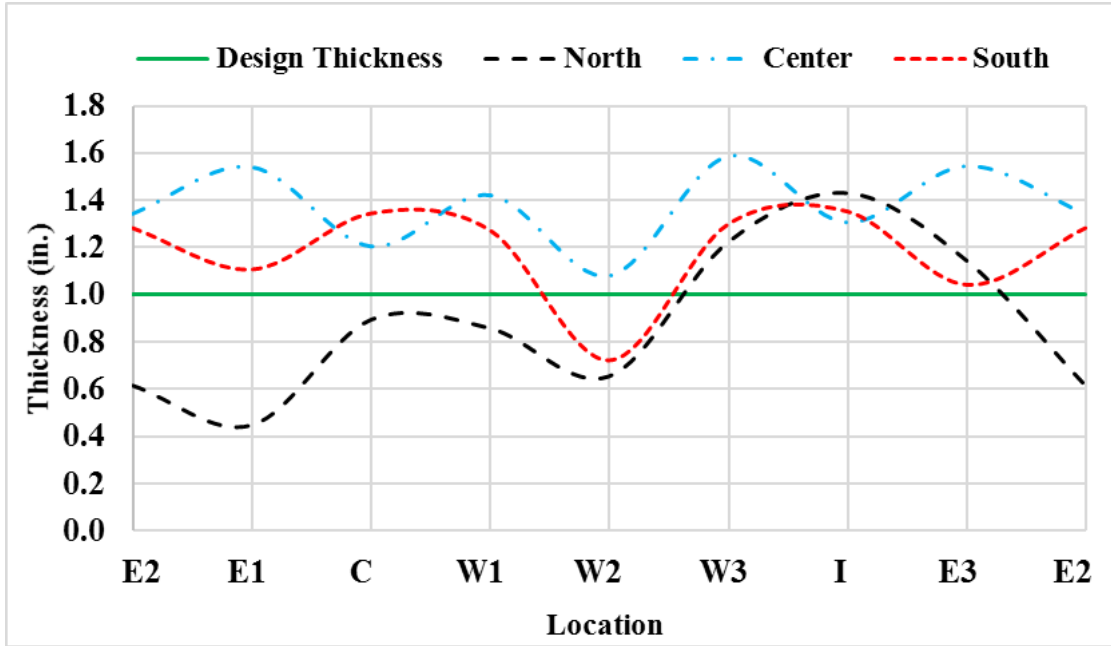


Figure 4-130. Thickness measurement for the 1-in. thick cementitious SAPL renewed circular CMP.

4.2.3.4. Circular SAPL Result Comparison

Result comparison between the bare (i.e., unlined) invert-cut circular CMP and SAPL renewed samples showed that application of 1, 2 and 3-in. thick cementitious SAPL on the invert-cut pipe arch CMPs have increased the load carrying capacity for 79.71, 113.9, and 174.73 % respectively. In all the applied thicknesses, the improvement rate for the SAPL renewed circular CMPs were higher than the SAPL renewed pipe arch CMPs. Table 4-2 presents the ultimate load results and the load carrying capacity enhancement using different SAPL thickness.

Table 4-2. Circular CMP test results

Testing Pipe Samples	SAPL Material	Ultimate Load (Kips)	Improvement (%)
Bare Pipe Arch	-	39.93	-
1 in. Thick SAPL	Geopolymer	71.76	79.71
2 in. Thick SAPL	Geopolymer	85.42	113.9
3 in. Thick SAPL	Geopolymer	109.7	174.73

Figure 4-131 illustrates the results of load versus crown deflection of the bare invert-cut CMP, 1, 2, and 3-in. thick SAPL renewed invert-cut CMPs. Similar data, for springline expansion is presented in Figure 4-132. In both figures it can be observed that the 2 in. thick SAPL renewed CMP had lower crown deflection and springline expansion as expected. One of the possible reasons could be due to the irregularity of the geometry and existed shrinkage cracks in different locations which caused different failure pattern for this pipe.

Figure 4-133 illustrates the application of the SAPL increases the soil settlement value to fail the SAPL-CMP system. In other words, more soil settlement is needed to fail the SAPL

renewed CMP. It can be observed that more soil settlement is also needed for thicker SAPL and the thickness of the SAPL affects the soil surface displacement.

Figure 4-134 illustrates the results of the applied static load on the soil surface versus the applied pressure over the crown of the pipes. The AASHTO H20 truck equivalent pressure, obtained from the intact CMP test (see Figure 4-30), is shown in Figure 4-134. As the figure shows, all the SAPL renewed circular CMP samples could resist the equivalent AASHTO H20 truck pressure. The figure shows that the thicker the liner the higher load was required to fail the SAPL-CMP system. It can be concluded that all three thicknesses are sufficient for the AASHTO H20 truck load.

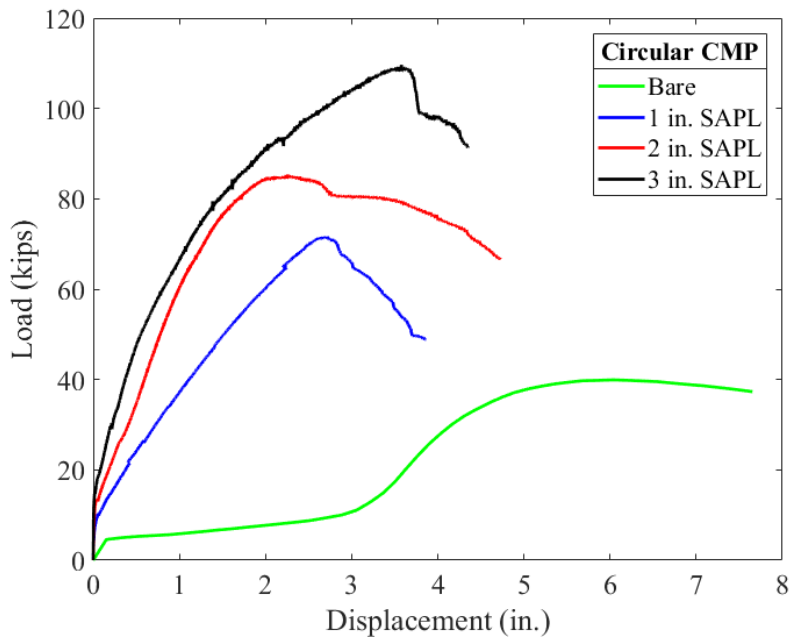


Figure 4-131. Load vs. crown displacement comparison graph.

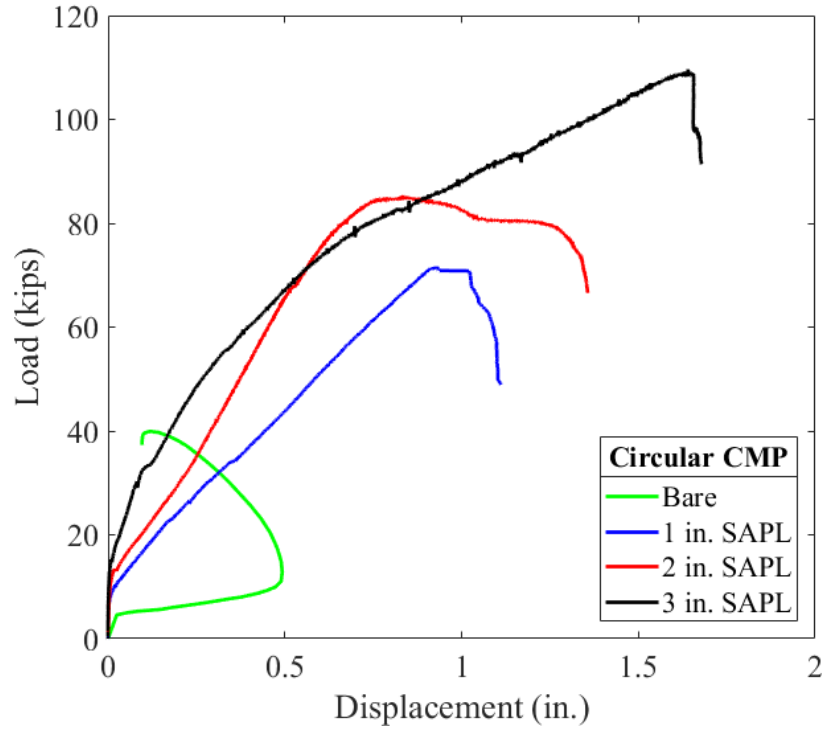


Figure 4-132. Load vs. springline displacement comparison graph.

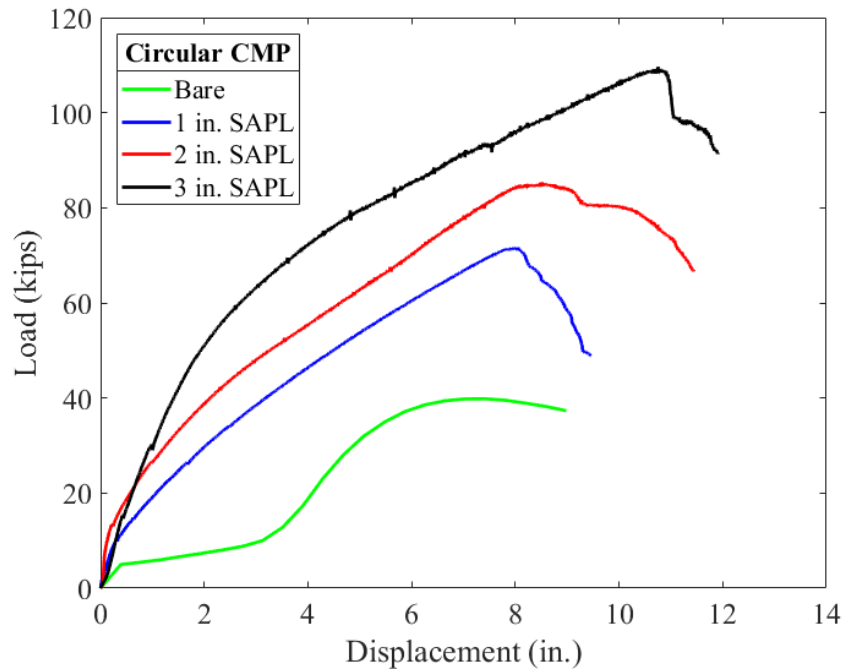


Figure 4-133. Load vs. soil surface settlement comparison graph.

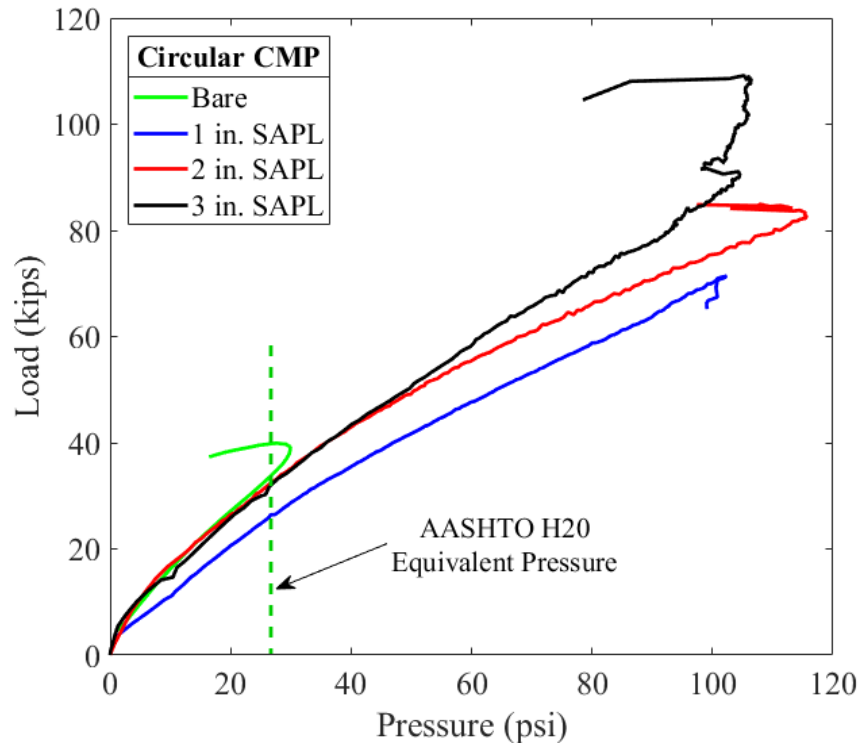


Figure 4-134. Load vs. pressure comparison graph.

4.2.3.5. Test Result for Mechanical Properties

The compressive strength of the samples was evaluated for the cubes, 3×6 , 4×8 , and 6×12 in. samples. The strength of the cubes and 4×8 -cylinder samples were examined for 24 hours, 7 and 28 days curing time. Rest of the samples were tested only for 7 and 28 days. All the Detailed test results are presented in APPENDIX D.

The cube samples were tested according to the ASTM C109. The load was applied at the rate of 300 lb/sec, as described in the test guideline. Figure 4-135 illustrates the box plot of the cube samples result that shows the cube samples had an average compressive strength of 2753 psi after 24 hours of curing. After 7 days the strength of the samples was increased up to 4442 psi. The compressive strength increased further for 56.6% at the end of 28 days where the compressive strength reached average value of 6958 psi. Figure 4-135 (top) the samples were broken at 45-degree planes that implies the load were applied uniformly over the samples.

All the cylinder samples were tested according to the ASTM C39 at the pressure rate of 30 psi/sec. The 3×6 in. spray-cast cylinder samples, were able to reach 3163 psi at the 7 days and 4331 psi at the end of 28 days. The sprayed cylinders showed about 36.92% increase from 7 to 28 days of curing. The hand-cast cylinders showed relatively higher compressive strength than the spray-cast cylinders at 7 day curing period and relatively lower strength at the 28-day curing time where the compressive strength of the hand-cast cylinders were 3977 and 4190 psi at 7 and 28 days respectively. Figure 4-136 illustrates the box plot of the 3×6 in. samples test results.

The 4×8 in. spray-cast cylinder samples showed that the geopolymer was able to achieve 1906 psi compressive strength within 24 hours. The 7 and 28 days test specimens showed 4724, and 6027 psi respectively. The comparison between the results showed that the geopolymer could

increase its strength for 216.2% during the 28 days of curing time. The hand-cast cylinders also showed similar results to the spray-cast samples. The results are presented in Figure 4-137. The hand-cast had compressive strength of 2476, 4966, and 5373 psi for the 24 hours, 7, and 28 days respectively. Direct comparison between the spray-cast and hand-cast specimens showed that the hand-cast samples had 29.9% higher, 5.12% higher, and 12.17% lower strength than the spray-cast specimens in 24 hours 7 and 28 days, respectively.

The 6 × 12 in. spray-cast cylinder samples achieved 4742 psi at the end of 7 days curing time which was 11.9% lower than the 28 day cured samples. The 6 × 12 in. samples at the end of 28 days had the average value of 4176 psi that are illustrated in Figure 4-138.

The results from all different specimens are compared for both 7 and 28 days curing time and are presented in Figure 4-139. The result comparison illustrates that in the absence of large aggregates the smaller samples could result in higher compressive strength. In addition, the lower compressive strength of larger samples revealed that although the geopolymer was reinforced with micro fibers, the fibers could not contribute to the compressive strength. The total average compressive strength value for all the specimens at 7 and 28 days were 4,336 and 5,176 psi respectively.

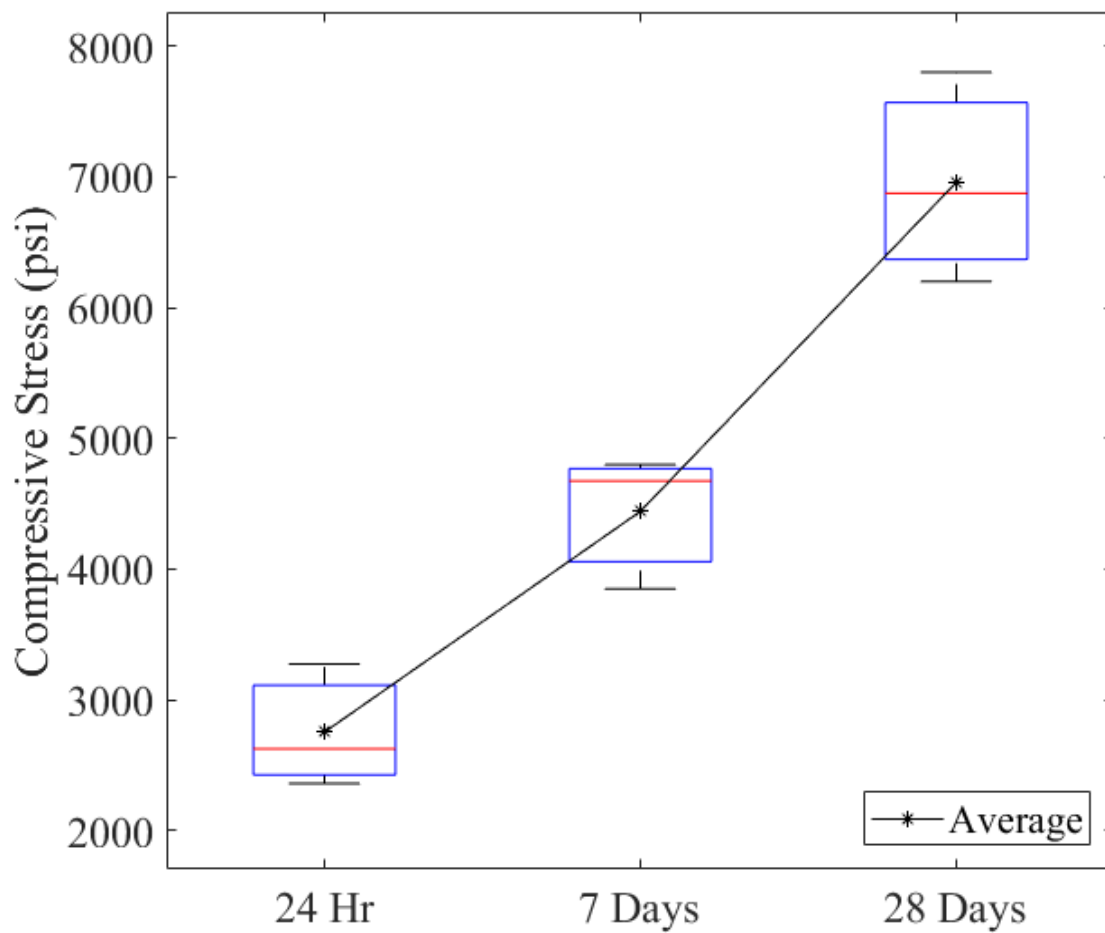
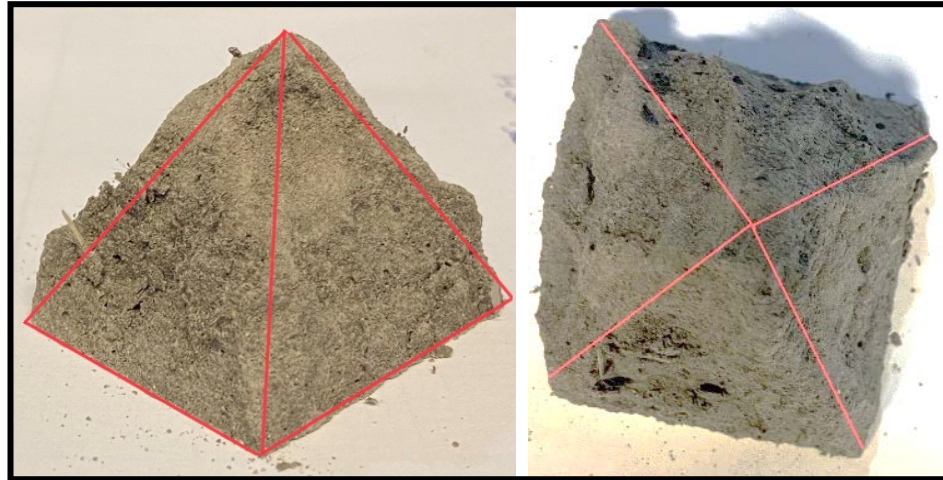


Figure 4-135. Cube samples taken from SAPL batch sprayed on circular CMPs: (top) broken cube samples with 45-degree failure planes, and (bottom) box plot of the results.

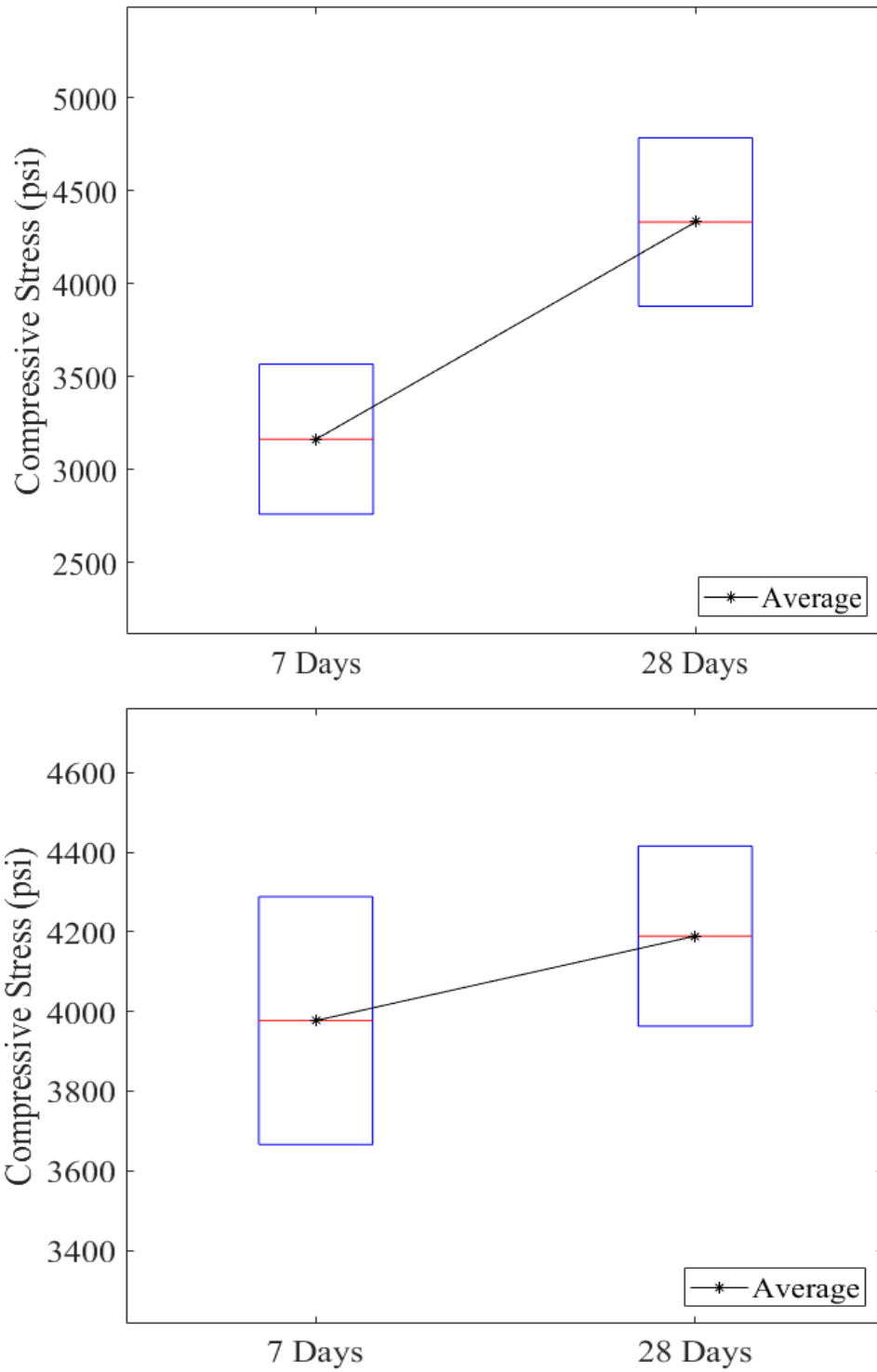


Figure 4-136. Box plot for the 3×6 -cylinder samples taken from SAPL batch sprayed on circular CMPs: (top) spray cast, (bottom) hand cast.

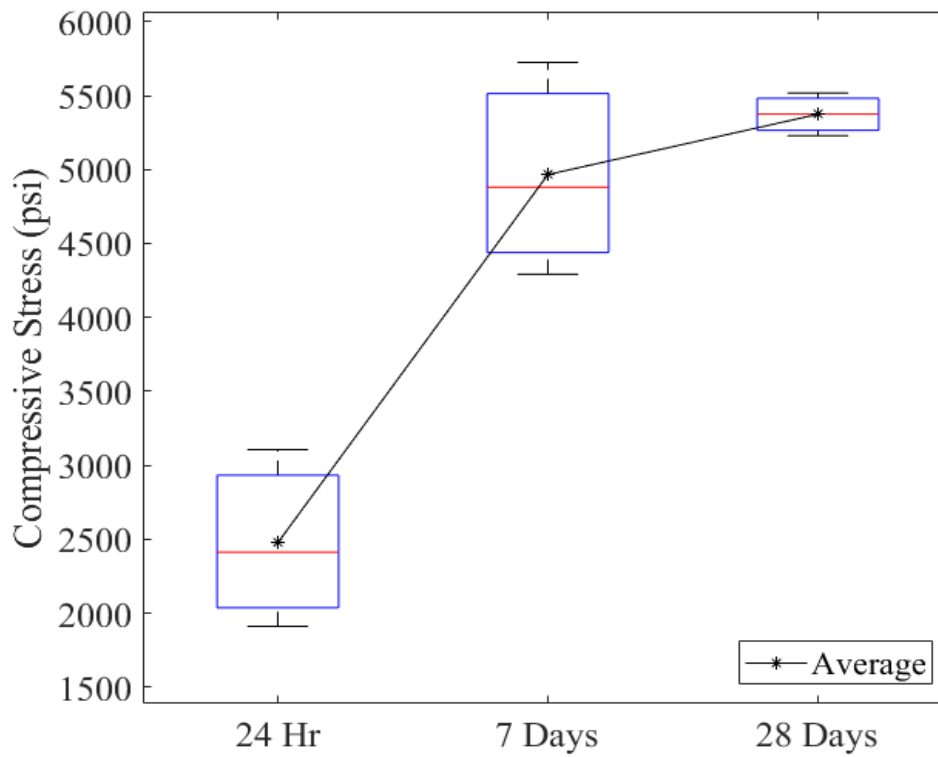
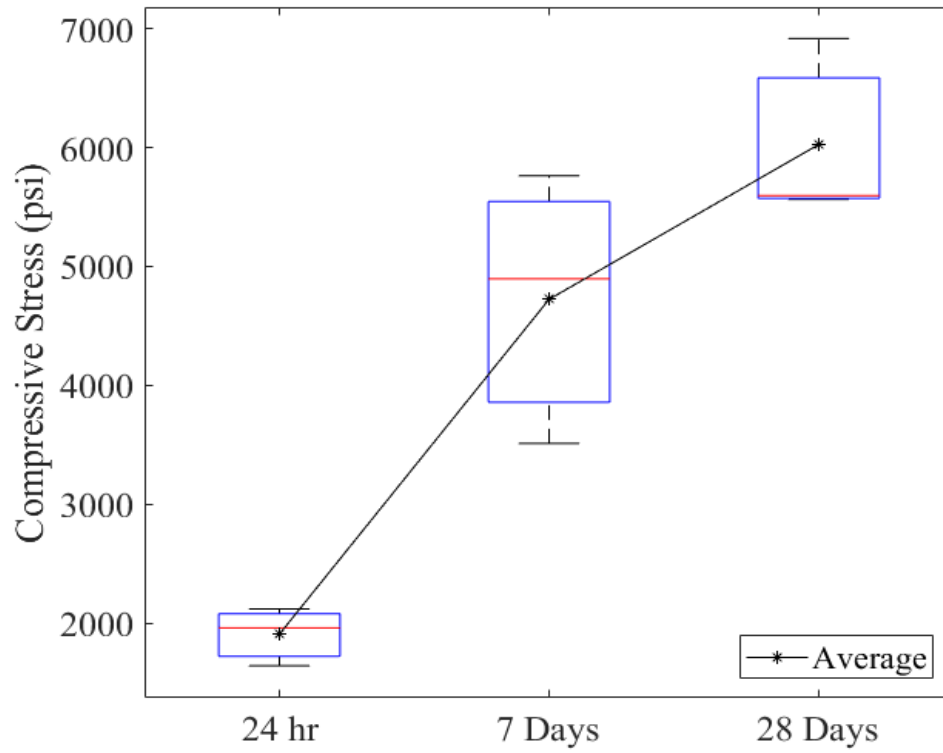


Figure 4-137. Box plot for the 4×8 cylinder samples taken from SAPL batch sprayed on circular CMPs: (top) spray cast, (bottom) hand cast.

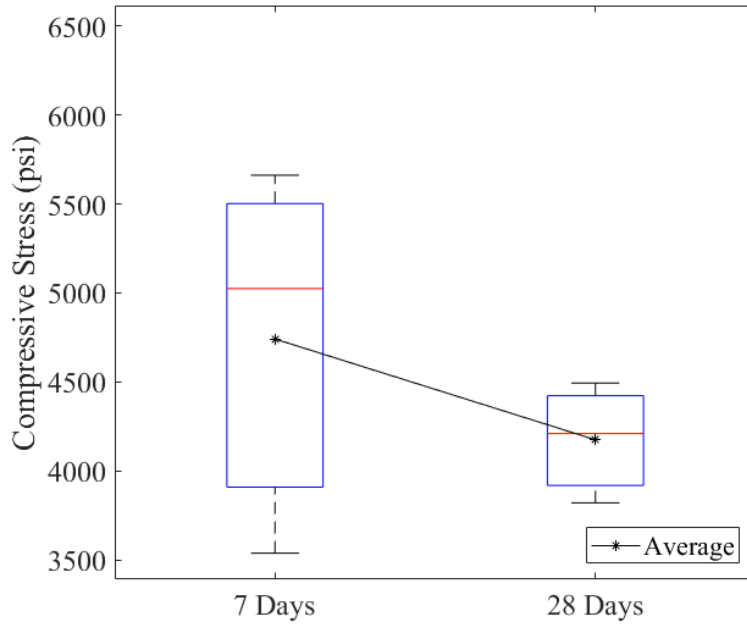


Figure 4-138. Box plot for the 6 × 12-cylinder samples taken from SAPL batch sprayed on circular CMPs.

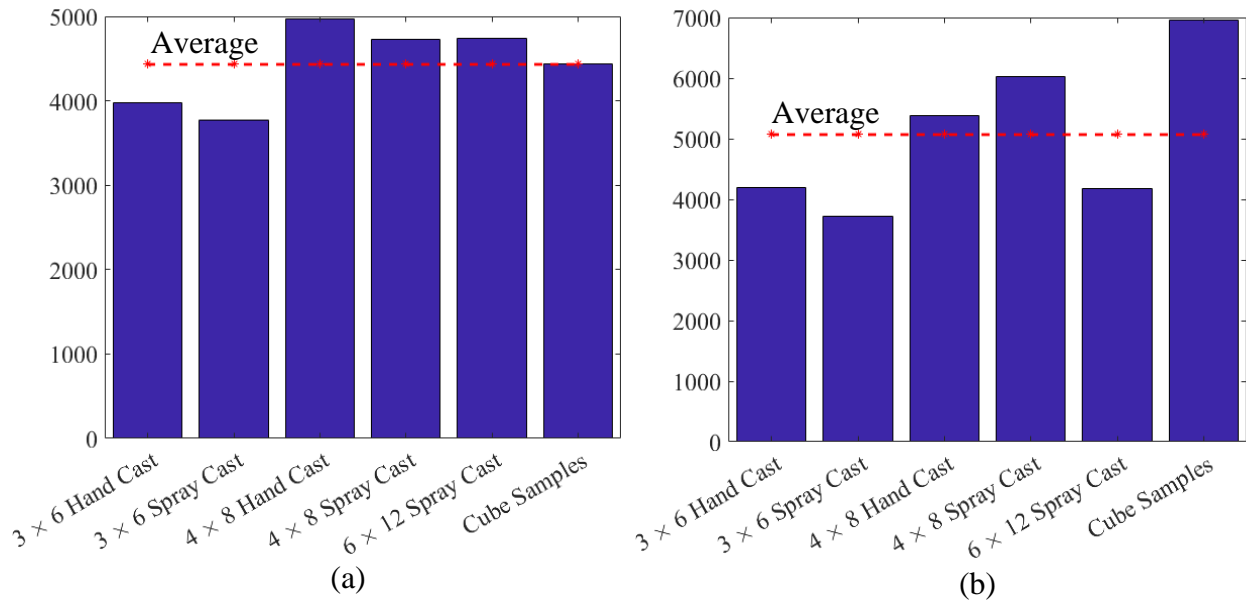


Figure 4-139. Bar chart results for: (a) 7 days, and (b) 28 days samples.

4.2.3.6. Proposed Design Equation

The applicability of CIPP design equations for both partially (i.e., equation (36)) and fully (i.e., equation (39)) deteriorated culverts as well as Iowa equation and Watkins' formula were investigated with the results obtained from the experimental test.

The modified Iowa formula, which is demonstrated in equation (41), is conceptually derived by the division of the applied load over the resisting structures' stiffness as described below:

$$\Delta_y = \frac{\text{load}}{\text{pipe stiffness} + \text{soil stiffness}} \quad (50)$$

Therefore, in the existence of another resisting structure, which is the SAPL, it was improvised by the author to add the stiffness of the SAPL ring to the equation that yields:

$$\Delta_y = \frac{\text{load}}{\text{pipe stiffness} + \text{soil stiffness} + \text{SAPL stiffness}} \quad (51)$$

As a result, the Modified Iowa formula can be adopted for the SAPL as follows:

$$\Delta_y = \frac{D_L \cdot K \cdot W_c}{E \cdot \frac{I}{R^3} + 0.061 \cdot E' + E_{SAPL} \cdot I_{SAPL} / R_{SAPL}^3} \quad (52)$$

AASHTO equation, demonstrated in equation (42), included the dead load and its coefficient to the modified Iowa equation. Therefore, by inclusion of SAPL stiffness to the AASHTO equation, the equation yields to:

$$\Delta_t = \frac{K_B \cdot (D_L \cdot P_{Sp} + C_L \cdot P_L) \cdot D_o}{1000 \cdot (E_p \cdot I_p / R^3 + 0.061 \cdot M_s + E_{SAPL} \cdot I_{SAPL} / R^3)} \quad (53)$$

Figure 4-140 illustrates the comparison results from the CIPP design equations, Watkins' formula, AASHTO Thermoplastic equation and the test results. All the results are plotted for the crown deflection equal to 1% of the CMP diameter (i.e., 1 in.). At this deflection, the crown pressure of the pipe samples was obtained from the soil box test results and were compared with the corresponding values obtained from the equations. It should be noted that for the experimental data, illustrated by the green squares in Figure 4-140, the averaged thickness values, obtained from thickness measurement results, was used. It can be observed that the both CIPP design equations do not represent the test data and are not applicable for SAPL. The Watkins' formula has lower prediction at lower SAPL thickness. However, the adapted AASHTO formula follows the test data's trend which indicates that the adapted analytical approach is a good candidate to be selected as a base equation for a fully deteriorated invert renewed with cementitious SAPL.

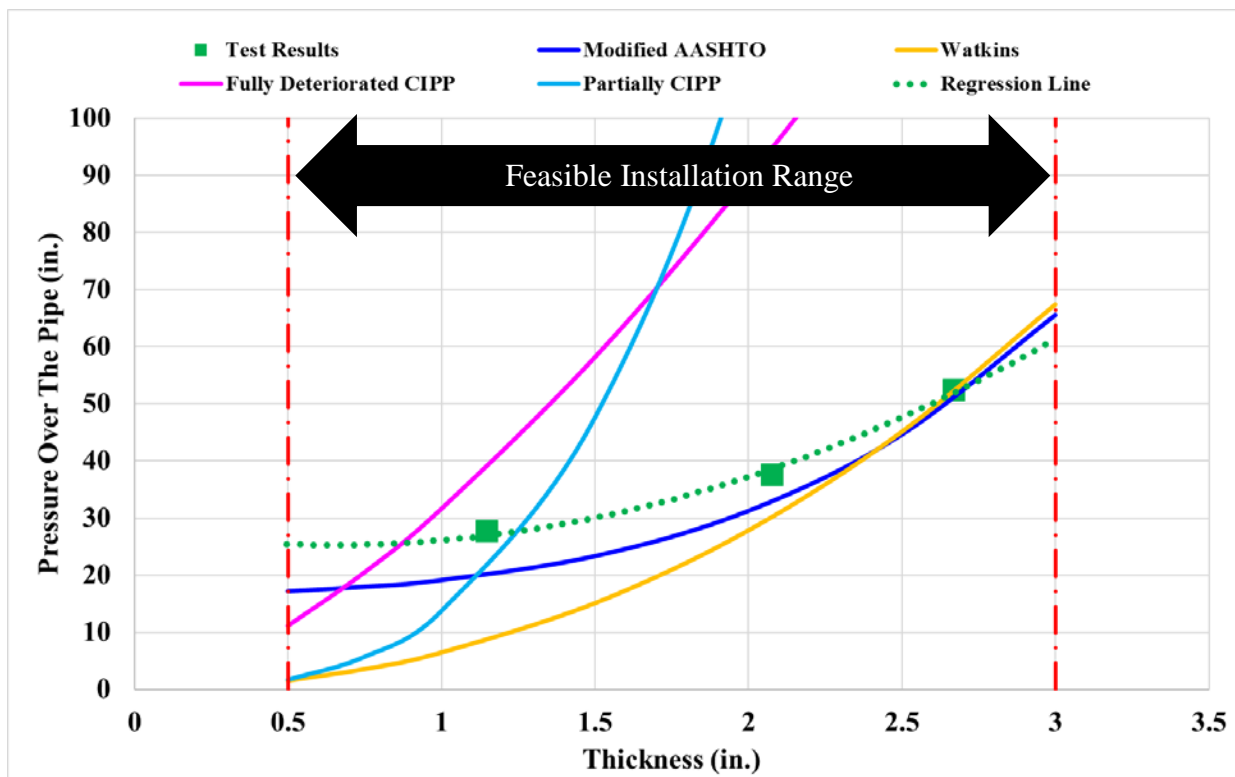


Figure 4-140. Test result comparison with different available equations.

The modified AASHTO equation can also be adapted based on the test results by inclusion of an experimental enhancement factor/coefficient. To find the coefficients, first, a non-linear regression analysis was conducted on the three data points to find a numerical model representing the three data points obtained from the test results. This regression line was necessary to produce more data point to better fit the AASHTO equation with the test results. The equation of regression line from the three data points is as follows:

$$P = 6.5005 \cdot t^2 - 8.3812 \cdot t + 28. \quad (54)$$

The R^2 for this regression line is 0.9937. Once the equation of the regression curve was obtained, 7 data points of $t = 0.5, 0.75, 1, 1.5, 2, 2.5,$ and 3 were selected. These values are the typical SAPL installation thicknesses installed in field. For the known values, a non-linear regression analysis, also known as non-linear curve fitting, was conducted using the modified AASTHO equation to adopt the equation based on the soil box test results. Therefore, the adopted equation yields to:

$$\Delta_t = \frac{K_B \cdot (D_L \cdot P_{sp} + C_L \cdot P_L \cdot X1) \cdot D_o}{1000 \cdot (E_p \cdot I_p / R^3 + 0.061 \cdot M_s + X2 \cdot E_{SAPL} \cdot I_{SAPL} / R^3)} \quad (55)$$

Where the $X1 = 0.69$ and $X2 = 0.1$. The R^2 and the SSE value for this equation was 0.9996 and 0.000935 respectively that shows the adopted equation and the test results are in excellent conformity. Figure 4-141 illustrates the test result comparison with the adapted modified-AASHTO equation (i.e., equation (55)). The coefficients improved the overall trend and proximity of the pressure values obtained from the equation and from the experimental test results. To verify the accuracy of develop equation, a residual analysis for the regression equation was conducted and the results are presented in Figure 4-142. In addition to that, a two-sample t-test was conducted to investigate whether the two sets of data, obtained from the experimental test and the adopted

modified-AASHTO equation, are significantly different or not. The result of the t-test is presented in Table 4-3 demonstrates that the two data sets are not significantly different. Therefore, the equation (55) can be suggested for fully invert deteriorated circular CMP renewed with cementitious SAPLs.

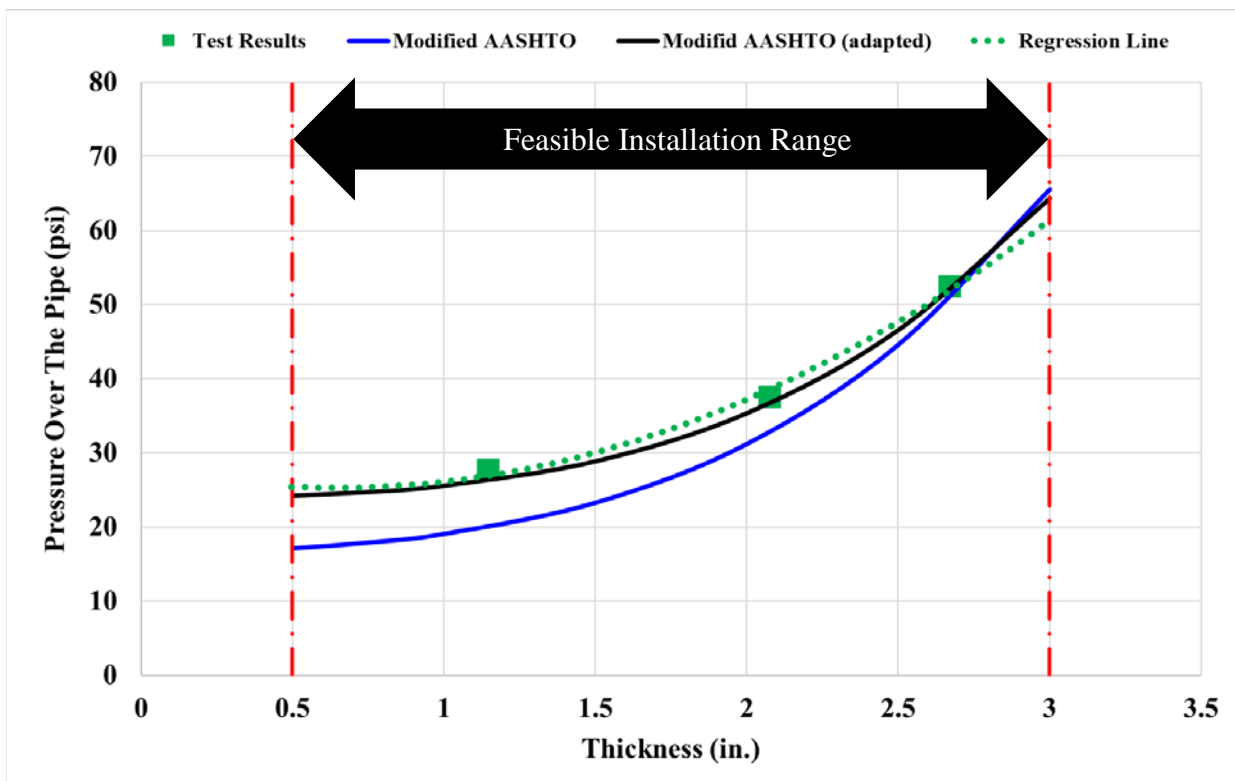


Figure 4-141. Test result comparison with adapted modified-AASHTO equation.

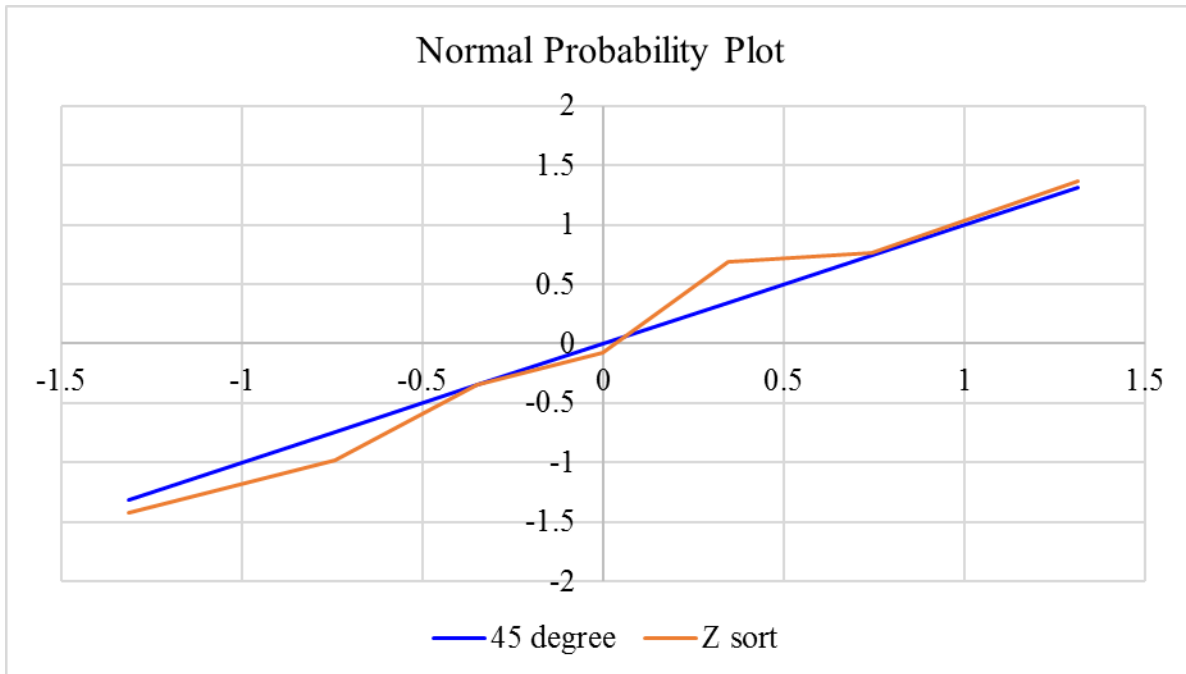


Figure 4-142. Residual analysis for the test result and the adopted AASHTO equation.

Table 4-3. T-Test results.

<i>T-Test</i>	<i>Variable 1</i>	<i>Variable 2</i>
Mean	36.17920089	35.70414286
Variance	189.7312726	223.4103568
Observations	7	7
Hypothesized Mean Difference	0	
Df	12	
t Stat	0.061836686	
P(T<=t) one-tail	0.475855449	
t Critical one-tail	1.782287556	
P(T<=t) two-tail	0.951710898	
t Critical two-tail	2.17881283	

CHAPTER 5. CONCLUSIONS, LIMITATIONS, AND RECOMMENDATIONS FOR FUTURE RESEARCH

5.1. Summary

This dissertation presented results of nine full-scale structural tests including three control tests (i.e., unlined), three pipe arch culverts, and three circular culverts renewed with cementitious SAPL tests. The invert section of the culverts was cut to simulate fully invert deteriorated culverts in service. The structural capacity of these culverts with and without SAPL were investigated. The installation issues and recommendations were provided for cementitious SAPL. Different aspects of SAPL were studied in detail. Shrinkage cracks and post failure cracks (i.e., after testing) were measured and discussed. Ultimately, the feasibility of several design equations, applicable to a fully deteriorated culvert was investigated, and based on the analytical and numerical results, a SAPL design equation was developed for circular culverts renewed with cementitious SAPL.

5.2. Conclusions

The control test was conducted with three CMPs including, intact circular CMP, invert-cut pipe arch CMP, and invert-cut circular CMP. The intact circular CMP was subjected to load using 10 × 20 in. load pad, which the dimension is selected based on the AASTHO H20 truck tire size. The intact circular CMP was able to reach the AASHTO H20 service load (i.e., 16 kips). The test showed that the AASHTO H20 service load produces vertical pressure over the crown of the pipe with the magnitude of 25.72 psi. The intact CMP reached the deflection limit of 5% after occurrence of the local buckling at the crown and failed at the load of 24.85 kips.

The invert-cut circular CMP was able to withstand the equivalent AASHTO H20 service load which was the vertical force applied to the soil surface and is corresponding to the 25.72 psi pressure over the crown of the pipe, obtained from the intact circular CMP test. The initial load carrying capacity of the invert-cut circular CMP was due to the frictional resistance of the CMP-soil system. The friction is a function of the CMP-soil contact area and consequently length of the CMP. In the field conditions, the length of culvert barrel is longer than the tested pipe samples. A longer CMP can have a higher frictional resistance that locks the pipe in place, therefore, may reduce or eliminate CMP's movement. Resistance to the CMP circumferential movement may facilitate or increase the chance of local buckling failure. The strength of the invert-cut circular CMP was highly dependent on its ring stiffness. The invert-cut arch CMP was able to carry the superimposed load by taking advantage of its arch shape to transfer the vertical load to the soil at its flat bottom area. The pipe failed at 39.93 kips.

The invert-cut pipe arch CMP was not able to reach the equivalent load prior to ultimate failure. The test results showed that the invert-cut arch CMP had 47% lower ultimate load bearing capacity than the invert-cut circular CMP. The invert-cut pipe arch CMP was able to take the applied load to its ultimate failure without showing significant horizontal movement, in contrast with the invert-cut circular.

Considering the pipe sample length, the frictional resistance factor, and the higher loading capacity of the circular pipe sample, it can be inferred the less risk of circular CMP collapse over the arch CMP in a fully deteriorated invert condition.

The application of cementitious SAPL improved the ultimate load carrying capacities of the fully invert deteriorated pipe arch CMPs by 72.73, 104.4, and 151.44%, respectively. The invert-cut pipe arch CMPs with the design thickness of 1, 2, and 3 inches had the averaged

thicknesses of 1.105, 1.818, and 2.638 inches respectively. All three pipes had shrinkage cracks on the crown, invert and haunch area. The crack measurements showed that the existed shrinkage cracks at the haunch area, near the springline, were closed at after the applied load. This was due to generated compressive stress at haunch area near the springline. At the end of the tests, major cracks were created at the crown and both invert-cut gaps on the invert of the pipe arch CMPs.

The invert-cut circular CMPs with the design thickness of 1, 2, and 3 inches had the averaged thicknesses of 1.47, 2.01, and 2.678 inches respectively. Similar the pipe arch samples, it was observed that the vendor was failed to install uniform thickness of 3 in. One of the possible reason was due to low accuracy of the hand-spray installation method. The application of cementitious SAPL improved the ultimate load carrying capacities of the fully invert deteriorated circular CMPs by 79.71, 113.9, and 174.73%, respectively, as illustrated in Figure 5-1. All three pipes had shrinkage cracks on the crown, invert and springline. The crack measurements showed that the existed shrinkage cracks at the springline were closed at after the applied load. This was due to generated compressive stress at the springline as a result of applied vertical load over the crown of the pipe. At the end of the tests, major cracks were created at the crown and both invert-cut gaps on the invert of the pipe arch CMPs.

The created cracks at the gap area of the invert-cut location for all six SAPL renewed CMP samples, implies that the cementitious SAPL was not a fully structural liner, if a fully structural liner is defined as a stand-alone structural pipe inside the host pipe. It was found that the cementitious SAPL's structural integrity was dependent on the host pipe, especially at the crown area.

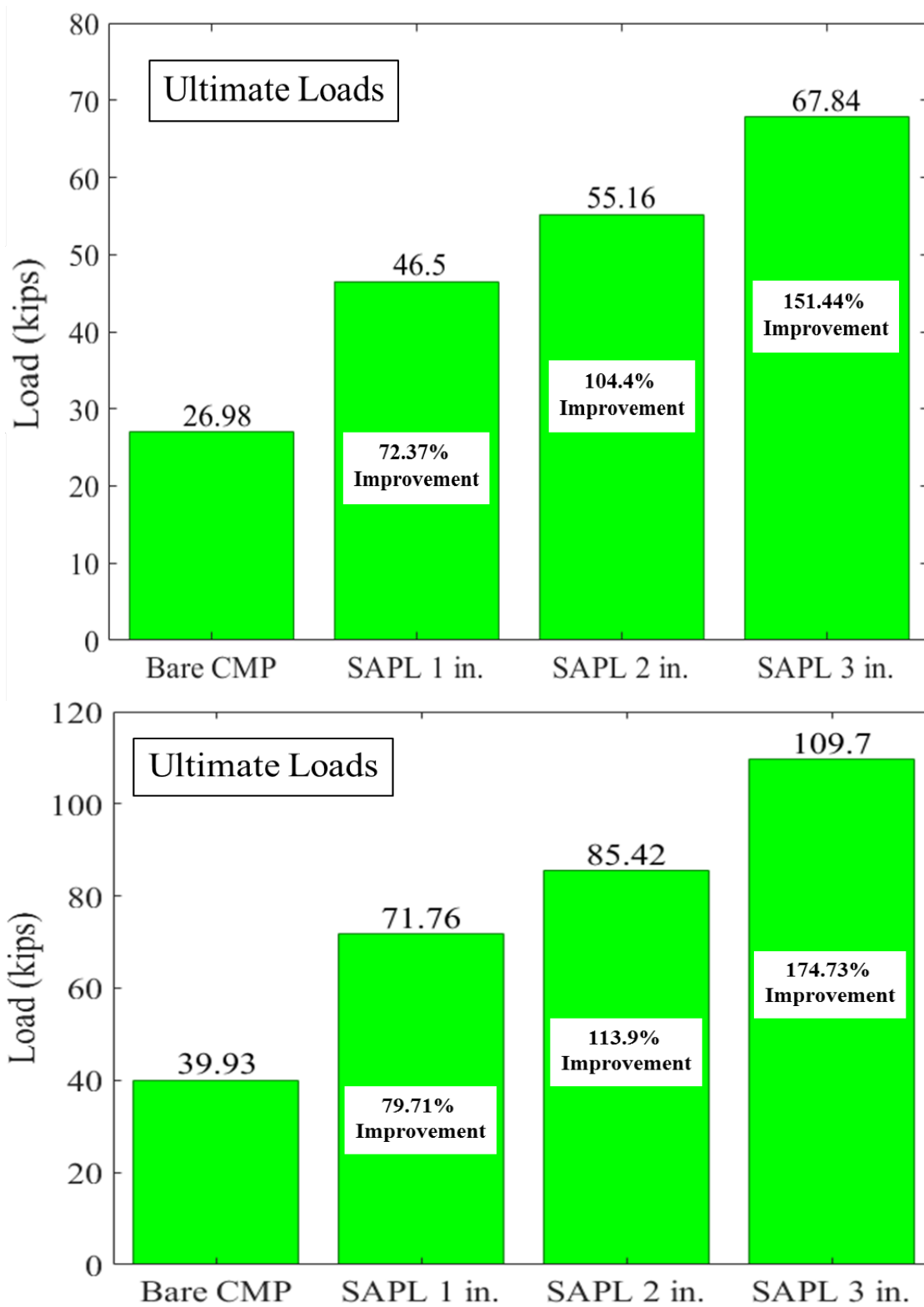


Figure 5-1. SAPL improvement on fully deteriorated CMPs: (top) pipe arch, (bottom) circular.

The physical property test of the cementitious SAPL showed that the geopolymer SAPL was able to reach the compressive strength of 2,753, 4,443, and 6,958 psi at the end of 24 hours, 7 and 28 days, respectively. To increase the compressive and tensile strength of the geopolymer SAPL mortar, utilization of macro fibers was suggested based on the investigation that is presented in this dissertation. In addition, the evaluations on the need of filling the host pipe's corrugation showed that filling the corrugations with SAPL will result in both hydraulic and structural capacity enhancement of the renewed culvert.

The investigation of the applicability of deferent design equations including Watkins formula, partially and fully CIPP design equations showed that none of these equations could represent the SAPL-CMP behavior under the applied vertical load. However, the modified AASHTO equation for flexible thermoplastic pipes could follow the trend of the test results. Two enhancement factors were added to the AASHTO equation where the factors were obtained from statistical analysis and the accuracy of the developed equation was verified residual and t-test analyses. It was found that the developed adopted-AASHTO equation could represent the test data and can potentially be used for design of cementitious SAPLs in fully invert deteriorated circular CMPs.

5.3. Limitations and Recommendations for Future Research

The developed equation presented in this dissertation is only verified with the experimental data laid within the scope of this study. The developed equation is recommended to be only used between the thicknesses 0.5 to 3 inches as this is the feasible range of cementitious SAPL installation without required mesh reinforcements.

Further investigation is recommended for other parameters involved in the developed equation like the effect of depth of cover, different soil material, different pipe diameter, etc.,. However, since the soil box testing of different scenarios, mentioned earlier is both time and financial expensive, it is recommended to utilize finite element analysis (FEA) on the current soil box results to verify the FEA model, and thereafter, to conduct parametric study on the aforementioned parameters with FEA model. The result can be compared with the outcomes of the proposed design equation.

APPENDIX A. Load Pad Design

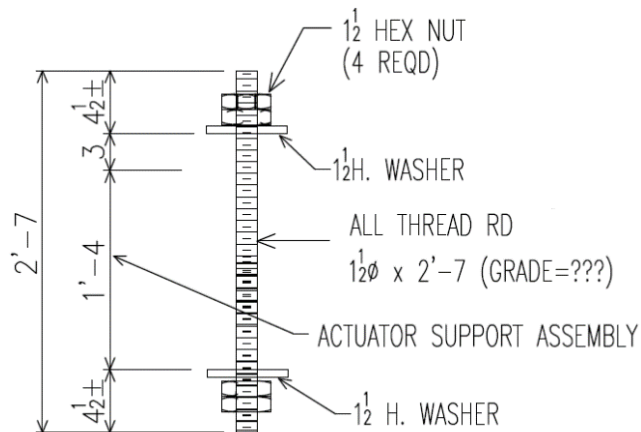
1. Plates:

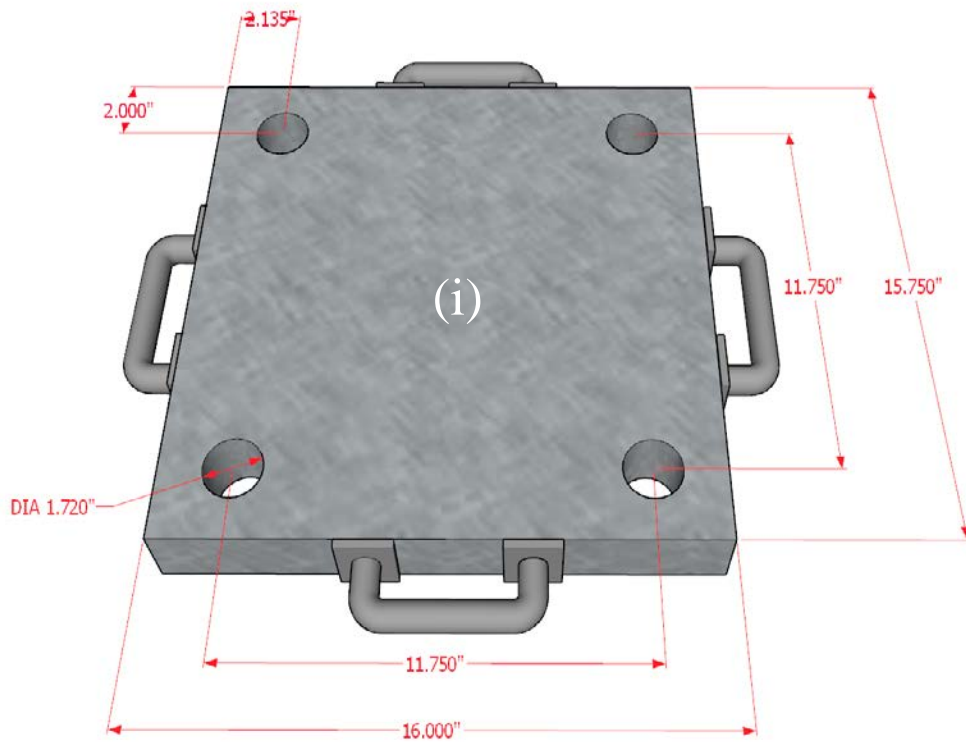
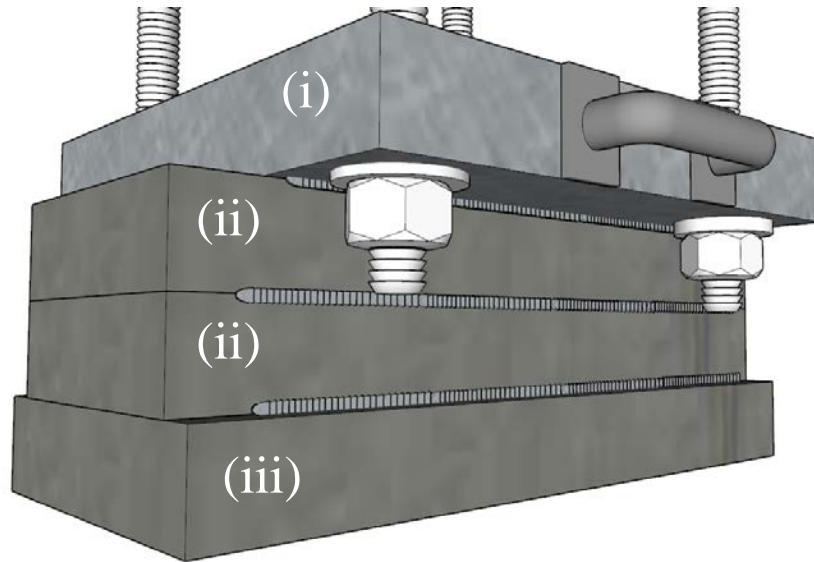
Plate name	Load Pad Size (in)	Quantity
(i)	16×15.75×2	1
(ii)	7×20×2	2
(iii)	10×20×2	1
(iv)	20×40×2	1

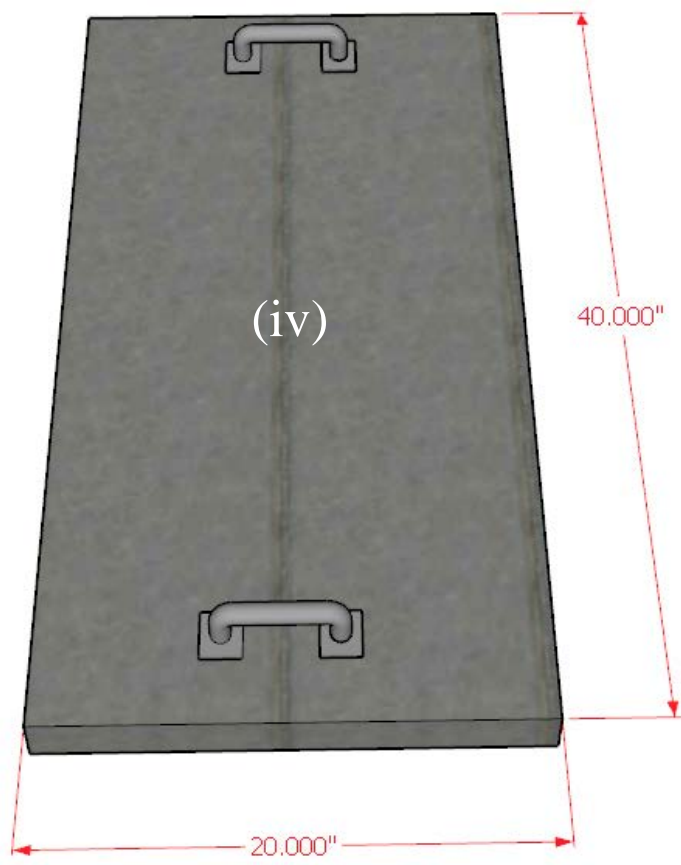
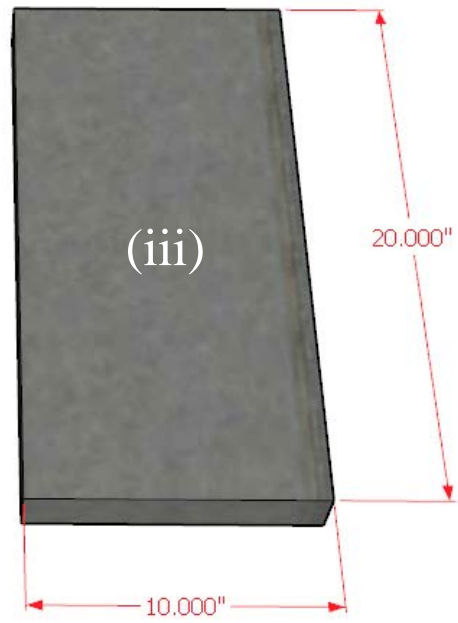
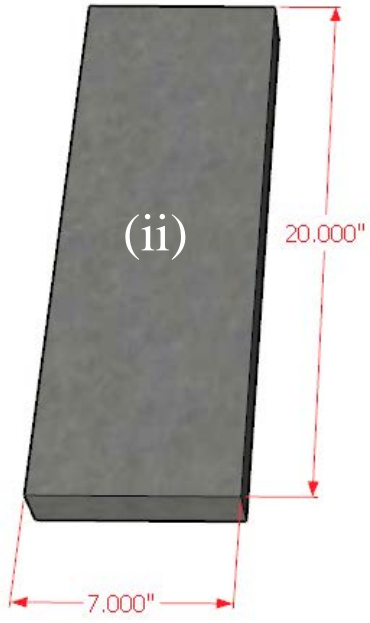
**The plates a, b, and c should to be welded together according to the figures.

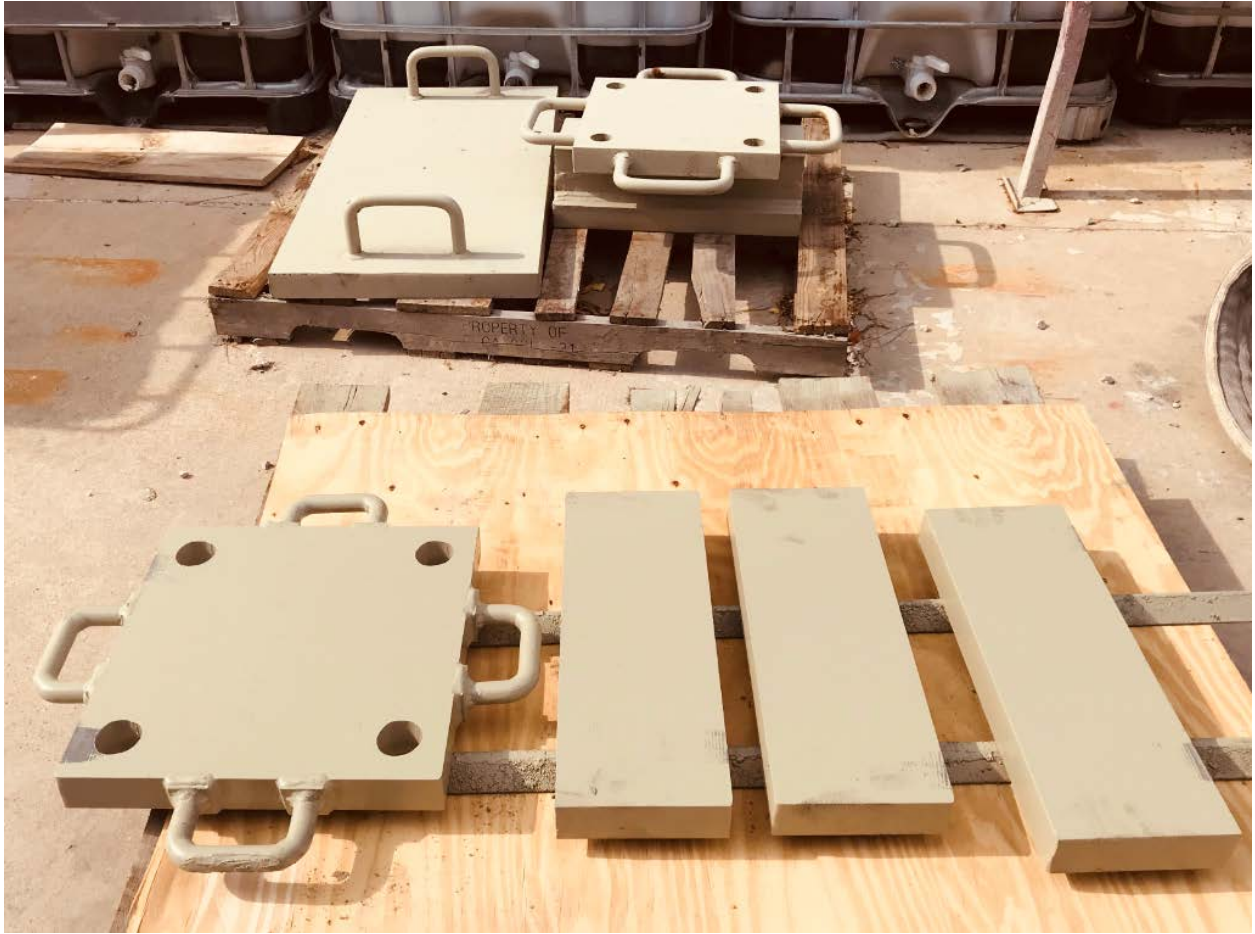
2. Bolts and Nuts:

Item	Dimension (in.)	Quantity
Bolt	1 ½ × 31	4
Nut	1 ½ Hex (A563)	4
Washer	1 ½ (F436)	4



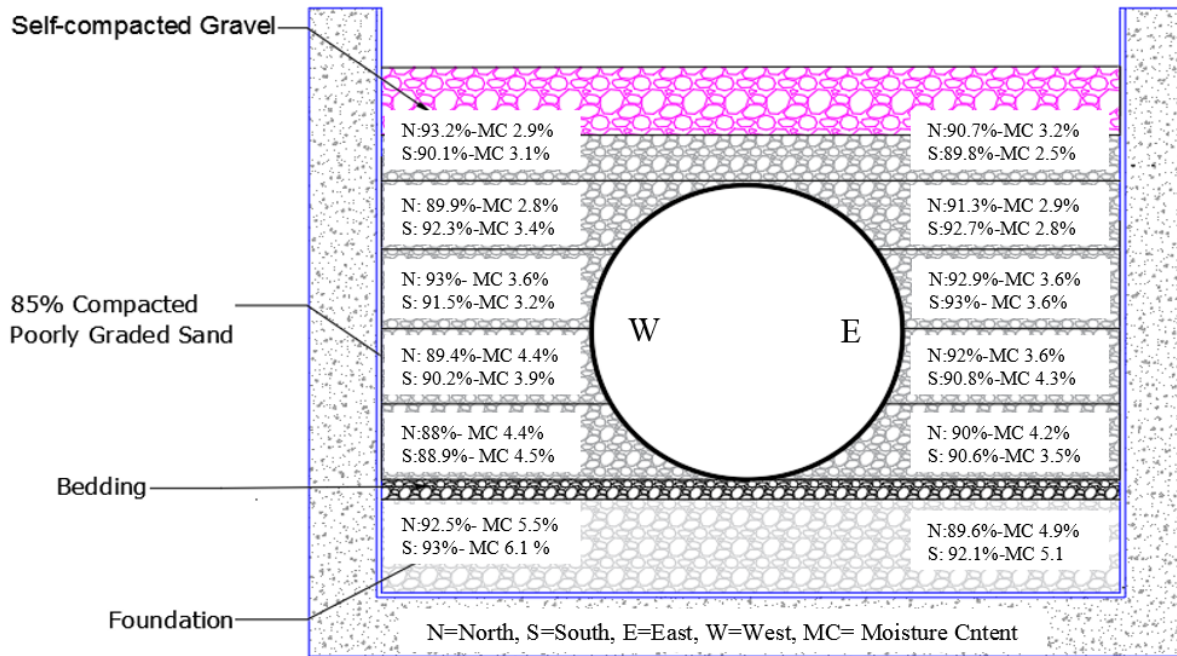
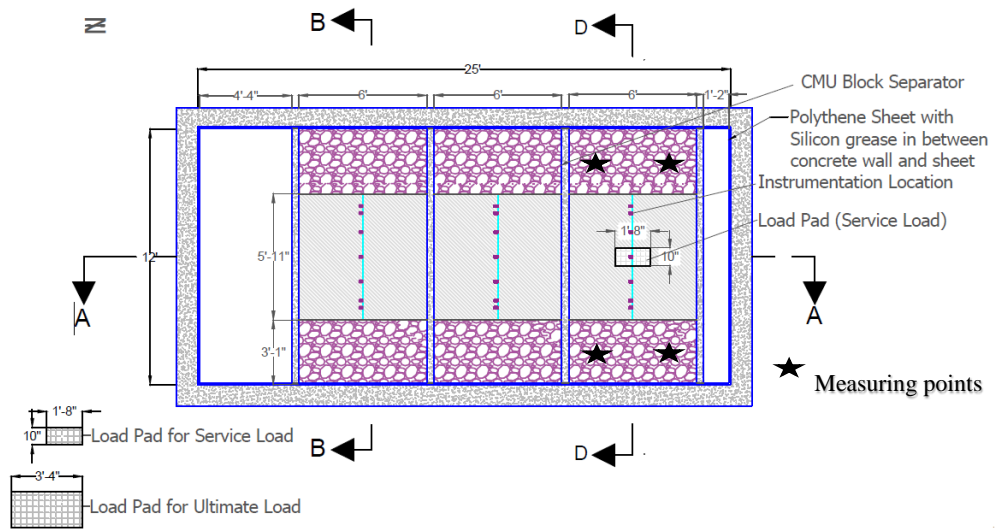




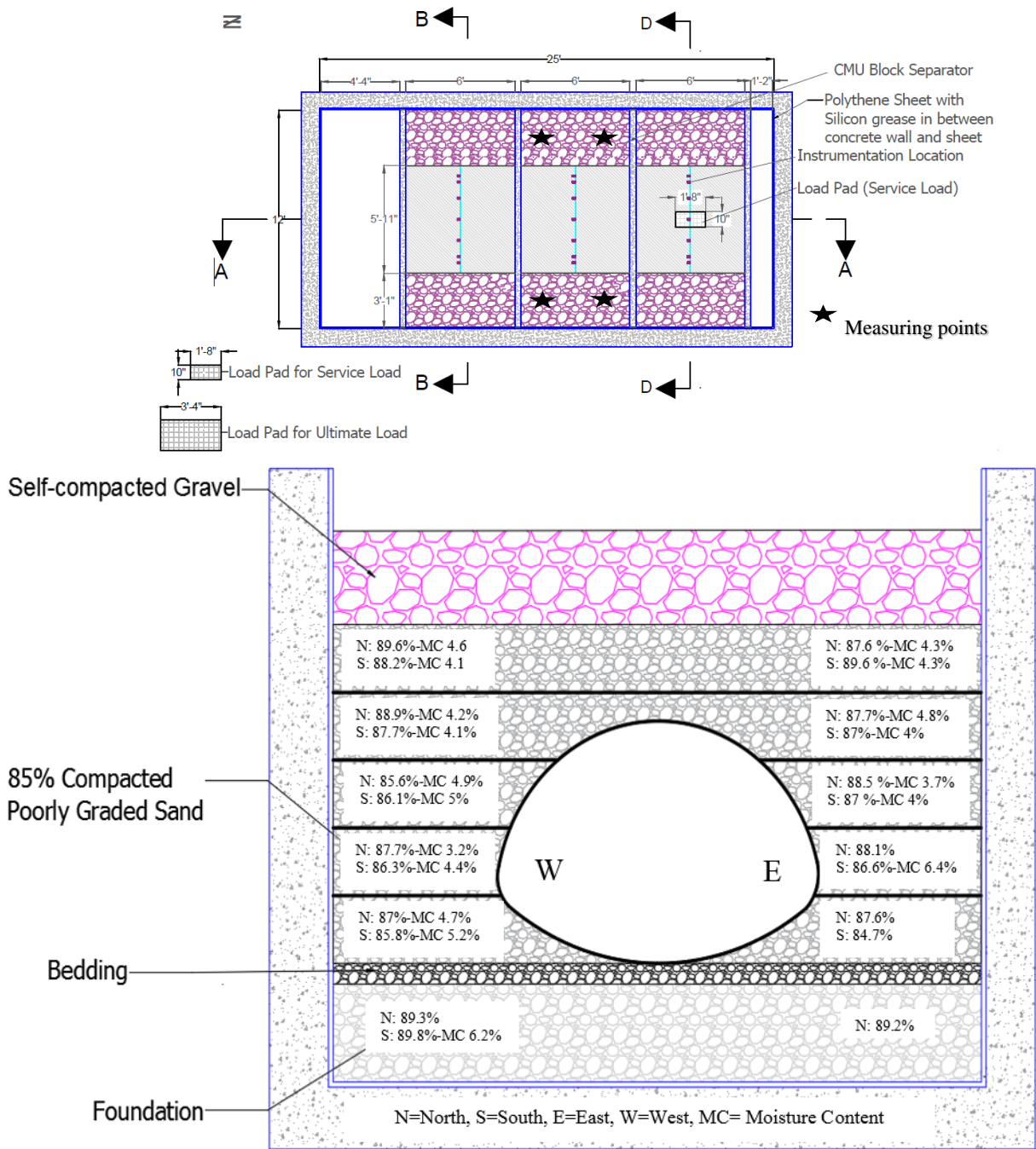


APPENDIX B. Compaction Measurement

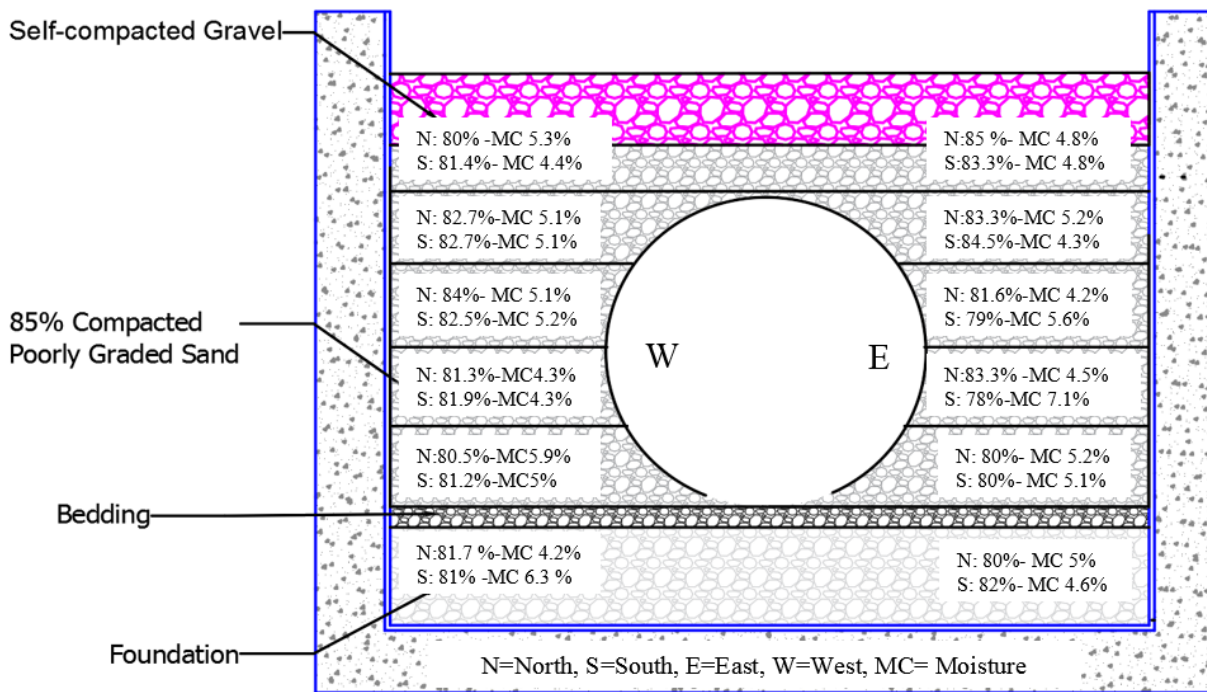
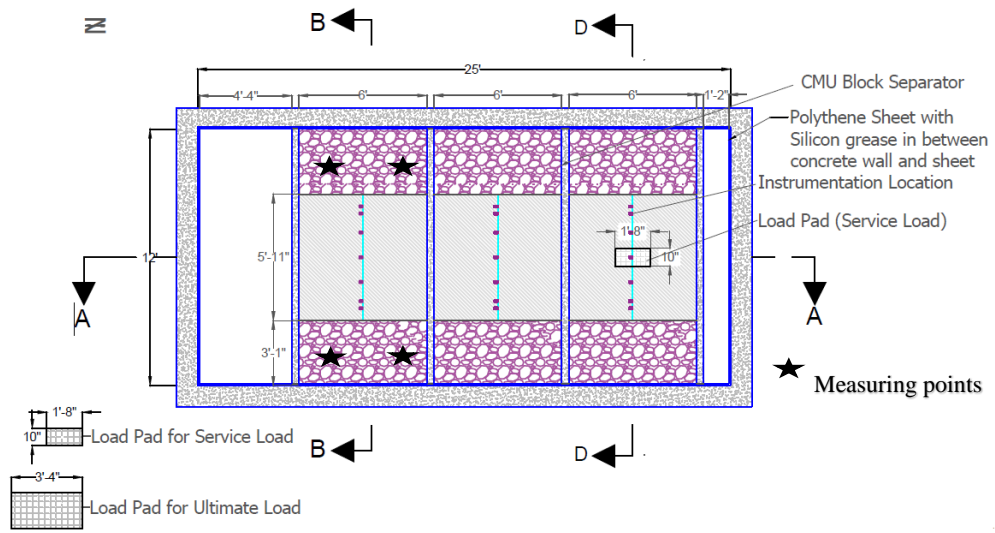
The compaction measurement was conducted through a nuclear density measurement gauge. The measured maximum proctor density was 115.2 pcf, obtained from the standard proctor compaction test. The measurements have carried out in 6 layers at two repetitions for both East and West locations of the pipe. The measured values for control test measurements are demonstrated in the figures below.



Compaction results for control test, intact CMP sample.



Compaction results for control test, invert-cut pipe arch CMP sample



Compaction results for control test, invert-cut circular CMP sample

APPENDIX C. GeoCast® Data Sheet

GeoCast® Geopolymer Mortar

Concrete Pipes and Culverts Rehabilitation

GENERAL

GeoCast® Geopolymer Mortar is for rehabilitation of horizontal concrete and corrugated steel culvert pipes; and vertical shafts, main sewers and stormwater drain workings. The Geocast® Geopolymer Mortar restores inverts in existing deteriorated pipes, stops water infiltration and exfiltration and prevents undercutting of pipe beddings. The Geocast® GM contains ANSI 61/ NSF 61 approved cement, and offers the [optional] benefit of DCI® Corrosion Inhibitor; a liquid admixture that's added to the mix during batching **that protects steel pipes and reinforcement against salt water chlorides**. The GeoCast® GM is comprised of inorganic microsilica geopolymer minerals, pozzolan binders, polypropylene fibers and select admixtures for protecting concrete [brick] and Fiberglass manholes against hydrogen sulfide (H₂S) attack.

APPLICATIONS

The GeoCast® Mortar is a wet-mix [dry] gunned shotcrete, pneumatically used (hand applied) or as a centrifugally applied liner for existing stormwater pipes, sanitary sewers and manhole rehabilitation. It provides extreme workability and applications to +3-inch thickness in one application.

- Abrasion and crack resistant mortar gains high early strength quickly, provides increased bond and reduced permeability.
- **Enhanced freeze thaw durability for northern regions.**
- Structural reinstatement of damaged concrete and brick tunnels, lift station wet wells, filtration basins, WTP constructions, bridges, parking garages, and dam structures to extend their service life beyond their original design.

PROTECTION LEVELS

GeoCast® Geopolymer Mortar protects against microbiologically induced corrosion (MIC), sulfates, chlorides, water vapor transmission and acids to pH 2.

YIELD

For estimating purpose only, adjust for waste, and cut-offs that reduces the coverage:

Approximately	7.4 ft ² at 1-in. thickness
	0.63 ft ³ per 75 lb. bag
Working time:	254-minutes (73°F)

PACKAGING

Stocked in 75 lb. bags, pallets and truckloads.
Shelf life 1 year when properly stored.

MIXING

Use clean, potable water. Do not add Portland cement or any admixture to this product

TECHNICAL INFORMATION

Property	PSI		
Compressive Strength	24h	7d	28d
ASTM C 109	2,800	6,370	8,290
Flexural Strength	24h	7d	28d
ASTM C 293	*	1,170	1,665
Splitting Tensile Strength			28d
ASTM C 496			685
Modulus of Elasticity			
ASTM C 496/ C 469M			3.85 x 10 ⁶
Shrinkage at 50% RH			
ASTM C 596			-0.178%
Chemical Resistance-90 days:			
ASTM C 267			
2,000 ppm (sulfuric acid)			0% weight loss No defects
20,000 ppm (sulfuric acid)			0.15% weight loss Slight discoloration
Freeze Thaw Resistance-300 cycles			
ASTM C 666			98%
Slant Shear Bond Strength			28d
ASTM C 882			2,930
Rapid Chloride Permeability			28d
ASTM C 1202			311 & Very low
Density			145 ± 2 lbs.

EQUIPMENT

The applicator shall use an approved Sewer Manhole Masters™ Repair Trailer or approved equal.

PLACEMENT/ CURING

Ambient temperatures and job conditions will govern specific curing. Take special care during hot or cold weather. Place immediately by hand, pneumatic shotcrete {gunite}; or centrifugal spray method. Follow ACI 302 Guide for Concrete Floors and Slab Construction and ACI 308 Standard Practice for Curing Concrete to avoid any shrinkage cracking problems due to decreased bleeding. Protect the cement from hot weather extremes, air movement and dry conditions, and direct sunlight. Cure as soon as the surface begins to harden, cover with plastic sheets or use an acceptable liquid membrane-forming curing compound per ASTM C 309 Liquid membrane-Forming Compounds Having Special Properties. The curing compound shall contain a minimum of 25 % solids and prevent water loss of up to 0.4-kg/m³ in 72 hours. Apply the curing compound in layers while the cement is still soft to keep the cement moist and at a favorable temperature during the early hardening period. Make no application when the ambient temperatures are less than 40°F or freezing temperature is expected within 24-hour. Trail batches are recommended.

STORAGE

Store in unopen containers in a clean dry area raised up off the floor.

SAFETY

Caution: contains fused calcium hydrates—May Cause Eye and Skin Irritation. Clean up with soap and water. Avoid prolong exposure. Wash with water immediately after handling. If skin problems arise, flush with water and get medical help. Store in a dry, cool place, and stocked in a 75-lb bag. Keep out of reach of children.

TECHNICAL SERVICE

Manufacturer provides technical and on-site assistance within 48-hours' notice.

WARRANTY

The manufacturer warrants this product to be of good quality and free from defects within the warranty period. Failure does not include acts of

God, consequential damage resulting from workmanship, mechanical and chemical maltreatment or exposure not customarily used in connection with the structure. The manufacturer's liability and the Buyer's single remedy in connection with the product shall be limited to replacement of the product not conforming to this warranty. The manufacturer reserves the right to determine whether any claim is specifically related to another cause. The corporation makes no other warranties, either expressed or implied and in no event intends to infringe on any established patents or trademarks.

Customer Service:

Standard Cement Materials, Inc.
www.standardcement.com
[www.sales@standardcement.com](mailto:sales@standardcement.com)
2019.

APPENDIX D. Compressive Strength Test Results

Table D-1. Pipe arch CMP's SAPL batch.

Casting Date:		6/13/2020				
Testing Date:		6/14/2020 (24 Hours)				
Specimen Size (in.)	Casting Type	Replicate Number	Applied Force (lb.)	F'c (psi)	Ave. Force (lb.)	Ave. F'c (psi)
4x8	Spray	1	23500.0	1871.0	24600	1958.6
		2	33900.0	2699.0		
		3	22900.0	1823.2		
		4	18100.0	1441.1		
Testing Date:		6/22/2020 (7 Days)				
Specimen Size	Casting Type	Replicate Number	Applied Force (lb)	F'C (psi)	Ave. Force (lb.)	Ave. F'c (psi)
4x8	Hand	1	31300.0	2492.0	38700.0	3081.2
		2	41300.0	3288.2		
		3	43500.0	3463.4		
	Spray	1	34500.0	2746.8	35566.7	2831.7
		2	37100.0	2953.8		
		3	35100.0	2794.6		
6x12	Spray	1	116000.0	4104.7	96500.0	3414.7
		2	77000.0	2724.7		
3x6	Hand	1	30600.0	4331.2	27250.0	3857.0
		2	23900.0	3382.9		
	Spray	1	26800.0	3793.3	24550.0	3474.9
		2	22300.0	3156.4		
Cube (2x2x2)	Hand	1	17400.0	4350.0	21040.0	5260.0
		2	25200.0	6300.0		
		3	20000.0	5000.0		
		4	22200.0	5550.0		
		5	20400.0	5100.0		
Testing Date:		7/10/2020 (28 Days)				
Specimen Size	Casting Type	Replicate Number	Applied Force (lb)	F'C (psi)	Ave. Force (lb.)	Ave. F'c (psi)
4x8	Hand	1	40200.0	3200.6	44033.3	3505.8
		2	38000.0	3025.5		
		3	53900.0	4291.4		
	Spray	1	63000.0	5015.9	57200.0	4554.1
		2	74300.0	5915.6		
		3	34300.0	2730.9		
6x12	Spray	1	85800.0	3036.1	113300.0	4009.2
		2	66100.0	2339.0		
		3	188000.0	6652.5		
3x6	Hand	1	27000.0	3857.1	28100.0	3995.1
		2	29200.0	4133.1		
	Spray	1	32000.0	4529.4	31250.0	4423.2
		2	30500.0	4317.1		
Cube (2x2x2)	Hand	1	22100.0	5525.0	25725.0	6431.3
		2	27200.0	6800.0		
		3	28800.0	7200.0		
		4	24800.0	6200.0		

Table D-2. Circular CMP's SAPL batch.

Casting Date:		7/18/2020				
Testing Date:		7/19/2020 (24 Hours)				
Specimen Size (in.)	Casting Type	Replicate Number	Applied Force (lb.)	F'c (psi)	Ave. Force (lb.)	Ave. F'c (psi)
Cube (2x2x2)	Hand	1	10500	2625	11013.6	2753.4
		2	9440.8	2360.2		
		3	13100	3275		
4x8	Spray	1	26600.0	2117.8	23933.3	1905.5
		2	20600.0	1640.1		
		3	24600.0	1958.6		
	Hand	1	39000.0	3105.1	31100.0	2476.1
		2	30300.0	2412.4		
		3	24000.0	1910.8		
Testing Date:		7/26/2020 (7 Days)				
Specimen Size	Casting Type	Replicate Number	Applied Force (lb)	F'C (psi)	Ave. Force (lb.)	Ave. F'c (psi)
4x8	Hand	1	61300.0	4880.6	62366.7	4965.5
		2	71900.0	5724.5		
		3	53900.0	4291.4		
	Spray	1	72400.0	5764.3	59333.3	4724.0
		2	61500.0	4896.5		
		3	44100.0	3511.1		
6x12	Spray	1	142000.0	5024.8	134000.0	4741.7
		2	160000.0	5661.7		
		3	100000.0	3538.6		
3x6	Hand	1	25900.0	3666.0	28100.0	3977.4
		2	30300.0	4288.7		
	Spray	1	19500.0	2760.1	22350.0	3163.5
		2	25200	3566.88		
Cube (2x2x2)	Hand	1	18700.0	4675.0	17766.7	4441.7
		2	19200.0	4800.0		
		3	15400.0	3850.0		
Testing Date:		8/17/2020 (28 Days)				
Specimen Size	Casting Type	Replicate Number	Applied Force (lb)	F'C (psi)	Ave. Force (lb.)	Ave. F'c (psi)
4x8	Hand	1	67500	5374.2	65666.7	5228.2
		2	69300	5517.5		
		3	60200	4793.0		
	Spray	1	86900.0	6918.8	75700.0	6027.1
		2	70300.0	5597.1		
		3	69900.0	5565.3		
6x12	Spray	1	127000.0	4494.0	118000.0	4175.5
		2	119000.0	4210.9		
		3	108000.0	3821.7		
3x6	Hand	1	28000.0	3963.2	29600.0	4189.7
		2	31200.0	4416.1		
	Spray	1	33800	4784.15	30600.0	4331.2
		2	27400.0	3878.3		
Cube (2x2x2)	Hand	1	31200	7800.0	27833.3	6958.3
		2	24800	6200.0		
		3	27500	6875.0		

APPENDIX E. Thickness Measurement Results

Table E-1. Pipe arch CMPs renewed with SAPL

Cell 1 (Close to Wall)					
Angle	Nominal Thickness	US	Caliper		
		Location	North	Center	South
0	1	E2	0.886	1.220	1.080
45		E1	0.864	1.770	1.516
90		Crown	1.015	1.173	1.013
135		W1	0.846	1.501	1.174
180		W2	1.209	1.604	0.704
225		W3	0.885	1.640	1.216
270		Invert	1.098	0.740	0.623
315		E3	0.881	1.090	0.899
360		E2	0.886	1.220	1.080
Cell 2 (Middle Cell)					
Angle	Nominal Thickness	US	Caliper		
		Location	North	Center	South
0	2	E2	1.738	1.935	1.805
45		E1	1.555	1.886	1.686
90		Crown	1.935	2.005	2.216
135		W1	1.615	1.924	1.820
180		W2	1.823	1.878	1.912
225		W3	1.695	1.650	1.801
270		Invert	1.632	1.914	2.040
315		E3	1.665	1.772	1.715
360		E2	1.738	1.935	1.805
Cell 3 (Close to Door)					
Angle	Nominal Thickness	US	Caliper		
		Location	North	Center	South
0	3	E2	2.518	2.434	3.311
45		E1	2.31	2.725	3.142
90		Crown	2.128	2.122	2.657
135		W1	2.616	3.304	2.723
180		W2	3.42	3.382	2.603
225		W3	2.195	2.919	2.849
270		Invert	2.32	1.978	2.433
315		E3	2.146	2.192	2.533
360		E2	2.518	2.434	3.311

Table E-2. Circular CMPs renewed with SAPL

Cell 1 (Close to Wall)					
Angle	Nominal Thickness	US	Caliper		
		Location	North	Center	South
0	1	E2	0.615	1.342	1.285
45		E1	0.447	1.540	1.109
90		Crown	0.894	1.204	1.347
135		W1	0.858	1.421	1.276
180		W2	0.654	1.079	0.723
225		W3	1.223	1.586	1.301
270		Invert	1.431	1.305	1.356
315		E3	1.146	1.544	1.044
360		E2	0.615	1.342	1.285
Cell 2 (Middle Cell)					
Angle	Nominal Thickness	US	Caliper		
		Location	North	Center	South
0	2	E2	1.939	2.169	1.923
45		E1	2.230	1.915	2.290
90		Crown	2.349	2.522	2.136
135		W1	2.425	2.450	2.290
180		W2	2.080	1.768	1.515
225		W3	1.827	1.877	1.670
270		Invert	1.930	2.178	2.621
315		E3	2.012	2.062	1.859
360		E2	1.939	2.169	1.923
Cell 3 (Close to Door)					
Angle	Nominal Thickness	US	Caliper		
		Location	North	Center	South
0	3	E2	2.383	3.211	2.215
45		E1	3.114	3.322	3.285
90		Crown	3.251	3.6	3.09
135		W1	2.898	2.886	3.2
180		W2	2.952	2.435	2.141
225		W3	1.89	2.29	2.305
270		Invert	1.539	2.212	2.676
315		E3	2.361	2.517	2.727
360		E2	2.383	3.211	2.215

APPENDIX F. Crown Crack Width Measurement for Circular CMP

Samples

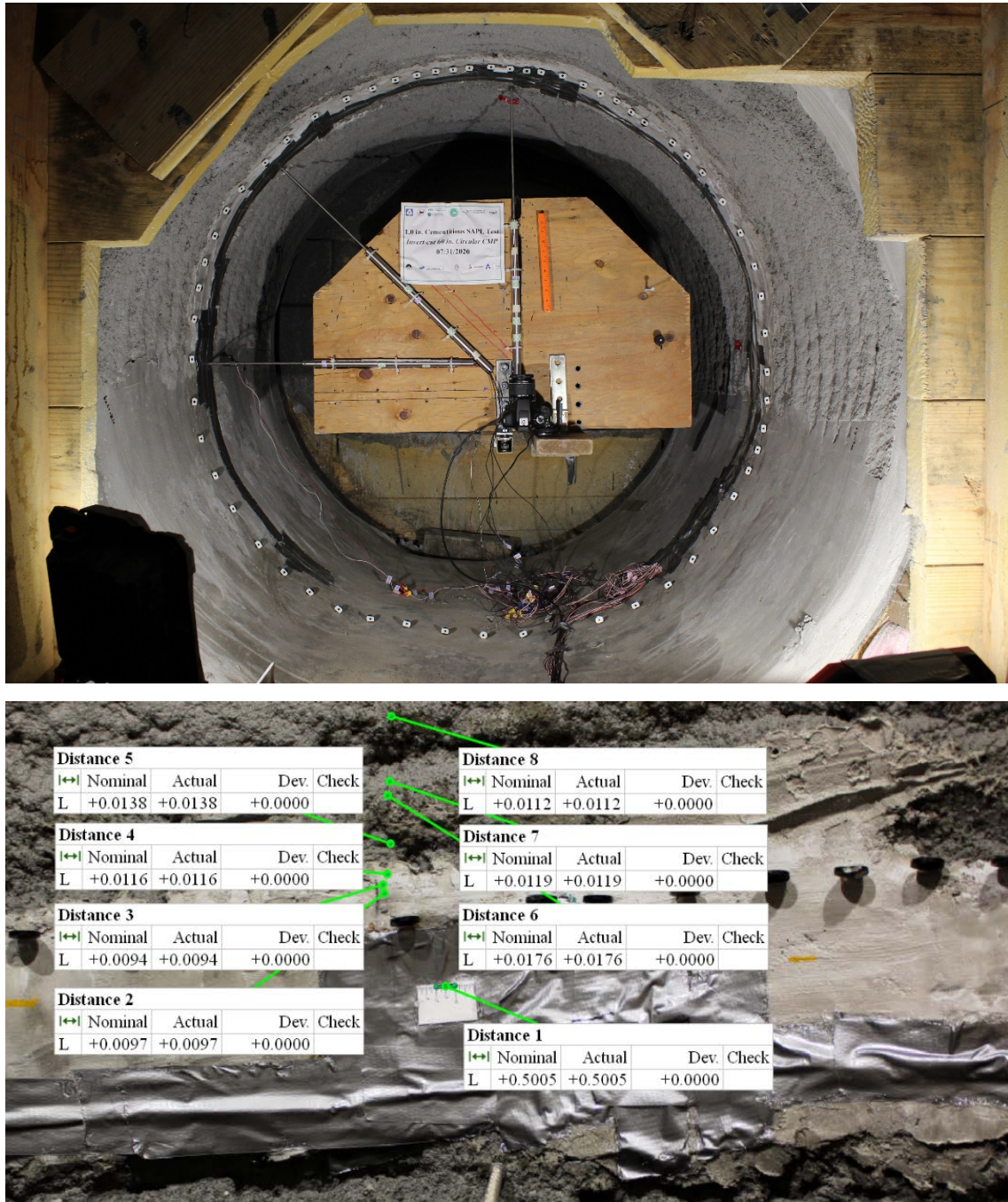


Figure F-1. Crack width measurement on the crown of the 1 in. SAPL renewed circular CMP at the beginning of the test.

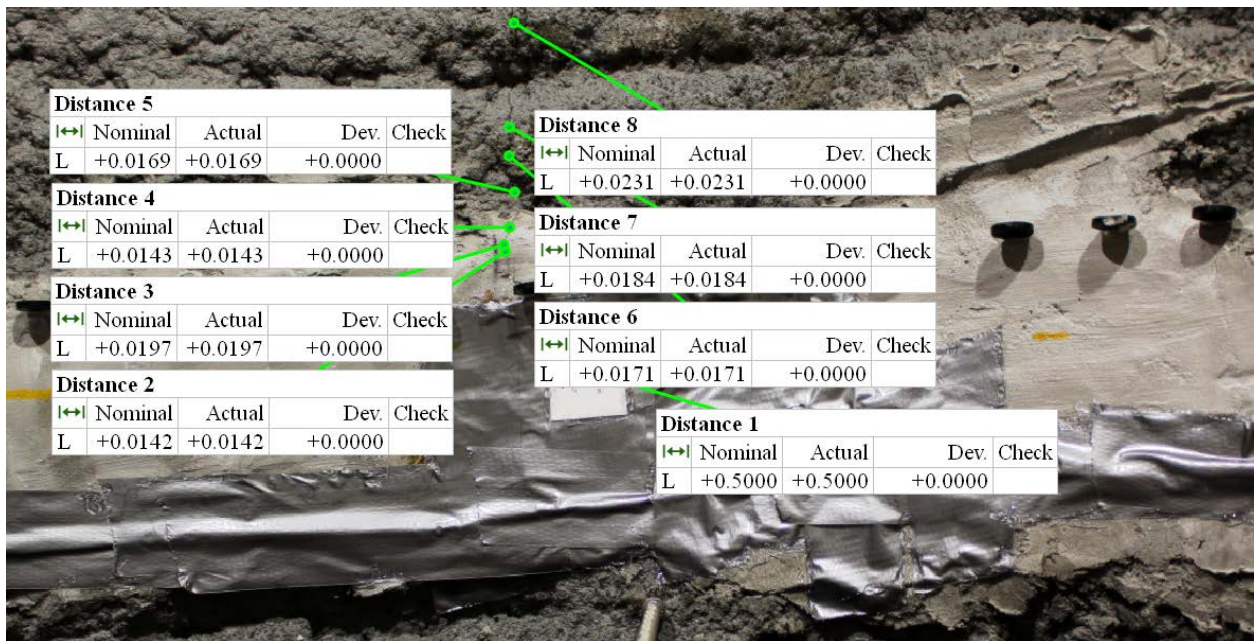
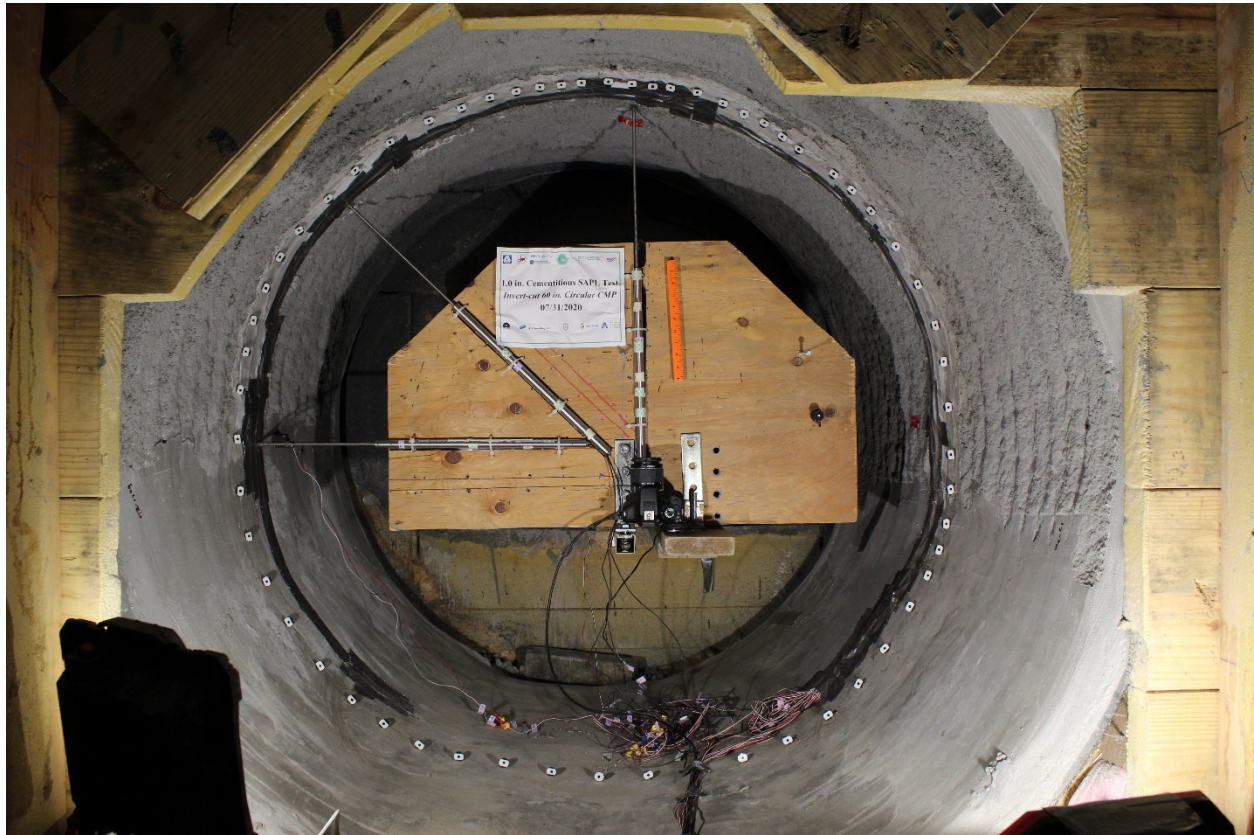


Figure F-2. Crack width measurement on the crown of the 1 in. SAPL renewed circular CMP at the load 10.4 kips.

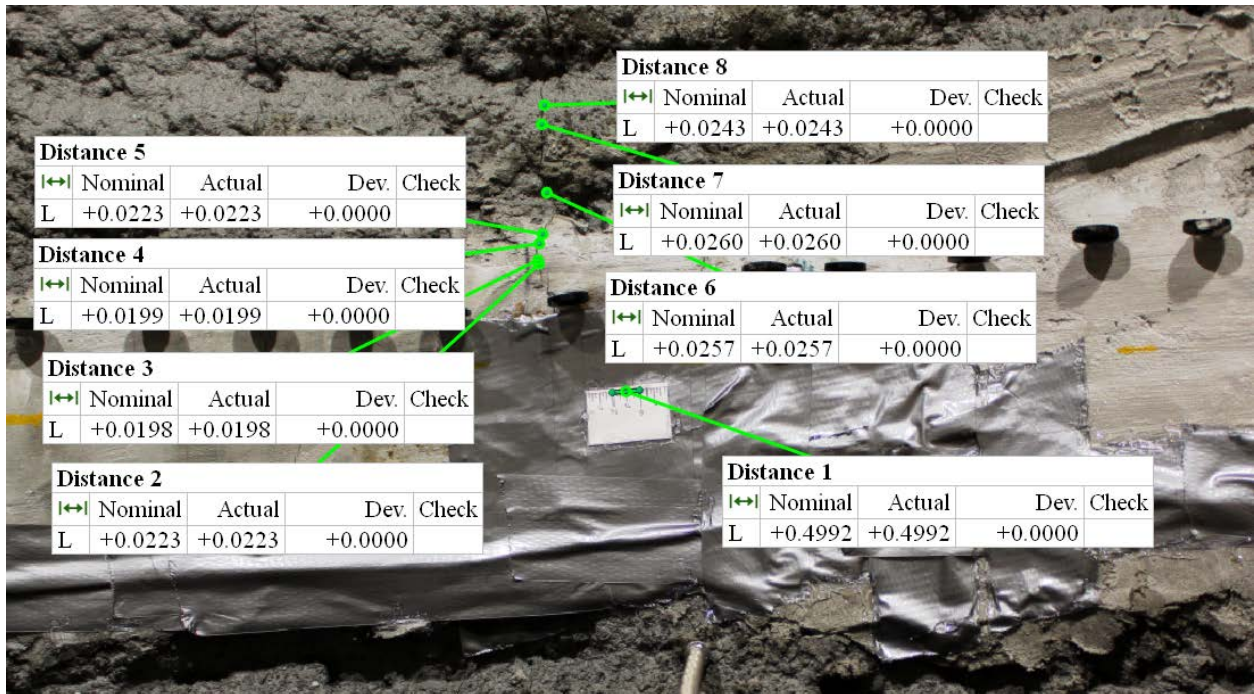
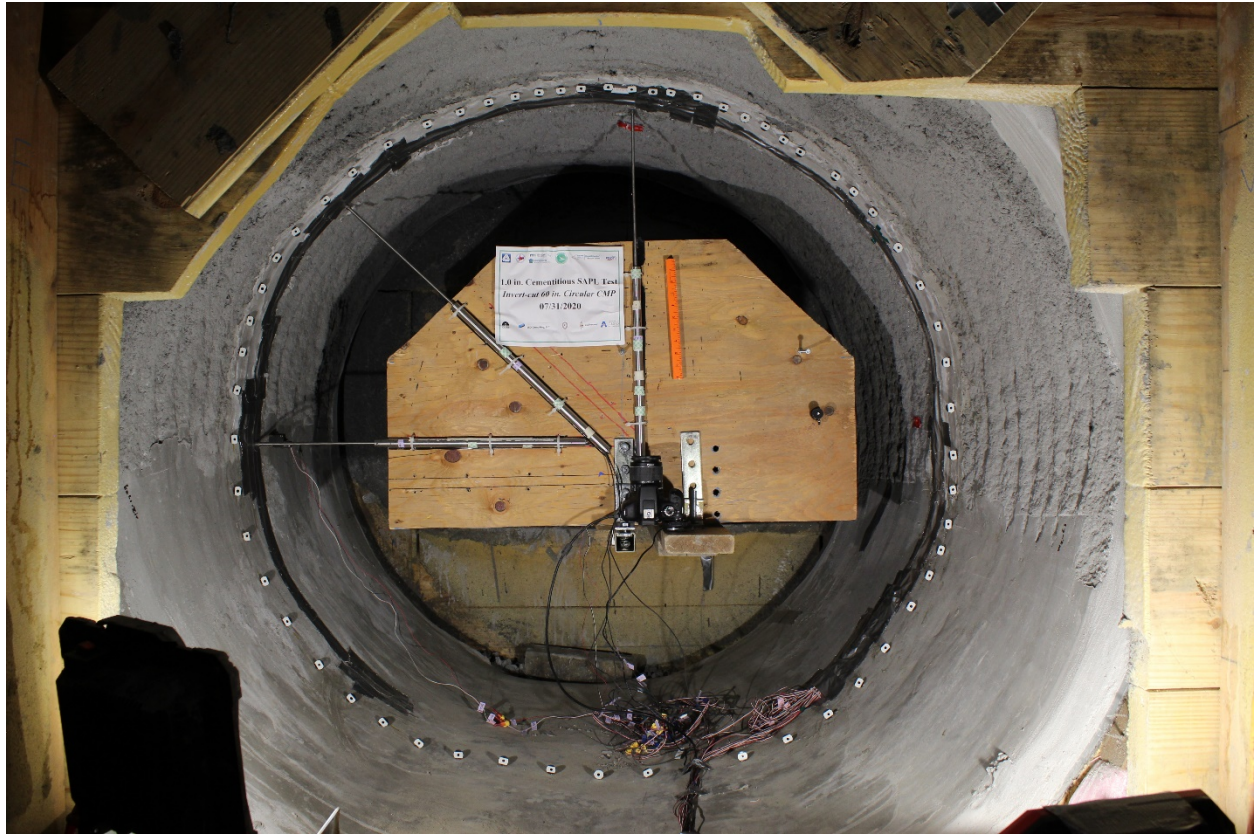


Figure F-3. Crack width measurement on the crown of the 1 in. SAPL renewed circular CMP at the load 26.45 kips.

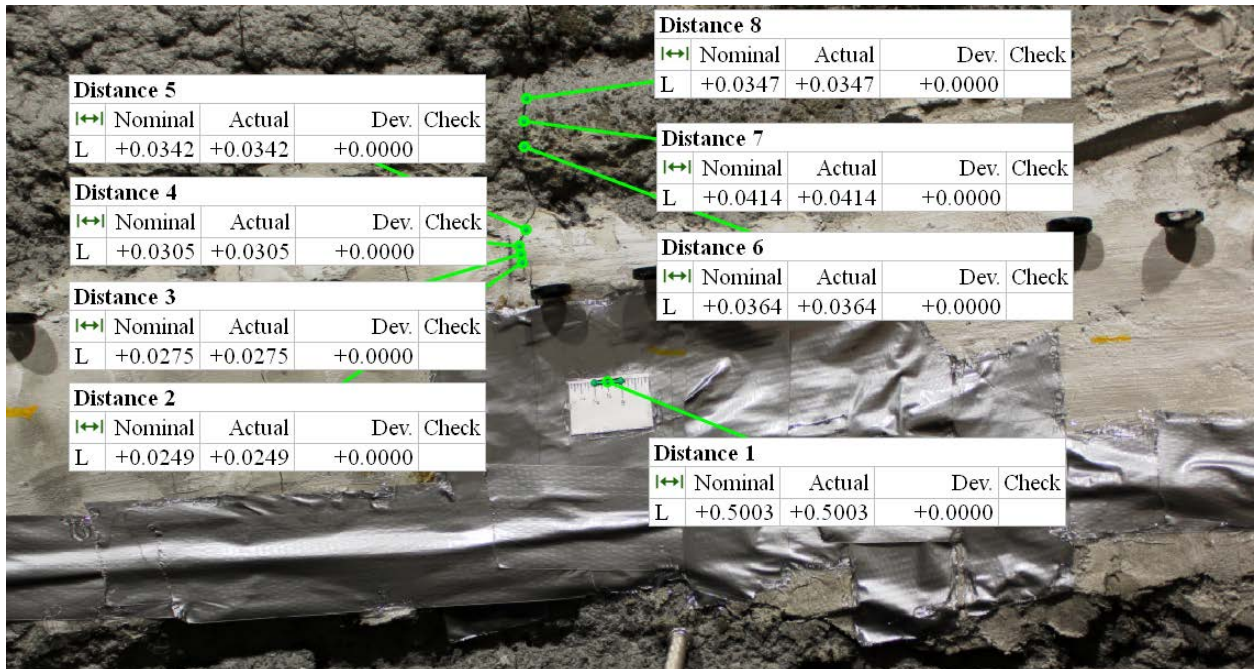


Figure F-4. Crack width measurement on the crown of the 1 in. SAPL renewed circular CMP at the load 39.1 kips.

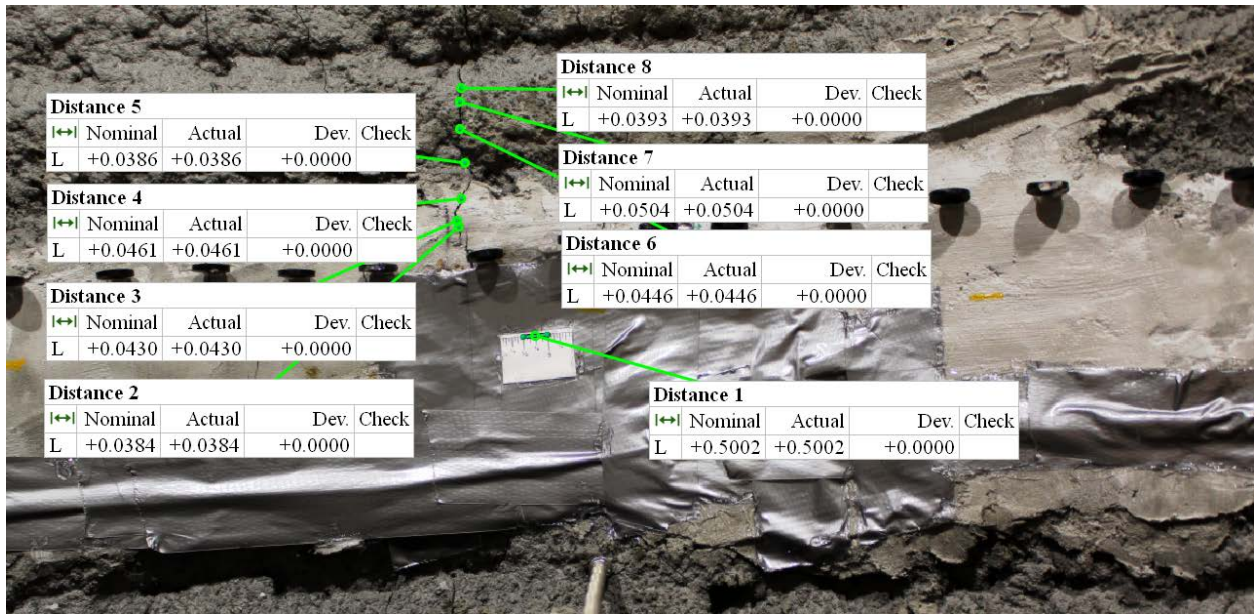
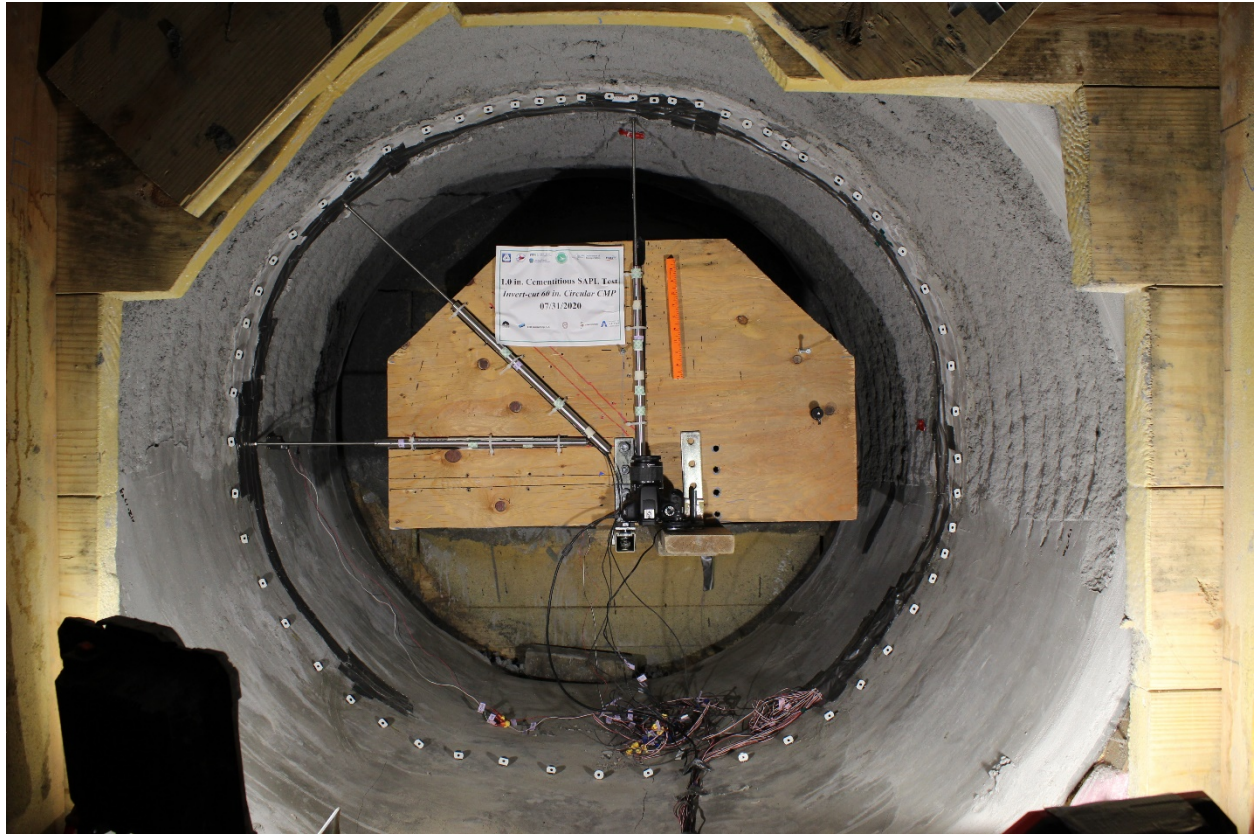


Figure F-5. Crack width measurement on the crown of the 1 in. SAPL renewed circular CMP at the load 45.2 kips.

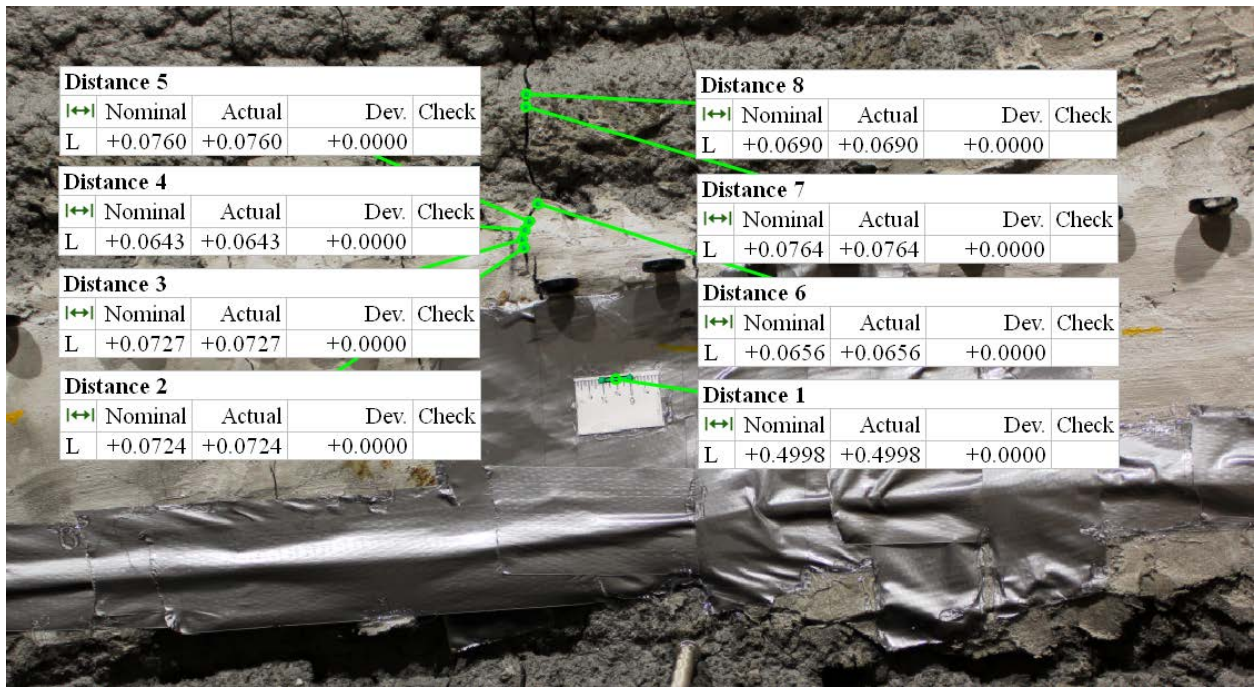
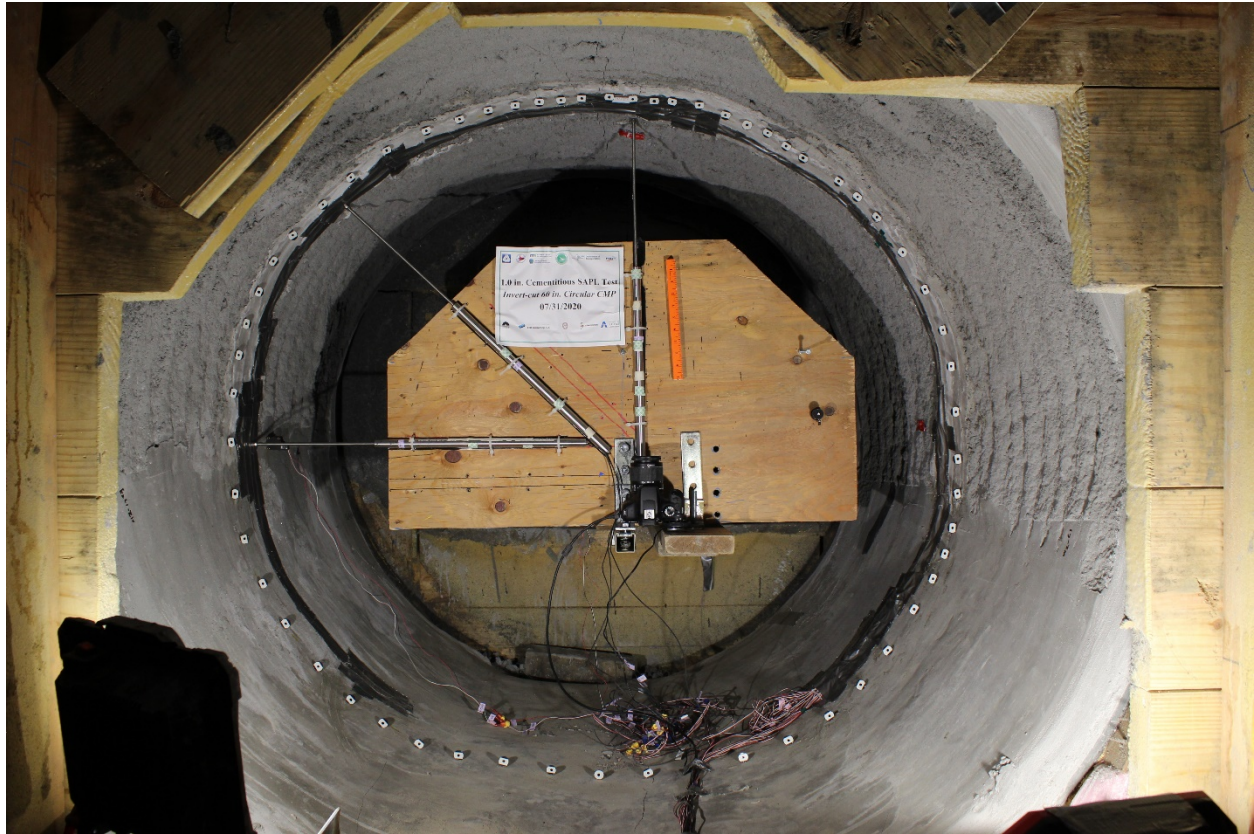


Figure F-6. Crack width measurement on the crown of the 1 in. SAPL renewed circular CMP at the load 58.5 kips.

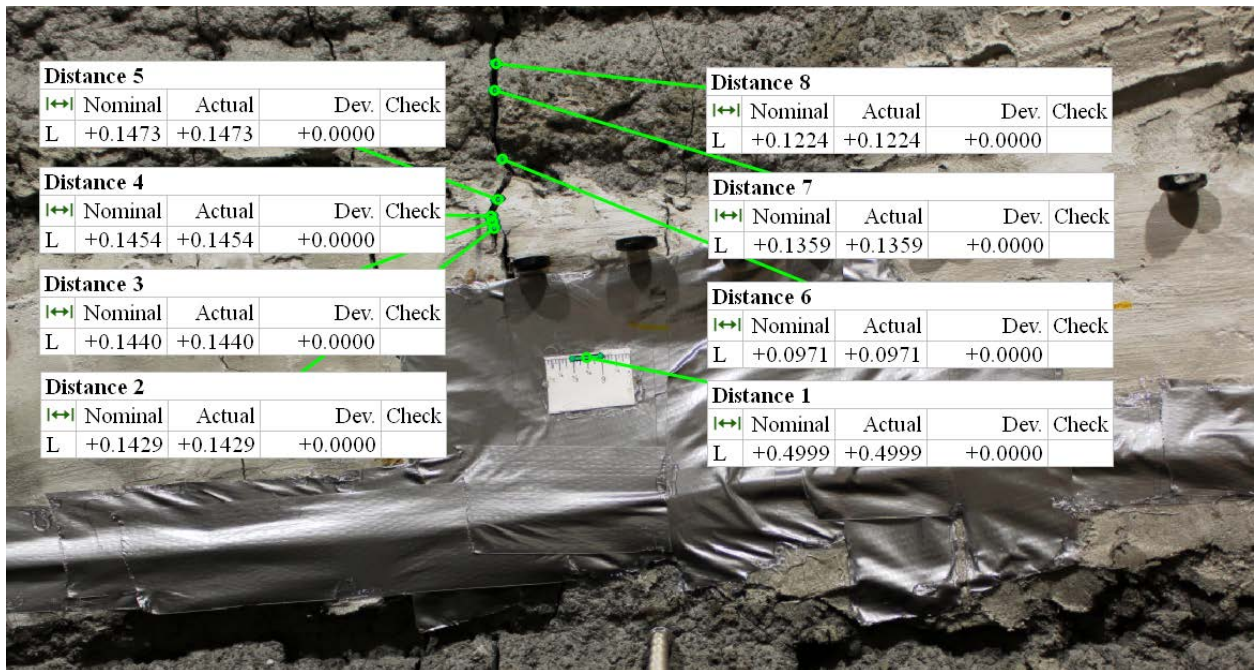
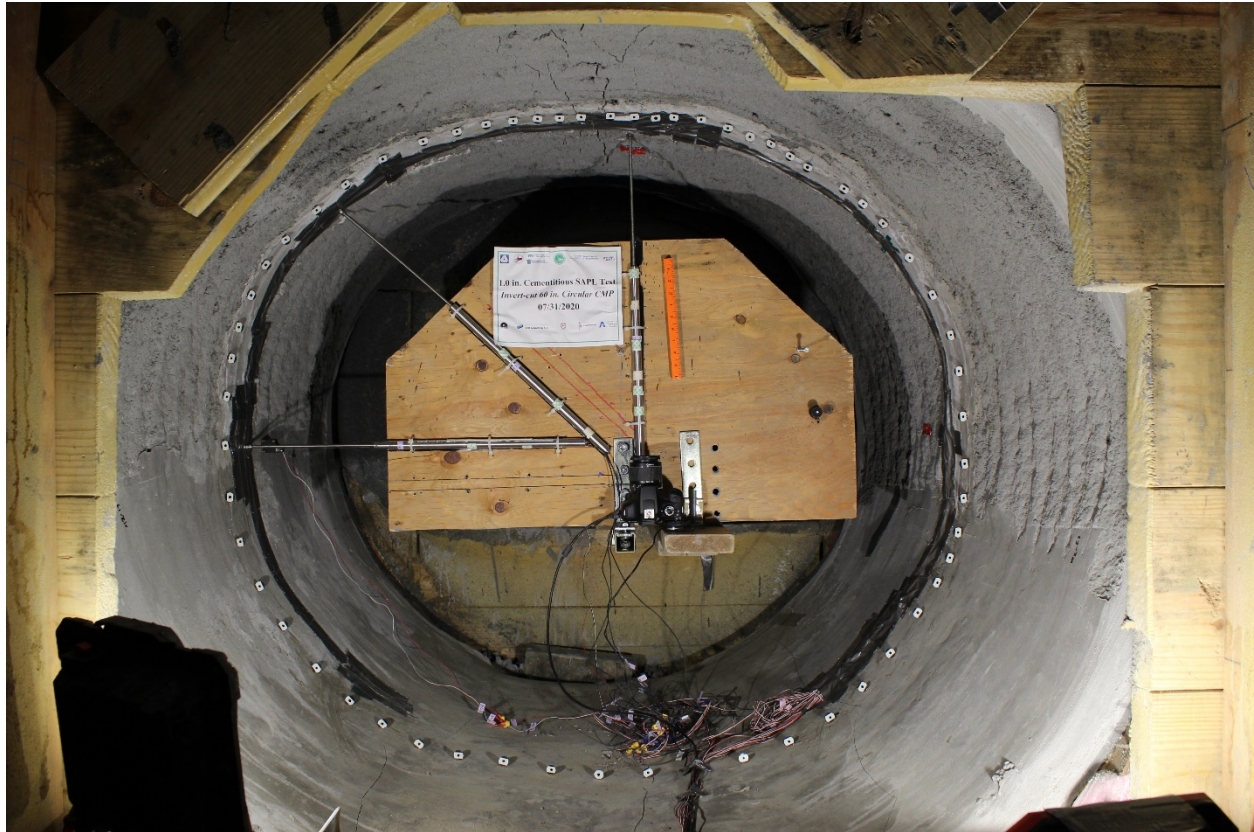


Figure F-7. Crack width measurement on the crown of the 1 in. SAPL renewed circular CMP at the load 71.7 kips.

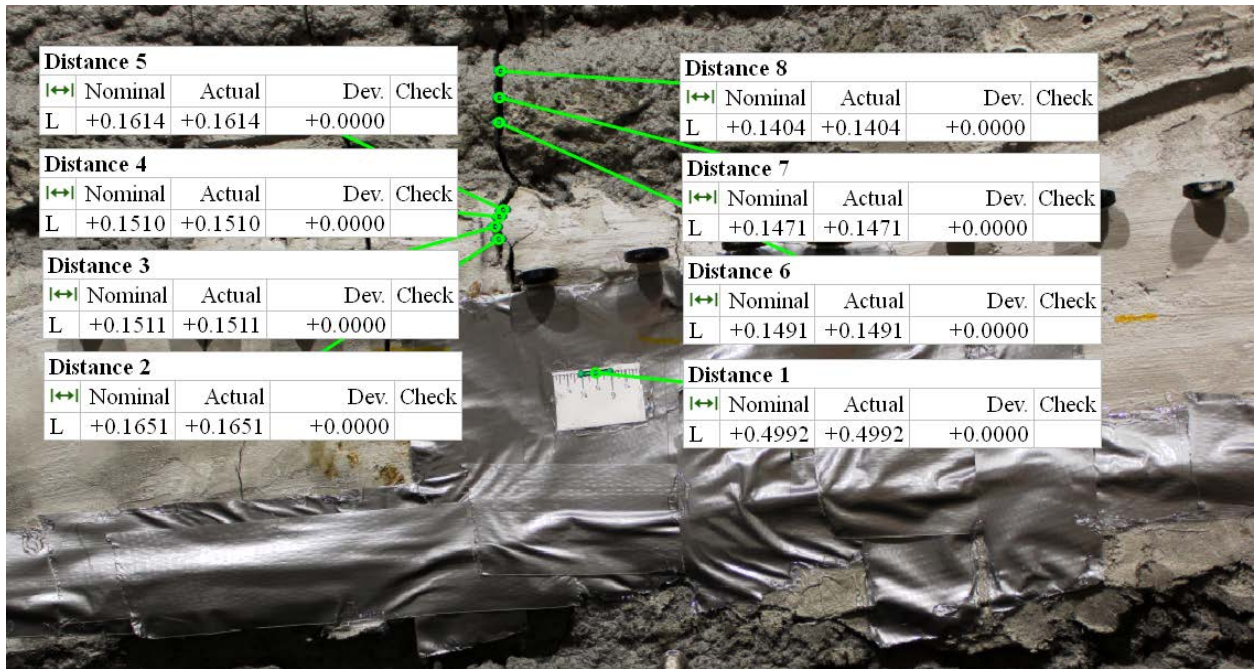
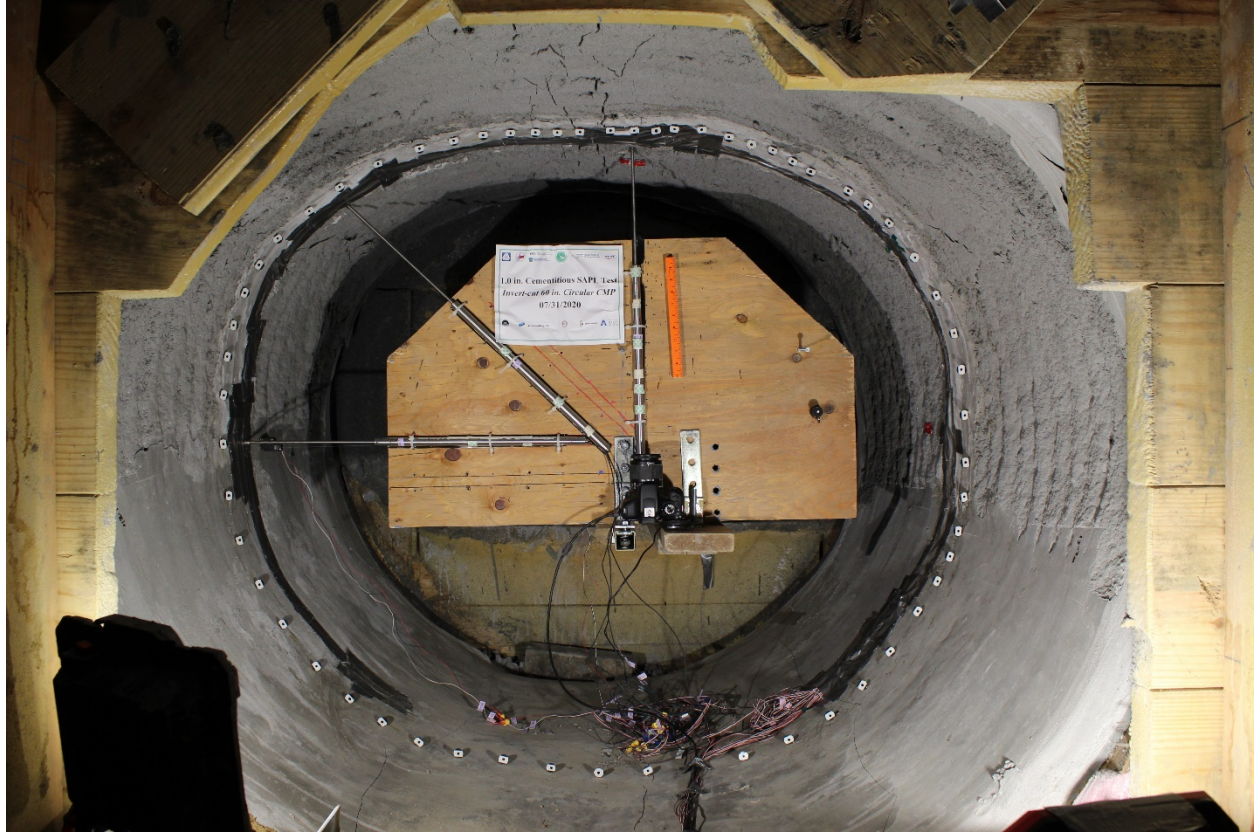


Figure F-8. Crack width measurement on the crown of the 1 in. SAPL renewed circular CMP at the end of the test.



Figure F-9. Crack width measurement on the crown of the 2 in. SAPL renewed circular CMP at the beginning of the test.

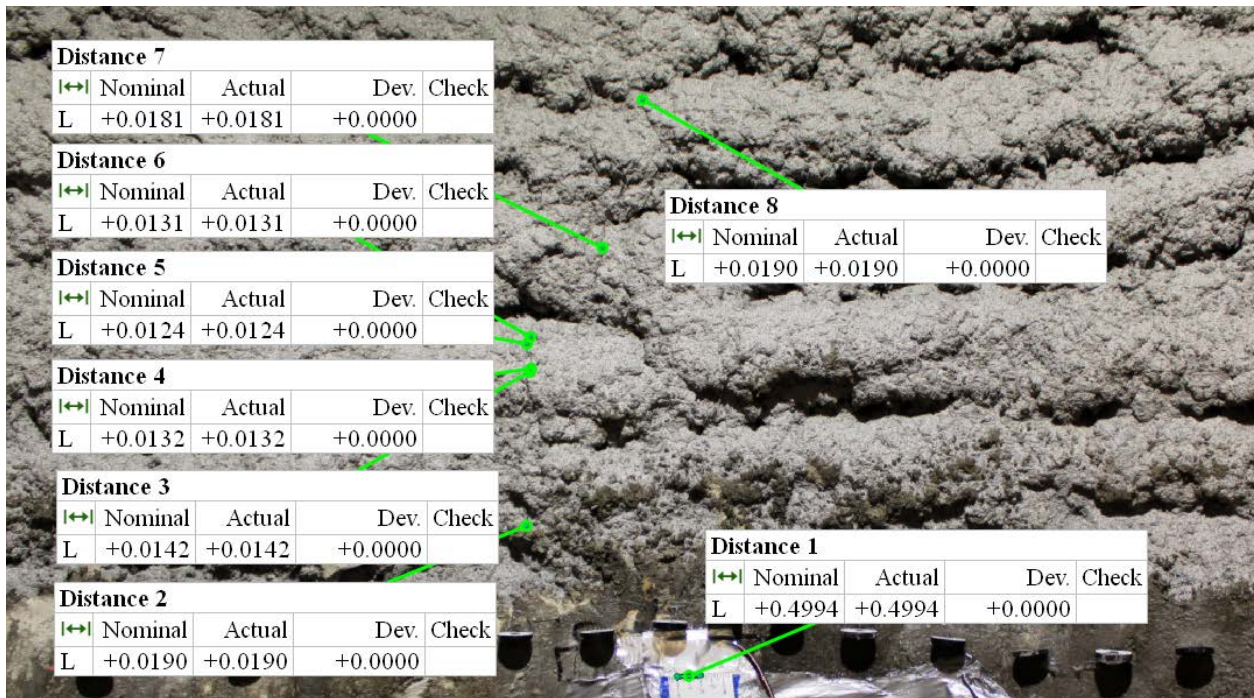


Figure F-10. Crack width measurement on the crown of the 2 in. SAPL renewed circular CMP at the load 14 kips.

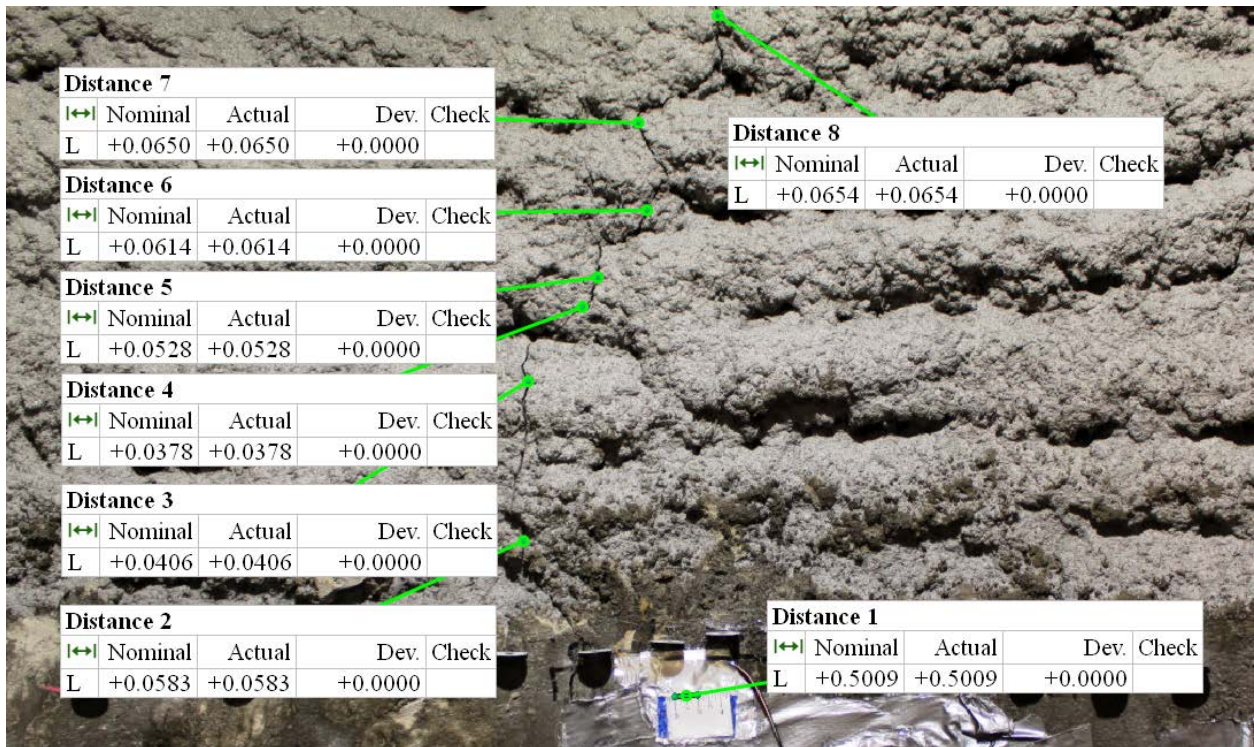
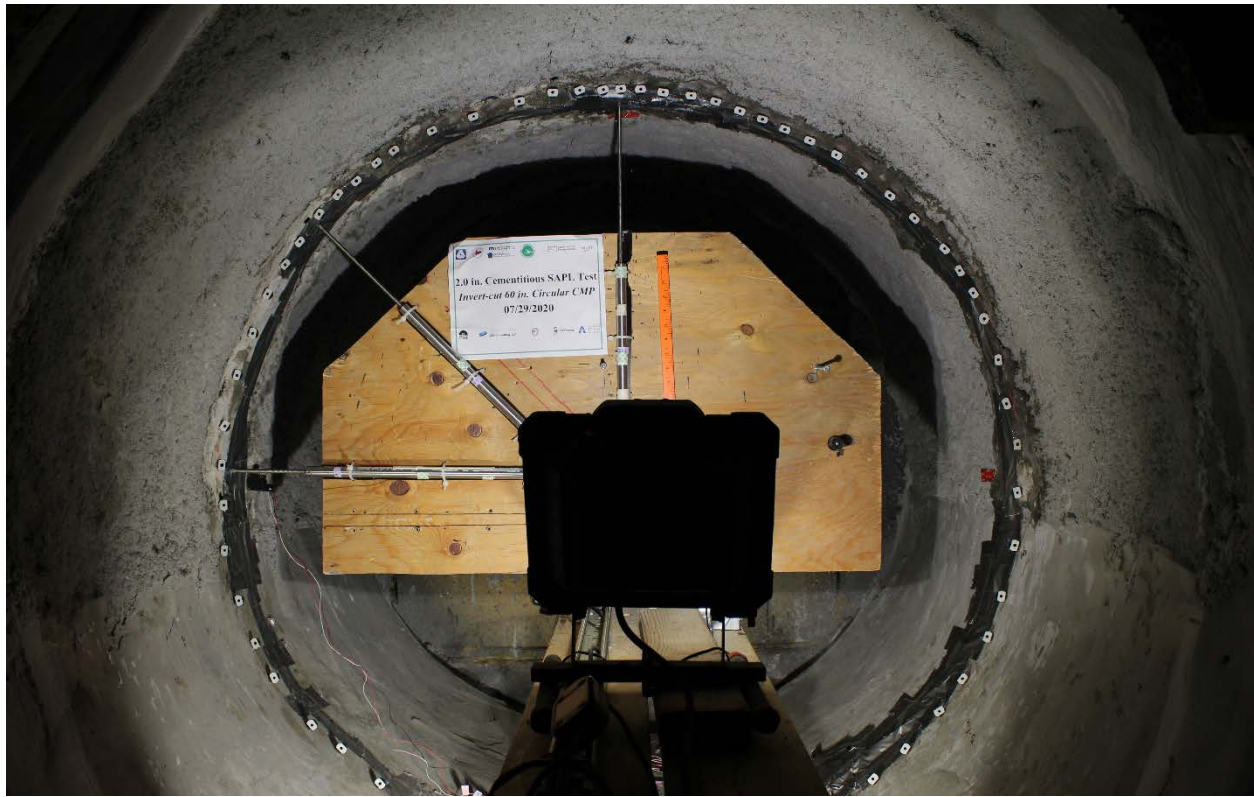


Figure F-11. Crack width measurement on the crown of the 2 in. SAPL renewed circular CMP at the load 33.92 kips.

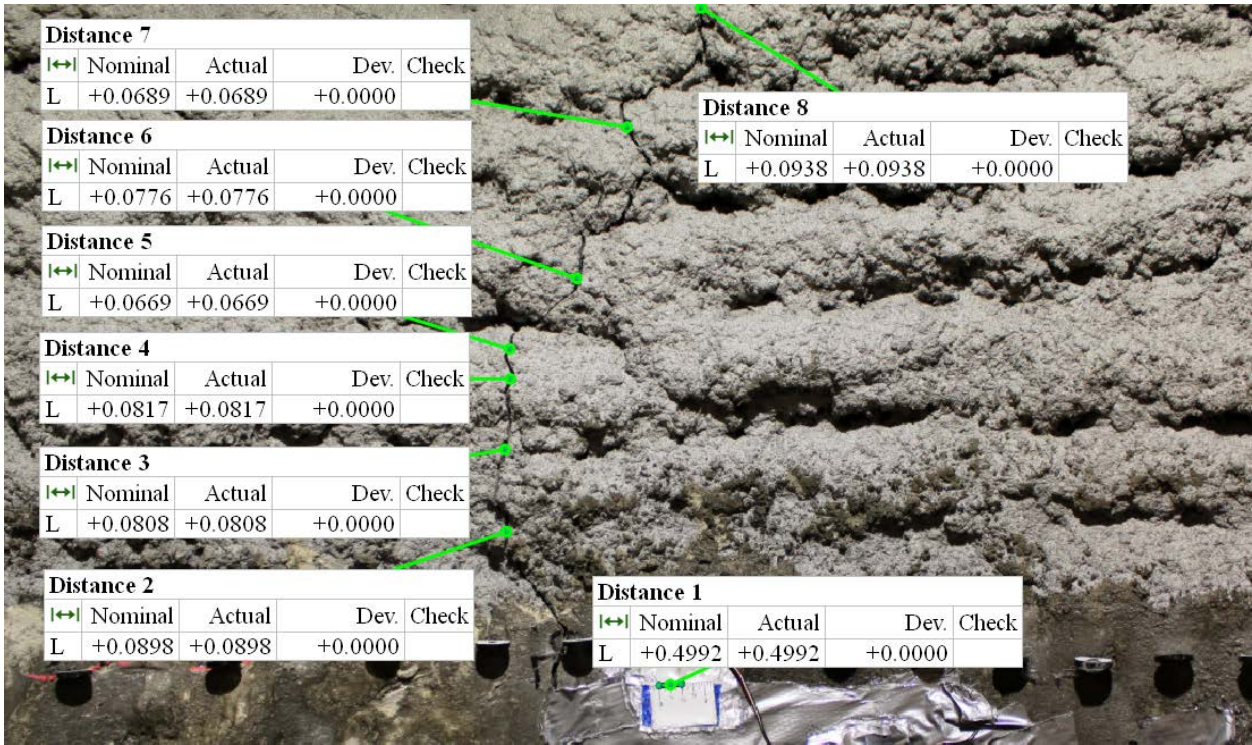


Figure F-12. Crack width measurement on the crown of the 2 in. SAPL renewed circular CMP at the load 52.6 kips.

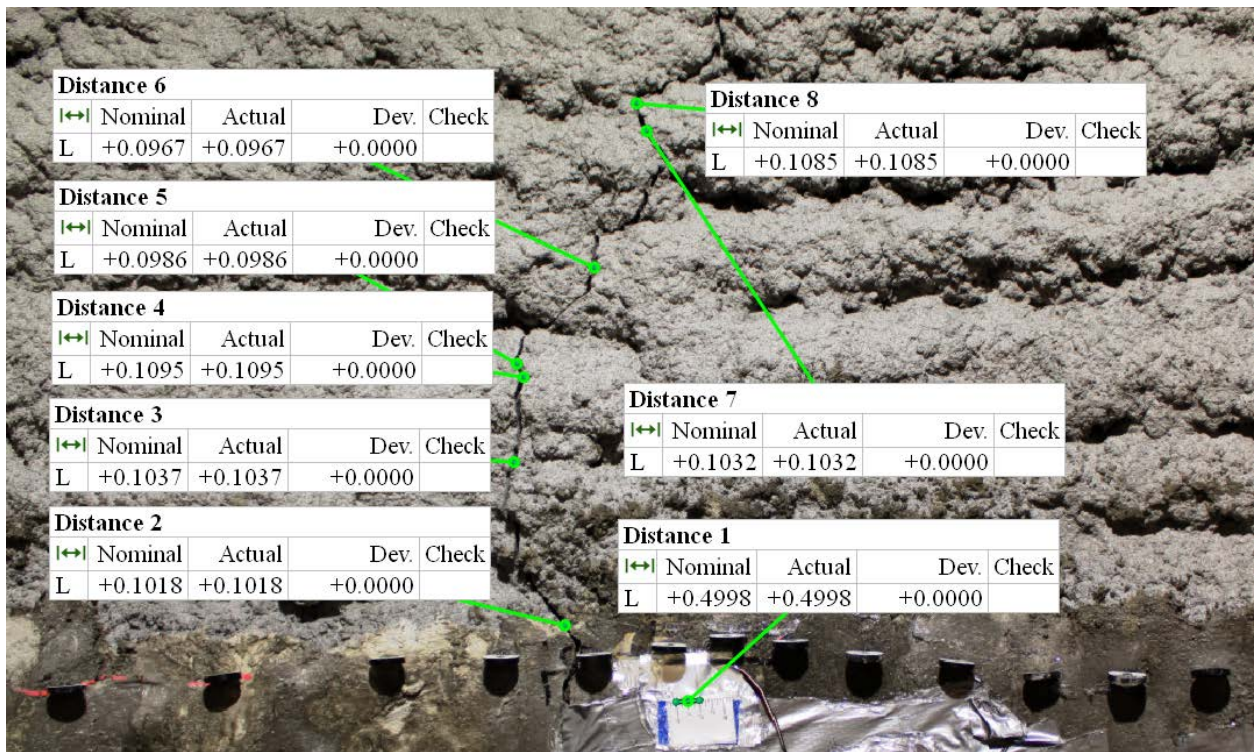
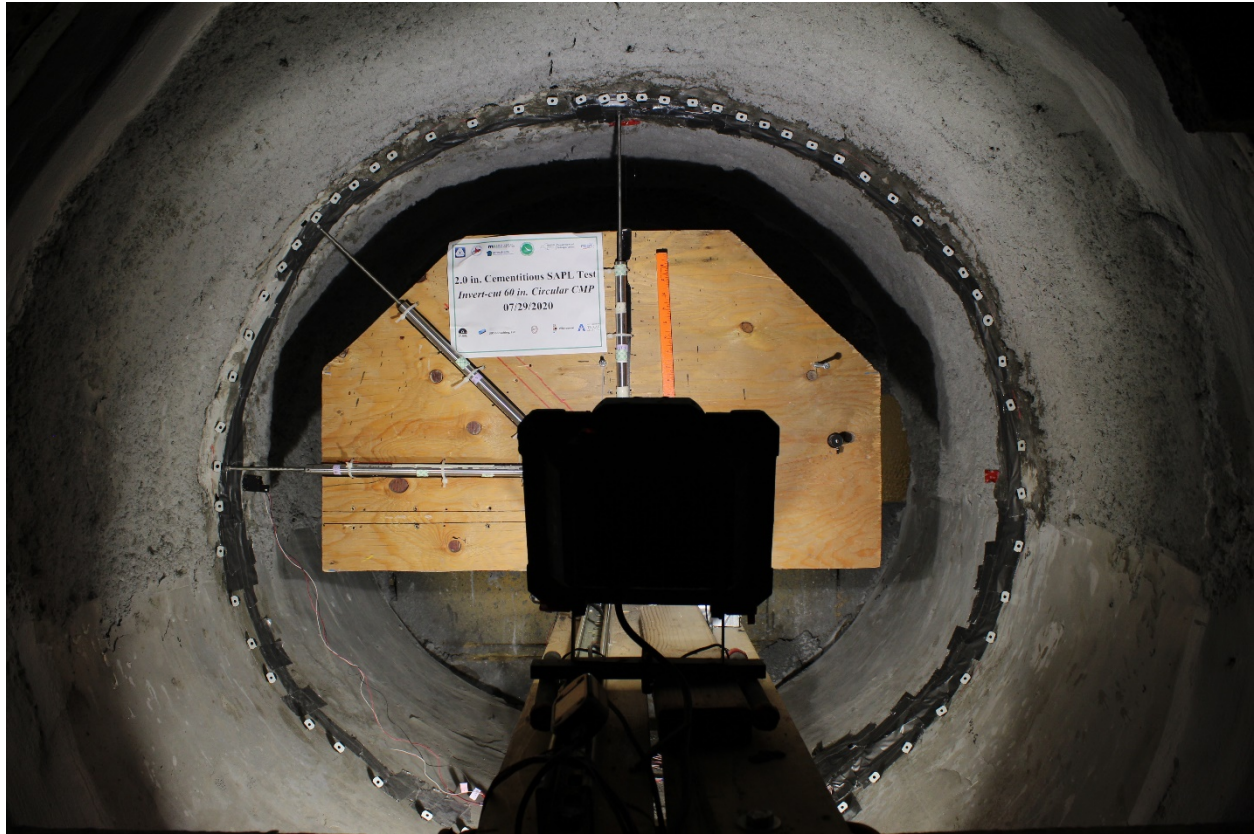


Figure F-13. Crack width measurement on the crown of the 2 in. SAPL renewed circular CMP at the load 67.6 kips.

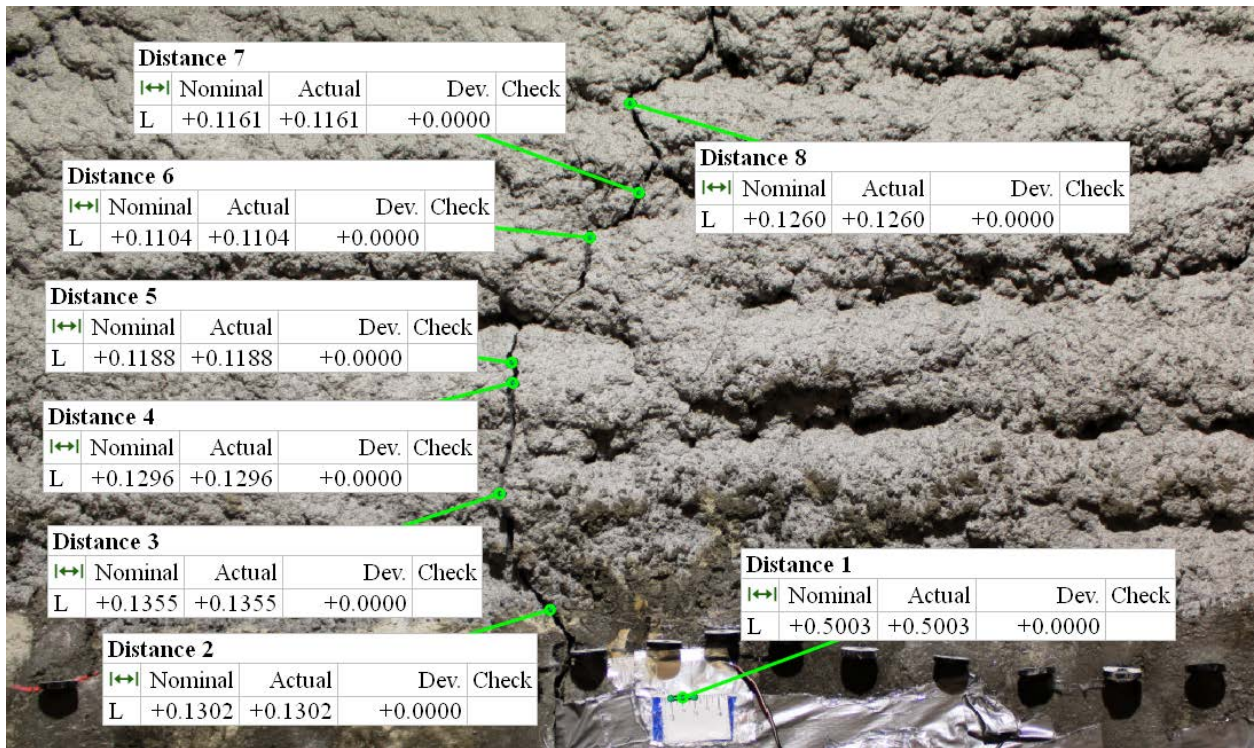


Figure F-14. Crack width measurement on the crown of the 2 in. SAPL renewed circular CMP at the load 81.2 kips.

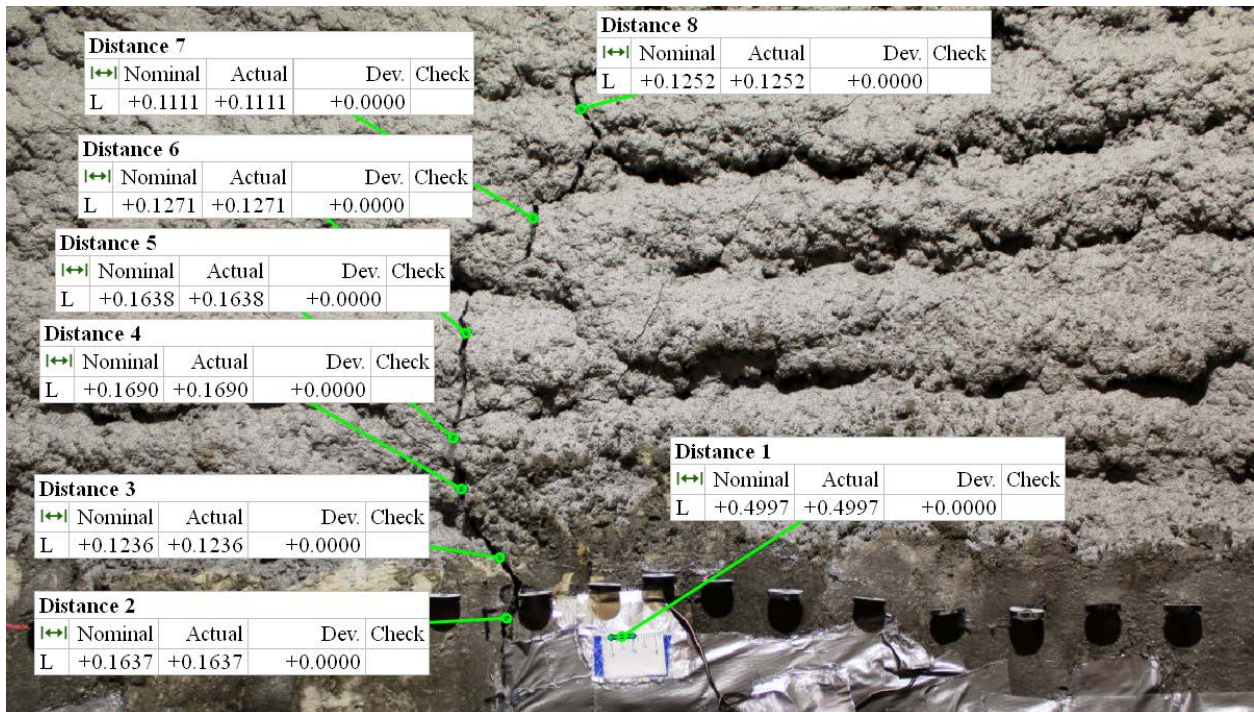
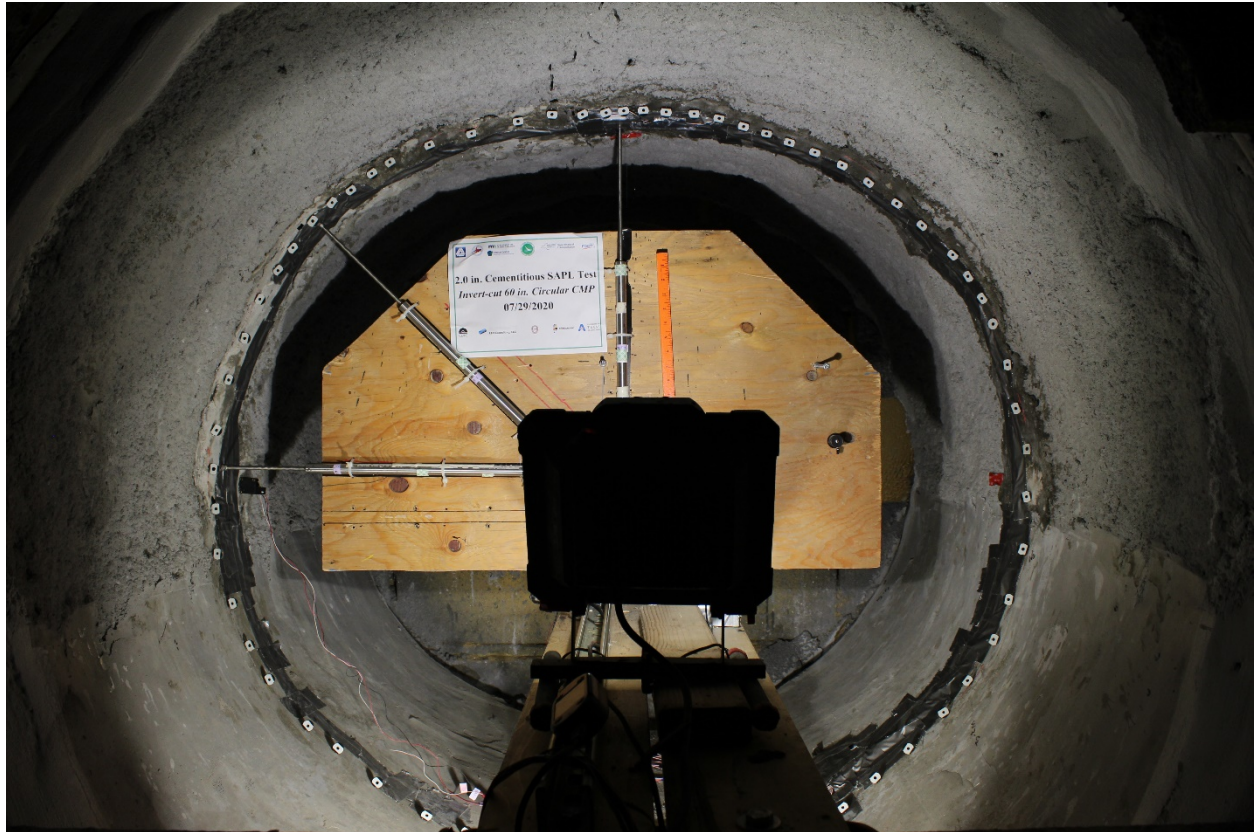


Figure F-15. Crack width measurement on the crown of the 2 in. SAPL renewed circular CMP at the load 85.3 kips.

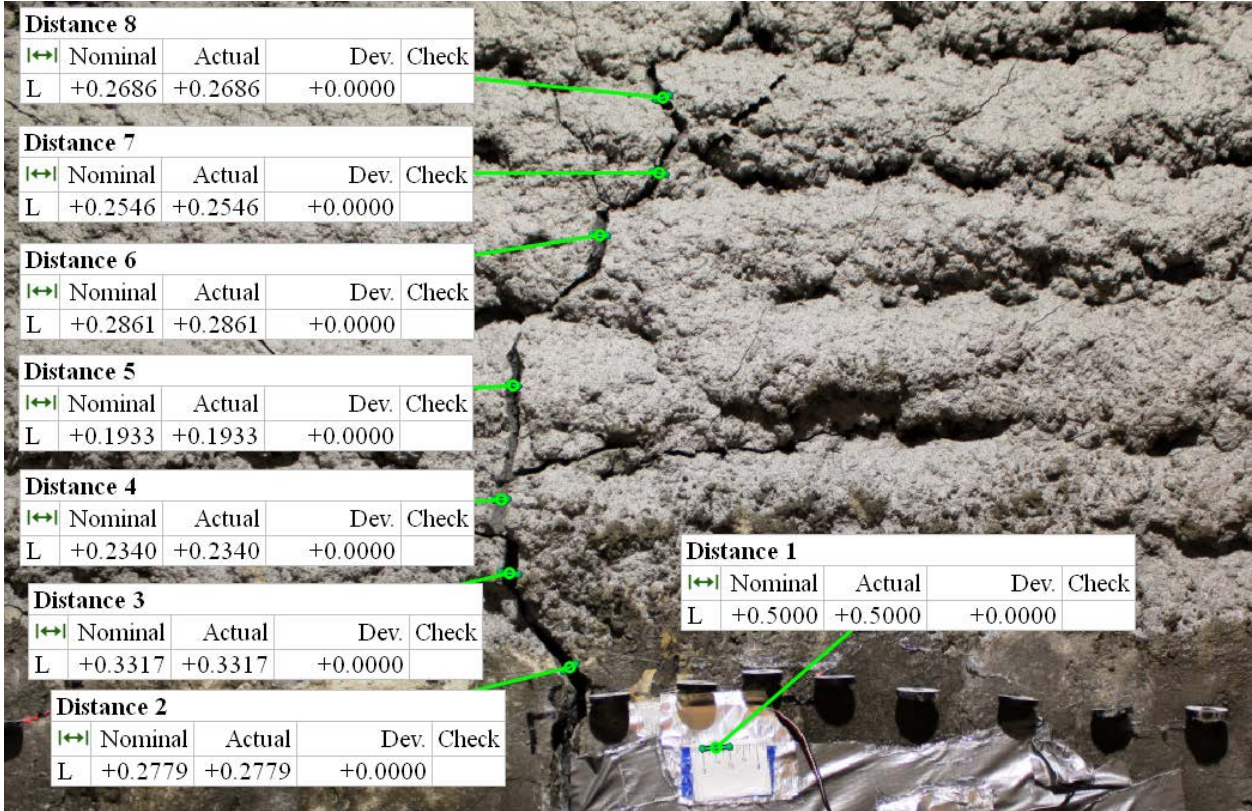


Figure F-16. Crack width measurement on the crown of the 2 in. SAPL renewed circular CMP at the end of the test.

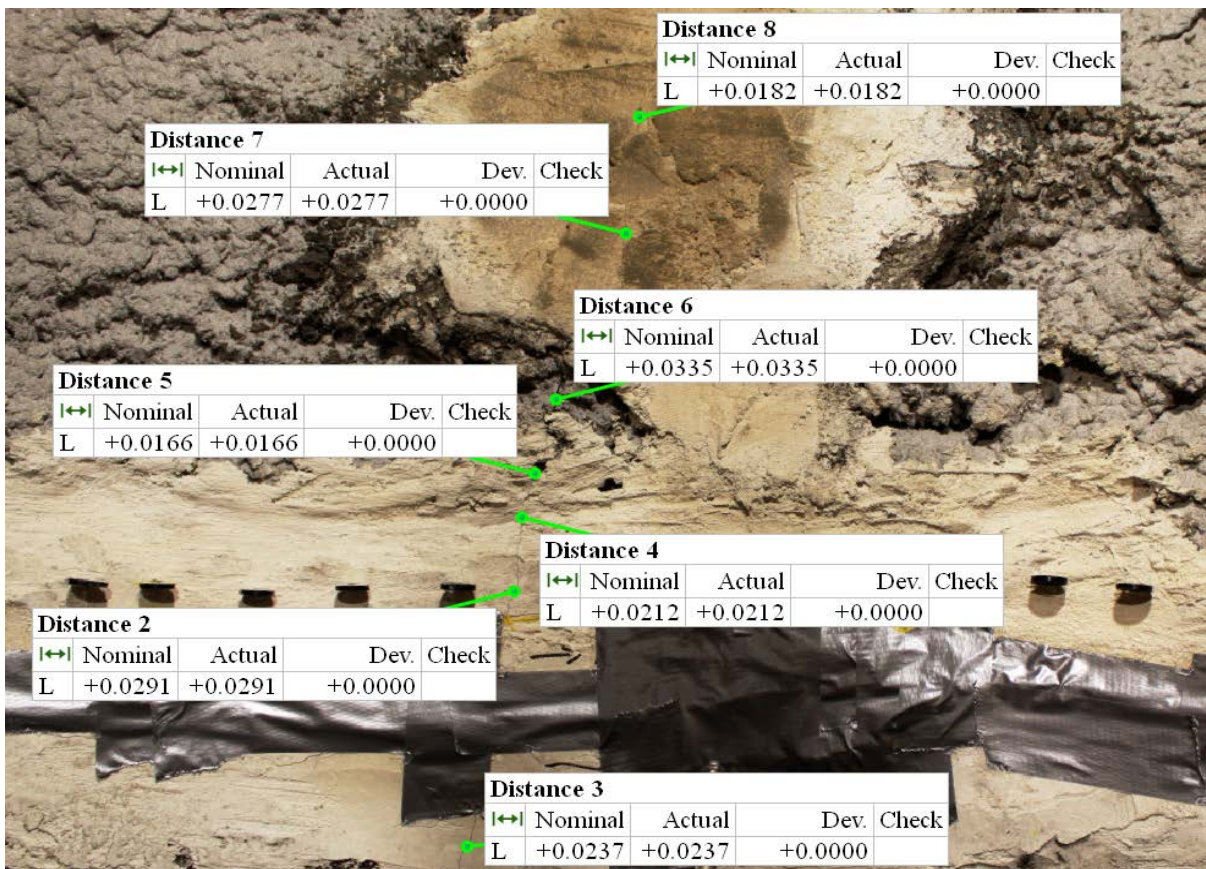


Figure F-17. Crack width measurement on the crown of the 3 in. SAPL renewed circular CMP at the beginning of the test.

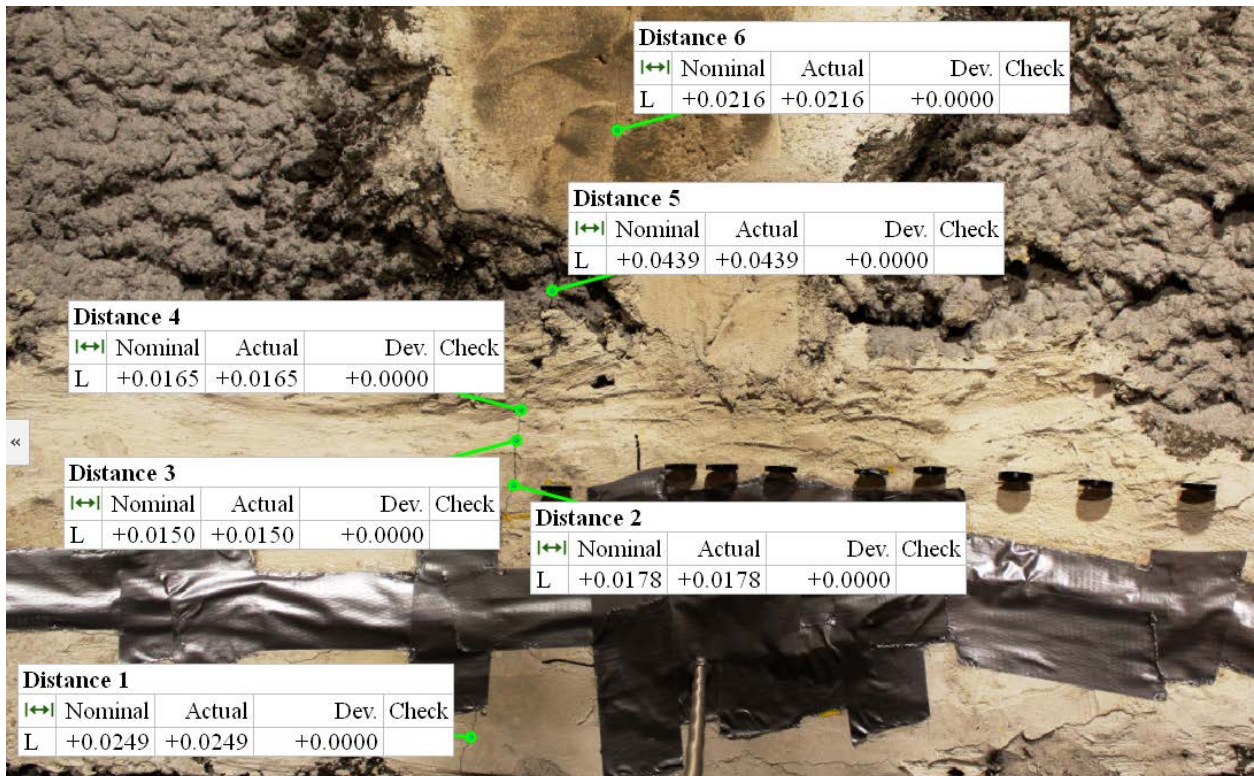


Figure F-18. Crack width measurement on the crown of the 3 in. SAPL renewed circular CMP at the load of 15.6 kips.

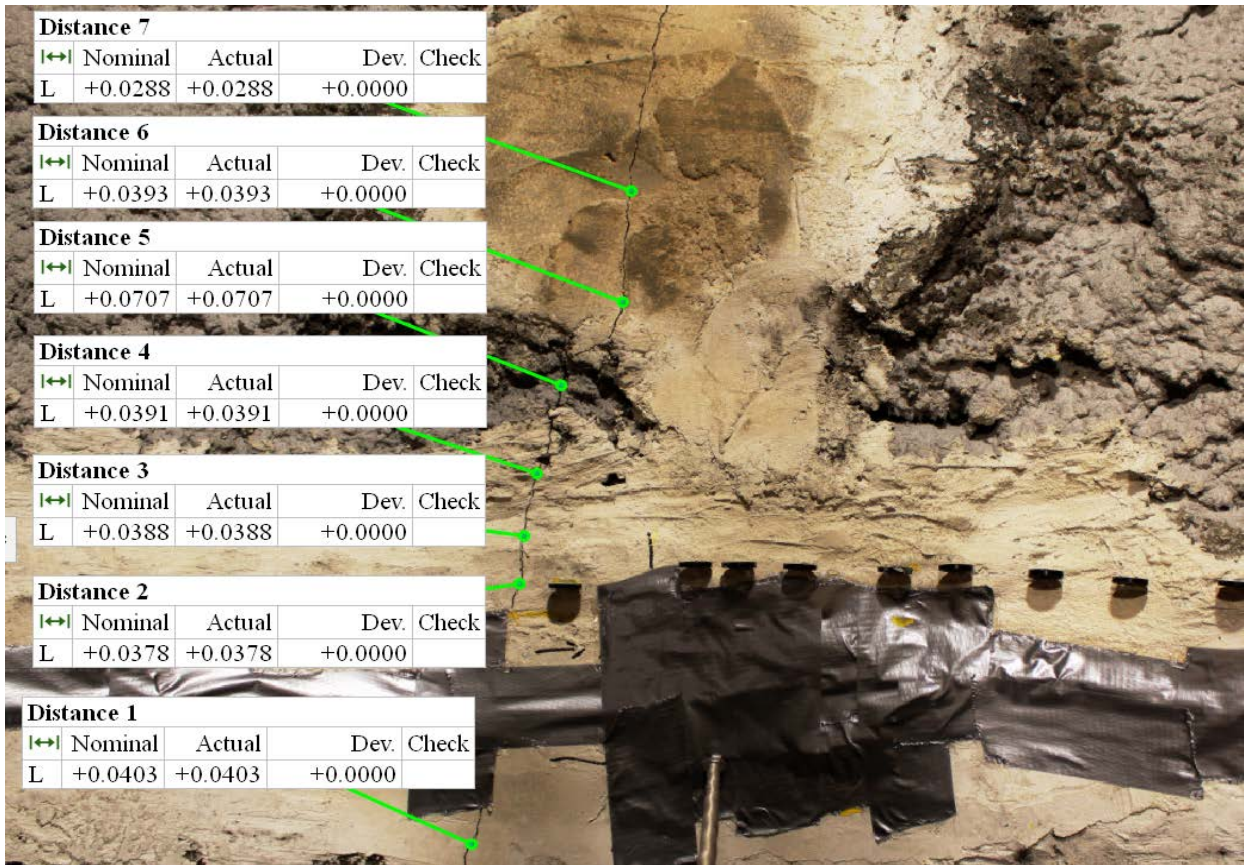


Figure F-19. Crack width measurement on the crown of the 3 in. SAPL renewed circular CMP at the load of 30.2 kips.

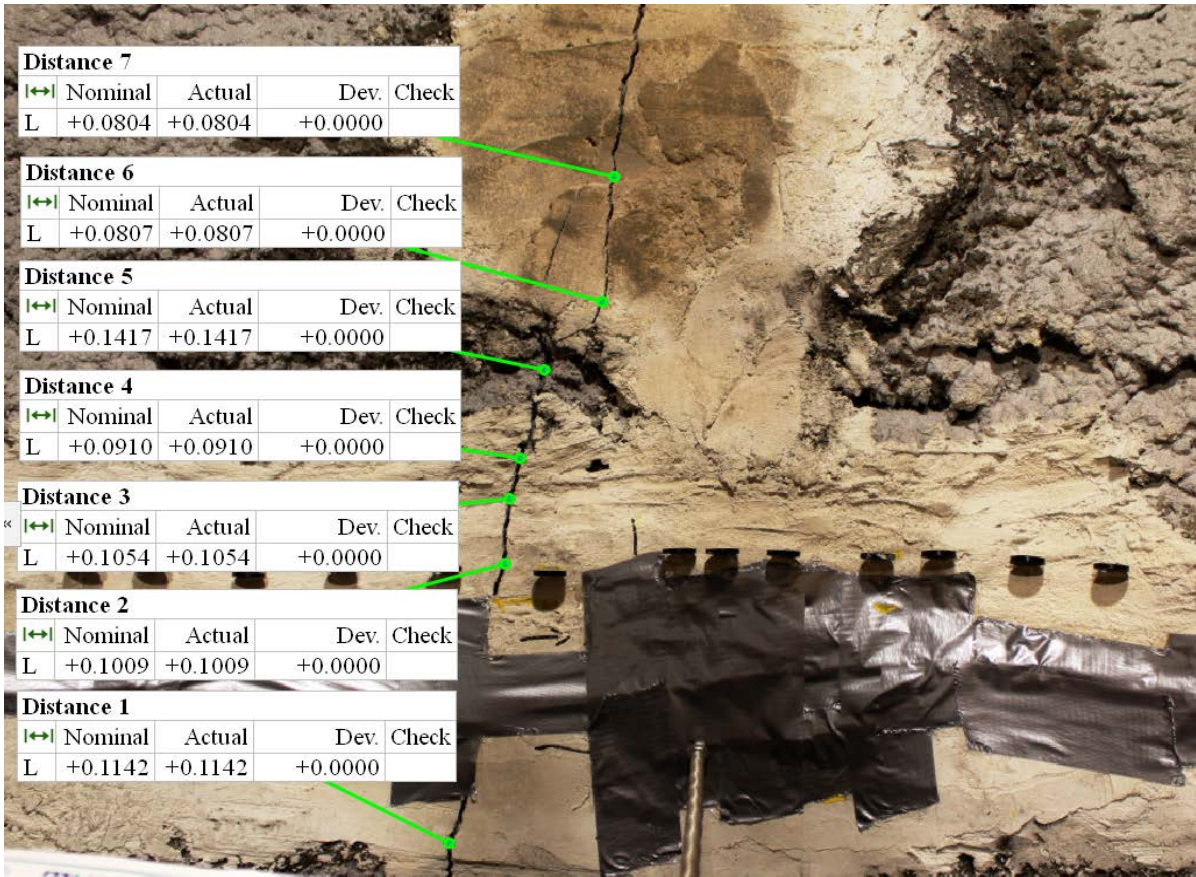


Figure F-20. Crack width measurement on the crown of the 3 in. SAPL renewed circular CMP at the load of 59.5 kips.

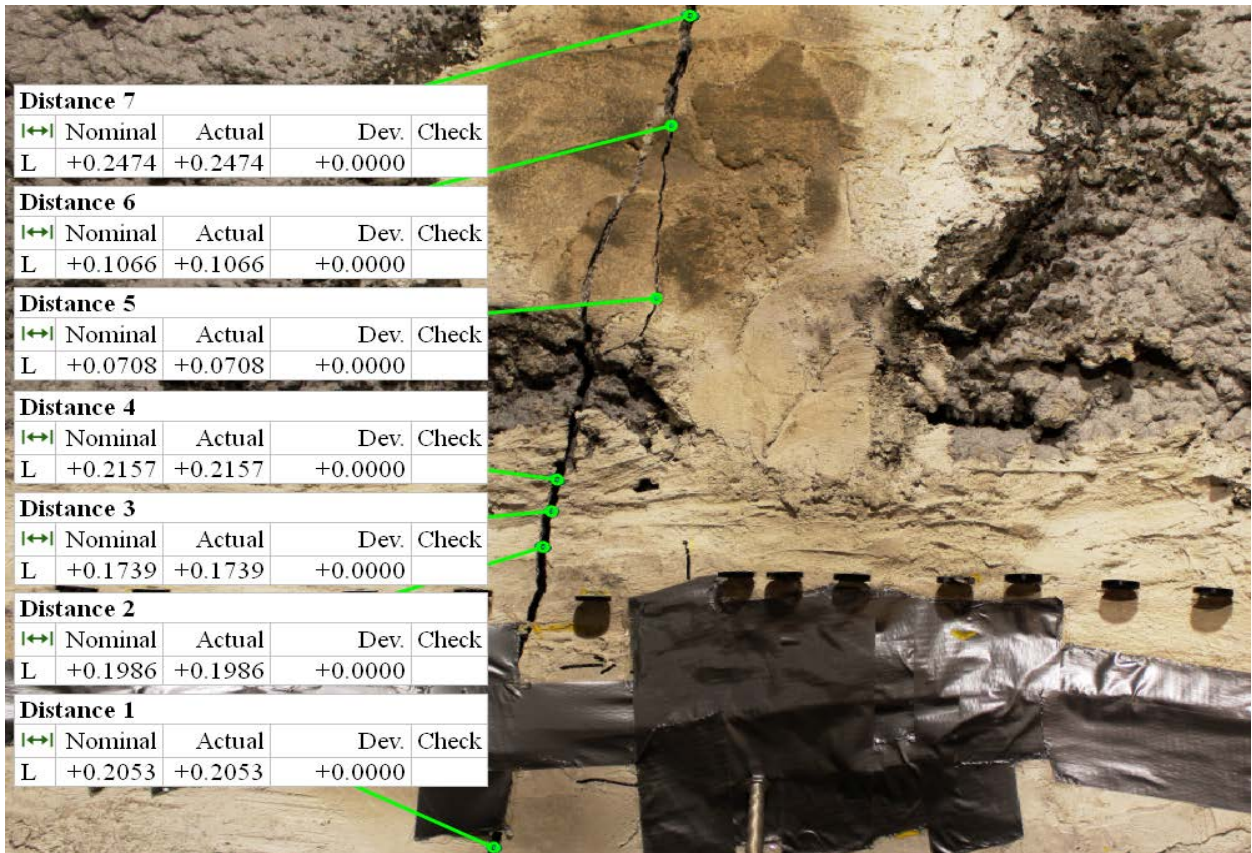


Figure F-21. Crack width measurement on the crown of the 3 in. SAPL renewed circular CMP at the load of 84 kips.

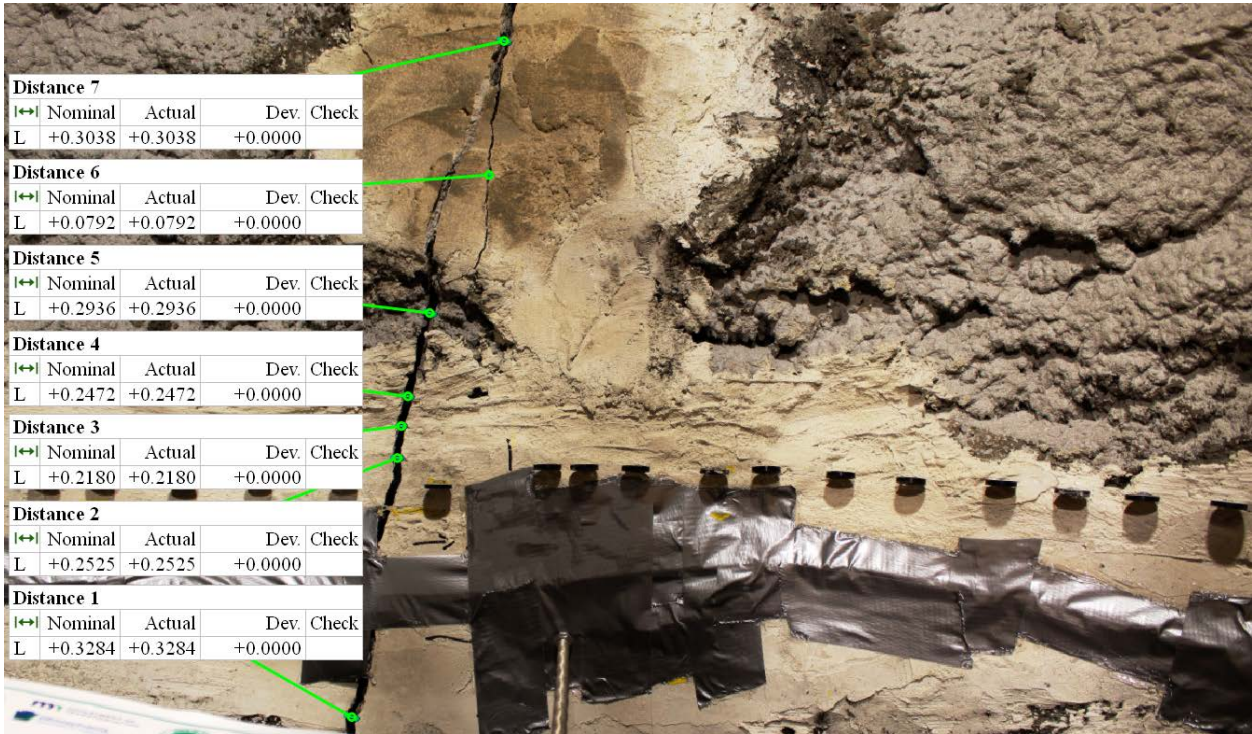


Figure F-22. Crack width measurement on the crown of the 3 in. SAPL renewed circular CMP at the load of 93.8 kips.

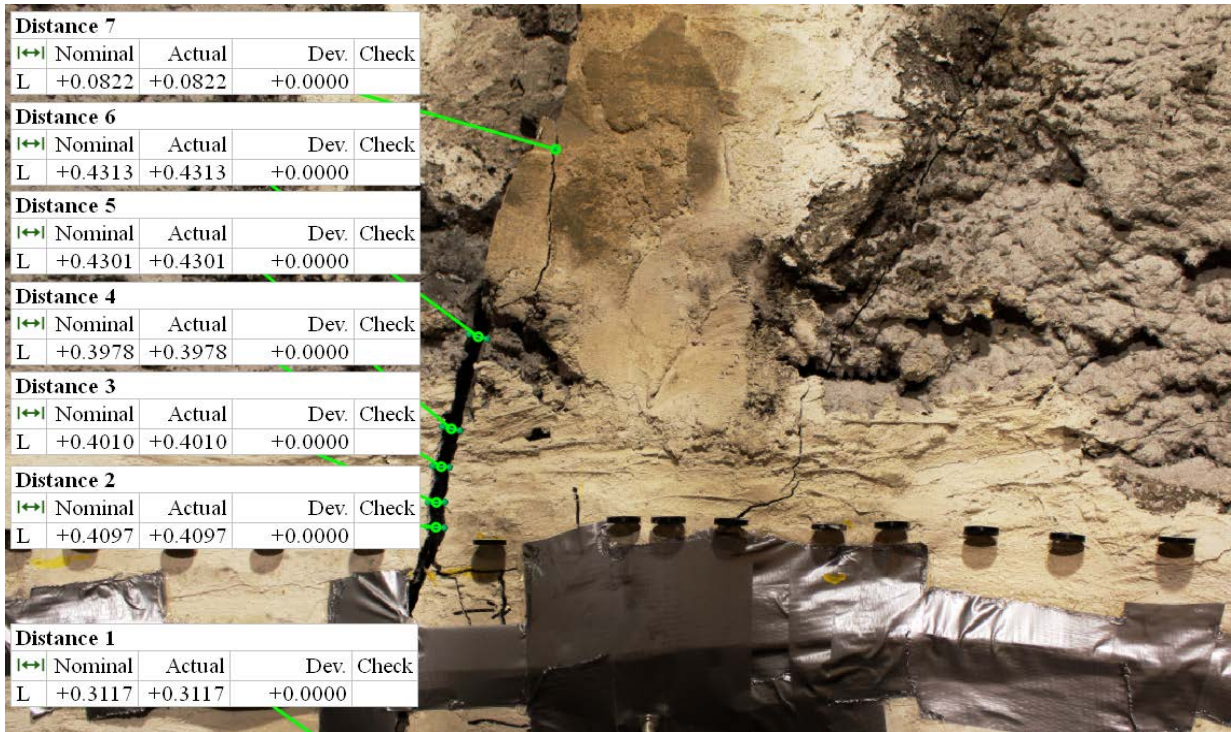


Figure F-23. Crack width measurement on the crown of the 3 in. SAPL renewed circular CMP at the load of 109.2 kips.

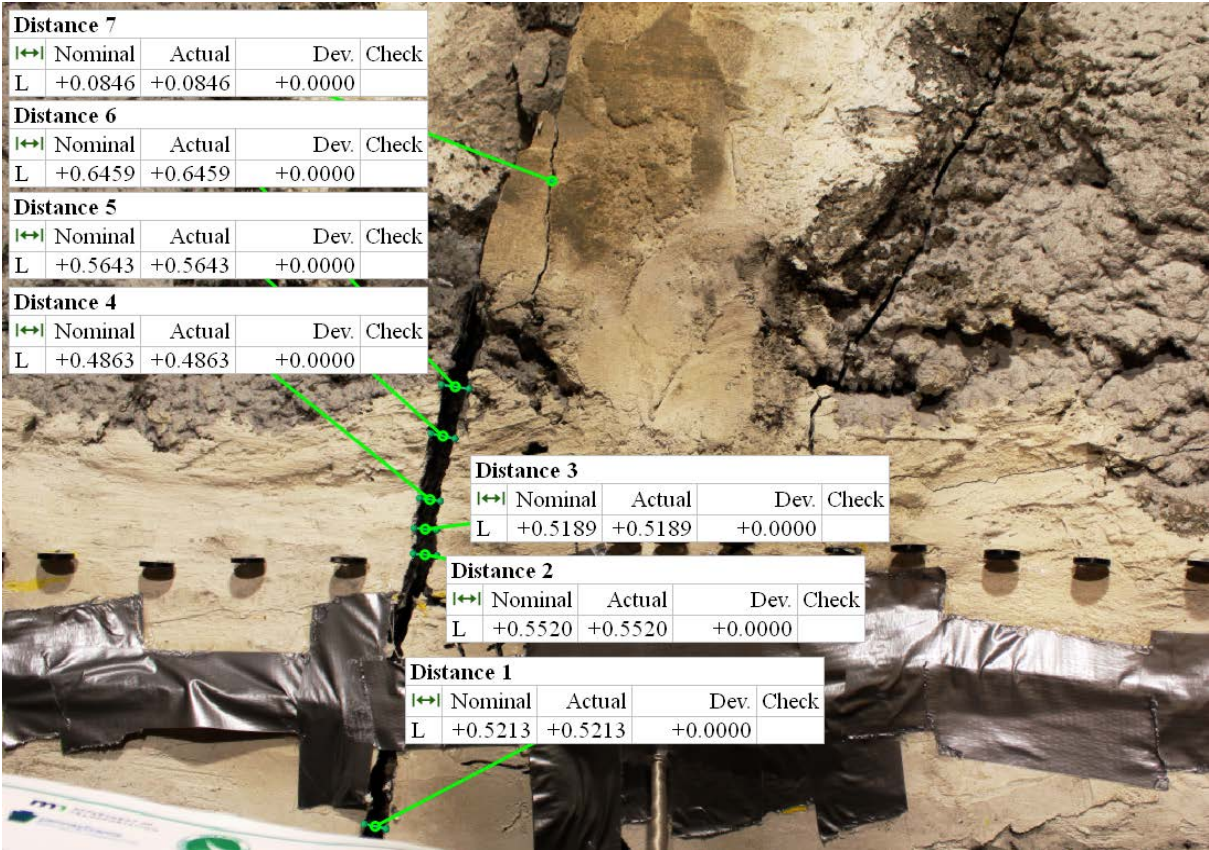


Figure F-24. Crack width measurement on the crown of the 3 in. SAPL renewed circular CMP at the end of the test.

APPENDIX G. Gallery of Soil Box Test Pictures



Figure G-1. CMP delivery, donated by Contech Engineering Solutions.



Figure G-2. CMP unloading and storage



Figure G-3. Partition wall construction and soil box preparation.

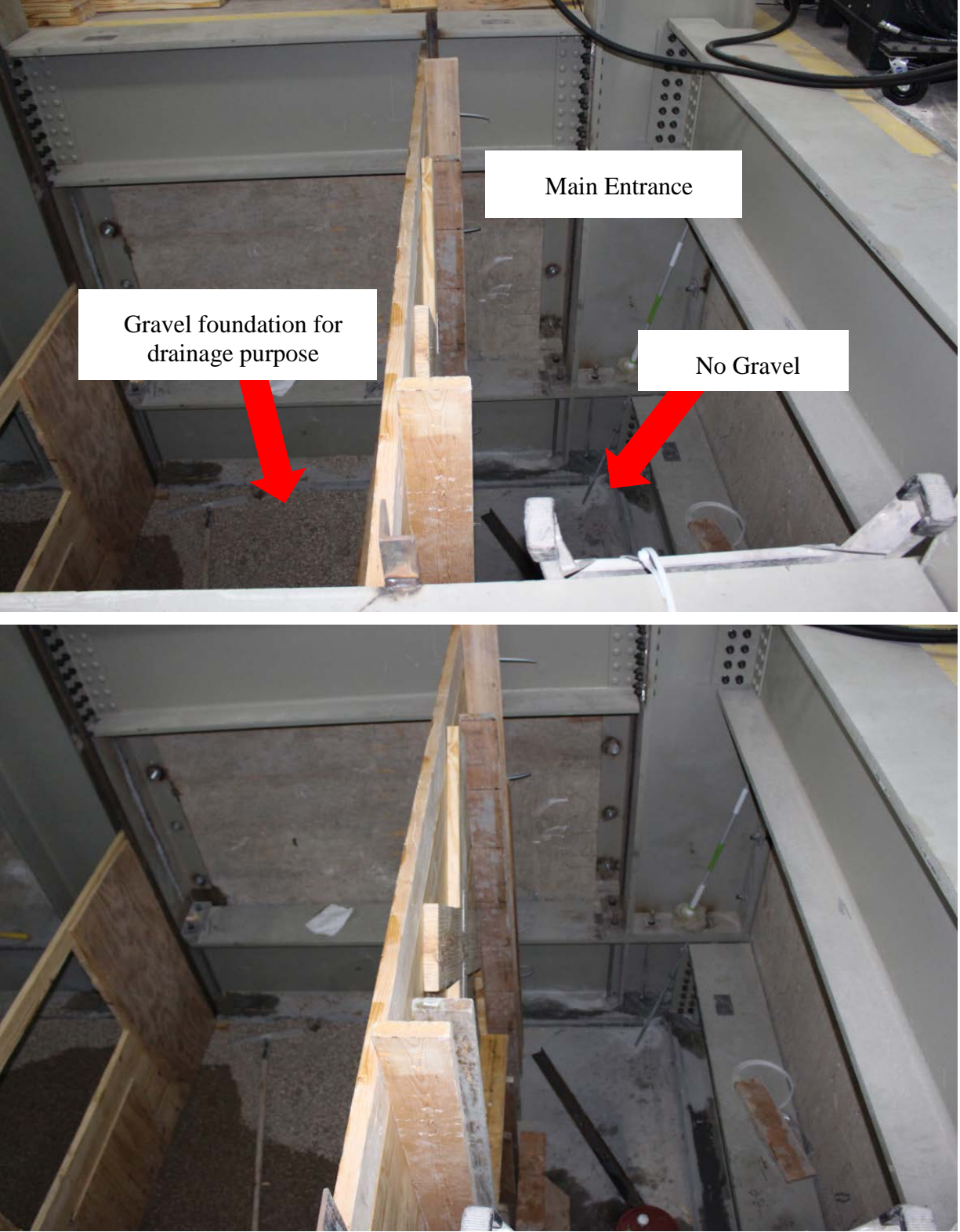


Figure G-4. Soil box preparation



Figure G-5. Foundation Preparation using SP soil



Figure G-6. Foundation compaction, leveling, and scratching.



Figure G-7. Foundation and pipe's top leveling check.



Figure G-8. Pipe installation.



Figure G-9. CMP installation.



Figure G-10. Pipe-wall gap sealing.



Figure G-11. Pipe preparation.



Figure G-12. Outside strain gauge installation



Figure G-13. Strain gauge physical protection.



Figure G-14.PVC duct to protect the strain gauges wires.



Figure G-15. Soil material handling.



Figure G-16. Soil placement inside soil box



Figure G-17. Soil placement using casting bucket.



Figure G-18. Surface leveling and earth pressure cell installation.



Figure G-19. Aggregate top surface leveling.



Figure G-20. Standard Cement vendor on site.



Figure G-21. Wet geopolymer mortar.



Figure G-22. Cementitious SAPL mixing and pumping.



Figure G-23. SAPL Spraying and surface finishing.



Figure G-24. Spray applied lining installation.



Figure G-25. Spraying and troweling.



Figure G-26. MTS hydraulic actuator applying a static load over the soil surface.



Figure G-27. Load pad penetration in to the soil at the end of test.

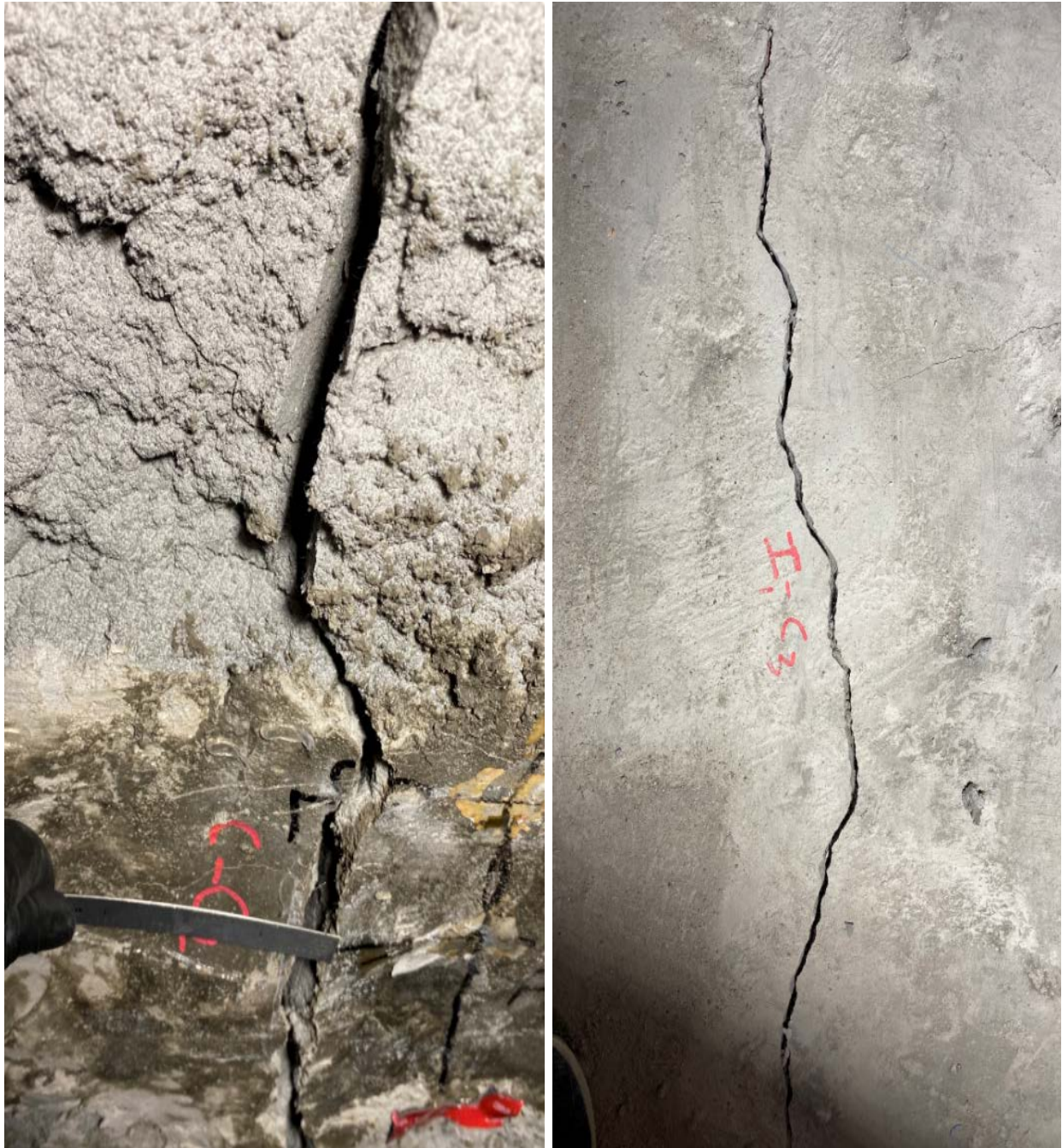


Figure G-28. Longitudinal cracks on the circular CMP at: (left) crown, and (right) invert of the SAPL.



Figure G-29. Crack opening at the crown location of the 3-in. thick circular SAPL renewed CMP at the end of the test.



Figure G-30. Longitudinal cracks at the both gaps of the invert-cut section.

REFERENCES

- AASHTO. (2017). *AASHTO LRFD bridge design specifications*. Fourth edition with 2008 interim revisions. Washington, D.C. : American Association of State Highway and Transportation Officials, [2008] ©2007.
- ACPA. (2008). “The infrastructure is collapsing.” American Concrete Pipe Association.
- Ahmadi, M., Hatami, M., Rahgozar, P., Shirkhanloo, S., Abed, S., Kamalzadeh, H., and Flood, I. (2020). “Development of an ESCO Risk Assessment Model as a Decision-Making Tool for the Energy Savings Certificates Market Regulator: A Case Study.” *Applied Sciences*, Multidisciplinary Digital Publishing Institute, 10(7), 2552.
- Al-Lami, B. (2020). “Performance of Cracked Reinforced Concrete Pipes Subjected to Different Environmental Conditions.” The University of Texas at Arlington.
- Al-Naddaf, M., Han, J., Xu, C., and Rahmaninezhad, S. M. (2018). “Effect of Geofom on Vertical Stress Distribution on Buried Structures Subjected to Static and Cyclic Footing Loads.” *Journal of Pipeline Systems Engineering and Practice*, 10(1), 04018027.
- Alzabeebee, S., Chapman, D. N., and Faramarzi, A. (2018). “A comparative study of the response of buried pipes under static and moving loads.” *Transportation Geotechnics*, 15, 39–46.
- American Association of State Highway and Transportation Officials (AASHTO). (2017). *AASHTO LRFD Bridge Construction Specification*. American Association of State Highway and Transportation Officials (AASHTO).
- American Iron and Steel Institute. (1999). *Modern Sewer Design*. AMERICAN IRON AND STEEL INSTITUTE, Washington, DC.
- Arnoult, J. D. (1986). “Culvert inspection manual.” *US Department of Transportation, Federal Highway Administration, Report# FHWA-IP-86-2*.
- Arockiasamy, M., Chaallal, O., and Limpeteeprakarn, T. (2006). “Full-Scale Field Tests on Flexible Pipes under Live Load Application.” *Journal of Performance of Constructed Facilities*, 20(1), 21–27.

- ASCE. (2010). *Trenchless renewal of culverts and storm sewers*. (L. Osborn, ed.), ASCE.
- ASCE. (2017). *Infrastructure Report Card*. ASCE.
- ASTM-C497. (2003). “Standard Test Methods for Concrete Pipe, Concrete Box Sections, Manhole Sections, or Tile.” *ASTM International*.
- ASTM-D2412. (2018). “Standard Test Method for Determination of External Loading Characteristics of Plastic Pipe by Parallel-Plate Loading.” *ASTM International*, 08.04(Reapproved), 1–3.
- ASTM A796. (2017). “Standard Practice for Structural Design of Corrugated Steel Pipe , Pipe-Arches , and Arches for Storm and Sanitary Sewers and Other.” ASTM international, West Conshohocken, PA.
- ASTM A979. (2003). “Standard Specification for Concrete Pavements and Linings Installed in Corrugated Steel Structures in the Field 1.” 03(Reapproved 2009), 1–5.
- ASTM C109. (2010). “Standard Test Method for Compressive Strength of Hydraulic Cement Mortars (Using 2-in. or [50-mm] Cube Specimens).” *ASTM International*, 04(C109/C109M – 11b), 1–9.
- ASTM C39. (2015). “Standard Test Method for Compressive Strength of Cylindrical Concrete Specimens.” *ASTM International*, 1–7.
- ASTM C76. (2015). “Standard Specification for Reinforced Concrete Culvert , Storm Drain , and Sewer Pipe.” *ASTM International*, 1–7.
- ASTM C822. (2019). “Standard Terminology Relating to Concrete and Concrete Aggregates.” *ASTM International*, 1–9.
- ASTM D1556. (2015). “Standard Test Method for Density and Unit Weight of Soil in Place by Sand-Cone Method.” ASTM international.
- ASTM D1633. (2013). “Standard Test Methods for Compressive Strength of Molded Soil-Cement Cylinders.” *ASTM International*, 00(Reapproved 2007), 1–5.
- ASTM D2167. (2015). “Standard Test Method for Density and Unit Weight of Soil in Place by the Rubber Balloon Method.” ASTM international.

- ASTM D2412. (2018). “Standard Test Method for Determination of External Loading Characteristics of Plastic Pipe by Parallel-Plate Loading.” *ASTM International*, 08.04(Reapproved), 1–3.
- ASTM D6780. (2019). “Standard Test Methods for Water Content and Density of Soil In situ by Time Domain Reflectometry (TDR).” *ASTM international*.
- ASTM D6913. (2004). “Standard Test Methods for Particle-Size Distribution (Gradation) of Soils Using Sieve Analysis.” *ASTM International, West Conshohocken, PA,*.
- ASTM D6938. (2017). “Standard Test Methods for In-Place Density and Water Content of Soil and SoilAggregate by Nuclear Methods (Shallow Depth).” *ASTM international*.
- ASTM F1216. (2009). “Standard Practice for Rehabilitation of Existing Pipelines and Conduits by the Inversion and Curing of a Resin-Impregnated Tube 12.” *ASTM International*.
- Banthia, N., Zanotti, C., and Sappakittipakorn, M. (2014). “Sustainable fiber reinforced concrete for repair applications.” *Construction and Building Materials*, Elsevier, 67, 405–412.
- Barchman, R. W. ., Moore, I. D., and Rowe, R. K. (2000). “The design of a laboratory facility for evaluating the structural response of small-diameter buried pipes.” *Canadian Geotechnical Journal*, 281–295.
- Bazant, Z. P., and Cao, Z. (1987). “Size Effect in Brittle Failure of Unreinforced Pipes.” (83), 369–373.
- Becerril García, D., and Moore, I. D. (2015). “Performance of deteriorated corrugated steel culverts rehabilitated with sprayed-on cementitious liners subjected to surface loads.” *Tunnelling and Underground Space Technology*, 47, 222–232.
- Berney, E. S., and Smith, D. M. (2008). *Mechanical and Physical Properties of ASTM C33 Sand. U.S. Army Corps of Engineers*.
- Bian, X., Tang, X., Shen, W., Ling, D., and Chen, Y. (2012). “An experimental study on a culvert buried in granular soil subjected to vehicle loads.” *Advances in Structural Engineering*, 15(6), 1031–1040.
- Brew, D. R. M., and Mackenzie, K. J. D. (2007). “Geopolymer synthesis using silica fume and sodium aluminate.” *Journal of Materials Science*, 42(11), 3990–3993.

- Bryden, P., El Naggar, H., and Valsangkar, A. (2015). "Soil-structure interaction of very flexible pipes: Centrifuge and numerical investigations." *International Journal of Geomechanics*, 15(6), 1–11.
- Caltrans. (2002). *Caltrans supplement to FHWA culvert repair practices manual. Design Information Bulletin No. 83-01*, Sacramento.
- CALTRANS. (2000). "Section 12 - Soil-Corrugated Metal Structure Interaction Systems." *Bridge Design Specifications*, 1–14.
- Caporossi, P., Mazzanti, P., and Bozzano, F. (2018). "Digital image correlation (DIC) analysis of the 3 December 2013 Montescaglioso landslide (Basilicata, southern Italy): Results from a multi-dataset investigation." *ISPRS International Journal of Geo-Information*, 7(9).
- Chaallal, O., Arockiasamy, M., and Godat, A. (2014). "Field Test Performance of Buried Flexible Pipes under Live Truck Loads." *Journal of Performance of Constructed Facilities*, 29(5), 04014124.
- Chapman, D. N., Fleming, P. R., Rogers, C. D. F., and Talby, R. (2007). "The response of flexible pipes buried in sand to static surface stress." *Geomechanics and Geoengineering*, Taylor & Francis, 2(1), 17–28.
- City of Dallas. (2011). *City of Dallas 2011 ADDENDUM to the Public Works Construction Standards – North Central Texas As Published by the North Central Texas Council of Governments*.
- Contech. (2019). "Contech Engineering Solutions." <<https://www.conteches.com/>>.
- Curran, P. (2016). "Make the right choice for metal coating for the right application." *Design World*, <<https://www.designworldonline.com/make-right-choice-metal-coating-right-application/>>.
- CVWD. (2013). *Coachella Valley Water District Pipe Materials for Non-Pressurized Pipeline Projects*.
- Cybersecurity & Infrastructure Security Agency. (2020). *Memorandum on Identification of Essential Critical Infrastructure Workers During COVID-19 Response*. U.S. Department of Homeland Security.

- Darabnoush Tehrani, A. (2016). “Finite Element Analysis for ASTM C-76 Reinforced Concrete Pipes with Reduced Steel Cage.” University of Texas at Arlington.
- Darabnoush Tehrani, A., Kohankar Kouchesfehaneh, Z., Chimaurya, H. R., Raut, S., Najafi, M., and Yu, X. (2020a). “Structural Evaluation of Invert-cut Circular and Arch Shape Corrugated Steel Pipes through Laboratory Testing.” *Canadian Journal of Civil Engineering*, (Soil-Structure Interaction of Buried Structures).
- Darabnoush Tehrani, A., Kohankar Kouchesfehaneh, Z., and Najafi, M. (2020b). “Pipe Profiling Using Digital Image Correlation.” *Pipelines 2020*, American Society of Civil Engineers, Reston, VA, 36–45.
- Darabnoush Tehrani, A., Kohankar Kouchesfehaneh, Z., Najafi, M., Syar, J. E., and Kampbell, N. E. (2019). “Evaluation of Filling the Valleys of Corrugated Metal Pipes by Trenchless Spray Applied Pipe Linings.” *Pipelines 2019: Multidisciplinary Topics, Utility Engineering, and Surveying*, ASCE, Nashville, 84–94.
- Darabnoush Tehrani, A., Kouchesfehaneh Kohankar, Z., and Najafi, M. (2020c). “Review and Recommendations for Structural Testing of Buried Gravity Storm Drain Pipes and Culverts.” *Canadian Journal of Civil Engineering*, (Soil–structure interaction of buried structures).
- Davidovits, J. (1991). “Geopolymers: inorganic polymeric new materials.” *Journal of Thermal Analysis and calorimetry*, Akadémiai Kiadó, co-published with Springer Science+ Business Media BV ..., 37(8), 1633–1656.
- Davidovits, J. (2015). *Geopolymer Chemistry and Applications*. J. Davidovits.–Saint-Quentin, France.
- Dawood, E. T., and Ramli, M. (2011). “High strength characteristics of cement mortar reinforced with hybrid fibres.” *Construction and building materials*, Elsevier, 25(5), 2240–2247.
- Ellison, D., Sever, F., Oram, P., Lovins, W., Romer, A., Duranceau, S. J., and Bell, G. (2010). “Global review of spray-on structural lining technologies.” *Water Research Foundation, Denver*, 1–184.
- Entezarmahdi, A. (2015). “Testing, analysis and classification of no-dig manhole rehabilitation

- materials.” The University of Texas at Arlington.
- Falter, B. (1996). “Structural analysis of sewer linings.” *Tunnelling and Underground Space Technology*, Elsevier, 11, 27–41.
- FDOT. (2019). “Florida Department of Transportation.” <<https://www.fdot.gov/>>.
- FHWA. (2012). *Hydraulic Design of Highway Culverts, Third Edition*.
- García, D. B., and Moore, I. D. (2015). “Performance of deteriorated corrugated steel culverts rehabilitated with sprayed-on cementitious liners subjected to surface loads.” *Tunnelling and Underground Space Technology*, Elsevier, 47, 222–232.
- GEOKON. (2019). “Pressure Cells.” <<https://www.geokon.com/4800>>.
- Gere, J. M., and Timoshenko, S. P. (1998). *Mechanics of materials*. Chapman and Hall.
- Ghahremannejad, M., and Abolmaali, A. (2018). “Prediction of shear strength of reinforced concrete beams using displacement control finite element analysis.” *Engineering Structures*, Elsevier, 169(January), 226–237.
- Gumbel, J. (2001). “New Approach To Design of Circular Liner Pipe.” *Pipelines 2001: Advances in Pipelines Engineering and Construction*, 1–18.
- Ham, S., and Darabnoush Tehrani, A. (2019). “2D Random Shape of Aggregate Model using Image Processing and Convex Combination Theory.” *Transportation Research Board (TRB)*.
- Han, J., Ph, D., and Corey, R. (2016). “Report # MATC-KU : 146 Final Report Geosynthetic Reinforcement to Protect Underground Pipes against Damage from Construction and Traffic.”
- Henning, S. (2020). *Long-Term Performance of a Microsilica Based Cement Liner In Aggressive Sewer Manhole Wastewater Environments*.
- Howarth, G. A. (2003). “Polyurethanes, polyurethane dispersions and polyureas: Past, present and future.” *Surface Coatings International Part B: Coatings Transactions*, 86(2), 111–118.
- Iucolano, F., Liguori, B., and Colella, C. (2013). “Fibre-reinforced lime-based mortars: A possible resource for ancient masonry restoration.” *Construction and Building Materials*,

Elsevier, 38, 785–789.

- Kang, J., Parker, F., and Yoo, C. H. (2008). “Soil-structure interaction for deeply buried corrugated steel pipes Part II: Imperfect trench installation.” *Engineering Structures*, 30(3), 588–594.
- Khatri, D. K., Han, J., Corey, R., Parsons, R. L., and Brennan, J. J. (2015). “Laboratory evaluation of installation of a steel-reinforced high-density polyethylene pipe in soil.” *Tunnelling and Underground Space Technology*, Elsevier Ltd, 49, 199–207.
- Kohankar Kouchesfehni, Z. (2020). “Development of a Structural Design Methodology for Polymeric Spray Applied Pipe Linings.” The University of Texas at Arlington.
- Kohankar Kouchesfehni, Z., Darabnoush Tehrani, A., Najafi, M., and Syar, J. (2020). “Laboratory Testing of Invert-cut Corrugated Metal Pipes Renewed with Polymeric Spray Applied Pipe Lining.” *Transportation Geotechnics*, Elsevier, 100413.
- Kohankar Kouchesfehni, Z., Darabnoush Tehrani, A., Najafi, M., Syar, J. E., and Ed Kampbell, P. E. (2019). “Adding Additional Reinforcement to Improve the Structural Performance of Spray Applied Pipe Lining Rehabilitation Technology: A Review.” *Pipelines 2019: Multidisciplinary Topics, Utility Engineering, and Surveying*, ASCE, Nashville.
- Kohankar Kouchesfehni, Z., and Ghasemi, M. R. (2013a). “Investigating the Cross-Section and Structural Geometry Effects on Response of Flat Scissor-Type Structures in Deployed Configuration.” *7th National Congress on Civil Engineering-University of Sistan and Baluchestan (7NCCE)*.
- Kohankar Kouchesfehni, Z., and Ghasemi, M. R. (2013b). “Investigating the Effects of Joint Size and Members’ Flexural Rigidity on Response of Flat Scissor-Type Structures in Deployed Configuration.” *7th National Congress on Civil Engineering-University of Sistan and Baluchestan (7NCCE)*.
- Kohankar Kouchesfehni, Z., Paggioli, K., Najafi, M., and Miglio, A. (2018). “Evaluation of Structural Design Methodologies for Large Diameter Pipeline Renewal Design.” *Pipelines 2018: Condition Assessment, Construction, and Rehabilitation*, American Society of Civil Engineers Reston, VA, 327–332.

- Kohankar Kouchesfehiani, Z., Tabesh, A., and Najafi, M. (2017). "Risk Identification for Pipeline Installation by Horizontal Directional Drilling." *Proc. International Congress on Underground Infrastructure, Water Management and Trenchless Technology (ICUWT)*, 85–92.
- Kraus, E., Oh, J., and Fernando, E. G. (2014). "Impact of repeat overweight truck traffic on buried utility facilities." *Journal of Performance of Constructed Facilities*, 28(4), 1–9.
- Kunecki, B., and Kubica, E. (2004). "Full-scale laboratory tests and FEM analysis of corrugated steel culverts under standardized railway load." *Archives of Civil and Mechanical Engineering*, Vol. 4, no(December), 41–53.
- Leonards, G. A., and Stetkar, R. E. (1978). "Performance of buried flexible conduits: Interim report." Purdue University.
- Liu, B., Wang, Z., Xu, W., Sun, H., and Wang, X. (2016). "Comparative Experimental Study and FE Analysis of Corrugated Steel Pipe Culverts with Different Stiffness." *The Open Civil Engineering Journal*, 10(1), 549–563.
- Liu, Y., Moore, I. D., and Hoult, N. A. (2020). "Field Monitoring of a Corrugated Steel Culvert Using Multiple Sensing Technologies." *Journal of Pipeline Systems Engineering and Practice*, 11(3), 1–10.
- Lougheed, A. C. (2008). "Limit States Testing of A Buried Deep corrugated Large-Span Box Culvert." Queen's University.
- Luk, G. K. (2001). "Pipeline rehabilitation with fiber-reinforced mortar lining." *Journal of infrastructure systems*, American Society of Civil Engineers, 7(3), 116–122.
- Mahgoub, A., and El Naggar, H. (2019). "Using TDA as an engineered stress-reduction fill over preexisting buried pipes." *Journal of Pipeline Systems Engineering and Practice*, 10(1), 1–15.
- Mahgoub, A., and El Naggar, H. (2020). "Innovative Application of Tire-Derived Aggregate around Corrugated Steel Plate Culverts." *Journal of Pipeline Systems Engineering and Practice*, 11(3), 1–18.
- Mai, V. T., Hoult, N. A., and Moore, I. D. (2013). "Effect of deterioration on the performance of

- corrugated steel culverts.” *Journal of Geotechnical and Geoenvironmental Engineering*, 141(4), 1–11.
- Mai, V. T., Hoult, N., and Moore, I. (2018). “Numerical evaluation of a deeply buried pipe testing facility.” *Advances in Structural Engineering*, 21(16), 2571–2588.
- Masada, T. (2017a). *Structural Benefits of Concrete Paving of Steel Structural Benefit of Concrete Paving of Steel Culvert Inverts*.
- Masada, T. (2017b). *Structural Benefit of Concrete Paving of Steel Culvert Inverts*. Ohio.
- Masada, T., Fekrat, A., and Hurd, J. (2020). “Structural Performance of Deteriorated Metal Culverts Rehabilitated Through Invert Concrete Paving.” *Transportation Research Record*, 2674(3), 248–257.
- Matthews, J. C., Simicevic, J., Kestler, M. A., and Piehl, R. (2012). *Decision Analysis Guide for Corrugated Metal Culvert Rehabilitation and Replacement Using Trenchless Technology*.
- Micro-Epsilon. (2019). “Micro-Epsilon.” <<https://www.micro-epsilon.com/>>.
- Moore, I. D., and García, D. B. (2015a). “Ultimate Strength Testing of Two Deteriorated Metal Culverts Repaired with Spray-On Cementitious Liners.” *Transportation Research Board*, (2522), 139–147.
- Moore, I. D., and García, D. B. (2015b). “Ultimate Strength Testing of Two Deteriorated Metal Culverts Repaired with Spray-On Cementitious Liners.” *Transportation Research Record: Journal of the Transportation Research Board*, 2522(1), 139–147.
- Moser, A. P., and Folkman, S. L. (2008). *Buried pipe design*. McGraw-Hill New York.
- Munro, S. M., Moore, I. D., and Brachman, R. W. I. (2009). “Laboratory Testing to Examine Deformations and Moments in Fiber-Reinforced Cement Pipe.” *Journal of Geotechnical and Geoenvironmental Engineering*, 135(11), 1722–1731.
- Najafi, A. M., Salem, S., Bhattachar, D., and Salman, B. (2008). *An Asset Management Approach for Drainage Infrastructure and Culverts*. Midwest Regional University Transportation Center.

- Najafi, M. (2010). *Trenchless Technology Piping: Installation and Inspection: Installation and Inspection*. McGraw Hill Professional.
- Najafi, M. (2013). *Trenchless technology: Planning, equipment, and methods*. McGraw Hill Professional.
- Najafi, M. (2016). *Pipeline infrastructure renewal and asset management*. McGraw Hill Professional.
- Najafi, M., and Gokhale, S. (2005). *Trenchless technology: Pipeline and utility design, construction, and renewal*. McGraw-Hill New York.
- NCSPA. (2008). “Corrugated Steel Pipe Design Manual.” National Corrugated Steel Pipe Association, Dallas.
- NCSPA. (2017). “Spiral Rib Pipe.” *The National Corrugated Steel Pipe Association*, <<https://ncspa.org/steel-product/spiral-rib-pipe/>>.
- Nehdi, M. L., Mohamed, N., and Soliman, A. M. (2016). “Investigation of buried full-scale SFRC pipes under live loads.” *Construction and Building Materials*, Elsevier Ltd, 102, 733–742.
- Okoye, F. N., Durgaprasad, J., and Singh, N. B. (2016). “Effect of silica fume on the mechanical properties of fly ash based-geopolymer concrete.” *Ceramics International*, Elsevier, 42(2), 3000–3006.
- Omara, A.-A. M. (1997). “Analysis of cured-in-place pipes (CIPP) installed in circular and oval deteriorated host pipes.” Louisiana Tech University.
- OMEGA. (2019). “LVDT.” <www.omega.com>.
- Park, Y., Abolmaali, A., Kim, Y. H., and Ghahremannejad, M. (2016). “Compressive strength of fly ash-based geopolymer concrete with crumb rubber partially replacing sand.” *Construction and Building Materials*, Elsevier Ltd, 118(2016), 43–51.
- PCPIPE. (2016). “Types of Corrugation.” <<http://www.pcpipes.com/products/typesofcorrugation.html>>.
- Pocock, R. G., Lawrence, G. J. L., and Taylor, M. E. (1980). “Behaviour of a Shallow Buried

Pipeline Under Static and Rolling Wheel Loads.”

- Potter, J. C. (1986). *Evaluation of Buried Concrete-Lined Corrugated Metal Pipe*. Department of the Army Waterways Experiment Station, Washington , DC.
- Rahman, M. M., Sameen, S., Hafiza, R., and Sadeque, M. A. (2013). “Behavior of Polymeric Fiber as an Alternative Reinforcement to Iron Wire Mesh in Ferro cement Elements under Flexural Load.” 1(5), 3–6.
- Rakitin, B. A. (2010). “Stress–strain state of large diameter non–pressure reinforced concrete pipes.” Ph. D. thesis, Department of Civil Engineering, South Ural State University
- Rakitin, B., and Xu, M. (2014). “Centrifuge modeling of large-diameter underground pipes subjected to heavy traffic loads.” *Canadian Geotechnical Journal*, 51(4), 353–368.
- Ramakrishnan, V., Tolmare, N. S., and Brik, V. B. (1998). *Performance evaluation of 3-D basalt fiber reinforced concrete & basalt rod reinforced concrete*.
- Regier, C., Hault, N. A., and Moore, I. D. (2016). “Laboratory Study on the Behavior of a Horizontal-Ellipse Culvert during Service and Ultimate Load Testing.” *Journal of Bridge Engineering*, 22(3), 04016131.
- Regier, C., Moore, I. D., and Hault, N. A. (2018). “Remaining strength of deteriorated corrugated steel culverts.” *Journal of Pipeline Systems Engineering and Practice*, 9(2).
- Roesler, J. R., and Gaedicke, M. C. (2004). “Fiber reinforced concrete for airfield rigid pavements.” Citeseer.
- Royer, J., and Iseley, T. (2017). “Laboratory testing and analysis of geopolymer pipe-lining technology for rehabilitation of sewer & storm water conduits, part II - CMP culvert analysis.” *NASTT’s No-Dig Show and ISTT’s 35th International No-Dig*, 1–10.
- Sargand, S. M., and Hazen, G. A. (1998). *STRUCTURAL EVALUATION AND PERFORMANCE OF PLASTIC PIPE. VOLUME I AND II*.
- Sargand, S. M., Hazen, G. A., White, K., and Moran, A. (2001a). “Time-dependent deflection of thermoplastic pipes under deep burial.” *Transportation Research Record*, (1770), 236–242.
- Sargand, S. M., Khoury, I., Hussein, H. H., and Masada, T. (2018). “Load Capacity of

- Corrugated Steel Pipe with Extreme Corrosion under Shallow Cover.” *Journal of Performance of Constructed Facilities*, 32(4), 04018050.
- Sargand, S. M., Masada, T., and Schehl, D. J. (2001b). “Soil pressure measured at various fill heights above deeply buried thermoplastic pipe.” *Transportation Research Record*, (1770), 227–235.
- Schluter, J. C., and Shade, J. W. (1999). “Flexibility factor or pipe stiffness: Significant stiffness considerations.” *Transportation research record*, SAGE Publications Sage CA: Los Angeles, CA, 1656(1), 45–50.
- Schrock, B. J., and Gumbel, J. (1997). “Pipeline Renewal–1997.” *North American No-Dig*, 97.
- Sharma, J. R. (2013). “Development of a Model for Estimation of Buried Large Diameter Thin-Walled Steel Pipe Deflection due to External Loads.” The University of Texas at Arlington.
- Sharma, J. R., Najafi, M., Zheng, Z., and Jain, A. (2011). “Laboratory Test of Statically-loaded Large Diameter Steel Pipe with Native Backfill.” *ASCE*, 1598–1609.
- Singh, B., Ishwarya, G., Gupta, M., and Bhattacharyya, S. K. (2015). “Geopolymer concrete: A review of some recent developments.” *Construction and Building Materials*, 85, 78–90.
- Sivaselvan, M. V., Reinhorn, A. M., Shao, X., and Weinreber, S. (2007). “Dynamic force control with hydraulic actuators using added compliance and displacement compensation Mettupalayam.” *Earthquake Engineering & Structural Dynamics*, (056), 1–6.
- Syar, J. E., Najafi, M., Kohankar Kouchesfehaneh, Z., Korkey, S., and Darabnoush Tehrani, A. (2019). “Use of Spray Applied Pipe Linings as a Structural Renewal for Gravity Storm Water Conveyance Conduits.” North American Society for Trenchless Technology (NASTT), Chicago, Illinois, WM-T5-05.
- Syar, J. E., Najafi, M., Kouchesfehaneh Kohankar, Z., and Darabnoush Tehrani, A. (2020). “Soil Box Testing Details of Spray Applied Pipe Linings as a Structural Renewal for Gravity Storm Water Conveyance Conduits.” *NASTT’s 2020 No-Dig Show*, North American Society for Trenchless Technology (NASTT), Denver, WM-T4-03.
- Szafran, J., and Matusiak, A. (2017). “Structural behaviour and compressive strength of concrete rings strengthened with a polyurea coating system.” (December).

- Tafreshi, S. N. M., Mehrjardi, G. T., and Dawson, A. R. (2012). “Buried Pipes in Rubber-Soil Backfilled Trenches under Cyclic Loading.” *Journal of Geotechnical and Geoenvironmental Engineering*, 138(11), 1346–1356.
- Takou, M., Abolmaali, A., and Park, Y. (2017). “Field deflection-measurement techniques and finite-element simulation for large-diameter steel pipes with controlled low-strength material.” *Journal of Pipeline Systems Engineering and Practice*, 8(4), 1–15.
- Tavakoli Mehrjardi, G., Moghaddas Tafreshi, S. N., and Dawson, A. R. (2012). “Combined use of geocell reinforcement and rubber-soil mixtures to improve performance of buried pipes.” *Geotextiles and Geomembranes*, Elsevier Ltd, 34, 116–130.
- Tetreault, J., Hoult, N. A., and Moore, I. D. (2018). “Pre- and post-rehabilitation behaviour of a deteriorated horizontal ellipse culvert.” *Canadian Geotechnical Journal*, 55(3), 329–342.
- Thepot, O. (2000). “A new design method for non-circular sewer linings.” *Tunnelling and Underground Space Technology*, Elsevier, 15, 25–41.
- Tognon, A. R., Rowe, R. K., and Brachman, R. W. I. (1999). “Evaluation of side wall friction for a buried pipe testing facility.” *Geotextiles and Geomembranes*, Elsevier, 17(4), 193–212.
- Trautmann, B. C. H., Asce, A. M., Rourfce, T. D. O., Asce, M., and Kulhawy, F. H. (1986). “UPLIFT FORCE-DISPLACEMENT RESPONSE OF BURIED PIPE.” *ASCE Journal of Geotechnical Engineering*, I(9), 1061–1076.
- TxDOT. (2014). “Test Procedure for FIELD METHOD FOR DETERMINING IN-PLACE DENSITY OF SOILS AND BASE MATERIALS PART I — NUCLEAR GAUGE METHOD.” 1–15.
- Wagener, B., and E. Leageid, E. (2014). “Culvert Repair Best Practices , Speci cations and Special Provisions – Best Practices Guidelines.” (January).
- Walker, D., and Guan, S. (1997). “Protective linings for steel pipe in potable water service.” *NACE Northern Area International Conference Corrosion Prevention*, 10–11.
- Wang, F., Han, J., Khatri, D. K., Parsons, R. L., Brennan, J. J., and Guo, J. (2016). “Field installation effect on steel-reinforced high-density polyethylene pipes.” *Journal of Pipeline Systems Engineering and Practice*, 7(1), 1–7.

- Water Infrastructure Network. (2001). *Water Infrastructure Now: Recommendations for clean and safe water in the 21st century*. Water Infrastructure Network (WIN), Washington, DC.
- Watkins, R. K., and Anderson, L. R. (1999). *Structural mechanics of buried pipes*. CRC press.
- Whidden, W. R. (2009). *Buried flexible steel pipe: Design and structural analysis*. American Society of Civil Engineers.
- Wyant, D. C. (2002). *Assessment and rehabilitation of existing culverts*. Transportation Research Board.
- Yeau, K. Y., Sezen, H., and Fox, P. J. (2009). “Load Performance of In Situ Corrugated Steel Highway Culverts.” *Journal of Performance of Constructed Facilities*, 23(1), 32–39.
- Young, W. C., and Budynas, R. G. (1989). *Roark ’s Formulas for Stress and Strain*. McGraw Hill.
- Zanotti, C., Banthia, N., and Plizzari, G. (2014). “A study of some factors affecting bond in cementitious fiber reinforced repairs.” *Cement and Concrete Research*, Elsevier, 63, 117–126.

BIOGRAPHY

Amin Darabnough Tehrani is currently a post-doctoral fellow in civil engineering department of the University of Texas at Arlington. He serves as a researcher at the CUIRE research center in UTA. Amin received his Master of Science in civil engineering with structural emphasis in 2016. His expertise lies in pipe structural analysis, numerical simulation, pipe installation and rehabilitation using trenchless technology. Amin is a member of four American Water Works Association (AWWA) standard and educational committees, where the committees develop standards and guidelines to educate engineers with the available trenchless technology techniques to rehabilitate the deteriorated water pipelines. Amin Has published several peer reviewed international journal articles as well as related highly attended conferences such as ASCE Pipelines, NASTT's No-Dig show etc. He has mainly been involved in multiple national- and state-level research projects. Amin received multiple scholastic recognition awards including NASSCO Scholarship in 2019 and 2020, NCT-TAWWA Scholarship in 2019, ASCE UESI Student Scholarship 2020, NASTT SC Chapter Scholarship 2018 and 2019, etc. Amin is also one the recipients of the International Society for Trenchless Technology (ISTT) Academic Award of the year 2019 for his excellent performance in structural evaluation of the trenchless technique “spray applied pipe linings (SAPLs)” for deteriorated gravity pipes, presented in this dissertation.

